

Exploring Substitutional and Vibronic Effects in Organic Donor–Acceptor Chromophores using Quantum Chemistry

Inaugural-Dissertation

zur Erlangung des Doktorgrades
der Mathematisch-Naturwissenschaftlichen Fakultät
der Heinrich-Heine-Universität Düsseldorf

vorgelegt von

Jeremy Markus Kaminski
aus Neuss

Düsseldorf, Februar 2025

aus dem Institut für Theoretische Chemie und Computerchemie
der Heinrich-Heine-Universität Düsseldorf

Gedruckt mit der Genehmigung der
Mathematisch-Naturwissenschaftlichen Fakultät der
Heinrich-Heine-Universität Düsseldorf

Berichterstattende:

1. Univ.-Prof. Dr. Christel M. Marian
2. PD Dr. Oliver Weingart

Tag der mündlichen Prüfung: 05. Juni 2025

Eidesstattliche Erklärung

Ich versichere an Eides statt, dass die Dissertation von mir selbständig und ohne unzulässige fremde Hilfe unter Beachtung der „Grundsätze zur Sicherung guter wissenschaftlicher Praxis an der Heinrich-Heine-Universität Düsseldorf“ erstellt worden ist. Darüber hinaus versichere ich, dass diese Dissertation in dieser oder vergleichbarer Form keiner anderen Prüfungsbehörde vorgelegt und, abgesehen von den aufgeführten Teilpublikationen, auch noch nicht veröffentlicht wurde.

Düsseldorf, den 11. Februar 2025

(Jeremy Markus Kaminski)

Danksagung

Eine Promotion wird nicht im Alleingang gemeistert. Es ist ein Gemeinschaftsprojekt und ich danke allen, die den Weg mit mir gegangen sind und ihren Anteil dazu beigetragen haben.

Zuerst möchte ich mich bei meiner Doktormutter Prof. Dr. Christel Marian bedanken, für die schöne Zeit im Arbeitskreis, die vielen Gespräche privater und beruflicher Natur, und die gemeinsame Beforschung eines spannenden Themengebiets. Es hat mich sehr gefreut, dass ich während meiner Masterarbeit fast schon selbstverständlich "gefragt" wurde, ob ich denn weitermachen würde. Das hat eine schöne Promotionszeit eingeläutet.

Dr. Oliver Weingart danke ich sehr für das Zweitgutachten. Auch wenn sein Arbeitsort mittlerweile nicht mehr im Arbeitskreis ist, steht er immer noch bei allen Anliegen und Problemstellungen bereit.

Wie schon zu Beginn der Masterarbeit wurde auch der Beginn der Promotionszeit aus bekannten Gründen im Homeoffice bestritten. Ich erinnere mich gerne an die langen Videocalls und gemeinsamen digitalen Kaffeepausen mit Dennis Dombrowski und Fabian Meitza zurück.

Im Büroalltag konnte ich mich bis zum letzten Arbeitstag an einem tollen Team erfreuen. Danke, Simon Metz und Hannah Jeuken, ihr seid meine ständigen Begleiter im Studium gewesen und wir hatten immer eine schöne Zeit in unserem gemeinsamen Büro. Ich danke Simon Metz und Tobias Böhmer nicht nur für das Korrekturlesen dieser Dissertation, sondern auch für jeglichen kreativen Input, wenn es bei mir mal an Kreativität gefehlt hat. Auch bin ich dankbar für die Zeit, die ihr euch für alle Problemstellungen und Gespräche genommen habt. Danke, Markus Putscher, für den lustigen Ausflug zum Workshop nach Polen und die zahlreichen Spiele- und Laufevents. Jasper Guhl danke ich vor allem für die stets gute Versorgung mit Kaffee.

Spannende und abenteuerreiche Ausflüge bleiben unvergessen: die STC in Heidelberg, die ICEL in London im Stadion des FC Chelsea, mit einem extravaganteren Conference Dinner im Natural History Museum, und die MMQC in Mariapfarr, wo intensiver Austausch auch auf der Skipiste stattgefunden hat. Die Arbeitsatmosphäre war super und es hat unglaublich viel Spaß gemacht. Meinetwegen hätte es noch lange so weitergehen können. Ich bin davon überzeugt, dass diese Arbeitskreis-Zusammensetzung die beste aller Zeiten war, und ich freue mich, ein Teil davon gewesen zu sein.

Mein Dank gilt auch dem festen Inventar des Arbeitskreises: Martin Kleinschmidt für seine mittlerweile zertifizierte Fähigkeit, Probleme zu lösen, und Gudrun Brauwers für die vielen Gespräche über die Jahre.

Ich danke den Mitgliedern des Graduiertenkollegs ModISC, insbesondere der ersten Kohorte und Martina Holz, für unvergessliche Retreats in Radevormwald und Bergisch Gladbach, aber auch allen anderen Doktorierenden und Professoren für das gute Miteinander. Die Zeit im Graduiertenkolleg hat die Promotion bereichert. Ein besonderer Dank gilt meinen Kollaborationspartnerinnen und -partnern für die erfolgreiche Zusammenarbeit: Elisabeth Pankert, Julia Wiefermann, Wiebke Haselbach, Dragana Schmeinck, Bárbara Elza Nogueira de Faria und Tobias Böhmer.

Ich möchte mich bei Prof. Dr. Shirin Faraji und ihrer neuen Gruppe bedanken, die uns Doktorierende aus der alten Arbeitsgruppe sehr freundlich aufgenommen und in der letzten Phase unserer Arbeit ausgehalten haben.

Der letzte große Dank gilt meiner Familie und meinen Freunden für die wichtige Unterstützung abseits des Uni-Alltags. Insbesondere danke ich meinen Eltern, ohne die ich bis hierhin nicht gekommen wäre, und meiner Freundin Lena Halbrügge, die mir eine sehr große Stütze in der Schreibphase war und mein Leben bereichert hat.

Der Deutschen Forschungsgemeinschaft (DFG) möchte ich für die finanzielle Unterstützung dieser Promotion im Graduiertenkolleg ModISC (GRK 2482 / Projektnummer 396890929) danken.

Kurzzusammenfassung

Die Effizienz thermisch aktivierter verzögerter Fluoreszenz (TADF) wird durch den Charakter und das Zusammenspiel angeregter Zustände bestimmt. Dies erfordert Emitter-Designs, die eine Kommunikation zwischen diesen Zuständen ermöglichen. Eine zentrale Herausforderung ist dabei das Ausbalancieren von Eigenschaften, wie der Singulett-Triplett-Energieaufspaltung, der Spin-Bahn-Kopplung (SOC) und dem Überlapp von Elektronendichte zwischen Donor und Akzeptor. Dadurch können effizientes reverses Intersystem Crossing (rISC) und hohe Photolumineszenz-Quantenausbeuten sichergestellt werden. Diese im Graduiertenkolleg ModISC durchgeführte Arbeit gibt einen Einblick in die Mechanismen bekannter blau-emittierender TADF-Emitter und zeigt, wie deren Eigenschaften moduliert und optimiert werden können.

Die photophysikalischen Eigenschaften von Through-Bond-Charge-Transfer-(TBCT)-Emitttern werden maßgeblich durch die Donor-Akzeptor-Torsion beeinflusst. Relaxierte Scans entlang der Potentialhyperflächen des Grund- und angeregten Zustands zeigen, dass durch Donor-Akzeptor-Torsionsmoden ein dynamischer Relaxationsmechanismus hervorgerufen wird. So wird für nahezu senkrechte Konformationen schnelles (r)ISC beobachtet, während für planare Konformationen die Fluoreszenz dominiert.

Im Gegensatz zu TBCT-Emitttern induzieren bei Through-Space-Charge-Transfer-(TSCT)-Emitttern niederfrequente Normalmoden starke Kopplungen zwischen den angeregten Zuständen durch eine Veränderung des Donor-Akzeptor-Abstands, sowie deren Orientierung zueinander. Darüber hinaus wurde die Notwendigkeit der Berücksichtigung von spinvibronischen Effekten hervorgehoben und durch die Berechnung von (nicht-)radiativen Ratenkonstanten in Herzberg-Teller-Näherung gestützt. Dazu wurden numerische Gradienten der SOC- und Übergangsdipolmoment-Matrixelemente entlang aller Normalmoden bestimmt. Typischerweise sind die einflussreichsten Normalmoden, die die spinvibronische Kopplung steuern, in der Akzeptorebene lokalisierte Schwingungen.

Sowohl für TBCT- als auch TSCT-Systeme sind, jenseits der üblicherweise betrachteten Singulett- und Triplett-CT-Zustände, lokal angeregte Zustände auf dem Akzeptor verantwortlich zur Überwindung des ansonsten El-Sayed-verbotenen Triplett-zu-Singulett-Prozesses, um die experimentell beobachteten TADF-Eigenschaften erklären zu können. Ferner wurden chemische Modifikationen untersucht, um den TADF-Prozess gezielt zu optimieren. Dazu zählen die Variation von Substituenten in *ortho*- oder *para*-Position, Donor-Akzeptor-Regioisomere, die Stärke und Rigidität von Donor und Akzeptor, die Donor-Akzeptor-Orientierung durch gezielte Substitution sowie die Verlängerung des π -Systems. Dabei hängen die Ergebnisse stark von der Umgebung ab. Insbesondere das häufig verwendete Lösungsmittel Toluol stellte eine quantenchemische Herausforderung dar, da es bei expliziter Berücksichtigung ohne direkte Beteiligung an den molekularen Übergängen einen erheblichen elektrostatischen Einfluss ausübt.

Abstract

Thermally activated delayed fluorescence (TADF) efficiency is governed by the nature and interplay of multiple excited states, requiring emitter designs that facilitate effective communication between them. A key challenge in TADF emitter design is balancing important properties such as the singlet–triplet energy gap, spin–orbit coupling (SOC), and sufficient electron density overlap between donor and acceptor to ensure efficient reverse intersystem crossing (rISC) and high photoluminescence quantum yields. This work, conducted within the framework of the ModISC research training group, aims to provide quantum chemical insights into existing TADF emitters, modulate their efficiency, and contribute to the development of new blue-light TADF emitters.

In through-bond charge-transfer (TBCT) emitters, donor–acceptor torsions critically influence the photophysical properties. Relaxed scans along ground- and excited-state potential energy surfaces confirm that torsional dynamics affect the excited-state decay mechanisms. Rotation along the donor–acceptor linkage results in fast (reverse) ISC processes for conformations near perpendicularity, whereas fluorescence is predominantly observed for more planar conformations.

In through-space charge-transfer (TSCT) emitters, different key degrees of freedom are introduced compared to TBCT emitters, *i.e.*, donor–acceptor distance and their tilt angle. Low-frequency vibrations that alter these degrees of freedom are crucial for inducing significant couplings between the excited states. Furthermore, the necessity of accounting for spin-vibronic effects was emphasized and supported by the calculation of (non-)radiative rate constants within a Herzberg–Teller-like framework, employing numerical gradients of SOC and transition dipole moment matrix elements along all vibrational normal modes. Most influential normal modes driving the spin-vibronic coupling are typically in-plane vibrations localized on the acceptor moiety.

For both TBCT and TSCT systems it was demonstrated that, beyond the commonly considered lowest-energy singlet and triplet CT states, acceptor-localized triplet states provide a pathway to overcome the otherwise El-Sayed forbidden triplet–to–singlet upconversion process to explain the experimentally observed TADF characteristics.

Chemical modifications were explored to modulate and fine-tune the TADF performance. These include the variation of substituents in *ortho*- or *para*-position, donor–acceptor regioisomers, donor and acceptor strength and rigidity, donor–acceptor orientation through targeted substitution and π -system elongation.

Moreover, results strongly depend on the environment. In particular, the commonly used solvent toluene poses a challenge, as it exerts a significant electrostatic influence in explicit considerations without directly participating in the molecular transitions.

List of Publications

- [I] **J. M. Kaminski**, A. Rodríguez-Serrano, F. Dinkelbach, H. Miranda-Salinas, A. P. Monkman, & C. M. Marian. Vibronic effects accelerate the intersystem crossing processes of the through-space charge transfer states in the triptycene bridged acridine–triazine donor–acceptor molecule TpAT-tFFO. *Chem. Sci.*, 13(23):7057–7066, 2022.

Contribution: Quantum chemical investigation of ground and excited states belonging to conformer (Me→Ph) and computation of all (spin-)vibronic interactions including the calculation of (non-)radiative rate constants within the FC and FC+HT approximation, preparation of Figures 3-6 and 8-11, contributions to writing and revising the manuscript.

- [II] W. Haselbach, **J. M. Kaminski**, L. N. Kloeters, T. J. J. Müller, O. Weingart, C. M. Marian, P. Gilch & B. E. Nogueira de Faria. A Thermally Activated Delayed Fluorescence Emitter Investigated by Time-Resolved Near-Infrared Spectroscopy. *Chem. Eur. J.*, 29(2):e202202809, 2023.

Contribution: All quantum chemical investigations presented in this work, writing of results in section about quantum chemical computations, revising the manuscript.

- [III] J. Wiefermann, **J. M. Kaminski**, E. Pankert, D. Hertel, K. Meerholz, C. M. Marian & T. J. J. Müller. Highly Luminescent Blue Emitter with Balanced Hybridized Locally and Charge-Transfer Excited-States Emission. *ChemPhotoChem*, 7(3):e202200265, 2023.

Contribution: All quantum chemical investigations presented in this work, writing and visualization of results in section about quantum chemical calculations, revising the manuscript.

- [IV] H. Miranda-Salinas, A. Rodríguez-Serrano, **J. M. Kaminski**, F. Dinkelbach, N. Hiromichi, Y. Kusakabe, H. Kaji, C. M. Marian & A. P. Monkman. Conformational, Host, and Vibrational Effects Giving Rise to Dynamic TADF Behavior in the Through-Space Charge Transfer, Triptycene Bridged Acridine-Triazine Donor Acceptor TADF Molecule TpAT-tFFO. *J. Phys. Chem. C*, 127(18):8607–8617, 2023.

Contribution: Quantum chemical investigation of ground and excited states belonging to conformer (Me→Ph) and computation of all (spin-)vibronic interactions including the calculation of (non-)radiative rate constants within the FC and FC+HT approximation, preparation of Figure 1, contributions to writing the quantum chemical sections and revising the manuscript.

- [V] **J. M. Kaminski**, T. Böhmer & C. M. Marian. Balancing TADF Properties in π -Bridged Donor–Acceptor Systems by Sterical Constraints: The Best of Three Worlds. *J. Phys. Chem. C*, 128(33):13711–13721, 2024.

Contribution: Quantum chemical investigation of compounds **1-H**, **2-Me** and **3-ⁱPr** and computation of all relaxed scans, (hybrid) solvent model approaches and spin-vibronic interactions, preparation of Figures 3, 4 and 6, writing the first draft and revising the manuscript.

- [VI] **J. M. Kaminski**, T. V. Chu & C. M. Marian. How Donor–Bridge–Acceptor Orientation and Chemical Modification Affect the TADF Abilities of Boron-Based Emitters. *ChemPhotoChem*, e202500033, 2025.

Contribution: All quantum chemical investigations of **DPACoOB**, **DMACoOB**, **DPAoOB** and **DPACoSB**, preparation of all figures, writing the first draft and revising the manuscript.

Manuscripts in Preparation

- [I] D. Sretenović, L. N. Kloeters, **J. M. Kaminski**, T. Böhmer, P. Schmeinck, S. Felekyan, O. Opanasyuk, G. A. Sommer, M. Chalani, G. J. Reiß, C. Janiak, C. M. Marian, R. Kühnemuth, T. J. J. Müller & C. A. M. Seidel. The effect of conformational constraints and oxygen quenching on TADF in donor–acceptor systems. Manuscript in preparation for *Chemical Science*.

Contribution: Quantum chemical investigation of compounds **1-H**, **2-Me** and **3-ⁱPr** and computation of all relaxed scans, contributions to writing of results regarding the quantum chemical calculations.

Contents

1	Introduction	1
1.1	Organic Light Emitting Diodes	4
1.2	Emitter Generations	5
2	Theoretical Methods	11
2.1	Density Functional Theory	11
2.2	Time-Dependent Density Functional Theory	13
2.3	Toward Range-Separated Hybrid Density Functionals	15
2.3.1	Density Functional Approximation	15
2.3.2	Global Hybrid Functionals	16
2.3.3	LR-Corrected and RSH Density Functionals	16
2.4	DFT/MRCI	19
2.5	Dispersion Correction	22
2.6	Solvent and Environment	23
2.6.1	Polarizable Continuum Models	24
2.6.2	Non-Equilibrium PCM	26
2.6.3	Hybrid Models Combining Implicit and Explicit Solvation . .	27
2.7	Rate Constants and Vibronic Spectra	29
2.7.1	Radiative Processes	30
2.7.2	Non-Radiative Processes	31
2.7.3	Calculation of TDM and SOC Gradients	34
2.7.4	Time-Dependent Approaches	35
3	Through-Bond Charge-Transfer Emitters	37
3.1	Donor–Acceptor Orientation in TAA-TPN	38
3.1.1	Methodological Details	40
3.1.2	Excited-State Absorption	42
3.1.3	Conformers and Absorption	45
3.1.4	Excited-State Decay Mechanism	46
3.1.5	Solvent Effects	49

Contents

3.2	Chemical Modification of Molecular Units in TAA-TPN	51
3.2.1	Donor Strength	51
3.2.2	π -System Length and Acceptor Strength	54
3.2.3	Pyridine Acceptors	58
4	Through-Space Charge-Transfer Emitters	65
4.1	Highly Efficient TADF Mechanism in TpAT-tFFO	66
4.1.1	Conformational Analysis	67
4.1.2	Vibronic Effects on (Non-)Radiative Rate Constants	69
4.2	TADF Emitters using Triarylboron Acceptors	73
4.2.1	Conformational Analysis on Absorption and Emission Process	74
4.2.2	Vibronic Effects on (Non-)Radiative Rate Constants	77
4.2.3	Chemical Modification of the Molecular Units in ortho- and para-appended systems	79
5	Conclusion and Future Perspectives	81
	Bibliography	85
	Abbreviations	113
A	Technical Details	I
B	Additional Material	III
B.1	Through-Bond Charge-Transfer Emitters	III
B.2	Through-Space Charge-Transfer Emitters	XII
C	Publications and Manuscripts in Preparation	XIII

1 Introduction

The use of **Organic Light Emitting Diodes (OLEDs)** marks a major trend in the field of display technologies. OLEDs attract attention due to their ability to achieve high efficiency while being thin and lightweight and offering excellent color quality, wide viewing angles, ultrafast response rates, and true black colors in display applications [1]. Unlike **Liquid Crystal Displays (LCDs)**, OLED displays can independently control the emission of each pixel (red, green, blue), generating light without the need for backlighting. This enables the realization of large screens with high resolutions as well as flexible screen designs.

Currently, the Asia-Pacific region represents the largest market for OLED panels, with key players including **SAMSUNG DISPLAY CO., LTD.**, **LG DISPLAY CO., LTD.**, and **SONY CORPORATION**. While the market concentration remains relatively low, since the technology is still too expensive for the mid-range market, Europe is projected to experience the fastest-growing market for OLED panels between 2024 and 2029 [2].

The core component of an OLED is the emitting layer. Within the OLED market, only first- and second-generation emitters have been commercially used so far. In terms of energy efficiency, production costs, and environmental considerations, third- and fourth-generation emitters would be advantageous. Unfortunately, these are less stable and have a shorter lifetime in devices. Achieving stable and highly efficient blue OLEDs, in particular, remains a significant challenge. The highest-energy emission of all visible colors introduces numerous degradation mechanisms. Additionally, the precise balance of device parameters is crucial for high-performance blue OLEDs. As a starting point, photochemically stable, bright **Thermally Activated Delayed Fluorescence (TADF)**-type emitters are needed [3, 4].

Historically, research in both academia and industry has proven to be highly relevant for advancing OLED technology. Significant breakthroughs have been achieved in both sectors [5]. Nevertheless, the field of TADF-OLEDs remains far from fully explored or understood. In this context, the present work focuses on the quantum chemical characterization of existing TADF emitters to gain new insights for future studies in emitter design and quantum chemical evaluation. Additionally, novel emitter classes

that have emerged within the graduate school GRK2482 **Modulation of Intersystem Crossing (ModISC)** (since 10/2019) are also being investigated.

The ModISC program integrates expertise from organic and inorganic synthesis, photophysical and electrochemical characterization, OLED device fabrication, quantum chemical characterization, and science communication. These areas are closely interconnected within four major projects. This collaborative approach aims to develop efficient blue emitters, progressing from synthesis to characterization and integration into OLED devices. Through these efforts, various influences on the **Intersystem Crossing (ISC)** process are being examined, with the goal of beneficially modulating it to achieve desirable TADF properties.

This work has made significant contributions to the scientific discussion surrounding TADF emitters. Using the example of **Through-Bond Charge-Transfer (TBCT)** emitters, the importance of adjusting the relative orientation of donor and acceptor units has been highlighted. It was demonstrated that the TADF properties of the system can be positively influenced and fine-tuned through targeted substitution effects and specific environmental effects.

For the quantum chemical characterization, the necessity of accounting for vibronic effects in donor–acceptor conjugates was emphasized. This was supported by the calculation of radiative and non-radiative rate constants within a **Herzberg-Teller (HT)**-like scheme. Importantly, it was shown that, beyond the commonly considered lowest-energy singlet and triplet **Charge-Transfer (CT)** states, the involvement of other excited states, such as **Locally Excited (LE)** states localized on the donor or acceptor, must be included in the excited-state decay mechanism. The widely used solvent toluene poses a quantum chemical challenge, as it exerts a significant electrostatic influence in explicit considerations without directly participating in the transitions occurring on the molecule.

In the case of **Through-Space Charge-Transfer (TSCT)** emitters, a highly efficient design principle for TADF was revisited. By enabling communication through space due to the spatial proximity of donor and acceptor units, TSCT emitters represent an equally promising alternative to TBCT emitters. Within the aforementioned principles a comprehensive explanation of the complex excited-state decay mechanism for a TADF emitter with non-radiative rate constants between the singlet and triplet manifolds reaching up to 10^7 s^{-1} could be provided.

Roadmap

To introduce the topic of this thesis, the introduction (Chapter 1) begins with general information on OLEDs (Section 1.1) and emitter generations (Section 1.2). Chapter 2 on theoretical methods is tailored specifically to the application areas of the presented projects. It highlights the key aspects and considerations relevant to these studies. The chapter does not aim to provide a comprehensive theoretical overview but rather focuses on presenting the core concepts necessary for the work described in this thesis. Additional details are available in the technical details section (Chapter A).

The primary focus of this thesis is on TADF emitters. The results are categorized and presented based on the type of emitter under investigation. Two main categories are distinguished: TBCT emitters (Chapter 3) and TSCT emitters (Chapter 4). Chapter 5, Conclusion and Future Perspectives, concludes the thesis.

The appendix provides additional material related to the projects (Chapter B) and contains all publications presented within this thesis (Chapter C).

1.1 Organic Light Emitting Diodes

OLED devices consist of several organic layers stacked on top of one another, with a total thickness typically in the range of a few hundred nanometers (see Figure 1.1 and Ref. [6]). When electric current is applied, holes and electrons are injected into these layers. Ideally, the charge carriers recombine in the emitting layer, creating tightly bound Frenkel excitons (hole-electron pairs with radii of around 1 nm) by strong Coulombic interactions that subsequently excite the emitting molecules. In such a thin-film structure, light can only be emitted at angles smaller than the limiting angle for total internal reflection at the glass-air interface, which corresponds to about 20% of the light generated [6]. The remaining light is reflected at different interfaces inside the device, followed by reabsorption and thermalization, which results in a significant loss of excitation energy and reduction of the **External Quantum Efficiency (EQE)**. These reductions can be minimized through optimized OLED device design, enabling better control over processes such as hole and electron transport and their recombination (see Ref. [7] exemplary for electron transport layers). Additional optimization can be achieved by carefully selecting materials and layer thicknesses or employing external measures [8].

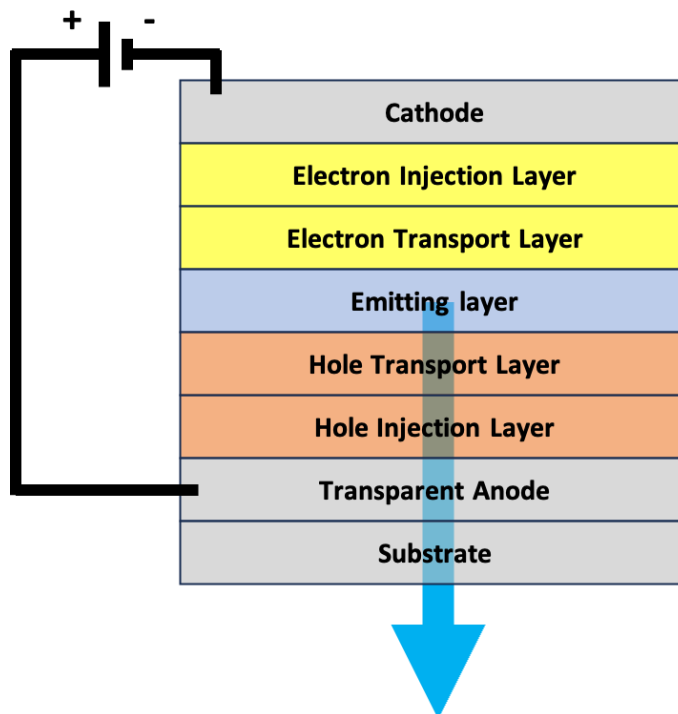


Figure 1.1: Schematic structure of a multilayer OLED device stack using the example of a through-the-bottom-emitting OLED, following Ref. [6].

Recently, research has focused on matrix or host materials, as excitons often are generated there. For the quantum chemical characterization of emitter molecules in the emitting layer, these matrix or host materials are of critical importance. They provide structural rigidity to the emitting layer and exert electrostatic effects.

1.2 Emitter Generations

While device modifications primarily influence the EQE, many scientific research groups focus on selecting suitable emitting materials to achieve the highest possible **I**nternal **Q**uantum **E**fficiency (IQE). When emitter molecules are excited via electric current, the process does not follow the selection rules for single electronic excitations by electric dipole radiation, which typically generate (almost) exclusively singlet excitons [9]. Instead, different spin combinations of an electron-hole pair result in three eigenstates with total spin equals one (triplet state) and one eigenstate with total spin equals zero (singlet state), which leads to a statistical population ratio of 25% singlet and 75% triplet excited states [10, 11] (see Figure 1.2).

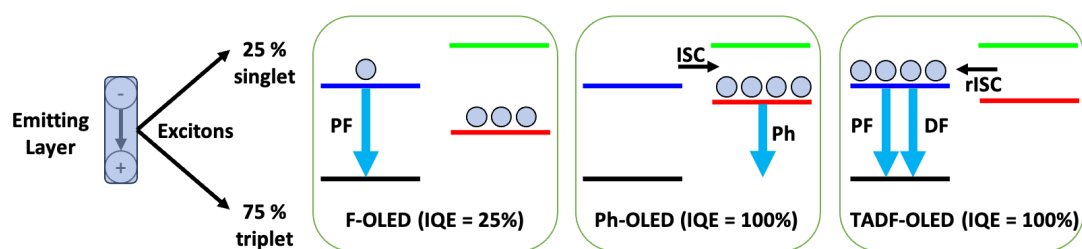


Figure 1.2: Prominent emitter generations for the use in the emitting layer of OLED devices. **F-OLED**: Fluorescent (F) emitters showing PF (maximum IQE = 25%), **Ph-OLED**: Phosphorescent (Ph) emitters showing phosphorescence (maximum IQE = 100%), **TADF-OLED**: TADF emitters showing PF and DF (maximum IQE = 100%). Fourth generation emitters combine a TADF dopant and a fluorescent emitter (hyperfluorescence) or a phosphorescent dopant and a fluorescent emitter (hyperphosphorescence), interacting via excitation energy transfer (maximum IQE = 100%).

First Generation: F-OLEDs

Most organic emitter molecules are fluorescent emitters, representing the first generation of luminescent materials used in OLED devices. Initially, in the 1960s, electroluminescence was observed in single crystals of anthracene and admixtures of tetracene [12]. A significant breakthrough made in 1987 when TANG and VAN SLYKE introduced the first

efficient low-voltage OLED device [13]. For a comprehensive overview of historical milestones in both academia and industry, see the review by HONG ET AL. [5].

However, the IQE of first-generation luminescent materials is limited to 25%, because triplet excitons cannot be directly harvested via fluorescence. To achieve highly efficient OLED devices, it is necessary to access the triplet excitons as well.

Second Generation: Ph-OLEDs

In the 1990s, emitters that deactivate via phosphorescence were introduced in OLEDs for the first time. With ISC from excited singlet to triplet states, followed by emission via phosphorescence, an IQE of up to 100% became achievable. The breakthrough for this second-generation luminescent materials was the utilization of metal complexes exhibiting an osmium [14], platinum [15] or iridium [16, 17] core. The best-performing OLEDs with red and green emitters can achieve an EQE of approximately 30%.

However, for blue emitters, first-generation materials offer several advantages compared to the second-generation ones, including longer operational lifetimes in OLEDs, higher color purity, and greater flexibility in molecular design strategies [18]. Additionally, the use of expensive, scarce, and toxic transition metals in phosphorescent emitters presents challenges for recycling and limits their large-scale industrial application.

Third Generation: TADF-OLEDs

In 2012, a significant breakthrough was achieved with the official establishment of third-generation luminescent materials [19]. Emitters deactivate via the mechanism of TADF. This phenomenon has been known for many years, *e.g.*, observed in the early 1960s for eosin [20], but lost attention due to weak efficiencies. In recent years, the development of various design principles has brought TADF into the spotlight as a highly interesting research topic, offering new possibilities for efficient luminescent materials [21]. Especially, there is great interest in developing highly efficient blue emitters, which remains a challenging task [1, 3].

TADF refers to thermally activated delayed fluorescence and describes two characteristics. First, a **D**elayed **F**luorescence (DF) signal can be observed alongside the **P**rompt **F**luorescence (PF) from an electronically excited singlet state. This delay arises from a process called **r**everse **I**ntersystem **C**rossing (rISC), which enables the transfer of triplet excitons back into the singlet manifold, followed by a second fluorescence signal to be measured at a later time, typically with the same characteristics as the PF. Consequently, TADF allows OLED devices to surpass the efficiency limit, *i.e.*, the EQE, typically expected for fluorescent materials.

Second, for rISC to occur, the energy barrier for the back-transfer of excited-state population must be surmountable through thermal activation. This is determined by the energy difference ΔE_{ST} between the singlet and triplet states involved, which is ideally, as a rule of thumb, in the lower 100 meV range. This energy difference is directly related to the electron exchange energy J , calculated from the electron density overlap of the dominant orbitals involved, see Eq. 1.1.

$$\Delta E_{ST} = E_S - E_T = 2J \quad (1.1)$$

Additionally, moderate **Spin–Orbit Coupling (SOC)** is required to couple the triplet and singlet manifolds, allowing the rISC process to occur. And, finally, fluorescence should be sufficiently strong to observe TADF. This is determined by the oscillator strength of the corresponding transition. These criteria are all desirable for the TADF process to be fast. Unfortunately, some of these factors may be in conflict with each other, necessitating the search for the best possible compromise.

TADF Mechanism: Modification Options

The TADF mechanism can be quite complex and is influenced by a variety of modification options.

- (a) **LE Triplet States:** Transitions between singlet and triplet CT excited states described by the same orbitals are expected to be slow according to the El-Sayed rules. However, experiments and quantum chemical calculations reveal that excited states typically exhibit a mixture of different state characters, such as CT and LE for donor–acceptor compounds, which is of great importance for elucidating the TADF mechanism. The inclusion of excited states beyond the lowest CT states is considered in the vibrationally coupled spin-orbit coupling mechanism. It describes a deactivation pathway in which a triplet LE state (${}^3\text{LE} / T_{\text{LE}}$) mediates the otherwise forbidden ${}^3\text{CT} / T_{\text{CT}} \rightsquigarrow {}^1\text{CT} / S_{\text{CT}}$ transition via rISC [22–24]. The ${}^3\text{LE} / T_{\text{LE}}$ state, which is typically energetically close to the ${}^1\text{CT} / S_{\text{CT}}$ and ${}^3\text{CT} / T_{\text{CT}}$ states, can be reached through small molecular vibrations, thus facilitating the transition (see Section 4.1). Additionally, the consideration of higher electronically excited states can be important as well. These indirectly contribute to spin-vibronic interactions or actively participate in the decay pathway. The corresponding rISC transitions $T_{n \geq 2} \rightsquigarrow S_{m \geq 1}$, commonly referred to as hot exciton or HIGHrISC [25] processes, are followed by **Internal Conversion (IC)** to the lowest excited singlet state and subsequent emission in the form of fluorescence. Alongside **Triplet–Triplet Annihilation (TTA)** and classical

TADF, the hot exciton mechanism is a generally accepted theoretical framework explaining how fluorescent materials can surpass the limitation of spin statistics for first-generation OLEDs (see Section 3.2).

- (b) **Emitter Design:** Structural modifications of the emitter molecule give rise to various CT states differing in their properties and excited-state characteristics. In the literature, a distinction is made, among other classifications, between TBCT and TSCT emitters, based on the relative orientation of donor and acceptor units. In both cases, excitation involves transfer of electron density from the donor to the acceptor (see Chapter 3 – 4). For another class of compounds, referred to as **Hybridized Local and Charge-Transfer (HLCT)** emitters, structural modifications determine the mixing of CT and LE character within the excited state (see Section 3.2). In such emitters, the S_1 state typically exhibits both CT and LE contributions, with hole and particle reflecting this hybrid nature. In particular, when the energy difference between S_1 and T_1 states is insurmountably large, a higher triplet state $T_{n \geq 2}$ can strongly couple to the hybrid S_1 state. A notable benefit of HLCT emitters is the significantly enhanced fluorescence rate constant, attributed to the higher amount of local excitation compared to classical CT emitters [26]. Furthermore, by employing donors and acceptors with moderate strengths, it becomes feasible to achieve pure-blue and deep-blue emission. Importantly, this mechanism prevents the formation of long-lived T_1 excitons, thereby reducing efficiency roll-off in the respective devices. Additional insights into this concept are provided by MA AND CO-WORKERS in Ref. [27].
- (c) **Environmental and Substitutional Effects:** Environmental and substitutional effects significantly influence excited-state properties and subsequent decay mechanisms, as demonstrated in a combined experimental and theoretical study for flavine derivatives by BRACKER ET AL. [28, 29]. Similarly, the behavior of an emitter molecule in an OLED can be influenced by the matrix material in which it is embedded, potentially differing from its behavior when dissolved in solution [30, 31] (see Section 3.1).

For other modification strategies, see for example Refs. [32, 33]. The conceptual development, synthesis, and characterization of various TADF emitter molecules have yielded numerous design principles that not only significantly improve third-generation luminescent materials but are also expected to be relevant in advancing fourth-generation OLED emitters [34].

Fourth Generation: HF-OLEDs

Hyperfluorescent and hyperphosphorescent systems, first introduced in 2014 by NAKANOTANI ET AL. [18], represent an innovative combination of two established emitter generations. In these systems, a TADF or phosphorescent molecule acts as an assistant dopant to a fluorescent emitter. For the hyperfluorescence mechanism to take place, an overlap between the fluorescence spectrum of the TADF molecule and the absorption spectrum of the emitter is essential. This enables singlet-to-singlet **F**örster **R**esonance **E**nergy **T**ransfer (FRET). In addition, other transitions, such as direct triplet-to-singlet FRET, are also conceivable and have been discussed in the literature, such as in the work by DE SOUSA ET AL. [35]. These transitions rely on additional conditions, shared with hyperphosphorescent systems, such as non-negligible SOC between triplet and singlet states and an overlap between the phosphorescence spectrum (of the donor) and the absorption spectrum (of the acceptor). However, in all cases, short-range triplet-to-triplet Dexter energy transfer should be avoided, as the triplet excitons can not be used for emission in the fluorescent emitter.

The combination of two emitter generations offers significant advantages: the potential for achieving 100% IQE from the TADF or phosphorescent dopant, coupled with the fast and narrowband emission of the fluorescent emitter. This synergistic effect leads to enhanced electroluminescence intensity, higher color purity, and improved overall device efficiency [36].

Other Mechanisms

- (a) **TTA emitters:** As mentioned earlier, TTA can explain how the IQE of first-generation OLEDs can exceed 25%. This mechanism recovers part of the otherwise lost triplet excitons for light emission by allowing two molecules in an excited triplet state to interact, producing one molecule in an excited singlet state and another in the ground state. This process is only feasible if the energy of the S_1 state is less than or equal to twice the energy of the triplet state. Consequently, a theoretical IQE of up to 62.5% can be achieved [37]. The most representative TTA materials are anthracene derivatives. For specific examples, see Ref. [27].
- (b) **IST emitters:** Analogous to the TADF mechanism, DF can also be observed in **I**nverted **S**inglet-**T**riplet gap (IST) emitters. The key distinction lies in the inverted singlet-triplet gap, which means that the excited S_1 state is lower in energy than the T_1 state. This phenomenon was first attributed to energetically low-lying doubly excited singlet configurations, which can interact with the singlet state but not with the triplet state [38]. Such behavior has been observed in heptazine and

similar systems [39]. Although the concept of expecting improved exciton back-transfer with an inverted singlet–triplet gap seems promising, quantum chemical calculations urge caution. Using higher-level quantum chemical methods, the inverted energy gaps often diminish and may even acquire a positive sign [38]. Furthermore, another study indicates that a large inverted singlet–triplet gap is not necessarily beneficial for the TADF process [40]. However, achieving chemical accuracy in quantitative predictions for such large systems remains challenging.

- (c) **MR emitters:** Contrary to the **Long-Range** (LR)-CT observed in classical *para*-appended donor–acceptor conjugates, **Multi-Resonance** (MR) emitters, as pioneered by HATAKEYAMA AND CO-WORKERS [41], such as DABNA and its derivatives, exhibit **Short-Range** (SR)-CT states. In these systems, the electron densities are localized on neighboring atoms within heteroacenes. The rigid molecular structures of these emitters enable small Stokes shifts and narrowband emissions (Ref. [21], Chapter 11).

2 Theoretical Methods

2.1 Density Functional Theory

To describe a system of N interacting non-relativistic electrons, it is necessary to solve the static Schrödinger equation

$$\hat{H}\Psi_j(x_1, \dots, x_N) = E_j\Psi_j(x_1, \dots, x_N) \quad (2.1)$$

within the **Born-Oppenheimer** (BO) approximation and with $x_j \equiv (r_j, \sigma_j)$ including space and spin coordinates. Wavefunction-based methods, *e.g.*, coupled cluster methods or **Configuration Interaction** (CI) expansions, aim to obtain the solution by describing the wave function as exactly as possible. However, for large numbers of electrons calculating the full wave function is computationally not feasible. Fortunately, the complete wave function often contains more information than is necessary for predicting most properties of interest. This has motivated the development of methods based on approximations. Among these, **Density Functional Theory** (DFT) has become a widely used and highly popular approach. It offers a computationally efficient alternative, enabling the treatment of larger molecular systems while still providing reliable results for many electronic properties [42]. Based on the Thomas-Fermi theory [43, 44], HOHENBERG and KOHN established the theoretical foundation of DFT with their seminal work on the inhomogeneous electron gas [45]. They demonstrated that all properties of a stationary system in its electronic ground state can be determined solely from the one-electron density. It is a physical observable that can be intuitively interpreted and visualized. Compared to wavefunction-based methods, the density formulation offers a significant advantage: it depends only on three spatial coordinates, regardless of the number of electrons in the system. This reduction in complexity greatly enhances the feasibility of applying DFT to large many-electron systems. Proven by *reductio ad absurdum*, HOHENBERG and KOHN demonstrated a one-to-one correspondence between the external potential, typically the Coulomb potential of the nuclei in most applications, and the ground-state electron density. If the electron density is known exactly, the true total energy of the system can be determined. The theorems by HOHENBERG and KOHN

2 Theoretical Methods

also apply to inhomogeneous density distributions, thereby enabling their application to a wide range of systems, including atoms and molecules [45].

In search of the unknown energy functional that would yield the exact solution, KOHN and SHAM introduced the most influential approximation in 1965 [46]. The system consisting of N interacting electrons is described by a fictitious Kohn-Sham (KS)-system consisting of N non-interacting electrons (electron-electron interaction $V_{ee} = 0$).

$$E[n(r)] = T_s[n(r)] + V_{ne}[n(r)] + J[n(r)] + E_{xc}[n(r)] \quad (2.2)$$

The total energy is defined by the kinetic energy $T_s[n(r)]$ of the fictitious KS-system, the potential energy $V_{ne}[n(r)]$ between nuclei and electrons and the Coulomb self-interaction $J[n(r)]$ of the electron density. The so-called exchange-correlation functional $E_{xc}[n(r)]$ contains all terms that cannot be determined exactly, namely the true kinetic energy $T[n(r)]$ of the interacting system minus that of the fictitious KS-system and the exchange interaction $K[n(r)]$ between electrons [47].

$$E_{xc}[n(r)] = T[n(r)] - T_s[n(r)] - K[n(r)] \quad (2.3)$$

Solutions for the exchange-correlation functional $E_{xc}[n(r)]$ are diverse and play a central role in KS-DFT. A comprehensive overview, along with detailed explanations, is provided in Section 2.3.

In KS-DFT, the many-body ground-state wave function is approximated by a single Slater determinant, where the single-particle orbitals $\phi_i(r)$ are solutions of the KS-equations. The ground-state electron density $n(r)$ is then constructed from the N lowest-energy single-particle KS-orbitals, in accordance with the conventional Aufbau principle [48, 49].

$$\epsilon_i \phi_i(r) = \left[-\frac{\nabla^2}{2} + v_{KS}(r) \right] \phi_i(r) \quad (2.4)$$

$$n(r) = \sum_i^{occ} |\phi_i|^2 \quad (2.5)$$

Since the KS-potential $v_{KS}(r)$ itself depends on the derivative of the exchange-correlation functional E_{XC} with respect to the electron density $n(r)$, the N one-electron equations can only be solved self-consistently [48, 49].

$$v_{KS}(r) = \frac{\partial E_{XC}}{\partial n(r)} \quad (2.6)$$

The idea to have a simple yet exact theoretical framework capable of determining numerous properties of a system remains a fundamental challenge in theoretical chemistry. In the context of DFT, only approximate solutions are achievable due to the requirement for an accurate exchange-correlation energy functional. While increasingly precise approximations are continually being developed, there is no systematic way to achieve arbitrarily high accuracy using sufficient computational resources [50].

The challenge is aptly summarized by MAITRA ET AL., who formulated it as follows: "The acrobatics of the functionals involved that allow noninteracting electrons to reproduce the exact density of an interacting system remain an intriguing, important, and fun research area" [51].

In recent years, the application of machine learning to electronic structure theory has gained significant attention. This raises the question of whether machine learning can propose or enhance density functional approximations, potentially leading to substantial improvements in the accuracy and efficiency of DFT [52]. Given the rapid advancements in this field, significant progress can be expected in the coming years.

2.2 Time-Dependent Density Functional Theory

In order to investigate time-dependent processes, such as the excitation of an emitter molecule, the previously introduced KS-DFT framework is not sufficient, as it is limited to describing the stationary ground state. At the time, no theorem existed that connected the electron density of an excited state to its corresponding properties. This limitation was eventually overcome with the development of **Time-Dependent Density Functional Theory (TDDFT)**, which provided the necessary extension to address dynamic phenomena.

Analogous to the Hohenberg-Kohn-theorems, RUNGE and GROSS have proven a one-to-one correspondence between the time-dependent external potential and the time-dependent electron density for many-body systems evolving from a fixed initial state [53], based on the Runge-Gross action integral functional. This result implies that knowledge of the electron density determines the external potential that generated it and, consequently, the dynamics of the system.

The challenge of calculating the time-dependent electron density, however, initially remains an open question. Similar to static KS-DFT, the interacting system can be replaced by a fictitious non-interacting system. In this approach, the KS-electrons obey the time-dependent Schrödinger equation. If the KS-potential is known, the corresponding KS-orbitals can be computed, ultimately yielding the time-dependent electron density.

$$i\frac{\partial}{\partial t}\phi_i(r, t) = \left[-\frac{\nabla^2}{2} + v_{KS}(r, t) \right] \phi_i(r, t) \quad (2.7)$$

$$n(r, t) = \sum_i^{occ} |\phi_i(r, t)|^2 \quad (2.8)$$

Comparable to static KS-DFT, the KS-potential is divided into the external potential, the known one-electron terms for the KS-system, and the exchange-correlation potential. The latter contains all many-body effects that cannot be determined exactly. In static KS-DFT the exchange-correlation potential is derived from the exchange-correlation energy, which is linked to the total energy calculated from the variationally solved KS-equations. However, in time-dependent systems, there is no analogous variational principle for minimizing the total energy, as demonstrated by HOHENBERG and KOHN [45]. Instead, the action integral functional \tilde{A}_{XC} has been introduced to solve these expressions (for further details, see Ref. [54]).

$$v_{XC}(r, t) = \left. \frac{\partial \tilde{A}_{XC}}{\partial n(r, \tau)} \right|_{n(r, t)} \quad (2.9)$$

Excited-state energies and other properties of interest can be determined via the linear response of a ground-state solution to time-dependent electric fields. To achieve this, additional approximations are introduced: (i) Assuming that the external potential is weak, it can be expressed using perturbation theory. Consequently, the time-dependent electron density can be expanded in a Taylor series with respect to the perturbation. In the so-called linear response-KS-TDDFT, only the first-order terms of this expansion are considered. (ii) The time-dependent exchange-correlation potential is replaced by the time-independent one using the instantaneous electron density. This so-called adiabatic approximation assumes that the system remains instantaneously in equilibrium at all times. As a result, the description of excited states is limited to single excitations. (iii) Finally, the Tamm-Dancoff approximation provides a robust framework for calculating useful excited-state potential energy surfaces and mitigates triplet state instabilities [55–57].

Ultimately, several challenges arise in linear response-TDDFT regarding the accurate description of Rydberg and CT excited states. These issues stem from the approximate nature of the exchange-correlation functional [58, 59] and the necessity of explicitly including two- and higher-electron excitations when using standard density functionals [51].

Progress has been made through the development of more suitable functionals (see Section 2.3). For CT excited states, improvements include the incorporation of

greater spatial non-locality in the exchange-correlation functional, whereas for double excitations, strong frequency dependencies in the exchange-correlation kernel have proven crucial [51].

2.3 Toward Range-Separated Hybrid Density Functionals

DFT is, by construction, an exact theory. However, the greatest challenge remains in finding an accurate description of the exchange-correlation energy functional. Unfortunately, the one-electron density is not known at all places at the same time, leaving the exact functional to be unknown. To address this, suitable approximations have to be found, which remains an active area of research. Up to date, a wide variety of density functionals have been developed (for a detailed overview, see Ref. [60]) and can be categorized into different classes based on their underlying approximations.

2.3.1 Density Functional Approximation

The first class of functionals is based on the computation of exchange and correlation via **Local Density Approximation (LDA)**, **Local Spin Density Approximation (LSDA)** or **Generalized Gradient Approximation (GGA)**, the latter also including gradients of the electron density. Prominent examples are the PBE [61] and B97-D [62] functionals. An extension, known as meta-GGA, goes beyond by incorporating second derivatives of the electron density as well as KS-orbital kinetic-energy densities.

$$E_{xc} = E_x^{DFA} + E_c^{DFA} \quad (2.10)$$

Density Functional Approximation (DFA) functionals face significant challenges, including poor descriptions of LR interactions and the so-called self-interaction error. The latter arises from the incomplete cancellation of the Hartree-like Coulomb interaction for one-electron densities, leading to inaccuracies. Consequently, the exchange-correlation potential exhibits an exponential decay rather than the correct $1/r_{12}$ behavior, where r_{12} represents the distance between two electrons. Moreover, common density functionals struggle to accurately describe systems with non-integer numbers of electrons [63, 64]. This issue is particularly pronounced in cases where a single electron is delocalized over spatially separated fragments, which is relevant for CT or transition states in chemical reactions.

2.3.2 Global Hybrid Functionals

A significant breakthrough in the 1990s was the development of hybrid density functionals, which have been used very frequently. These functionals combine DFT with a fraction of exact exchange, which is defined in KS-DFT using the same formalism as in **H**artree-**F**ock (HF) theory. The resulting **G**lobal **H**ybrid (GHs) systematically improve spurious issues stemming from the locality problem, such as the one-electron self-interaction error and its extensions to many-electron systems. Prominent examples include PBE0 [65] (25% exact + 75% DFA exchange), BH-LYP [66, 67], and B3LYP [67–70] functionals.

$$E_{xc}^{GH} = aE_x^{HF} + (1 - a)E_x^{DFA} + E_c^{DFA} \quad (2.11)$$

While GHs successfully model a large number of ground-state and excited-state properties, they still suffer from a density overdelocalization in the LR regime, resulting in an incorrect $-a/r_{12}$ behavior instead of the correct $-1/r_{12}$ decay. This leads to an underestimation of energetic properties, such as **I**onization **P**otentials (IPs) and intra- or intermolecular CT excitations, and to the dissociation of open-shell complexes. To address these issues, numerous alternatives to GHs have been developed. These approaches aim to circumvent the locality problem, correct self-interaction and orbital dependence errors, and effectively bridge density-based and wavefunction-based methods.

2.3.3 LR-Corrected and RSH Density Functionals

Significant performance improvements were achieved with the introduction of range-separated exchange schemes, a concept pioneered in the early 2000s especially by SAVIN (for a detailed overview, see Refs. [71–73]). These schemes provide a physically sound solution by enforcing the correct $-1/r_{12}$ asymptotic behavior of the exchange potential by decomposing the Coulomb operator into a SR (first summand in Eq. 2.12) and a LR (second summand in Eq. 2.12) term [74].

$$\frac{1}{r_{12}} = \frac{1 - [\alpha + \beta \cdot \text{erf}(\omega r_{12})]}{r_{12}} + \frac{\alpha + \beta \cdot \text{erf}(\omega r_{12})}{r_{12}} \quad (2.12)$$

The error function erf and its complement $1 - \text{erf}$ smoothly connect the SR and LR components of the Coulomb operator through a range-separation parameter ω . It is equivalent to the inverse of a distance and determines how fast the range-separation switches from the SR to the LR regime. In addition, the parameter α defines a global r_{12} -independent exact-exchange contribution. Assuming that $\beta = 1 - \alpha$ ensures self-interaction errors to be asymptotically canceled by the exact exchange [63].

$$E_{xc}^{RSH} = aE_x^{SR-HF} + (1-a)E_x^{SR-DFA} + bE_x^{LR-HF} + (1-b)E_x^{LR-DFA} + E_c^{DFA} \quad (2.13)$$

This approach effectively combines the advantages of both HF and semilocal DFT. In the SR regime, semilocal DFT provides dynamical correlation and error cancellation between exchange and correlation. Contrary, in the LR regime, exchange is dominated by HF and is poorly described by semilocal DFT [51]. By construction, the exchange-correlation functional exhibits the correct LR behavior. As a result, the description of LR phenomena, *i.e.*, long chain polarizabilities, CT and Rydberg excitations, non-linear optical properties and dissociation of two-center three-electron bonds, has been significantly improved. However, the LR correction can in some cases reduce the accuracy of results. This issue can be addressed by decreasing the fraction of HF exchange in the LR regime, although it introduces an incorrect behavior in the exchange-correlation potential [75]. An improvement is offered in so-called double-hybrid functionals, which incorporate unoccupied orbitals into the construction of correlation functionals, thereby describing exchange and correlation in a hybrid format [76]. Nevertheless, the results are highly sensitive to the choice of the range-separation parameter ω .

The range-separation parameter ω should be optimized to ensure reasonable and meaningful results for all types of states, *e.g.*, describing CT and LE transitions on the same level. Several optimal tuning procedures have been proposed in the literature [77–79].

- (a) **Empirical parametrization:** Minimizing errors for general or specific properties of interest [80], resulting in ω -values typically ranging between 0.2 and 0.5 bohr⁻¹.
- (b) **Non-empirical, but system-dependent parametrization:** Optimal tuning procedure based on the fulfillment of Koopman’s theorem within the KS-framework, enforcing the agreement of the negative **H**ighest **O**ccupied **M**olecular **O**rbital (HOMO) energy $-\epsilon_H$ and the IP. Both values are combined in Eq. 2.14.

$$J(\omega) = \left(|\epsilon_H^\omega(N) + IP^\omega(N)| \right)^2 + \left(|\epsilon_H^\omega(N+1) + IP^\omega(N+1)| \right)^2 \quad (2.14)$$

The goal is to minimize the target function $J(\omega)$, which corresponds to achieving the best agreement between $-\epsilon_H$ and IP. Although this method is computationally expensive, it delivers very good results and is recommended in the literature due

to its success in ground-state and excited-state applications. Additionally, it can potentially be implemented in a self-consistent fashion.

- (c) **Non-empirical parametrization:** Procedure imposing an additional physical constraint when deriving the density functional, *e.g.*, by enforcing the exact treatment of the total ground-state energy of the hydrogen atom [73].

Since many theoretical studies require the quantum chemical treatment of solvent effects (see Section 2.6), the question arises whether **Polarizable Continuum Model (PCM)** and **Optimally Tuned (OT)-Range-Separated Hybrid (RSH)** functionals can be combined. There is an ongoing debate about whether the PCM should be included directly into the optimal tuning procedure or if the solvent effects should be considered afterwards. In general, these are two independently developed methods: the optimal tuning of RSH functionals, which was developed for accurate descriptions of electronic structure and optical properties in the gas phase, and the PCM, which provides a well-approximated treatment of solvent effects with minimal additional computational cost [81].

In TDDFT, orbital-relaxation effects are not well described. The use of an optimal tuning procedure directly scales the asymptotic Coulomb interaction, which is similar to the effect of dielectric screening [82]. However, considering PCM in the tuning procedure leads to several problems: (i) The range-separation parameter ω tends to zero [83], which causes excitation energies to be underestimated as the LR correction becomes negligible. This issue is believed to stem from the use of equilibrium PCM. A suitable description of IPs requires the consideration of different time scales on which nuclear and electronic degrees of the solvent respond to the change of the solute, namely a non-equilibrium solvation [84] (see Section 2.6). (ii) The inclusion of PCM causes the tuning to become unbalanced. Total energies, and thus the IPs, are more strongly affected by the solvent than the DFT eigenvalues. (iii) The use of explicit solvation urges caution, if orbitals are no longer localized on the chromophore, but expand to the solvent molecules. Otherwise, it results in reasonable range-separation parameters and molecular properties.

Since the results with explicit solvation and in the gas phase are typically very similar, and the investigated properties of the molecule are better reproduced when PCM is not directly included in the tuning procedure, it is recommended to perform the tuning in the gas phase first and to include environmental effects afterwards [81, 83]. Given the importance of LR interactions and processes, and the goal of achieving a well-balanced description of CT and LE states, this approach is considered useful for the projects in this work. However, it should be noted that for solvents that can strongly interact with the chromophore and its orbitals, *e.g.*, by the formation of hydrogen bonds and π - π -interactions, the results can deviate markedly from reality.

2.4 DFT/MRCI

DFT and TDDFT perform well in optimizing the ground and excited states of emitter molecules, and can also be used to analyze certain photophysical properties. Nonetheless, their accuracy is highly dependent on the choice of the density functional. In 1999, GRIMME and WALETZKE developed a method combining two existing theories, DFT and **M**ulti-**R**eference **C**onfiguration **I**nteraction (MRCI), to improve the description of excited-state properties [85]. This approach has since become a well-established semi-empirical quantum chemical method for efficiently calculating excited-state properties of organic molecules.

In its original formulation, the DFT/MRCI demonstrates great efficiency in the evaluation of singlet and triplet excited states, which mainly originate from local one-electron transitions. The approach aims to incorporate dynamical correlation effects, where electrons are close to each other, via the single-reference DFT method, while treating non-dynamical or static correlation, where electrons are far apart, via the multi-reference CI method. The MRCI wave function is constructed using KS-orbitals and a closed- or single open-shell anchor configuration. It is expanded in a basis of spin (ω) and space (w) symmetry-adapted **C**onfiguration **S**tate **F**unctions (CSFs), which are built from linear combinations of Slater determinants as basis functions. For interactions between two CSFs, four distinct cases can be identified (Eqs. 2.15, 2.17, 2.18 and 2.19). Since the CI matrix is typically diagonal-dominant, the first class of matrix elements (Eq. 2.15) represents the most important interactions. The computation of CI matrix elements is implemented using formulas derived from SEGAL and WETMORE [86, 87]. The resulting eigenvalue problem is solved using an iterative multi-root Davidson procedure. Further developments led to redesigned Hamiltonians, namely R2016 [88], R2017, R2018 [89] and R2022 [90], while the first and last Hamiltonians have been used in this work.

(a) **Same spin- and spatial occupations (diagonal matrix element):**

$$\begin{aligned}
 \langle \omega w | \hat{H}^{DFT/CI} | \omega w \rangle = & E^{KS} + \sum_i F_{ii}^{KS} \Delta w_i + \frac{1}{2} \sum_{i \neq j} V_{ijij} \Delta w_i \Delta w_j \\
 & + \frac{1}{2} \sum_{i \neq j} V_{ijji} \left(-\frac{1}{2} \Delta w_i \Delta w_j + \frac{1}{2} w_i w_j - w_i + \eta_{ij}^{ji} \right) \\
 & + \frac{1}{2} \sum_i V_{iiii} \left(\frac{1}{2} \Delta w_i \Delta w_i + \frac{1}{2} w_i w_i - w_i \right) \\
 & + \Delta E_{DFT/MRCI}
 \end{aligned} \quad (2.15)$$

with total KS energy E^{KS} , KS canonical orbital energies F_{ii}^{KS} , two-electron integrals V_{ijij} , occupation number w_i of the i -th orbital in configuration w , occupation difference Δw_i of the i -th orbital with respect to the anchor configuration, one/two-electron spin-coupling coefficients η_i^j/η_{ij}^{ji} and DFT/MRCI correction terms $\Delta E_{\text{DFT/MRCI}}$ depending on the used Hamiltonian, respectively. In the original formulation a scaling factor $p_J = 1 - x_{HF}$ was introduced for the Coulomb part, with x_{HF} representing the exact exchange of the used density functional (here, BH-LYP with $x_{HF} = 0.5$). Additionally, another scaling factor ${}^m p[N_o]$ was introduced for the exchange part, which depends on the state multiplicity m (singlet/triplet) and the number of open shells N_o .

$$\Delta E_{\text{DFT/MRCI}}^{\text{original}} = \frac{1}{n_{exc}} \sum_{i \in c} \sum_{j \in a}^{n_{exc}} \left(p_J V_{ijij} - {}^m p[N_o] V_{ijji} \right) \quad (2.16)$$

with excitation class n_{exc} and creation (c) and annihilation (a) of electrons. The exchange scaling is generalized in the R2016 Hamiltonian, making it spin-invariant for all state multiplicities. For the latest R2022 Hamiltonian, the Coulomb and exchange corrections are divided into two cases: one for double excitations originating from the same orbital p^{he} and another for those coming from different orbitals p^{hee} [90].

(b) Different spin- and same spatial occupations (off-diagonal matrix element):

$$\langle \omega w | \hat{H}^{DFT/CI} | \omega' w' \rangle = \langle \omega w | \hat{H}^{CI} | \omega' w' \rangle \quad (2.17)$$

These matrix elements are calculated exactly in the original approach or being scaled by $(1 - p_X)$ in the redesigned Hamiltonians [88, 90].

(c) One-electron occupation difference in spatial part (off-diagonal matrix element):

$$\begin{aligned} \langle \omega w | \hat{H}^{CI} | \omega' w' \rangle &= F_{ij}^{HF} \eta_i^j + \sum_{k \neq i, j} V_{ikjk} \Delta w'_k \eta_i^j \\ &+ \sum_{k \neq i, j} V_{ikkj} \left(\frac{1}{2} \Delta w'_k \eta_i^j + w'_k \eta_i^j - \eta_i^j + \eta_{ik}^{kj} \right) \\ &+ V_{iii} \left(\frac{1}{2} \Delta w'_i + \frac{1}{2} w'_i \right) \eta_i^j - V_{ijjj} \left(\frac{1}{2} \Delta w'_j + \frac{1}{2} w'_j - 1 \right) \eta_i^j \end{aligned} \quad (2.18)$$

(d) **Two-electron occupation difference in spatial part (off-diagonal matrix element):**

$$\langle \omega_W | \hat{H}^{CI} | \omega''_W \rangle = \left(V_{ikjl} \eta_{ik}^{jl} + V_{iklj} \eta_{ik}^{lj} \right) \left[\left(1 + \delta_{ik} \right) \left(1 + \delta_{jl} \right) \right]^{-1} \quad (2.19)$$

All off-diagonal matrix elements, which include electron occupation differences in the spatial part, experience energy-dependent scaling to avoid double counting of electron correlation arising from the mixed DFT and MRCI approach. This damping function depends on the energy difference $\Delta E_{\omega\omega'}$ between two CSFs and ensures the incorporation of non-dynamical electron correlation when they are in energetic proximity (original: Eq. 2.20, R2016: Eq. 2.21, R2022: Eq. 2.20 with $p_1 = 1 - 2p_J^{hee} + p_X^{hee}$).

$$\langle \omega_W | \hat{H}^{DFT/CI} | \omega'_W \rangle = \langle \omega_W | \hat{H}^{CI} | \omega'_W \rangle p_1 e^{-p_2 \Delta E_{\omega\omega'}^4} \quad (2.20)$$

$$\langle \omega_W | \hat{H}^{DFT/CI} | \omega'_W \rangle = \langle \omega_W | \hat{H}^{CI} | \omega'_W \rangle \frac{p_1}{1 + (p_2 \Delta E_{\omega\omega'})^5 \arctan(p_2 \Delta E_{\omega\omega'})^5} \quad (2.21)$$

with $\Delta E_{\omega\omega'} \approx \sum_{i \in c} F_{ii}^{KS} - \sum_{i \in a} F_{ii}^{KS}$.

Several approximations are made to enhance computational efficiency. For dynamical correlation, which is calculated using DFT at low computational cost, a large number of CSFs is not required. Therefore, a selection procedure is employed that considers the most important configurations based on an energy gap criterion and an energy cutoff E_{sel} (original: 1.1 Hartree, redesigned versions: standard 1.0 Hartree, tight 0.8 Hartree). Afterwards, CSFs with a certain weight (original: > 0.007 , redesigned: > 0.003) in the intermediately generated wave function serve as the reference space for a second or third run, typically sufficient to reach convergence. Two-electron integrals are calculated using the resolution of the identity approximation, and auxiliary basis functions allow for two-electron integrals to be precalculated and stored. For further technical aspects, see Ref. [89].

With its extensions and developments, the DFT/MRCI approach has become a powerful tool to characterize the excited-state properties of larger emitter molecules, especially relevant for organic donor–acceptor compounds and transition metal complexes, as well as metal organic frameworks and biomolecules. The DFT/MRCI provides reasonable excited-state energies and properties based on the BH-LYP density functional, instead of calculating results dependent on the choice of the best performing functional for a specific problem. However, the optimized geometries used as input for the DFT/MRCI

method still depend on the chosen density functional. Ultimately, a balanced description of various singly or doubly excited states, including LE, CT and mixed transitions, is achieved, enabling highly accurate results in the range of chemical accuracy.

2.5 Dispersion Correction

Dispersion interactions are present in every system and describe the attractive interaction between two atoms or molecules at large distances. The name of dispersion forces is derived from the similarity between the quantum mechanical treatment of these interactions and the mathematical description of optical dispersion. Dispersion interactions can be understood as the interaction between two mutually induced dipoles, which arise from the construction of the wave function via several CSFs, showing that dispersion is a purely electron correlation effect. For a detailed example on the He dimer, see the work by Truhlar [91]. Dispersion is typically described using a multipole series, starting with terms of the form R_{ij}^{-6-n} with $n = 0, 1, 2, \dots$, which are proportional to the interaction between two interacting dipoles. Depending on the interatomic distance R_{ij} , a distinction must be made between dispersion and damped dispersion, occurring at LR distances and at **van der Waals** (vdW) distances, respectively.

In DFT, LR correlation is sometimes poorly described or entirely omitted, depending on the chosen approximation for the exchange-correlation functional. Various possibilities have been developed, with Grimme's empirical dispersion correction [92–94] being the most prominent. In the DFT-DX series with $X = 1, 2, 3$ and 4 , expressions typically in the form of LR dispersion terms multiplied by a damping factor are added as a subsequent correction if the description of accurate intermolecular forces is not provided solely by DFT (Eqs. 2.22 and 2.23). These corrections not only account for dispersion and damped dispersion but also include other electrostatic interactions that are treated at lower level.

$$E_{DFT-D} = E_{KS-DFT} + E_{disp} \quad (2.22)$$

with

$$E_{disp} = - \sum_{i=1}^{N_{at}-1} \sum_{j=i+1}^{N_{at}} \frac{C_6^{ij}}{R_{ij}^6} f_{damp}(R_{ij}) \quad (2.23)$$

and

$$f_{damp}(R_{ij}) = \frac{1}{1 + a(R_{ij}/R_r)^{-12}} \quad (2.24)$$

The equations presented above were proposed by CHAI and HEAD-GORDON based on the original DFT-D1 and DFT-D2 formulations developed by GRIMME. In earlier

versions, the dispersion correction includes a global scaling factor s_6 , typically set to one. In addition to the empirical atomic pairwise dispersion coefficient C_6^{ij} , a damping coefficient $f_{damp}(R_{ij})$ (see Eq. 2.24) ensures the dispersion correction diminishing to zero below vdW-radii, *i.e.*, for distances of typical bond lengths, which is defined by the sum of vdW-radii of the respective atom pair R_r [92]. The traditional zero-damping method works well for standard density functionals, but introduces a repulsive force at short interatomic distances. This repulsion arises from enforcing the dispersion energy to zero, which may falsify the results compared to calculations without dispersion correction. To address this issue, the finite-damping method proposed by BECKE and JOHNSON provides a constant contribution of the dispersion energy to the total correlation energy from each bonded atom pair [94, 95].

In the latest versions, the exponent in the denominator has been adjusted to ensure that the dispersion correction contributes less than 1% for typical covalent bond distances [93]. Additionally, extensions were developed accounting for three-body non-additive dispersion effects, which correct the overestimation of π - π -interactions. However, the consideration of intermolecular dispersion effects is relatively straightforward, whereas intramolecular dispersion corrections are less trivial and necessitate careful application and evaluation.

2.6 Solvent and Environment

The consideration of environmental effects is crucial for accurately characterizing an emitter, which, in the experiment is typically embedded in either a solution or a matrix material. This is particularly true for the widely studied class of CT transitions, where the treatment of environmental effects is inevitable. In the CT process, charge separation of hole and electron on donor and acceptor, respectively, can be significantly influenced by factors such as a highly polar environment. Consequently, it is essential to either accurately account for environmental effects during quantum chemical calculations or to estimate their impact in a reliable and meaningful way.

Various solvent models have been developed and are further improved, differing particularly in the computational demands and the accuracy with which they describe environmental effects. The following sections present and discuss a selection of the most relevant models. These are applied in quantum chemistry to describe phenomena such as the aggregation of molecules, crystal effects, and the layering of emitter molecules within the emitting layer of an OLED.

2.6.1 Polarizable Continuum Models

From a computational perspective, the most economical and straightforward approach is to describe the solvent as a dielectric medium, where the emitter molecule, referred to as solute, is embedded within a cavity. However, this approach neglects the atomistic character of the solvent and excludes all explicit chemical interactions between the solvent and the solute [81]. The central challenge lies in accurately describing solute-solvent interactions, which can be categorized based on their physical origin into electrostatic, cavitation, dispersion and repulsive forces. These effects are included perturbationally through a reaction potential, which acts on the solute studied *ab initio* in the gas phase and contains nuclear repulsion contributions.

In the following, the cavity modulation is defined to characterize the solute-solvent interaction side. A well-defined cavity should (i) have a physical meaning, (ii) reproduce the molecular shape, (iii) exclude the solvent, and (iv) contain the largest possible portion of the solute charge distribution within its boundaries. Although some overlap with the charge distribution of the medium is unavoidable, it is assumed to be negligible [96]. Using vdW spheres to represent both solute and solvent, two surfaces are commonly employed: the **Solvent Accessible Surface (SAS)** and the **Solvent Excluded Surface (SES)**. The SAS defines a surface which the center of the solvent molecules cannot enter, whereas the SES represents a surface that is inaccessible to the entire solvent vdW sphere (see Figure 2.1).

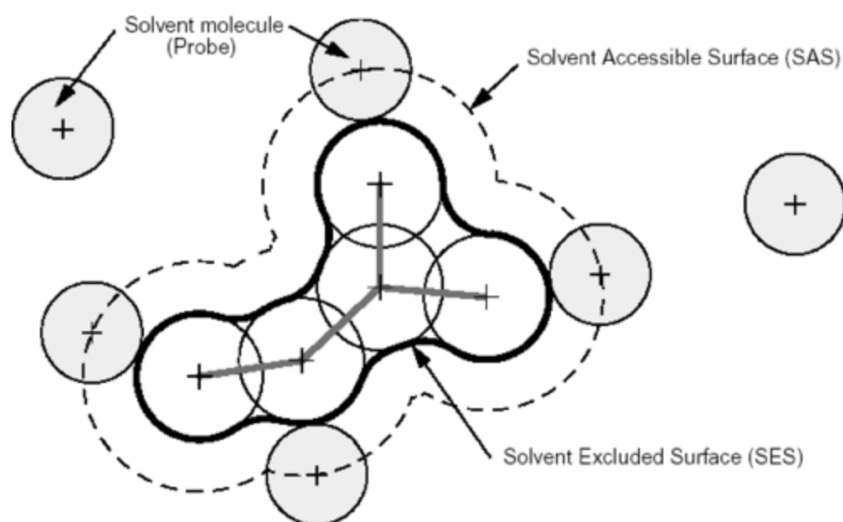


Figure 2.1: Several cavity models to describe the embedding of the solute in the solvent during quantum chemical calculations, as outlined in Ref. [96].

The calculation of vdW and SAS using a set of spheres centered on single atoms or groups with given radii is straightforward. Contrary, calculating the SES is more

complex. To address this, an algorithm was developed that systematically evaluates whether the solvent, represented as a vdW-sphere, can pass between pairs of solute spheres based on their radii and overlap. If so, additional spheres are added to define the surface more accurately. Once the set of spheres has been determined, it is subdivided into equilateral triangles, forming a pentakis-dodecahedron. For higher accuracy, each triangle can be further divided into four smaller triangles [97]. The algorithm identifies and eliminates triangles created at the intersection volume of spheres and whose centers lie inside the overlapping volume of the spheres. The remaining triangles, referred to as tesserae, form the envelope surface [98]. The SES is considered the most precise representation of the molecular surface. The algorithm iteratively optimizes this surface using two key parameters: the overlapping factor, which determines the extent of overlap between spheres, and the minimum radius for the smallest sphere that can be generated. The electrostatic component of the solvent reaction potential can be described by a set of induced point charges q_i placed at the centers of the tesserae that form the surface of the cavity, in which the solute is embedded. The charge distribution assigned to the solute polarizes the dielectric medium, which, in turn, polarizes the solute. This mutual polarization is self-consistent and must be solved iteratively. By considering only Coulomb interactions between the solvent and the solute and assuming the dielectric response to be isotropic and linear, leads to solving the Poisson equation

$$-\nabla[\epsilon(r)\nabla V(r)] = 4\pi\rho(r) \quad (2.25)$$

where $\epsilon(r)$ is the dielectric function within the medium and $V(r)$ describes the sum of electrostatic and reaction potential V_M and V_R , generated by the charge distribution of the solute and the polarization of the dielectric medium, respectively. The latter is represented by continuous surface charges $\sigma(r)$, located on the cavity surface, from which the set of induced point charges are derived. The polarization charges can be subdivided into either created by solute nuclei or electrons, respectively. Calculating the resulting electrostatic interactions requires knowledge of the potentials exerted by the solute nuclei and electrons, the corresponding point charges, and the one-particle density matrix [99]. Under specific boundary conditions, $\epsilon(r)$ is set to one inside the cavity and to a value greater than one in the medium. In addition to the cavity and $\epsilon(r)$, both to produce $\sigma(r)$, only the charge density $\rho(r)$ of the solute has to be defined.

A wide variety of PCM versions have been developed. For a comprehensive overview, see the review article by TOMASI ET AL. [96]. In the following, the **Integral Equation Formalism (IEF)-PCM** is briefly discussed, as this is the default PCM implementation in Gaussian 16 and was the only PCM model utilized to produce the results presented in this work [100, 101].

Classical reaction field methods are almost exclusively limited to deal with linear, isotropic, homogeneous dielectrics, for which the Poisson equation (see Eq. 2.25) applies. However, the reformulated IEF-PCM is able to describe interactions with intrinsically anisotropic dielectrics with tensorial permittivity or even ionic solutions. To achieve this, the Poisson operator is replaced by a modified version, with potentials $V(r)$ being redefined using so-called Green functions $G(x, y)$, which describe a potential produced at position x by a unit point charge located at position y [100]. After reformulations, the reaction potential V_R can be represented as a single-layer potential, where the continuous surface charges are uniquely determined by solving an equation containing two integral operators, which give the method its name. Further simplifications show that the surface charges $\sigma(r)$ depend only on the potential V_M . This is important because it represents an implicit correction for the error that arises when the solute charge is located outside the cavity [102]. For further details, see Ref. [96].

In Gaussian 16, a continuous surface charge description is used to ensure continuity, smoothness and robustness of the reaction field, also providing continuous derivatives with respect to atomic positions and external perturbing fields. The solute-solvent interaction side is modeled using spherical Gaussian functions located at each tessera. Discontinuities in the surface derivatives are eliminated by effectively smoothing the regions where the spheres intersect [103].

Contrary to the more complex description of electrostatic interactions, the remaining terms are straightforward to compute. The cavitation free energy describes the work required to create the cavity in a continuous medium and is calculated via the hard sphere theory of PIEROTTI and REISS. Solute-solvent dispersion and repulsion interactions are typically computed using the classical approximation proposed by FLORIS and TOMASI. For further details, the relevant formulas are discussed in Ref. [104].

2.6.2 Non-Equilibrium PCM

The PCM enables an appropriate description of solvent effects with low computational costs. However, the procedure described earlier assumes that solute and solvent are in equilibrium, *e.g.*, after geometry optimization. For time-dependent electron or energy transfer processes and nuclear vibrations, *i.e.*, vertical excitation, the modulation of solvation effects has to reflect the dynamical nature of these phenomena. Therefore, non-equilibrium PCM divides the polarization charges into fast and slow components. This aims to represent the idea that the electron density within the solvent responds almost instantaneously to changes in the electronic state of the solute, while orientational degrees of freedom, *i.e.*, the reorganization of solvent molecules, respond much more slowly [81]. The fast component is determined by the optical dielectric constant, which

depends on the refractive index of the solvent. The total charges are associated with the static dielectric constant. The slow component can be computed from the total and fast charges [104].

In addition to the classical description of PCM, corrected schemes address non-equilibrium solvation. Initially, the solvent equilibrates with the electronic ground-state of the solute. Upon electronic excitation, the charge distribution of the solute changes rapidly, necessitating a corresponding adjustment of the solvent degrees of freedom. Due to their differing response times, a slow evolution from non-equilibrium to equilibrium solvation occurs. Significant changes of the solvent or solute can lead to strongly differing configurations for both regimes.

To simulate the coupling between the emitter molecule and continuum solvent models, a two-step process is employed: (i) Immediately after the vertical transition, the final state of the solute interacts with a solvent polarization frozen to the initial state of the solute, and (ii) the dynamic component of the solvent polarization rearranges to equilibrate with the final state charge density of the solute. In linear-response models, this rearrangement is computed from the transition density. Contrary, state-specific models, such as the corrected **Linear-Response** (cLR) approach, compute it using the difference in electron densities between the initial and final states, including a density-dependent relaxation of the solvent polarization [105]. In principle, the cLR model perturbatively estimates the state-specific polarization of the solvent using the excited-state density. This is a significant advancement because the linear-response model often fails for CT states due to their vanishing transition density. However, state-specific approaches face the challenge of calculating gradients for excited states, which is more complex compared to linear-response theory in the ground state [82]. While computationally efficient, state-specific models may inadequately describe the effects for electron density changes becoming very large due to electronic excitation, *e.g.*, for CT excited states. Alternative state-specific formulations have been developed, including the **Vertical Excitation Model** (VEM) [106], the IBSF model by IMPROTA ET AL. [107], and the cLR² approach by GUIDO ET AL. [108]. Rather different from these approaches, the combination of **Restricted Open-Shell Kohn-Sham** (ROKS) and PCM was recently proposed by the groups of GRIMME and MEWES [82, 109, 110]. This orbital-optimized DFT approach for excited states offers improved descriptions of CT excitations in dielectric environments.

2.6.3 Hybrid Models Combining Implicit and Explicit Solvation

Hybrid models combine explicit solvent molecules with an implicit dielectric medium. This strategy accounts for explicit solute-solvent interactions within the first solvation layer while approximating the influence of additional solvation layers at low computa-

tional costs. Several strategies exist to construct a meaningful explicit solvation layer, from which the most relevant are summarized below.

- (a) **Chemical Intuition:** Explicit solvent molecules can be strategically positioned around the solute based on chemical intuition. This approach is straightforward in cases where interactions are well-understood, such as the formation of hydrogen bonds. However, it becomes more challenging for systems, such as donor–acceptor compounds, where π - π -interactions may occur between a solvent molecule and the solute (see for example Ref. [111] for two benzene molecules). In addition, a significant limitation lies in identifying configurations that represent optimal solute-solvent arrangements. Since this approach only represents a small subset of configurations, it is most appropriate for test purposes or cases involving small molecules.
- (b) **The *CREST* Program:** Originally developed for conformational sampling purposes, the *CREST* program offers the opportunity to automatically generate an explicit solvent layer around the solute. This is carried out time-efficiently for all solvents of interest using the built-in **Quantum Cluster Growth (QCG)** feature [112]. The program requires the Cartesian coordinates of both the solute and the solvent. At each step of adding one solvent molecule, the interaction energy surface between the solute and the growing solvent shell is analyzed to determine the optimal complexation position for the next solvent molecule. This process continues until the solute is fully and consistently surrounded by a minimum number of solvent molecules, forming the complete solvent layer. Repulsive wall potentials are employed to ensure well-shaped solute-solvent clusters [113]. However, in the standard setup, *CREST* tends to overestimate π - π -interactions, leading to unrealistically short distances between solvent and solute or within the solute itself. Nevertheless, the generated cluster ensembles represent valuable input geometries for following higher-level calculations.
- (c) **QM/MM Approach:** The solute, calculated at **Quantum Mechanical (QM)** level of theory, is embedded in a solvent molecule box with movable and immovable layers, which are treated at **Molecular Mechanical (MM)** level. This allows to include a significantly larger number of explicit solvent molecules. There are at least two key challenges to address initially: (i) Electrons are only considered implicitly through a force field in the MM description. Accordingly, electronic rearrangements and chemical bond formations are not captured. (ii) When combining two subsystems calculated at different levels of theory, their mutual interaction must be adequately defined. In the recommended additive scheme,

the QM and MM subsystems are computed separately using methods of choice, and their interaction is then explicitly taken into account using an embedding scheme. This approach allows for the consideration of mutual polarization between the two subsystems. When the boundary is defined by a chemical bond, special care must be taken to accurately describe the communication between the two subsystems. The choice of a suitable force field is crucial, as it must account for all relevant interactions. For example, in a solvent box consisting of toluene molecules, π - π -interactions must be included. Combined QM/MM approaches are widely applicable, ranging from molecular dynamics simulations and geometry optimizations to the calculation of free energy surfaces and computational spectroscopy [114].

2.7 Rate Constants and Vibronic Spectra

The calculation of rate constants and spectra is essential for understanding the excited-state decay mechanism in potent emitter molecules for OLED devices. Therefore, various couplings, principles and assumptions have to be introduced.

The **Franck-Condon (FC)** approximation is employed to describe radiative and non-radiative processes. Since electronic transitions occur significantly faster than nuclear motion [115], absorption or emission processes are typically regarded as vertical transitions, *i.e.*, without changes to the nuclear configuration. In addition to the electronic coupling, the probability of a transition depends on the transition energy and the overlap of vibrational states in the initial and final states, referred to as FC factors. The relationship between this overlap and the **Potential Energy Surface (PES)** of the electronic states is governed by the energy gap law [116, 117]. Using the harmonic oscillator model for both PESs, and assuming the normal modes and frequencies of the two electronic states to be identical except for displacements in the origins of the normal coordinates, the energy gap law can be categorized into two scenarios: (i) In the strong coupling limit, the PESs are significantly displaced horizontally relative to each other. Close to the intersection point of the PESs, the vibrational overlap becomes substantial. Therefore, the transition probability exhibits a Gaussian-like dependence with increasing ΔE_{ST} . Nevertheless, for large values of ΔE_{ST} , the harmonic model gives entirely unrealistic results. (ii) Contrary, in the weak coupling limit, when the horizontal displacement of the PESs is small, the transition probability decreases exponentially with increasing ΔE_{ST} . This behavior is typical for excited states with similar excitation character.

The HT approach goes beyond the FC approximation by accounting for the variation of electronic coupling with respect to displacements along molecular vibrational modes [24, 117]. This approach is particularly important in cases where electronic transitions are symmetry-forbidden in the FC approximation but can be re-enabled through molecular vibrations. Additionally, these can enhance the transition probability of processes that are not strictly forbidden. To incorporate these effects, a Taylor expansion of the matrix element of interest, *i.e.*, the **Transition Dipole Moment** (TDM) μ for fluorescence or the SOC for ISC/rISC, is performed with respect to the vibrational coordinates Q_A of the equilibrium geometry Q_0 , typically truncated after the first derivative term.

2.7.1 Radiative Processes

Radiative deactivation through photon emission in principle follows Kasha's rule [118], which states that emission occurs from the lowest electronically excited singlet or triplet state, referred to as fluorescence ($S_1 \rightarrow S_0$) or phosphorescence ($T_1 \rightarrow S_0$). However, as a rule allows exceptions, anti-Kasha emission is also discussed in literature, for example by DEMCHENKO ET AL. [119]. While fluorescence occurs rapidly, with rate constants of 10^6 – 10^9 s⁻¹, phosphorescence, which involves spin inversion, is much slower and can exhibit lifetimes of up to seconds.

In particular, fluorescence is important for the TADF emitters explored in this thesis. Besides stimulated emission, which occurs due to external influences, spontaneous emission is crucial for understanding the excited-state decay mechanisms of chromophores. The corresponding Einstein coefficient quantifies fluorescence by describing the probability per unit time of an electron in the excited state decaying spontaneously to the ground state. The rate constant k_F or lifetime τ_F can be determined via the Einstein relation in the electric dipole approximation μ_{el} for the spontaneous emission process *in vacuo* and in atomic units:

$$k_{F_{a \rightarrow GS}} = \frac{1}{\tau_F} = \frac{4}{3c^3 \hbar^4} |\langle \Psi_{GS} | \hat{\mu}_{el} | \Psi_a \rangle|^2 (E_{GS} - E_a)^3 \quad (2.26)$$

with c representing the vacuum speed of light, \hbar Planck's constant divided by 2π , Ψ_a and Ψ_{GS} initial and final (ground-state) state wave functions and E_a or E_{GS} their respective energies. The calculated lifetime represents an upper limit (**Photoluminescence Quantum Yield** (PLQY) = 1). With PLQY < 1, the lifetime τ_F will be shorter [120]. Alternatively, the fluorescence lifetime or rate constant can be determined using the integral of the emission spectrum (see Eq. 2.27), employing for example our in-house program *VIBES* [121–123].

$$k_F^{FC} = \int I^{FC}(\omega) d\omega \quad (2.27)$$

The emission intensity is proportional to ΔE^3 . Straightforward for the emission maximum, weighting to achieve the correct intensity ratio for the remaining transitions in the FC spectrum is performed by multiplying by $\tilde{\nu}^3$ and dividing by $\tilde{\nu}_{max}^3$. However, this correction is not applied automatically in the *VIBES* program. To calculate the fluorescence rate constant within the HT approximation, *i.e.*, including electric dipole transition moments and their numerical derivatives, normalizing the HT emission spectrum and calculating a rate constant from it is not straightforward. Only in the uncorrected FC spectrum, the sum of all FC factors equals one. Then, the areas of the FC and HT spectra can be related to each other, in order to calculate vibronic fluorescence rate constants (see Eq. 2.28), with $S^{FC}(\omega)$ and $S^{HT}(\omega)$ representing the respective spectral densities [124].

$$k_F^{HT} = \int I^{HT}(\omega) d\omega = \frac{4}{3c^3\hbar} \frac{\int S^{HT}(\omega) \omega^3 d\omega}{\int S^{FC}(\omega) d\omega} \quad (2.28)$$

2.7.2 Non-Radiative Processes

Non-radiative deactivation occurs via IC, ISC or (internal) vibrational relaxation. IC describes a transition between states of the same multiplicity (*e.g.*, $S_n \rightarrow S_{n-1}$ or $T_n \rightarrow T_{n-1}$) mediated by the nuclear momentum operator, with typical rate constants of about 10^{12} s^{-1} . ISC describes a spin-forbidden transition between states of different multiplicity (*e.g.*, $S \rightarrow T$), enabled by SOC, with typical rate constants of up to 10^7 s^{-1} in purely organic compounds. The reverse process, referred to as rISC, is especially important for the third generation of OLEDs (see Section 1.2). In principle, the microscopic reversibility principle should apply for ISC and rISC, *i.e.*, when a system is in equilibrium, each process occurs at the same rate as its reverse. However, due to the approximations employed, such as modeling the PES around the optimized minima as harmonic potentials and treating electronic and vibrational couplings separately, the forward and reverse processes are not identical. For the common case where the triplet state is lower in energy than the singlet state, thermal activation is required to overcome the barrier. Consequently, the rISC process is temperature-dependent and occurs at a slower rate than ISC.

El-Sayed rules [117, 125, 126] qualitatively describe the rate of ISC for single excitations. In addition to the change in multiplicity, the change in the character of the excitation is speed-determining. Quantitatively, rate constants for ISC and rISC are calculated using Fermi's golden rule (see Eq. 2.29), with Ψ_a and Ψ_b representing the initial and final

2 Theoretical Methods

state wave functions. It is derived from first-order time-dependent perturbation theory and is based on the squared transition amplitude between the initial and final states, divided by time. The perturbation is assumed to be small, ensuring that the response of the system remains linear.

$$k_{NR_{a \rightarrow b}} = \frac{2\pi}{\hbar} \left| \langle \Psi_b | \hat{O} | \Psi_a \rangle \right|_{Q_0}^2 \delta(E_a - E_b) \quad (2.29)$$

The electronic coupling between two states of different multiplicity is enabled via SOC. It is a relativistic effect, which acts on both angular momentum and spin. SOC is naturally incorporated into the Dirac equation for electrons with spin $s = 1/2$ and is typically used as a perturbative correction to non-relativistic theories. This coupling causes the mixing of electronic orbital and spin degrees of freedom, leading to the fact that the electronic states are no longer pure states. Based on DFT/MRCI calculations, the **Spin–Orbit Coupling Kit** (SPOCK) computes **Spin–Orbit Coupling Matrix Elementss** (SOCMEs) by utilizing the Breit-Pauli Hamilton operator (see Eq. 2.30). It contains both one-electron and two-electron terms that describe the interaction between electron i and nucleus I (or electron j), involving the angular momentum operator ($\hat{r}_{iI} \times \hat{p}_i$), the spin operator \hat{s}_i , the atomic number Z_I , the electron mass m_e , the speed of light c and the electron-nucleus distance r_{iI} [127].

$$\hat{H}_{SO}^{BP} = \frac{1}{2m_e^2 c^2} \sum_I \sum_i \frac{Z_I}{r_{iI}^3} (\hat{r}_{iI} \times \hat{p}_i) \hat{s}_i - \frac{1}{2m_e^2 c^2} \sum_i \sum_{j \neq i} \frac{1}{r_{ij}^3} (\hat{r}_{ij} \times \hat{p}_i) (\hat{s}_i + 2\hat{s}_j) \quad (2.30)$$

To reduce computational effort, the **Spin–Orbit Mean-Field** (SOMF) approximation is employed, which simplifies the two-electron term by replacing it with a mean-field, leading to an effective one-electron spin–orbit operator [128]. Additionally, neglecting all multicenter SOC terms and replacing them with a sum of atomic mean-fields, referred to as **Atomic Mean-Field Integral** (AMFI) approximation, merely introduces errors by the one-center approximation of up to 5% for light-element compounds [127, 129].

The application of the BO approximation and the FC principle simplifies the expression in Eq. 2.29 into a product of an electronic coupling matrix element at fixed nuclear coordinates and a term for nuclear vibrational transitions (see Eq. 2.31), exemplarily for the ISC process based on the formulas provided in Refs. [24, 117].

$$k_{ISC_{a \rightarrow b}}^{FC} = \frac{2\pi}{\hbar} \sum_{\gamma} \left| \langle \psi_{T_b}^{\gamma} | \hat{H}_{SO} | \psi_{S_a} \rangle \right|_{Q_0}^2 \sum_k |\langle \nu_{bk} | \nu_{aj} \rangle|^2 \delta(E_{aj} - E_{bk}) \quad (2.31)$$

The combination of FC factors and the Delta-Dirac-function is referred to as FC weighted density of states. It describes the probability of finding initial and final vibrational states

that satisfy the energy conservation criterion. To account for temperature effects in the calculation, a temperature-dependent population of vibrational states is simulated using a Boltzmann distribution in the initial state.

$$k_{ISC_{a \rightarrow b}}^{FC,T} = \frac{2\pi}{\hbar} \sum_{\gamma} \left| \langle \psi_{T_b^{\gamma}} | \hat{H}_{SO} | \psi_{S_a} \rangle \right|_{Q_0}^2 \sum_j \frac{1}{Z} e^{-\frac{(E_{aj}-E_{a0})}{k_B T}} \sum_k |\langle \nu_{bk} | \nu_{aj} \rangle|^2 \delta(E_{aj} - E_{bk}) \quad (2.32)$$

Note that the thermal vibrational partition function $Z = \sum_j e^{-\frac{(E_{aj}-E_{a0})}{k_B T}}$ is constant and not affected by preceding summations. This term describes the probability of finding the molecule in a particular vibrational state j . For the rISC process, the rate constants must be multiplied by 1/3, as the triplet population will be equally distributed across all three sublevels, given that, in organic molecules, the zero-field splitting is almost non-existent.

Similar to the TDM, the SOC is also confined to a specific nuclear configuration, but it is not always constant and depends on vibrational motion. In addition to the direct SOC, which is driven by the electronic character of the states, vibrational SOC, which refers to the vibrational dependence of the SOCMEs on the motion along a particular nuclear degree of freedom, can be included in a HT-like approach (see Eq. 2.33).

$$k_{ISC_{a \rightarrow b}}^{FC+HT,T} = \frac{2\pi}{\hbar} \sum_{\gamma} \sum_j \frac{1}{Z} e^{-\frac{(E_{aj}-E_{a0})}{k_B T}} \left| \langle \nu_{bk} | \langle \psi_{T_b^{\gamma}} | \hat{H}_{SO} | \psi_{S_a} \rangle \right|_{Q_0}^2 + \sum_M \left| \frac{\partial \langle \psi_{T_b^{\gamma}} | \hat{H}_{SO} | \psi_{S_a} \rangle}{\partial Q_M} \right|_{Q_0} Q_M |\nu_{aj}\rangle \right|^2 \delta(E_{aj} - E_{bk}) \quad (2.33)$$

Due to the summation of the static matrix element and its gradient, squaring the mixed vibrational and electronic term leads to three different terms, resulting from the resolution via the binomial formula: (i) FC/FC term (see Eq. 2.32), (ii) mixed FC/HT term, and (iii) HT/HT-Term [24]. Thus, the total rate constant for the ISC process is: $k_{ISC} = k_{ISC}^{FC/FC} + k_{ISC}^{FC/HT} + k_{ISC}^{HT/HT}$.

In addition to the FC term (see Eq. 2.34, first row) and the HT terms (see Eq. 2.34, second row), interactions with higher excited states in close energetic proximity are significant. These contributions, referred to as spin-vibronic terms (see Eq. 2.34, third row), involve a mixture of SOC and Non-Adiabatic Coupling (NAC) within the triplet or singlet manifolds [24] and emerge exclusively at second-order perturbation theory.

$$\begin{aligned}
\hat{H}_{SO} = \sum_{\gamma} & \left(\langle \psi_{S_1} | \hat{H}_{SO} | \psi_{T_1^{\gamma}} \rangle \right. \\
& + \sum_M \frac{\partial \langle \psi_{S_1} | \hat{H}_{SO} | \psi_{T_1^{\gamma}} \rangle}{\partial Q_M} Q_M + \frac{1}{2} \sum_M \sum_N \frac{\partial^2 \langle \psi_{S_1} | \hat{H}_{SO} | \psi_{T_1^{\gamma}} \rangle}{\partial Q_M \partial Q_N} Q_M Q_N \\
& \left. + \sum_n \frac{\langle \psi_{S_1} | \hat{H}_{SO} | \psi_{T_n^{\gamma}} \rangle \langle \psi_{T_n^{\gamma}} | \hat{T}_N | \psi_{T_1^{\gamma}} \rangle}{E_{T_n} - E_{S_1}} + \sum_m \frac{\langle \psi_{S_1} | \hat{T}_N | \psi_{S_m} \rangle \langle \psi_{S_m} | \hat{H}_{SO} | \psi_{T_1^{\gamma}} \rangle}{E_{S_m} - E_{T_1}} \right) \quad (2.34)
\end{aligned}$$

Since the influence of third-party states is implicitly included through CI, and HT terms similarly increase, like the spin-vibronic terms, when other states approach in energy, a clear distinction between vibrational and spin-vibronic coupling becomes challenging [117]. Nonetheless, incorporating SOC or TDM gradients is both beneficial and essential for enhancing the accuracy of calculated rate constants, particularly in organic donor–acceptor compounds.

2.7.3 Calculation of TDM and SOC Gradients

The TDM and SOC gradients cannot be calculated analytically using the DFT/MRCI program, as the configurations are selected individually. Instead, these gradients are computed numerically via displacements along the vibrational modes obtained from frequency analyses at the (TD-)DFT level of theory. This process involves evaluating the matrix elements at the displaced geometries relative to the static element, using the *GRADIENATOR* script (see Figure 2.2).

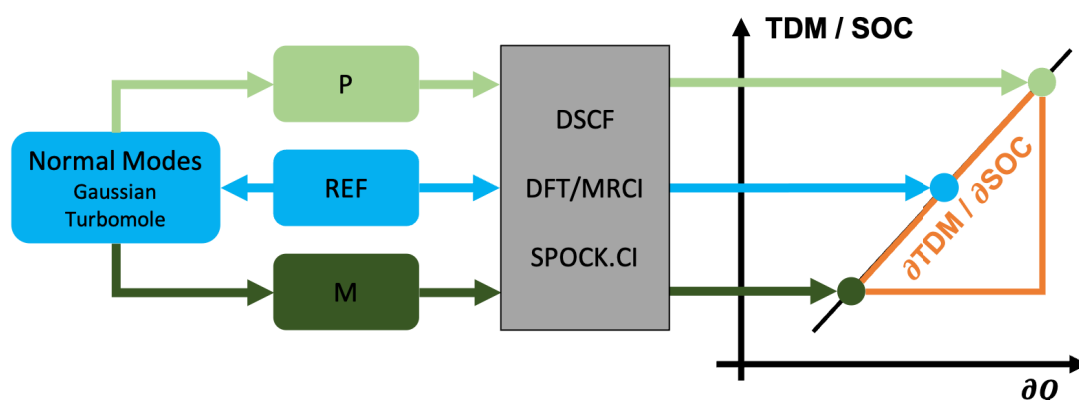


Figure 2.2: Schematic picture of the *GRADIENATOR* workflow.

Starting from the optimized relaxed structure (**REF**), the *GRADIENATOR* script generates displaced structures in the positive (**P**) and negative (**M**) directions along the com-

puted vectors of the analytically determined vibrational modes. DFT/MRCI(+SPOCK) calculations are then performed on each of these geometries.

It is crucial that the displacement magnitude remains small, as a linear approximation is employed to calculate the SOC and TDM gradients. This approximation assumes that the matrix elements around the reference point **REF** vary linearly. Thus, the change between **M** and **P** can be calculated using a two-point finite difference method.

To ensure accurate computation, the *GRADIENATOR* script was modified as part of this work to print out a warning if the matrix elements at the displaced geometries (**M/P**) do not change symmetrically around the reference point (**REF**). This guarantees that the static element lies along the straight line formed between the matrix elements in both directions. The right- and left-sided gradients must match within a certain threshold to satisfy this condition.

Finally, the calculated numerical gradients are incorporated into the rate constant calculations using the *VIBES* program.

2.7.4 Time-Dependent Approaches

In time-independent approaches, calculating all FC factors for large molecules is computationally challenging. To address this issue, time-dependent approaches often reformulate Fermi’s golden rule in the framework of the Heisenberg picture (see Eq. 2.35).

$$k_{NR_{a \rightarrow b}}^{FC,corr} = \frac{2\pi}{\hbar} \left| \langle \Psi_b | \hat{O} | \Psi_a \rangle \right|_{Q_0}^2 \int_{-\infty}^{\infty} f_{corr}(t) dt \quad (2.35)$$

Numerical integration of the correlation function in the time domain provides the FC-weighted density of states. The normal modes of the initial (Q_a) and final (Q_b) states are related via the Duschinsky transformation: $Q_a = JQ_b + K$, where J is the Duschinsky rotation matrix, and K is the displacement vector that accounts for differences between the two sets of normal modes [115]. Using Fermi’s golden rule in the framework of the Heisenberg picture also enables the calculation of vibronic spectra, requiring only the Fourier transform of the correlation function. Such spectra are typically computed employing the adiabatic Hessian model. However, an improved description can be achieved using the **V**ertical **H**essian (VH) approach, particularly for transitions involving vibrational modes such as donor—acceptor rotations and other low-frequency modes with high displacements. For further details, see Refs. [130, 131].

3 Through-Bond Charge-Transfer Emitters

The focus of this chapter is the quantum chemical investigation of potential or experimentally verified TADF emitters. Modifications to the emitter framework, possible environmental effects, and the importance of vibronic effects are discussed to interpret experimentally observed TADF properties and to investigate new molecules that may serve as TADF emitters. Special attention is given to blue TADF emitters, a class of molecules that has been extensively studied in recent years.

Within the ModISC research training group, emitters based on the well-established principle of relatively linear *para*-connected donor–acceptor molecular arrangements (see Figure 3.1) incorporating a triarylamine (TAA)-based donor moiety were taken as the starting point.

These emitters belong to the class of TBCT emitters, in which the donor and acceptor are directly connected by a single σ -bond or some linker. Electronic communication between the donor and acceptor is facilitated through π -conjugation, with strong coupling mediated by covalent bonds [132].

TAA-based compounds are well-known in the field of TADF and OLEDs. Triphenylamine is a particularly strong donor with good hole-transporting and injection abilities [133]. Additionally, it introduces thermal stability to the system and offers many possibilities for chemical modification.

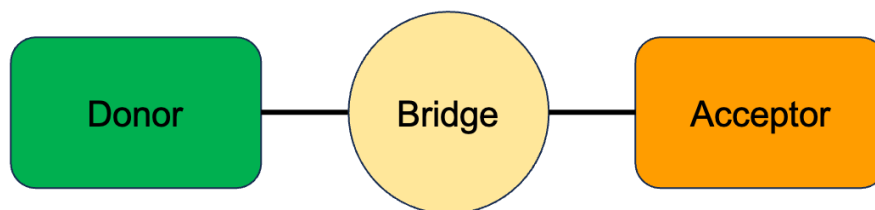


Figure 3.1: Schematic picture of *para*-appended TBCT emitters consisting of donor, bridge, and acceptor units.

To design efficient TADF emitters, luminescent materials with CT emission aim for balancing several factors: modulating the singlet–triplet energy gap ΔE_{ST} , maintaining

sufficient emission oscillator strength, and minimizing non-radiative decay from the singlet excited state [132, 134]. Interruption of the π -conjugation between donor and acceptor minimizes the mutual coupling of electron densities, which also reduces the energy gap between the singlet and triplet states belonging to the same transition. This leads to increased rISC rate constants. At the same time, donor and acceptor must remain in spatial proximity to communicate with each other. In contrast, increased radiative decay rate constants require an overlap of electron densities and the extension of π -conjugated systems [34, 135].

One of the simplest strategies to modulate these factors is to introduce conformational twisting between the directly connected donor and acceptor moieties. Other common approaches involve using connecting groups to spatially separate the donor and acceptor while ensuring some overlap of the frontier orbitals involved in the CT excitation, thereby maintaining weak electronic coupling. Examples of such approaches include single σ -bonds, twisted conjugated linkers, and three-dimensional π -conjugated spacers [136].

3.1 Donor–Acceptor Orientation in TAA-TPN

The initial series of molecules investigated in this work, referred to as **TAA-TPN**, consists of a triarylamine (**TAA**) donor and a terephthalonitrile (**TPN**) acceptor unit (see Figure 3.2). Four emitter molecules (**Em**), each with different substituents in *ortho*-position relative to the donor–acceptor linkage, were compared. These substituents were selected to influence the conformation purely through steric demand, without inducing substantial electronic effects. The emitters are numbered and ordered by the increasing steric demand of the substituents: **Em1-H**, **Em2-Me**, **Em3-*i*Pr** and **Em4-diMe**.

The aim of this study is to investigate the effect of varying the steric influence of an *ortho*-positioned substituent relative to the donor–acceptor linkage, and its impact on the experimentally observed TADF properties of molecule **Em2-Me**.

The following section provides a summary of the current state of research at the beginning of my PhD project.

Experimentally, **Em2-Me** was identified as a highly potent biaryl TADF emitter, exhibiting PLQYs of 80% in toluene and 90% in PMMA at room temperature [137]. The decay time constants for prompt and delayed fluorescence were measured as 21 ns and 30 μ s, respectively. From an Arrhenius plot analysis, the singlet–triplet energy gap was estimated to be $\Delta E_{ST} = 120$ meV. Upon excitation at $\lambda_{exc} = 378$ nm, the molecule exhibits bluish-green CT emission with a maximum at $\lambda_{max} = 492$ nm. The CT character was confirmed by a solvatochromic redshift of approximately 3400 cm^{-1} in

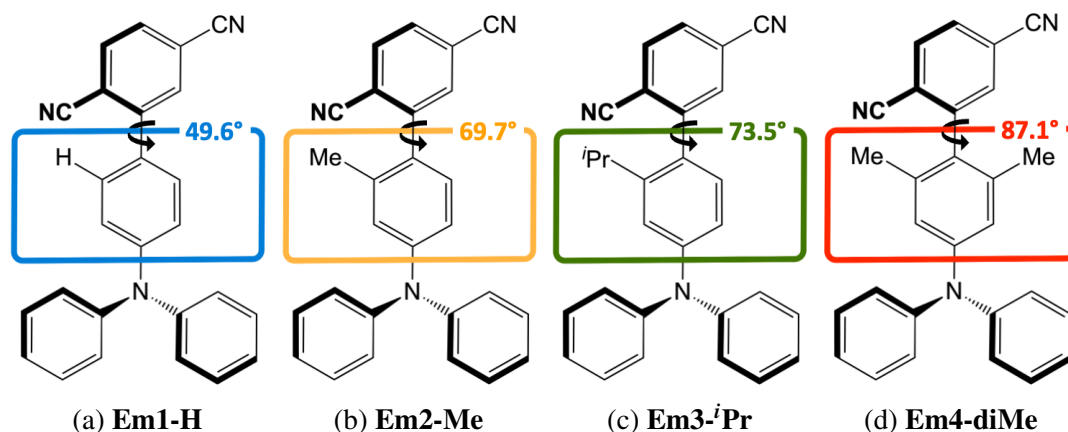


Figure 3.2: Investigated emitter series consisting of a triarylamine (TAA) donor and a terephthalonitrile (TPN) acceptor unit. Labeling: Consecutive numbers in the order of increasing substitutional effect plus name of the substituent. Differences are highlighted by colored boxes. The dihedral angle between the phenylene bridge of TAA and the TPN acceptor of the most stable conformer is indicated in the upper right of each colored box.

polar solvents, observed across the series toluene, tetrahydrofurane and dichloromethane. Subsequent TDDFT calculations at B3LYP/6-31G** level of theory at the optimized ground-state geometry estimated $\Delta E_{ST} = 104$ meV. These calculations also revealed excited states with configurations other than CT, located about 0.5 eV higher in energy, which are necessary to couple the singlet and triplet manifolds.

Initial quantum chemical investigations at PBE0/TZVP level of theory [138] involved conformational analyses in the electronic ground-state, identifying four conformers with varying donor–acceptor dihedral angles. The torsional scan revealed an almost mirror-symmetrical profile at 180 degrees, with two double minima. This symmetry suggested that investigating one side of the torsional scan would suffice, with results transferable to the other side. It was concluded that the dihedral angle significantly influences the absorption behavior and the excited-state processes. In the adiabatic picture, the lowest CT states showed a larger splitting compared to experimental results. Additionally, a locally excited triplet state experienced substantial energetic relaxation when the donor and acceptor were arranged perpendicularly. Finally, initial analyses of the emission maximum in various solvent environments, using PCM and the cLR approach, indicated major challenges in accurately describing the solvatochromic redshift observed experimentally.

3.1.1 Methodological Details

These findings necessitate more detailed quantum chemical investigations of **Em2-Me**. The first step toward improving the results involved switching from hybrid to RSH density functionals. As outlined in Section 2.3, RSH functionals provide a more balanced and accurate energetic description of CT states relative to states of different character. Since the electronic ground and excited states are optimized using DFT and TDDFT, respectively, the impact of this approach should already be noticeable in the resulting calculations.

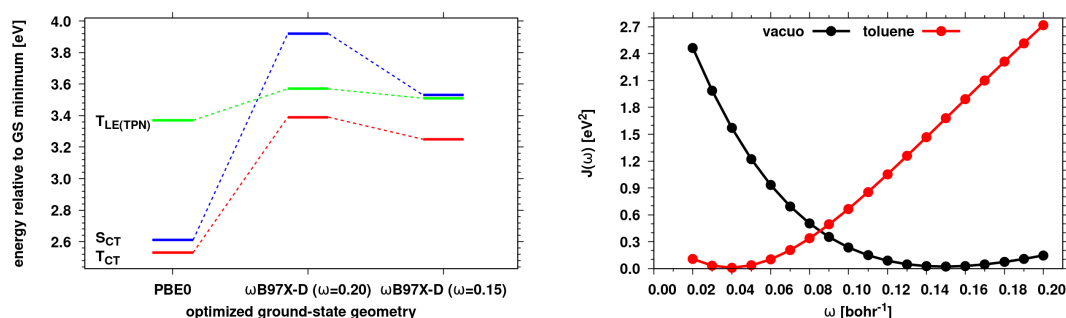


Figure 3.3: **Left:** TDDFT energy level diagram showing vertical excitation energies at various optimized geometries using PBE0/def2-SV(P) or ω B97X-D/def2-SV(P) level of theory for **Em2-Me** in toluene. The standard and optimal system-specific range-separation parameter ω are used. **Right:** Optimal tuning procedure for range-separation parameter ω in vacuo (black) and toluene (red) for the optimized electronic ground-state at ω B97X-D/def2-TZVP level of theory.

The options for selecting density functionals seem endless, as each is tailored to address specific challenges. In this work, the ω B97X-D functional was chosen because it yields reliable results for excitation energies on average and includes DFT-D3 dispersion corrections [77, 139]. A critical factor in such functionals is the range-separation parameter ω . In quantum chemistry programs, it is implemented with a standard value optimized for a selected test set of molecules and properties. To fully exploit the advantages of the functional, a non-empirical optimal tuning procedure was applied. The standard and optimized values for ω can differ significantly, which strongly influences the results, as illustrated in Figure 3.3. Molecule-specific adaptation of ω can be achieved through various procedures, with the one based on the fulfilment of Koopman’s theorem being the most recommended in literature (see Section 2.3). When simulating environmental effects, a decision must be made whether to optimize the optimal range-separation parameter ω *in vacuo* or in solution. As shown in Figure 3.3, the values derived in toluene are far too small (as discussed in Section 2.3), so that the

optimal parameters obtained *in vacuo* are used for subsequent calculations. Energies and photophysical properties were then analyzed using DFT/MRCI level of theory in the presence of a solvent model.

A comparison of PBE0 and ω B97X-D results for the first conformer (see Section 3.1.3) reveals notable differences in the optimized ground-state and excited-state geometries within a toluene environment using the PCM, especially in the donor–acceptor dihedral angle. With both setups, the geometries of the ground state (PBE0: 65°, ω B97X-D: 70°) and S_{CT} excited state (PBE0: 76°, ω B97X-D: 66°) are relatively similar, with donor–acceptor dihedral angles differing by maximum of 10 degrees. In contrast, the T_{CT} state (PBE0: 61°, ω B97X-D: 42°) adopts a significantly smaller dihedral angle.

At the TDDFT level of theory, PBE0 underestimates the CT excited state energies, leading to strongly bathochromically shifted fluorescence emission compared to experimental results (see Table 3.1). Conversely, the ω B97X-D emission shows a hypsochromic shift. At the DFT/MRCI level of theory, ω B97X-D does not affect the adiabatic S_{CT} energy compared to PBE0, with similar CT character (PBE0: 85% CT, ω B97X-D: 80% CT, based on TheoDORE one-electron transition density matrix analysis). However, the T_{CT} state exhibits more LE character (PBE0: 62% CT, ω B97X-D: 40% CT, based on TheoDORE one-electron transition density matrix analysis), resulting in larger adiabatic singlet–triplet energies (see Table 3.1).

Table 3.1: **Em2-Me**: Overview of S_{CT} and T_{CT} vertical (v, at optimized ground-state geometry) and adiabatic (a, at respective optimized excited-state geometry relative to ground-state minimum) excitation energies in eV and vertical fluorescence emission wavelength at the optimized S_{CT} geometry in eV (nm). The relevant electronic states were optimized using (TD-)DFT at PBE0/def2-SV(P) or ω B97X-D ($\omega = 0.15$ bohr⁻¹)/def2-SV(P) level of theory. All properties were calculated at TDDFT or DFT/MRCI level of theory,

		S_{CT} (v)	T_{CT} (v)	S_{CT} (a)	T_{CT} (a)	λ_{em}
PBE0	TDDFT	2.62	2.53	2.37	2.23	2.13 (582)
	DFT/MRCI	3.06	2.84	2.94	2.67	2.65 (468)
ω B97X-D	TDDFT	3.53	3.25	3.22	2.49	2.92 (425)
	DFT/MRCI	3.10	2.91	2.94	2.50	2.56 (484)
Experiment [137]						2.52 (492)

Two literature-supported conclusions can be drawn from this comparison: (i) OT-RSH functionals are more capable of equally describing all properties necessary for characterizing a TADF emitter [82]. (ii) Comparing adiabatic energy differences with experimental 0–0 energies provides little insight into whether the optimized

geometries are realistic. It is much more critical to compare vertical energies, such as the calculated and experimental emission wavelengths. JACQUEMIN has emphasized that the geometric contribution to fluorescence emission is much stronger than for the absorption process [140]. Based on these observations and the obtained results (see Table 3.1), the ω B97X-D functional with an optimized range-separation parameter $\omega = 0.15 \text{ bohr}^{-1}$ is employed in the following discussion. The large adiabatic energy gap for a TADF emitter will be further addressed in the subsequent sections.

First, a quantum chemical validation is sought to confirm that the geometries of the excited states optimized with ω B97X-D, particularly the T_{CT} state, are reliable.

3.1.2 Excited-State Absorption

The reliability of the optimized excited-state geometries was validated in collaboration with PETER GILCH's research group (Heinrich Heine University Düsseldorf, Germany). They developed an experimental setup utilizing time-resolved Near-Infrared (NIR) spectroscopy to energetically localize all relevant excited states for emitters in solution, and to determine the energy differences between them [141]. Further details are presented in **Publication II**. This collaboration provided a twofold benefit: our computational results were used to evaluate whether the measured spectra and the experimentally determined excited-state energies were consistent with the chosen setup, while the experimental findings offered critical insights into whether the optimized geometries for the S_{CT} and T_{CT} states reflected accurate donor–acceptor conformations.

In the experiment, transient difference spectra are obtained using the pump-probe technique. Initially, the population resides in the electronic ground state. A pump pulse is applied to excite the majority of population to an excited state, followed by a probe pulse that records population changes as a function of wavelength and time. The observable processes include (i) the **Excited-State Absorption** (ESA), which is measured with a positive signal, (ii) **Stimulated Emission** (SE) from the excited state back to the ground state, contributing with a negative signal, and (iii) ground-state bleach, the decrease in signal of the ground-state absorption caused by depopulation due to the pump pulse, also contributing with a negative signal. Upon excitation, mainly excited singlet states are populated. However, in a TADF emitter, part of the population transitions to the triplet manifold via ISC. Consequently, depending on the time delay of the probe pulse, spectra can be recorded in the singlet and triplet manifold, respectively. To simulate these processes as accurately as possible and characterize the key transitions in the measured spectra, ESA was calculated at the optimized S_{CT} and T_{CT} geometries. Additionally, the stimulated emission from S_{CT} to the ground state was taken into account

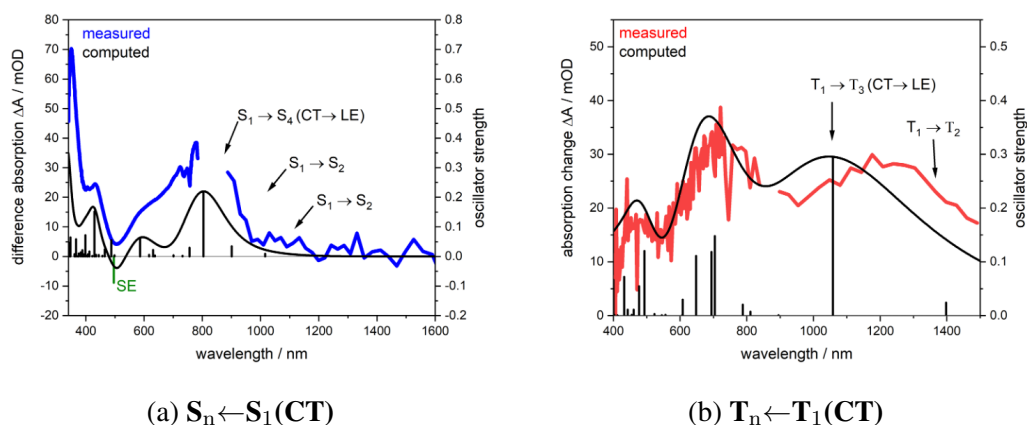


Figure 3.4: Experimental and calculated spectra for (a) $S_n \leftarrow S_1(\text{CT})$ and (b) $T_n \leftarrow T_1(\text{CT})$ processes combining ESA and SE in toluene for **Em2-Me**. The experimental setup is based on the fact that the visible and NIR ranges are calculated separately from each other and combined as one spectrum. This creates a gap in the range between 800 nm and 900 nm. The calculated DFT/MRCI-R2016 line spectra were broadened with Gaussians of 1850 cm^{-1} or 4000 cm^{-1} Full Width at Half Maximum (FWHM) for $S_n \leftarrow S_1(\text{CT})$ and $T_n \leftarrow T_1(\text{CT})$, respectively.

by subtracting the transition with a positive oscillator strength from the calculated ESA spectrum.

Figure 3.4 presents a comparison between theory and experiment for the $S_n \leftarrow S_1(\text{CT})$ and $T_n \leftarrow T_1(\text{CT})$ transitions. The agreement is convincing, with the band structure of the measured spectrum being well reproduced. From the comparison with quantum chemical calculations, the CT→LE transition ($S_4 \leftarrow S_1$ or $T_3 \leftarrow T_1$) is identified as particularly important due to its high measured and computed intensity. This demonstrates the ability of the experimental setup, in conjunction with quantum chemical calculations, to energetically locate and characterize excited states. To ensure that the observed agreement between theory and experiment is not coincidental, the dependence of calculated ESA spectra on the donor–acceptor dihedral angle was investigated. Relaxed scans along the PESs of the S_{CT} and T_{CT} excited states were performed (see **Manuscript I**, Figure 5), with the donor–acceptor angle systematically varied and fixed in steps of 5 degrees. Results for angles ranging from 25° to 90° are shown in Figure 3.5.

The calculated ESA spectra are highly sensitive to the donor–acceptor dihedral angle. Across the spectra, all absorption bands experience a hypsochromic shift (for the singlet transitions) and a bathochromic shift (for the triplet transitions), along with changes in the intensity ratios. In comparison to the experimental spectrum, altering the dihedral angle in the excited state would lead to a less satisfactory agreement with experimental

3 Through-Bond Charge-Transfer Emitters

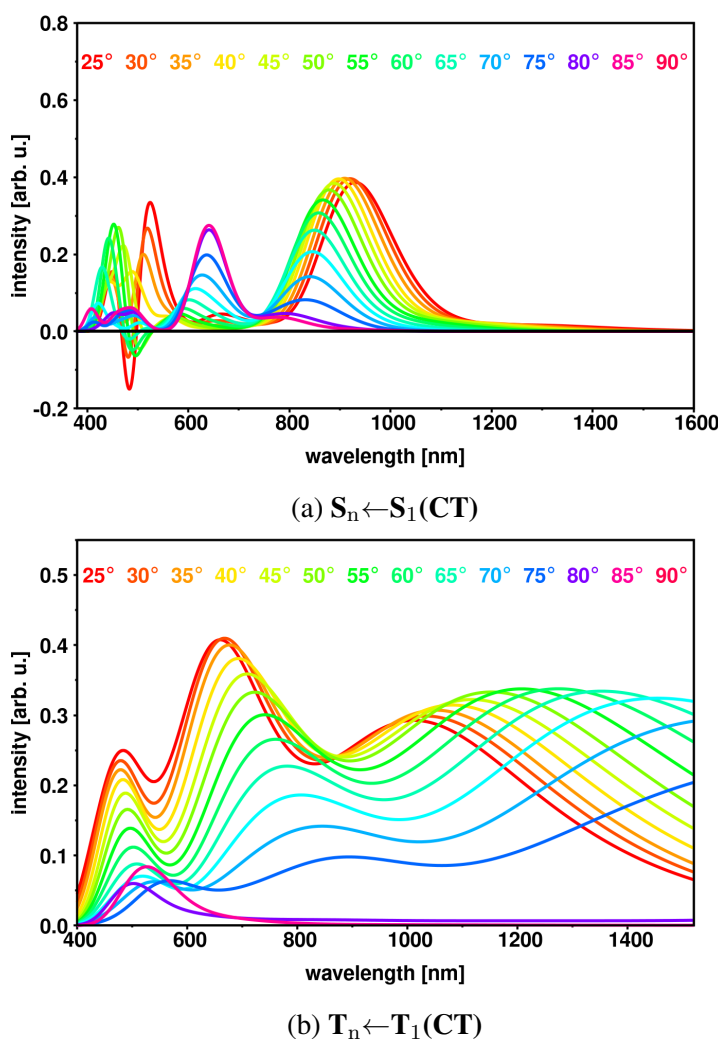


Figure 3.5: Simulated spectra for (a) $S_n \leftarrow S_1(\text{CT})$ and (b) $T_n \leftarrow T_1(\text{CT})$ processes combining ESA and SE in toluene with respect to fixed donor–acceptor configurations between **TAA** and **TPN** along the relaxed excited-state PES for **Em2-Me**. The calculated DFT/MRCI-R2016 line spectra were broadened with Gaussians of 1850 cm^{-1} or 4000 cm^{-1} FWHM for $S_n \leftarrow S_1(\text{CT})$ and $T_n \leftarrow T_1(\text{CT})$, respectively.

data. This provides sufficient evidence that the optimized geometries of S_{CT} and T_{CT} states are reliable and can be used for further investigations.

Determining energy differences between excited states offers an additional advantage in the context of vibronic interactions. They play an important role in TBCT emitters as well as in TSCT emitters (discussed in Chapter 4), particularly in the context of non-adiabatic couplings. These interactions are essential for describing processes such as ISC and rISC, which directly influence whether TADF can occur. The calculation of spin-vibronic interactions (see Eq. 2.34) requires the energy difference between excited states, as these values appear in the denominator of the relevant equations. Consequently,

precise determination of the energetic positions of excited states is of great importance for understanding and predicting these processes [141].

3.1.3 Conformers and Absorption

From a theoretical point of view, it remains to be demonstrated why TADF is expected for emitter **Em2-Me**. Further analyses were conducted as part of **Publication V** and **Manuscript I**, in collaboration with the research groups of CLAUD A. M. SEIDEL and THOMAS J. J. MÜLLER (Heinrich Heine University Düsseldorf, Germany).

To better understand the TADF properties of **Em2-Me** described by SOMMER ET AL. [137], the influence of specific donor–acceptor conformations on TADF was investigated for the entire TAA-TPN series.

For **Em1-H** and **Em2-Me** (see Figure 3.2), two conformers were identified with donor–acceptor dihedral angles ranging between 0 and 180 degrees. Despite the partially symmetrical substitution, these conformers are not energetically equivalent due to the helical arrangement of the TAA moiety. The increasing steric demand of the substituent drives the donor–acceptor arrangement closer to a perpendicular orientation. At this arrangement, π -conjugation along the TBCT axis is minimized. Among the investigated emitters, **Em1-H** shows the strongest stabilization of its conformers relative to a perfectly perpendicular arrangement, which increases the energy difference between the conformers. Conformational analysis of **Em4-diMe** reveals only one conformer, as the PES becomes very flat. For **Em3-ⁱPr**, however, the donor–acceptor dihedral angle is not sufficient to fully describe the conformational space. As shown in **Manuscript I**, the isopropyl group rotation introduces a second conformer, which is presented in a two-dimensional relaxed scan of the ground-state PES. For better comparability, the following results are described for the first conformer, unless otherwise stated.

This substitution effect imposes conformational constraints, which manifest in distinct properties of the molecule. In the electronic ground state, this is particularly evident in the absorption behavior, which exhibits clear variations with changes in the donor–acceptor dihedral angle. Notable correlations emerge, such as the decrease in oscillator strength for the CT transition as the torsion angle increases. Nevertheless, it was necessary to determine whether this substitution induces purely steric effects or also exerts an electronic influence. To address this question, a relaxed scan of the ground-state PES for **Em2-Me** was performed, with fixed donor–acceptor dihedral angles. Fortunately, both approaches produced consistent results, supporting the hypothesis that substitution effects can be effectively used to analyze different donor–acceptor conformations (see Figure 3.6).

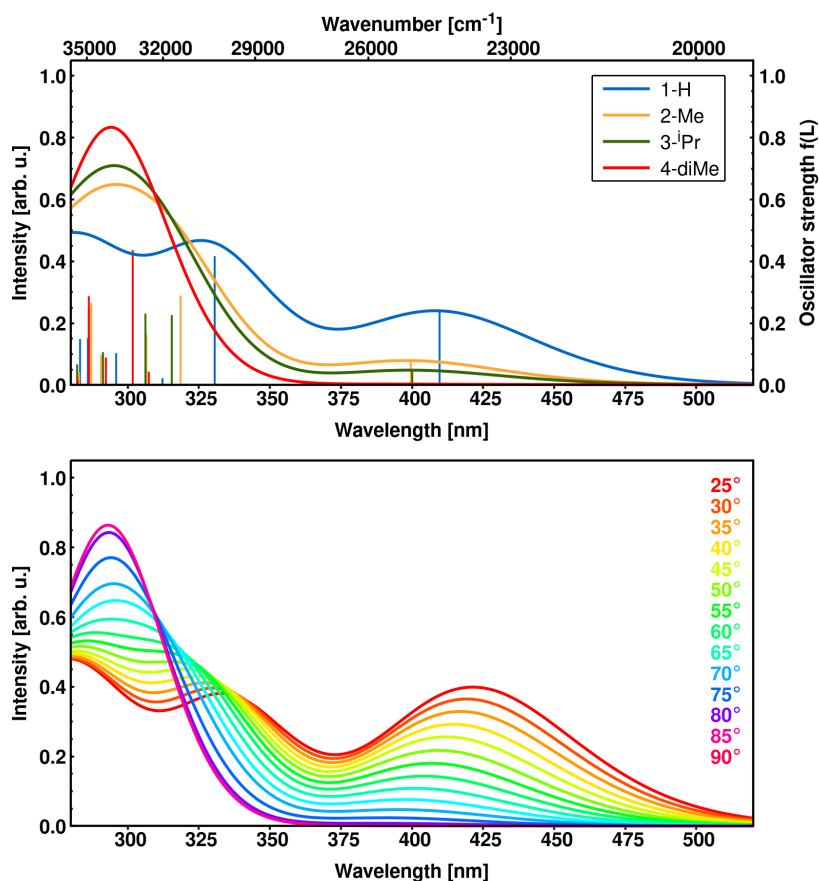


Figure 3.6: **Top:** Computed absorption spectra of **Em1-H** (blue), **Em2-Me** (orange), **Em3-*i*Pr** (green) and **Em4-diMe** (red) in toluene solution. **Bottom:** Simulated absorption spectra of **Em2-Me** at fixed donor–acceptor dihedral angles along a relaxed scan of the electronic ground-state PES. All DFT/MRCI-R2016 line spectra were broadened with Gaussians of 4400 cm^{-1} FWHM.

3.1.4 Excited-State Decay Mechanism

While optimizations of the S_{CT} and T_{CT} excited states was straightforward, the predicted T_{LE} state, expected to be energetically close to the T_{CT} state, could not be found. Relaxed scans along the donor–acceptor dihedral angle reveal that the T_{LE} PES has a minimum at 90 degrees (see **Manuscript I**, Figure 5, second and third rows).

Figure 3.7 shows the vertical excitation energies of the lowest-energy states at their respective optimized geometries for **Em2-Me**. As already expected from the state of research, a LE state localized on the **TPN** moiety can be identified. This $T_{LE(TPN)}$ state is energetically below the CT states when the donor and acceptor are arranged perpendicularly and should be considered in the excited-state decay pathway.

Across the entire emitter series, the emission wavelength from the S_{CT} state remains nearly unchanged upon photoexcitation. Interestingly, for all molecules, the S_{CT} and

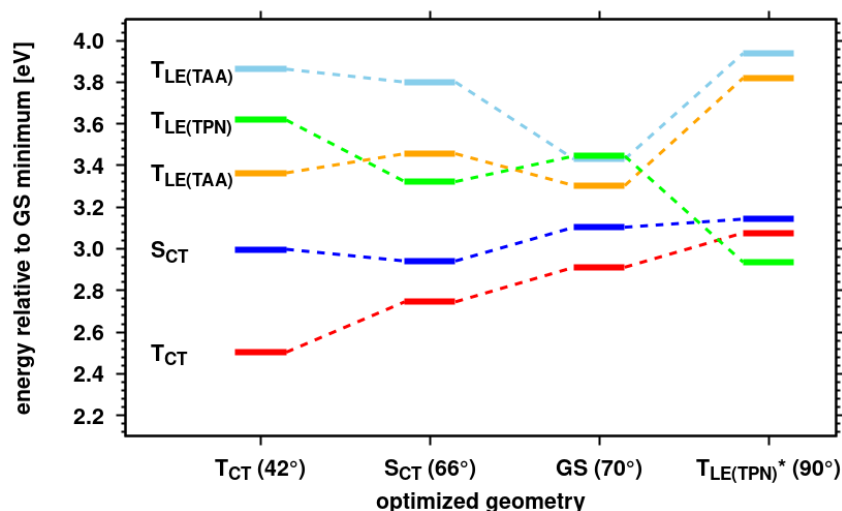


Figure 3.7: DFT/MRCI-R2016 energy level diagram showing vertical excitation energies relative to the electronic ground-state at various optimized geometries for **Em2-Me** at ω B97X-D/def2-SV(P) level of theory using the optimized range-separation parameter of $\omega = 0.15 \text{ bohr}^{-1}$. The asterisk denotes that the $T_{LE(TPN)}$ minimum is assumed to be at 90° from relaxed scans along the donor–acceptor dihedral angle. Excited-state labelling: S_{CT} blue, T_{CT} red, $T_{LE(TPN)}$ green, $T_{LE(TAA)}$ orange, and $T_{LE(TAA)}$ skyblue. The dihedral angle between the phenylene bridge of **TAA** and the **TPN** acceptor of each optimized excited state is indicated in brackets.

T_{CT} geometries differ significantly in the donor–acceptor dihedral angle, as observed for **Em2-Me**. This leads to relatively large adiabatic singlet–triplet energy gaps ΔE_{ST} , which decrease progressively from **Em1-H** to **Em4-diMe**. This trend aligns with experimental findings: **Em1-H** exhibits no TADF, in contrast to all other investigated molecules, while the fraction of DF increases relative to PF across the series, despite similar total PLQY values (**Em1-H**: 76%, **Em2-Me**: 67%, **Em3-ⁱPr**: 67%, **Em4-diMe**: 81%). Relaxed scans along the PESs of the S_1 and T_1 states provide insights into the key parameters for efficient TADF, namely ΔE_{ST} , SOC and TDM μ of S_{CT} state emission. As noted in prior studies, *e.g.*, Refs. [142, 143], these properties are strongly influenced by the donor–acceptor torsion, making it nearly impossible to optimize all of them simultaneously. For a perfectly perpendicular donor–acceptor arrangement, achieving efficient TADF becomes highly unlikely within the classical framework of TBCT emitters, where both S_1 and T_1 are CT states. Considering the electronic ground state, the TADF process is commonly described using a 3-state model, encompassing the electronic states involved in the excited-state decay mechanism (see Figure 3.8, left). In this case, it is crucial to consider additional effects that can influence the behavior of these emitters [30, 144]. While many quantum chemical calculations are performed

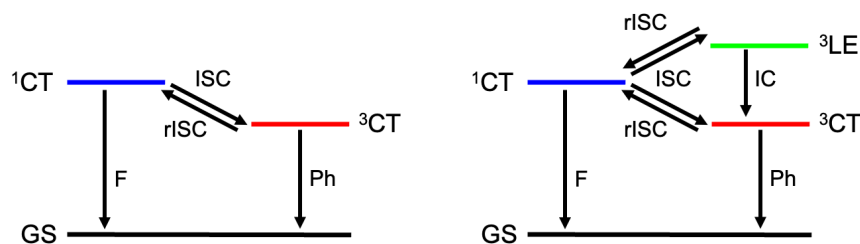


Figure 3.8: Schematic picture comparing state diagrams consisting of three (left) or four (right) electronic states, which are necessary to describe the excited-state decay mechanism of an emitter molecule.

at stationary points, dynamic effects must not be neglected as the molecule is not entirely rigid and should at least be discussed during evaluation, or calculated when feasible [145]. One such dynamic effect is the donor–acceptor torsion, a low-frequency vibrational mode that plays a crucial role. When the molecule is distorted from an orthogonal arrangement, key parameters for efficient TADF improve at donor–acceptor dihedral angles between 85° and 95° . At these angles, the singlet–triplet energy gap ΔE_{ST} increases slightly, but the SOC and TDM, which were previously close to zero, exhibit a much more pronounced increase [146] (see **Publication V**, Figures 3 and 4). Another important finding emerged from the relaxed triplet-state scan. As the dihedral angle decreases, moving donor and acceptor closer to coplanarity, the CT character of the lowest triplet state begins to mix with contributions from a $T_{LE(TAA)}$ state. Notably, in the range of 80° to 100° , the energetically lowest triplet state undergoes a character change during optimization, transitioning from a CT to a LE state. The coupling between different types of states is significantly larger than the coupling between two CT states that involve the same orbitals (see Section 2.7). Furthermore, the excited-state decay pathway can be changed, as shown in Ref. [147].

Experimental evidence suggests the involvement of an additional excited triplet state in the excited-state decay mechanism (see Figure 3.8, right). The rate constant for ISC increases with rising temperature, indicating a process requiring activation energy. In a 3-state model, this behavior would not be expected, as ISC from S_1 to T_1 is typically barrierless. Consequently, the model is expanded to include an additional excited triplet state, resulting in a total of four states of interest. This expanded model resolves two distinct ISC processes, $S_{CT} \rightsquigarrow T_{CT}$ and $S_{CT} \rightsquigarrow T_{LE}$ transitions, with the latter showing a decreasing barrier from **Em2-Me** to **Em4-diMe**. Additionally, one rISC process, $T_{CT} \rightsquigarrow S_{CT}$, also exhibits a decreasing barrier from **Em2-Me** to **Em4-diMe**. These findings align with our quantum chemical calculations (see **Manuscript I**).

While the ISC processes are well described within this framework, the rISC process requires a more complex analysis. Unlike ISC, rISC is strongly dependent on the donor–acceptor dihedral angle. Efficient rISC necessitates stronger geometric changes [145]. A comparison across the series from **Em1-H** to **Em4-diMe** reveals that the dihedral angle increases for the optimized T_{CT} state, consistent with the observed increase in DF fraction in the experiment. Traditionally, rate constants for the entire TADF process are calculated using a static description, based on equilibrated populations of the excited singlet and triplet states at their respective optimized minimum geometries. However, such an approach fails to adequately explain the TADF properties of these and many similar compounds for the reasons outlined above. A quantum dynamical treatment of the TADF process is prohibitively expensive due to the microsecond time scale involved in TADF kinetics.

To address this limitation, the dynamical behavior of the system undergoing large-amplitude motions was investigated using the VH method, avoiding the need of costly dynamics simulations. This approach has been recently illustrated by FERRER ET AL. [130] and implemented in the *VIBES* program by BÖHMER ET AL. [131]. The VH method involves calculating the PES of the final state at the geometry of the initial state, based on the initial population or optimized initial PES and Hessian of the final state. The PES of the final state is then extrapolated, assuming that the nuclear coordinates remain fixed during the transition. Dynamic behavior is introduced by manually varying the geometry of the initial state to simulate possible structural changes. This method provides a more realistic estimation of rate constants for the TADF process (see **Publication V**, Figure 8).

3.1.5 Solvent Effects

Finally, a literature-known challenge in computational chemistry is addressed, which arises when modeling the solvent environment using continuum models. For donor–acceptor compounds with small static dipole moments in the ground state, absorption properties can be reliably described using the PCM. In contrast, excited states with CT character, where the electron and hole are spatially separated, leading to large static dipole moments, are strongly affected by the solvent environment, thus emission properties can be hardly described via the PCM. The stabilization of CT states increases with solvent polarity, while LE states are much less influenced. To ensure a balanced description of both CT and LE states, it is crucial to select a solvent model that is appropriate for the molecule size and the desired level of accuracy [109] (see Section 2.6).

In experiments with TADF dyes, toluene, a non-polar solvent, is often used. With a static dielectric constant of $\epsilon = 2.3807$ [148], toluene has a minor polar effect, comparable

with solvents like n-hexane ($\epsilon = 1.8799$) [149]. Despite this low static dielectric constant, toluene can significantly influence the photophysical processes of the emitter, *e.g.*, Ref. [142]. Specifically, emission from CT states is strongly bathochromically shifted. Attempts to reproduce these experimental results using the cLR model were unsuccessful [146] (see **Publication V**, Supporting Information Table S6). This failure highlights a limitation of implicit solvent models: they do not inherently account for explicit interactions between the solvent molecules and the emitter. Toluene, for instance, is known for its ability to exert π - π -interactions [111]. To investigate this effect, two explicit toluene molecules were included in the quantum mechanical description. These two molecules were sufficient to reduce the adiabatic singlet–triplet energy gap by nearly half, from 0.44 eV to 0.26 eV, without significantly influencing the S_{CT} and T_{CT} geometry of the emitter. The impact of explicit solvation was strongest for the S_{CT} state, which has a more pronounced CT character and is therefore more susceptible to stabilization through excitonic interactions with toluene. In parallel, further investigations were conducted to explore other factors influencing the computational results, including the choice of Hamiltonian and basis set. Comparisons were made between the R2016 and R2022 Hamiltonians, as well as between def2-SV(P) vs. def2-TZVP basis sets (see Tables B.2–B.4). Using the R2022 Hamiltonian led to a hypsochromic shift in the excitation energies of S_{CT} and T_{CT} , while expanding the basis set resulted in a bathochromic shift. These factors can influence each other, potentially canceling out errors introduced by the methods. On average, the originally employed computational protocol can be considered reasonable, with the knowledge that numerous factors influence the results, and compensating errors are possible.

Further advancements and refinements of such hybrid approaches could be achieved by employing a combined QM/MM approach to simulate more complete solvation environment of the emitter. For reasons of time and computational cost, this approach has not been used in the scope of the present work. Nevertheless, the trend of explicit solvation effects was investigated to provide insights into the impact of solvent interactions. Other promising methods, such as the state-specific spin-unrestricted Kohn-Sham approach combined with the polarizable continuum model (UKS/PCM), have shown interesting results for various TADF emitters, including the investigated compound **Em2-Me** (for the adiabatic S_1 – T_1 energy gap, see Ref. [110], TPA-Ph2CN). These methods represent a valuable avenue for future research (see Section 2.6). Note that only the lowest excited states S_1 and T_1 can be adequately described within this framework, while the T_2 state, which appears to play an important role in the decay mechanism, remains inaccessible. This limitation highlights the need for further

methodological advancements to capture the full range of excited states contributing to the photophysical processes of these systems.

To validate whether the solvent model accurately describes the energetic characteristics of the excited states, time-resolved NIR spectroscopy presented in **Publication II** was applied to the entire **TAA-TPN** emitter series. This approach identified an intense CT→LE transition in both the singlet and triplet ESA spectra. In polar solvents, the strong energetic relaxation of the CT state, coupled with the negligible influence on the LE state, should manifest as a detectable hypsochromic shift of the corresponding signal. Substitution and the resulting different conformations of emitters **Em1-H** to **Em4-diMe** also impact the ESA spectra. For the singlet transitions (see Table B.1, Figures 3.5a and B.1a), the CT→LE band shifts to shorter wavelengths, which can be attributed to the nearly constant energies of the S_{CT} state and an energetic increase of the $S_{LE(TPN)}$ state. For the triplet transitions (see Table B.1, Figures 3.5b and B.1b), the trend is reversed. Increasing the dihedral angle of the optimized T_1 geometries leads to increasing T_{CT} and decreasing $T_{LE(TPN)}$ energies. This observation aligns with the relaxed T_1 scan results, where the states cross at a certain point. Consequently, the CT→LE band exhibits a bathochromic shift.

In conclusion, the combined experimental and quantum chemical analyses presented in **Publication II**, **Publication V** and **Manuscript I** provided a comprehensive explanation of the complex excited-state decay mechanism for compounds **Em2-Me**, **Em3-ⁱPr** and **Em4-diMe**.

3.2 Chemical Modification of Molecular Units in TAA-TPN

The substitution effects on the phenylene unit of the donor, which is connected to the acceptor, as presented in Section 3.1, primarily influenced the donor–acceptor dihedral angle. Following the idea of ModISC (see Chapter 1), additional modification strategies can be explored to control and fine-tune the properties of the investigated system. These modifications could involve changes to the electronic nature of the substituents, variations in molecular rigidity, or adjustments to the environment, such as solvent effects or incorporation of specific intermolecular interactions.

3.2.1 Donor Strength

To explore the modification of donor strength, two emitters, **Em2-Me** and **Em4-diMe**, from the previous study were chosen as a starting point. Methoxy groups were introduced

in *para*-position relative to the nitrogen atom on the terminal aryl moieties to enhance the donor strength through their mesomeric and inductive effects. The resulting systems, as shown in Figure 3.9, are **Em2-Me+diOMe**, which has already been synthesized and characterized, and **Em4-diMe+diOMe**, a fictitious test molecule designed to evaluate the influence of this modification on the best-performing molecule in the emitter series in terms of TADF.

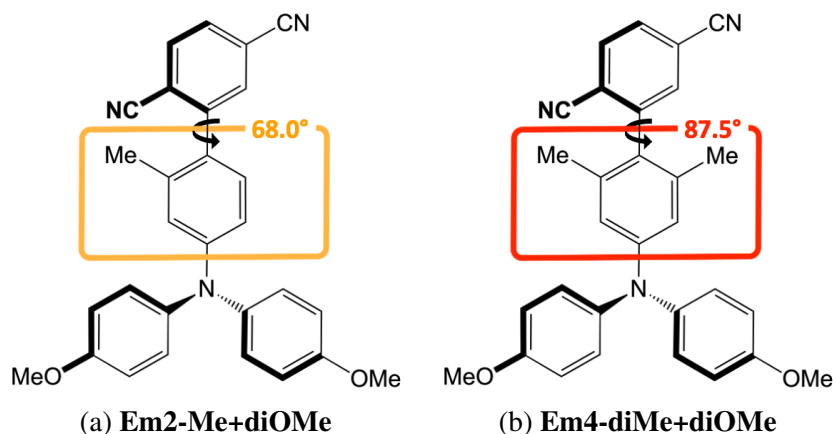


Figure 3.9: Modified emitters based on **Em2-Me** and **Em4-diMe** shown in Figure 3.2 with two additional methoxy groups added at the terminal phenyl groups of the donor moiety in *para*-position with respect to the nitrogen. The dihedral angle between the phenylene bridge and the TPN acceptor of the most stable conformer is indicated in the upper right of each colored box.

The introduction of methoxy groups to enhance the donor strength shows minimal influence on the donor–acceptor dihedral angle in the electronic ground state. In the excited state, the CT character is notably enhanced, as reflected in the increased static dipole moment difference between the ground state and the S_1 state: **Em2-Me**: 22.9 D \rightarrow **Em2-Me+diOMe**: 24.0 D and **Em4-diMe**: 24.0 D \rightarrow **Em4-diMe+diOMe**: 25.8 D. This enhanced CT character affects the excited-state decay pathway. As shown in Figure 3.10, the increased donor strength stabilizes the CT states, preventing the crossing of CT and LE triplet states. Additionally, the adiabatic singlet–triplet energy gap reduces: **Em2-Me**: 438 meV \rightarrow **Em2-Me+diOMe**: 229 meV and **Em4-diMe**: 333 meV \rightarrow **Em4-diMe+diOMe**: 265 meV. Experimental results from **Manuscript I** reveal that **Em2-Me+diOMe** exhibits enhanced TADF properties, with an increased fraction of DF and a higher rISC rate constant compared to **Em2-Me**. However, this comes at the cost of a significantly reduced total fluorescence quantum yield, which is almost halved. Quantum chemically calculations suggest that fluorescence rate constants only marginally decrease, indicating that the reduction in PF might be due to faster IC to the

ground state. This is consistent with the strongly reduced energy difference between S_1 and the ground state.

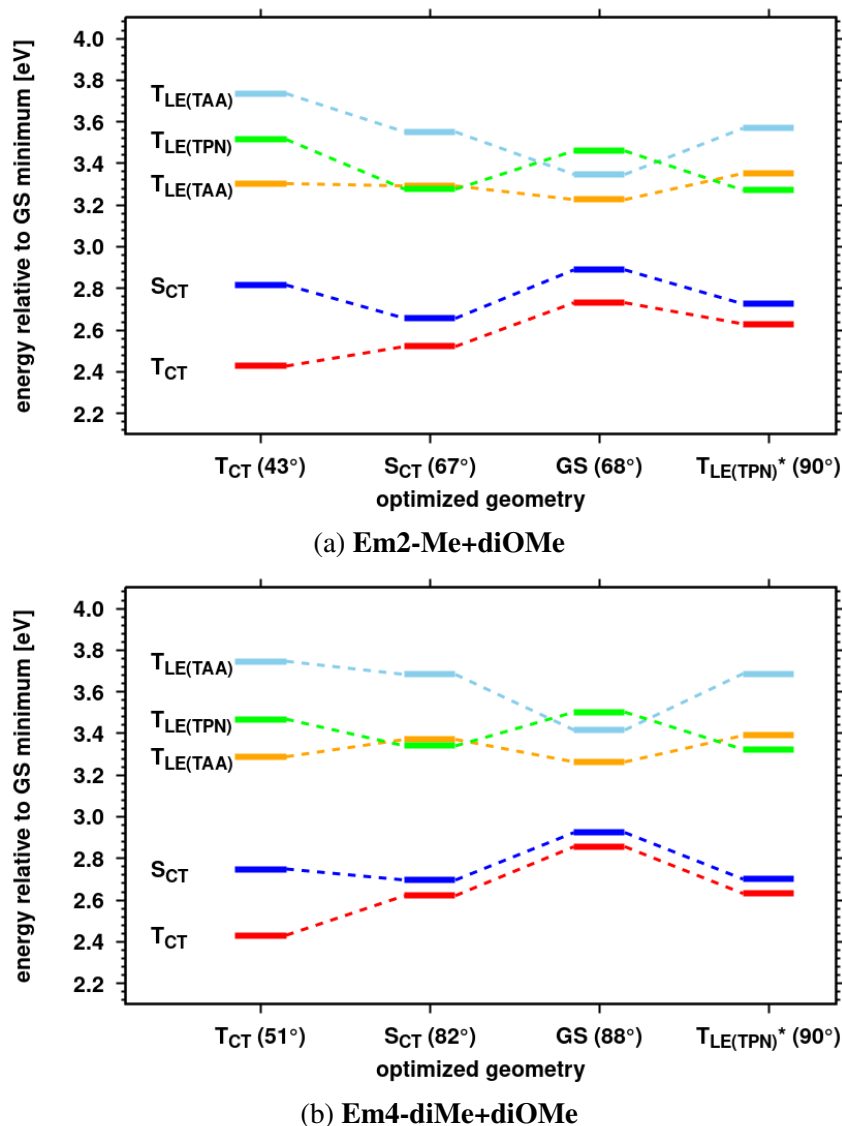


Figure 3.10: DFT/MRCI-R2016 energy level diagrams showing vertical excitation energies relative to the electronic ground-state at various optimized geometries for (a) **Em2-Me+diOMe** and (b) **Em4-diMe+diOMe**. The asterisk denotes that the $T_{LE(TPN)}$ minimum is assumed to be at 90° from relaxed scans along the donor–acceptor dihedral angle. Excited-state labelling: S_{CT} blue, T_{CT} red, $T_{LE(TPN)}$ green, $T_{LE(TAA)}$ orange, and $T_{LE(TAA)}$ skyblue. The dihedral angle between the phenylene bridge of **TAA** and the **TPN** acceptor of each optimized excited state is indicated in brackets.

The evaluation of whether synthesizing **Em4-diMe+diOMe** is worthwhile suggests that several factors weigh against its practicality. The dimethylated emitter **Em4-diMe** already exhibits a larger proportion of DF compared to **Em2-Me+diOMe**, making

it a more suitable candidate. Nevertheless, increasing the donor strength introduces several drawbacks: (i) The total fluorescence quantum yield can decrease significantly, as demonstrated in the results of **Em2-Me+diOMe**. (ii) The strong energetic relaxation of the CT states results in a bathochromically shifted emission, moving it out of the desired blue wavelength regime. (iii) The increased CT character leads to broader emission spectra, experimentally determined by the FWHM, reducing color purity. Given the goal of improving blue-emitting molecules and the findings from **Manuscript I** and Ref. [150], this approach does not meet the desired criteria. Finally, the results emphasize the versatility of the **TAA-TPN** system and highlight the potential for donor strength modulation to fine-tune TADF properties.

3.2.2 π -System Length and Acceptor Strength

It is also conceivable to adjust the size of the π -system or modify the acceptor moiety. To explore these modifications, systems were investigated in collaboration with the research group of THOMAS J. J. MÜLLER (Heinrich Heine University Düsseldorf, Germany). These systems, illustrated in Figures 3.11 and 3.14, were based on quantum chemical and experimental predictions.

When comparing **Em2-Me** and **TAA-p-CN** (Figure 3.12), the removal of one cyano group reduces the acceptor strength, leading to an energetic increase of the CT states. Furthermore, the absence of a substituent in the *ortho*-position relative to the donor–acceptor linkage allows the molecule to adopt a more planar orientation. This planarization increases the ΔE_{ST} between the S_1 and T_1 CT states (see also **Em1-H** and **Em2-Me**). This planarization also diminishes the CT character of the S_1 and T_1 states, while enhancing the LE character, predominantly localized on the **TAA** donor. This results in a mixed CT/LE character (see also difference densities, Figure B.2). As a consequence, the S_1 emission undergoes a hypsochromic shift, which is confirmed by results obtained using the VH method, showing emission wavelengths of 505 nm for **Em2-Me** and 433 nm for **TAA-p-CN** (see Figure B.3). For **TAA-p-CN**, with an adiabatic ΔE_{ST} value of 0.76 eV between S_1 and T_1 , the conventional TADF mechanism becomes unlikely. In the next step, the π -system was extended by introducing a phenylene unit (see also Ref. [151], pp. 203–231).

Diphenylamino-terphenyl-based donor–acceptor conjugates were previously presented as highly deep-blue luminescent emitters in an experimental study by WIEFERMANN ET AL. (Ref. [152]). Among these, compound **3a**, referred to here as **TAA-Ph-p-CN**, was particularly noteworthy. Crystal structure analysis revealed anti-parallel donor–acceptor packing arrangements, with shortest intermolecular distances of approximately 3.4 Å. The recorded emission spectra were obtained using an excitation wavelength

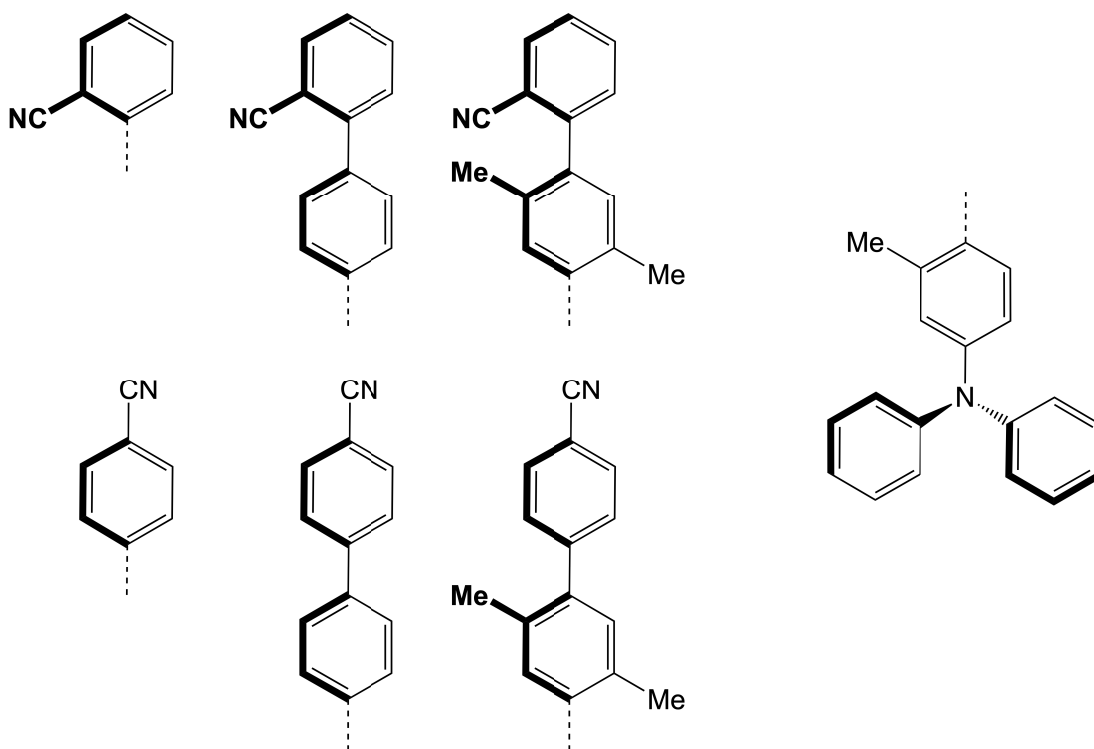


Figure 3.11: Schematic representation of the **TAA**-based donor moiety (right), which is combined with phenyl- (**o**-CN, **p**-CN) and terphenyl-based (**Ph-o**-CN, **Ph-p**-CN, **PhdiMe-o**-CN, **PhdiMe-p**-CN) acceptor moieties (left) having one cyano group in *ortho*- or *para*-position with respect to the donor–acceptor linkage.

corresponding to the absorption maximum (309 nm), showing deep-blue emission in toluene at 431 nm with a remarkable PLQY of 99%. In the molecular series presented by WIEFERMANN ET AL. [152] (cp. Figure 3.11), **TAA-Ph-p-CN** exhibited the narrowest FWHM, measured as 3159 cm^{-1} in toluene. It also performed exceptionally well in the solid state, achieving a FWHM of 2271 cm^{-1} and a PLQY of 98%, with a slightly bathochromically shifted emission maximum at 450 nm. Lifetime analysis showed fast radiative rate constants of 10^8 s^{-1} and moderate non-radiative rate constants of 10^6 s^{-1} . The steric effects causing conformational twisting between the donor and acceptor moieties were found to induce non-radiative decay rates comparable to those of PF. Initial quantum chemical calculations at the CAM-B3LYP/6-311++G** level of theory identified the S_1 state of **TAA-Ph-p-CN** as having ^1CT (**TAA**→**biphenyl**) character at the optimized ground-state geometry.

Finally, **TAA-Ph-p-CN** demonstrated consistently high PLQY values close to one across all investigated environments, including solution, solid state, and PMMA film. Its emission spectrum consistently displayed the lowest FWHM while maintaining

deep-blue emission. Owing to these exceptional properties, this molecule was further investigated, with results published alongside its synthesis and application in an OLED device in **Publication III**, Ref. [153]. Again, the results are obtained using the OT-RSH density functional ω B97X-D. Methodological details as depicted for **Em2-Me** (see Section 3.1) can be found in the appendix (see Figure B.4 and Table B.5).

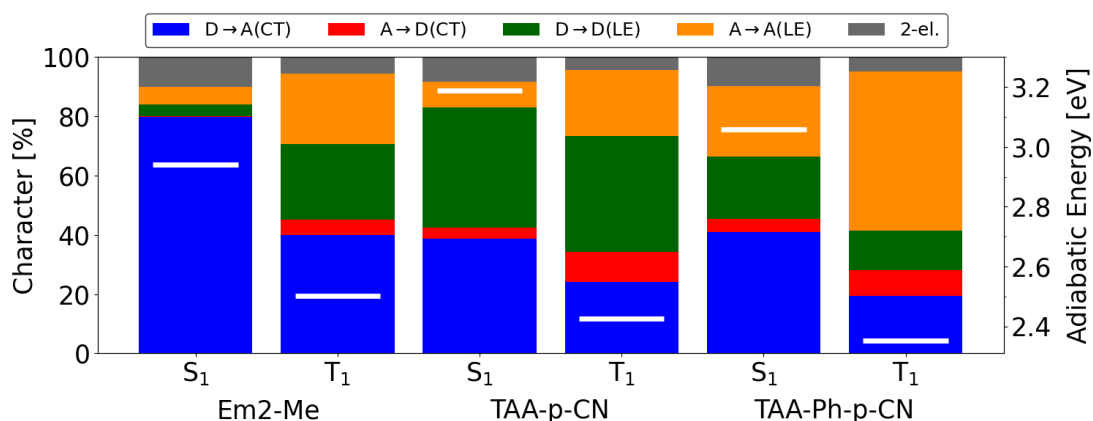


Figure 3.12: Fragment-based analysis of the one-electron transition density matrix (using the TheoDORÉ program package) for the vertical singlet and triplet state DFT/MRCI-R2016 wave functions and corresponding adiabatic excitation energies (white lines) at the S₁ and T₁ geometries in toluene for **Em2-Me**, **TAA-p-CN** and **TAA-Ph-p-CN**.

Quantum chemical calculations for **TAA-Ph-p-CN** reveal that one-electron transition density matrix analyses at the optimized excited-state geometries indicate an increased admixture of LE character compared to **Em2-Me** and **TAA-p-CN**. This leads to states with mixed CT/LE character. The moderate donor and acceptor strengths reduce the CT character of the excitation, which in turn increases the S₁–T₁ energy gap due to the proportionality between exchange interaction and ΔE_{ST} . The higher S₁ and T₁ energies compared to **Em2-Me** align with the experimentally observed hypsochromically shifted fluorescence emission wavelengths: **Em2-Me**: 492 nm and **TAA-Ph-p-CN**: 431 nm. Similar to the non-extended donor–acceptor conjugate **TAA-p-CN**, the adiabatic ΔE_{ST} between S₁ and T₁ remains large (0.703 eV, Figure 3.12), effectively ruling out a classical TADF process from the T₁ state. Notably, the T₂ state was successfully optimized and found to be nearly degenerate with the S₁ state, with a $\Delta E_{S_1-T_2}$ of –0.002 eV (see Figure 3.13).

Although unsuitable for a classical TADF process, the class of HLCT emitters has been introduced in the literature as a solution to the challenge posed by large singlet–triplet energy gaps. Examples include dimethylacridine as a donor and anthracene as an acceptor. Similarly, **TAA** and *para*-benzonitrile (**TAA-p-CN**) are promising building blocks for

such a decay mechanism, as demonstrated in Figure 20 of Ref. [27]. The defining characteristic of HLCT emitters, as described in the literature, is the combination of two distinct characters within a single excitation. The exciton localization (LE state) increases the radiative transition rate, leading to a high PLQY. Simultaneously, the exciton delocalization (CT state) reduces the exciton binding energy and ΔE_{ST} , facilitating rISC from higher-lying triplet to singlet states and resulting in a high proportion of radiative singlet excitons. Importantly, CT and LE characters are not merely mixed but form a single hybridized excited state [27]. To optimize the performance of such emitters, it is crucial to design them in a way that minimizes IC between T_n and T_1 while maximizing rISC between T_n and S_1 or similar transitions.

The design of **TAA-Ph-p-CN** is comparable to the HLCT emitter presented by LIU ET AL. [154], but features a simpler phenylene bridge. This modification introduces additional LE character compared to previously reported non-elongated donor–acceptor conjugates [155] and fully engages the phenylene bridge in the excitation of the S_1 state. The balanced CT/LE character of the S_1 state is supported experimentally by varying solvent polarity and deriving the fluorescence rate constant from luminescence decay measurements, alongside quantum chemical analyses of absorption and emission behavior. The HLCT character appears to persist across all solvents analyzed [153], as demonstrated by the Lippert-Mataga analysis in **Publication III**, consistent with findings in Ref. [156]. When evaluating the criteria for HLCT emitters, **TAA-Ph-p-CN** exhibits strong fluorescence in the blue wavelength regime with an oscillator strength greater than one. However, the coupling between the T_2 and S_1 states is relatively weak, which challenges its classification as a true HLCT emitter. Rate constants calculated using the FC approximation indicate that the $T_2 \rightsquigarrow S_1$ rISC process is rather slow, owing to the small SOC.

Similar results were observed when the emitter was embedded in a DPEPO matrix and integrated into an OLED device. The device achieved only an EQE of 2%. Based on the expected outcoupling efficiency of the device (see Section 1.1), this corresponds to an IQE of approximately 10%. While this IQE aligns with a PLQY of 94%, it is relatively low considering the anticipated contribution of additional triplet excitons from the HIGHrISC process. The weak coupling between the triplet and singlet manifolds suggests that the $T_2 \rightsquigarrow S_1$ process contributes only marginally to the IQE. The high PLQY is primarily attributed to the generation of singlet excitons, which can be explained by the exceptionally high oscillator strength of the S_1 state after optimization. This increased oscillator strength arises from enhanced π -delocalization due to the extensive planarization of the phenyl rings. Despite these limitations, **TAA-Ph-p-CN** remains a highly promising deep-blue fluorescent emitter. Its performance could be further

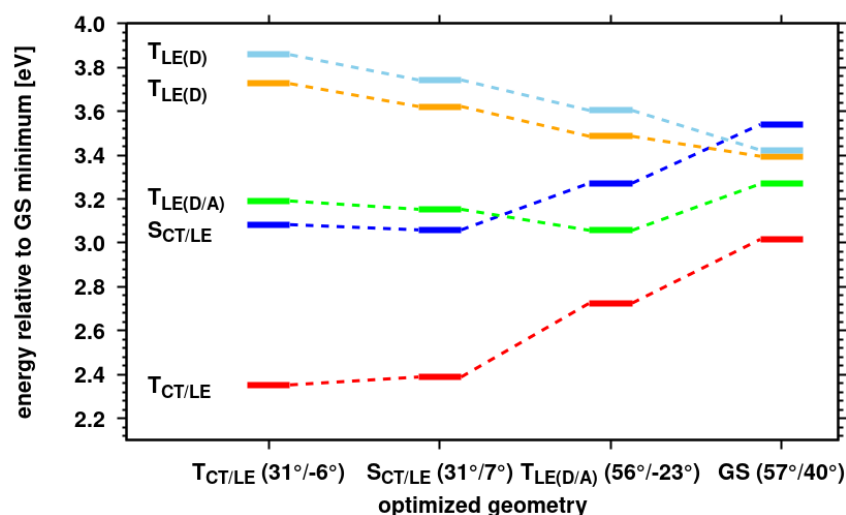


Figure 3.13: DFT/MRCI-R2016 energy level diagram showing vertical excitation energies relative to the electronic ground-state at various optimized geometries for **TAA-Ph-p-CN**. The excited states are labelled as follows: $S_{CT/LE}$ blue, $T_{CT/LE}$ red, $T_{LE(D/A)}$ green, $T_{LE(D)}$ orange, $T_{LE(D)}$ skyblue. The dihedral angles between the phenylene bridges of **TAA** and the acceptor and between the phenyl rings within the acceptor of each optimized excited state are indicated in brackets.

improved by optimizing the OLED device design. Additionally, other applications, such as its use as a host dopant in combination with a TADF emitter for white OLEDs, similar to the approach demonstrated by WANG ET AL. [156], are conceivable.

3.2.3 Pyridine Acceptors

At last, another class of molecules arising from modifications to the acceptor moiety is discussed. The synthesis and photophysical characterization of these triphenylamine-pyridine chromophores are presented in Ref. [157] and Ref. [151], pp. 80–111.

In this series, various substituents were introduced in the *meta*-position relative to the donor–acceptor linkage, focusing less on steric effects and more on their inductive and mesomeric influences. The substituents include **-Me**, **-H**, **-Cl**, **-COOMe**, **-CHO**, **-CF₃**, and **-CN**. In the solid state, all compounds exhibit deep-blue emission, except for **TAA-Py-m-CHO**, which shows sky-blue emission ($\lambda_{\max} = 495$ nm). In dichloromethane solution, the emission maxima are slightly bathochromically shifted, with the strongest shifts observed for **TAA-Py-m-COOMe** and **TAA-Py-m-CN**, whereas **TAA-Py-m-CHO** exhibits a hypsochromic shift. An analysis of the substituent series does not reveal a clear trend. Experimental ΔE_{ST} values, determined from low-temperature fluorescence and phosphorescence spectra at 77 K, suggest that electron-withdrawing

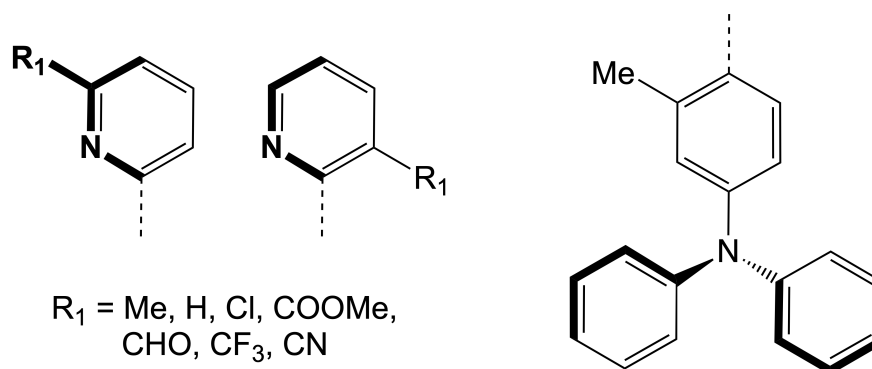


Figure 3.14: Schematic representation of the **TAA**-based donor moiety (right), which is combined with pyridine-based (**Py**) acceptor moieties (left) having one substituent in *ortho*- or *meta*-position relative to the donor–acceptor linkage.

substituents slightly reduce the singlet–triplet energy gap. The lowest value, measured for **TAA-Py-m-CHO** at 0.51 eV (determined from low-temperature phosphorescence and room-temperature fluorescence) in toluene, remains relatively high, making TADF unlikely. This suggests that the *meta*-position is generally unfavorable for achieving small ΔE_{ST} values within this series.

Initial quantum chemical calculations at PBE0/6-311G** level of theory in toluene (PCM) reveal that the longest-wavelength absorption band exhibits CT character for all molecules except for **TAA-Py-m-CHO**, which shows combined CT/LE character. Furthermore, **TAA-Py-m-CHO** appears to play a unique role, warranting further investigation to clarify the experimental findings. Studies of this compound in solvents of varying polarity reveal a more complex excited-state decay pathway. After excitation at $\lambda_{\text{exc}} = 365$ nm, a short-wavelength emission band is observed in non-polar solvents such as cyclohexane, toluene, and benzene. In more polar solvents, including 1,4-dioxane, tetrahydrofuran, ethyl acetate, and dichloromethane, two emission bands are observed. For **TAA-Py-m-CHO**, it was hypothesized that dual fluorescence might contribute to the observed emission process. Dual fluorescence is a phenomenon that depends on solvent polarity and has been observed in non-isolated molecules. It was first reported by LIPPERT ET AL. in 1961 for DMABN. This phenomenon requires the presence of two excited singlet states, connected by a reaction coordinate [158]. Typically, the PES wells of these states are separated by a barrier, with each excited state being the lowest-energy state at its respective optimized geometry. Thus, distinct excited-state characters coexist on the same PES. In the case of DMABN, ZACHARIASSE ET AL. [159] demonstrated that a configuration change at the amino group, from pyramidal to planar, facilitates dual fluorescence. For donor–acceptor conjugates, the reaction coordinate

likely involves the donor–acceptor torsional mode. While vibronic coupling between the S_1 and S_2 states is considered essential for the process, other processes, such as IC, may also play a significant role. These processes are indirectly influenced by the solvent environment, as it impacts the relative energies of the excited states. According to the literature, for **TAA-Py-m-CHO**, the high-energy emission band has been attributed to a locally excited (LE) state. In more polar solvents, a second lower-energy emission band appears, which is assigned to an intramolecular CT state.

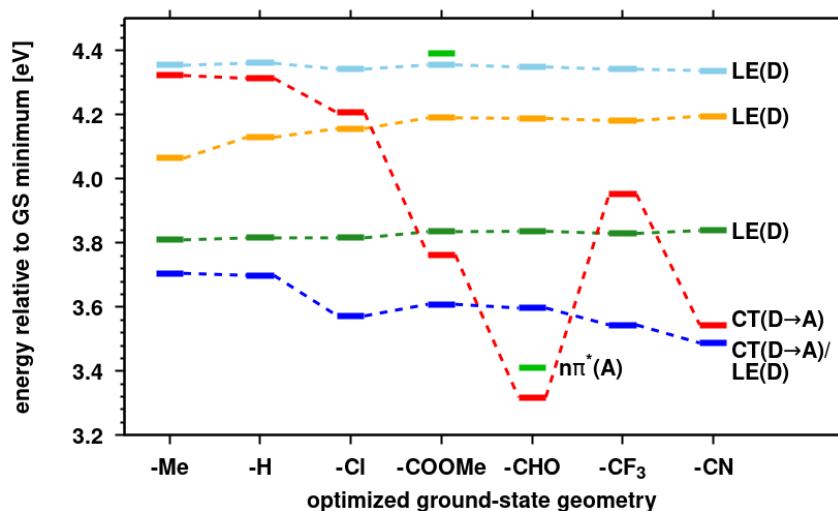


Figure 3.15: DFT/MRCI-R2016 energy level diagram showing vertical excitation energies at the optimized ground-state geometries for **TAA-Py** with various substituents in *meta*-position to the donor–acceptor linkage, including **-Me**, **-H**, **-Cl**, **-COOMe**, **-CHO**, **-CF₃**, and **-CN**. All energies are calculated relative to the electronic ground-state. The excited singlet states are labelled as follows: CT(D→A)/LE(D) blue, CT(D→A) red, $n\pi^*(A)$ green, LE(D) forest-green, LE(D) orange, and LE(D) skyblue.

In the experiment, excitation was carried out at the absorption maximum, which, according to computed oscillator strengths from quantum chemical calculations, corresponds to a transition into the CT(D→A)/LE(D) state (see Figure 3.15, blue). This state is energetically the lowest in the investigated series of molecules, except for **TAA-Py-m-CHO**, where an additional CT state and an $n\pi^*(A)$ state localized on the acceptor are located at lower energies. The energetic position of the LE(D) states remains unaffected by the choice of the substituent. Only states involving the acceptor are modified, including the pure CT(D→A) state, which is strongly stabilized for **TAA-Py-m-COOMe**, **TAA-Py-m-CHO**, and **TAA-Py-m-CN**, and the mixed CT/LE state, which consistently retains a significant local contribution on the **Ph-Me** bridge and is stabilized by up to 0.2 eV. Notably, the described $n\pi^*(A)$ state is significantly stabilized for **TAA-Py-m-CHO**, even

compared to **TAA-Py-m-COOMe** and all other states, bringing it into close energetic proximity to the CT and CT(D→A)/LE(D) states. This raises the question of the role the $n\pi^*$ state may play in the emission process. For **TAA-Py-m-CF₃**, the stabilization of the CT(D→A) state is not too pronounced. According to the -I and +M effects, contrary to the ordering presented in Ref. [157], **TAA-Py-m-CF₃** should be placed after **TAA-Py-m-Cl**, which would better align with the trend observed for the CT state.

For **TAA-Py-m-CHO**, the calculated absorption spectra in vacuo, cyclohexane, and tetrahydrofuran show minimal differences in both the energetic position of the absorption bands and their intensity, consistent with experimental trends (see Figure B.5). This behavior can be attributed to the small static dipole moment in the electronic ground state (4.15 Debye). The absorption maximum at 345 nm, corresponding to the $S_3 \leftarrow S_0$ transition, is bathochromically shifted by approximately 100 meV relative to the experiment. The second absorption band at 296 nm, with a relative intensity of about 40%, represents the $S_5 \leftarrow S_0$ transition and is hypsochromically shifted by around 150 meV relative to the experiment. The vertical absorption appears to be inadequately described, as the intensity ratio and the energetic separation between the two bands are not accurately reproduced (see Figure B.5). In detail, torsional analysis along the donor–acceptor linkage suggests that slight twisting between the donor and acceptor results in only a minor energetic increase on the ground-state PES, as discussed in Section 3.1. This implies that, at room temperature, conformations around the minimum structure contribute to the absorption behavior of the molecule. Compared to the minimum geometry, rotation along the dihedral angle induces a hypsochromic shift of the most intense absorption band and a reduction in intensity. The LE states S_4 and S_5 remain unchanged in position but gain slightly in intensity. Consequently, the experimental intensity ratio and the broad band structure can be well reproduced. These findings emphasize the strong influence of geometry on the energetic position and intensity ratio of the two absorption bands (see Table B.7 and Figure B.6), in agreement with the observations in Section 3.1.

Optimization of the excited states *in vacuo* retains the same energetic order as observed at the ground-state geometry. Considering solvent effects, as expected, increasing polarity destabilizes the $n\pi^*$ states while stabilizing the CT $\pi\pi^*$ states. This leads to substantial variations in the energetic positions of the states. Upon excitation to the $S_{CT/LE}$, which is the lowest excited state at its optimized geometry *in vacuo*, the system relaxes along the S_1 PES via the $S_{n\pi^*}$ state to the S_{CT} , consistent with torsional motion around the donor–acceptor dihedral angle (see Figure 3.16). In contrast, calculations in cyclohexane show that the $n\pi^*$ state, due to its energetic destabilization, no longer

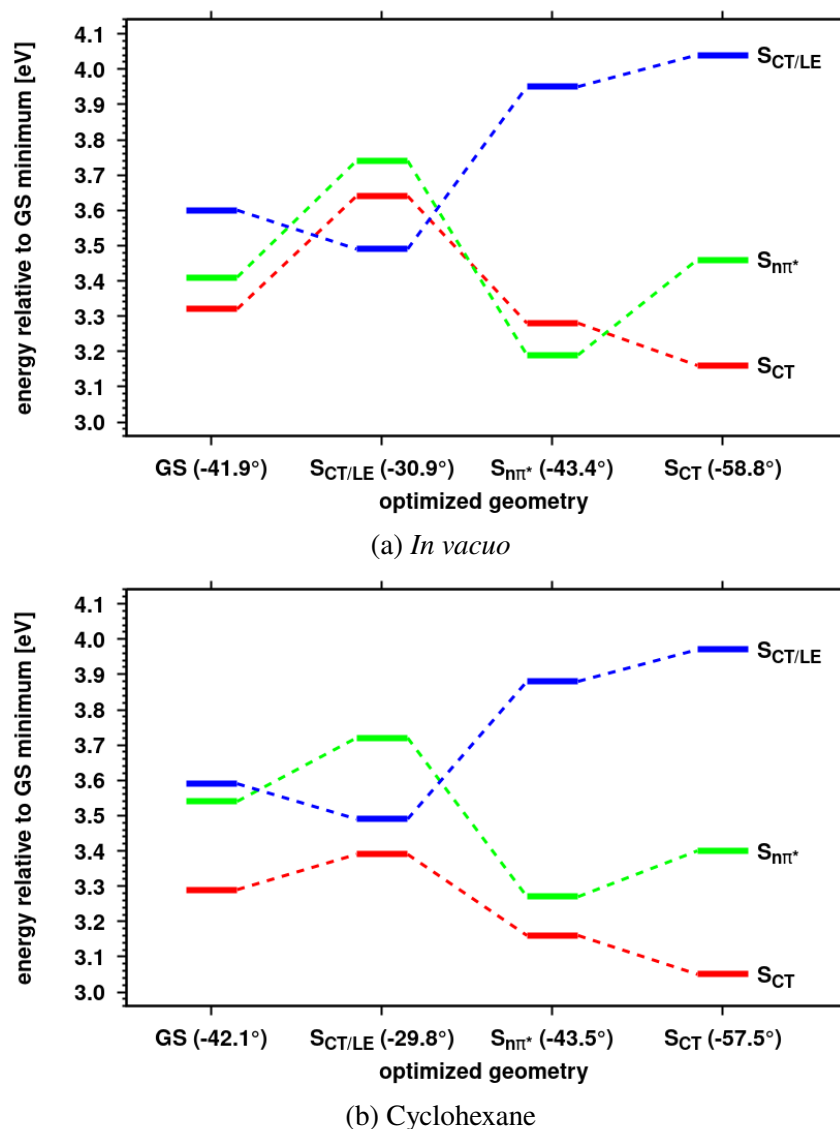


Figure 3.16: DFT/MRCI-R2016 energy level diagram showing vertical excitation energies relative to the electronic ground-state at the optimized ground-state geometries for **TAA-Py-m-CHO**. The excited states are labelled as follows: S_{CT/LE} blue, S_{CT} red, and S_{nπ*} green.

contributes to the S₁ PES. With increasing solvent polarity, the CT state is further stabilized, and in highly polar solvents, the CT state alone dominates the S₁ PES.

For a comparison with experimentally observed emission wavelengths, the inclusion of continuum models alone is insufficient for organic donor–acceptor compounds (see Section 2.6). To account for solvent relaxation effects in the excited state within an implicit solvent model, the cLR method can be employed. While this method works well for molecules with a polar ground state, it performs inadequately for the present case, where the ground state is non-polar. Specifically, for states with CT character, the

cLR method poorly describes interactions with the ground-state charge field, leading to an overestimation of solvent relaxation effects. Consequently, the pure CT state is excessively stabilized. Nevertheless, the expectation that emission from the pure CT state undergoes a stronger bathochromic shift compared to the CT/LE state can still be confirmed as a trend using the cLR method.

It remains unclear, how the experimental finding that a single band is observed at 406 nm in cyclohexane and two bands at 426 nm and 585 nm in tetrahydrofuran can be explained by an excited-state decay mechanism. Since the CT and CT/LE states in more polar solvents do not share a common S_1 PES, dual fluorescence cannot be assumed. Instead of dual fluorescence, a combination of fluorescence and phosphorescence originating from the $n\pi^*$ states might be possible. This is supported by experimentally measured fluorescence and phosphorescence spectra at 77 K, where two bands can also be observed (see Ref. [151], pp. 106–108). Calculated rate constants for phosphorescence and fluorescence from the $n\pi^*$ states, with 10^3 s^{-1} and 10^5 s^{-1} , respectively, exhibit significant values. The fluorescence rate constant from the CT/LE state, with 10^8 s^{-1} , is the highest. Nonetheless, it can be assumed that this state is only minimally populated. Ultimately, fluorescence from the CT state, with a rate constant of 10^6 s^{-1} , is moderate and typical for organic donor–acceptor conjugates.

Evaluating the TADF properties of the investigated triphenylamine-pyridine chromophores, the inductive and mesomeric effects of different substituents strongly influence the positions of the lowest singlet and triplet states (see Table B.6). Notably, the adiabatic singlet–triplet gap lies between 0.8 eV and 1.0 eV due to the presence of a low-lying triplet state, suggesting that any population reaching the triplet state will no longer be available for emission from the singlet state. This issue is observed in many of these nitrogen derivatives, such as quinoline-based compounds studied at their ground-state geometry, where the T_1 state shows an increasing LE character. These findings also explain the experimentally observed reduction in PLQY for some of these molecules. Ultimately, the observation of TADF for this class of compounds appears highly unlikely.

Further modifications, as outlined in Figure 3.14, have been investigated. Changing the substitution pattern from *meta* to *ortho* (see Ref. [151], pp. 112–138) proves to be promising and leads to a reduction in ΔE_{ST} , investigated for **TAA-Py-o-CHO** and **TAA-Py-o-CN**. Experimentally, ΔE_{ST} values of 0.06 eV in PMMA films and 0.08 eV in toluene have been observed for **TAA-Py-o-CHO**. For the additional effect of donor enhancement, see Ref. [151], pp. 139–158.

4 Through-Space Charge-Transfer Emitters

TBCT emitters face certain challenges. First, the strong through-bond interactions often induce a significant bathochromic shift in emission, which is particularly undesirable for achieving blue fluorescence emission [134, 160]. Second, the *para*-connectivity of TBCT emitters makes them more susceptible to intramolecular vibrations and rotations, especially along the donor–acceptor connection axis [143]. These dynamic motions can lead to emission loss [161] through a reduction in oscillator strength and the radiative decay rate constant. Furthermore, they accelerate non-radiative decay processes [162]. As discussed earlier in Sections 3.1 and 3.2, the properties of these systems are highly dependent on the donor–acceptor torsion angle, demonstrating the critical influence of conformational constraints on performance.

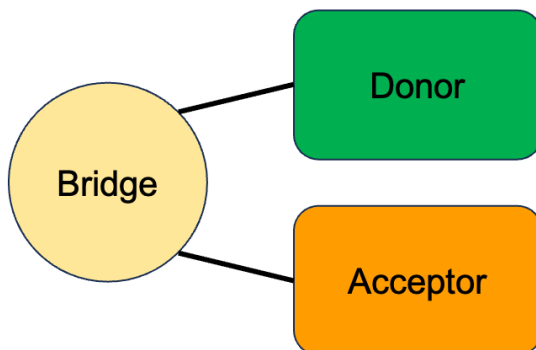


Figure 4.1: Schematic representation of TSCT emitters consisting of donor, bridge, and acceptor units.

To address the challenges associated with TBCT emitters, the principle of TSCT emitters was introduced, where electronic communication occurs through space via strong intramolecular π - π dipolar interactions. One implementation of this principle involves the CT transition taking place intermolecularly between two neighboring molecules, reminiscent of an exciplex state. In this scenario, donor and acceptor do not need to be covalently connected. This type of interaction offers a significant advantage due to the well-separated electron densities on the donor and acceptor, respectively,

resulting in a very small singlet–triplet energy gap [134, 160]. However, exciplexes come with their own set of challenges. The spatial arrangement of the neighboring molecules is difficult to control and predict. This results in the loss of crucial information, such as whether the molecules interact during excitation and, if so, whether they are optimally oriented relative to one another.

A more effective approach involves physically separating the donor and acceptor via an electronically inert bridging group (see Figure 4.1), arranging them in a pseudofacial manner while keeping them spatially close [132, 134]. Unlike the randomly oriented donor and acceptor in exciplex systems, this emitter design provides a deeper understanding of through-space interactions in exciplex-like systems [132, 135]. A critical feature is the spacer connecting donor and acceptor, which serves multiple purposes: it rigidifies the molecular structure, ensures spatial proximity, and controls the mutual relative orientation of donor and acceptor.

4.1 Highly Efficient TADF Mechanism in TpAT-tFFO

In collaboration with the research groups of ANDREW P. MONKMAN (University of Durham, United Kingdom) and HIRONORI KAJI (Kyoto University, Japan), a TSCT TADF emitter named **TpAT-tFFO** (Figure 4.2) was investigated. This molecule demonstrates remarkably high rate constants for the rISC process, reaching up to 10^7 s^{-1} [163]. This is particularly noteworthy because the molecule is purely organic and therefore cannot benefit from heavy atom effects or similar characteristics typically associated with high rISC rate constants. Therefore, it continues to be a subject of research, *e.g.*, as part of a CT excimer, as presented by the workgroups of HIRONORI KAJI and MALTE C. GATHER [164].

TpAT-tFFO is composed of a 9,9-dimethylacridane (**A**) donor unit and a 2,4-diphenyl-1,3,5-triazine (**T**) acceptor unit, connected by a tryptycene (**Tp**) scaffold, placing donor and acceptor in a slightly tilted face-to-face (**tFF**) arrangement. It represents the TSCT counterpart of the extensively studied TBCT TADF emitter **DMAC-TRZ** [30, 31, 142]. Preceding theoretical considerations and quantum chemical calculations [163] identified the almost inert bridging moiety as advantageous, as it allows for an optimal distance (**O**) between donor and acceptor. This configuration ensures near-degeneracy of the LE triplet and CT singlet/triplet state energy levels, promoting strong resonance. Consequently, the excited states exhibit mixed CT/LE character, or the LE state enables overcoming the El-Sayed forbidden $^1\text{CT} \leftrightarrow ^3\text{CT}$ transition [162, 165]. A state model was proposed

comprising ^1CT , ^3CT and ^3LE states, with derived rate constants for fluorescence, ISC and rISC in the range of $10^6 - 10^7 \text{ s}^{-1}$.

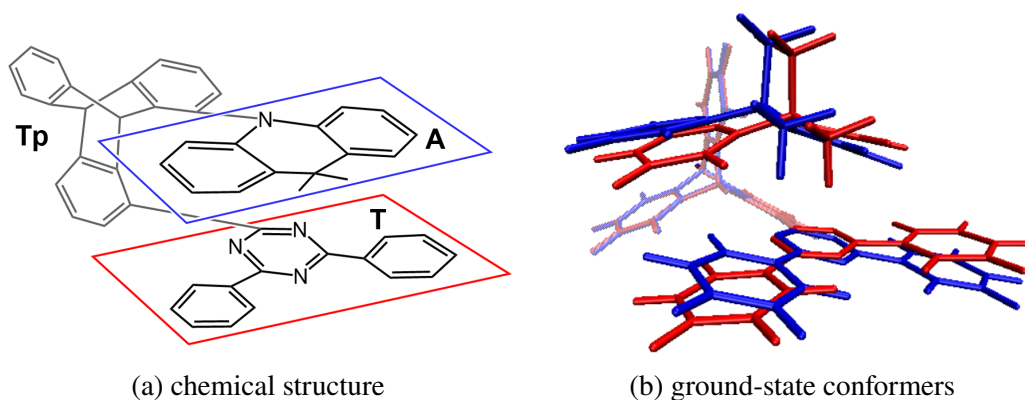


Figure 4.2: (a) Chemical structure of **TpAT-tFFO**. (b) Overlays of **TpAT-tFFO** molecular frames visualizing the coordinate displacements between the ground-state minimum nuclear arrangements (red: Me→N, blue: Me→Ph) while minimizing the root mean squares deviations of the **Tp** bridges.

4.1.1 Conformational Analysis

More precise experimental studies by ANDREW P. MONKMAN's work group [166] have led to new insights that cannot be fully explained by the previous theoretical model. In absorption measurements conducted in toluene, a weak band arising from the TSCT transition was observed, consistent with the earlier findings by WADA ET AL. In addition, the fluorescence emission measurements revealed two distinct channels for PF, both with the same onset of CT emission but exhibiting different rate constants ($2.4 \times 10^6 \text{ s}^{-1}$ and $6.7 \times 10^5 \text{ s}^{-1}$). Our quantum chemical calculations provide an explanation for that. Two ground-state conformers (Me→N and Me→Ph) exist, each with its own excited ^1CT state, whose geometrical structures differ primarily in the spatial orientation of donor and acceptor relative to each other (see Figure 4.2 for ground-state geometries). In the electronic ground state, the two conformers are nearly energetically equivalent ($\Delta E \approx 20 \text{ meV}$), and easily interconvertible. However, in the excited state, it is not possible due to high reorganization energy, thus accounting for dual fluorescence observed experimentally. Despite having nearly identical emission maxima for both CT states (503 nm and 499 nm), which results in a single observed emission band, the fluorescence rate constants differ. Calculations using the FC approximation yielded rate constants of $7.0 \times 10^5 \text{ s}^{-1}$ and $2.0 \times 10^5 \text{ s}^{-1}$, in line with the experimental data.

Considering the updated scenario of two interconvertible conformers, the excited-state decay pathway becomes significantly more complex. For the analysis of non-radiative processes, in total five electronically excited states can influence the decay process: ^1CT , ^3CT and ^3LE states belonging to the first conformer, referred to as Me \rightarrow N, and $^1\text{CT}'$ and $^3\text{CT}'$ states associated with the second conformer, referred to as Me \rightarrow Ph. Optimization of these excited states reveals a picture where each of these states is lowest in energy within the singlet or triplet manifold at their respective geometry (Figure 4.3). Notably, all five excited states are located within a small energetic window in an adiabatic picture. Their interactions were initially investigated using linearly interpolated paths between two optimized structures [167] (**Publication I**, Figure 7). Transitions between the ^1CT and $^1\text{CT}'$ states, as well as between the ^3CT and $^3\text{CT}'$ states, can occur along a reaction coordinate with an intermediate transition state. The high reorganization energy explaining the dual PF from two distinct excited states observed experimentally, is also evident, as these states remain energetically well-separated at their respective ^1CT or $^1\text{CT}'$ minima. The ^3LE state plays a key role in the decay mechanism, showing (avoided) crossings with both $^1\text{CT}/^3\text{CT}$ and $^1\text{CT}'/^3\text{CT}'$ states, all in favor of strongly coupled states through non-adiabatic interactions.

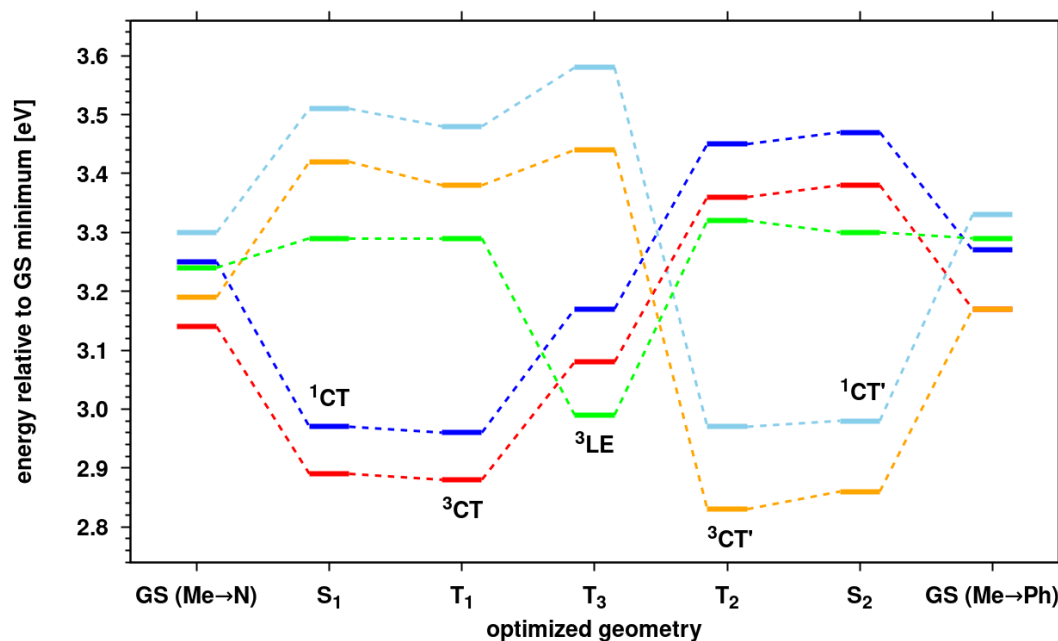


Figure 4.3: DFT/MRCI-R2016 energy level diagram showing vertical excitation energies at various optimized geometries. All energies are calculated relative to the most stable ground-state conformer GS (Me \rightarrow Ph). The excited states are labelled at their respective minimum geometry: ^1CT blue, ^3CT red, ^3LE green, $^1\text{CT}'$ skyblue, $^3\text{CT}'$ orange.

4.1.2 Vibronic Effects on (Non-)Radiative Rate Constants

Rate constants for fluorescence and ISC/rISC initially were calculated within the FC approximation. However, the vibrational dependence of SOC and TDM matrix elements has proven critical for understanding the excited-state decay of TBCT emitters [31, 168, 169]. Certain vibrational modes, such as the donor–acceptor torsional mode, can be readily identified influencing the excited-state decay pathway, especially in the case of symmetry-forbidden transitions. In contrast, for TSCT emitters it is less straightforward. In general, the best approach is to include all vibrational modes in the analysis, regardless of the emitter type. The vibronic effects for **TpAT-tFFO** were considered using a HT-like approach for the radiative and non-radiative rate constants. Especially the calculation of the numerical gradients is computationally demanding due to the need to evaluate 528 displaced geometries. To make the calculations feasible, the number of excited states considered in the DFT/MRCI framework was reduced, and solvent effects were excluded, although cyclohexane would be appropriate to align with the experimental conditions in *Zeonex*[®].

For each ISC and rISC process, derivatives of the SOCMEs with respect to displacements along all normal modes were determined. The evaluation (**Publication I**, Figures S35 - S39) indicates that gradients for transitions between CT states within the same geometrical cluster are very small, whereas they are considerably larger when a change in the geometrical cluster occurs. This is also reflected in the averaged static SOCMEs (**Publication I**, Table 2). Both values increase when there is a change in either the electronic character or geometrical cluster. High-frequency vibrational modes are not particularly relevant for enhancing these processes [167]. Instead, it is necessary to determine whether the largest gradients contribute most to the acceleration of the calculated rate constants. Additionally, it must be considered which vibrational modes dominate the calculated rate constants or emission spectra. For instance, modes involving the triazine moiety exhibiting a large gradient are critical for the rISC process starting from the ³LE state [166] (**Publication IV**, p. 862). In addition, low-frequency vibrations below 100 cm⁻¹ have a dominant overall contribution and should be easily accessible, as little energy is required to excite them. This trend is also observed for the respective fluorescence processes.

Vibrational modes Q_1 , Q_9 and Q_{12} (see Figure 4.4) are particularly interesting as they change both the tilt angle and the interplanar distance between donor and acceptor. This enables the molecule to dynamically access various spatial and orientational donor–acceptor configurations. Displacements along Q_9 and Q_{12} , as shown in Figure 4.5, correspond to an energetic increase of only 2 meV on the ground-state PES.

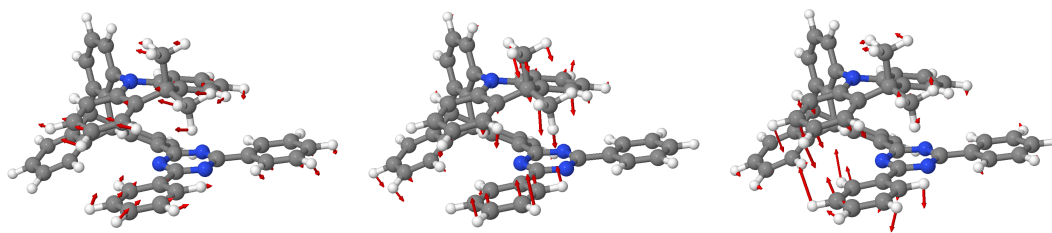


Figure 4.4: Low-frequency vibrational modes Q_1 (left), Q_9 (middle) and Q_{12} (right) from *Gaussian 16* frequency analysis at the optimized GS (Me→N) geometry.

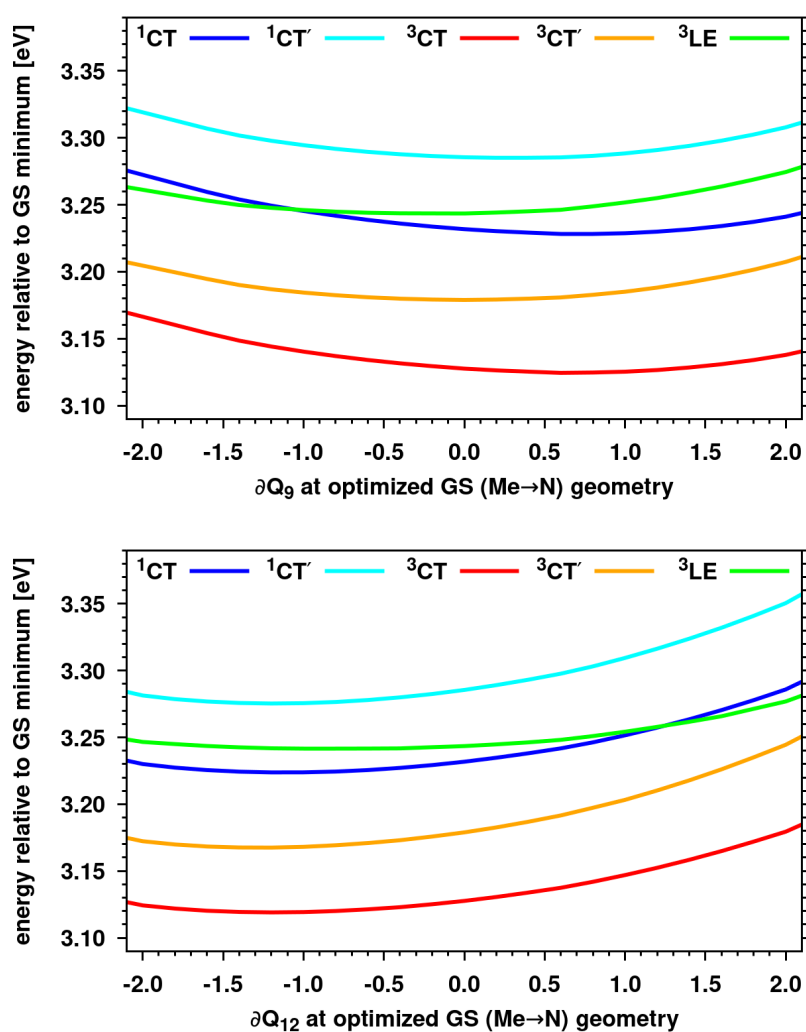


Figure 4.5: Excited-state energies for displacements along vibrational modes Q_9 and Q_{12} at the optimized ground-state conformer GS (Me→N). The energy, which is needed to exert the shown displacements is in the range of 2 meV.

In the excited state, depending on the ground-state conformer, $^1\text{CT}/^3\text{LE}$ or $^1\text{CT}'/^3\text{LE}$ states can already be energetically tuned into and out of resonance. Moreover, the

electron exchange energy and SOC are highly sensitive to changes in the donor–acceptor tilt or distance. This was also observed by WADA ET AL., who demonstrated enhanced SOC for tilted configurations compared to coplanar arrangements [163]. The oscillator strength for the $^1\text{CT} \leftarrow \text{GS}$ transition is weak in the **M** direction and strong for the $^1\text{CT}' \leftarrow \text{GS}$ transition, whereas the opposite is true in the **P** direction. Consequently, even small-amplitude vibrational motions can induce substantial dynamic variations in the excited-state decay pathway.

The inclusion of vibrational effects in the electronic coupling demonstrates that transitions within a geometrical cluster are significantly accelerated due to the mixing of orbital characters, which can be understood as indirect intensity borrowing from El-Sayed allowed transitions. In addition to electronic coupling, the vibrational overlap is decisive in determining the magnitude of the rate constants. For **TpAT-tFFO**, ISC and rISC processes are faster for nested states within the same geometrical cluster, although SOCMEs are smaller. The final FC+HT rate constants are presented in Figure 4.6 and fit much better to the experimental values than the respective FC rate constants.

Nonetheless, the calculated singlet–triplet gap is overestimated. Therefore, variations in the adiabatic energy difference were investigated. According to the energy gap law, in the weak coupling regime (within the same geometrical cluster), the $^1\text{CT} \leftrightarrow ^3\text{CT}$ and $^1\text{CT}' \leftrightarrow ^3\text{CT}'$ ISC transitions are accelerated by approximately one order of magnitude when ΔE_{ST} is reduced to the experimentally observed value of 0.02 eV, whereas corresponding rISC processes are accelerated even more strongly. In the strong coupling regime (between different geometrical clusters), the $^1\text{CT} \leftrightarrow ^3\text{CT}'$ and $^1\text{CT}' \leftrightarrow ^3\text{CT}$ ISC transitions are reduced by roughly one order of magnitude, whereas corresponding rISC rate constants increase, but much less pronounced than in the weak coupling limit. These findings also highlight that rISC is much more strongly thermally activated than the ISC process. IC could not be computed in this study, as its calculation for a molecule with 90 atoms is computationally too expensive with the current implementation available in our working group [170].

Figure 4.6 illustrates the proposed excited-state decay mechanism, with all states plotted according to the adiabatic energies at their optimized geometries. The high reorganization energies between the $^1\text{CT}/^1\text{CT}'$ and $^3\text{CT}/^3\text{CT}'$ states, as well as the easily interconvertible ground-state conformers, result in two distinct deactivation pathways. Non-adiabatic couplings between CT and LE triplet states ensure that the ^3LE state can act as a mediator state for highly efficient rISC processes, specifically $^3\text{CT} \rightsquigarrow ^3\text{LE} \rightsquigarrow ^1\text{CT}$ and $^3\text{CT}' \rightsquigarrow ^3\text{LE} \rightsquigarrow ^1\text{CT}'$. Together with fluorescence and ISC, the experimentally observed 98% DF can be achieved. Molecular vibrations significantly contribute to the decay mechanism by dynamically modulating the properties of the molecule, switching

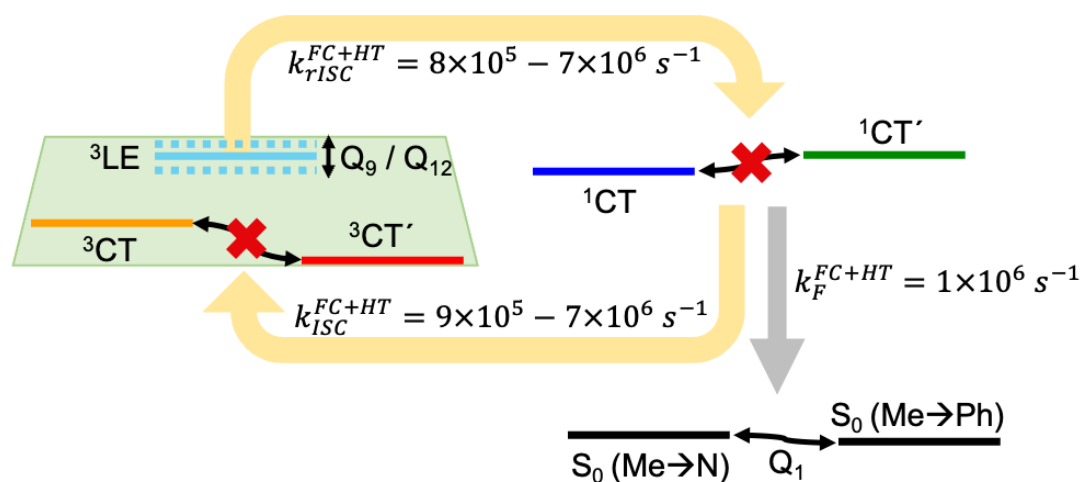


Figure 4.6: Proposed scheme for excited-state decay mechanism of **TpAT-tFFO**.

between high $rISC$ and high $PLQY/k_F$. The elucidation of vibrational effects also provides explanations for the experimentally observed fast non-radiative rate constants. However, the extraordinary DF is not solely attributed to its high $rISC$ rate constant. It is equally crucial that the rate constants k_F , k_{ISC} and k_{rISC} are carefully balanced while potential loss pathways are specifically slowed or suppressed [171]. Finally, organic TSCT TADF emitters exhibit significantly enhanced ISC processes due to the interplay between vibronic and spin–orbit coupling. This is recognized as a general characteristic of these systems and can be extrapolated to other TSCT molecules.

In comparison to TBCT emitters, intramolecular interactions and steric hindrance in TSCT emitters lead to more restricted vibrational and rotational motions, which reduces non-radiative decays and improves the PLQY [161, 162]. Thus, the principle of TSCT represents a highly effective molecular design strategy for achieving efficient TADF emitters, while also obtaining blue emission.

As a further development, in addition to TSCT emitters like **TpAT-tFFO**, CHEN ET AL. [136] have introduced covalent cages composed of triazatruxene (donor) and triphenyltriazene (acceptor) units. These macrocyclic architectures spatially arrange donor and acceptor units in face-to-face fashion, connected by three electronically inert pillars. This design facilitates efficient charge separation and through-space interactions. Furthermore, the relatively rigid cage skeleton restricts conformational freedom, providing significant advantages for understanding the electronic states and photophysical dynamics of these systems.

4.2 TADF Emitters using Triarylboron Acceptors

In the pursuit of finding efficient blue TADF emitters, boron-based donor–acceptor systems have increasingly been the subject of research [172–181]. Boron-based TADF emitters are particularly notable for their versatility in modification and their efficiency, which stems from the strong electron-accepting properties of the sp^2 -hybridized, tri-coordinate boron atom. These properties are characterized by the empty $p(B)$ -orbital and the $p(B)-\pi^*$ conjugation between the boron atom and the attached π -systems.

Initially, the aim was to investigate another molecule with TSCT characteristics that would be easy to chemically modify and ideally had already been investigated as a TBCT emitter. A desirable feature was a design principle similar to the emitters discussed in Chapter 3 to enable a comprehensive comparative study. This led to the molecule **DPACoOB** [182] being studied, which consists of a 9,9-diphenylacridane (**DPAC**) donor and a 10H-phenoxaboranyl (**OB**) acceptor crosslinked in the *ortho*-position at a methylated phenyl bridge. The *para*-appended counterpart **DPACpOB** is also known in the literature (in partially modified forms) [183, 184].

In a bachelor's thesis supervised as part of this work, Tu V. CHU examined the quantum chemical influence of *ortho*- and *para*-connectivity between the donor and acceptor via a bridge, as well as the effects of a modified donor on the experimentally observed TADF properties. This study was subsequently expanded: first, the starting emitter **DPACoOB** was characterized in detail. Additionally, donor modifications were extended to include a third donor, substitution effects on the bridge were explored, and chemical modifications in the acceptor were investigated (see **Publication VI**).

DPACoOB is one of three in a series studied by MUBAROK ET AL. [182], where the influence of different acceptor moieties, namely 9-boraanthryl (**BA**), 10H-phenoxaboranyl (**OB**) and dimesitylboryl (**B**), on the luminescence was analyzed. These emitters have a rigid backbone due to the *ortho*-connectivity of donor and acceptor. The crystal structure of **DPACoOB** indicates the presence of π - π -interactions between one phenyl group of **DPAC** and the **OB** plane, with a distance similar to the face-to-face alignment observed in **TpAT-tFFO** (see Section 4.1). Additionally, a non-bonding electronic interaction between the nitrogen atom of **DPAC** and the boron atom may be assumed from their short interatomic distance. Hence, the boron atom is sterically and electronically protected, which improves the chemical and thermal stability of the emitter [182].

In toluene and in a DPEPO film with 20 wt% of the respective boryl compound, broad emission spectra typical for CT transitions are observed in the sky-blue wavelength regime, with $\lambda_{\max} = 485$ nm and $\lambda_{\max} = 451$ nm, respectively, at room temperature. Only small structural deformations between the ground- and excited-state geometries were expected in solution, which was presumed owing to the rigid cyclic boryl groups.

In comparison to toluene, a substantial rigidochromic blue-shift by 34 nm was observed in film, which was attributed to the steric effects from the *ortho*-**DPAC** and methyl groups, as well as the rigidity of the cyclic boryl moiety. Intriguingly, the experimental spectra between 77 K and 298 K differ significantly with a strong hypsochromic shift of more than 3000 cm^{-1} . In the end, temperature-dependent photoluminescence decay curves, along with measured PLQY values in oxygen-free (99%) and air-saturated (6.1%) solutions, confirm that DF, which accounts for half of the total emission, plays a crucial role in the decay pathway of the investigated emitters.

4.2.1 Conformational Analysis on Absorption and Emission Process

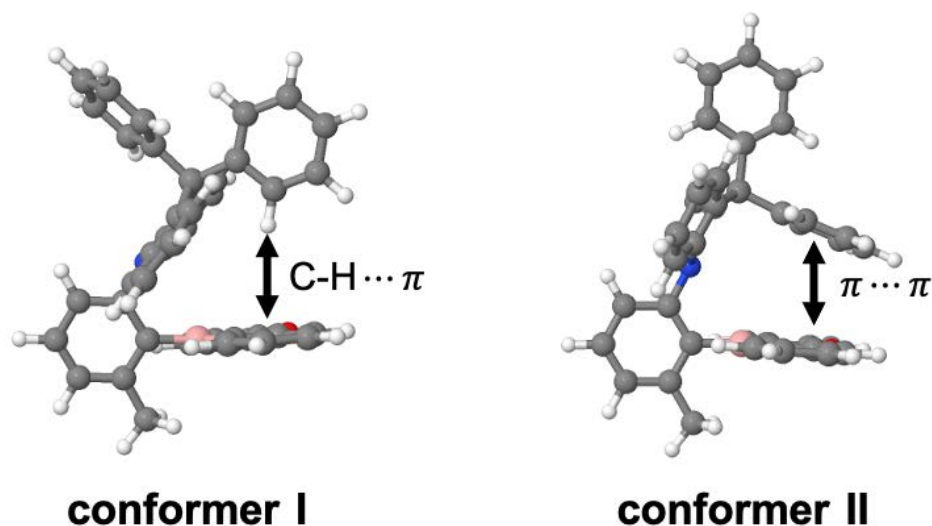


Figure 4.7: Optimized electronic ground-state conformers of **DPACoOB** at PBE0/def2-SV(P) level of theory in toluene. Conformers **I** and **II** exhibit either C-H $\cdots\pi$ or $\pi\cdots\pi$ interactions, respectively.

The ground-state optimization revealed two conformers (see Figure 4.7), **conformer I** and **conformer II**, which differ in the orientation of one **DPAC** phenyl residues relative to the **OB** acceptor and the curvature of the acridane moiety. This results in C-H- π -interactions, similar to the corresponding **DMAC** compound studied in Ref. [185], and π - π -interactions, consistent with the reported crystal structure [182]. Similar to **TpAT-tFFO** (see Section 4.1), a second conformer was considered useful to potentially describe the special characteristics of the experimentally observed emission properties of **DPACoOB**. In the electronic ground state, the π - π -interactions are highly stabilizing, making **conformer II** the energetically preferred form ($\Delta E = 0.24$ eV).

Initial calculations were performed using the PBE0 functional with DFT-D3-BJ dispersion corrections. However, comparing **conformer II** with the crystal structure revealed that the described π - π -interactions were overestimated, as evidenced by an underestimated distance of up to 0.3 Å between the **DPAC** phenyl residue and the **OB** plane. Drawing on insights from projects on TBCT emitters (see Chapter 3), additional calculations were performed using a LR-corrected and a RSH density functional to evaluate their ability to accurately describe the key geometric parameters as well as absorption and emission behavior. It was found that including DFT-D3-BJ dispersion corrections, either explicitly or through the density functional, led to too strong intramolecular π - π -interactions (for geometric parameters, see **Publication VI**, Tables S2 and S3). Moreover, for absorption and emission properties computed with the DFT/MRCI method, no significant differences were observed for **DPACoOB** (for a comparison of absorption spectra, see **Publication VI**, Table S1 and Figure S1). Consequently, all final results were generated using the PBE0 functional without dispersion corrections.

For **conformer II**, the experimental spectrum is well reproduced, even though with a systematic hypsochromic shift of 0.10 – 0.15 eV compared to the experimental spectrum. In contrast, the agreement between calculation and experiment is hardly given for **conformer I**. Given the large ΔE between the ground-state conformers, any significant contribution from **conformer I** can be excluded.

The adiabatic excitation energies (see Figure 4.8) reveal a particularly interesting picture. Notably, three excited states, *i.e.*, S_{CT} , T_{CT} , and $T_{LE(A)}$, are relevant for accurately describing the excited-state decay pathway, as they are located within a small energy window, even at the ground-state geometry. For **conformer I**, the CT states are energetically more stable than those of **conformer II**, which contrasts with the energy ordering observed on the ground-state PES. Energetically lower-lying CT states could explain the experimentally observed bathochromically shifted emission at 298 K.

Fluorescence spectra were calculated for the emissive S_{CT} state at different temperatures in toluene and compared to experimental data [182] (see Figure 4.9). For **conformer II**, at 77 K, there is good agreement between the calculated ($\lambda_{max} = 414$ nm) and experimental ($\lambda_{max} = 422$ nm) spectra. At higher temperatures, the computed spectrum exhibits a bathochromic shift of 1113 cm^{-1} (0.14 eV), resulting in $\lambda_{max} = 434$ nm. In contrast, the experimental spectrum shows a significantly larger red-shift of 3078 cm^{-1} (0.38 eV) to $\lambda_{max} = 485$ nm. This discrepancy suggests that the observed shift cannot be attributed solely to the temperature effect caused by a change in the Boltzmann population of the vibrational levels. For **conformer I**, however, the calculated emission maximum at 298 K ($\lambda_{max} = 498$ nm) matches the experimental value well.

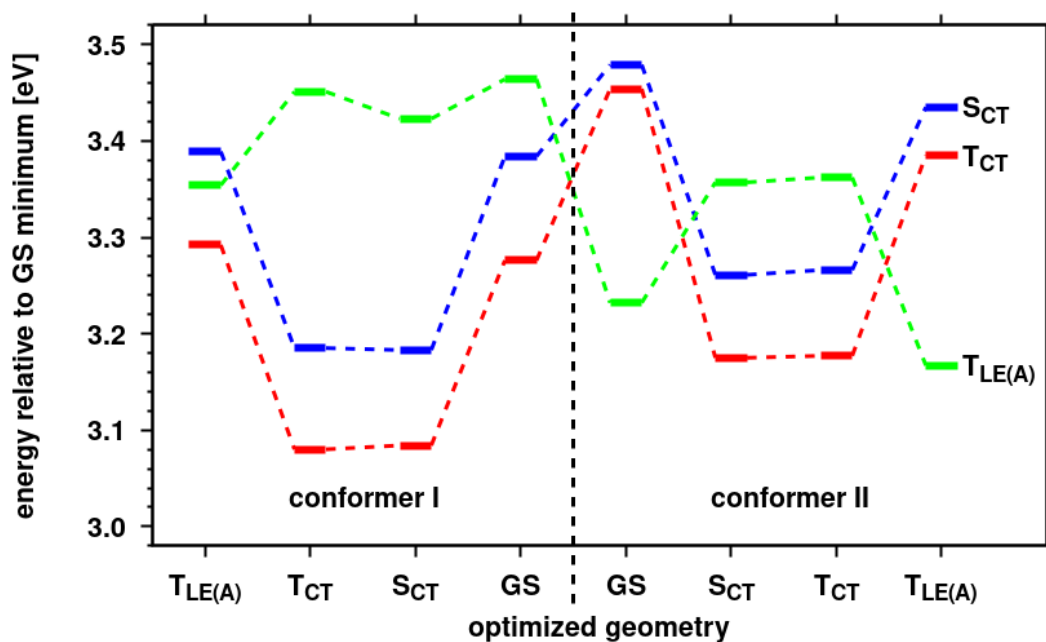


Figure 4.8: DFT/MRCI-R2016 energy level diagram showing vertical excitation energies at various optimized geometries. All energies are calculated relative to the most stable ground-state conformer **II**. The excited states are labelled as follows: S_{CT} blue, T_{CT} red, $T_{LE(A)}$ green.

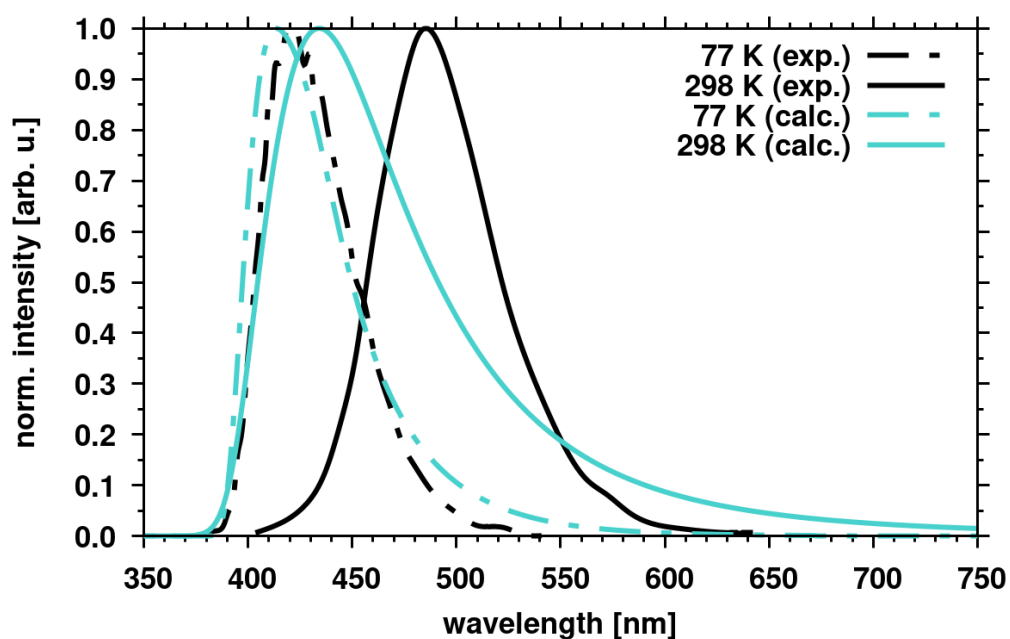


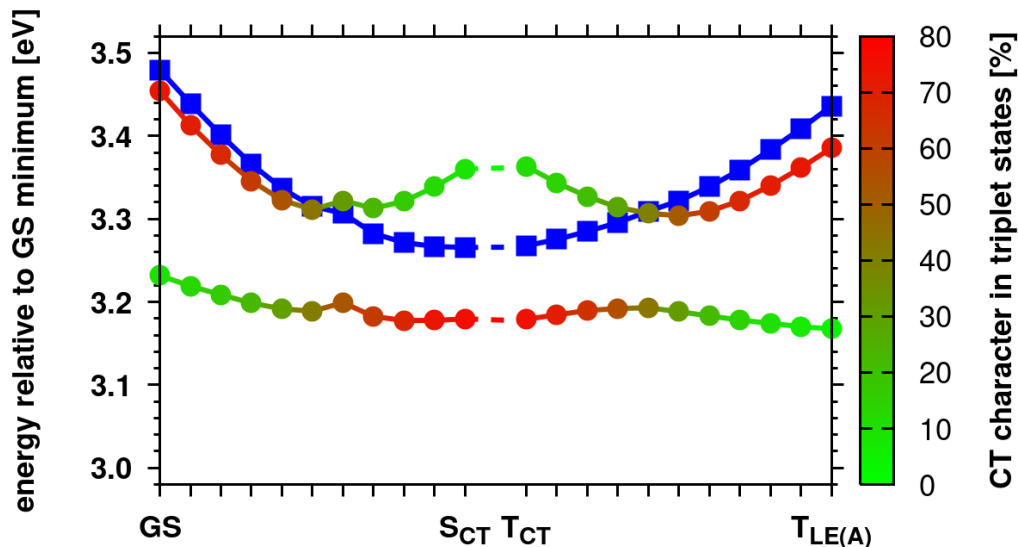
Figure 4.9: **DPACoOB, conformer II**: Calculated (turquoise) and experimental (black) emission spectra in toluene at 77 K (dashed lines) and 298 K (solid lines).

For **conformer I** to participate in the emission process, an efficient pathway must exist to transfer the excited-state population from **conformer II** to **conformer I**. To investigate this, Nudged Elastic Band (NEB) calculations were performed to estimate the energetic barriers associated with conformational interconversion. The results suggest that the energetic barriers on both the ground-state and S_{CT} state PESs are ranging between 0.40–0.60 eV (starting from the MEP minimum, see **Publication VI**, Figures S11 and S12). These values indicate that such transitions are relatively unlikely under typical experimental conditions. If not in the ground state and excited S_{CT} states, there could only be another transition occurring in higher-lying excited states. From an experimental perspective, no evidence supports this hypothesis. Therefore, it is reasonable to assume that **conformer I** coincidentally matches the experimental emission. Consequently, this suggests that **conformer I** plays any role in the excited-state decay mechanism, and it is thus excluded from further analysis. It can be assumed that the significant bathochromic shift of the emission is due to solvent relaxation in the excited state, a phenomenon that could not be calculated in the context of this study. Nevertheless, prior indications suggest that toluene behaves in a particularly complex manner. At 77 K, the agreement remains good as toluene is in its solid phase; in contrast, at 298 K, it is expected to adapt significantly to the conditions in the excited state.

4.2.2 Vibronic Effects on (Non-)Radiative Rate Constants

Geometry relaxation in the excited state places S_{CT} , T_{CT} , and $T_{LE(A)}$ in an energetic window of less than 100 meV, with the T_{CT} and $T_{LE(A)}$ states being almost degenerate. As shown in Section 4.1, the close energetic proximity of the LE and CT states, combined with potential vibronic interactions, plays a crucial role in the photophysical behavior [186]. This is further corroborated by analyzing the one-particle transition density matrices along linearly interpolated pathways (see Figure 4.10): during the absorption process, *i.e.*, going from the FC region to the S_{CT} optimized geometry, the electronic structure of the T_1 state changes gradually from a CT contribution of about 10% at the ground-state geometry to about 75% at the S_{CT} minimum geometry. In contrast, the S_1 state largely retains its CT character. Along this relaxation pathway, the S_1 and T_2 PESs intersect while T_1 and T_2 undergo an avoided crossing. We may therefore expect strong vibronic coupling between these states. A similar picture is observed along a linearly interpolated pathway connecting the T_{CT} and $T_{LE(A)}$ minima. In addition to angular motions of the π -stacked **DPAC** phenyl residue, C–C stretching modes in the **OB** acceptor are excited. The low-frequency vibrational modes promoting the non-adiabatic couplings are torsional and rocking motions of the **OB** acceptor as

well as a scissoring mode between the **DPAC** phenyl group and the acceptor moiety, similar to **TpAT-tFFO** (see Section 4.1).



Linearly interpolated pathways $\text{GS} \rightarrow \text{S}_{\text{CT}}$ and $\text{T}_{\text{CT}} \rightarrow \text{T}_{\text{LE(A)}}$

Figure 4.10: **DPACoOB**: Linearly interpolated pathways between the optimized ground-state and S_{CT} , as well as between the optimized T_{CT} and $\text{T}_{\text{LE(A)}}$ geometries (**conformer II**). DFT/MRCI-R2016 vertical energies of the relevant excited singlet (boxes) and triplet (circles) states relative to the ground-state minimum in eV. The S_1 state can be characterized along the pathways as S_{CT} state (blue), whereas the T_1 and T_2 states change their character according to TheoDORE analysis of the one-particle transition density matrices between T_{CT} (red) and $\text{T}_{\text{LE(A)}}$ (green).

Table 4.1: FC and FC+HT rate constants [s^{-1}] at 300 K for fluorescence (F), ISC, and rISC between low-lying singlet and triplet state minima of **DPACoOB** including SOC for conformer **II**.

Process	Transition	FC	FC+HT
F	$\text{S}_{\text{CT}} \rightarrow \text{S}_0$	5.2×10^6	5.4×10^6
ISC	$\text{S}_{\text{CT}} \rightsquigarrow \text{T}_{\text{CT}}$	3.8×10^4	3.0×10^6
ISC	$\text{S}_{\text{CT}} \rightsquigarrow \text{T}_{\text{LE(A)}}$	7.7×10^6	9.6×10^6
rISC	$\text{T}_{\text{CT}} \rightsquigarrow \text{S}_{\text{CT}}$	4.4×10^2	7.9×10^4
rISC	$\text{T}_{\text{LE(A)}} \rightsquigarrow \text{S}_{\text{CT}}$	1.3×10^4	7.6×10^4

The fluorescence rate constant (see Table 4.1) matches the expectations for a purely organic donor–acceptor system. Spin-vibronic interactions increase the rate constant

only marginally. The radiative lifetime of 185 ns, determined in HT approximation, agrees very well with the measured PF lifetime of 173.4 ns [182].

In contrast, for the $S_{CT} \leftrightarrow T_{CT}$ transitions, the inclusion of spin-vibronic interactions accelerates these ISC and rISC processes by up to two orders of magnitude (see Table 4.1), comparable to the observed impact in **TpAT-tFFO** (see Section 4.1). In HT approximation, the back-transfer of triplet excitons reaches a rate constant of 10^5 s^{-1} , providing an explanation for the experimentally observed DF. Component-averaged derivatives of the SOCMEs relative to nuclear displacements along all vibrational normal modes (see **Publication VI**, Figures S3–S8) identify high-frequency in-plane vibrations of the acceptor as the most prominent promoting modes of the $S_{CT} \leftrightarrow T_{CT}$ ISC and rISC processes. C–C stretching modes with harmonic frequencies around 1600 cm^{-1} accelerate the $S_{CT} \leftrightarrow T_{LE(A)}$ non-radiative processes.

As in the earlier presented studies, vibronic effects owing to low-frequency vibrations changing the donor–acceptor orientation, strongly coupled triplet states with CT and LE character and spin-vibronic effects through in-plane high-frequency vibrations localized on the acceptor were determined to be crucial in explaining the excited-state decay mechanisms of TSCT as well as TBCT emitters.

4.2.3 Chemical Modification of the Molecular Units in *ortho*- and *para*-appended systems

Donor, bridge, and acceptor units can be systematically modified to fine-tune the photophysical properties of the emitter molecule (see **Publication VI**, Figure 1).

In the *ortho*-regioisomer, **DPACoOB**, three distinct donor motifs, *i.e.*, **DPAC**, **DMAC**, and **DPA**, were investigated. **DPAC** and **DMAC** exhibit relatively rigid structures, whereas **DPA** is more flexible. Consequently, **DPAC** and **DPA** show π - π -interactions between the phenyl residue and the **OB** acceptor plane, while **DMAC**, lacking flexible phenyl groups, instead facilitates C–H- π -interactions. These π - π -interactions differ: in **DPAC**, the interacting phenyl group is electronically inert, whereas in **DPA**, it actively participates in the CT excitation.

These differences affect the adiabatic excitation energies (see **Publication VI**, Figure 8). As π - π -stacking increases from **DMAC** to **DPA/DPAC**, the $T_{LE(A)}$ state shifts slightly to higher energies. A comparison of **DPAC** and **DMAC** shows that the absence of π - π -interactions stabilizes the CT states in energy, consistent with the expected competing effects of charge transfer and π - π -interactions. **DPA** represents a special case, as its phenyl group is directly participating in the electronic transition, improving donor–acceptor communication and further stabilizing the CT states.

Based on the energetic ordering of the three excited states, **DMAC** is expected to exhibit the most favorable TADF performance, consistent with the experimentally observed higher ratio of DF to PF compared to **DPAC**, followed by **DPAC** and **DPA**.

In the *para*-regioisomer **DPACpOB**, the donor–acceptor orientation was initially expected to be easily manipulated through steric effects, as demonstrated for the **TAA-TPN** series (see Section 3.1). To investigate this, a systematic substitution on the phenylene bridge in *ortho*-position relative to the acceptor was performed using varying numbers of methyl groups, *i.e.*, **0-Me**, **1-Me** and **2-Me**. Since these methyl groups have no significant electronic effects, they serve as ideal probes for analyzing structural influences on the photophysical properties of the emitter.

In the **TAA-TPN** series, the donor and acceptor were directly connected. In contrast, in **DPACpOB**, the phenylene bridge linking the **DPAC** donor and **OB** acceptor is not part of the donor itself. As a result, substitution in the *ortho*-position relative to the bridge–acceptor linkage does not enforce a perpendicular donor–acceptor orientation with increasing steric demand. This effect is only observed when the bridge is part of the donor, directly linking both moieties. Surprisingly, at the optimized ground-state geometries, increasing steric hindrance instead reduces the dihedral angle between the donor and acceptor, bringing them closer to coplanarity (**0-Me**: $41^\circ \rightarrow$ **1-Me**: $15^\circ \rightarrow$ **2-Me**: 2°). Counterintuitively, while the adiabatic excitation energies of the CT states are modulated, the singlet–triplet gap remains unchanged. Only the position of the $T_{LE(A)}$ state remains stable, meaning that methyl substitution primarily adjusts the relative energies of the CT and LE states (see **Publication VI**, Figure 9).

5 Conclusion and Future Perspectives

This work was conducted within the framework of the ModISC research training group, with the goal of performing quantum chemical characterizations of existing TADF emitters to gain new insights for future emitter designs and computational evaluations, as well as contributing to the development of new efficient blue-light TADF emitters. Various factors influencing the ISC process have been systematically investigated, aiming to optimize and fine-tune the TADF efficiency.

Quantum chemical calculations are essential for estimating or explaining photo- and electrochemical properties. A common approach involves extracting general insights from calculations performed at the optimized ground-state geometry, *i.e.*, the determination of the singlet–triplet energy gap ΔE_{ST} . In contrast, this work emphasizes that more advanced quantum chemical calculations especially in the excited states often reveal the complexity of certain decay mechanisms.

First, the classical *para*-appended TBCT emitters were introduced, where communication is facilitated through π -conjugation. For this class of molecules, the choice of computational setup was critically evaluated, comparing the hybrid PBE0 and the RSH ω B97X-D density functionals to achieve the best balance between accuracy and computational cost. While PBE0 generally provides reliable results, the OT-RSH density functional ω B97X-D was chosen for the investigated TBCT molecules, as the results most accurately align with the experimentally observed vertical emission energies. Further validation of the optimized geometries was achieved through good agreement with ESA spectra, measured via time-resolved NIR spectroscopy. Relaxed scans along the ground- and excited-state PESs confirm the donor–acceptor torsion to be one of the most critical degrees of freedom influencing the photophysical properties. For the **TAA-TPN** series, the influence of an acceptor-localized triplet state, alongside the S_{CT} and T_{CT} states, could be observed for nearly perpendicular conformations. In addition, rotations along the donor–acceptor linkage introduce a dynamic nature of the excited-state decay mechanism. These findings demonstrate fast ISC/rISC processes for conformations near perpendicularity, whereas fluorescence is predominantly observed

for more planar conformations. Through targeted substitution in *ortho*-position of the donor–acceptor linkage, it was demonstrated that the TADF properties of the system can be effectively modulated and fine-tuned. Moreover, the results highlight a strong solvent dependence, observed both experimentally and theoretically. In particular, for quantum chemical simulations the commonly used solvent toluene poses a challenge, as it exerts a significant electrostatic influence in explicit considerations without directly participating in the molecular transitions. This was explicitly tested by including two toluene molecules in the QM region.

Chemical modifications were explored to optimize the TADF performance of the **TAA-TPN** series. The introduction of two methoxy groups enhanced the donor strength, lowering the CT energy and inducing a bathochromic shift in the emission wavelength. Extending the π -system facilitated stronger electronic communication between the donor and acceptor, resulting in a hybridized CT and LE S_1 state with significantly increased PLQY. In combination with a reduced acceptor strength by removing one cyano group, TADF was initially suppressed due to a large adiabatic ΔE_{ST} between the S_1 and T_1 states. Nonetheless, the T_2 state was found to be energetically degenerate with the S_1 state, offering an alternative pathway for efficient triplet back-transfer via a hot exciton mechanism. This beneficial effect could not be realized in the fabricated OLED device. The molecule remains a highly fluorescent emitter, which, when combined with other molecules via excitation energy transfer, can contribute to an efficient emission process. Investigations on pyridine acceptors revealed that TADF is unlikely due to a strongly energetically lowered triplet state, resulting in adiabatic singlet–triplet gaps of nearly 1 eV. Modifying the acceptor substituent to vary inductive and mesomeric effects led to the identification of two promising molecules, featuring **-CHO** and **-CN** groups. When these groups were attached in the *ortho*-position rather than the *para*-position relative to the donor–acceptor linkage, improved key parameters were observed.

Second, TSCT emitters were introduced, where communication occurs through space owing to the spatial proximity of the donor and acceptor units. This introduces different key degrees of freedom compared to TBCT emitters, such as the donor–acceptor distance and their tilt angle. Using two representative molecules, the highly efficient TADF emitter **TpAT-tFFO** and the boron-based **DPACoOB**, the necessity of accounting for spin-vibronic effects was emphasized. This was supported by the calculation of radiative and non-radiative rate constants within a HT-like framework, employing numerical gradients of SOC and TDM matrix elements along all vibrational normal modes. It was demonstrated that, beyond the commonly considered lowest-energy singlet and triplet CT states, LE states must be included in the excited-state decay mechanism. The near-degeneracy of S_{CT} , T_{CT} , and $T_{LE(A)}$ states creates conditions for near-barrierless rISC,

with the $T_{LE(A)}$ state providing a pathway to overcome the El-Sayed forbidden transition between the CT states to explain the experimentally observed TADF characteristics.

Two ground-state conformers of **TpAT-tFFO** were identified, along with singlet CT excited states corresponding to either the (Me→N) or (Me→Ph) conformer. The minimal energy difference between their optimized minima, combined with their interconvertibility in the ground state and a simultaneously high reorganization energy in the excited state, accounts for the observed dual PF characteristics. Nevertheless, almost the entire emission of **TpAT-tFFO** occurs via DF. A total of five electronically excited states were necessary to describe two efficient pathways following the excitation of the molecule: ${}^3CT \rightsquigarrow {}^3LE \rightsquigarrow {}^1CT$ and ${}^3CT' \rightsquigarrow {}^3LE \rightsquigarrow {}^1CT'$, with the 3LE state serving as a mediator for efficient upconversion of triplet population to the singlet manifold. While in-plane vibrational modes localized on the triazine acceptor moiety drive the spin-vibronic coupling, low-frequency vibrational modes that alter the donor–acceptor distance and tilt angle are crucial for inducing significant couplings between the excited states.

In the investigated boron-based emitter molecule **DPACoOB**, the experimental emission at room temperature exhibits a strong bathochromic shift compared to its maximum at 77 K. To explain this behavior, two conformers were found: **conformer I**, which aligns well with the emission at 298 K and **conformer II**, which aligns well with the emission at 77 K. Unlike in **TpAT-tFFO**, the interconversion in **DPACoOB** involves not only a phenyl rotation but also the inversion of the acridane core. Computed pathways on the singlet ground- and excited-state PES reveal high energy barriers, which, given the experimental conditions, are considered insurmountable. **Conformer II** accurately describes the excited-state decay pathway of **DPACoOB**, again involving an acceptor-localized triplet state as a mediator in the triplet-to-singlet upconversion process. Incorporating spin-vibronic effects successfully explains the experimentally observed TADF. In-plane vibrational normal modes localized on the acceptor moiety drive the spin-vibronic coupling, as evaluated from SOC gradients within an HT-like framework.

Finally, the systematic chemical modification of the donor, bridge, and acceptor demonstrates how CT and LE states can be fine-tuned relative to each other. In the *para*-regioisomer, **DPACpOB**, the substitutional effect differs from that observed in the **TAA-TPN** series. Here, the phenylene unit connecting the donor and acceptor is not part of the donor itself. As a result, substitution in the *ortho*-position relative to the bridge–acceptor linkage does not enforce a perpendicular orientation of donor and acceptor with increasing steric demand. This effect is only observed when the bridge is part of the donor, directly linking donor and acceptor.

5 Conclusion and Future Perspectives

TADF efficiency is governed by the nature and interplay of multiple excited states, where emitter design is able to realize the communication between these states. The design of TADF molecules always requires a compromise of many properties. Interruption of π -conjugation between donor and acceptor minimizes the mutual coupling of electron densities, thus minimizing the singlet–triplet energy gap and accelerating the rISC rate constant. Simultaneously, maintaining donor and acceptor close to each other prevents completely isolated systems which cannot communicate. In contrast, maximizing absorption and emission oscillator strength, connected to the radiative decay rate constant, and increase the PLQY requires the extension of the π -conjugated systems of donor and acceptor or some overlap of their electron densities.

In the future, exploring new mechanisms and expanding design principles will be crucial for advancing TADF and OLED research. TADF emitters in combination with fluorescent ones as hyperfluorescence systems (4th generation) presents a promising approach to further enhance efficiency and color purity. Alternative decay mechanisms such as in MR- and TTA-based systems are gaining significant attention in this field. However, the search for efficient blue emitters that can be seamlessly integrated into OLED devices remains a key challenge. Ultimately, the goal is to advance OLED technology to the point where efficient OLED devices become the standard choice for everyone in the future.

Bibliography

- [1] X. Cai and S.-J. Su, “Marching Toward Highly Efficient, Pure-Blue, and Stable Thermally Activated Delayed Fluorescent Organic Light-Emitting Diodes,” *Adv. Func. Mater.*, vol. 28, no. 43, p. 1802558, 2018.
- [2] Mordor Intelligence Research and Advisory, “Analyse der Marktgröße und des Marktanteils von OLED-Panels – Wachstumstrends und Prognosen (2024 – 2029),” 2023. <https://www.mordorintelligence.com/de/industry-reports/oled-panel-market> [Accessed: (08.01.2025)].
- [3] E. Tankelevičiūtė, I. D. Samuel, and E. Zysman-Colman, “The Blue Problem: OLED Stability and Degradation Mechanisms,” *J. Phys. Chem. Lett.*, vol. 15, no. 4, pp. 1034–1047, 2024.
- [4] A. Monkman, “Why Do We Still Need a Stable Long Lifetime Deep Blue OLED Emitter?,” *ACS Appl. Mater. Interfaces*, vol. 14, no. 18, pp. 20463–20467, 2022.
- [5] G. Hong, X. Gan, C. Leonhardt, Z. Zhang, J. Seibert, J. M. Busch, and S. Bräse, “A Brief History of OLEDs—Emitter Development and Industry Milestones,” *Adv. Mater.*, vol. 33, no. 9, p. 2005630, 2021.
- [6] W. Brütting, J. Frischeisen, T. D. Schmidt, B. J. Scholz, and C. Mayr, “Device efficiency of organic light-emitting diodes: Progress by improved light outcoupling,” *Phys. Status Solidi A*, vol. 210, no. 1, pp. 44–65, 2013.
- [7] R. Meerheim, M. Furno, S. Hofmann, B. Lüssem, and K. Leo, “Quantification of energy loss mechanisms in organic light-emitting diodes,” *Appl. Phys. Lett.*, vol. 97, no. 25, p. 253305, 2010.
- [8] M. C. Gather and S. Reineke, “Recent advances in light outcoupling from white organic light-emitting diodes,” *J. Photon. Energy*, vol. 5, no. 1, p. 057607, 2015.
- [9] F. Hinderer, *Auswahlregeln*, pp. 11–18. Wiesbaden: Springer Fachmedien Wiesbaden, 2020.

- [10] C. Adachi and A. S. Sandanayaka, “The Leap from Organic Light-Emitting Diodes to Organic Semiconductor Laser Diodes,” *CCS Chem.*, vol. 2, no. 4, pp. 1203–1216, 2020.
- [11] T. J. Penfold, “On Predicting the Excited-State Properties of Thermally Activated Delayed Fluorescence Emitters,” *J. Phys. Chem. C*, vol. 119, no. 24, pp. 13535–13544, 2015.
- [12] M. Pope, H. P. Kallmann, and P. Magnante, “Electroluminescence in Organic Crystals,” *J. Chem. Phys.*, vol. 38, no. 8, pp. 2042–2043, 1963.
- [13] C. W. Tang and S. A. VanSlyke, “Organic electroluminescent diodes,” *Appl. Phys. Lett.*, vol. 51, no. 12, pp. 913–915, 1987.
- [14] Y. Ma, H. Zhang, J. Shen, and C. Che, “Electroluminescence from triplet metal—ligand charge-transfer excited state of transition metal complexes,” *Synth. Met.*, vol. 94, no. 3, pp. 245–248, 1998.
- [15] M. Baldo, D. O’Brien, Y. You, A. Shoustikov, S. Sibley, M. Thompson, and S. Forrest, “Highly efficient phosphorescent emission from organic electroluminescent devices,” *Nature*, vol. 395, no. 6698, pp. 151–154, 1998.
- [16] M. Baldo, S. Lamansky, P. Burrows, M. Thompson, and S. Forrest, “Very high-efficiency green organic light-emitting devices based on electrophosphorescence,” *Appl. Phys. Lett.*, vol. 75, no. 1, pp. 4–6, 1999.
- [17] C. Adachi, M. A. Baldo, M. E. Thompson, and S. R. Forrest, “Nearly 100% internal phosphorescence efficiency in an organic light-emitting device,” *J. Appl. Phys.*, vol. 90, no. 10, pp. 5048–5051, 2001.
- [18] H. Nakanotani, T. Higuchi, T. Furukawa, K. Masui, K. Morimoto, M. Numata, H. Tanaka, Y. Sagara, T. Yasuda, and C. Adachi, “High-efficiency organic light-emitting diodes with fluorescent emitters,” *Nat. Commun.*, vol. 5, no. 1, p. 4016, 2014.
- [19] H. Uoyama, K. Goushi, K. Shizu, H. Nomura, and C. Adachi, “Highly efficient organic light-emitting diodes from delayed fluorescence,” *Nature*, vol. 492, no. 7428, pp. 234–238, 2012.
- [20] C. Parker and C. Hatchard, “Triplet-singlet emission in fluid solutions. Phosphorescence of eosin,” *Trans. Faraday Soc.*, vol. 57, pp. 1894–1904, 1961.

- [21] J. M. Dos Santos, D. Hall, B. Basumatary, M. Bryden, D. Chen, P. Choudhary, T. Comerford, E. Crovini, A. Danos, J. De, S. Diesing, M. Fatahi, M. Griffin, A. K. Gupta, H. Hafeez, L. Hämmerling, E. Hanover, J. Haug, T. Heil, D. Karthik, S. Kumar, O. Lee, H. Li, F. Lucas, C. F. R. Mackenzie, A. Mariko, T. Matulaitis, F. Millward, Y. Olivier, Q. Qi, I. D. W. Samuel, N. Sharma, C. Si, L. Spierling, P. Sudhakar, D. Sun, E. Tankelevičiūtė, M. Duarte Tonet, J. Wang, T. Wang, S. Wu, Y. Xu, L. Zhang, and E. Zysman-Colman, “The Golden Age of Thermally Activated Delayed Fluorescence Materials: Design and Exploitation,” *Chem. Rev.*, vol. 124, no. 24, pp. 13736–14110, 2024.
- [22] M. K. Etherington, J. Gibson, H. F. Higginbotham, T. J. Penfold, and A. P. Monkman, “Revealing the spin–vibronic coupling mechanism of thermally activated delayed fluorescence,” *Nat. Commun.*, vol. 7, no. 1, p. 13680, 2016.
- [23] J. Gibson, A. P. Monkman, and T. J. Penfold, “The Importance of Vibronic Coupling for Efficient Reverse Intersystem Crossing in Thermally Activated Delayed Fluorescence Molecules,” *ChemPhysChem*, vol. 17, no. 19, pp. 2956–2961, 2016.
- [24] T. J. Penfold, E. Gindensperger, C. Daniel, and C. M. Marian, “Spin-Vibronic Mechanism for Intersystem Crossing,” *Chem. Rev.*, vol. 118, no. 15, pp. 6975–7025, 2018.
- [25] K. A. Thom, F. Wieser, K. Diestelhorst, A. Reiffers, C. Czekelius, M. Kleinschmidt, M. Bracker, C. M. Marian, and P. Gilch, “Acridones: Strongly Emissive HIGHrISC Fluorophores,” *J. Phys. Chem. Lett.*, vol. 12, no. 24, pp. 5703–5709, 2021.
- [26] I. Bala, R. A. K. Yadav, M. Devi, J. De, N. Singh, K. Kailasam, J. Jayakumar, J.-H. Jou, C.-H. Cheng, and S. K. Pal, “High-performing D– π –A– π –D benzothiadiazole-based hybrid local and charge-transfer emitters in solution-processed OLEDs,” *J. Mater. Chem. C*, vol. 8, no. 47, pp. 17009–17015, 2020.
- [27] Y. Xu, P. Xu, D. Hu, and Y. Ma, “Recent progress in hot exciton materials for organic light-emitting diodes,” *Chem. Soc. Rev.*, vol. 50, no. 2, pp. 1030–1069, 2021.
- [28] M. Bracker, M. K. Kubitz, C. Czekelius, C. M. Marian, and M. Kleinschmidt, “Computer-Aided Design of Fluorinated Flavin Derivatives by Modulation of Intersystem Crossing and Fluorescence,” *ChemPhotoChem*, vol. 6, no. 7, p. e202200040, 2022.

- [29] M. K. Kubitz, W. Haselbach, D. Sretenović, M. Bracker, M. Kleinschmidt, R. Kühnemuth, C. A. Seidel, P. Gilch, and C. Czekelius, “Increasing the Fluorescence Quantum Yield and Lifetime of the Flavin Chromophore by Rational Design,” *ChemPhotoChem*, vol. 7, no. 7, p. e202200334, 2023.
- [30] D. A. Phan Huu, S. Saseendran, R. Dhali, L. G. Franca, K. Stavrou, A. Monkman, and A. Painelli, “Thermally activated delayed fluorescence: polarity, rigidity, and disorder in condensed phases,” *J. Am. Chem. Soc.*, vol. 144, no. 33, pp. 15211–15222, 2022.
- [31] K. Stavrou, L. G. Franca, T. Böhmer, L. M. Duben, C. M. Marian, and A. P. Monkman, “Unexpected Quasi-Axial Conformer in Thermally Activated Delayed Fluorescence DMAC-TRZ, Pushing Green OLEDs to Blue,” *Adv. Func. Mater.*, vol. 33, no. 25, p. 2300910, 2023.
- [32] P. Li, W. Li, Y. Zhang, P. Zhang, X. Wang, C. Yin, and R. Chen, “Recent Progress of Thermally Activated Delayed Fluorescent Materials with Narrowband Red, Green, and Blue (RGB) Emission,” *ACS Mater. Lett.*, vol. 6, no. 5, pp. 1746–1768, 2024.
- [33] Y. Im, M. Kim, Y. J. Cho, J.-A. Seo, K. S. Yook, and J. Y. Lee, “Molecular Design Strategy of Organic Thermally Activated Delayed Fluorescence Emitters,” *Chem. Mater.*, vol. 29, no. 5, pp. 1946–1963, 2017.
- [34] T.-T. Bui, F. Goubard, M. Ibrahim-Ouali, D. Gigmes, and F. Dumur, “Recent advances on organic blue thermally activated delayed fluorescence (TADF) emitters for organic light-emitting diodes (OLEDs),” *Beilstein J. Org. Chem.*, vol. 14, no. 1, pp. 282–308, 2018.
- [35] L. E. de Sousa, L. dos Santos Born, P. H. de Oliveira Neto, and P. de Silva, “Triplet-to-singlet exciton transfer in hyperfluorescent OLED materials,” *J. Mater. Chem. C*, vol. 10, no. 12, pp. 4914–4922, 2022.
- [36] J. Adachi, H. Kakizoe, P. K. D. Tsang, and A. Endo, “10.1: Invited Paper: Hyperfluorescence™; a Game Changing Technology of OLED Display,” *SID Int. Symp. Dig. Tech. Pap.*, vol. 50, no. S1, pp. 95–98, 2019.
- [37] D. Y. Kondakov, “Triplet–triplet annihilation in highly efficient fluorescent organic light-emitting diodes: current state and future outlook,” *Philos. Trans. R. Soc. A*, vol. 373, no. 2044, p. 20140321, 2015.

- [38] A. Dreuw and M. Hoffmann, “The inverted singlet–triplet gap: a vanishing myth?,” *Front. Chem.*, vol. 11, p. 1239604, 2023.
- [39] N. Aizawa, Y.-J. Pu, Y. Harabuchi, A. Nihonyanagi, R. Ibuka, H. Inuzuka, B. Dhara, Y. Koyama, K.-i. Nakayama, S. Maeda, *et al.*, “Delayed fluorescence from inverted singlet and triplet excited states,” *Nature*, vol. 609, no. 7927, pp. 502–506, 2022.
- [40] F. Dinkelbach, M. Bracker, M. Kleinschmidt, and C. M. Marian, “Large Inverted Singlet–Triplet Energy Gaps Are Not Always Favorable for Triplet Harvesting: Vibronic Coupling Drives the (Reverse) Intersystem Crossing in Heptazine Derivatives,” *J. Phys. Chem. A*, vol. 125, no. 46, pp. 10044–10051, 2021.
- [41] T. Hatakeyama, K. Shiren, K. Nakajima, S. Nomura, S. Nakatsuka, K. Kinoshita, J. Ni, Y. Ono, and T. Ikuta, “Ultrapure Blue Thermally Activated Delayed Fluorescence Molecules: Efficient HOMO-LUMO Separation by the Multiple Resonance Effect,” *Adv. Mater.*, vol. 28, no. 14, pp. 2777–2781, 2016.
- [42] A. Dreuw and M. Head-Gordon, “Single-Reference ab Initio Methods for the Calculation of Excited States of Large Molecules,” *Chem. Rev.*, vol. 105, no. 11, pp. 4009–4037, 2005.
- [43] L. H. Thomas, “The calculation of atomic fields,” *Math. Proc. Camb. Phil. Soc.*, vol. 23, no. 5, pp. 542–548, 1927.
- [44] E. Fermi, “Eine statistische Methode zur Bestimmung einiger Eigenschaften des Atoms und ihre Anwendung auf die Theorie des periodischen Systems der Elemente,” *Zeitschrift für Physik*, vol. 48, no. 1, pp. 73–79, 1928.
- [45] P. Hohenberg and W. Kohn, “Inhomogeneous Electron Gas,” *Phys. Rev.*, vol. 136, no. 3B, pp. B864–B871, 1964.
- [46] W. Kohn and L. J. Sham, “Self-Consistent Equations Including Exchange and Correlation Effects,” *Phys. Rev.*, vol. 140, no. 4A, pp. A1133–A1138, 1965.
- [47] R. G. Parr, “Density Functional Theory,” *Annu. Rev. Phys. Chem.*, vol. 34, no. 1, pp. 631–656, 1983.
- [48] F. Nogueira, A. Castro, and M. A. L. Marques, *A Tutorial on Density Functional Theory*, pp. 218–256. Springer Berlin Heidelberg, 2003.
- [49] M. A. L. Marques and E. K. U. Gross, *Time-Dependent Density Functional Theory*, pp. 144–184. Springer Berlin Heidelberg, 2003.

- [50] W. Kohn, A. D. Becke, and R. G. Parr, “Density Functional Theory of Electronic Structure,” *J. Phys. Chem.*, vol. 100, no. 31, pp. 12974–12980, 1996.
- [51] N. T. Maitra, “Double and Charge-Transfer Excitations in Time-Dependent Density Functional Theory,” *Annu. Rev. Phys. Chem.*, vol. 73, no. 1, pp. 117–140, 2022.
- [52] B. Kalita, L. Li, R. J. McCarty, and K. Burke, “Learning to Approximate Density Functionals,” *Acc. Chem. Res.*, vol. 54, no. 4, pp. 818–826, 2021.
- [53] E. Runge and E. K. Gross, “Density-Functional Theory for Time-Dependent Systems,” *Phys. Rev. Lett.*, vol. 52, no. 12, pp. 997–1000, 1984.
- [54] R. Van Leeuwen, “Causality and Symmetry in Time-Dependent Density-Functional Theory,” *Phys. Rev. Lett.*, vol. 80, no. 6, pp. 1280–1283, 1998.
- [55] S. Hirata and M. Head-Gordon, “Time-dependent density functional theory within the Tamm–Dancoff approximation,” *Chem. Phys. Lett.*, vol. 314, no. 3-4, pp. 291–299, 1999.
- [56] F. Furche and R. Ahlrichs, “Adiabatic time-dependent density functional methods for excited state properties,” *J. Chem. Phys.*, vol. 117, no. 16, pp. 7433–7447, 2002.
- [57] M. E. Casida, “Time-dependent density-functional theory for molecules and molecular solids,” *J. Mol. Struct.: THEOCHEM*, vol. 914, no. 1-3, pp. 3–18, 2009.
- [58] D. J. Tozer, “Relationship between long-range charge-transfer excitation energy error and integer discontinuity in Kohn–Sham theory,” *J. Chem. Phys.*, vol. 119, no. 24, pp. 12697–12699, 2003.
- [59] A. Dreuw and M. Head-Gordon, “Failure of Time-Dependent Density Functional Theory for Long-Range Charge-Transfer Excited States: The Zincbacteriochlorin–Bacteriochlorin and Bacteriochlorophyll–Spheroidene Complexes,” *J. Am. Chem. Soc.*, vol. 126, no. 12, pp. 4007–4016, 2004.
- [60] N. Mardirossian and M. Head-Gordon, “Thirty years of density functional theory in computational chemistry: an overview and extensive assessment of 200 density functionals,” *Mol. Phys.*, vol. 115, no. 19, pp. 2315–2372, 2017.
- [61] J. P. Perdew, K. Burke, and M. Ernzerhof, “Generalized Gradient Approximation Made Simple,” *Phys. Rev. Lett.*, vol. 77, no. 18, pp. 3865–3868, 1996.

- [62] S. Grimme, "Semiempirical GGA-type density functional constructed with a long-range dispersion correction," *J. Comput. Chem.*, vol. 27, no. 15, pp. 1787–1799, 2006.
- [63] J. P. Zobel, A. Kruse, O. Baig, S. Lochbrunner, S. I. Bokarev, O. Kühn, L. González, and O. S. Bokareva, "Can range-separated functionals be optimally tuned to predict spectra and excited state dynamics in photoactive iron complexes?," *Chem. Sci.*, vol. 14, no. 6, pp. 1491–1502, 2023.
- [64] C. Wang and Q. Zhang, "Understanding Solid-State Solvation-Enhanced Thermally Activated Delayed Fluorescence Using a Descriptor-Tuned Screened Range-Separated Functional," *J. Phys. Chem. C*, vol. 123, no. 7, pp. 4407–4416, 2018.
- [65] C. Adamo and V. Barone, "Toward reliable density functional methods without adjustable parameters: The PBE0 model," *J. Chem. Phys.*, vol. 110, no. 13, pp. 6158–6170, 1999.
- [66] A. D. Becke, "A new mixing of Hartree–Fock and local density-functional theories," *J. Chem. Phys.*, vol. 98, no. 2, pp. 1372–1377, 1993.
- [67] C. Lee, W. Yang, and R. G. Parr, "Development of the Colle-Salvetti correlation-energy formula into a functional of the electron density," *Phys. Rev. B*, vol. 37, no. 2, pp. 785–789, 1988.
- [68] A. D. Becke, "Density-functional thermochemistry. III. The role of exact exchange," *J. Chem. Phys.*, vol. 98, no. 7, pp. 5648–5652, 1993.
- [69] S. H. Vosko, L. Wilk, and M. Nusair, "Accurate spin-dependent electron liquid correlation energies for local spin density calculations: a critical analysis," *Can. J. Phys.*, vol. 58, no. 8, pp. 1200–1211, 1980.
- [70] P. J. Stephens, F. J. Devlin, C. F. Chabalowski, and M. J. Frisch, "Ab Initio Calculation of Vibrational Absorption and Circular Dichroism Spectra Using Density Functional Force Fields," *J. Phys. Chem.*, vol. 98, no. 45, pp. 11623–11627, 1994.
- [71] H. Iikura, T. Tsuneda, T. Yanai, and K. Hirao, "A long-range correction scheme for generalized-gradient-approximation exchange functionals," *J. Chem. Phys.*, vol. 115, no. 8, pp. 3540–3544, 2001.

- [72] J. Toulouse, F. Colonna, and A. Savin, “Long-range–short-range separation of the electron-electron interaction in density-functional theory,” *Phys. Rev. A*, vol. 70, no. 6, p. 062505, 2004.
- [73] É. Brémond, Á. J. Pérez-Jiménez, J. C. Sancho-García, and C. Adamo, “Range-separated hybrid density functionals made simple,” *J. Chem. Phys.*, vol. 150, no. 20, p. 201102, 2019.
- [74] J. P. Dombroski, S. W. Taylor, and P. M. Gill, “KWIK: Coulomb Energies in O(N) Work,” *J. Phys. Chem.*, vol. 100, no. 15, pp. 6272–6276, 1996.
- [75] O. A. Vydrov and G. E. Scuseria, “Assessment of a long-range corrected hybrid functional,” *J. Chem. Phys.*, vol. 125, no. 23, p. 234109, 2006.
- [76] C. A. Ullrich, *Time-Dependent Density-Functional Theory: Concepts and Applications*. OUP Oxford, 2011.
- [77] D. Jacquemin, B. Moore, A. Planchat, C. Adamo, and J. Autschbach, “Performance of an Optimally Tuned Range-Separated Hybrid Functional for 0–0 Electronic Excitation Energies,” *J. Chem. Theory Comput.*, vol. 10, no. 4, pp. 1677–1685, 2014.
- [78] R. Baer, E. Livshits, and U. Salzner, “Tuned Range-Separated Hybrids in Density Functional Theory,” *Annu. Rev. Phys. Chem.*, vol. 61, no. 1, pp. 85–109, 2010.
- [79] L. Kronik, T. Stein, S. Refaely-Abramson, and R. Baer, “Excitation Gaps of Finite-Sized Systems from Optimally Tuned Range-Separated Hybrid Functionals,” *J. Chem. Theory Comput.*, vol. 8, no. 5, pp. 1515–1531, 2012.
- [80] J.-D. Chai and M. Head-Gordon, “Systematic optimization of long-range corrected hybrid density functionals,” *J. Chem. Phys.*, vol. 128, no. 8, p. 084106, 2008.
- [81] L. Kronik and S. Kümmel, “Dielectric Screening Meets Optimally Tuned Density Functionals,” *Adv. Mater.*, vol. 30, no. 41, p. 1706560, 2018.
- [82] T. Froitzheim, S. Grimme, and J.-M. Mewes, “Either Accurate Singlet–Triplet Gaps or Excited-State Structures: Testing and Understanding the Performance of TD-DFT for TADF Emitters,” *J. Chem. Theory Comput.*, vol. 18, no. 12, pp. 7702–7713, 2022.
- [83] O. S. Bokareva, G. Grell, S. I. Bokarev, and O. Kühn, “Tuning Range-Separated Density Functional Theory for Photocatalytic Water Splitting Systems,” *J. Chem. Theory Comput.*, vol. 11, no. 4, pp. 1700–1709, 2015.

- [84] T. B. de Queiroz and S. Kümmel, “Charge-transfer excitations in low-gap systems under the influence of solvation and conformational disorder: Exploring range-separation tuning,” *J. Chem. Phys.*, vol. 141, no. 8, p. 084303, 2014.
- [85] S. Grimme and M. Waletzke, “A combination of Kohn–Sham density functional theory and multi-reference configuration interaction methods,” *J. Chem. Phys.*, vol. 111, no. 13, pp. 5645–5655, 1999.
- [86] R. W. Wetmore and G. A. Segal, “Efficient generation of configuration interaction matrix elements,” *Chem. Phys. Lett.*, vol. 36, no. 4, pp. 478–483, 1975.
- [87] G. A. Segal, R. W. Wetmore, and K. Wolf, “Efficient methods for configuration interaction calculations,” *Chem. Phys.*, vol. 30, no. 2, pp. 269–297, 1978.
- [88] I. Lyskov, M. Kleinschmidt, and C. M. Marian, “Redesign of the DFT/MRCI Hamiltonian,” *J. Chem. Phys.*, vol. 144, no. 3, p. 034104, 2016.
- [89] C. M. Marian, A. Heil, and M. Kleinschmidt, “The DFT/MRCI method,” *WIREs Comput. Mol. Sci.*, vol. 9, p. e1394, 2019.
- [90] D. R. Dombrowski, T. Schulz, M. Kleinschmidt, and C. M. Marian, “R2022: A DFT/MRCI Ansatz with Improved Performance for Double Excitations,” *J. Phys. Chem. A*, vol. 127, no. 8, pp. 2011–2025, 2023.
- [91] D. G. Truhlar, “Dispersion Forces: Neither Fluctuating Nor Dispersing,” *J. Chem. Educ.*, vol. 96, no. 8, pp. 1671–1675, 2019.
- [92] S. Grimme, “Accurate description of van der Waals complexes by density functional theory including empirical corrections,” *J. Comput. Chem.*, vol. 25, no. 12, pp. 1463–1473, 2004.
- [93] S. Grimme, J. Antony, S. Ehrlich, and H. Krieg, “A consistent and accurate ab initio parametrization of density functional dispersion correction (DFT-D) for the 94 elements H–Pu,” *J. Chem. Phys.*, vol. 132, no. 15, p. 154104, 2010.
- [94] S. Grimme, S. Ehrlich, and L. Goerigk, “Effect of the damping function in dispersion corrected density functional theory,” *J. Comput. Chem.*, vol. 32, no. 7, pp. 1456–1465, 2011.
- [95] S. Grimme, “Density functional theory with London dispersion corrections,” *WIREs Comput. Mol. Sci.*, vol. 1, no. 2, pp. 211–228, 2011.

- [96] J. Tomasi, B. Mennucci, and R. Cammi, "Quantum Mechanical Continuum Solvation Models," *Chem. Rev.*, vol. 105, no. 8, pp. 2999–3094, 2005.
- [97] J. Pascual-Ahuir, E. Silla, J. Tomasi, and R. Bonaccorsi, "Electrostatic interaction of a solute with a continuum. Improved description of the cavity and of the surface cavity bound charge distribution," *J. Comput. Chem.*, vol. 8, no. 6, pp. 778–787, 1987.
- [98] J.-L. Pascual-Ahuir, E. Silla, and I. Tunon, "GEPOL: An improved description of molecular surfaces. III. A new algorithm for the computation of a solvent-excluding surface," *J. Comput. Chem.*, vol. 15, no. 10, pp. 1127–1138, 1994.
- [99] V. Barone, M. Cossi, and J. Tomasi, "Geometry optimization of molecular structures in solution by the polarizable continuum model," *J. Comput. Chem.*, vol. 19, no. 4, pp. 404–417, 1998.
- [100] E. Cancès, B. Mennucci, and J. Tomasi, "A new integral equation formalism for the polarizable continuum model: Theoretical background and applications to isotropic and anisotropic dielectrics," *J. Chem. Phys.*, vol. 107, no. 8, pp. 3032–3041, 1997.
- [101] J. Tomasi, B. Mennucci, and E. Cancès, "The IEF version of the PCM solvation method: an overview of a new method addressed to study molecular solutes at the QM ab initio level," *J. Mol. Struct.: THEOCHEM*, vol. 464, no. 1-3, pp. 211–226, 1999.
- [102] B. Mennucci and J. Tomasi, "Continuum solvation models: A new approach to the problem of solute's charge distribution and cavity boundaries," *J. Chem. Phys.*, vol. 106, no. 12, pp. 5151–5158, 1997.
- [103] G. Scalmani and M. J. Frisch, "Continuous surface charge polarizable continuum models of solvation. I. General formalism," *J. Chem. Phys.*, vol. 132, no. 11, p. 114110, 2010.
- [104] M. Cossi and V. Barone, "Solvent effect on vertical electronic transitions by the polarizable continuum model," *J. Chem. Phys.*, vol. 112, no. 5, pp. 2427–2435, 2000.
- [105] C. A. Guido, D. Jacquemin, C. Adamo, and B. Mennucci, "Electronic Excitations in Solution: The Interplay between State Specific Approaches and a Time-Dependent Density Functional Theory Description," *J. Chem. Theory Comput.*, vol. 11, no. 12, pp. 5782–5790, 2015.

- [106] A. V. Marenich, C. J. Cramer, D. G. Truhlar, C. A. Guido, B. Mennucci, G. Scalmani, and M. J. Frisch, "Practical computation of electronic excitation in solution: vertical excitation model," *Chem. Sci.*, vol. 2, no. 11, pp. 2143–2161, 2011.
- [107] R. Improta, V. Barone, G. Scalmani, and M. J. Frisch, "A state-specific polarizable continuum model time dependent density functional theory method for excited state calculations in solution," *J. Chem. Phys.*, vol. 125, no. 5, p. 054103, 2006.
- [108] C. A. Guido, A. Chrayteh, G. Scalmani, B. Mennucci, and D. Jacquemin, "Simple Protocol for Capturing Both Linear-Response and State-Specific Effects in Excited-State Calculations with Continuum Solvation Models," *J. Chem. Theory Comput.*, vol. 17, no. 8, pp. 5155–5164, 2021.
- [109] J.-M. Mewes, "Modeling TADF in organic emitters requires a careful consideration of the environment and going beyond the Franck–Condon approximation," *Phys. Chem. Chem. Phys.*, vol. 20, no. 18, pp. 12454–12469, 2018.
- [110] L. Kunze, A. Hansen, S. Grimme, and J.-M. Mewes, "PCM-ROKS for the Description of Charge-Transfer States in Solution: Singlet–Triplet Gaps with Chemical Accuracy from Open-Shell Kohn–Sham Reaction-Field Calculations," *J. Phys. Chem. Lett.*, vol. 12, no. 35, pp. 8470–8480, 2021.
- [111] S. Tsuzuki, K. Honda, T. Uchimaru, M. Mikami, and K. Tanabe, "Origin of Attraction and Directionality of the π - π Interaction: Model Chemistry Calculations of Benzene Dimer Interaction," *J. Am. Chem. Soc.*, vol. 124, no. 1, pp. 104–112, 2002.
- [112] P. Pracht, F. Bohle, and S. Grimme, "Automated exploration of the low-energy chemical space with fast quantum chemical methods," *Phys. Chem. Chem. Phys.*, vol. 22, no. 14, pp. 7169–7192, 2020.
- [113] S. Spicher, C. Plett, P. Pracht, A. Hansen, and S. Grimme, "Automated Molecular Cluster Growing for Explicit Solvation by Efficient Force Field and Tight Binding Methods," *J. Chem. Theory Comput.*, vol. 18, no. 5, pp. 3174–3189, 2022.
- [114] G. Groenhof, *Introduction to QM/MM Simulations*, pp. 43–66. Totowa, NJ: Humana Press, 2013.
- [115] S. Banerjee, A. Baiardi, J. Bloino, and V. Barone, "Temperature Dependence of Radiative and Nonradiative Rates from Time-Dependent Correlation Function Methods," *J. Chem. Theory Comput.*, vol. 12, no. 2, pp. 774–786, 2016.

- [116] R. Englman and J. Jortner, "The energy gap law for radiationless transitions in large molecules," *Mol. Phys.*, vol. 18, no. 2, pp. 145–164, 1970.
- [117] C. M. Marian, "Understanding and Controlling Intersystem Crossing in Molecules," *Annu. Rev. Phys. Chem.*, vol. 72, no. 1, pp. 617–640, 2021.
- [118] M. Kasha, "Characterization of electronic transitions in complex molecules," *Discuss. Faraday Soc.*, vol. 9, pp. 14–19, 1950.
- [119] A. P. Demchenko, V. I. Tomin, and P.-T. Chou, "Breaking the Kasha Rule for More Efficient Photochemistry," *Chem. Rev.*, vol. 117, no. 21, pp. 13353–13381, 2017.
- [120] S. Strickler and R. A. Berg, "Relationship between Absorption Intensity and Fluorescence Lifetime of Molecules," *J. Chem. Phys.*, vol. 37, no. 4, pp. 814–822, 1962.
- [121] M. Etinski, J. Tatchen, and C. M. Marian, "Time-dependent approaches for the calculation of intersystem crossing rates," *J. Chem. Phys.*, vol. 134, no. 15, p. 154105, 2011.
- [122] M. Etinski, J. Tatchen, and C. M. Marian, "Thermal and solvent effects on the triplet formation in cinnoline," *Phys. Chem. Chem. Phys.*, vol. 16, no. 10, pp. 4740–4751, 2014.
- [123] M. Etinski, V. Rai-Constapel, and C. M. Marian, "Time-dependent approach to spin-vibronic coupling: Implementation and assessment," *J. Chem. Phys.*, vol. 140, no. 11, p. 114104, 2014.
- [124] A. Manian, R. Shaw, I. Lyskov, W. Wong, and S. Russo, "Modeling radiative and non-radiative pathways at both the Franck–Condon and Herzberg–Teller approximation level," *J. Chem. Phys.*, vol. 155, no. 5, p. 054108, 2021.
- [125] M. El-Sayed, "The Radiationless Processes Involving Change of Multiplicity in the Diazenes," *J. Chem. Phys.*, vol. 36, no. 2, pp. 573–574, 1962.
- [126] M. El-Sayed, "Spin–Orbit Coupling and the Radiationless Processes in Nitrogen Heterocyclics," *J. Chem. Phys.*, vol. 38, no. 12, pp. 2834–2838, 1963.
- [127] C. M. Marian, "Spin–orbit coupling and intersystem crossing in molecules," *WIREs Comput. Mol. Sci.*, vol. 2, no. 2, pp. 187–203, 2012.

- [128] B. A. Heß, C. M. Marian, U. Wahlgren, and O. Gropen, “A mean-field spin-orbit method applicable to correlated wavefunctions,” *Chem. Phys. Lett.*, vol. 251, no. 5-6, pp. 365–371, 1996.
- [129] B. Schimmelpfennig, “AMFI, an atomic mean-field spin-orbit integral program,” *University of Stockholm*, 1996.
- [130] F. J. A. Ferrer and F. Santoro, “Comparison of vertical and adiabatic harmonic approaches for the calculation of the vibrational structure of electronic spectra,” *Phys.Chem. Chem. Phys.*, vol. 14, no. 39, pp. 13549–13563, 2012.
- [131] T. Böhmer, M. Kleinschmidt, and C. M. Marian, “Toward the improvement of vibronic spectra and non-radiative rate constants using the vertical Hessian method,” *J. Chem. Phys.*, vol. 161, no. 9, p. 094114, 2024.
- [132] S. Kumar, L. G. Franca, K. Stavrou, E. Crovini, D. B. Cordes, A. M. Slawin, A. P. Monkman, and E. Zysman-Colman, “Investigation of Intramolecular Through-Space Charge-Transfer States in Donor–Acceptor Charge-Transfer Systems,” *J. Phys. Chem. Lett.*, vol. 12, no. 11, pp. 2820–2830, 2021.
- [133] S. Tao, L. Li, J. Yu, Y. Jiang, Y. Zhou, C.-S. Lee, S.-T. Lee, X. Zhang, and O. Kwon, “Bipolar Molecule as an Excellent Hole-Transporter for Organic-Light Emitting Devices,” *Chem. Mater.*, vol. 21, no. 7, pp. 1284–1287, 2009.
- [134] S. Shao and L. Wang, “Through-space charge transfer polymers for solution-processed organic light-emitting diodes,” *Aggregate*, vol. 1, no. 1, pp. 45–56, 2020.
- [135] H. Miranda-Salinas, Y.-T. Hung, Y.-S. Chen, D. Luo, H.-C. Kao, C.-H. Chang, K.-T. Wong, and A. Monkman, “Controlling through-space and through-bond intramolecular charge transfer in bridged D–D′–A TADF emitters,” *J. Mater. Chem. C*, vol. 9, no. 28, pp. 8819–8833, 2021.
- [136] L. Chen, C. Li, E. Fu, M. Li, Y. Kuboi, Z.-Y. Li, Z. Chen, J. Chen, X. Liu, X. Tang, *et al.*, “A Donor–Acceptor Cage for Thermally Activated Delayed Fluorescence: toward a New Kind of TADF Exciplex Emitters,” *ACS Mater. Lett.*, vol. 5, no. 5, pp. 1450–1455, 2023.
- [137] G. A. Sommer, L. N. Mataranga-Popa, R. Czerwieniec, T. Hofbeck, H. H. Homeier, T. J. Müller, and H. Yersin, “Design of Conformationally Distorted Donor–Acceptor Dyads Showing Efficient Thermally Activated Delayed Fluorescence,” *J. Phys. Chem. Lett.*, vol. 9, no. 13, pp. 3692–3697, 2018.

- [138] Y. Acar, “Quantenchemische Untersuchung der photophysikalischen Eigenschaften von Terephthalnitril-basierten Donor-Akzeptor-Fluorophoren,” masters thesis, Heinrich Heine University Düsseldorf, Düsseldorf, Germany, 2017. Available at <https://www.theochem.hhu.de/abschlussarbeiten/master-und-diplomarbeiten>.
- [139] H. Sun, C. Zhong, and J.-L. Bredas, “Reliable Prediction with Tuned Range-Separated Functionals of the Singlet–Triplet Gap in Organic Emitters for Thermally Activated Delayed Fluorescence,” *J. Chem. Theory Comput.*, vol. 11, no. 8, pp. 3851–3858, 2015.
- [140] D. Jacquemin, “What is the Key for Accurate Absorption and Emission Calculations, Energy or Geometry?,” *J. Chem. Theory Comput.*, vol. 14, no. 3, pp. 1534–1543, 2018.
- [141] W. Haselbach, J. M. Kaminski, L. N. Kloeters, T. J. Müller, O. Weingart, C. M. Marian, P. Gilch, and B. E. Nogueira de Faria, “A Thermally Activated Delayed Fluorescence Emitter Investigated by Time-Resolved Near-Infrared Spectroscopy,” *Chem. Eur. J.*, vol. 29, no. 2, p. e202202809, 2023.
- [142] R. Dhali, D. A. P. Huu, F. Bertocchi, C. Sissa, F. Terenziani, and A. Painelli, “Understanding TADF: a joint experimental and theoretical study of DMAC-TRZ,” *Phys. Chem. Chem. Phys.*, vol. 23, no. 1, pp. 378–387, 2021.
- [143] S. Ahmad, J. Eng, and T. J. Penfold, “Conformational Control of Donor–Acceptor Molecules Using Non-covalent Interactions,” *J. Phys. Chem. A*, vol. 128, no. 38, pp. 8035–8044, 2024.
- [144] P. Rajamalli, D. Chen, S. M. Suresh, Y. Tsuchiya, C. Adachi, and E. Zysman-Colman, “Planar and Rigid Pyrazine-Based TADF Emitter for Deep Blue Bright Organic Light-Emitting Diodes,” *Eur. J. Org. Chem.*, vol. 2021, no. 16, pp. 2285–2293, 2021.
- [145] T. J. Penfold and J. Gibson, *The Role of Vibronic Coupling for Intersystem Crossing and Reverse Intersystem Crossing Rates in TADF Molecules*, ch. 9, pp. 297–330. John Wiley & Sons, Ltd, 2018.
- [146] J. M. Kaminski, T. Böhmer, and C. M. Marian, “Balancing TADF Properties in π -Bridged Donor–Acceptor Systems by Sterical Constraints: The Best of Three Worlds,” *J. Phys. Chem. C*, vol. 128, no. 33, pp. 13711–13721, 2024.

- [147] S.-J. Woo, Y.-H. Kim, and J.-J. Kim, "Dihedral Angle Distribution of Thermally Activated Delayed Fluorescence Molecules in Solids Induces Dual Phosphorescence from Charge-Transfer and Local Triplet States," *Chem. Mater.*, vol. 33, no. 14, pp. 5618–5630, 2021.
- [148] F. I. Mopsik, "Dielectric Properties of Slightly Polar Organic Liquids as a Function of Pressure, Volume, and Temperature," *J. Chem. Phys.*, vol. 50, no. 6, pp. 2559–2569, 1969.
- [149] F. I. Mopsik, "Dielectric Constant of N-Hexane as a Function of Temperature, Pressure, and Density," *J. Res. Natl. Bur. Stand. A Phys. Chem.*, vol. 71, no. 4, p. 287, 1967.
- [150] G. A. Sommer, *Masuda-Borylierung-Suzuki-Kupplung als effizientes Werkzeug zum Aufbau von Wirk- und Effektstoffen*. Phd thesis, Heinrich Heine University Düsseldorf, Düsseldorf, Germany, 2018. Available at <https://docserv.uni-duesseldorf.de/servlets/DocumentServlet?id=45969>.
- [151] J. Wiefermann, *Synthese und Charakterisierung konformationell verdrillter Triphenylamin-Chromophore als potentielle TADF-Emitter*. Phd thesis, Heinrich Heine University Düsseldorf, Düsseldorf, Germany, 2023. Available at <https://docserv.uni-duesseldorf.de/servlets/DocumentServlet?id=63673>.
- [152] J. Wiefermann, P. Schmeinck, C. Ganter, and T. J. Müller, "Highly Deep-Blue Luminescent Twisted Diphenylamino Terphenyl Emitters by Bromine-Lithium Exchange Borylation-Suzuki Sequence," *Chem. Eur. J.*, vol. 28, no. 29, p. e202200576, 2022.
- [153] J. Wiefermann, J. M. Kaminski, E. Pankert, D. Hertel, K. Meerholz, C. M. Marian, and T. J. Müller, "Highly Luminescent Blue Emitter with Balanced Hybridized Locally and Charge-Transfer Excited-States Emission," *ChemPhotoChem*, vol. 7, no. 3, p. e202200265, 2023.
- [154] X. Liu, W. Liu, W. Dongyu, X. Wei, L. Wang, H. Wang, Y. Miao, H. Xu, J. Yu, and B. Xu, "Deep-blue fluorescent emitter based on a 9,9-dioctylfluorene bridge with a hybridized local and charge-transfer excited state for organic light-emitting devices with EQE exceeding 8%," *J. Mater. Chem. C*, vol. 8, no. 40, pp. 14117–14124, 2020.
- [155] T. Liu, X. Chen, J. Zhao, W. Wei, Z. Mao, W. Wu, S. Jiao, Y. Liu, Z. Yang, and Z. Chi, "Hybridized local and charge-transfer excited state fluorophores enabling

- organic light-emitting diodes with record high efficiencies close to 20%,” *Chem. Sci.*, vol. 12, no. 14, pp. 5171–5176, 2021.
- [156] S. Wang, L. Peng, F. He, Y. Ming, H. Qi, Y. Liu, D. Ma, S. Ying, and S. Yan, “A Breakthrough in Color-Tunable All-Fluorescent White OLEDs through the Cooperation Between a New Blue HLCT Fluorophore and a Long-Wavelength TADF Emitter,” *Adv. Opt. Mater.*, vol. 12, no. 21, p. 2400503, 2024.
- [157] J. Wiefermann and T. J. Müller, “Synthesis and electronic properties of torsionally constrained blue-emissive triphenylamine-pyridine chromophores,” *Dyes Pigm.*, vol. 212, p. 111134, 2023.
- [158] M. Aydemir, S. Xu, C. Chen, M. R. Bryce, Z. Chi, and A. P. Monkman, “Photophysics of an Asymmetric Donor–Acceptor–Donor TADF Molecule and Reinterpretation of Aggregation-Induced TADF Emission in These Materials,” *J. Phys. Chem. C*, vol. 121, no. 33, pp. 17764–17772, 2017.
- [159] K. Zachariasse, M. Grobys, T. Von Der Haar, A. Hebecker, Y. V. Il’ichev, O. Morawski, I. Rückert, and W. Kühnle, “Photo-induced intramolecular charge transfer and internal conversion in molecules with a small energy gap between S_1 and S_2 . Dynamics and structure,” *Journal of Photochemistry and Photobiology A: Chemistry*, vol. 105, no. 2–3, pp. 373–383, 1997.
- [160] J.-T. Ye, L. Wang, H.-Q. Wang, X.-M. Pan, H.-M. Xie, and Y.-Q. Qiu, “Effective Impact of Dielectric Constant on Thermally Activated Delayed Fluorescence and Nonlinear Optical Properties: Through-Bond-/Space Charge Transfer Architectures,” *J. Phys. Chem. C*, vol. 122, no. 33, pp. 18850–18859, 2018.
- [161] F. Ma, H. Ji, D. Zhang, K. Xue, P. Zhang, Z. Qi, and H. Zhu, “Adjusting the photophysical properties of AIE-active TADF emitters from through-bond to through-space charge transfer for high-performance solution-processed OLEDs,” *Dyes Pigm.*, vol. 188, p. 109208, 2021.
- [162] T. Zhang, Y. Xiao, H. Wang, S. Kong, R. Huang, V. Ka-Man Au, T. Yu, and W. Huang, “Highly Twisted Thermally Activated Delayed Fluorescence (TADF) Molecules and Their Applications in Organic Light-Emitting Diodes (OLEDs),” *Angew. Chem. Int. Ed.*, vol. 62, no. 39, p. e202301896, 2023.
- [163] Y. Wada, H. Nakagawa, S. Matsumoto, Y. Wakisaka, and H. Kaji, “Organic light emitters exhibiting very fast reverse intersystem crossing,” *Nat. Photon.*, vol. 14, pp. 643–649, 2020.

- [164] C.-K. Moon, Y. Yasuda, Y. Kusakabe, A. Popczyk, S. Fukushima, J. F. Butscher, H. Kaji, and M. C. Gather, “Electrochemically induced hyperfluorescence based on the formation of charge-transfer excimers,” 2025.
- [165] E. Zysman-Colman, “Molecular designs offer fast exciton conversion,” *Nat. Photon.*, vol. 14, no. 10, pp. 593–594, 2020.
- [166] H. Miranda-Salinas, A. Rodríguez-Serrano, J. M. Kaminski, F. Dinkelbach, N. Hiromichi, Y. Kusakabe, H. Kaji, C. M. Marian, and A. P. Monkman, “Conformational, Host, and Vibrational Effects Giving Rise to Dynamic TADF Behavior in the Through-Space Charge Transfer, Triptycene Bridged Acridine-Triazine Donor Acceptor TADF Molecule TpAT-tFFO,” *J. Phys. Chem. C*, vol. 127, no. 18, pp. 8607–8617, 2023.
- [167] J. M. Kaminski, A. Rodríguez-Serrano, F. Dinkelbach, H. Miranda-Salinas, A. P. Monkman, and C. M. Marian, “Vibronic effects accelerate the intersystem crossing processes of the through-space charge transfer states in the triptycene bridged acridine–triazine donor–acceptor molecule TpAT-tFFO,” *Chem. Sci.*, vol. 13, no. 23, pp. 7057–7066, 2022.
- [168] S. Metz, T. Böhmer, B. Raunischke, and C. M. Marian, “Intersystem crossing and intramolecular triplet excitation energy transfer in spiro [9,10-dihydro-9-oxoanthracene-10,2′-5′,6′-benzindan] investigated by DFT/MRCI methods,” *Can. J. Chem.*, vol. 101, no. 9, pp. 633–640, 2022.
- [169] D. Püschel, J. Wiefermann, S. Hédé, T. Heinen, L. Pfeifer, O. Weingart, M. Suta, T. J. Müller, and C. Janiak, “Molecular design of phenazine-5, 10-diyl-dibenzonitriles and the impact on their thermally activated delayed fluorescence properties,” *J. Mater. Chem. C*, vol. 11, no. 26, pp. 8982–8991, 2023.
- [170] M. Bracker, *Entwicklung und Anwendung von nichtadiabatischen Kopplungs-Matrixelementen für DFT/MRCI-Wellenfunktionen*. Phd thesis, Heinrich Heine University Düsseldorf, Düsseldorf, Germany, 2022. Available at <https://docserv.uni-duesseldorf.de/servlets/DocumentServlet?id=59536>.
- [171] J. U. Kim, I. S. Park, C.-Y. Chan, M. Tanaka, Y. Tsuchiya, H. Nakanotani, and C. Adachi, “Nanosecond-time-scale delayed fluorescence molecule for deep-blue OLEDs with small efficiency rolloff,” *Nat. Commun.*, vol. 11, no. 1, pp. 1–8, 2020.
- [172] K. Suzuki, S. Kubo, K. Shizu, T. Fukushima, A. Wakamiya, Y. Murata, C. Adachi, and H. Kaji, “Triarylboron-Based Fluorescent Organic Light-Emitting Diodes

- with External Quantum Efficiencies Exceeding 20%,” *Angew. Chem.*, vol. 127, no. 50, pp. 15446–15450, 2015.
- [173] L. Ji, S. Griesbeck, and T. B. Marder, “Recent developments in and perspectives on three-coordinate boron materials: a bright future,” *Chem. Sci.*, vol. 8, no. 2, pp. 846–863, 2017.
- [174] G. Turkoglu, M. E. Cinar, and T. Ozturk, “Triarylborane-Based Materials for OLED Applications,” *Molecules*, vol. 22, no. 9, p. 1522, 2017.
- [175] S. K. Mellerup and S. Wang, “Boron-Doped Molecules for Optoelectronics,” *Trends Chem.*, vol. 1, no. 1, pp. 77–89, 2019.
- [176] Z. Huang, S. Wang, R. D. Dewhurst, N. V. Ignatév, M. Finze, and H. Braunschweig, “Boron: Its Role in Energy-Related Processes and Applications,” *Angew. Chem. Int. Ed.*, vol. 59, no. 23, pp. 8800–8816, 2020.
- [177] S. S. Kothavale and J. Y. Lee, “Three- and Four-Coordinate, Boron-Based, Thermally Activated Delayed Fluorescent Emitters,” *Adv. Opt. Mater.*, vol. 8, no. 22, p. 2000922, 2020.
- [178] H. Lee, D. Karthik, R. Lampande, J. H. Ryu, and J. H. Kwon, “Recent Advancement in Boron-Based Efficient and Pure Blue Thermally Activated Delayed Fluorescence Materials for Organic Light-Emitting Diodes,” *Front. Chem.*, vol. 8, p. 373, 2020.
- [179] H. J. Kim and T. Yasuda, “Narrowband Emissive Thermally Activated Delayed Fluorescence Materials,” *Adv. Opt. Mater.*, vol. 10, no. 22, p. 2201714, 2022.
- [180] J.-Y. Yoo, S. W. Kang, T. H. Ha, and C. W. Lee, “Thermally activated delayed fluorescence emitters with a LUMO-extended boron-containing acceptor for high-efficiency and long-lifetime blue OLEDs,” *J. Mater. Chem. C*, vol. 12, pp. 14045–14053, 2024.
- [181] J. Park, S. Han, U. Jo, S. C. Kim, D. R. Lee, H. J. Ahn, J. Y. Kim, J.-H. Baek, and J. Y. Lee, “Boron-based thermally activated delayed fluorescence host materials as universal hosts for blue phosphorescent organic light-emitting diodes,” *Mater. Today*, vol. 75, pp. 27–36, 2024.
- [182] H. Mubarak, W. Lee, T. Lee, J. Jung, S. Yoo, and M. H. Lee, “Impact of Boron Acceptors on the TADF Properties of Ortho-Donor-Appended Triarylboron Emitters,” *Front. Chemistry*, vol. 8, p. 538, 2020.

- [183] Y. Kitamoto, T. Namikawa, D. Ikemizu, Y. Miyata, T. Suzuki, H. Kita, T. Sato, and S. Oi, "Light blue and green thermally activated delayed fluorescence from 10*H*-phenoxaborin-derivatives and their application to organic light-emitting diodes," *J. Mater. Chem. C*, vol. 3, no. 35, pp. 9122–9130, 2015.
- [184] Y. H. Lee, D. Lee, T. Lee, J. Lee, J. Jung, S. Yoo, and M. H. Lee, "Impact of boryl acceptors in para-acridine-appended triarylboron emitters on blue thermally activated delayed fluorescence OLEDs," *Dyes Pigm.*, vol. 188, p. 109224, 2021.
- [185] J. Kim, T. Lee, J. Y. Ryu, Y. H. Lee, J. Lee, J. Jung, and M. H. Lee, "Highly Emissive ortho-Donor–Acceptor Triarylboranes: Impact of Boryl Acceptors on Luminescence Properties," *Organometallics*, vol. 39, no. 12, pp. 2235–2244, 2020.
- [186] P. K. Samanta, D. Kim, V. Coropceanu, and J.-L. Brédas, "Up-Conversion Intersystem Crossing Rates in Organic Emitters for Thermally Activated Delayed Fluorescence: Impact of the Nature of Singlet vs Triplet Excited States," *J. Am. Chem. Soc.*, vol. 139, no. 11, pp. 4042–4051, 2017.
- [187] J.-D. Chai and M. Head-Gordon, "Long-range corrected hybrid density functionals with damped atom–atom dispersion corrections," *Phys. Chem. Chem. Phys.*, vol. 10, no. 44, pp. 6615–6620, 2008.
- [188] Y. Jiang, Z. Hu, B. Zhou, C. Zhong, Z. Sun, and H. Sun, "Accurate Prediction for Dynamic Hybrid Local and Charge Transfer Excited States from Optimally Tuned Range-Separated Density Functionals," *J. Phys. Chem. C*, vol. 123, no. 9, pp. 5616–5625, 2019.
- [189] O. A. Vydrov, J. Heyd, A. V. Krukau, and G. E. Scuseria, "Importance of short-range versus long-range Hartree-Fock exchange for the performance of hybrid density functionals," *J. Chem. Phys.*, vol. 125, no. 7, p. 074106, 2006.
- [190] O. A. Vydrov, G. E. Scuseria, and J. P. Perdew, "Tests of functionals for systems with fractional electron number," *J. Chem. Phys.*, vol. 126, no. 15, p. 154109, 2007.
- [191] T. M. Henderson, A. F. Izmaylov, G. Scalmani, and G. E. Scuseria, "Can short-range hybrids describe long-range-dependent properties?," *J. Chem. Phys.*, vol. 131, no. 4, p. 044108, 2009.

List of Figures

1.1	Schematic structure of a multilayer OLED device stack using the example of a through-the-bottom-emitting OLED, following Ref. [6].	4
1.2	Prominent emitter generations for the use in the emitting layer of OLED devices. F-OLED : Fluorescent (F) emitters showing PF (maximum IQE = 25%), Ph-OLED : Phosphorescent (Ph) emitters showing phosphorescence (maximum IQE = 100%), TADF-OLED : TADF emitters showing PF and DF (maximum IQE = 100%). Fourth generation emitters combine a TADF dopant and a fluorescent emitter (hyperfluorescence) or a phosphorescent dopant and a fluorescent emitter (hyperphosphorescence), interacting via excitation energy transfer (maximum IQE = 100%).	5
2.1	Several cavity models to describe the embedding of the solute in the solvent during quantum chemical calculations, as outlined in Ref. [96].	24
2.2	Schematic picture of the <i>GRADIENATOR</i> workflow.	34
3.1	Schematic picture of <i>para</i> -appended TBCT emitters consisting of donor, bridge, and acceptor units.	37
3.2	Investigated emitter series consisting of a triarylamine (TAA) donor and a terephthalonitrile (TPN) acceptor unit. Labeling: Consecutive numbers in the order of increasing substitutional effect plus name of the substituent. Differences are highlighted by colored boxes. The dihedral angle between the phenylene bridge of TAA and the TPN acceptor of the most stable conformer is indicated in the upper right of each colored box.	39

- 3.3 **Left:** TDDFT energy level diagram showing vertical excitation energies at various optimized geometries using PBE0/def2-SV(P) or ω B97X-D/def2-SV(P) level of theory for **Em2-Me** in toluene. The standard and optimal system-specific range-separation parameter ω are used. **Right:** Optimal tuning procedure for range-separation parameter ω in vacuo (black) and toluene (red) for the optimized electronic ground-state at ω B97X-D/def2-TZVP level of theory. 40
- 3.4 Experimental and calculated spectra for (a) $S_n \leftarrow S_1$ (CT) and (b) $T_n \leftarrow T_1$ (CT) processes combining ESA and SE in toluene for **Em2-Me**. The experimental setup is based on the fact that the visible and NIR ranges are calculated separately from each other and combined as one spectrum. This creates a gap in the range between 800 nm and 900 nm. The calculated DFT/MRCI-R2016 line spectra were broadened with Gaussians of 1850 cm^{-1} or 4000 cm^{-1} FWHM for $S_n \leftarrow S_1$ (CT) and $T_n \leftarrow T_1$ (CT), respectively. 43
- 3.5 Simulated spectra for (a) $S_n \leftarrow S_1$ (CT) and (b) $T_n \leftarrow T_1$ (CT) processes combining ESA and SE in toluene with respect to fixed donor–acceptor configurations between **TAA** and **TPN** along the relaxed excited-state PES for **Em2-Me**. The calculated DFT/MRCI-R2016 line spectra were broadened with Gaussians of 1850 cm^{-1} or 4000 cm^{-1} FWHM for $S_n \leftarrow S_1$ (CT) and $T_n \leftarrow T_1$ (CT), respectively. 44
- 3.6 **Top:** Computed absorption spectra of **Em1-H** (blue), **Em2-Me** (orange), **Em3-ⁱPr** (green) and **Em4-diMe** (red) in toluene solution. **Bottom:** Simulated absorption spectra of **Em2-Me** at fixed donor–acceptor dihedral angles along a relaxed scan of the electronic ground-state PES. All DFT/MRCI-R2016 line spectra were broadened with Gaussians of 4400 cm^{-1} FWHM. 46
- 3.7 DFT/MRCI-R2016 energy level diagram showing vertical excitation energies relative to the electronic ground-state at various optimized geometries for **Em2-Me** at ω B97X-D/def2-SV(P) level of theory using the optimized range-separation parameter of $\omega = 0.15\text{ bohr}^{-1}$. The asterisk denotes that the $T_{LE(TPN)}$ minimum is assumed to be at 90° from relaxed scans along the donor–acceptor dihedral angle. Excited-state labelling: S_{CT} blue, T_{CT} red, $T_{LE(TPN)}$ green, $T_{LE(TAA)}$ orange, and $T_{LE(TAA)}$ skyblue. The dihedral angle between the phenylene bridge of **TAA** and the **TPN** acceptor of each optimized excited state is indicated in brackets. 47

3.8	Schematic picture comparing state diagrams consisting of three (left) or four (right) electronic states, which are necessary to describe the excited-state decay mechanism of an emitter molecule.	48
3.9	Modified emitters based on Em2-Me and Em4-diMe shown in Figure 3.2 with two additional methoxy groups added at the terminal phenyl groups of the donor moiety in <i>para</i> -position with respect to the nitrogen. The dihedral angle between the phenylene bridge and the TPN acceptor of the most stable conformer is indicated in the upper right of each colored box.	52
3.10	DFT/MRCI-R2016 energy level diagrams showing vertical excitation energies relative to the electronic ground-state at various optimized geometries for (a) Em2-Me+diOMe and (b) Em4-diMe+diOMe . The asterisk denotes that the $T_{LE(TPN)}$ minimum is assumed to be at 90° from relaxed scans along the donor–acceptor dihedral angle. Excited-state labelling: S_{CT} blue, T_{CT} red, $T_{LE(TPN)}$ green, $T_{LE(TAA)}$ orange, and $T_{LE(TAA)}$ skyblue. The dihedral angle between the phenylene bridge of TAA and the TPN acceptor of each optimized excited state is indicated in brackets.	53
3.11	Schematic representation of the TAA -based donor moiety (right), which is combined with phenyl- (o-CN , p-CN) and terphenyl-based (Ph-o-CN , Ph-p-CN , PhdiMe-o-CN , PhdiMe-p-CN) acceptor moieties (left) having one cyano group in <i>ortho</i> - or <i>para</i> -position with respect to the donor–acceptor linkage.	55
3.12	Fragment-based analysis of the one-electron transition density matrix (using the TheoDORE program package) for the vertical singlet and triplet state DFT/MRCI-R2016 wave functions and corresponding adiabatic excitation energies (white lines) at the S_1 and T_1 geometries in toluene for Em2-Me , TAA-p-CN and TAA-Ph-p-CN	56
3.13	DFT/MRCI-R2016 energy level diagram showing vertical excitation energies relative to the electronic ground-state at various optimized geometries for TAA-Ph-p-CN . The excited states are labelled as follows: $S_{CT/LE}$ blue, $T_{CT/LE}$ red, $T_{LE(D/A)}$ green, $T_{LE(D)}$ orange, $T_{LE(D)}$ skyblue. The dihedral angles between the phenylene bridges of TAA and the acceptor and between the phenyl rings within the acceptor of each optimized excited state are indicated in brackets.	58

3.14	Schematic representation of the TAA -based donor moiety (right), which is combined with pyridine-based (Py) acceptor moieties (left) having one substituent in <i>ortho</i> - or <i>meta</i> -position relative to the donor–acceptor linkage.	59
3.15	DFT/MRCI-R2016 energy level diagram showing vertical excitation energies at the optimized ground-state geometries for TAA-Py with various substituents in <i>meta</i> -position to the donor–acceptor linkage, including -Me , -H , -Cl , -COOMe , -CHO , -CF₃ , and -CN . All energies are calculated relative to the electronic ground-state. The excited singlet states are labelled as follows: CT(D→A)/LE(D) blue, CT(D→A) red, $n\pi^*(A)$ green, LE(D) forest-green, LE(D) orange, and LE(D) skyblue.	60
3.16	DFT/MRCI-R2016 energy level diagram showing vertical excitation energies relative to the electronic ground-state at the optimized ground-state geometries for TAA-Py-m-CHO . The excited states are labelled as follows: $S_{CT/LE}$ blue, S_{CT} red, and $S_{n\pi^*}$ green.	62
4.1	Schematic representation of TSCT emitters consisting of donor, bridge, and acceptor units.	65
4.2	(a) Chemical structure of TpAT-tFFO . (b) Overlays of TpAT-tFFO molecular frames visualizing the coordinate displacements between the ground-state minimum nuclear arrangements (red: Me→N, blue: Me→Ph) while minimizing the root mean squares deviations of the Tp bridges.	67
4.3	DFT/MRCI-R2016 energy level diagram showing vertical excitation energies at various optimized geometries. All energies are calculated relative to the most stable ground-state conformer GS (Me→Ph). The excited states are labelled at their respective minimum geometry: 1CT blue, 3CT red, 3LE green, $^1CT'$ skyblue, $^3CT'$ orange.	68
4.4	Low-frequency vibrational modes Q_1 (left), Q_9 (middle) and Q_{12} (right) from <i>Gaussian 16</i> frequency analysis at the optimized GS (Me→N) geometry.	70
4.5	Excited-state energies for displacements along vibrational modes Q_9 and Q_{12} at the optimized ground-state conformer GS (Me→N). The energy, which is needed to exert the shown displacements is in the range of 2 meV.	70
4.6	Proposed scheme for excited-state decay mechanism of TpAT-tFFO	72

4.7	Optimized electronic ground-state conformers of DPACoOB at PBE0/def2-SV(P) level of theory in toluene. Conformers I and II exhibit either C–H··· π or π ··· π interactions, respectively.	74
4.8	DFT/MRCI-R2016 energy level diagram showing vertical excitation energies at various optimized geometries. All energies are calculated relative to the most stable ground-state conformer II . The excited states are labelled as follows: S _{CT} blue, T _{CT} red, T _{LE(A)} green.	76
4.9	DPACoOB, conformer II : Calculated (turquoise) and experimental (black) emission spectra in toluene at 77 K (dashed lines) and 298 K (solid lines).	76
4.10	DPACoOB : Linearly interpolated pathways between the optimized ground-state and S _{CT} , as well as between the optimized T _{CT} and T _{LE(A)} geometries (conformer II). DFT/MRCI-R2016 vertical energies of the relevant excited singlet (boxes) and triplet (circles) states relative to the ground-state minimum in eV. The S ₁ state can be characterized along the pathways as S _{CT} state (blue), whereas the T ₁ and T ₂ states change their character according to TheoDORE analysis of the one-particle transition density matrices between T _{CT} (red) and T _{LE(A)} (green). . . .	78
B.1	Calculated spectra for (a) S _n ←S ₁ (CT) and (b) T _n ←T ₁ (CT) processes combining ESA and SE in toluene for Em1-H , Em2-Me , Em3-ⁱPr , and Em4-diMe . The calculated DFT/MRCI-R2016 line spectra were broadened with Gaussians of 1850 cm ⁻¹ or 4000 cm ⁻¹ FWHM for S _n ←S ₁ (CT) and T _n ←T ₁ (CT), respectively.	III
B.2	Difference densities (± 0.001) of the excited states at their optimized geometries in toluene. Areas losing electron density in comparison to the electronic ground-state are shown in red, areas gaining electron density in yellow.	VII
B.3	Calculated fluorescence emission spectra (S ₁ →S ₀) in toluene using the VH method for Em2-Me (orange), TAA-p-CN (black), and TAA-Ph-p-CN (green) at 298 K.	VIII
B.4	TAA-Ph-p-CN : Optimal tuning procedure for the range-separation parameter ω <i>in vacuo</i> (black) and toluene (red) for the optimized electronic ground-state at ω B97X-D/def2-TZVP level of theory. . . .	VIII
B.5	TAA-Py-m-CHO : Experimental (dashed lines) and computed (solid lines) absorption spectra <i>in vacuo</i> (orange), cyclohexane (CHX, black), and tetrahydrofuran (THF, green). All DFT/MRCI-R2016 line spectra were broadened with Gaussians of 2500 cm ⁻¹ FWHM.	X

B.6	TAA-Py-m-CHO : Simulated absorption spectra <i>in vacuo</i> for unrelaxed scan along donor–acceptor dihedral angle (minimum structure 320). All DFT/MRCI-R2016 line spectra were broadened with Gaussians of 2500 cm ^{−1} FWHM.	XI
B.7	TDDFT energies at the optimized ground-state geometry GS (Me→N) in vacuo at PBE0/def2-SV(P) or LC- ω PBE/6-31+G* level of theory using the standard range-separation parameter $\omega = 0.40$ bohr ^{−1} and the optimized value $\omega = 0.1664$ bohr ^{−1} from Ref. [163]. The excited states are labeled as follows: ¹ CT blue, ³ CT orange, ¹ CT' forest-green, ³ CT' red, ³ LE skyblue. For LC- ω PBE ($\omega = 0.40$ bohr ^{−1}), the CT singlet and triplet states are located at energies higher than 4.5 eV.	XII

List of Tables

3.1	Em2-Me : Overview of S_{CT} and T_{CT} vertical (v, at optimized ground-state geometry) and adiabatic (a, at respective optimized excited-state geometry relative to ground-state minimum) excitation energies in eV and vertical fluorescence emission wavelength at the optimized S_{CT} geometry in eV (nm). The relevant electronic states were optimized using (TD-)DFT at PBE0/def2-SV(P) or ω B97X-D ($\omega = 0.15 \text{ bohr}^{-1}$)/def2-SV(P) level of theory. All properties were calculated at TDDFT or DFT/MRCI level of theory,	41
4.1	FC and FC+HT rate constants [s^{-1}] at 300 K for fluorescence (F), ISC, and rISC between low-lying singlet and triplet state minima of DPACoOB including SOC for conformer II	78
B.1	Calculated spectra for $S_n \leftarrow S_1(CT)$ and $T_n \leftarrow T_1(CT)$ processes combining ESA and SE in toluene for Em1-H , Em2-Me , Em3-ⁱPr , and Em4-diMe . The longest-wavelength absorption maximum of the singlet ($S_4 \leftarrow S_1$) or triplet ($T_3 \leftarrow T_1$) spectrum is given with the corresponding oscillator strength.	III
B.2	Overview of characteristic properties for Em2-Me comparing the R2016 and R2022 Hamiltonians, implicit and hybrid solvent models, as well as SV(P) and TZVP basis sets at the optimized ground-state geometry (donor–acceptor dihedral angles: PCM 63.4°, PCM+2expl. 69.7°). Optimization was employed at ω B97X-D/def2-SV(P) level of theory using an optimally tuned range-separation parameter of $\omega = 0.15 \text{ bohr}^{-1}$. DFT/MRCI-R2016 results for energies E in eV and dipole moments μ in debye. Excited-state character [CT/LE(TAA)/LE(TPN)] in % using the TheoDORE program package.	IV

B.3	Overview of characteristic properties for Em2-Me comparing the R2016 and R2022 Hamiltonians, implicit and hybrid solvent models, as well as SV(P) and TZVP basis sets at the optimized S_1 state geometry (donor–acceptor dihedral angles: PCM 64.3°, PCM+2expl. 65.9°). Optimization was employed at ω B97X-D/def2-SV(P) level of theory using an optimally tuned range-separation parameter of $\omega = 0.15 \text{ bohr}^{-1}$. DFT/MRCI-R2016 results for energies E in eV and dipole moments μ in debye. Excited-state character [CT/LE(TAA)/LE(TPN)] in % using the TheoDORE program package.	V
B.4	Overview of characteristic properties for Em2-Me comparing the R2016 and R2022 Hamiltonians, implicit and hybrid solvent models, as well as SV(P) and TZVP basis sets at the optimized T_1 state geometry (donor–acceptor dihedral angles: PCM 41.0°, PCM+2expl. 41.7°). Optimization was employed at ω B97X-D/def2-SV(P) level of theory using an optimally tuned range-separation parameter of $\omega = 0.15 \text{ bohr}^{-1}$. DFT/MRCI-R2016 results for energies E in eV and dipole moments μ in debye. Excited-state character [CT/LE(TAA)/LE(TPN)] in % using the TheoDORE program package.	VI
B.5	TAA-Ph-p-CN : Overview of S_{CT} and T_{CT} vertical (v, at optimized GS geometry) and adiabatic (a, at respective optimized excited-state geometry relative to GS minimum) excitation energies in eV and vertical fluorescence emission wavelength at the optimized S_{CT} geometry in eV (nm). The relevant electronic states were optimized using (TD-)DFT at PBE0/def2-SV(P) or ω B97X-D ($\omega = 0.14 \text{ bohr}^{-1}$)/def2-SV(P) level of theory. All properties were calculated at TDDFT or DFT/MRCI level of theory,	IX
B.6	TAA-Py-m-X : DFT/MRCI-R2016 excitation energies of the first excited singlet and triplet state at the ground-state and their respective optimized geometries at PBE0/def2-TZVP level of theory <i>in vacuo</i> in eV. Substituents X include -Me , -H , -Cl , -COOMe , -CHO , -CF3 , and -CN	IX
B.7	Relative energies E_{rel} in eV, wavelengths in nm and oscillator strengths (in brackets) of the five energetically lowest excited singlet states for structures in the potential well close to the global minimum for TAA-Py-m-CHO <i>in vacuo</i>	XI

Abbreviations

AMFI	A tomic M ean- F ield I ntegral
BO	B orn- O ppenheimer
CI	C onfiguration I nteraction
cLR	corrected L inear- R esponse
CSF	C onfiguration S tate F unction
CT	C harge- T ransfer
DPEPO	bis[2-(d iphenylphosphino) p henyl] e ther o xide
DF	D elayed F luorescence
DFA	D ensity F unctional A pproximation
DFT	D ensity F unctional T heory
DMABN	4-(d imethylamino) b enzonitrile
EQE	E xternal Q uantum E fficiency
ESA	E xcited- S tate A bsorption
FC	F ranck- C ondon
FRET	F örster R esonance E nergy T ransfer
FWHM	F ull W idth at H alf M aximum
GGA	G eneralized G radient A pproximation
GH	G lobal H ybrid
HF	H artree- F ock
HLCT	H ybridized L ocal and C harge- T ransfer
HOMO	H ighest O ccupied M olecular O rbital
HT	H erzberg- T eller
IC	I nternal C onversion
IEF	I ntegral E quation F ormalism

Abbreviations

IP	I onization P otential
IQE	I nternal Q uantum E fficiency
ISC	I ntersystem C rossing
IST	I nverted S inglet– T riplet gap
KS	K ohn- S ham
LCD	L iquid C rystal D isplay
LDA	L ocal D ensity A pproximation
LE	L ocally E xcited
LR	L ong- R ange
LSDA	L ocal S pin D ensity A pproximation
MM	M olecular M echanical
ModISC	M odulation of I ntersystem C rossing
MR	M ulti- R esonance
MRCI	M ulti- R eference C onfiguration I nteraction
NAC	N on- A diabatic C oupling
NEB	N udged E lastic B and
NIR	N ear- I nfrared
OLED	O rganic L ight E mitting D iode
OT	O ptimally T uned
PCM	P olarizable C ontinuum M odel
PES	P otential E nergy S urface
PF	P rompt F luorescence
PLQY	P hotoluminescence Q uantum Y ield
PMMA	p olymethyl m ethacrylate
QCG	Q uantum C luster G rowth
QM	Q uantum M echanical
rISC	r everse I ntersystem C rossing
ROKS	R estricted O pen- S hell K ohn- S ham
RSH	R ange- S eparated H ybrid
SAS	S olvent A ccessible S urface

SE	Stimulated Emission
SES	Solvent Excluded Surface
SOC	Spin–Orbit Coupling
SOCME	Spin–Orbit Coupling Matrix Elements
SOMF	Spin–Orbit Mean-Field
SPOCK	Spin–Orbit Coupling Kit
SR	Short-Range
TAA	triarylamine
TADF	Thermally Activated Delayed Fluorescence
TBCT	Through-Bond Charge-Transfer
TDDFT	Time-Dependent Density Functional Theory
TDM	Transition Dipole Moment
TheoDORE	Theoretical Density, Orbital Relaxation and Exciton Analysis
TPN	terephthalonitrile
TSCT	Through-Space Charge-Transfer
TTA	Triplet–Triplet Annihilation
vdW	van der Waals
VEM	Vertical Excitation Model
VH	Vertical Hessian

A Technical Details

RSH Density Functionals

- **ω B97X-D:** The ω B97X-D functional was used in **Publications II, III, V** and **Manuscript I** and shows excellent performance for various energy properties [80, 187] and for emitter molecules having hybridized CT and LE character [188].

$$E_{xc}^{\omega B97X} = c_x E_x^{SR-HF} + E_x^{SR-B97} + E_x^{LR-HF} + E_c^{B97} \quad (\text{A.1})$$

It consists of 100% LR and about 22% SR exact exchange ($c_x = 0.22$), which is special for LR corrected hybrid functionals, a modified B97 exchange density functional for SR interactions and B97 correlation density functional. The empirically fitted standard range-separation parameter ω is set to 0.20 bohr^{-1} .

Furthermore, this functional includes empirical atom-atom dispersion corrections to provide the missing LR-vdW-interactions without additional computational costs. In more detail, at short interatomic distances no dispersion correction is needed, whereas the correct asymptotic pairwise vdW-potentials are enforced by damping function, including parameter a with its optimum value at $a = 6.0$ that controls the strength of dispersion correction (for details see Section 2.5).

- **LC- ω PBE:** The LC- ω PBE functional was used in **Publications I and IV** and performs well for many molecular properties, whether in equilibrium, transition state or dissociation limit [75].

$$E_{xc}^{LC-\omega PBE} = E_x^{SR-PBE}(\omega) + E_x^{LR-HF}(\omega) + E_c^{PBE} \quad (\text{A.2})$$

The best empirically fitted parameter set, which provides barrier heights and equilibrium thermochemistry data consistently accurate, was found to be $\omega = 0.4 \text{ bohr}^{-1}$, $a = 0$ and $b = 1$ [189, 190]. This translates to 100% SR interactions described by DFA and 100% LR interactions described by HF. Further development was done in a recommended version called LC- ω HPBE [191] offering the possibility of calculating also excited state geometries.

B Additional Material

B.1 Through-Bond Charge-Transfer Emitters

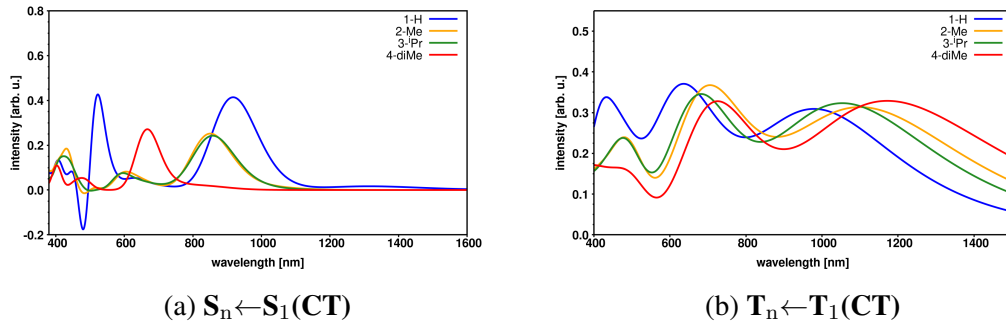


Figure B.1: Calculated spectra for (a) $S_n \leftarrow S_1(CT)$ and (b) $T_n \leftarrow T_1(CT)$ processes combining ESA and SE in toluene for **Em1-H**, **Em2-Me**, **Em3-*i*Pr**, and **Em4-diMe**. The calculated DFT/MRCI-R2016 line spectra were broadened with Gaussians of 1850 cm^{-1} or 4000 cm^{-1} FWHM for $S_n \leftarrow S_1(CT)$ and $T_n \leftarrow T_1(CT)$, respectively.

Table B.1: Calculated spectra for $S_n \leftarrow S_1(CT)$ and $T_n \leftarrow T_1(CT)$ processes combining ESA and SE in toluene for **Em1-H**, **Em2-Me**, **Em3-*i*Pr**, and **Em4-diMe**. The longest-wavelength absorption maximum of the singlet ($S_4 \leftarrow S_1$) or triplet ($T_3 \leftarrow T_1$) spectrum is given with the corresponding oscillator strength.

		Em1-H	Em2-Me	Em3-<i>i</i>Pr	Em4-diMe
$S_4 \leftarrow S_1$	E [eV]	1.35	1.47	1.45	1.59
	E [nm]	917	846	853	780
	f(L)	0.41324	0.22224	0.19568	0.00715
$T_3 \leftarrow T_1$	E [eV]	1.24	1.11	1.17	1.05
	E [nm]	998	1119	1063	1177
	f(L)	0.28427	0.29419	0.30605	0.31498

Table B.2: Overview of characteristic properties for **Em2-Me** comparing the R2016 and R2022 Hamiltonians, implicit and hybrid solvent models, as well as SV(P) and TZVP basis sets at the optimized ground-state geometry (donor–acceptor dihedral angles: PCM 63.4°, PCM+2expl. 69.7°). Optimization was employed at ω B97X-D/def2-SV(P) level of theory using an optimally tuned range-separation parameter of $\omega = 0.15$ bohr⁻¹. DFT/MRCI-R2016 results for energies E in eV and dipole moments μ in debye. Excited-state character [CT/LE(TAA)/LE(TPN)] in % using the TheodORE program package.

Solvent Model		PCM						PCM + 2 expl.		
Hamiltonian		R2016		R2022		R2016		R2016		R2022
Basis Set	SV(P)	TZVP	SV(P)	TZVP	SV(P)	TZVP	SV(P)	TZVP	SV(P)	TZVP
μ (GS)	1.75	1.90	1.75	1.90	1.61	1.77	1.62	1.78		
E(S _{I,vert.})	3.10	3.01	3.27	3.14	2.90	2.83	3.12	3.01		
μ (S _I)	26.97	27.03	26.56	26.64	24.32	24.45	23.88	24.05		
Character	80/6/4	79/7/5	80/6/4	78/6/5	78/6/6	76/6/7	78/6/6	75/6/7		
E(T _{I,vert.})	2.91	2.85	3.09	2.99	2.72	2.66	2.95	2.85		
μ (T _I)	20.28	21.54	19.53	21.01	20.07	20.67	19.50	20.21		
Character	59/22/11	62/20/10	58/21/13	61/19/11	64/14/12	64/14/13	63/14/14	63/13/13		
Δ E _{ST,vert.}	0.19	0.16	0.18	0.15	0.18	0.17	0.17	0.16		

Table B.3: Overview of characteristic properties for **Em2-Me** comparing the R2016 and R2022 Hamiltonians, implicit and hybrid solvent models, as well as SV(P) and TZVP basis sets at the optimized S_1 state geometry (donor–acceptor dihedral angles: PCM 64.3°, PCM+2expl. 65.9°). Optimization was employed at ω B97X-D/def2-SV(P) level of theory using an optimally tuned range-separation parameter of $\omega = 0.15 \text{ bohr}^{-1}$. DFT/MRCI-R2016 results for energies E in eV and dipole moments μ in debye. Excited-state character [CT/LE(TAA)/LE(TPN)] in % using the TheoDORE program package.

Solvent Model	PCM						PCM + 2 expl.					
	R2016		R2022		R2016		R2016		R2022		R2022	
Hamiltonian												
Basis Set	SV(P)	TZVP	SV(P)	TZVP	SV(P)	TZVP	SV(P)	TZVP	SV(P)	TZVP	SV(P)	TZVP
$E(S_{1,\text{vert.}})$	2.56	2.47	2.74	2.61	2.35	2.28	2.58	2.47	2.35	2.28	2.58	2.47
$E(S_{1,\text{adia.}})$	2.94	2.86	3.11	2.99	2.73	2.70	2.96	2.89	2.73	2.70	2.96	2.89
$\mu(S_1)$	24.66	24.68	24.31	24.34	23.16	23.21	22.80	22.85	23.16	23.21	22.80	22.85
Character	80/4/6	77/5/8	80/4/6	77/5/8	78/4/6	76/5/8	78/4/7	76/4/8	78/4/6	76/5/8	78/4/7	76/4/8
$\lambda_{F,\text{vert.}}$	484	502	452	475	528	544	481	502	528	544	481	502
k_F	2.6×10^7	2.3×10^7	3.1×10^7	2.6×10^7	2.2×10^7	2.0×10^7	2.8×10^7	2.5×10^7	2.2×10^7	2.0×10^7	2.8×10^7	2.5×10^7
$E(T_{1,\text{vert.}})$	2.36	2.29	2.54	2.44	2.19	2.13	2.42	2.34	2.19	2.13	2.42	2.34
$E(T_{1,\text{adia.}})$	2.74	2.69	2.92	2.82	2.57	2.55	2.80	2.75	2.57	2.55	2.80	2.75
$\mu(T_1)$	20.32	21.13	19.17	20.34	20.67	21.03	19.91	20.40	20.67	21.03	19.91	20.40
Character	65/10/17	65/10/16	61/10/20	63/10/18	70/8/13	68/8/13	68/8/14	67/8/14	70/8/13	68/8/13	68/8/14	67/8/14
$\Delta E_{\text{ST,adia.}}$	0.44	0.36	0.41	0.33	0.26	0.24	0.26	0.22	0.26	0.24	0.26	0.22

Table B.4: Overview of characteristic properties for **Em2-Me** comparing the R2016 and R2022 Hamiltonians, implicit and hybrid solvent models, as well as SV(P) and TZVP basis sets at the optimized T_1 state geometry (donor-acceptor dihedral angles: PCM 41.0°, PCM+2expl. 41.7°). Optimization was employed at ω B97X-D/def2-SV(P) level of theory using an optimally tuned range-separation parameter of $\omega = 0.15$ bohr⁻¹. DFT/MRCI-R2016 results for energies E in eV and dipole moments μ in debye. Excited-state character [CT/LE(TAA)/LE(TPN)] in % using the TheodORE program package.

Solvent Model		PCM		PCM + 2 expl.			
Hamiltonian		R2016		R2022		R2016	
Basis Set	SV(P)	TZVP	SV(P)	TZVP	SV(P)	TZVP	SV(P)
E(S_{1,vert.})	2.53	2.46	2.74	2.63	2.37	2.30	2.61
E(S_{1,adia.})	3.00	2.96	3.21	3.13	2.88	2.85	3.13
μ (S₁)	19.66	19.84	19.39	19.65	18.53	18.68	18.27
Character	59/15/13	56/15/14	59/15/13	56/15/15	60/12/13	57/12/15	61/12/14
E(T_{1,vert.})	2.03	2.00	2.23	2.16	1.95	1.92	2.18
E(T_{1,adia.})	2.50	2.50	2.70	2.66	2.47	2.46	2.70
μ (T₁)	13.71	14.34	13.03	13.74	14.16	14.70	13.48
Character	40/26/24	39/26/24	38/26/25	38/26/25	45/21/23	43/20/24	43/21/24
$\Delta E_{ST,adia.}$	0.44	0.36	0.41	0.33	0.26	0.24	0.26
							0.22

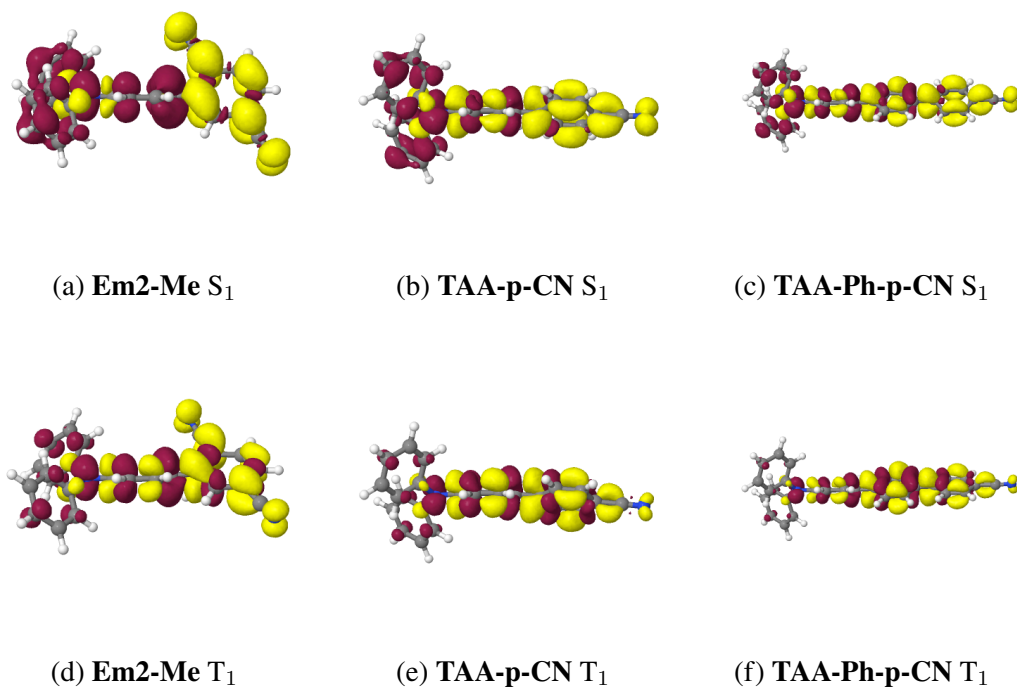


Figure B.2: Difference densities (± 0.001) of the excited states at their optimized geometries in toluene. Areas losing electron density in comparison to the electronic ground-state are shown in red, areas gaining electron density in yellow.

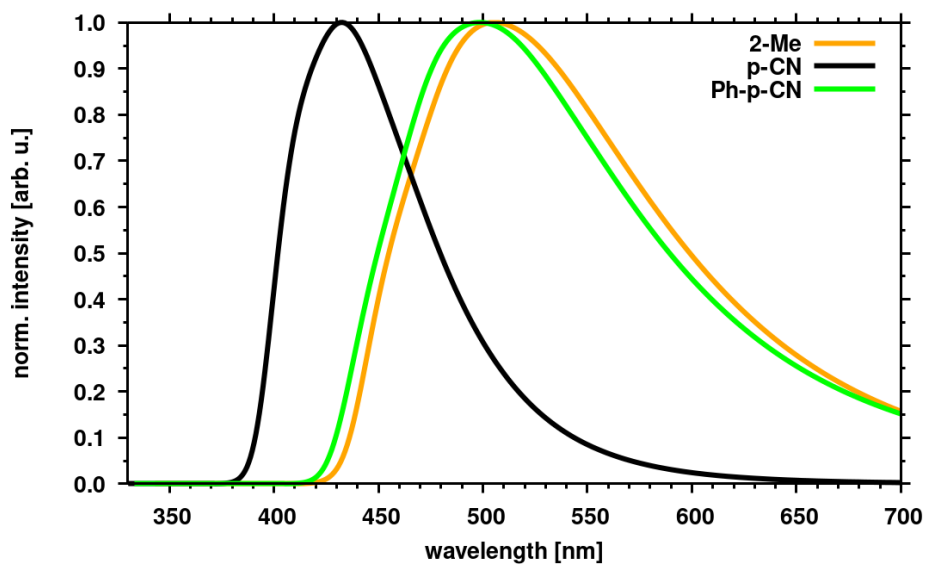


Figure B.3: Calculated fluorescence emission spectra ($S_1 \rightarrow S_0$) in toluene using the VH method for **Em2-Me** (orange), **TAA-p-CN** (black), and **TAA-Ph-p-CN** (green) at 298 K.

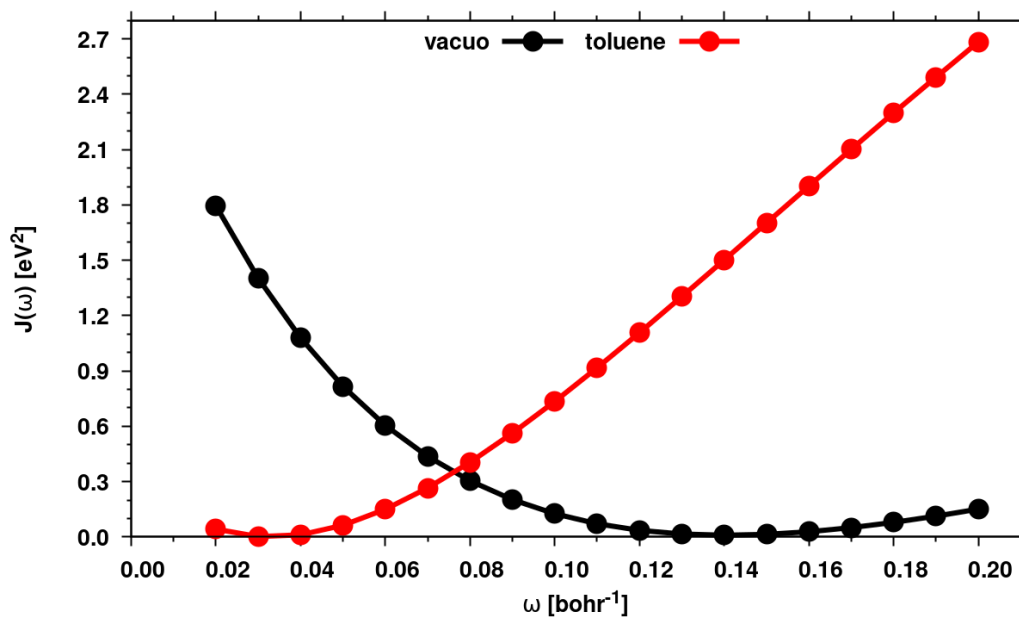


Figure B.4: **TAA-Ph-p-CN**: Optimal tuning procedure for the range-separation parameter ω in *vacuo* (black) and toluene (red) for the optimized electronic ground-state at ω B97X-D/def2-TZVP level of theory.

Table B.5: **TAA-Ph-p-CN**: Overview of S_{CT} and T_{CT} vertical (v, at optimized GS geometry) and adiabatic (a, at respective optimized excited-state geometry relative to GS minimum) excitation energies in eV and vertical fluorescence emission wavelength at the optimized S_{CT} geometry in eV (nm). The relevant electronic states were optimized using (TD-)DFT at PBE0/def2-SV(P) or ω B97X-D ($\omega = 0.14 \text{ bohr}^{-1}$)/def2-SV(P) level of theory. All properties were calculated at TDDFT or DFT/MRCI level of theory,

		S_{CT} (v)	T_{CT} (v)	S_{CT} (a)	T_{CT} (a)	λ_{em}
PBE0	TDDFT	3.16	2.85	2.90	2.11	2.69 (461)
	DFT/MRCI	3.42	2.83	3.07	2.36	2.82 (439)
ω B97X-D	TDDFT	3.92	3.30	3.45	2.11	3.02 (410)
	DFT/MRCI	3.55	2.96	3.06	2.35	2.68 (462)
Experiment [152]						2.88 (431)

Table B.6: **TAA-Py-m-X**: DFT/MRCI-R2016 excitation energies of the first excited singlet and triplet state at the ground-state and their respective optimized geometries at PBE0/def2-TZVP level of theory *in vacuo* in eV. Substituents X include -Me, -H, -Cl, -COOMe, -CHO, -CF₃, and -CN.

	-Me	-H	-Cl	-COOMe	-CHO	-CF ₃	-CN
S₁, vert. @ S₀	3.71	3.70	3.57	3.61	3.32	3.54	3.49
T₁, vert. @ S₀	3.04	3.03	2.94	2.98	2.89	2.93	2.89
$\Delta E_{ST,vert}$	0.67	0.67	0.63	0.63	0.43	0.61	0.60
S₁, adia. @ S₁	3.65	3.66	3.54	3.55	3.16	3.54	3.39
T₁, adia. @ T₁	2.63	2.67	2.61	2.65	2.61	2.62	2.57
$\Delta E_{ST,adia}$	1.02	0.99	0.93	0.90	0.55	0.92	0.82

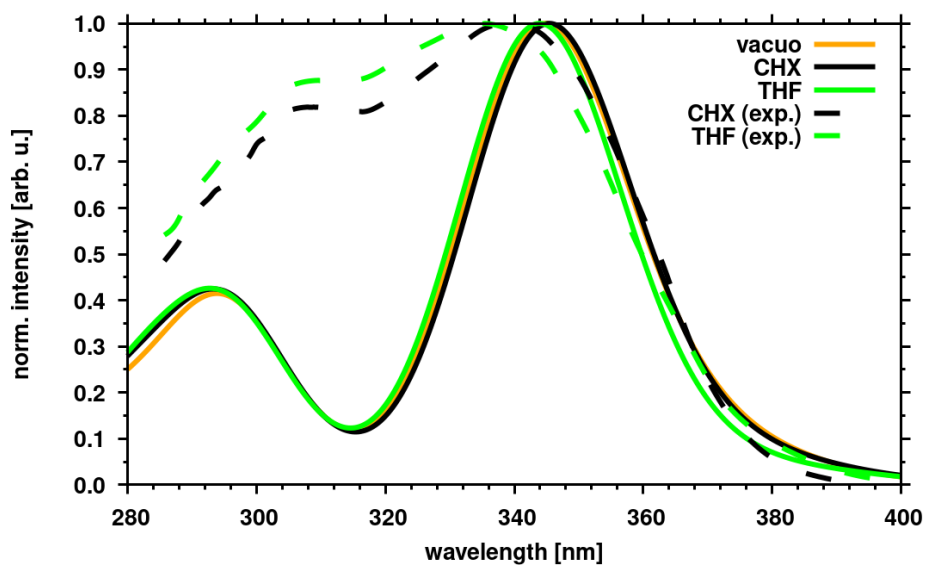


Figure B.5: **TAA-Py-m-CHO**: Experimental (dashed lines) and computed (solid lines) absorption spectra *in vacuo* (orange), cyclohexane (CHX, black), and tetrahydrofuran (THF, green). All DFT/MRCI-R2016 line spectra were broadened with Gaussians of 2500 cm^{-1} FWHM.

Table B.7: Relative energies E_{rel} in eV, wavelengths in nm and oscillator strengths (in brackets) of the five energetically lowest excited singlet states for structures in the potential well close to the global minimum for **TAA-Py-m-CHO** *in vacuo*.

Structure	E_{rel}	S_1	S_2	S_3	S_4	S_5
280	0.0703	354 (0.002)	330 (0.001)	306 (0.433)	317 (0.049)	292 (0.279)
290	0.0615	356 (0.006)	333 (0.000)	319 (0.306)	315 (0.241)	293 (0.276)
300	0.0392	359 (0.014)	336 (0.001)	327 (0.572)	318 (0.045)	293 (0.273)
310	0.0152	362 (0.031)	338 (0.010)	334 (0.637)	319 (0.030)	293 (0.269)
320	0.0000	366 (0.060)	347 (0.019)	341 (0.671)	319 (0.026)	293 (0.264)
330	0.0281	370 (0.102)	341 (0.038)	345 (0.670)	320 (0.024)	294 (0.257)
340	0.0973	375 (0.125)	342 (0.015)	348 (0.709)	320 (0.024)	294 (0.251)

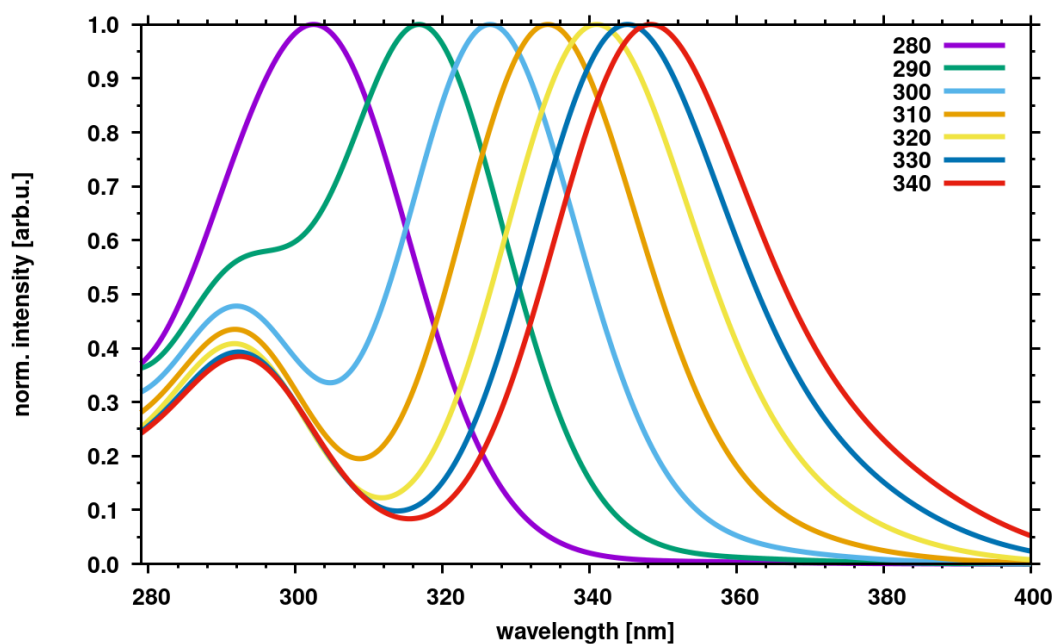


Figure B.6: **TAA-Py-m-CHO**: Simulated absorption spectra *in vacuo* for unrelaxed scan along donor–acceptor dihedral angle (minimum structure 320). All DFT/MRCI-R2016 line spectra were broadened with Gaussians of 2500 cm^{-1} FWHM.

B.2 Through-Space Charge-Transfer Emitters

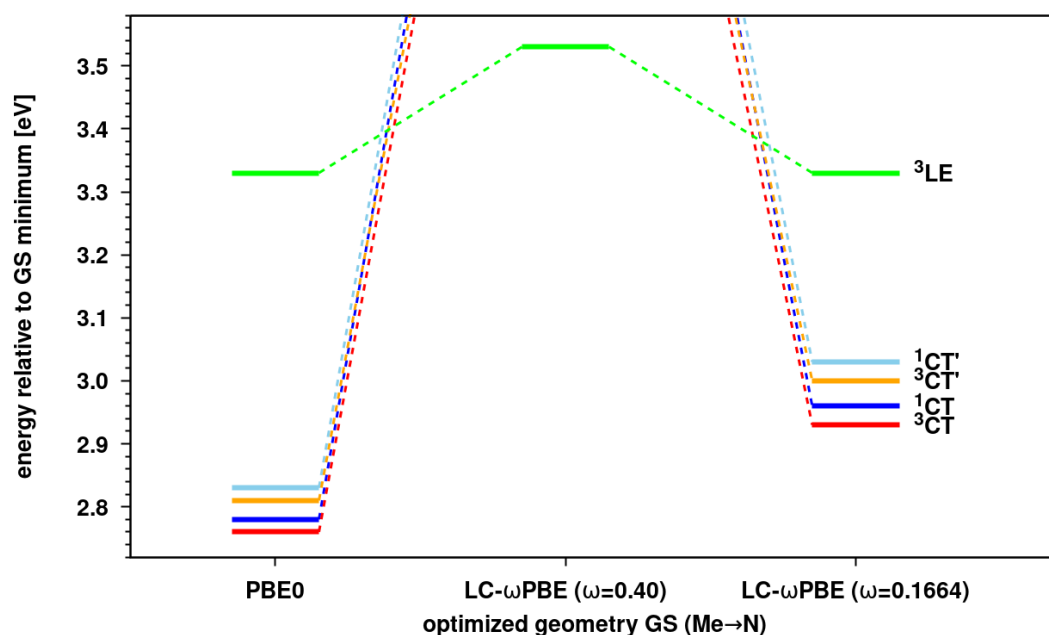


Figure B.7: TDDFT energies at the optimized ground-state geometry GS (Me→N) in vacuo at PBE0/def2-SV(P) or LC- ω PBE/6-31+G* level of theory using the standard range-separation parameter $\omega = 0.40 \text{ bohr}^{-1}$ and the optimized value $\omega = 0.1664 \text{ bohr}^{-1}$ from Ref. [163]. The excited states are labeled as follows: 1 CT blue, 3 CT orange, 1 CT' forest-green, 3 CT' red, 3 LE skyblue. For LC- ω PBE ($\omega = 0.40 \text{ bohr}^{-1}$), the CT singlet and triplet states are located at energies higher than 4.5 eV.

C Publications and Manuscripts in Preparation

Publication I

Vibronic effects accelerate the intersystem crossing processes of the through-space charge transfer states in the triptycene bridged acridine–triazine donor–acceptor molecule TpAT-tFFO

J. M. Kaminski, A. Rodríguez-Serrano, F. Dinkelbach, H. Miranda-Salinas, A. P. Monkman, & C. M. Marian

Chem. Sci., 13(23):7057–7066, 2022

DOI: 10.1039/d1sc07101g

Contribution: Quantum chemical investigation of ground and excited states belonging to conformer (Me→Ph) and computation of all (spin-)vibronic interactions including the calculation of (non-)radiative rate constants within the FC and FC+HT approximation, preparation of Figures 3-6 and 8-11, contributions to writing and revising the manuscript.

Cite this: *Chem. Sci.*, 2022, 13, 7057

All publication charges for this article have been paid for by the Royal Society of Chemistry

Vibronic effects accelerate the intersystem crossing processes of the through-space charge transfer states in the triptycene bridged acridine–triazine donor–acceptor molecule TpAT-tFFO†

Jeremy M. Kaminski,^a Angela Rodríguez-Serrano,^a Fabian Dinkelbach,^a Hector Miranda-Salinas,^b Andrew P. Monkman^b and Christel M. Marian^{*a}

Quantum chemical studies employing combined density functional and multireference configuration interaction methods suggest five excited electronic states to be involved in the prompt and delayed fluorescence emission of TpAT-tFFO. Three of them, a pair of singlet and triplet charge transfer (CT) states (S_1 and T_1) and a locally excited (LE) triplet state (T_3), can be associated with the (Me \rightarrow N) conformer, the other two CT-type states (S_2 and T_2) form the lowest excited singlet and triplet states of the (Me \rightarrow Ph) conformer. The two conformers, which differ in essence by the shearing angle of the face-to-face aligned donor and acceptor moieties, are easily interconverted in the electronic ground state whereas the reorganization energy is substantial in the excited singlet state, thus explaining the two experimentally observed time constants of prompt fluorescence emission. Forward and reverse intersystem crossing between the singlet and triplet CT states is mediated by vibronic spin–orbit interactions involving the LE T_3 state. Low-frequency vibrational modes altering the distance and alignment of the donor and acceptor π -systems tune the S_1 and T_3 states (likewise S_2 and T_3) into and out of resonance. The enhancement of intersystem crossing due to the interplay of vibronic and spin–orbit coupling is considered a general feature of organic through-space charge-transfer thermally activated delayed fluorescence emitters.

Received 20th December 2021

Accepted 16th February 2022

DOI: 10.1039/d1sc07101g

rsc.li/chemical-science

1 Introduction

Recently, Kaji and co-workers¹ presented combined experimental and theoretical studies of TpAT-tFFO, a thermally activated delayed fluorescence (TADF) emitter constituted by 9,9-dimethyl-9,10-dihydroacridine as a donor (A), 2,4-diphenyl-1,3,5-triazine as an acceptor (T) and triptycene (Tp) as a bridge connecting the subunits A and T in a tilted face-to-face (tFF) configuration with optimal (O) distance (Fig. 1).

A key feature of a TADF emitter is an efficient reverse intersystem crossing (rISC) from the triplet manifold to the first excited singlet state by which triplet as well as singlet excitons can be harvested in an organic light-emitting diode (OLED). In principle, therefore internal quantum efficiencies of up to 100% can be reached in a TADF OLED. Because of the through-space

configuration of the donor and acceptor moieties in TpAT-tFFO ($d_{DA} = 4.72$ Å), the spatial overlap between HOMO and LUMO is very small which in turn leads to a minuscule energy separation between the lowest excited singlet and triplet states. While a small singlet–triplet energy gap ($\Delta E_{ST} < 0.1$ eV) is favorable for thermally activated processes such as rISC, the negligible spatial overlap of the hole and particle densities results in a moderate $S_1 \rightarrow S_0$ transition dipole moment in accordance with the comparably low fluorescence rate constant of $k_F = 1.1 \times 10^6$ s^{−1} deduced from experiment.¹ With ISC and rISC rate constants of $k_{ISC} = 5.2 \times 10^7$ s^{−1} and $k_{rISC} = 1.2 \times 10^7$ s^{−1}, respectively, at room temperature (RT) in doped film, the ISC

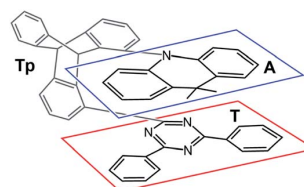


Fig. 1 Chemical structure TpAT-tFFO with its donor (A, blue box), acceptor (T, red box), and linker (Tp, unframed) subunits.

^aInstitute of Theoretical and Computational Chemistry, Heinrich-Heine-University Düsseldorf, D-40204 Düsseldorf, Germany. E-mail: christel.marian@hhu.de

^bDept of Physics, OEM Research Group, Durham University, Durham, DH1 3LE, UK. E-mail: a.p.monkman@durham.ac.uk

† Electronic supplementary information (ESI) available: Details of the electronic structure data, TDDFT energies, scans along normal modes and linearly interpolated paths, spin–orbit coupling matrix elements and their derivatives with respect to normal modes. See <https://doi.org/10.1039/d1sc07101g>



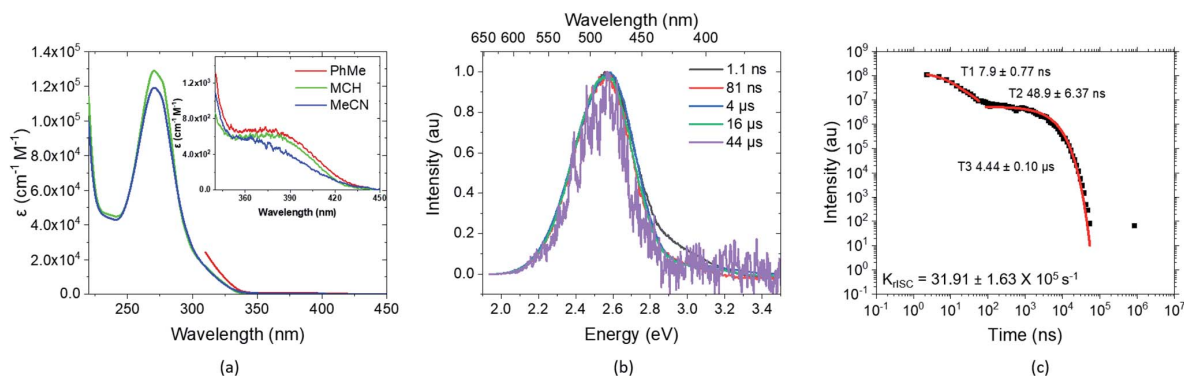


Fig. 2 Experimental key results on the photophysics of **TpAT-tFFO**, presented in detail in ref. 2. (a) Extinction coefficients in different solvents and close-up of the direct CT absorption band in the inset, (b) time-resolved spectral frames of the PhMe degassed solution at different times and (c) decay, lifetimes and k_{rISC} of the same PhMe solution (all solution concentrations are $20 \mu\text{M L}^{-1}$).

and rISC processes are an order of magnitude faster than prompt fluorescence in this molecule, *i.e.*, the excited singlet and triplet populations can largely equilibrate before emitting delayed fluorescence with a radiative lifetime of $4.1 \mu\text{s}$.¹

Newer time-resolved measurements in various solvents and host matrices by Monkman and coworkers, described in detail in a forthcoming publication,² suggest the excitation decay kinetics to be even more involved. Two components for the decay of prompt fluorescence with different time constants but essentially identical emission wavelengths are observed followed by delayed fluorescence in degassed solution at RT (Fig. 2). In mCBP host, in addition strong long-lived phosphorescence emission is seen at 20 K. While the absolute S_1 and T_1 energies change from host to host, their energy separation ΔE_{ST} stays surprisingly constant at about $0.016 \pm 0.002 \text{ eV}$.² These intriguing experimental observations call for a detailed quantum chemical study of the **TpAT-tFFO** donor-acceptor complex that can shed light on its excited-state decay processes.

Because ISC and rISC between singlet and triplet charge-transfer (CT) states of equal electronic structure are orbitally forbidden, spin-vibronic coupling with a nearby locally excited (LE) triplet state has been argued to be essential for enhancing the radiationless $^1\text{CT} \leftrightarrow ^3\text{CT}$ transitions in both, through-bond and through-space donor-acceptor complexes.^{1,3–12} Quantum chemical calculations on **TpAT-tFFO** in the framework of time-dependent density functional theory (TDDFT)⁴ suggest the presence of a ^3LE state on the T acceptor in close energetic proximity of the lowest-lying ^1CT and ^3CT states. The results of this study further indicate that a tilted face-to-face (tFF) alignment of A and T gives rise to stronger spin-orbit coupling (SOC) between ^1CT and ^3LE (0.61 cm^{-1}) than the parallel face-to-face (pFF) alignment (0.05 cm^{-1}) of the donor and acceptor moieties while the SOC between ^1CT and ^3CT vanishes (0.00 cm^{-1}) in both conformations. Therefore, spin-vibronic effects are expected to play an essential role in the ISC and rISC transitions of this TADF emitter. This three-state model can, however, not explain the bi-exponential decay of the prompt fluorescence observed in the newer time-resolved experiments by the Monkman group.² To elucidate the mechanisms underlying the

considerably fast ISC and rISC of **TpAT-tFFO** found in experiment, we have characterized the electronic structures of its low-lying singlet and triplet states in the framework of density functional theory (DFT) and multi-reference configuration interaction (MRCI) methods and explored their interactions by means of associated spin-orbit coupling and property programs. The chosen computational protocol has proven to yield energies and rate constants that are sufficiently accurate to provide valuable insights into the kinetics of competitive radiative and nonradiative decay processes.^{13–17}

2 Computational methods

Electronic ground-state geometries of the **TpAT-tFFO** emitter were optimized using the Turbomole program package¹⁸ and DFT at the PBE0-D3(BJ)/def2-SV(P) level of theory^{19,20} including Grimme's dispersion correction (D3) together with Becke and Johnson (BJ) damping.^{21,22} Time-dependent DFT (TDDFT) was used for the optimization of the excited singlet states^{23–26} while the Tamm-Dancoff approximation (TDA) was utilized for the optimization of the excited triplet states.²⁷ Analytic harmonic vibrational frequencies were computed by means of Gaussian16.²⁸

Vertical and adiabatic excitation energies and optical electronic properties were calculated using the DFT/MRCI method.^{29–31} Up to 25 roots at the respective ground-state geometries and 10 roots at the excited-state geometries were determined for each singlet and triplet manifold in DFT/MRCI employing closed-shell BH-LYP^{32,33} orbitals as the one-particle basis. The parametrization of the Hamiltonian reported in Lyskov *et al.*³⁴ for the tight configuration selection threshold of $0.8E_{\text{h}}$ was employed (DFT/MRCI-R2016), which is specially designed for large multichromophoric systems. Fragment-based analyses of the singlet and triplet DFT/MRCI wavefunctions were performed by an extended version of the THEODORE tool box.^{17,35} Mutual spin-orbit coupling matrix elements (SOCMEs) between target singlet and triplet states were calculated with the spin-orbit coupling kit (SPOCK) developed in our group.^{36–38} Here, the SOC is described by using the Breit-Pauli

Hamiltonian and the atomic spin-orbit mean-field approximation.^{39,40} Rate constants for ISC and rISC between excited singlet and triplet states were determined in the framework of Fermi's golden rule approximation and a time-dependent Fourier transform approach as implemented in the VIBES program.^{41,42} Temperature effects were accounted to the rate constants by assuming a Boltzmann distribution in the initial electronic state. In the Franck-Condon (FC) approximation, the rate constant for the $S_a \rightsquigarrow T_b$ ISC at a given temperature T is computed as the sum of squared electronic SOCMEs between the initial singlet state S_a at its minimum geometry Q_0 and the three triplet sublevels T_b^α , multiplied by the Boltzmann and FC weighted density of vibrational states according to⁴⁴

$$k_{\text{ISC}_{ab}}^{\text{FC}}(T) = \frac{2\pi}{\hbar Z} \sum_{\alpha} \left| \langle \Psi_{T_b^\alpha} | \hat{H}_{\text{SO}} | \Psi_{S_a} \rangle \right|_{Q_0}^2 \times \sum_k e^{-\frac{(E_{ak}-E_{a0})}{k_B T}} \sum_j |\langle v_{bj} | v_{ak} \rangle|^2 \delta(E_{ak} - E_{bj}) \quad (1)$$

here k_B is the Boltzmann constant and $Z = \sum_k e^{-\frac{(E_{ak}-E_{a0})}{k_B T}}$ the partition function of the initial state. In the Herzberg-Teller (HT) approximation, the SOC is expanded as a function of the normal coordinates Q of the initial state about Q_0 and the expansion is terminated after the linear term.^{8,43,44}

$$k_{\text{ISC}_{ab}}^{\text{FC+HT}}(T) = \frac{2\pi}{\hbar Z} \sum_{\alpha} \sum_k e^{-\frac{(E_{ak}-E_{a0})}{k_B T}} \sum_j \langle v_{bj} | \langle \Psi_{T_b^\alpha} | \hat{H}_{\text{SO}} | \Psi_{S_a} \rangle \Big|_{Q_0} + \sum_A \frac{\partial \langle \Psi_{T_b^\alpha} | \hat{H}_{\text{SO}} | \Psi_{S_a} \rangle}{\partial Q_A} \Big|_{Q_0} Q_A |v_{ak}\rangle|^2 \delta(E_{ak} - E_{bj}) \quad (2)$$

Squaring this expression yields a pure FC term, a mixed FC/HT term and a HT/HT term. Similar formulas result for the reverse $S_a \leftarrow T_b$ process. The SOCME gradients in eqn (2) were determined by averaged two-point finite difference techniques. To this end, the nuclear framework was deflected from the respective minimum geometry in positive and negative directions of the dimensionless vibrational normal modes utilizing a step size of 0.1 units. Phase corrections were applied as described in earlier work.¹⁷

To check whether vibronic effects accelerate fluorescence as well, electric dipole transition moments and their numerical derivatives were employed to compute fluorescence in FC and HT approximation. Because the HT spectra are not properly normalized in the VIBES program, we made use of the closure relation for FC factors to normalize the HT spectrum and to determine fluorescence rate constants according to

$$k_F^{\text{HT}} = \int I^{\text{HT}}(\omega) d\omega = \frac{4}{3\hbar c_0^3} \frac{\int \omega^3 S^{\text{HT}}(\omega) d\omega}{\int S^{\text{FC}}(\omega) d\omega} \quad (3)$$

where $I^{\text{HT}}(\omega)$ is the frequency dependent intensity of the computed HT spectrum, \hbar is Planck's constant divided by 2π , c_0 is the vacuum speed of light and $S^{\text{HT}}(\omega)$ and $S^{\text{FC}}(\omega)$ are the HT

and FC spectral densities, respectively. Phosphorescence rate constants were determined in FC approximation using multi-reference spin-orbit configuration interaction (MRSOCI)³⁸ wavefunctions.

3 Computational results

3.1 Ground state

3.1.1 Conformer geometries. The optimization of the electronic ground state led to two different conformations (Fig. 3) which are almost energetically degenerate at DFT/MRCI-R2016 level of theory ($\Delta E = 0.02$ eV). A very shallow barrier separates the S_0 potential energy well of the (Me \rightarrow N) conformer (Fig. 3 left) from the one of the slightly more stable (Me \rightarrow Ph) conformer (Fig. 3 right). Vibrational mode 1 (Fig. S1†), which transforms the two ground state conformers into one another, exhibits a harmonic frequency of merely 8 cm^{-1} . Unless hindered by a rigid environment, the two conformers should be easily interconvertible in the electronic ground state at RT.

3.1.2 Absorption spectra. The absorption spectrum measured in apolar solvents and our computed vertical absorption spectra (Fig. 4) match very well, thus validating the computation protocol. The measurements cover a spectral range between ca. 250 and 450 nm. Two transitions, namely S_2

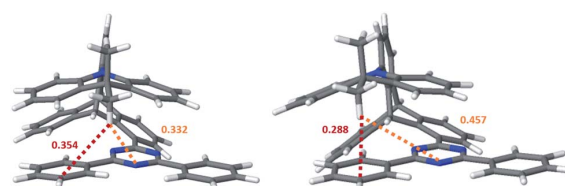


Fig. 3 Nuclear arrangements at the two ground state minima of TpAT-tFFO optimized at PBE0-D3(BJ)/def2-SV(P) level of theory (left: $S_0(\text{Me} \rightarrow \text{N})$; right: $S_0(\text{Me} \rightarrow \text{Ph})$). Distances between the proximal methyl hydrogen atom of the A donor and the triazine (orange) or phenyl (red) rings of the T acceptor are given in nm.

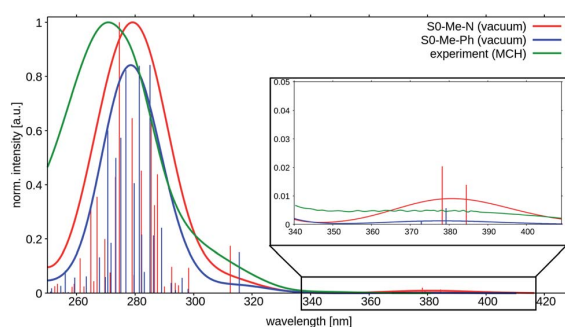


Fig. 4 Vertical absorption spectra at the two ground state minima of TpAT-tFFO at the DFT/MRCI-R2016 level of theory *in vacuo* (red: $S_0(\text{Me} \rightarrow \text{N})$, blue: $S_0(\text{Me} \rightarrow \text{Ph})$). The experimental UV-vis absorption spectrum of TpAT-tFFO (green) was recorded in MCH solution at RT. For details. See ref. 2.



$\leftarrow S_0$ and $S_1 \leftarrow S_0$, contribute to the weak band in the long wavelength regime. Both result from A-to-T CT transitions, with the electron density being transferred to the one or the other side of the T acceptor (*ca.* Fig. S4 and S7†). The calculations find three triplet states in this wavelength regime, too. T_1 and T_2 are CT states which exhibit very similar electron density distributions as their singlet counterparts whereas T_3 has predominantly LE(T) character. The low energy regime is the only part of the spectrum where the two conformers show marked variations. In particular, the oscillator strengths of the $S_2 \leftarrow S_0$ and $S_1 \leftarrow S_0$ electric dipole transitions are substantially smaller for the $S_0(\text{Me} \rightarrow \text{Ph})$ conformer than for the $S_0(\text{Me} \rightarrow \text{N})$ conformer on an absolute scale while their absorption wavelengths are nearly identical. To give an estimate of their relative intensities, we have normalized the calculated spectra, plotted in Fig. 4, with respect to the strong ^1LE transition of the $S_0(\text{Me} \rightarrow \text{N})$ conformer at *ca.* 275 nm. Qualitatively, the residual intensity of the experimental spectrum in the long wavelength regime (inset of Fig. 4) appears to match better with the absorption spectrum computed for the slightly more stable $S_0(\text{Me} \rightarrow \text{Ph})$ conformer. The shoulder in the experimental spectra at about 315 nm originates from the $S_3 \leftarrow S_0$ transition. Fragment-based analyses of the DFT/MRCI wavefunctions (Fig. S5 and S8†) reveal this transition to have mixed **Tp** linker-to-T acceptor CT and **Tp** LE character. The high oscillator strengths of the spectral lines forming the strong absorption band between approximately 290 and 260 nm originate from local $\pi\pi^*$ transitions. The intense lines in the 285 nm region are mainly due to ^1LE transitions on the T acceptor moiety whereas the spectrum in the 275 nm region is formed by local $^1\pi\pi^*(\text{A})$ donor transitions.

The shapes and positions of the experimental bands appear to be rather insensitive with respect to the solvent polarity as seen when comparing the spectral signatures of **TpAT-tFFO** in methyl cyclohexane (MCH), toluene (PhMe) and acetonitrile (MeCN) solution.^{1,2} The absorption spectrum recorded in toluene breaks off at about 300 nm where the solvent starts to absorb. At longer wavelength it is very similar to the spectra in other solvent environments. Similar observations were made for the quantum chemical modeling of the absorption. Test calculations on **TpAT-tFFO** in toluene solution led to nearly identical results as *in vacuo*, so that solvent effects have been neglected in the following. Note, however, the strong solvent-dependent Stokes shifts of the experimental emission wavelengths,² typical for CT transitions in liquid solution where the solvent shell can reorganize and adapt to the altered polarity of the solute in the excited state. In more rigid environments, where this reorganization is hindered at the time scale of the experiment, the experimental onset energies exhibit a much smaller variation.

3.2 Excited states

3.2.1 Geometries and electronic structures. To find a correspondence between the low-lying electronically excited states of **TpAT-tFFO** at the TDDFT (PBE0) and DFT/MRCI levels of theory, TDDFT single-point calculations at the electronic ground-state geometries of both conformers were carried out.

As may be expected, the energies of the CT states (S_1 , S_2 , T_1 and T_2) are somewhat underestimated by the TDDFT (PBE0) calculations in comparison to DFT/MRCI, while similar excitation energies are found for the T_3 LE state. More importantly, however, the electronic structures of these five states match very well at both levels of theory (compare Tables S1, S2, S9, and S11†) so that a TDDFT (PBE0) geometry optimization of the excited states is considered meaningful. If the optimally tuned range-separated LC- ω PBE functional, employed in previous theoretical work on **TpAT-tFFO**,¹ is used instead, blue shifts of the CT state energies (Tables S10 and S12†) by about 0.2 eV in comparison to the PBE0 results are observed, but the electronic structures of the five low-lying states do not significantly change.

The optimization of the first two excited singlet states (S_1 and S_2 , both CT states) and the first three excited triplet states (T_1 and T_2 : CT states, T_3 : LE state) yielded the desired minima on the potential energy surface (PES). Note, however, that the energetic order of the states may vary from geometry to geometry. To avoid confusion, we have kept the state designations used in the FC region of the (Me \rightarrow N) conformer. For example, the locally excited triplet state is the third triplet state at the ground-state geometry. Hence, the ^3LE state is named T_3 and it retains this name irrespective of the energetic order at other geometries. Difference densities visualizing the characters of the electronic states at their respective minimum geometries are displayed in Fig. 5.

In general, the geometry relaxation in the excited states leads to mild changes in the tilted alignment between A and T (up to 3.0°). In detail, some dihedral angles between the triazine molecular plane and the benzene moieties of A change. Furthermore, a distortion of the triazine moiety itself resulting from bond length alterations with respect to the electronic ground states can be made out in all excited state structures. To provide an overview over the particular displacements of the minimum geometries, we constructed overlays of the ground and excited state structures such that their **Tp** bridges exhibit minimal root mean square deviations (Fig. 6). With regard to their minimum nuclear arrangements, the electronic states can

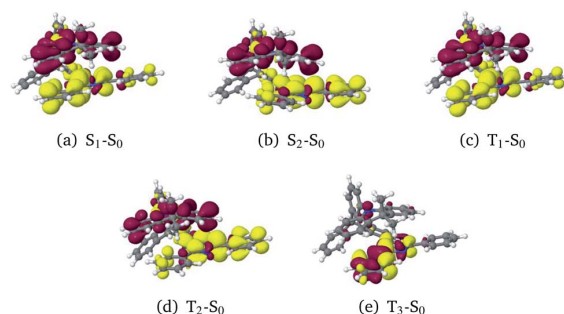


Fig. 5 Difference densities (± 0.001) of the excited states at their optimized geometries. Areas losing electron density in comparison to the electronic ground state are shown in red, areas gaining electron density in yellow.



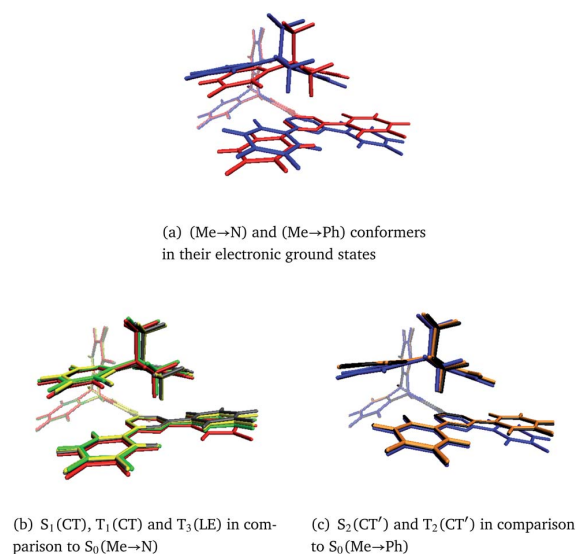


Fig. 6 Overlays of TpAT-tFFO molecular frames visualizing the coordinate displacements of the respective minimum nuclear arrangements while minimizing the root mean squares deviations of the **Tp** bridges. The following color codes have been used: red: $S_0(\text{Me} \rightarrow \text{N})$, blue: $S_0(\text{Me} \rightarrow \text{Ph})$, gray: $S_1(\text{CT})$, yellow: $T_1(\text{CT})$, green: $T_3(\text{LE})$, orange: $S_2(\text{CT}')$, black: $T_2(\text{CT}')$. Details of the electronic structure data can be found in Tables S1–S8 and Fig. S3–S26.†

be grouped into two clusters: $S_0(\text{Me} \rightarrow \text{N})$, $S_1(\text{CT})$, $T_1(\text{CT})$ and $T_3(\text{LE})$ exhibit similar relative orientations of the **A** and **T** subunits whereas $S_2(\text{CT}')$ and $T_2(\text{CT}')$ more closely resemble the $S_0(\text{Me} \rightarrow \text{Ph})$ conformer.

Surprisingly, the energies of the $S_1(\text{CT})$ and $S_2(\text{CT}')$ states are nearly degenerate after structural relaxation to their respective minima on the PES (Table 1). In contrast, they are separated vertically by more than 0.5 eV (Fig. S27†). In terms of a Marcus-type model, a substantial reorganization energy has to be overcome for a transition between their potential energy wells. A similar picture is obtained for the corresponding excited $T_1(\text{CT})$ and $T_2(\text{CT}')$ states. On an absolute scale, the calculated adiabatic ^1CT and ^3CT energies are in good agreement with experimental on-set energies of the singlet and triplet transitions in various host matrices (Table 1). Note, however, that the calculated adiabatic ΔE_{ST} values of 0.09 eV (S_1 – T_1) and 0.15 eV (S_2 – T_2) are significantly larger than the singlet–triplet energy gaps

derived experimentally (0.016 ± 0.002 eV) on the basis of temperature-dependent measurements in the solid state.

The potential energy scheme in Fig. S27† implies the existence of conical intersections between the CT and CT' states which have been located at energies approximately 0.15 eV above the respective minima. Optimization of the $T_3(\text{LE})$ energy brings this state adiabatically into near degeneracy with the excited singlet states (0.01 eV above). Due to the closer geometric resemblance of the S_1 and T_3 structures, their reorganization energy is much smaller than for the S_2 and T_3 pair of states. While being in qualitative agreement with the scheme proposed by Kaji and co-workers on the basis of their experimental and theoretical data, the results of our computational study paint a more intricate picture of the excited-state processes in TpAT-tFFO.

3.2.2 Linearly interpolated paths. To obtain a better overall view of possible excited-state transition pathways, linearly interpolated potential energy profiles (LIPs) between target singlet and triplet state minima were constructed. Fig. 7a shows a relaxation pathway connecting the ground state of the ($\text{Me} \rightarrow \text{N}$) conformer with the minimum of the $S_1(\text{CT})$ state. Several crossings in the vicinity of the FC region can be made out. In contrast, the energy profiles for transitions between excited singlet and triplet states with same character are very flat (Fig. S28a†). The conical intersection, found while optimizing the excited triplet states, is probably not as important for the relaxation pathway as Fig. 7c may suggest. When trying to connect the CT and CT' states directly, we detected a pathway with much smaller activation barrier (Fig. S27b†). Thus, in liquid solution both excited ^1CT states can be interconverted by a simultaneous torsional motion of the **A** and **T** units about their links to the **Tp** bridge at moderate cost, similar to a deflection along mode 1 in the electronic ground state (Fig. S1†). The CI connects the two lowest excited triplet states and the two lowest excited singlet states. In the geometrical vicinity of the crossing point, S_1/T_2 and S_2/T_1 intersections with sizeable SOCMEs are found that might contribute to singlet–triplet mixing by ISC or rISC. Note, however, that – in addition to the singlet–triplet energy gap and the mutual electronic coupling of the initial and final states – the overlap of their vibrational wavefunctions is an important factor contributing to the nonradiative transition rates.⁹ The $S_1(\text{CT})$ and $T_3(\text{LE})$ potentials are found to cross as well whereas $T_1(\text{CT})$ and $T_3(\text{LE})$ undergo an avoided crossing along the LIP connecting their

Table 1 Adiabatic DFT/MRCI excitation energies ΔE of low-lying singlet and triplet states of TpAT-tFFO in comparison with experimental on-sets in various hosts. Zero-point vibrational energy (ZPVE) corrections were computed at the (TD)DFT level of theory. All energies in eV

State		ΔE_0^0	ZPVE	Experimental on-sets ²
S_1	CT	2.97	−0.11	2.853 (UGH-3), 2.818 (mCBP), 2.893 (CzSi), 2.943 (zeonex)
S_2	CT'	2.98	−0.12	
T_1	CT	2.88	−0.11	2.839 (UGH-3), 2.800 (mCBP), 2.877 (CzSi), 2.930 (zeonex)
T_2	CT'	2.83	−0.12	
T_3	LE	2.99	+0.04	



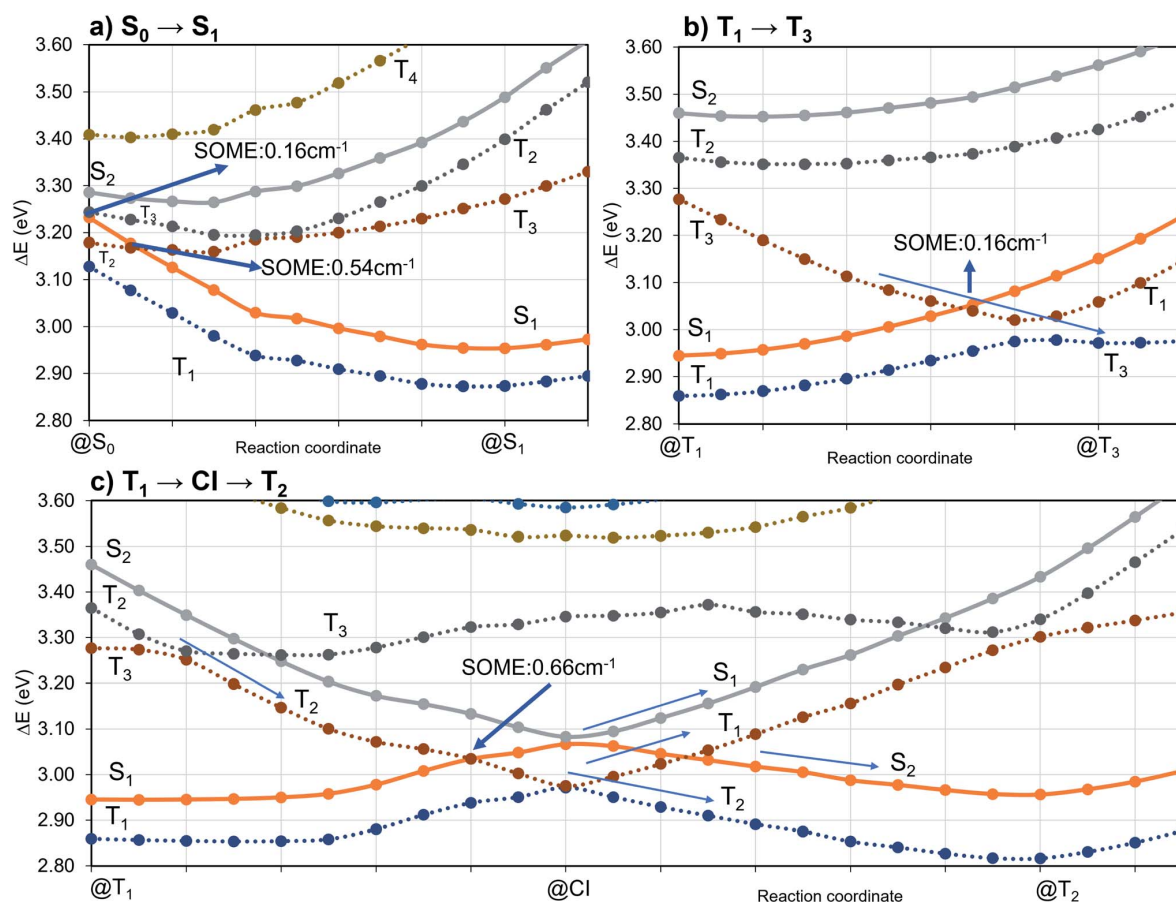


Fig. 7 DFT/MRCI energy profiles along linear interpolated pathways (LIPs) between target electronic state minima. Dashed lines correspond to triplet state PESs while solid lines correspond to singlet states.

minima (Fig. 7b). Although the SOCME between S_1 and T_3 is much smaller than for the S_1/T_2 pair of states, we will see that the T_3 (LE) state plays a decisive role in the ISC and rISC kinetics of the CT states.

To investigate the importance of the tilted face-to-face alignment of the donor and acceptor units for the photo-physics of **TpAT-tFFO**, the molecular frame was deflected along selected vibrational modes of the Me \rightarrow N conformer, namely vibrational mode 1 (Fig. S1†), which transforms the two ground state conformers into one another, and the vibrational modes 9 and 12 (Fig. 8), which are low-frequency modes that move the donor-acceptor π -systems closer to or further away from one another. Even small distortions along these modes are sufficient to reach a crossing between S_1 (CT) and T_3 (LE) (Fig. S2, S29 and S30†) while the ground-state energy increases only slightly. Additionally, these vibrational motions have large impact on the oscillator strengths of the $S_1 \leftarrow S_0$ and $S_2 \leftarrow S_0$ processes. We therefore expect dynamic processes beyond the FC approximation to play an important role.

3.2.3 Emission properties. As the S_1 (CT) and the S_2 (CT') states represent nearly isoenergetic minima on the PES of the

first excited singlet state, both may contribute to the fluorescence. The calculations find a broad 1 CT emission band with maximum at 503 nm for the isolated (Me \rightarrow N) conformer at 300 K in HT approximation which is blue shifted to 483 nm when cooling the molecule to 20 K. The corresponding emission maxima for the 1 CT emission of the (Me \rightarrow Ph) conformer lie at nearly identical positions, namely at 499 nm for a sample at 300 K and 478 nm at 20 K. With a value of $k_F^{HT} \approx 1.1 \times 10^6 \text{ s}^{-1}$, the

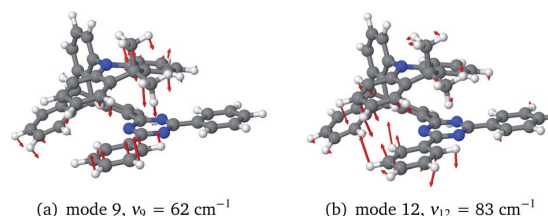


Fig. 8 Low-frequency ground-state vibrational modes of the (Me \rightarrow N) conformer moving the donor-acceptor π -systems closer to one another (positive deflection) or further away (negative deflection).

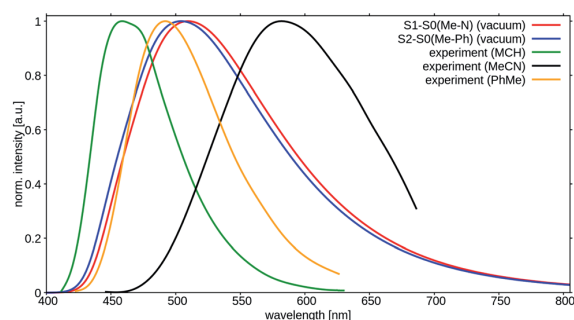


Fig. 9 Calculated room temperature fluorescence spectra of TpAT-tFFO (red: $S_1 \rightarrow S_0$ (Me \rightarrow N), blue: $S_2 \rightarrow S_0$ (Me \rightarrow Ph)) in comparison to experimental emission spectra in methyl cyclohexane (green), toluene (gold) and acetonitrile (black).²

radiative rate constant for the spontaneous fluorescence of the (Me \rightarrow Ph) conformer is somewhat smaller than for the corresponding value of the (Me \rightarrow N) conformer ($k_F^{\text{HT}} \approx 1.3 \times 10^6 \text{ s}^{-1}$) and might explain the occurrence of two prompt fluorescence components with essentially identical emission wavelengths in the latest experiments.² The HT values agree also well with the radiative rate constant of $1.1 \times 10^6 \text{ s}^{-1}$ derived experimentally by Kaji and coworkers.¹ HT coupling speeds up the fluorescence, but not to a substantial extent as may be judged from a comparison with the corresponding values in FC approximation, *i.e.*, $k_F^{\text{FC}} \approx 2.0 \times 10^5 \text{ s}^{-1}$ (Me \rightarrow Ph) and corresponding value of the (Me \rightarrow N) conformer ($k_F^{\text{FC}} \approx 7.0 \times 10^5 \text{ s}^{-1}$).

The peak positions of the experimental fluorescence spectra in liquid solution at RT are seen to vary substantially for different solvents (Fig. 9). The strong Stokes shift of the emission in MeCN in comparison to MCH solution is caused, for example, by the electrostatic interactions of the very polar CT state of the solute and the reorganized polar solvent environment. The fact that even the spectrum in toluene is red shifted is mostly attributed to π -stacking interactions between the solute and the solvent. Both, solvent reorganization and π -stacking effects are not included in our computational model. It is therefore not surprising that the peak positions of the computed $S_1 \rightarrow S_0$ and $S_2 \rightarrow S_0$ transitions do not agree well with the measured peak maxima in liquid solution (Fig. 9). The fact that the computed spectra show more pronounced tails in the long wavelength region than the experimental fluorescence spectrum is a consequence of the harmonic oscillator approximation that is not well obeyed by transitions involving higher vibrational levels of the electronic ground state.

Much better agreement is found when the calculated adiabatic excitation energies of the isolated molecules are compared with the experimental on-sets of the emission spectra in rigid matrices that prevent the reorganization of the solvent cage (Table 1).

In order to rationalize the long-time component of the emission observed experimentally at 20 K,² phosphorescence rate constants of the three low-lying triplet states were computed in FC approximation. Because vibronic interactions

had only a moderate effect on the fluorescence and the computational costs for evaluating them are substantial, we refrained from computing phosphorescence in HT approximation. Component-averaged phosphorescence rate constants of $k_P^{\text{FC}} \approx 0.4 \times 10^{-1} \text{ s}^{-1}$ (T_1), $k_P^{\text{FC}} \approx 1.0 \times 10^{-1} \text{ s}^{-1}$ (T_2), and $k_P^{\text{FC}} \approx 8.3 \times 10^{-1} \text{ s}^{-1}$ (T_3) were obtained corresponding to radiative lifetimes of 25 s, 10 s, and about 1 s, respectively. Looking only at the numbers, one might be tempted to attribute the emission on the 100 millisecond time scale to phosphorescence emission from the LE T_3 state that forms a shallow minimum on the first excited triplet energy surface. The LIPs in Fig. 7b suggest, however, strong nonadiabatic interactions between the T_3 and T_1 state in their crossing region energetically and geometrically close to the T_3 minimum. Moreover, motions altering the tilted face-to-face of the donor and acceptor moieties (compare Fig. S30†) lead to crossings between T_2 and T_3 . It can therefore be assumed that a triplet population in the T_3 potential well rapidly relaxes *via* internal conversion to the lower-lying T_1 or T_2 states. Hence, phosphorescence is expected to originate from the ^3CT states and not from the ^3LE state. In addition to phosphorescence, $T_1(\text{CT}) \rightarrow S_0$ and $T_2(\text{CT}) \rightarrow S_0$ nonradiative deactivation of the triplet population will occur, explaining the difference between the observed phosphorescence decay times (100 ms regime) and the much larger theoretical lifetime values (10 s regime) which correspond to purely radiative processes.

3.2.4 Intersystem crossing. The magnitudes of the spin-component averaged SOCMEs, presented in Table 2 at various minimum geometries, suggest at first sight that the $S_1 \leftrightarrow T_2$ and $S_2 \leftrightarrow T_1$ ISC and rISC processes dominate the singlet-triplet population transfer. This is, however, not the case because their vibrational overlaps are smaller than for states belonging to the same geometrical cluster. Taking the FC factors and the energy matching conditions of the Fermi golden rule expression for the probability of a nonradiative transition into consideration yields ISC and rISC rate constants, which are two orders of magnitude too small in comparison to experiment (Table S14†). It is well known, however, that spin-vibronic interactions can substantially enhance orbitally forbidden ISC and rISC processes.^{3–9} The computation of ISC and rISC rate constants of donor-acceptor compounds therefore requires to go beyond the FC approximation. Without going into details, there are two major routes to proceed, a dynamic and a static one. While the first route is optimally taken for simulating ultrafast

Table 2 Component-averaged spin-orbit matrix elements (SOCMEs, cm^{-1}) between low-lying singlet and triplet states calculated at the excited state minima of TpAT-tFFO

Interacting states	@ S_1	@ S_2	@ T_1	@ T_2	@ T_3
$\langle S_1 \hat{H}_{\text{SO}} T_1 \rangle$	0.027	—	0.039	—	—
$\langle S_1 \hat{H}_{\text{SO}} T_2 \rangle$	0.760	—	—	0.666	—
$\langle S_1 \hat{H}_{\text{SO}} T_3 \rangle$	0.170	—	—	—	0.142
$\langle S_2 \hat{H}_{\text{SO}} T_1 \rangle$	—	0.581	0.750	—	—
$\langle S_2 \hat{H}_{\text{SO}} T_2 \rangle$	—	0.082	—	0.087	—
$\langle S_2 \hat{H}_{\text{SO}} T_3 \rangle$	—	0.348	—	—	0.299



Table 3 Rate constants for direct and vibronic ISC/rISC (s^{-1}) between low-lying singlet and triplet state minima of **TpAT-tFFO** employing their computed adiabatic energy differences

Process/ temperature	ISC/20 K	ISC/300 K	rISC/20 K	rISC/300 K
$S_1(\text{CT}) \leftrightarrow T_1(\text{CT})$	4.3×10^5	8.8×10^5	—	2.3×10^4
$S_1(\text{CT}) \leftrightarrow T_2(\text{CT}')$	2.6×10^2	3.6×10^5	—	1.7×10^3
$S_1(\text{CT}) \leftrightarrow T_3(\text{LE})$	—	1.9×10^4	6.5×10^6	6.8×10^6
$S_2(\text{CT}')$	—	1.4×10^5	—	5.2×10^3
$S_2(\text{CT}') \leftrightarrow T_2(\text{CT}')$	3.3×10^6	6.5×10^6	—	3.4×10^4
$S_2(\text{CT}') \leftrightarrow T_3(\text{LE})$	—	1.2×10^3	2.7×10^5	8.4×10^5

nonadiabatic transitions, the static approach employed here is applicable to slower processes as it rests on a HT-type expansion of the spin–orbit interaction.^{8,43,44} Derivatives of the SOCMEs with respect to normal mode displacements were determined for all states of interest, despite the high computational effort.

The inclusion of vibrational SOC commonly enhances transitions between states with the same orbital character because they can get more mixed through displacements along the vibrational modes. In this way, ISC and rISC processes can indirectly borrow intensity from El-Sayed allowed transitions and are accelerated. Although the derivative couplings of the $S_1(\text{CT}) \leftrightarrow T_1(\text{CT})$ and $S_2(\text{CT}') \leftrightarrow T_2(\text{CT}')$ transitions are tiny (Fig. S35 and S36†), the HT terms increase the rate constants of these processes by an order of magnitude in comparison to the FC approximation. In general, the SOCME gradients for transitions between states with similar minimum nuclear arrangements are small in comparison to those for transitions between states belonging to different geometry clusters (Fig. S35–S39†). The largest SOCME gradients are found for vibrational modes located mainly on the triazine acceptor unit of **TpAT-tFFO**. Contrary to the expectations, the fastest ISC is calculated for the transition from $S_2(\text{CT}')$ to $T_2(\text{CT}')$ which is associated with the largest energy gap (Table 3). In addition, the $S_1(\text{CT}) \leftrightarrow T_3(\text{LE})$ rISC rate constant reaches values of the order of 10^7 s^{-1} . The avoided crossing along the LIP connecting the minima of the $T_1(\text{CT})$ and $T_3(\text{LE})$ potentials (Fig. 7b) suggests that the $T_3(\text{LE})$ state in turn interacts with the $T_1(\text{CT})$ state *via* nonadiabatic coupling and thus can act a mediator in the $S_1(\text{CT}) \leftrightarrow T_3(\text{LE}) \leftrightarrow T_1(\text{CT})$ rISC process. A strong coupling between the $T_2(\text{CT}')$ and $T_3(\text{LE})$ pair of states is observed when the π -systems of **A** and **T** are tilted (mode 12, Fig. 8 and S30†). T_3 may therefore act as a mediator of the $S_2(\text{CT}') \leftrightarrow T_3(\text{LE}) \leftrightarrow T_2(\text{CT}')$ rISC process as well.

The cause of the largest uncertainties regarding the computed ISC and rISC rate constants relates to the magnitude of the singlet–triplet energy separation. The ΔE_{ST} values are somewhat overestimated by our quantum chemical calculations (Table 1) and therefore diminish the vibrational overlaps in the weak coupling case with nested PESs of the initial and final states. $S_1 \leftrightarrow T_1$ and $S_2 \leftrightarrow T_2$ belong to this coupling case. The results of various test calculations employing energy-shifted singlet and triplet potentials with gaps ranging from 0.02 to 0.17 eV are displayed in Fig. 10.

Following the energy gap law of the weak coupling case,^{9,45} the rate constants of the $S_1 \rightarrow T_1$ and $S_2 \rightarrow T_2$ ISC transitions

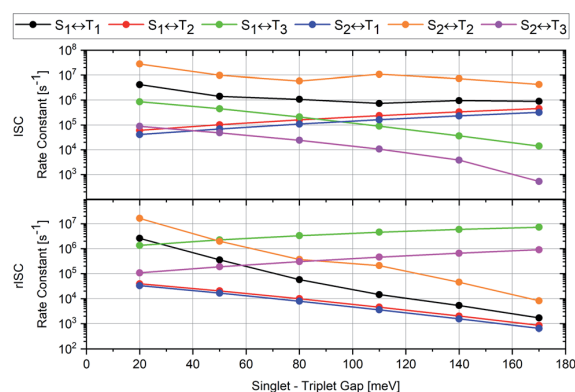


Fig. 10 Variation of the computed rate constants for ISC (upper panel) and rISC (lower panel) at 300 K with the adiabatic singlet–triplet energy separation of the initial and final states. Note the logarithmic scale of the ISC and rISC rate constants. The corresponding numerical data may be found in Tables S15 and S16.†

increase by roughly one order of magnitude when ΔE_{ST} is decreased to 0.02 eV, a value closer to the experimental estimates. As may be expected, the corresponding $S_1 \leftrightarrow T_1$ and $S_2 \leftrightarrow T_2$ rISC processes are affected even more strongly. Their rate constants are substantially enhanced when the singlet–triplet gap is reduced to 0.02 eV. Inverse trends are observed for the $S_1 \rightarrow T_2$ and $S_2 \rightarrow T_1$ ISC transitions which belong to the strong coupling case with substantial geometry displacements in at least some normal coordinates. Their rate constants are reduced by about one order of magnitude when the singlet–triplet gap gets smaller. In both directions, the $S_1 \leftrightarrow T_3$ transitions are preferred over the $S_2 \leftrightarrow T_1$ transitions, despite their smaller electronic SOCMEs (Table 2). These examples once again underscore that it is not sufficient to rely solely on the magnitude of the electronic SOCME when identifying possible ISC and rISC pathways. To get the whole picture, the inclusion of vibrational factors and vibronic interactions is mandatory for modelling ISC and rISC in donor–acceptor compounds.

4 Conclusions

All in all, the results of our quantum chemical studies support a kinetic model for the emission decay of **TpAT-tFFO** involving five electronically excited states which are coupled by spin–orbit and vibronic interactions. Three of these states, a pair of singlet and triplet CT states (S_1 and T_1) and a LE triplet state (T_3), can be associated with the (Me \rightarrow N) conformer of **TpAT-tFFO**. To

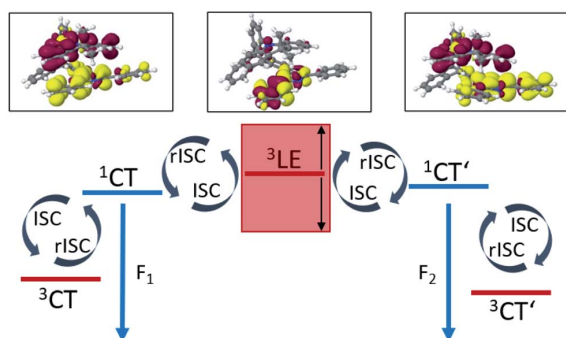


Fig. 11 Schematic excitation decay mechanism of the nearly degenerate (Me \rightarrow N) and (Me \rightarrow Ph) conformers of **TpAT-tFFO**. ISC and rISC processes are promoted by vibronic spin–orbit coupling. Low-frequency vibrations that diminish the distance between donor and acceptor π -systems tune the first excited singlet CT states of the conformers and the LE T_3 state into and out of resonance.

avoid confusion, the other two CT-type states that form the lowest excited singlet and triplet states, respectively, of the (Me \rightarrow Ph) conformer, have been named S_2 and T_2 because they are the second of their kind at the ground-state geometries of both conformers. The two conformers differ in essence by the tilt angle formed by the nearly parallel **A** donor and **T** acceptor moieties with the **Tp** bridge. While the two conformers are easily interconverted in the electronic ground state – given that the environment does not sterically hinder the transformation – this is not the case in the excited state where the reorganization energy is substantial. For this reason, dual fluorescence emission may occur.

Fig. 11 summarizes the most important findings with regard to the excitation decay mechanism. The emission energies of the two excited singlet potential energy wells are nearly identical, but the radiative rate constant of the (Me \rightarrow N) conformer is somewhat larger than the one of the (Me \rightarrow Ph) conformer. This explains why only one emission band but two different prompt fluorescence time constants have been observed experimentally.

Like in many donor–acceptor compounds, the ISC and rISC processes between the CT states of **TpAT-tFFO** are markedly accelerated by spin–vibronic interactions with a nearby LE triplet acceptor state, T_3 , located slightly above the S_1 and S_2 minima according to our calculations. While the computed ISC and rISC rate constants are sensitive with respect to the singlet–triplet energy separations, it is clear that $S_1(\text{CT}) \rightsquigarrow T_1(\text{CT})$ and $S_2(\text{CT}') \rightsquigarrow T_2(\text{CT}')$ ISC outcompete prompt fluorescence. For singlet–triplet energy gaps larger than 0.05 eV, rISC is fastest for the $S_1(\text{CT}) \leftarrow T_3(\text{LE})$ transition which is a slight downhill process. The avoided crossing of the $T_1(\text{CT})$ and $T_3(\text{LE})$ potentials suggests that the $T_3(\text{LE})$ and $T_1(\text{CT})$ states are strongly coupled by nonadiabatic interactions and that thus the $T_3(\text{LE})$ state can act as a mediator in the $S_1(\text{CT}) \leftarrow T_3(\text{LE}) \leftarrow T_1(\text{CT})$ rISC process at RT. The interconversion of the CT' states is promoted by the $T_3(\text{LE})$ state as well. Low-frequency vibrational modes that alter the tilt angle and the interplanar distance of the donor

and acceptor moieties play a decisive role in the nonadiabatic coupling of these triplet states. If the energy gaps between the lowest-lying ^1CT and ^3CT states of the (Me \rightarrow N) and (Me \rightarrow Ph) conformers, $S_1(\text{CT})$ – $T_1(\text{CT})$ and $S_2(\text{CT}')$ – $T_2(\text{CT}')$, are reduced to 0.02 eV, as suggested by the experimental data, the vibronically enhanced $S_1(\text{CT}) \leftrightarrow T_1(\text{CT})$ and $S_2(\text{CT}') \leftrightarrow T_2(\text{CT}')$ mechanisms prevail at RT.

At cryogenic temperatures, the $S_1(\text{CT}) \rightsquigarrow T_1(\text{CT})$ and $S_2(\text{CT}') \rightsquigarrow T_2(\text{CT}')$ ISC are still competitive with fluorescence whereas the corresponding rISC processes are not. $T_1(\text{CT}) \rightarrow S_0$ and $T_2(\text{CT}') \rightarrow S_0$ phosphorescence is held accountable for the long-time component of the emission observed experimentally at 20 K.

Turning our focus from the specific situation in **TpAT-tFFO** to more general aspects of the decay mechanism inherent to organic through-space charge transfer TADF emitters, our results suggest that the interplay between vibronic and spin–orbit effects is a key feature increasing the ISC and rISC probabilities in this class of chromophores. In particular, low-frequency shearing and breathing motions have the potential to alter the interplanar spacing of the donor and acceptor units and hence the energetic position of the singlet and triplet CT states in relation to low-lying triplet LE states. Intersections of the CT and LE potentials along these modes offer easy and efficient pathways for the interconversion of spin multiplicities in these light-element compounds despite the relatively small size of the spin–orbit coupling in comparison to transition metal complexes.

Data availability

Cartesian coordinates of all optimized minimum structures can be obtained upon request from the authors.

Author contributions

Jeremy M. Kaminski and Angela Rodríguez-Serrano (computational investigation, preparation of images and writing), Fabian Dinkelbach (software development and computational setup), Hector Miranda Salinas (experimental investigation and preparation of images), Andrew P. Monkman and Christel M. Marian (conceptualization, funding acquisition, project administration, supervision and writing).

Conflicts of interest

There are no conflicts to declare.

Acknowledgements

This research was funded by the Deutsche Forschungsgemeinschaft (DFG, German Research Foundation) – 396890929/GRK 2482 and MA1051/17-1. HMS acknowledges the Mexican National Council for Science and Technology, CONACYT for his studentship (2019-000021-01EXTF-00308). APM acknowledges the EPSRC for funding under grant number EP/T02240X/1.



Notes and references

- Y. Wada, H. Nakagawa, S. Matsumoto, Y. Wakisaka and H. Kaji, *Nat. Photonics*, 2020, **14**, 643–649.
- H. Miranda-Salinas, A. Rodriguez-Serrano, J. M. Kaminski, F. Dinkelbach, C. M. Marian and A. P. Monkman, to be published. Originally, a back-to-back publication of the experimental and theoretical studies on TpAT-tFFO in Chem. Science had been intended.
- B. T. Lim, S. Okajima, A. Chandra and E. Lim, *Chem. Phys. Lett.*, 1981, **79**, 22–27.
- M. Etherington, J. Gibson, H. F. Higginbotham, T. J. Penfold and A. P. Monkman, *Nat. Commun.*, 2016, **7**, 13680.
- J. Gibson, A. P. Monkman and T. J. Penfold, *ChemPhysChem*, 2016, **17**, 2956–2961.
- C. M. Marian, *J. Phys. Chem. C*, 2016, **120**, 3715–3721.
- I. Lyskov and C. M. Marian, *J. Phys. Chem. C*, 2017, **121**, 21145–21153.
- T. J. Penfold, E. Gindensperger, C. Daniel and C. M. Marian, *Chem. Rev.*, 2018, **118**, 6975–7025.
- C. M. Marian, *Annu. Rev. Phys. Chem.*, 2021, **72**, 617–640.
- Q. Li, J. Hu, J. Lv, X. Wang, S. Shao, L. Wang, X. Jing and F. Wang, *Angew. Chem., Int. Ed.*, 2020, **59**, 20174–20182.
- S. Kumar, L. G. Franca, K. Stavrou, E. Crovini, D. B. Cordes, A. M. Z. Slawin, A. P. Monkman and E. Zysman-Colman, *J. Phys. Chem. Lett.*, 2021, **12**, 2820–2830.
- Y. Song, M. Tian, R. Yu and L. He, *ACS Appl. Mater. Interfaces*, 2021, **13**, 60269–60278.
- V. Rai-Constapel, T. Villnow, G. Ryseck, P. Gilch and C. M. Marian, *J. Phys. Chem. A*, 2014, **118**, 11708–11717.
- T. Villnow, G. Ryseck, V. Rai-Constapel, C. M. Marian and P. Gilch, *J. Phys. Chem. A*, 2014, **118**, 11696–11707.
- R. Mundt, T. Villnow, C. T. Ziegenbein, P. Gilch, C. Marian and V. Rai-Constapel, *Phys. Chem. Chem. Phys.*, 2016, **18**, 6637–6647.
- M. Bracker, C. M. Marian and M. Kleinschmidt, *J. Chem. Phys.*, 2021, **155**, 014102.
- A. Rodriguez-Serrano, F. Dinkelbach and C. M. Marian, *Phys. Chem. Chem. Phys.*, 2021, **23**, 3668–3678.
- TURBOMOLE V7.0 2015, A development of University of Karlsruhe and Forschungszentrum Karlsruhe GmbH, TURBOMOLE GmbH, 1989–2007, since 2007; available from, <https://www.turbomole.com>.
- J. P. Perdew, K. Burke and M. Ernzerhof, *Phys. Rev. Lett.*, 1996, **77**, 3865–3868.
- C. Adamo and V. Barone, *J. Chem. Phys.*, 1999, **110**, 6158–6170.
- S. Grimme, J. Antony, S. Ehrlich and H. Krieg, *J. Chem. Phys.*, 2010, **132**, 154104.
- S. Grimme, S. Ehrlich and L. Goerigk, *J. Comput. Chem.*, 2011, **32**, 1456–1465.
- E. Runge and E. K. U. Gross, *Phys. Rev. Lett.*, 1984, **52**, 997–1000.
- M. A. L. Marques and E. K. U. Gross, *A Primer in Density Functional Theory*, Springer, Berlin, Heidelberg, 2003, pp. 144–184.
- A. Dreuw and M. Head-Gordon, *J. Am. Chem. Soc.*, 2004, **126**, 4007–4016.
- F. Furche and R. Ahlrichs, *J. Chem. Phys.*, 2002, **117**, 7433–7447.
- S. Hirata and M. Head-Gordon, *Chem. Phys. Lett.*, 1999, **314**, 291–299.
- M. J. Frisch, G. W. Trucks, H. B. Schlegel, G. E. Scuseria, M. A. Robb, J. R. Cheeseman, G. Scalmani, V. Barone, G. A. Petersson, H. Nakatsuji, X. Li, M. Caricato, A. V. Marenich, J. Bloino, B. G. Janesko, R. Gomperts, B. Mennucci, H. P. Hratchian, J. V. Ortiz, A. F. Izmaylov, J. L. Sonnenberg, D. Williams-Young, F. Ding, F. Lipparini, F. Egidi, J. Goings, B. Peng, A. Petrone, T. Henderson, D. Ranasinghe, V. G. Zakrzewski, J. Gao, N. Rega, G. Zheng, W. Liang, M. Hada, M. Ehara, K. Toyota, R. Fukuda, J. Hasegawa, M. Ishida, T. Nakajima, Y. Honda, O. Kitao, H. Nakai, T. Vreven, K. Throssell, J. A. Montgomery Jr, J. E. Peralta, F. Ogliaro, M. J. Bearpark, J. J. Heyd, E. N. Brothers, K. N. Kudin, V. N. Staroverov, T. A. Keith, R. Kobayashi, J. Normand, K. Raghavachari, A. P. Rendell, J. C. Burant, S. S. Iyengar, J. Tomasi, M. Cossi, J. M. Millam, M. Klene, C. Adamo, R. Cammi, J. W. Ochterski, R. L. Martin, K. Morokuma, O. Farkas, J. B. Foresman and D. J. Fox, *Gaussian 16, Revision A.03*, Gaussian, Inc, Wallingford CT, 2016.
- S. Grimme and M. Waletzke, *J. Chem. Phys.*, 1999, **111**, 5645–5655.
- C. M. Marian, A. Heil and M. Kleinschmidt, *Wiley Interdiscip. Rev.: Comput. Mol. Sci.*, 2019, **9**, e1394.
- M. Kleinschmidt, C. M. Marian, M. Waletzke and S. Grimme, *J. Chem. Phys.*, 2009, **130**, 044708.
- A. D. Becke, *J. Chem. Phys.*, 1993, **98**, 1372–1377.
- C. Lee, W. Yang and R. G. Parr, *Phys. Rev. B: Condens. Matter Phys.*, 1988, **37**, 785–789.
- I. Lyskov, M. Kleinschmidt and C. M. Marian, *J. Chem. Phys.*, 2016, **144**, 034104.
- F. Plasser, *J. Chem. Phys.*, 2020, **152**, 084108.
- M. Kleinschmidt, J. Tatchen and C. M. Marian, *J. Comput. Chem.*, 2002, **23**, 824–833.
- M. Kleinschmidt and C. M. Marian, *Chem. Phys.*, 2005, **311**, 71–79.
- M. Kleinschmidt, J. Tatchen and C. M. Marian, *J. Chem. Phys.*, 2006, **124**, 124101.
- B. A. Heß, C. M. Marian, U. Wahlgren and O. Gropen, *Chem. Phys. Lett.*, 1996, **251**, 365–371.
- B. Schimmelpfennig, *Atomic mean-field integral program AMFI*, University of Stockholm, 1996.
- M. Etinski, J. Tatchen and C. M. Marian, *Phys. Chem. Chem. Phys.*, 2014, **16**, 4740.
- M. Etinski, J. Tatchen and C. M. Marian, *J. Chem. Phys.*, 2011, **134**, 154105.
- J. Tatchen, N. Gilka and C. M. Marian, *Phys. Chem. Chem. Phys.*, 2007, **9**, 5209.
- M. Etinski, V. Rai-Constapel and C. M. Marian, *J. Chem. Phys.*, 2014, **140**, 114104.
- R. Englman and J. Jortner, *Mol. Phys.*, 1970, **18**, 145–164.



Electronic Supplementary Information

for

**Vibronic effects accelerate the intersystem crossing processes of the
through-space charge transfer states in the triptycene bridged
acridine-triazine donor-acceptor molecule TpAT-tFFO**

Jeremy M. Kaminski,^a Angela Rodríguez-Serrano,^a Fabian Dinkelbach,^a
Hector Miranda-Salinas,^b Andrew P. Monkman^b and Christel M. Marian^{*a}

^a Institute of Theoretical and Computational Chemistry,
Heinrich-Heine-University Düsseldorf, Universitätsstraße 1,
D-40225 Düsseldorf, Germany, E-mail: christel.marian@hhu.de

^b OEM research group, Dept. of Physics, Durham University,
Durham, UK, DH1 3LE, E-mail: a.p.monkman@durham.ac.uk

20.12.2021

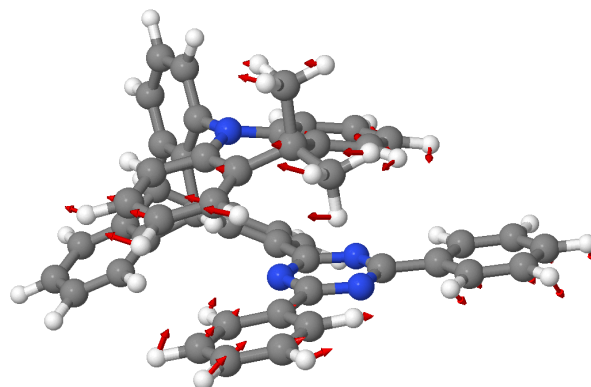


Figure S1: Vibrational mode 1 at the $S_0(\text{Me} \rightarrow \text{N})$ geometry in vacuo.

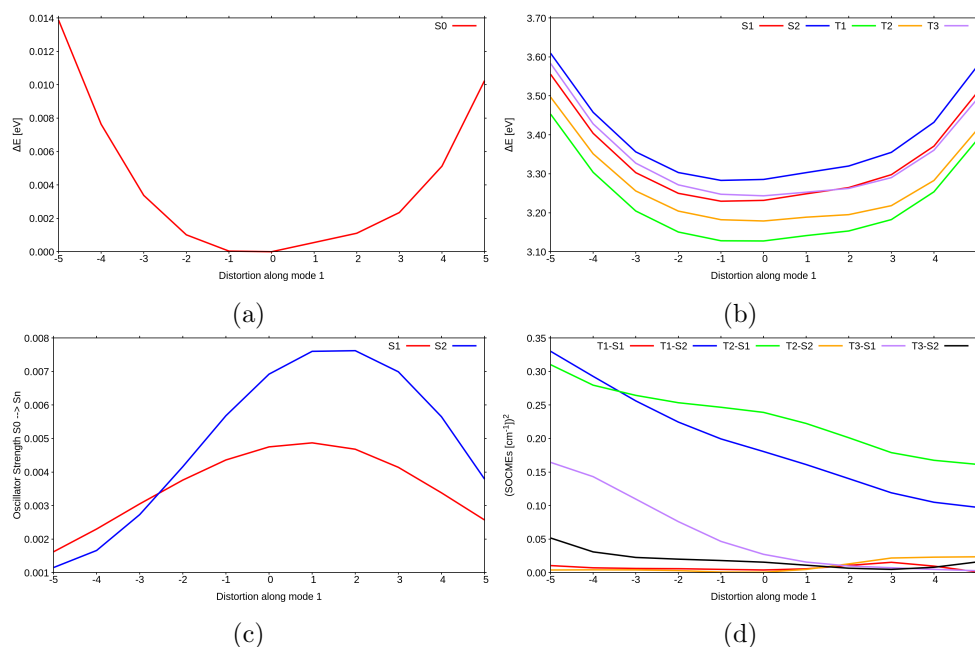


Figure S2: Scan along vibrational mode 1: (a) Relative DFT/MRCI ground state energy differences w.r.t. the undistorted $S_0(\text{Me} \rightarrow \text{N})$ geometry, (b) DFT/MRCI excitation energies w.r.t. the ground state energy at the undistorted $S_0(\text{Me} \rightarrow \text{N})$ geometry, (c) oscillator strengths for the $S_0 \rightarrow S_1$ and $S_0 \rightarrow S_2$ absorption processes, (d) sum of the squared SOCMEs for transitions discussed in this study.

Table S1: DFT/MRCI-R2016 vertical excitation energies and characterization of low-lying singlet and triplet states of **TpAT-tFFO** calculated at the $S_0(\text{Me} \rightarrow \text{N})$ geometry.

State	ΔE [eV]	f(L)	Transition	Character	%	μ [D]
S_0	0.02		GS		96	0.61
S_1	3.25	0.005	H \rightarrow L	CT	68	16.24
			H \rightarrow L+1		21	
S_2	3.30	0.007	H \rightarrow L+1	CT'	67	16.42
			H \rightarrow L		21	
T_1	3.14		H \rightarrow L	CT	70	15.37
			H \rightarrow L+1		16	
T_2	3.19		H \rightarrow L+1	CT'	67	14.43
			H \rightarrow L		14	
T_3	3.24		H-5 \rightarrow L	LE	25	0.39
			H-6 \rightarrow L		13	

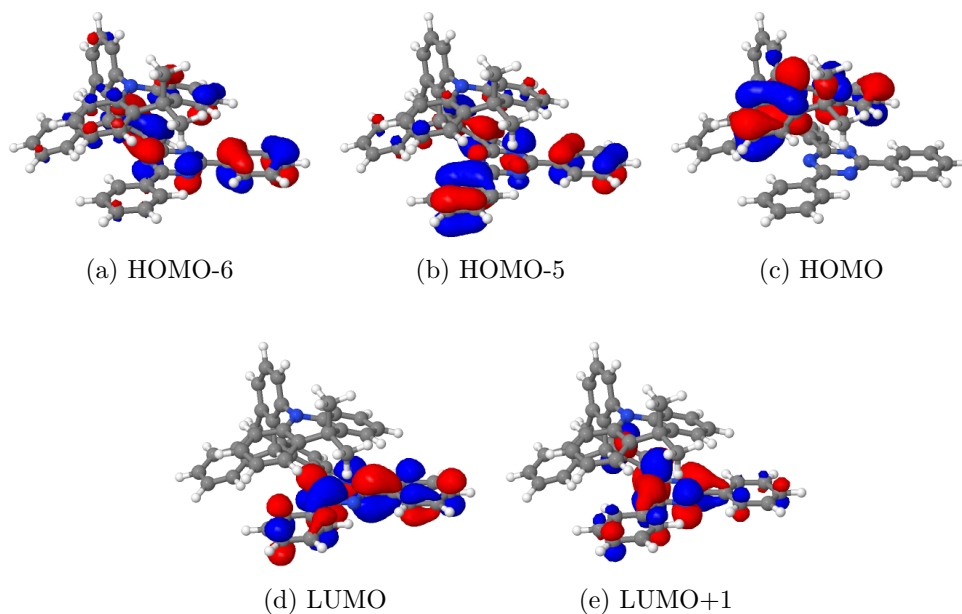


Figure S3: BH-LYP molecular orbitals (cutoff 0.03) at the $S_0(\text{Me} \rightarrow \text{N})$ geometry in vacuo.

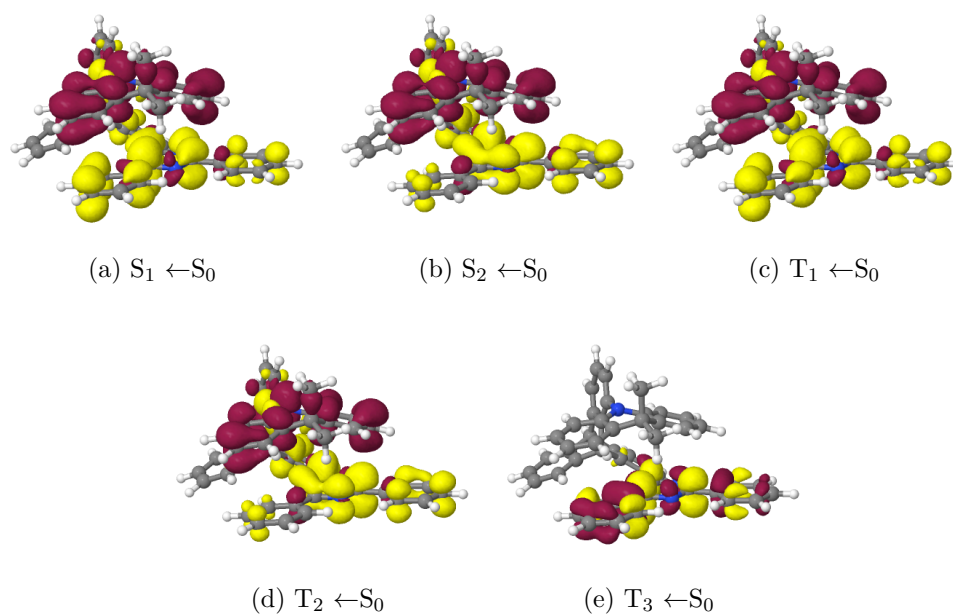


Figure S4: Difference densities (± 0.001) of the excited states at the $S_0(\text{Me} \rightarrow \text{N})$ geometry in vacuo. Areas losing electron density in comparison to the electronic ground state are shown in red, areas gaining electron density in yellow.

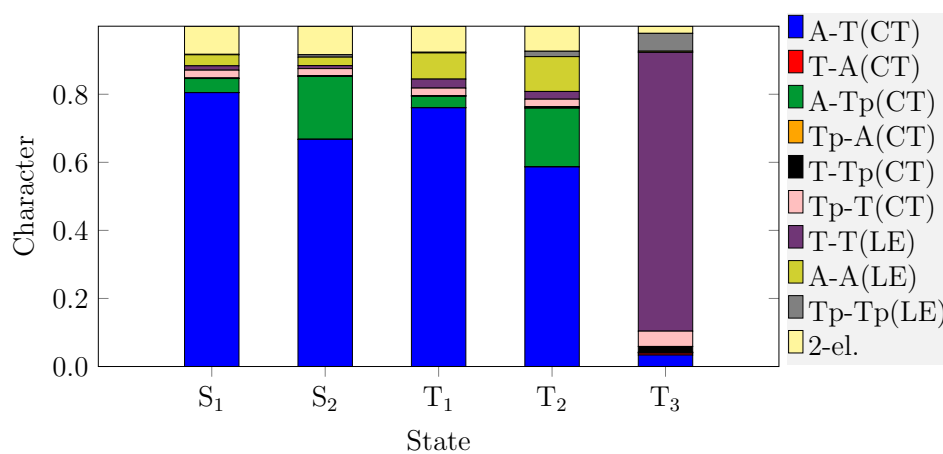


Figure S5: Fragment-based analysis for the vertical singlet and triplet state DFT/MRCI-R2016 wavefunctions at the $S_0(\text{Me} \rightarrow \text{N})$ geometry in vacuo.

Table S2: DFT/MRCI-R2016 vertical excitation energies and characterization of low-lying singlet and triplet states of **TpAT-tFFO** calculated at the $S_0(\text{Me} \rightarrow \text{Ph})$ geometry.

State	ΔE [eV]	f(L)	Transition	Character	%	μ [D]
S_0	0.00		GS		96	0.65
S_1	3.27	0.002	H \rightarrow L+1	CT	49	16.72
			H \rightarrow L		39	
S_2	3.33	0.000	H \rightarrow L	CT'	48	18.50
			H \rightarrow L+1		39	
T_1	3.17		H \rightarrow L	CT	71	14.41
T_2	3.17		H \rightarrow L+1	CT'	56	9.93
			H-5 \rightarrow L+1		10	
T_3	3.29		H \rightarrow L+1	LE/CT	29	6.93
			H-6 \rightarrow L		17	
			H-4 \rightarrow L		10	

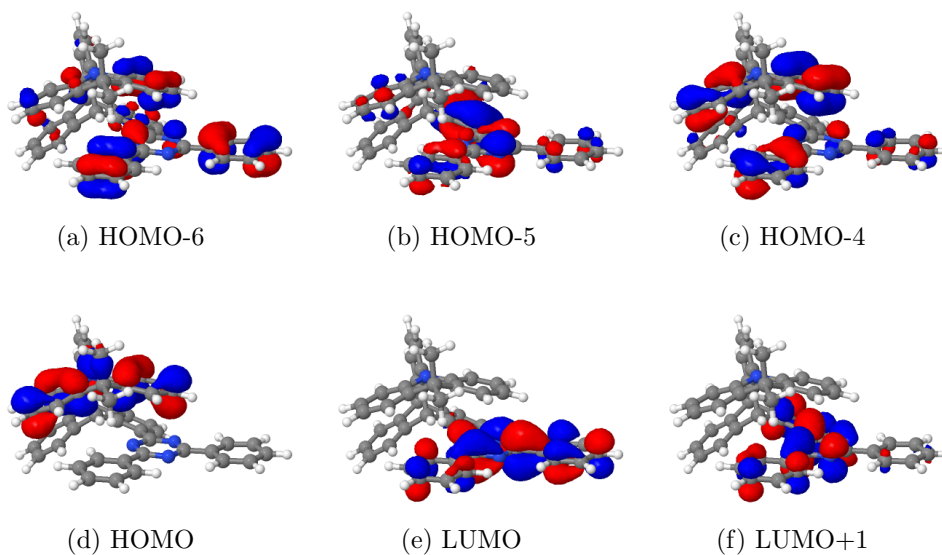


Figure S6: BH-LYP molecular orbitals (cutoff 0.03) at the $S_0(\text{Me} \rightarrow \text{Ph})$ geometry in vacuo.

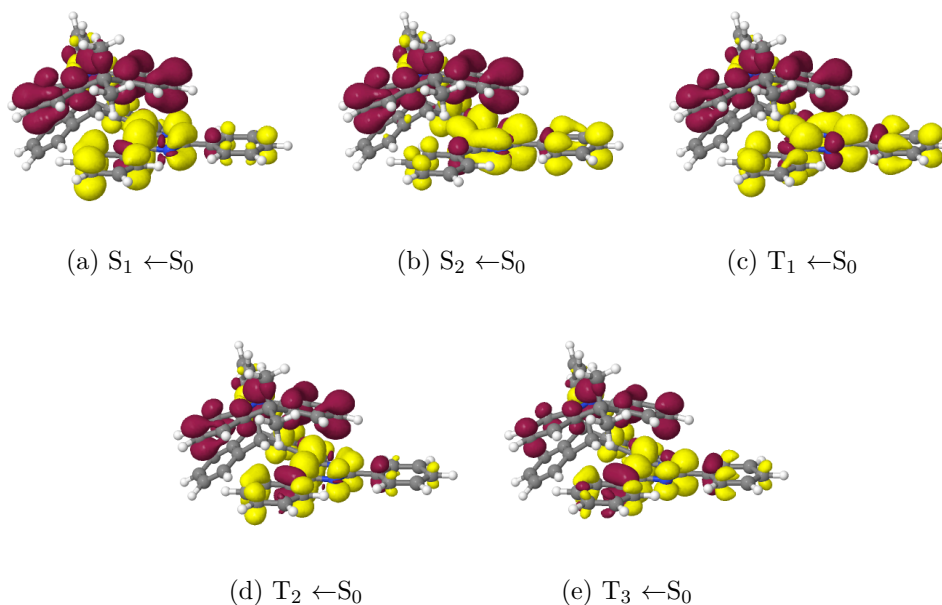


Figure S7: Difference densities (± 0.001) of the excited states at the $S_0(\text{Me} \rightarrow \text{Ph})$ geometry in vacuo. Areas losing electron density in comparison to the electronic ground state are shown in red, areas gaining electron density in yellow.

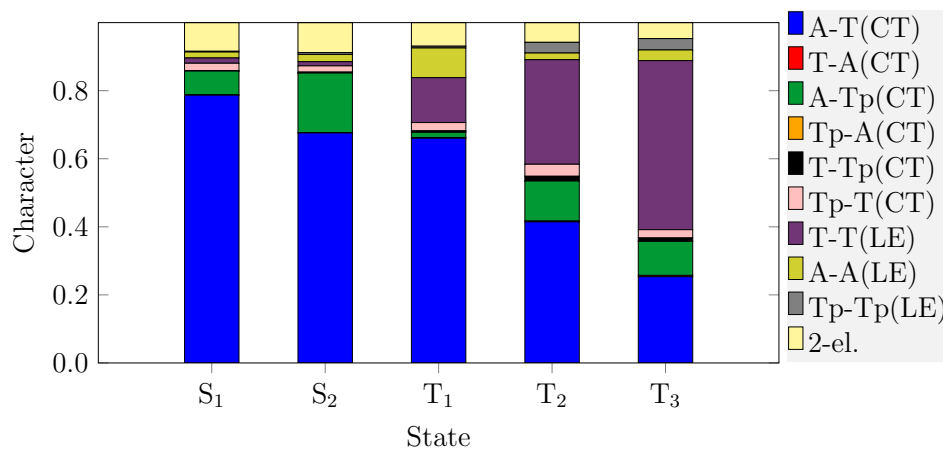


Figure S8: Fragment-based analysis for the vertical singlet and triplet state DFT/MRCI-R2016 wavefunctions at the $S_0(\text{Me} \rightarrow \text{Ph})$ geometry in vacuo.

Table S3: DFT/MRCI-R2016 vertical excitation energies and characterization of low-lying singlet and triplet states of **TpAT-tFFO** calculated at the S_1 geometry.

State	ΔE [eV]	Transition	Character	%	μ [D]
S_0	0.41	GS		96	0.45
S_1	2.97	H \rightarrow L	CT	90	15.65
S_2	3.51	H \rightarrow L+1	CT'	88	15.65
T_1	2.89	H \rightarrow L	CT	89	15.40
T_3	3.29	H-5 \rightarrow L	LE	25	1.49
		H-2 \rightarrow L		15	
		H-9 \rightarrow L		14	
T_2	3.42	H \rightarrow L+1	CT'	83	14.41

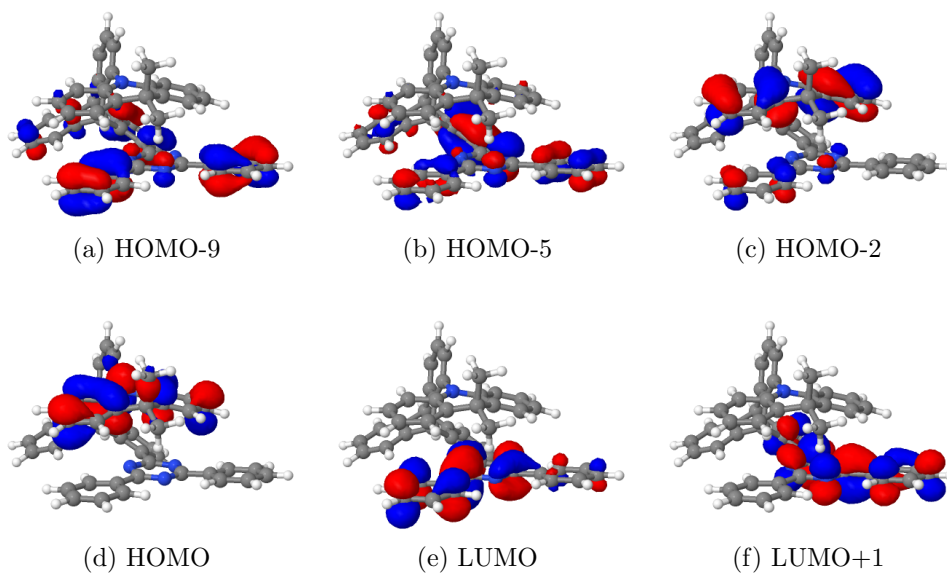


Figure S9: BH-LYP molecular orbitals (cutoff 0.03) at the S_1 geometry in vacuo.

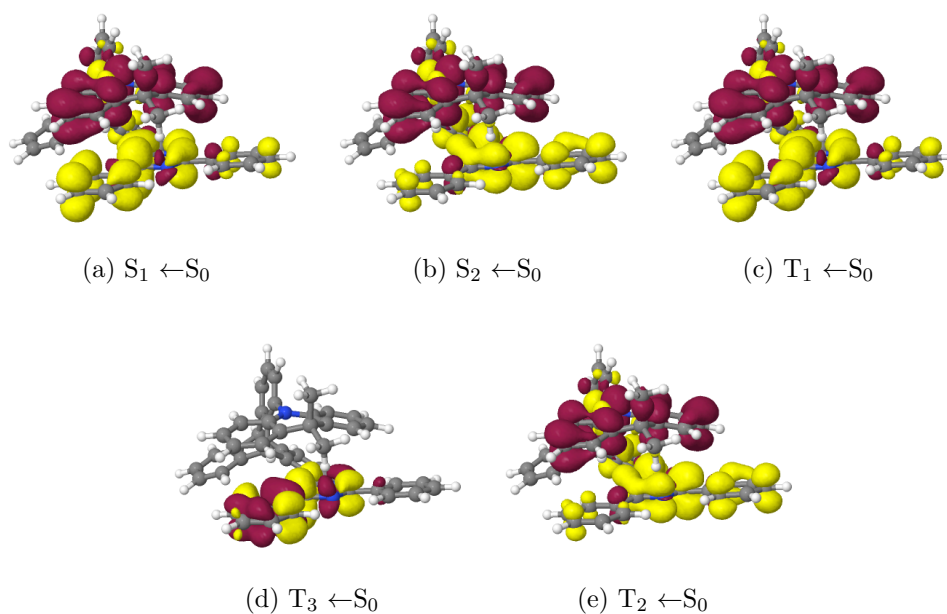


Figure S10: Difference densities (± 0.001) of the excited states at the S_1 geometry in vacuo. Areas losing electron density in comparison to the electronic ground state are shown in red, areas gaining electron density in yellow.

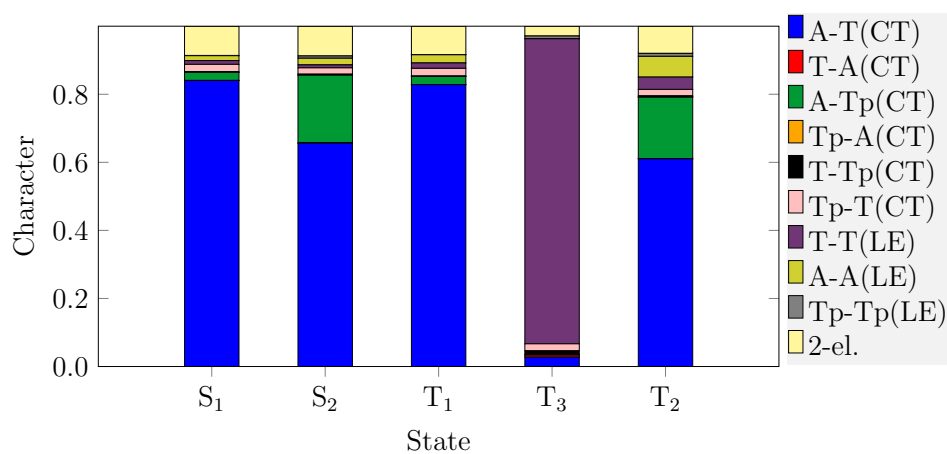
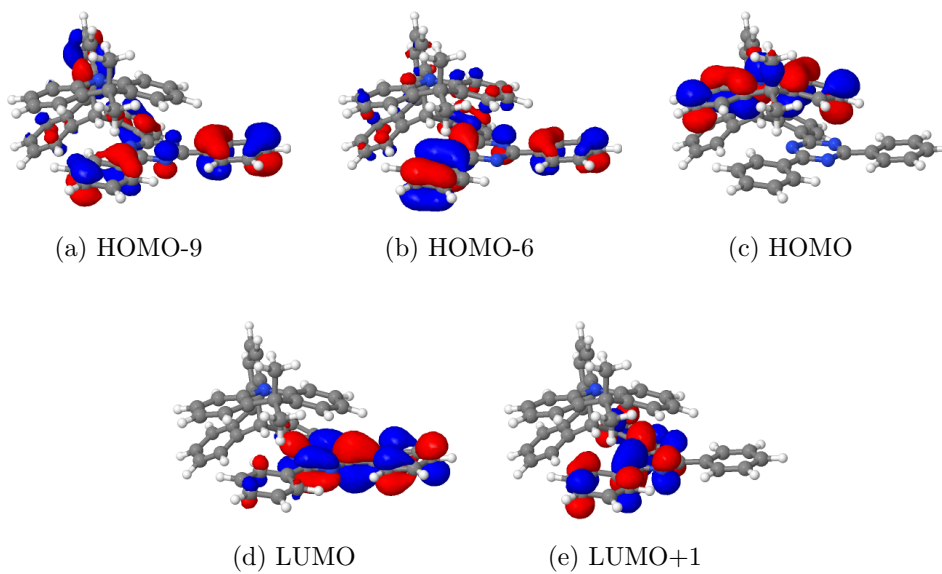


Figure S11: Fragment-based analysis for the vertical singlet and triplet state DFT/MRCI-R2016 wavefunctions at the S_1 geometry in vacuo.

Table S4: DFT/MRCI-R2016 vertical excitation energies and characterization of low-lying singlet and triplet states of **TpAT-tFFO** calculated at the S_2 geometry.

State	ΔE [eV]	Transition	Character	%	μ [D]
S_0	0.38	GS		96	1.08
S_2	2.98	H \rightarrow L	CT'	88	18.39
S_1	3.47	H \rightarrow L+1	CT	88	14.92
T_2	2.86	H \rightarrow L	CT'	83	16.77
T_3	3.30	H-6 \rightarrow L	LE	32	2.00
		H-9 \rightarrow L		16	
T_1	3.38	H \rightarrow L+1	CT	76	12.63

Figure S12: BH-LYP molecular orbitals (cutoff 0.03) at the S_2 geometry in vacuo.

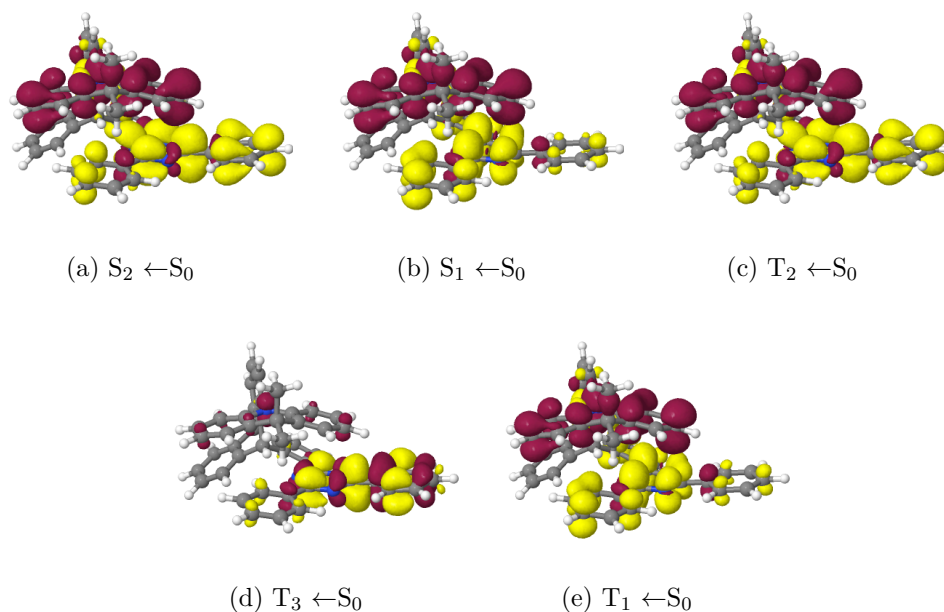


Figure S13: Difference densities (± 0.001) of the excited states at the S_2 geometry in vacuo. Areas losing electron density in comparison to the electronic ground state are shown in red, areas gaining electron density in yellow.

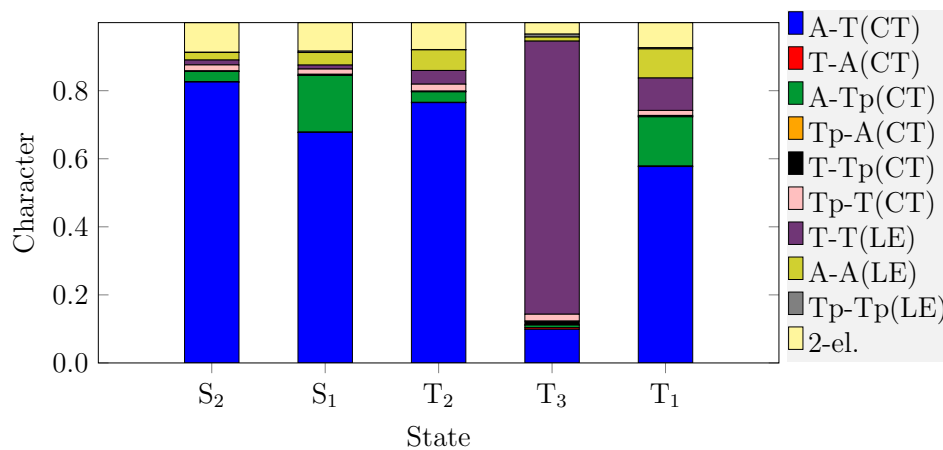
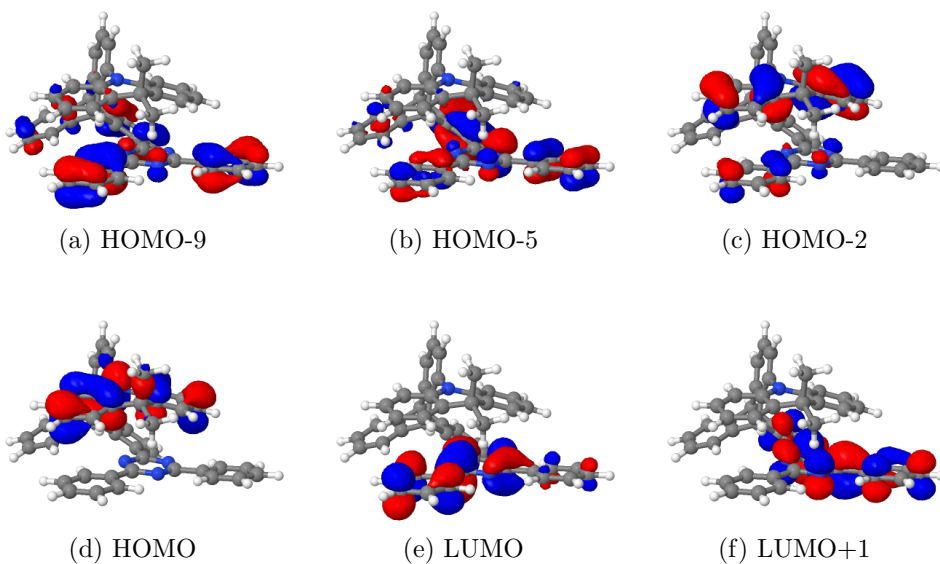


Figure S14: Fragment-based analysis for the vertical singlet and triplet state DFT/MRCI-R2016 wavefunctions at the S_2 geometry in vacuo.

Table S5: DFT/MRCI-R2016 vertical excitation energies and characterization of low-lying singlet and triplet states of **TpAT-tFFO** calculated at the T_1 geometry.

State	ΔE [eV]	Transition	Character	%	μ [D]
S_0	0.40	GS		96	0.43
S_1	2.96	H \rightarrow L	CT	90	15.40
S_2	3.48	H \rightarrow L+1	CT'	88	15.45
T_1	2.88	H \rightarrow L	CT	89	15.11
T_3	3.29	H-5 \rightarrow L	LE	27	1.51
		H-2 \rightarrow L		20	
		H-9 \rightarrow L		14	
T_2	3.38	H \rightarrow L+1	CT'	83	14.18

Figure S15: BH-LYP molecular orbitals (cutoff 0.03) at the T_1 geometry in vacuo.

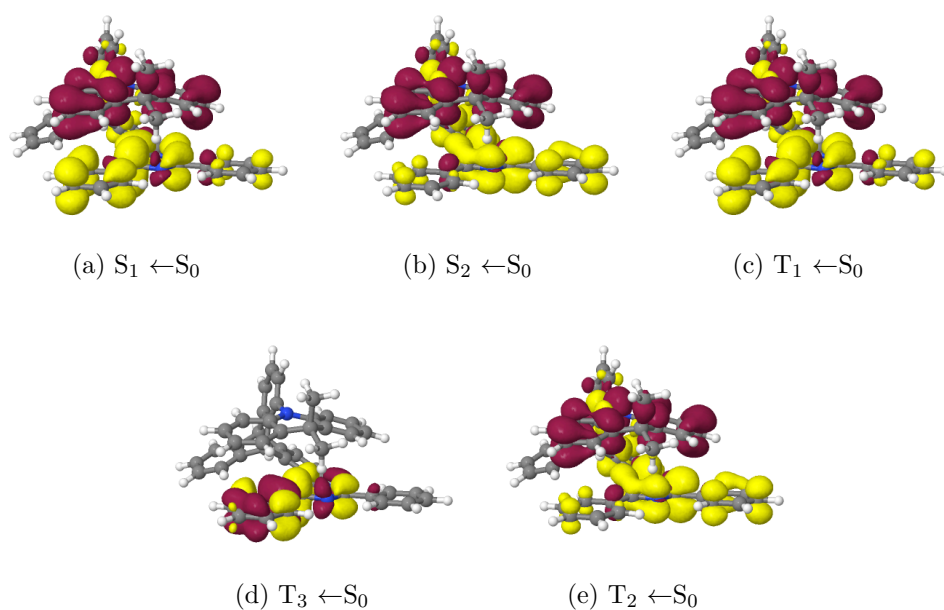


Figure S16: Difference densities (± 0.001) of the excited states at the T_1 geometry in vacuo. Areas losing electron density in comparison to the electronic ground state are shown in red, areas gaining electron density in yellow.

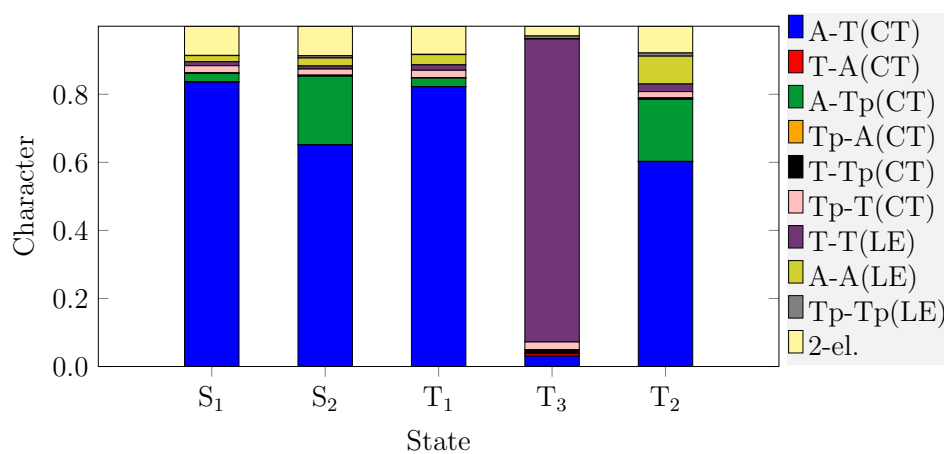


Figure S17: Fragment-based analysis for the vertical singlet and triplet state DFT/MRCI-R2016 wavefunctions at the T_1 geometry in vacuo.

Table S6: DFT/MRCI-R2016 vertical excitation energies and characterization of low-lying singlet and triplet states of **TpAT-tFFO** calculated at the CI geometry.

State	ΔE [eV]	Transition	Character	%	μ [D]
S ₀	0.24	GS		96	0.87
S ₂	3.08	H \rightarrow L+1	CT	67	14.54
		H \rightarrow L		21	
S ₁	3.10	H \rightarrow L	CT'	67	16.49
		H \rightarrow L+1		22	
T ₂	2.99	H \rightarrow L+1	CT	69	13.80
		H \rightarrow L		17	
T ₁	2.99	H \rightarrow L	CT'	67	15.58
		H \rightarrow L+1		18	
T ₃	3.36	H-5 \rightarrow L+1	LE	25	0.33
		H-6 \rightarrow L		20	
		H-2 \rightarrow L+1		13	

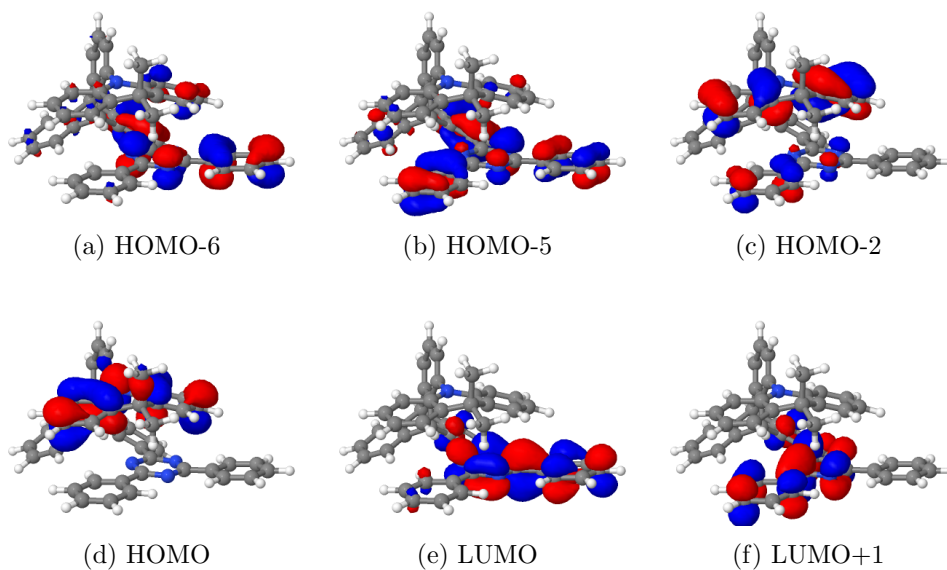


Figure S18: BH-LYP molecular orbitals (cutoff 0.03) at the CI geometry in vacuo.

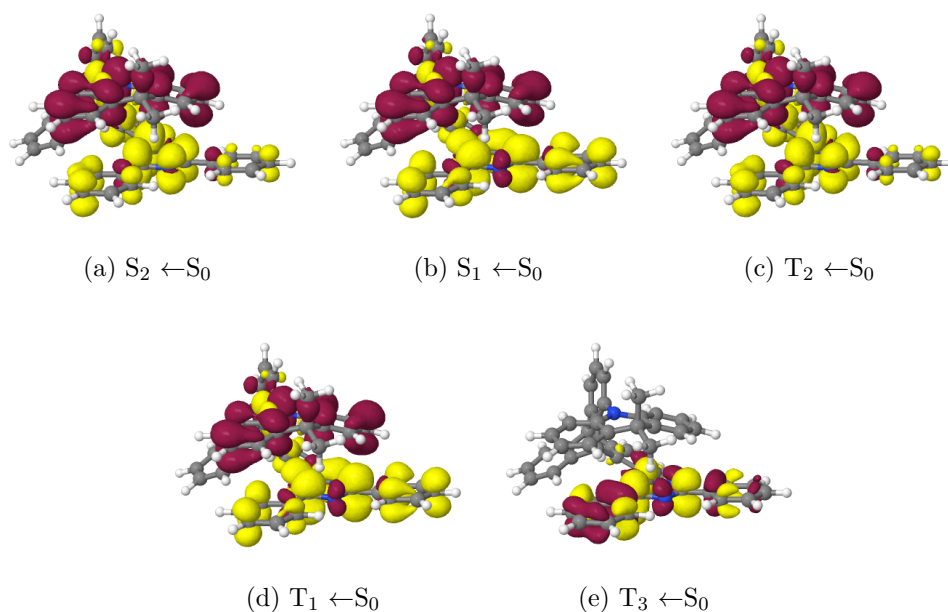


Figure S19: Difference densities (± 0.001) of the excited states at the CI geometry in vacuo. Areas losing electron density in comparison to the electronic ground state are shown in red, areas gaining electron density in yellow.

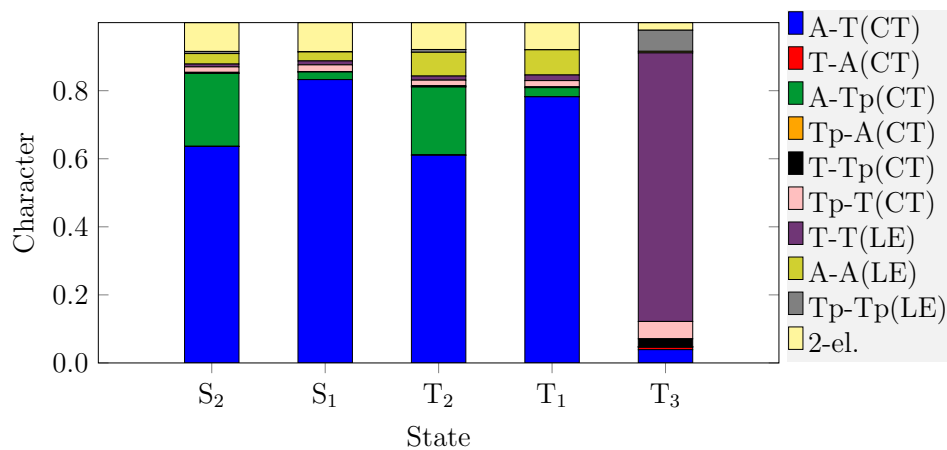


Figure S20: Fragment-based analysis for the vertical singlet and triplet state DFT/MRCI-R2016 wavefunctions at the CI geometry in vacuo.

Table S7: DFT/MRCI-R2016 vertical excitation energies and characterization of low-lying singlet and triplet states of **TpAT-tFFO** calculated at the T_2 geometry.

State	ΔE [eV]	Transition	Character	%	μ [D]
S_0	0.39	GS		96	1.00
S_2	2.97	H \rightarrow L	CT'	88	17.77
S_1	3.45	H \rightarrow L+1	CT	88	14.47
T_2	2.83	H \rightarrow L	CT'	82	15.77
T_1'	3.32	H \rightarrow L+1	LE/CT	30	4.78
		H-6 \rightarrow L		20	
		H-9 \rightarrow L		10	
T_1''	3.36	H \rightarrow L+1	CT/LE	53	8.62
		H-6 \rightarrow L		12	
		H-9 \rightarrow L		7	

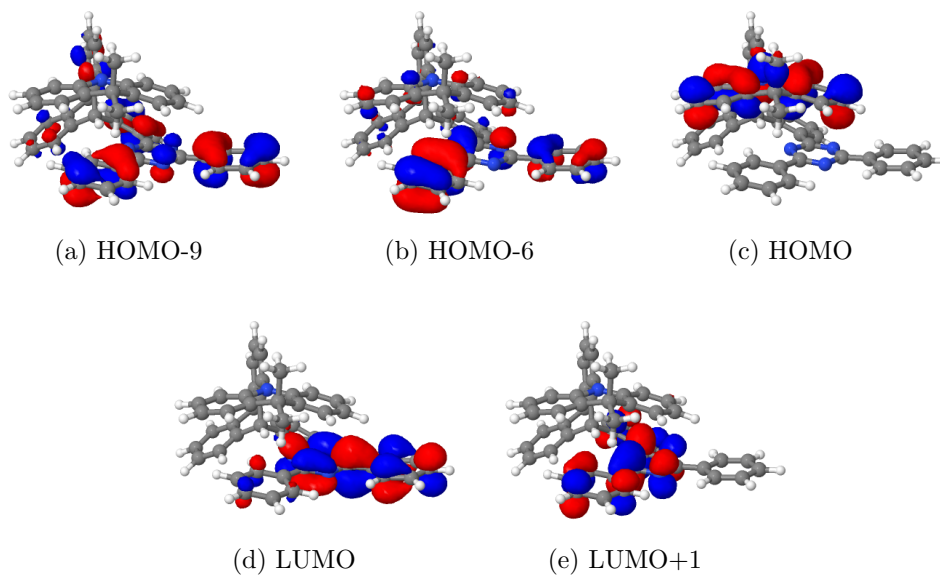


Figure S21: BH-LYP molecular orbitals (cutoff 0.03) at the T_2 geometry in vacuo.

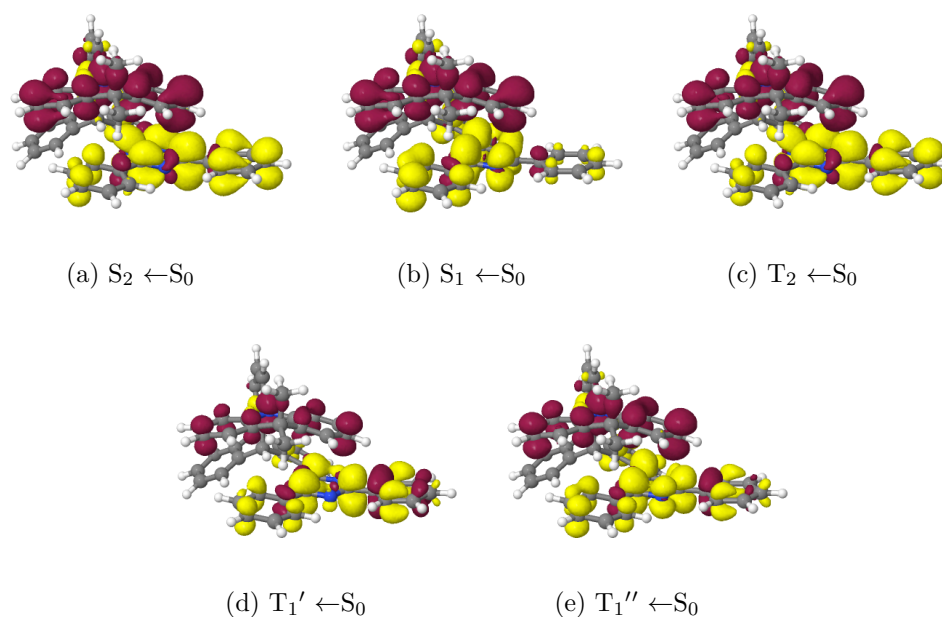


Figure S22: Difference densities (± 0.001) of the excited states at the T_2 geometry in vacuo. Areas losing electron density in comparison to the electronic ground state are shown in red, areas gaining electron density in yellow.

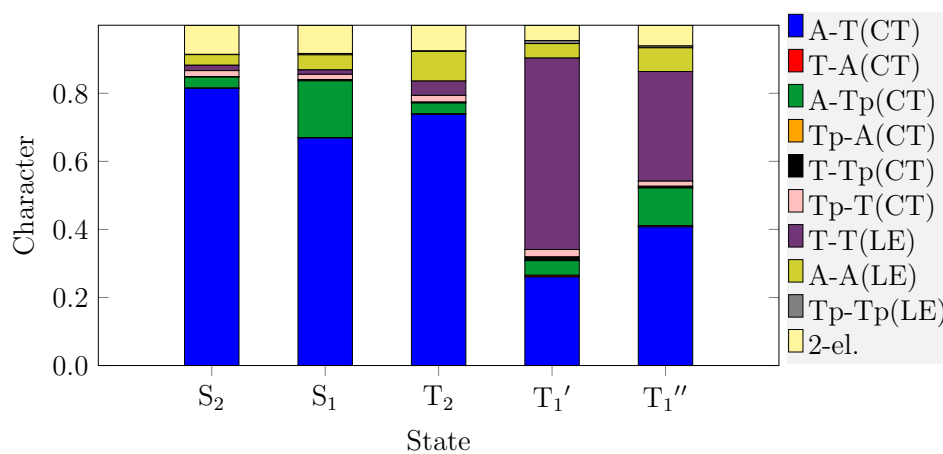


Figure S23: Fragment-based analysis for the vertical singlet and triplet state DFT/MRCI-R2016 wavefunctions at the T_2 geometry in vacuo.

Table S8: DFT/MRCI-R2016 vertical excitation energies and characterization of low-lying singlet and triplet states of **TpAT-tFFO** calculated at the T_3 geometry.

State	ΔE [eV]	Transition	Character	%	μ [D]
S_0	0.32	GS		96	0.46
S_1	3.17	H \rightarrow L	CT	89	15.88
S_2	3.58	H \rightarrow L+1	CT'	87	16.00
T_3	2.99	H-2 \rightarrow L	LE	35	2.26
		H-4 \rightarrow L		20	
T_1	3.08	H \rightarrow L	CT	78	14.09
T_2	3.44	H \rightarrow L+1	CT'	78	13.50

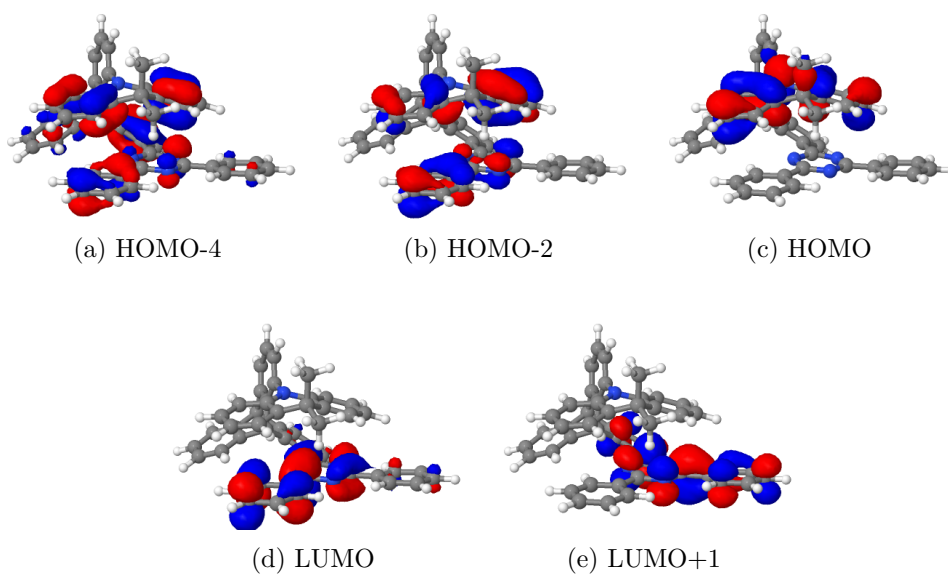


Figure S24: BH-LYP molecular orbitals (cutoff 0.03) at the T_3 geometry in vacuo.

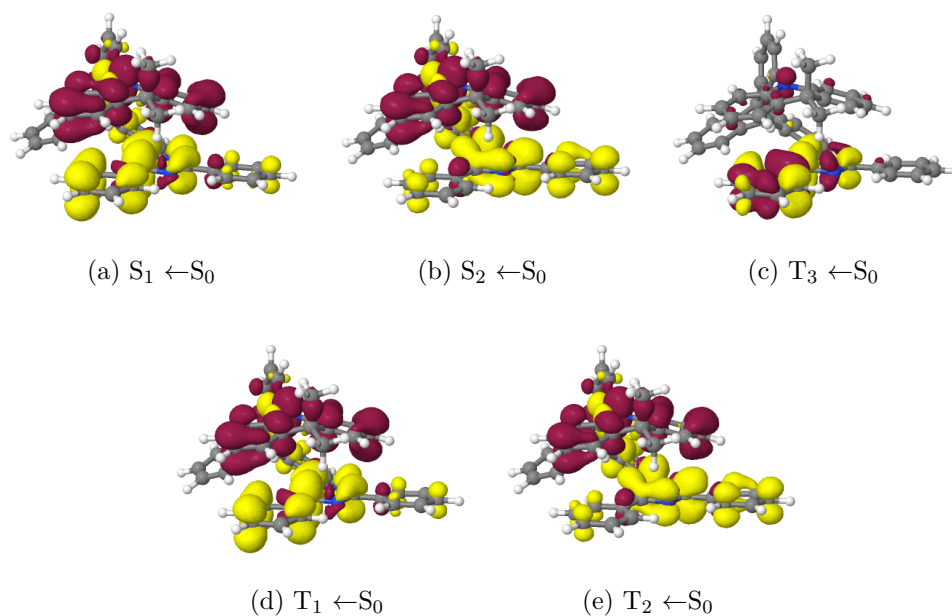


Figure S25: Difference densities (± 0.001) of the excited states at the T_3 geometry in vacuo. Areas losing electron density in comparison to the electronic ground state are shown in red, areas gaining electron density in yellow.

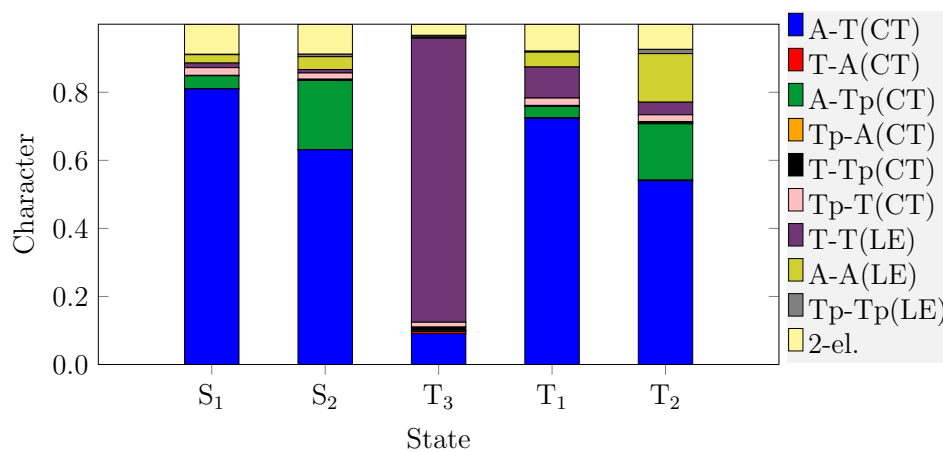


Figure S26: Fragment-based analysis for the vertical singlet and triplet state DFT/MRCI-R2016 wavefunctions at the T_3 geometry in vacuo.

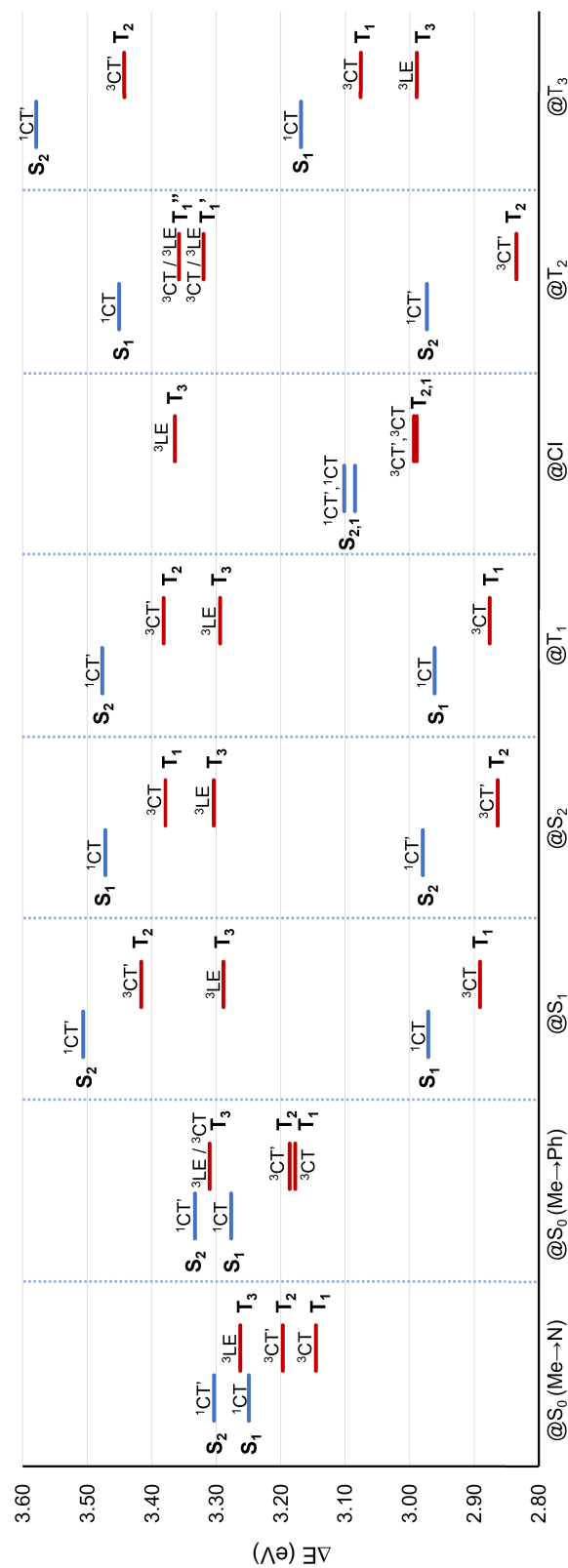


Figure S27: DFT/MRCI excitation energies (ΔE , eV) at optimized geometries. CI designates the conical intersection between the T₁ and T₂ PESs. The S₀ energy of the slightly more stable (Me→Ph) conformer has been chosen as common origin.

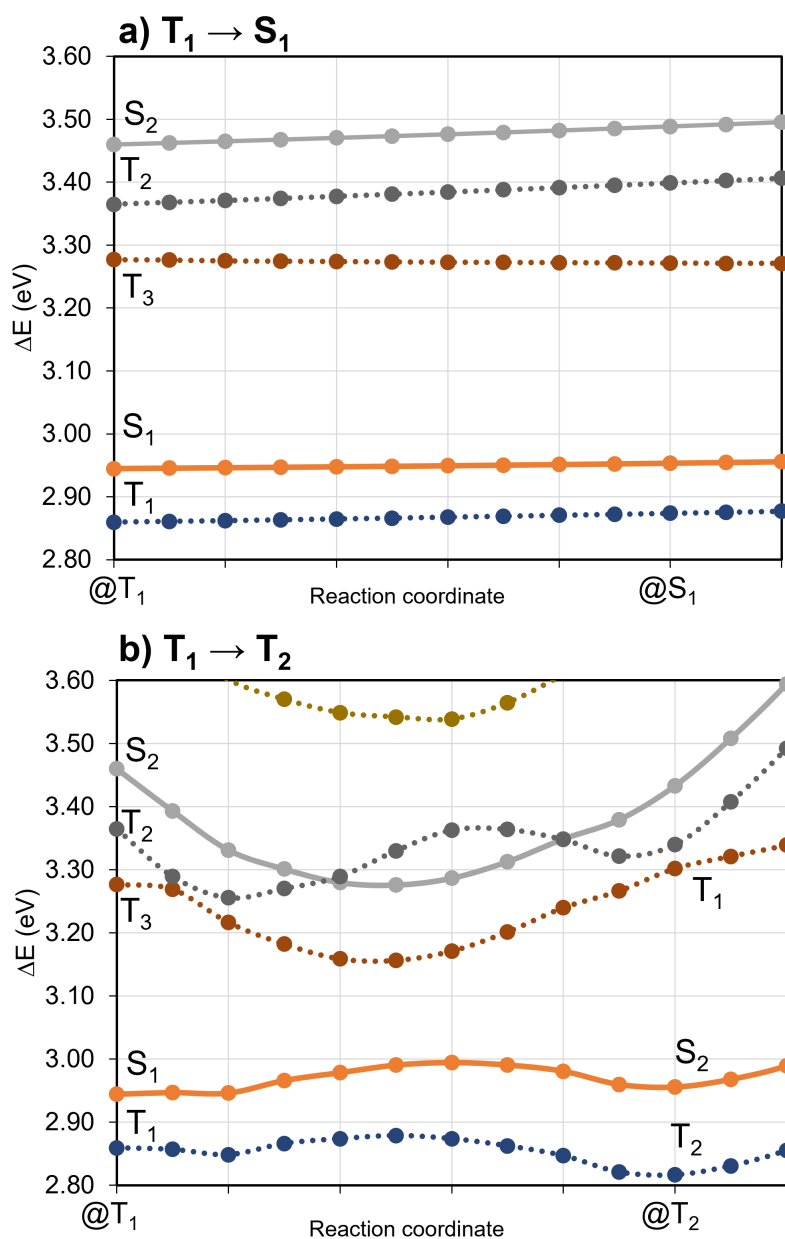


Figure S28: DFT/MRCI energy profiles along linear interpolated pathways (LIPs) between target electronic state minima. Dashed lines correspond to triplet state PESs while solid lines correspond to singlet states.

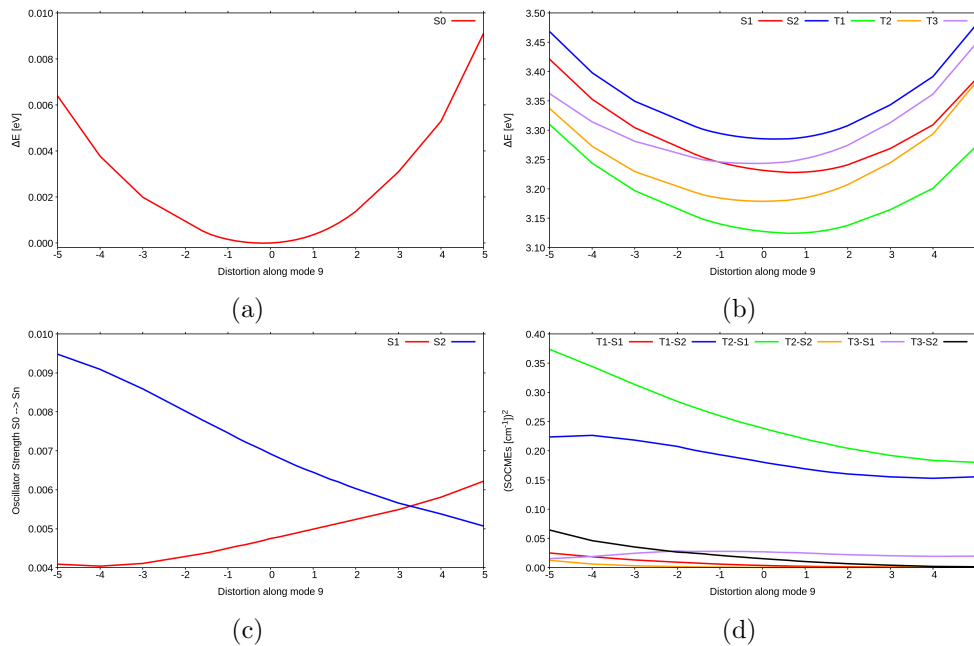


Figure S29: Scan along vibrational mode 9: (a) Relative DFT/MRCI ground state energy differences w.r.t. the undistorted $S_0(\text{Me} \rightarrow \text{N})$ geometry, (b) DFT/MRCI excitation energies w.r.t. the ground state energy at the undistorted $S_0(\text{Me} \rightarrow \text{N})$ geometry, (c) oscillator strengths for the $S_0 \rightarrow S_1$ and $S_0 \rightarrow S_2$ absorption processes, (d) sum of the squared SOCMEs for transitions discussed in this study.

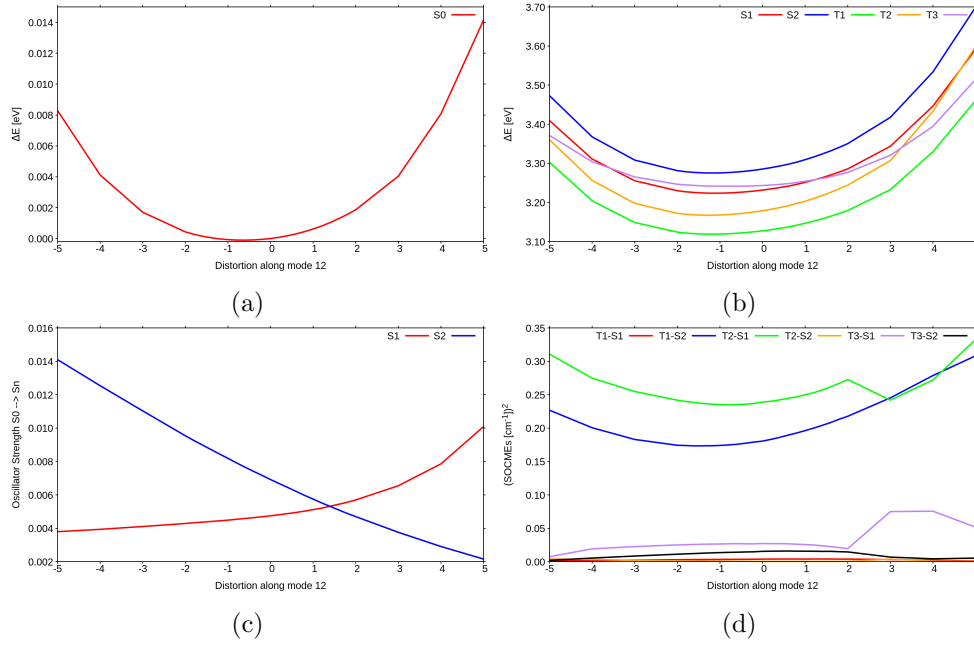


Figure S30: Scan along vibrational mode 12: (a) Relative DFT/MRCI ground state energy differences w.r.t. the undistorted $S_0(\text{Me} \rightarrow \text{N})$ geometry, (b) DFT/MRCI excitation energies w.r.t. the ground state energy at the undistorted $S_0(\text{Me} \rightarrow \text{N})$ geometry, (c) oscillator strengths for the $S_0 \rightarrow S_1$ and $S_0 \rightarrow S_2$ absorption processes, (d) sum of the squared SOCMEs for transitions discussed in this study.

Table S9: PBE0/def2-SV(P) TDDFT vertical excitation energies (including TDA approximation for triplet states) and characterization of low-lying singlet and triplet states of **TpAT-tFFO** calculated at the $S_0(\text{Me} \rightarrow \text{N})$ geometry.

State	ΔE [eV]	Transition	Character	%
S_1	2.78	H \rightarrow L	CT(A \rightarrow T)	89
		H \rightarrow L+1	CT(A \rightarrow T/Tp)	11
S_2	2.83	H \rightarrow L+1	CT(A \rightarrow T/Tp)	89
		H \rightarrow L	CT(A \rightarrow T)	11
T_1	2.76	H \rightarrow L	CT(A \rightarrow T)	91
T_2	2.81	H \rightarrow L+1	CT(A \rightarrow T/Tp)	91
T_3	3.33	H-6 \rightarrow L	LE(T/Tp)	22
		H-5 \rightarrow L	LE(T/Tp)	19
		H-5 \rightarrow L+1	LE(T/Tp)	11

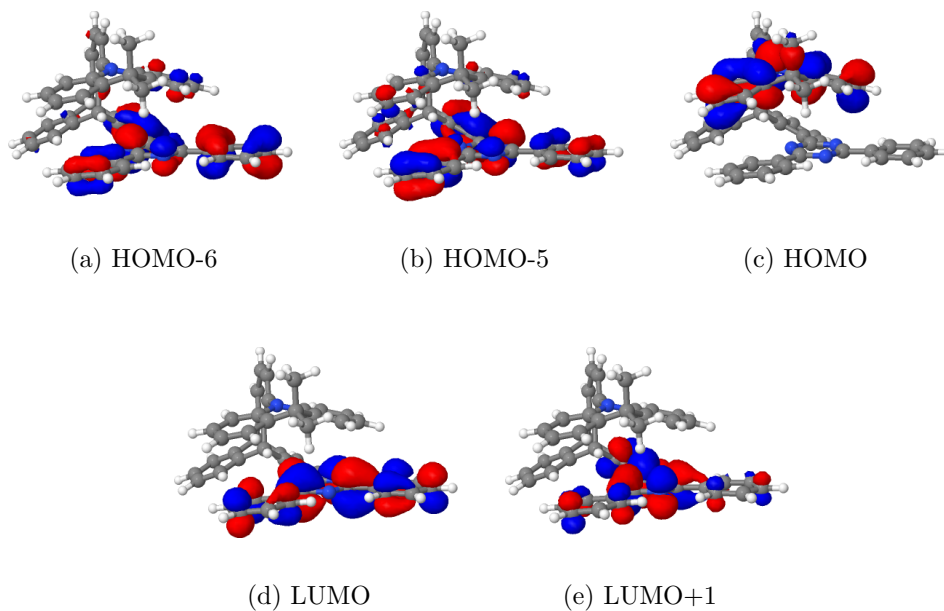


Figure S31: PBE0 molecular orbitals (cutoff 0.03) at the $S_0(\text{Me} \rightarrow \text{N})$ geometry in vacuo.

Table S10: LC- ω PBE/6-31+G(d) ($\omega = 0.1664$) TDDFT vertical excitation energies (including TDA approximation for triplet states) and characterization of low-lying singlet and triplet states of **TpAT-tFFO** calculated at the $S_0(\text{Me} \rightarrow \text{N})$ geometry.

State	ΔE [eV]	Transition	Character	%
S_1	2.96	H \rightarrow L	CT (A \rightarrow T)	56
		H \rightarrow L+1	CT (A \rightarrow T/Tp)	42
S_2	3.03	H \rightarrow L+1	CT (A \rightarrow T/Tp)	55
		H \rightarrow L	CT (A \rightarrow T)	40
T_1	2.93	H \rightarrow L	CT (A \rightarrow T)	62
		H \rightarrow L+1	CT (A \rightarrow T/Tp)	34
T_2	3.00	H \rightarrow L+1	CT (A \rightarrow T/Tp)	61
		H \rightarrow L	CT (A \rightarrow T)	32
T_3	3.33	H-5 \rightarrow L	LE(A/Tp)	21
		H-6 \rightarrow L	LE(A/Tp)	20

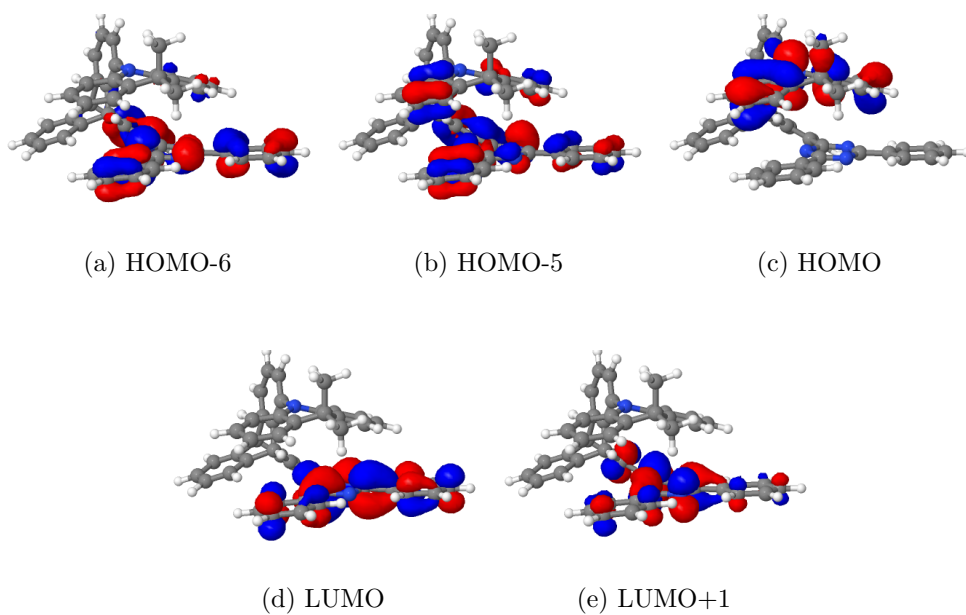


Figure S32: LC- ω PBE ($\omega = 0.1664$) molecular orbitals (cutoff 0.03) at the $S_0(\text{Me} \rightarrow \text{N})$ geometry in vacuo.

Table S11: PBE0/def2-SV(P) TDDFT vertical excitation energies (including TDA approximation for triplet states) and characterization of low-lying singlet and triplet states of **TpAT-tFFO** calculated at the $S_0(\text{Me} \rightarrow \text{Ph})$ geometry.

State	ΔE [eV]	Transition	Character	%
S_1	2.83	H \rightarrow L+1	CT(A \rightarrow T/Tp)	53
		H \rightarrow L	CT(A \rightarrow T)	46
S_2	2.87	H \rightarrow L	CT(A \rightarrow T)	53
		H \rightarrow L+1	CT(A \rightarrow T/Tp)	46
T_1	2.81	H \rightarrow L	CT(A \rightarrow T)	63
		H \rightarrow L+1	CT(A \rightarrow T/Tp)	35
T_2	2.84	H \rightarrow L+1	CT(A \rightarrow T/Tp)	63
		H \rightarrow L	CT(A \rightarrow T)	34
T_3	3.34	H-6 \rightarrow L	LE(A/Tp)	30
		H-5 \rightarrow L+1	LE(A/Tp)	30
		H-4 \rightarrow L	CT(A \rightarrow T)	10

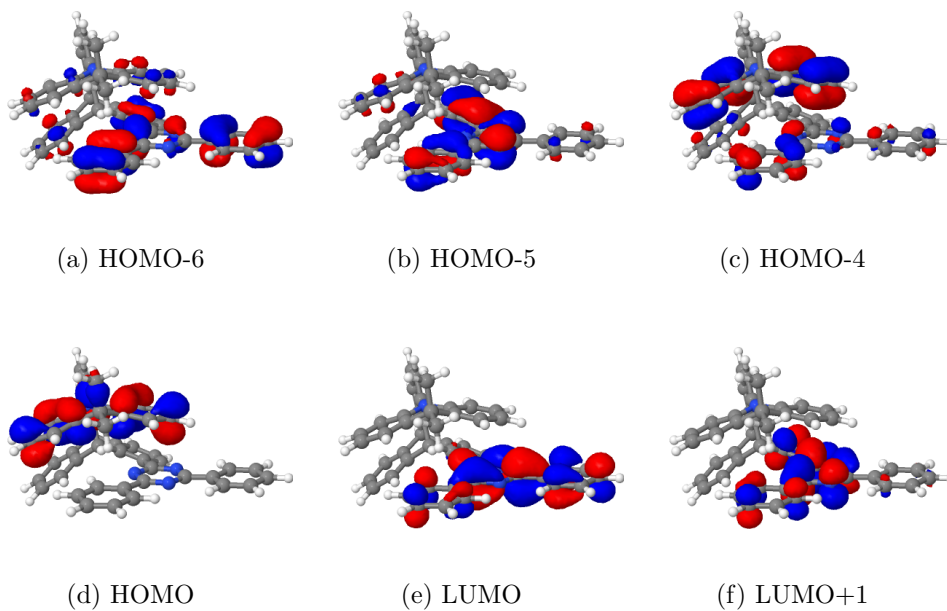


Figure S33: PBE0 molecular orbitals (cutoff 0.03) at the $S_0(\text{Me} \rightarrow \text{Ph})$ geometry in vacuo.

Table S12: LC- ω PBE/6-31+G(d) ($\omega = 0.1664$) TDDFT vertical excitation energies (including TDA approximation for triplet states) and characterization of low-lying singlet and triplet states of **TpAT-tFFO** calculated at the $S_0(\text{Me} \rightarrow \text{Ph})$ geometry.

State	ΔE [eV]	Transition	Character	%
S_1	3.01	H \rightarrow L+1	CT (A \rightarrow T/Tp)	55
		H \rightarrow L	CT (A \rightarrow T)	41
S_2	3.12	H \rightarrow L	CT (A \rightarrow T)	52
		H \rightarrow L+1	CT (A \rightarrow T/Tp)	41
T_1	2.99	H \rightarrow L	CT (A \rightarrow T)	47
		H \rightarrow L+1	CT (A \rightarrow T/Tp)	46
T_2	3.07	H \rightarrow L+1	CT (A \rightarrow T/Tp)	45
		H \rightarrow L	CT (A \rightarrow T)	40
T_3	3.35	H-5 \rightarrow L+1	LE(A/Tp)	28
		H-6 \rightarrow L	LE(A/Tp)	21

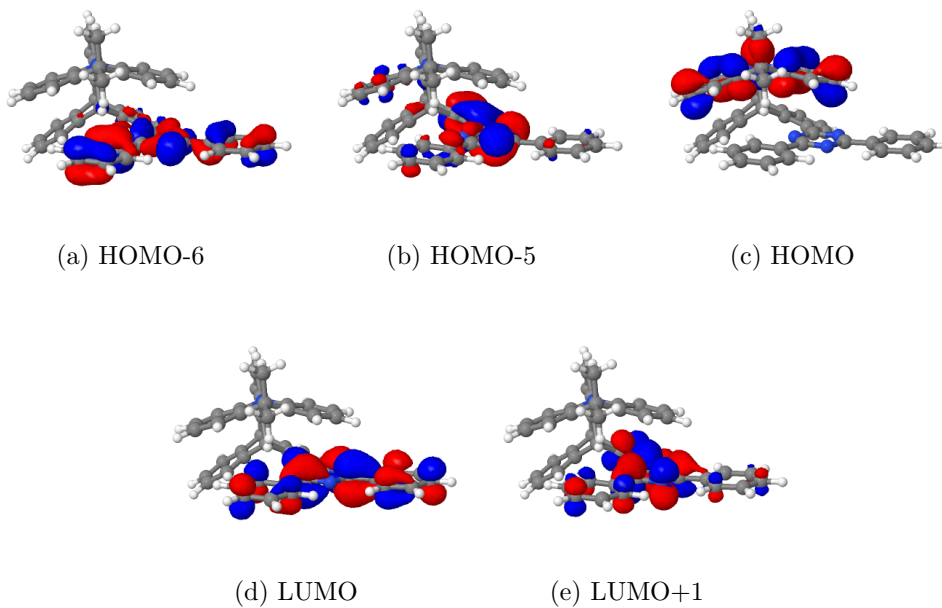


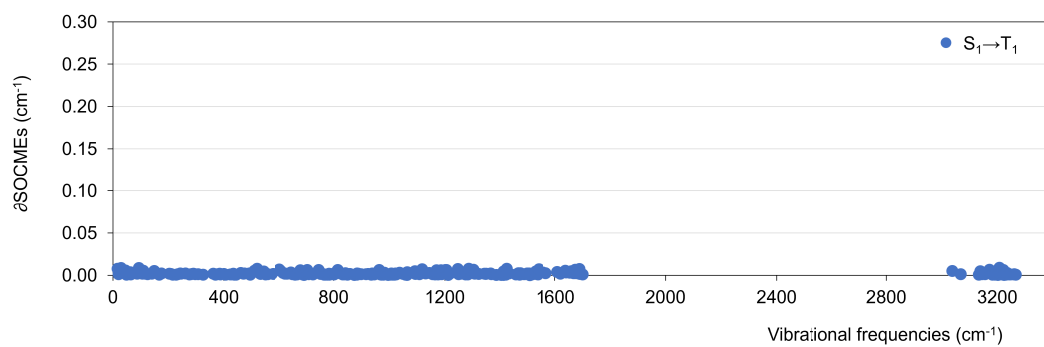
Figure S34: LC- ω PBE ($\omega = 0.1664$) molecular orbitals (cutoff 0.03) at the $S_0(\text{Me} \rightarrow \text{Ph})$ geometry in vacuo.

Table S13: PBE0/def2-SV(P) Adiabatic TDDFT excitation energies of low-lying singlet and triplet states of **TpAT-tFFO** (including TDA approximation for triplet states). Zero-point vibrational energy corrections were computed at the (TD)DFT level of theory.

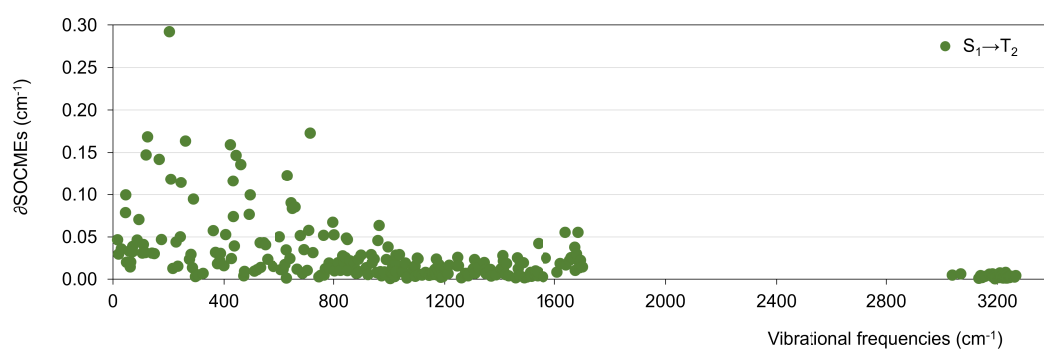
State	ΔE [eV]	Transition	Character	%	ZPVE
S ₁	2.47	H \rightarrow L	CT	99.8	-0.11
S ₂	2.49	H \rightarrow L+1	CT'	99.1	-0.12
T ₁	2.45	H \rightarrow L	CT	99.4	-0.11
T ₂	2.45	H \rightarrow L+1	CT'	97.3	-0.12
T ₃	3.09	H-2 \rightarrow L	LE	38.3	+0.04
		H-4 \rightarrow L		17.2	
		H-5 \rightarrow L		15.4	

Table S14: FC rate constants (direct ISC/rISC, s⁻¹) between low-lying singlet and triplet state minima of **TpAT-tFFO**. Values smaller than 1 s⁻¹ have been omitted.

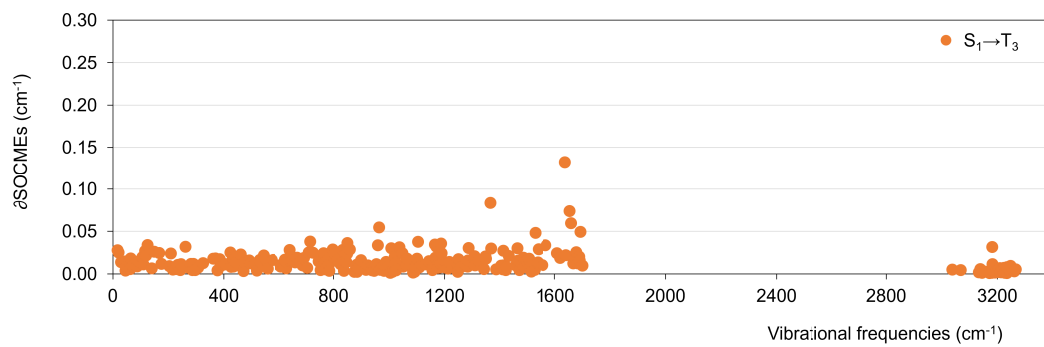
State	ISC (20 K)	ISC (300 K)	rISC (20 K)	rISC (300 K)
S ₁ (CT) \leftrightarrow T ₁ (CT)	9.8×10^3	8.7×10^4	—	5.2×10^3
S ₁ (CT) \leftrightarrow T ₂ (CT')	3.0×10^2	2.9×10^5	—	9.1×10^2
S ₁ (CT) \leftrightarrow T ₃ (LE)	—	9.5×10^3	5.0×10^6	2.2×10^6
S ₂ (CT') \leftrightarrow T ₁ (CT)	—	8.6×10^4	—	4.2×10^3
S ₂ (CT') \leftrightarrow T ₂ (CT')	1.3×10^5	5.3×10^5	—	2.6×10^3
S ₂ (CT') \leftrightarrow T ₃ (LE)	—	3.5×10^2	7.3×10^4	1.2×10^5



(a) $S_1(\text{CT}) \rightarrow T_1(\text{CT})$

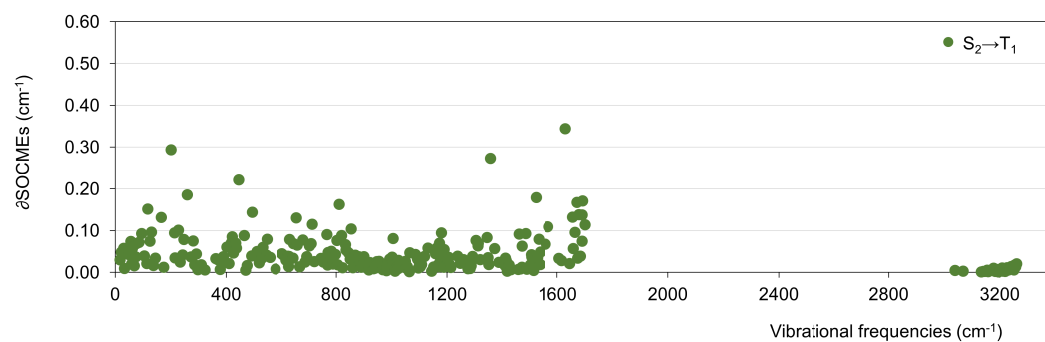


(b) $S_1(\text{CT}) \rightarrow T_2(\text{CT}')$

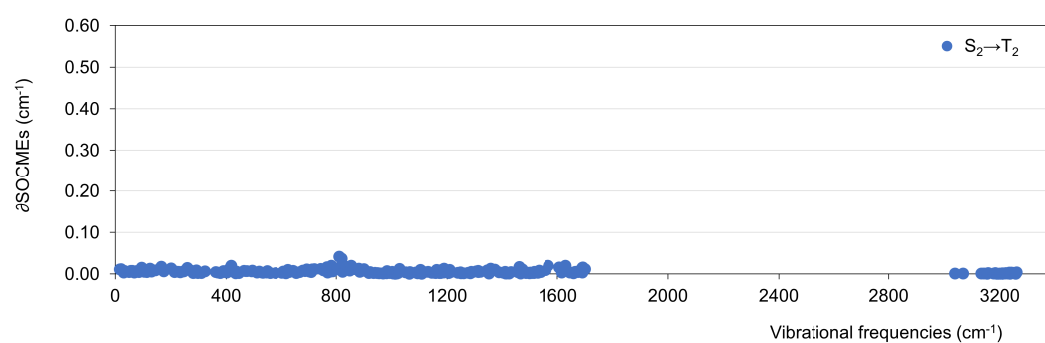


(c) $S_1(\text{CT}) \rightarrow T_3(\text{LE})$

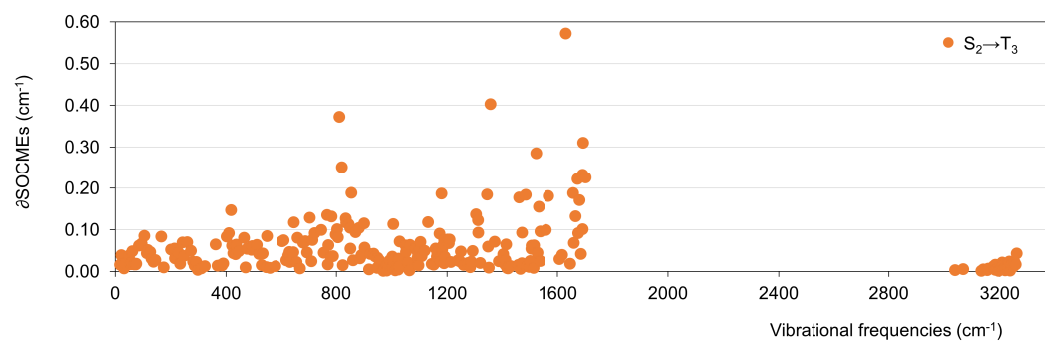
Figure S35: Important coupling vibrational normal modes calculated at the S_1 minimum of **TpAT-tFFO**.



(a) $S_2(\text{CT}') \rightarrow T_1(\text{CT})$

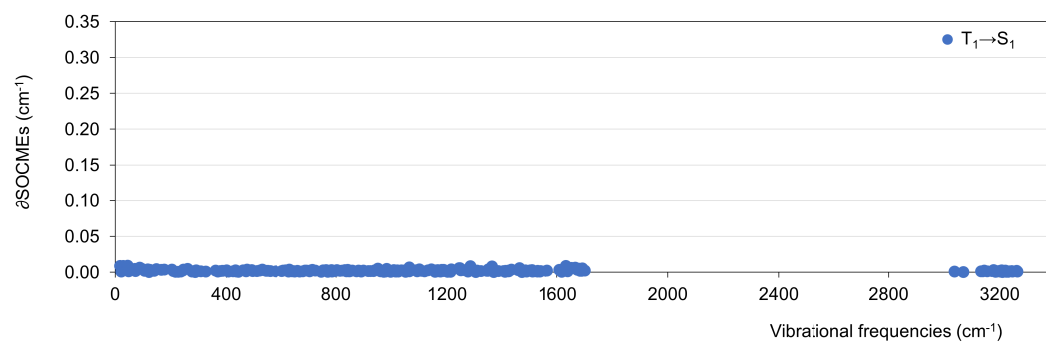


(b) $S_2(\text{CT}') \rightarrow T_2(\text{CT}')$

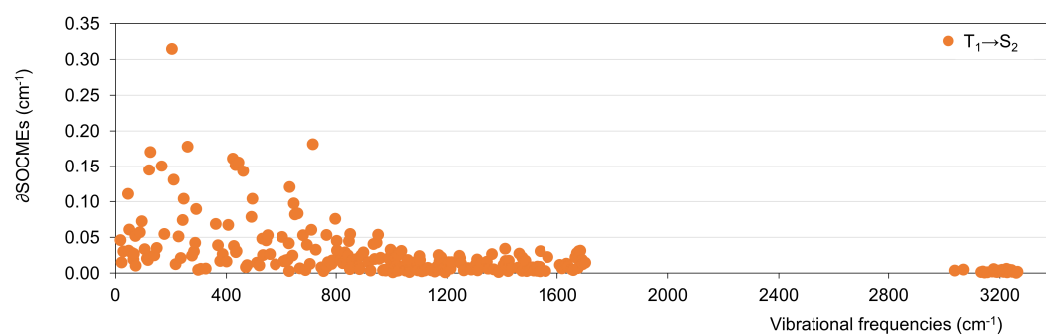


(c) $S_2(\text{CT}') \rightarrow T_3(\text{LE})$

Figure S36: Important coupling vibrational normal modes calculated at the S_2 minimum of **TpAT-tFFO**.

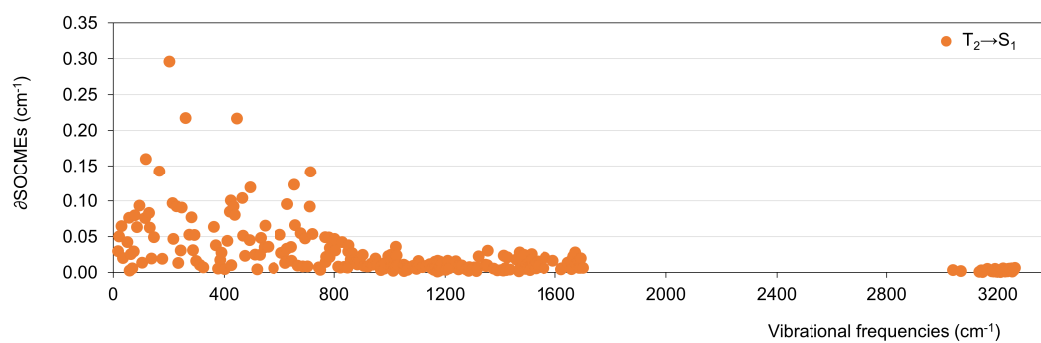


(a) $T_1(\text{CT}) \rightarrow S_1(\text{CT})$

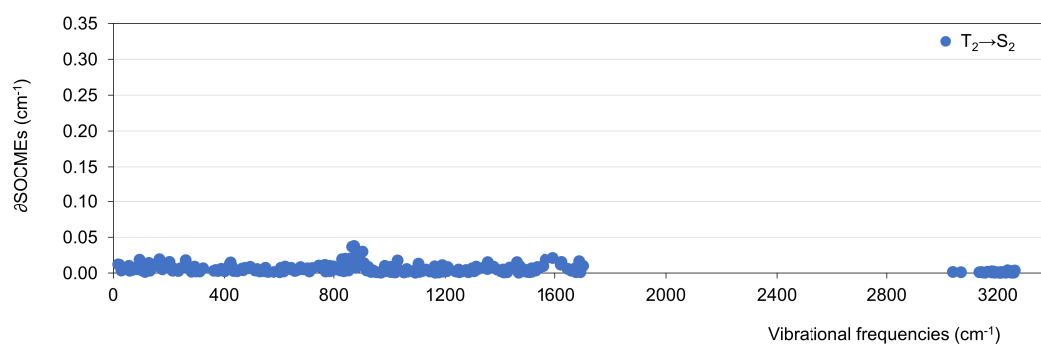


(b) $T_1(\text{CT}) \rightarrow S_2(\text{CT}')$

Figure S37: Important coupling vibrational normal modes calculated at the T_1 minimum of **TpAT-tFFO**.

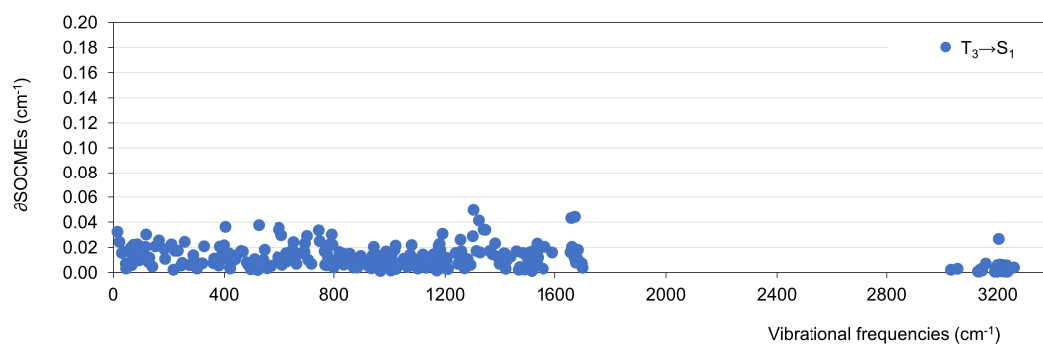


(a) $T_2(CT') \rightarrow S_1(CT)$

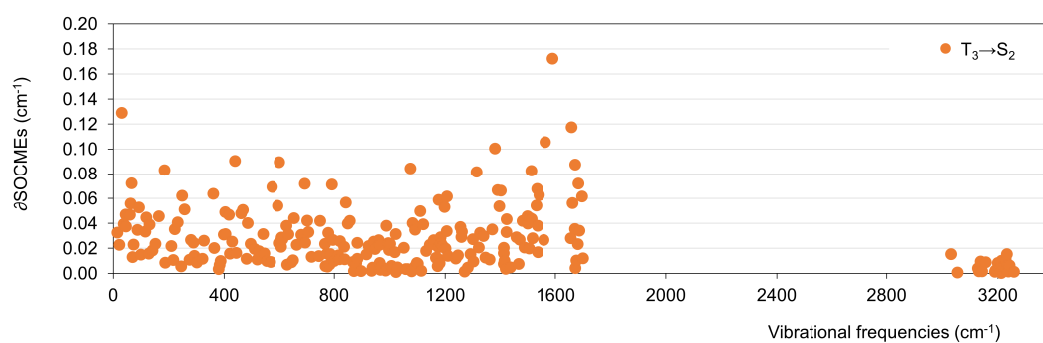


(b) $T_2(CT') \rightarrow S_2(CT')$

Figure S38: Important coupling vibrational normal modes calculated at the T_2 minimum of **TpAT-tFFO**.



(a) $T_3(\text{LE}) \rightarrow S_1(\text{CT})$



(b) $T_3(\text{LE}) \rightarrow S_2(\text{CT}')$

Figure S39: Important coupling vibrational normal modes calculated at the T_3 minimum of **TpAT-tFFO**.

Table S15: FC-HT rate constants (direct and vibronic ISC, s^{-1}) at 300 K with shifted potentials in the range of 20 and 170 meV between low-lying singlet and triplet state minima of **TpAT-tFFO**.

State	20 meV	50 meV	80 meV	110 meV	140 meV	170 meV
$S_1(\text{CT}) \rightarrow T_1(\text{CT})$	4.2×10^6	1.4×10^6	1.1×10^6	7.4×10^5	9.6×10^5	8.9×10^5
$S_1(\text{CT}) \rightarrow T_2(\text{CT}')$	6.0×10^4	1.0×10^5	1.6×10^5	2.4×10^5	3.4×10^5	4.6×10^5
$S_1(\text{CT}) \rightarrow T_3(\text{LE})$	8.6×10^5	4.5×10^5	2.1×10^5	9.0×10^4	3.6×10^4	1.4×10^4
$S_2(\text{CT}') \rightarrow T_1(\text{CT})$	4.1×10^4	6.9×10^4	1.1×10^5	1.6×10^5	2.3×10^5	3.2×10^5
$S_2(\text{CT}') \rightarrow T_2(\text{CT}')$	2.8×10^7	9.8×10^6	5.9×10^6	1.1×10^7	7.3×10^6	4.3×10^6
$S_2(\text{CT}') \rightarrow T_3(\text{LE})$	8.8×10^4	4.8×10^4	2.4×10^4	1.1×10^4	3.8×10^3	5.3×10^2

Table S16: FC-HT rate constants (direct and vibronic rISC, s^{-1}) at 300 K with shifted potentials in the range of 20 and 170 meV between low-lying singlet and triplet state minima of **TpAT-tFFO**.

State	20 meV	50 meV	80 meV	110 meV	140 meV	170 meV
$S_1(\text{CT}) \leftarrow T_1(\text{CT})$	2.6×10^6	3.6×10^5	5.8×10^4	1.5×10^4	5.3×10^3	1.7×10^3
$S_1(\text{CT}) \leftarrow T_2(\text{CT}')$	3.9×10^4	2.1×10^4	1.0×10^4	4.6×10^3	2.0×10^3	8.6×10^2
$S_1(\text{CT}) \leftarrow T_3(\text{LE})$	1.4×10^6	2.2×10^6	3.3×10^6	4.6×10^6	5.9×10^6	7.3×10^6
$S_2(\text{CT}') \leftarrow T_1(\text{CT})$	3.3×10^4	1.7×10^4	7.9×10^3	3.6×10^3	1.6×10^3	6.5×10^2
$S_2(\text{CT}') \leftarrow T_2(\text{CT}')$	1.7×10^7	2.0×10^6	3.7×10^5	2.1×10^5	4.6×10^4	8.2×10^3
$S_2(\text{CT}') \leftarrow T_3(\text{LE})$	1.1×10^5	1.9×10^5	3.1×10^5	4.6×10^5	6.6×10^5	9.1×10^5

Publication II

A Thermally Activated Delayed Fluorescence Emitter Investigated by Time-Resolved Near-Infrared Spectroscopy

W. Haselbach, **J. M. Kaminski**, L. N. Kloeters, T. J. J. Müller, O. Weingart, C. M.

Marian, P. Gilch & B. E. Nogueira de Faria

Chem. Eur. J., 29(2):e202202809, 2023

DOI: 10.1002/chem.202202809

Contribution: All quantum chemical investigations presented in this work, writing of results in section about quantum chemical computations, revising the manuscript.

VIP A Thermally Activated Delayed Fluorescence Emitter Investigated by Time-Resolved Near-Infrared Spectroscopy

Wiebke Haselbach,^[a] Jeremy M. Kaminski,^[b] Laura N. Kloeters,^[c] Thomas J. J. Müller,^[c] Oliver Weingart,^[b] Christel M. Marian,^[b] Peter Gilch,^{*,[a]} and Barbara E. Nogueira de Faria^[a]

Abstract: Emitters for organic light-emitting diodes (OLEDs) based on thermally activated delayed fluorescence (TADF) require small singlet (S_1)-triplet (T_1) energy gaps as well as fast intersystem crossing (ISC) transitions. These transitions can be mediated by vibronic mixing with higher excited states S_n

and T_n ($n=2, 3, 4, \dots$). For a prototypical TADF emitter consisting of a triarylamine and a dicyanobenzene moiety (TAA-DCN) it is shown that these higher states can be located energetically by time-resolved near-infrared (NIR) spectroscopy.

Introduction

Thermally activated delayed fluorescence (TADF) emitters are designed to convert singlet and triplet excitons efficiently into light.^[1] They show great potential for the application in organic light-emitting diodes (OLEDs).^[2] In OLEDs, excitons are generated by electron-hole recombination. Due to spin statistics, singlet and triplet excitons are generated in a 1:3 ratio, and emitters based on TADF can harvest both excitons to achieve 100% internal quantum efficiency.^[3]

Efficient TADF emitters ought to feature small singlet-triplet energy gaps as well as high rate constants for intersystem crossing (ISC) and reverse intersystem crossing (rISC) between singlet and triplet states.^[4] The energy gap (ΔE_{ST}) between the lowest singlet (S_1) and triplet (T_1) excited states ought to be of the order of the thermal energy $k_B T$.^[2c] It equals twice the exchange energy, and is small for a small overlap between hole and electron densities.^[1c] In a molecular orbital picture, the hole density is related to the highest occupied molecular orbital (HOMO) and the electron density to the lowest unoccupied

molecular orbital (LUMO) of the emitter. Small singlet-triplet energy gaps are commonly encountered in compounds with donor and acceptor moieties where the HOMO (LUMO) is mainly localized on the donor (acceptor) moiety.^[5] As a consequence, the relevant singlet and triplet excited states have a strong charge-transfer (CT) character. Concerning the kinetics, efficient TADF emitters ought to exhibit high rate constants for ISC and rISC, since the delayed fluorescence relies on the triplet-to-singlet energy up-conversion mechanism. However, between “pure” CT excited states the spin-orbit coupling (SOC) mediating ISC and rISC is very weak.^[6] There are two mechanisms, vibrational spin-orbit and spin-vibronic coupling, that can lift the forbiddenness of the ISC/rISC transitions.^[7] With perturbation theory, expressions for the impact on these mechanisms on the ISC/rISC rate constants can be derived. These expressions reveal an explicit and implicit (see, e.g., discussion in ref. [8]) influence of the energetic separation of CT and locally excited (LE) states (Figure 1) on these rate constants. Thus, it seems worthwhile to address the

[a] W. Haselbach, Prof. Dr. P. Gilch, Dr. B. E. Nogueira de Faria
Institut für Physikalische Chemie
Heinrich-Heine-Universität Düsseldorf
Universitätsstraße 1, 40225 Düsseldorf (Germany)
E-mail: gilch@hhu.de
Homepage: <https://www.gilch.hhu.de>

[b] J. M. Kaminski, Dr. O. Weingart, Prof. Dr. C. M. Marian
Institut für Theoretische Chemie und Computerchemie
Heinrich-Heine-Universität Düsseldorf
Universitätsstraße 1, 40225 Düsseldorf (Germany)

[c] L. N. Kloeters, Prof. Dr. T. J. J. Müller
Institut für Organische Chemie und Makromolekulare Chemie
Heinrich-Heine-Universität Düsseldorf
Universitätsstraße 1, 40225 Düsseldorf (Germany)

Supporting information for this article is available on the WWW under <https://doi.org/10.1002/chem.202202809>

© 2022 The Authors. Chemistry - A European Journal published by Wiley-VCH GmbH. This is an open access article under the terms of the Creative Commons Attribution Non-Commercial License, which permits use, distribution and reproduction in any medium, provided the original work is properly cited and is not used for commercial purposes.

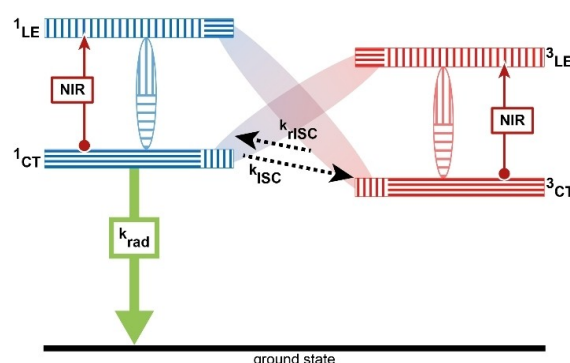


Figure 1. Scheme showing excited-state processes with ISC and rISC mediated by spin-vibronic coupling. Due to vibronic mixing, the lowest excited states of CT character (horizontal stripes) gain some LE character (vertical stripes). The transitions $^1CT \rightarrow ^1LE$ and $^3CT \rightarrow ^3LE$ are located in the NIR region.

respective energies experimentally. The energetic separations are related to $S_1 \rightarrow S_n$ and $T_1 \rightarrow T_n$ ($n=2, 3, 4, \dots$) transition energies that ought to be found in the near-infrared (NIR) region. Respective experiments are presented in the following.

A pulsed excitation promotes the emitter to the $S_1(^1\text{CT})$ state and the $S_1 \rightarrow S_n$ transitions can be monitored. After a suitable waiting time the $T_1(^3\text{CT})$ state will be populated and the $T_1 \rightarrow T_n$ transitions are accessed. Respective proof of principle experiments will be described here.

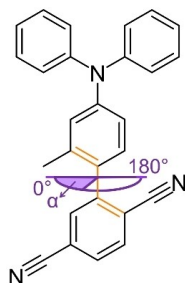
The TADF emitter TAA-DCN studied here consists of a triarylamine (TAA) donor and an 1,4-dicyanobenzene (DCN) acceptor moiety (Scheme 1). Dissolved in toluene and at room temperature, the compound was shown to be TADF active with a prompt fluorescence lifetime of 21 ns and a delayed one of 30 μs .^[9] According to temperature-dependent measurements its energy gap ΔE_{ST} was estimated to be 980 cm^{-1} (0.12 eV).^[9]

Here, femto- and nanosecond transient absorption measurements of TAA-DCN covering the UV/Vis to NIR range are reported on. $S_1 \rightarrow S_n$ and $T_1 \rightarrow T_n$ ($n=2, 3, 4, \dots$) transitions were observed and compared favourably with high-level quantum chemical computations. As these computations point to a non-Condon effect in the S_1 emission respective experiments were also conducted.

Results and Discussion

Quantum chemical computations

To assess the spectral range in which the lowest excited state transition $S_1 \rightarrow S_n$ and $T_1 \rightarrow T_n$ ($n=2, 3, 4, \dots$) are to be expected, quantum-chemical computations were performed. A previous TD-DFT (B3-LYP) study^[9] gives the first estimates for the vertical excitation energies. It places the $S_1 \rightarrow S_2$ transition at 1.01 eV and the $T_1 \rightarrow T_2$ one at 0.63 eV at the optimized ground state geometry. In the NIR experiments vertical energies with respect to the S_1 and T_1 geometries will be recorded. Furthermore, TD-DFT is known to have deficits when it comes to describe CT excitations in conjunction with standard hybrid density functionals such as B3-LYP.^[10] The CT states do not only appear at too low energies in the TD-DFT spectrum, also the twist angle of the donor and acceptor moieties is typically too large. To



Scheme 1. Structure of 4'-(diphenylamino)-2'-methyl-[1,1'-biphenyl]-2,5-dicarbonitrile (TAA-DCN). The dihedral angle α is indicated.

avoid these problems, geometry optimizations of the S_0 , S_1 , and T_1 states were performed with Gaussian16^[11] employing an optimally tuned range-separated hybrid density functional $\omega\text{B97X-D}^{[12]}$ ($\omega=0.15 \text{ Bohr}^{-1}$, details about the optimal tuning procedure in Figure S1 in the Supporting Information) in combination with a def2-TZVP basis set. In these computations, the solvent toluene (permittivity $\epsilon_r=2.38^{[13]}$) was considered implicitly using the polarizable continuum model (PCM) implemented in Gaussian16. Two rotamers were identified for TAA-DCN in the S_0 state (Figure S2). They differ in the dihedral angle α defined by the orientation of the m -(Ph_2N)-toluene and acceptor moieties (Scheme 1). The rotamer lowest in energy features an angle α of 70.2°. The second one ($\alpha=112.3^\circ$) is about 0.02 eV higher in energy. Thus, both rotamers should be present at room temperature with a slight preference for $\alpha=70.2^\circ$. The respective profile for the S_1 state (Figure S3) shows that this rotamer remains the one with the lowest energy. In the T_1 state (Figure S4), the minima are shifted to $\alpha=40^\circ$ and 150° . In this state, a barrier of ~ 0.35 eV separates the rotamers. This should preclude an interconversion on the timescales relevant here. Thus, to simplify the analysis and discussions, only the preferred rotamer, lowest in energy, with $\alpha=70.2^\circ$ will be considered further. In addition, the computed spectra signatures of the two conformers differ only slightly (Tables S1–S3). Vertical singlet excitation energies with respect to the optimized S_0 geometry were computed with the DFT/MRCI-R2016^[14] approach. The energies and the respective oscillator strengths are summarized in Table 1 and Figure 2. The energies are by ~ 0.5 eV higher than the ones computed previously,^[9] a behaviour already expected due to the different methods applied. The vertical $S_0 \rightarrow S_1$ energy computed here is in better agreement with the experiment (see below). The respective oscillator strength f amounts to 0.069. The colour bar code plotted in Figure 2 highlights the CT character of the excited states (see Tables S1–S3 for difference densities^[15]).

Starting with the S_0 geometry, TAA-DCN was geometry optimized in its S_1 state. The optimized S_1 structure of the predominant rotamer exhibits a dihedral angle α of 65.9°. The structural relaxation lowers the S_1 energy from 3.06 to 2.89 eV and the computed vertical emission energy amounts to 2.50 eV. Interestingly, this relaxation goes along with a slight increase of the oscillator strength f to 0.089. This is due to the more parallel arrangement between donor and acceptor moieties resulting in a more local excitation character. So, a dependence of the transition dipole moment on the nuclear coordinates, that is, a non-Condon effect,^[16] is predicted. Vertical excitation energies with respect to the S_1 geometry and the oscillator strengths of the spin- and electric dipole-allowed transitions are shown in Table 1 and Figure 2 (see Table S2 for the other rotamer). The computation places the lowest of these transitions ($S_1 \rightarrow S_2$) at 1.22 eV. The value is similar to the rough estimate given above and indicates that in the experiment we ought to search for this transition at ~ 1000 nm.

The T_1 state was also geometry optimized. The optimized T_1 structure exhibits a dihedral angle α of 41.4°. Its computed adiabatic energy amounts to 2.53 eV. This translates into a singlet-triplet gap ΔE_{ST} of 0.36 eV. This is roughly a factor of

Table 1. Vertical excitation energies [eV] and oscillator strengths for S_0 , S_1 , and T_1 equilibrium geometry of TAA-DCN in toluene.

Geometry	TD-DFT ^[a] S_0 vertical	Oscillator Strength	DFT/MRCI ^[b] S_0 vertical	Oscillator Strength	S_1 vertical (adiabatic)	Oscillator Strength	T_1 vertical (adiabatic)	Oscillator Strength
S_0	0	–	0	–	–2.50	0.089	–2.01	–
S_1	2.42	0.073	3.06	0.069	0 (2.89)	–	–	–
S_2	3.43	0.335	3.83	0.205	1.22	0.009	–	–
S_3	3.65	0.006	3.97	0.222	1.38	0.034	–	–
S_4	3.74	0.016	4.26	0.251	1.54	0.220	–	–
T_1	2.32	–	2.90	–	–	–	0 (2.53)	–
T_2	2.95	–	3.32	–	–	–	0.89	0.024
T_3	3.11	–	3.46	–	–	–	1.17	0.295
T_4	3.24	–	3.52	–	–	–	1.39	0.001

[a] TD-DFT vertical electronic transitions of TAA-DCN in toluene modelled according to the polarizable continuum model (PCM) for the ground state molecular geometry at the B3LYP/6-31G(d,p) level of theory from ref. [9]. [b] DFT/MRCI vertical electronic transitions of TAA-DCN in toluene modelled according to the polarizable continuum model (PCM) for the S_0 , S_1 , and T_1 equilibrium geometry at OT- ω B97X-D/def2-TZVP level of theory.

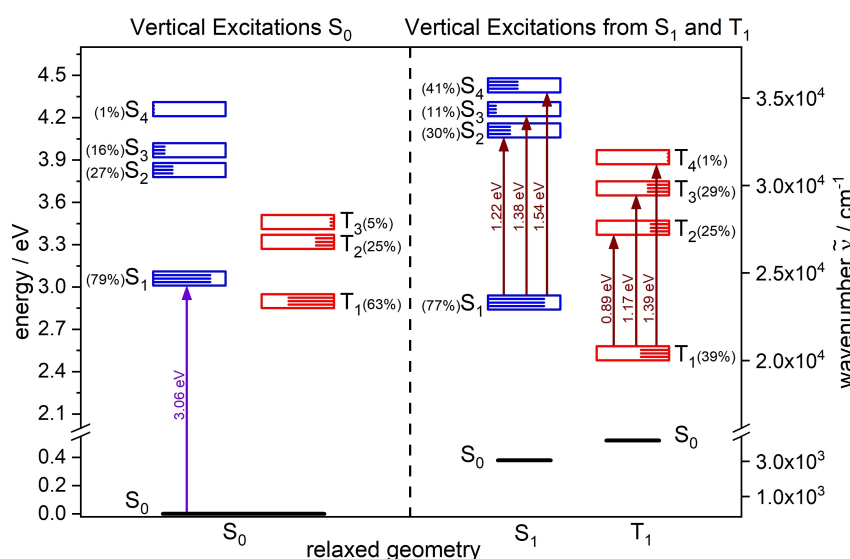


Figure 2. Computed vertical excitation energies of TAA-DCN in toluene and the CT character at the respectively optimized geometry for the relevant excited states. The vertical energies refer to the S_0 , S_1 , and T_1 equilibrium geometry. The CT character of the excited states is depicted by the coloured bars (with the corresponding values in brackets); it was obtained from a fragment-based analysis of the transition density matrix.

three higher than the earlier experimental value derived from kinetic data.^[9] The computed vertical excitations with respect to the T_1 geometry and the oscillator strengths of the spin- and electric dipole-allowed transitions are displayed in Table 1 and Figure 2 (see Table S3 for the other rotamer). According to these computations, the lowest transition ($T_1 \rightarrow T_2$) ought to be found at 0.89 eV or ~ 1400 nm. These quantum chemical predictions will now be compared with spectroscopic measurements.

Steady-state spectroscopy

TAA-DCN in toluene exhibits a lowest-energy absorption band peaking at around 382 nm with an absorption coefficient ϵ_{max} of $3844 \text{ M}^{-1}\text{cm}^{-1}$ (Figure 3). An experimental value for the

oscillator strength f was determined by first plotting the absorption coefficient $\epsilon(\tilde{\nu})$ as a function of wavenumber. To isolate the lowest energy transition, a Gaussian fit was performed (Figure 3a). From the integral of this Gaussian, $f^{[17]}$ was derived. It amounts to 0.09 and is close to the quantum chemical one of 0.07. Experimental excitation energies were determined from absorption and fluorescence spectra converted into the transition dipole representation^[17] (Figure 3b). Equating the respective absorption maximum with the vertical excitation energy for $S_0 \rightarrow S_1$ yields a value of 25830 cm^{-1} (3.20 eV) in good agreement with the computation. From the intersection of the normalized and redrawn absorption and emission spectra we deduce a 0–0 energy of 22676 cm^{-1} (2.81 eV). This is close to the computed adiabatic energy of 2.87 eV including zero-point vibrational energy corrections. The maximum of the emission is located at 19790 cm^{-1} (2.45 eV),

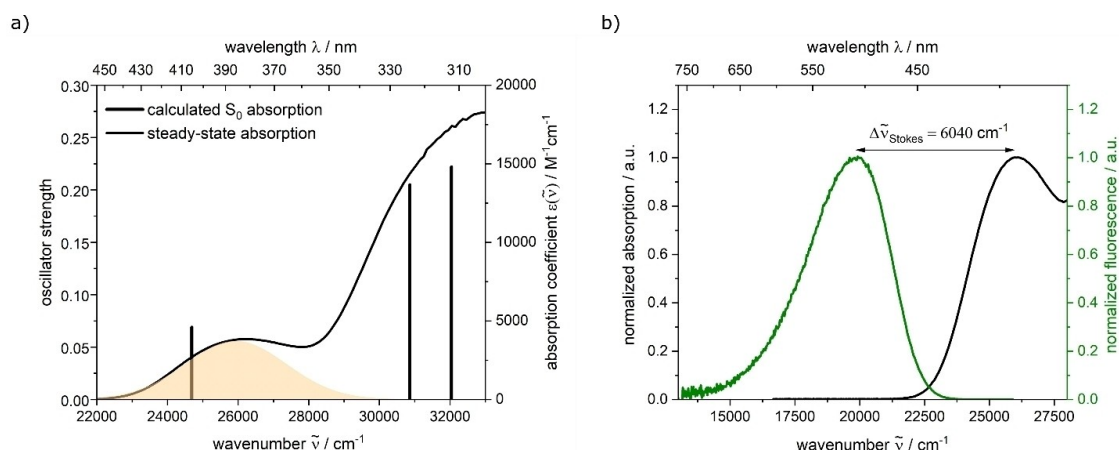


Figure 3. Absorption coefficient and fluorescence spectra of TAA-DCN in toluene. a) Comparison of measured absorption spectra ($\epsilon(\tilde{\nu})$, black line) and the calculated transitions from the S_0 state (sticks). The filled area represents the region used to determine the experimental oscillator strength. b) Spectra in the transition dipole representation. Absorption data are reported as absorption coefficient as a function of wavenumber ($\epsilon(\tilde{\nu})$) and were rescaled according to $\epsilon(\tilde{\nu})/\tilde{\nu}$, and fluorescence spectrum ($F(\tilde{\nu})$) according to $F(\tilde{\nu})/\tilde{\nu}^3$; then the rescaled spectra were normalized (for details see the Experimental Section). For the acquisition of the fluorescence spectrum, $\lambda_{\text{exc}} = 380$ nm.

again in good agreement with the computation. Absorption and emission maxima translate into Stokes shift of 6040 cm^{-1} .

Time-resolved spectroscopy

The S_1 state of TAA-DCN was characterized by femtosecond UV/Vis and nanosecond NIR absorption spectroscopy. In the femto-

second experiment, a TAA-DCN solution was excited with 400 nm laser pulses (Figure 4).

Around time zero, the excitation generates a broad excited state absorption (ESA) signature covering the complete detection range (360–730 nm). Maxima around 720, 435, and <350 nm are discernible. A pronounced minimum is located around 500 nm. With reference to the fluorescence spectrum (Figure 3), this is attributed to stimulated emission (SE). Note that in a transient absorption experiment SE gives a negative

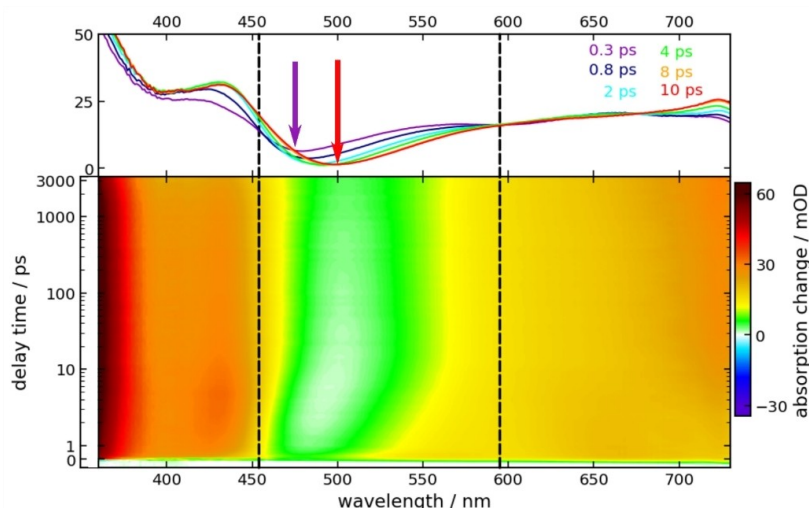


Figure 4. Femtosecond transient absorption of TAA-DCN in toluene ($c = 1.9$ mM) after excitation at 400 nm. In the contour representation, the difference absorption ΔA is shown as a function of the detection wavelength λ and the delay time t is colour coded. Selected transient spectra of up to 10 ps highlight the change in stimulated emission with time. The spectral region in which stimulated emission is expected is marked by the dashed lines. The arrows indicate the increase in the stimulated emission during solvent relaxation.

signal contribution. Here, this negative contribution “cuts into” a strong and broad positive one. Up ~ 10 ps changes of the SE contribution are observable (see also top panel in Figure 4). The SE spectrum shifts to the red (dynamic Stokes shift) and gains in signal strength. To quantify these changes, the SE contributions to the transient difference spectra were identified by overlaying the transient signal with the spontaneous emission (Figure 5a). From these contributions, the average emission wavenumbers $\langle\tilde{\nu}\rangle$, Eq. (1):

$$\langle\tilde{\nu}\rangle = \frac{\int_{\tilde{\nu}_{\min}}^{\tilde{\nu}_{\max}} \frac{\Delta A_{\text{SE}}(\tilde{\nu}, t)}{\tilde{\nu}} \tilde{\nu} d\tilde{\nu}}{\int_{\tilde{\nu}_{\min}}^{\tilde{\nu}_{\max}} \frac{\Delta A_{\text{SE}}(\tilde{\nu}, t)}{\tilde{\nu}} d\tilde{\nu}} \quad (1)$$

as well as the spectral integrals [Eq. (2)] were computed:

$$I(t) = \int_{\tilde{\nu}_{\min}}^{\tilde{\nu}_{\max}} \frac{\Delta A_{\text{SE}}(\tilde{\nu}, t)}{\tilde{\nu}} d\tilde{\nu} \quad (2)$$

The integration range $\tilde{\nu}_{\min} - \tilde{\nu}_{\max}$ was selected in such a way that only the SE contributes to the integral (Figure 5a).

The time dependencies of these quantities are plotted in Figure 5b. As a biexponential fit shows, the average emission wavenumber $\langle\tilde{\nu}\rangle$ approaches its steady state value with a time constant of 0.13 ps and 2.07 ps. Values of similar magnitude were determined in studies on dielectric relaxation of toluene.^[18] Thus, this shift seems to be, at least in parts, due to dielectric relaxation. The structures changes seen in the quantum chemical calculations are also expected to contribute to the dynamic shift and might also occur on this timescale. The

plot of integral $I(t)$ reveals an increase of the SE signal with time. As the SE integral is proportional to the oscillator strength this implies a non-Condon behaviour. To separate the additional rise due to non-Condon behaviour from the instrumentally limited one, the time trace was fitted with the following trial function [Eq. (3)]:

$$S(t, \tau_{\text{cc}}) = \text{IRF}(\tau_{\text{cc}}) \otimes [A_1 e^{-\frac{t}{\tau_1}} + A_2 e^{-\frac{t}{\tau_2}}] \quad (3)$$

$\text{IRF}(\tau_{\text{cc}}) \otimes$ stands for the convolution with the instrumental response function which was approximated by a gaussian function with $\tau_{\text{cc}} = 0.15$ ps (FWHM), $A_1 < 0$ is the amplitude associated with the rise time τ_1 , and $A_2 > 0$ is the signal after termination of the rise with the time constant τ_2 that was set to infinity, $A_1 + A_2$ equals the initial signal. The fit yields a rise time of 0.6 ps, an initial signal $A_1 + A_2$ of 2.3 and final one A_2 of 4.2. Thus, an increase in oscillator strength by a factor of around 2 is measured. The quantum chemical computation predicted only a smaller increase (a factor of 1.3), although it depends on the configuration selected (for $\alpha = 123.9^\circ$ a factor of 2.1 was estimated).

From ~ 10 ps until ~ 3 ns, the UV/Vis transient absorption signal is essentially constant. This is in line with the reported fluorescence lifetime of 21 ns.^[9] So, from ~ 10 ps onwards signals stem from the relaxed S_1 state of TAA-DCN. A spectral signal recorded after ~ 10 ps thus constitutes the short wavelength part of the $S_1 \rightarrow S_n$ spectrum. According to the quantum chemical computations described above, the long wavelength part of this spectrum ought to be centred around 1000 nm. This

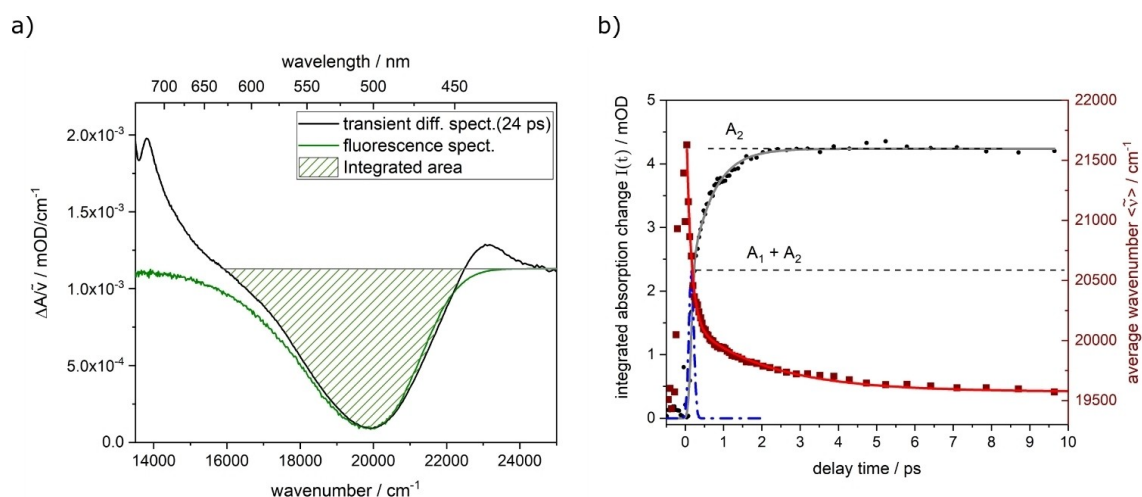


Figure 5. Analysis of the early behaviour of the stimulated emission. a) Comparison of the transient absorption spectrum with the steady-state fluorescence spectrum. An example transient absorption spectrum at a long (24 ps) delay time compared to the relaxation times is shown. For comparison, the fluorescence spectrum $F(\tilde{\nu})$ was redrawn according to $F(\tilde{\nu})/\tilde{\nu}^2$, and the transient absorption $\Delta A(\tilde{\nu})$ according to $\Delta A(\tilde{\nu})/\tilde{\nu}$ to arrive at the transition dipole representation. Then, the rescaled fluorescence (green line) was inverted and shifted to overlay the transient absorption spectrum. The marked area is proportional to the integral $I(24 \text{ ps})$. b) The spectrally integrated SE signal [Eq. (3)] is plotted as a function of time (shown in black). This signal $I(t)$ was fitted with the trial function (grey line) shown in Equation (4); the instrument-response function was approximated by a Gaussian function (with FWHM ~ 0.15 ps, plotted in blue). The evolution of the average emission wavenumber $\langle\tilde{\nu}\rangle$, dark red data points) is also shown with the respective double exponential fit (red line).

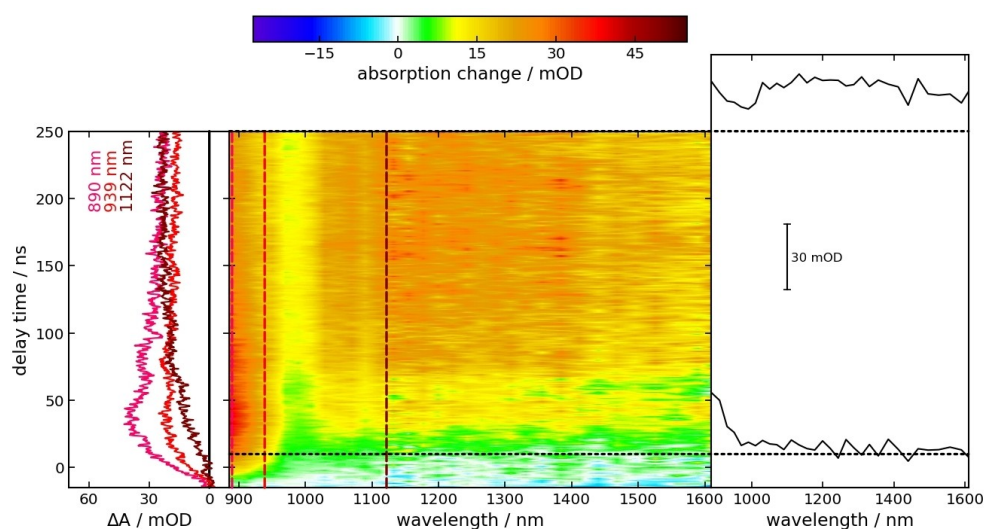


Figure 6. Nanosecond transient absorption of TAA-DCN in deoxygenated toluene ($c = 0.2$ mM) for the early-nanosecond range after excitation at 355 nm covering the NIR. The contour plot in the centre gives an overview. Time traces at indicated detection wavelengths are plotted on the left. Transient difference spectra at early and later times are shown on the right.

region is accessible by inspection of the early part of a nanosecond NIR experiment (Figure 6).

Around time zero, a difference absorption is observed which gradually increases from 1600 to 1000 nm. Below 1000 nm the signal sharply rises pointing to an absorption band peaking around 900 nm (not covered by our instrument). On the timescale of 10 ns the signal is seen to arise throughout most of the spectral region covered. The timescale of the rise matches the S_1 lifetime. We therefore assign the time zero spectrum to the S_1 state. By combining the “late” femtosecond UV/Vis and the “early” nanosecond NIR signals the experimental $S_1 \rightarrow S_n$ spectrum plotted in Figure 7 was obtained. For comparison, the quantum chemical stick spectrum (oscillator strengths as a function of wavelength) were convoluted with Gaussians. There is good agreement between measured and computed spectra.

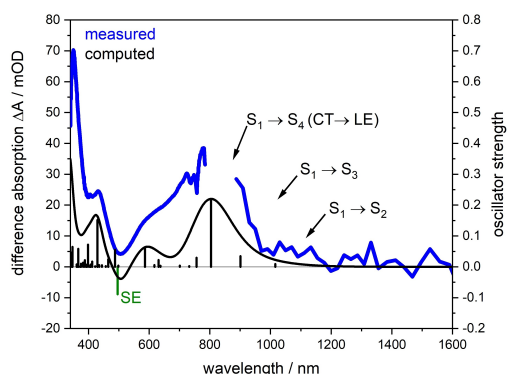


Figure 7. Comparison of the measured and computed $S_1 \rightarrow S_n$ spectra of TAA-DCN in toluene.

In particular, the lowest four transition $S_1 \rightarrow S_{2,3,4}$ can be identified. The $S_1 \rightarrow S_2$ and $S_1 \rightarrow S_3$ transitions are among CT states and the $S_1 \rightarrow S_4$, centred at around 800 nm, is a CT \rightarrow LE transition.

To obtain the $T_1 \rightarrow T_n$ spectrum, nanosecond UV/Vis spectroscopy and NIR probing were conducted. Hereby, the focus was laid on the microsecond time range, as the T_1 lifetime was reported to be 30 μ s.^[9] In the respective experiment, a broad excited state absorption extending from 400 to 1600 nm is observed at time zero (Figure 8). Peaks are discernible at 460, 710, and 1200 nm. The signal decays to zero on the timescale of 10 μ s. A global fit analysis yields a time constant τ_T of 19 μ s for this decay. This is shorter than the value of 30 μ s derived from the decay of the delayed fluorescence.^[9] We, thus, investigated the dependence of the lifetime τ_T on the TAA-DCN concentration (see in Figure S5). The experiment reveals a linear increase of $1/\tau_T$ with [TAA-DCN]. Such “self-quenching” is often observed for triplet states. A linear fit of the behaviour yields a quenching constant k_{sq} of $9.7 \cdot 10^7 \text{ M}^{-1} \text{ s}^{-1}$ and a lifetime τ_0^T for infinite dilution of 30.1 μ s. This value is very close the one reported early^[9] indicating that in both experiments the same state, namely, the T_1 one is monitored.

The experimental spectrum of this state is compared with the quantum chemical prediction in Figure 9. Again, a good agreement between measured and computed spectra is observed. Also, the lowest four transitions $T_1 \rightarrow T_{2,3,4}$ can be identified. The $T_1 \rightarrow T_2$ transition is among CT states and the $T_1 \rightarrow T_3$, centred at around 1100 nm, is a CT \rightarrow LE transition.

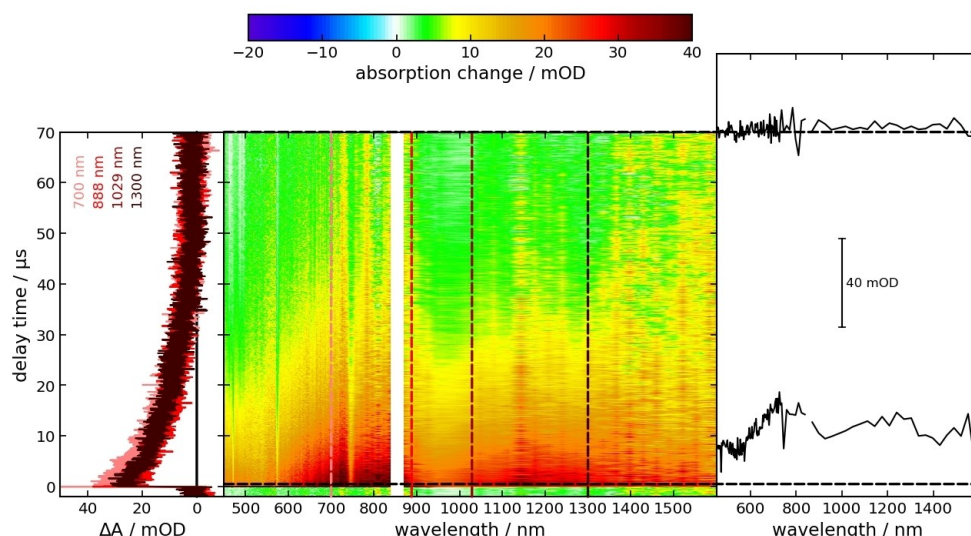


Figure 8. Nanosecond transient absorption of TAA-DCN in deoxygenated toluene ($c = 0.2$ mM) after excitation at 355 nm covering from visible to NIR for the microsecond range. The contour plot in the centre gives an overview. Time traces at indicated detection wavelengths are plotted on the left. Transient difference spectra at early and later times are shown on the right.

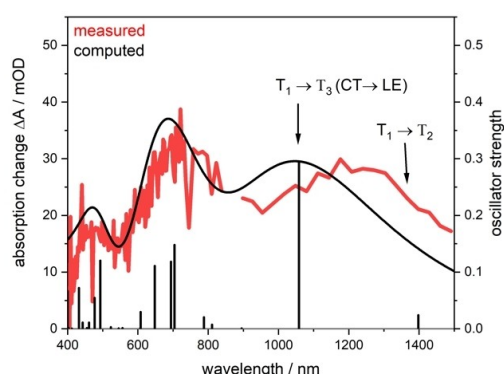


Figure 9. Comparison of the measured and computed $T_1 \rightarrow T_n$ spectra of TAA-DCN in toluene.

Conclusions

rISC and ISC transitions in TADF emitters can be mediated by vibronic mixing with higher excited singlet ($S_{n>1}$) and triplet ($T_{n>1}$) states into lower-energy excited states (S_1 and T_1). According to perturbation theory, the energy gaps between the lower-energy excited states and higher ones ought to affect this mixing.^[8] Here, it has been shown that, for a prototypical TADF emitter, the respective gaps are accessible experimentally by time-resolved NIR spectroscopy. The respective transition energies and oscillator strengths were well reproduced by quantum chemical computations. In the singlet, the lowest $^1CT \rightarrow ^1LE$ ($S_1 \rightarrow S_4$) transition was located at around 800 nm and in the triplet, the lowest $^3CT \rightarrow ^3LE$ ($T_1 \rightarrow T_3$) is at 1100 nm. In the future, we will shift these transitions by suitable substitutes

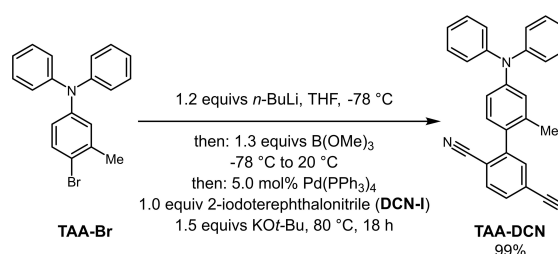
and/or solvents and investigate the impact of these shifts on the rate constants k_{ISC} and k_{rISC} .

Experimental Section

Sample and common conditions: The synthesis of TAA-DCN has been described previously,^[9] however, here we have transposed the BLEBS sequence (bromo-lithium-exchange-borylation-Suzuki)^[19] providing a higher-yielding access to the target molecule.

4-Bromo-3-methyl-*N,N*-diphenylaniline (TAA-Br) was converted by bromine-lithium exchange at -78 °C in THF to the lithiated derivative, which was reacted with trimethylborate to give the corresponding boronate complex. By subsequent Suzuki cross-coupling the boronate complex was reacted with 2-iodoterephthalonitrile (DCN-I) in the presence of potassium *tert*-butoxide and catalytic amounts of $Pd(PPh_3)_4$ as a catalyst at 80 °C for 18 h to give after isolation and purification TAA-DCN (Scheme 2).

TAA-DCN solutions were prepared in toluene ($\geq 99.7\%$, from Sigma-Aldrich). All measurements were carried out at room temperature (20 °C). For the steady-state absorption and fluorescence



Scheme 2. Synthesis of TAA-DCN by BLEBS in a one-pot fashion.

measurements fused silica cells (from Hellma analytics) of 1 cm path length were used. To avoid contributions of photo-products the sample solutions were pumped through fused silica flow cell in the femtosecond transient absorption measurements (1 mm path length) and in the nanosecond transient absorption measurements (5 mm path length in pump and 10 mm path length in probe direction). For the nsTA measurements all solutions were deaerated by purging with nitrogen (Air Liquide), and to prevent changes in the concentration, gases were saturated with the solvent.

Steady-state spectroscopy: Steady-state absorption was carried out with Lambda 19 spectrometer from PerkinElmer. Steady-state fluorescence was performed on FluoroMax-4 from Horiba Scientific. All fluorescence spectra were corrected for the solvent background and for the spectral sensitivity of the instruments. For fluorescence measurements the excitation was tuned to 380 nm, and the solutions were prepared to have an absorption below 0.05 in 1 cm cell at the excitation.

Femtosecond transient absorption spectroscopy: The setup was described in detail elsewhere.^[20] The pump pulses of 400 nm were obtained from the output of a Ti:Sa laser amplifier system (Coherent Libra, with 1 kHz of repetition rate and pulse duration of 100 fs (FWHM)) by second harmonic generation. The energy per pulse amounted to $\approx 1 \mu\text{J}$. The probe pulse was obtained by supercontinuum generation in CaF_2 . At the sample location, the diameter of the pump beam was about 160 μm , and the probe 100 μm . The relative polarization of pump and probe pulses was set to the magic angle. Raw data were corrected for the chirp and the solvent contribution. Absorptions of the sample solutions at 400 nm were adjusted to 0.7 in 1 mm cell.

Nanosecond laser flash photolysis: Nanosecond transient absorption data were performed with a laser flash photolysis spectrometer LP980 from Edinburgh Instruments. The excitation (pump pulse) was obtained by frequency tripling (355 nm) of the output of a Nd:YAG laser (Spotlight 600, InnoLas, Germany) with 5 Hz of repetition rate and 12 ns (FWHM) of pulse duration. The average pulse energy amounted to $\approx 5 \text{ mJ}$. The probe light was obtained from a pulsed xenon flash lamp (Osram XBO 150 W/CROFR). After passing the sample cell at a right angle geometry with respect to the pump, the transmitted probe light was dispersed by a grating monochromator and detected by two different detectors to cover the UV/Vis (photomultiplier Hamamatsu PMT-900) and the NIR (photodiode Hamamatsu InGaAs) spectral range. To obtain the transient signals, time traces were collected to cover the visible and near-infrared spectral range in different steps and averages to gain the best signal to noise ratio. Absorptions of the sample solutions at 355 nm were adjusted to 0.7 in 1 cm cell.

Data analysis: The oscillator strength was determined according to ref. [17], in which the integral covered the lowest absorption coefficient band. To this end, the absorption spectrum was decomposed in Gaussian components and only the lowest in energy entered in the analysis. To obtain the 0–0 excitation energy (E_{00}) and Stokes shifts, fluorescence spectra were converted from constant wavelength (λ) to constant wavenumber ($\tilde{\nu}$) bandpass by multiplying with λ^2 .^[21] Then, the absorption coefficient was rescaled according to $\epsilon(\tilde{\nu})/\tilde{\nu}$, and fluorescence spectrum according to $F(\tilde{\nu})/\tilde{\nu}^2$ to arrive at the transition dipole representation.^[17] Finally, the normalized corrected absorption and fluorescence spectra were plotted and the E_{00} was obtained from their intersection.

The transient absorption spectra ($\Delta A(\lambda, t)$) obtained here are function of the probe wavelength (λ) and the time delay (t) between pump and probe. To retrieve the time and wavelength dependencies for these measurements two approaches were used. In the first one, the stimulated emission spectra signal was analysed

for the early times. For that, the transient absorption $\Delta A(\tilde{\nu}, t)/\tilde{\nu}$ was compared to the steady-state fluorescence. The first step herein was to rescale the fluorescence spectrum according to $F(\tilde{\nu})/\tilde{\nu}^2$ to arrive at the transition dipole representation.^[23] For comparing both spectra, the rescaled fluorescence was then flipped and shifted. The spectral range in which both spectra overlaps were used latter to define the limits of the integrals analysed. And in the second approach, the nanosecond transient absorption data were analysed by global multi-exponential fit function [Eq. (4)].^[24]

$$\Delta A(\lambda, t) = \text{IRF} \otimes \sum_{i=1}^n \Delta A_i(\lambda) e^{-\frac{t}{\tau_i}} \quad (4)$$

which was convoluted with the response function (IRF) of the instrument. Here, the IRF was approximated by a Gaussian with a FWHM of 12 ns. The fit yields time constants τ_i and the respective decay associated difference spectra ΔA_i .

Quantum chemical computations: Electronic ground-state geometries of the TAA-DCN emitter were optimized with DFT at the $\omega\text{B97X-D/def2-TZVP}$ level of theory^[12,25] with $\omega = 0.15 \text{ Bohr}^{-1}$ (after optimal tuning procedure in vacuo) and including implicit toluene solvation through the polarizable continuum model (PCM)^[26] implemented in Gaussian16.^[11]

Time-dependent DFT (TDDFT)^[27] was used for the optimization of the excited states (Tamm-Dancoff approximation (TDA) for excited triplet states^[28]). Analytic harmonic vibrational frequencies were computed with Gaussian16.

Vertical and adiabatic excitation energies as well as optical electronic properties were calculated using the DFT/MRCI method.^[10b,14a,b] Up to 20 excited states in the singlet and triplet manifold (in case of ESA spectra 40 roots) employing closed-shell BH-LYP^[29] orbitals as the one-particle basis. The parametrization of the Hamiltonian reported by Lyskov et al.^[14c] (DFT/MRCI-R2016) was employed for the tight configuration selection threshold of 0.8 E_h , which is specially designed for large multichromophore systems.

Acknowledgements

This work was supported by the Deutsche Forschungsgemeinschaft (grant 396890929/GRK 2482, "ModISC"). We also thank the Center for Molecular and Structural Analytics @ Heinrich Heine University (CeMSA@HHU) for recording the mass and NMR spectra. We are grateful to our students Cornelius Treitner, Sebastian Bierhoff and Gülsüm Kinik for experimental support. We also thank Franziska Bergstein for technical support. Open Access funding enabled and organized by Projekt DEAL.

Conflict of Interest

The authors declare no conflict of interest.

Data Availability Statement

The data that support the findings of this study are available from the corresponding author upon reasonable request.

Keywords: intersystem crossing · NIR spectroscopy · thermally activated delayed fluorescence · time-resolved spectroscopy · UV/VIS spectroscopy

- [1] a) H. Uoyama, K. Goushi, K. Shizu, H. Nomura, C. Adachi, *Nature* **2012**, 492, 234–238; b) Y. Tao, K. Yuan, T. Chen, P. Xu, H. Li, R. Chen, C. Zheng, L. Zhang, W. Huang, *Adv. Mater.* **2014**, 26, 7931–7958; c) F. B. Dias, T. J. Penfold, A. P. Monkman, *Methods Appl. Fluoresc.* **2017**, 5, 012001.
- [2] a) T. Miwa, S. Kubo, K. Shizu, T. Komino, C. Adachi, H. Kaji, *Sci. Rep.* **2017**, 7, 1–8; b) T.-T. Bui, F. Goubard, M. Ibrahim-Ouali, D. Gimes, F. Dumur, *Beilstein J. Org. Chem.* **2018**, 14, 282–308; c) Y. Liu, C. Li, Z. Ren, S. Yan, M. R. Bryce, *Nat. Rev. Mater.* **2018**, 3, 1–20.
- [3] F. B. Dias, K. N. Bourdakos, V. Jankus, K. C. Moss, K. T. Kamtekar, V. Bhalla, J. Santos, M. R. Bryce, A. P. Monkman, *Adv. Mater.* **2013**, 25, 3707–3714.
- [4] a) F. B. Dias, J. Santos, D. R. Graves, P. Data, R. S. Nobuyasu, M. A. Fox, A. S. Batsanov, T. Palmeira, M. N. Berberan-Santos, M. R. Bryce, *Adv. Sci.* **2016**, 3, 1600080; b) P. L. dos Santos, M. K. Etherington, A. P. Monkman, *J. Mater. Chem. C* **2018**, 6, 4842–4853.
- [5] a) K. Shizu, H. Tanaka, M. Uejima, T. Sato, K. Tanaka, H. Kaji, C. Adachi, *J. Phys. Chem. C* **2015**, 119, 1291–1297; b) Y. Olivier, M. Moral, L. Muccioli, J.-C. Sancho-García, *J. Mater. Chem. C* **2017**, 5, 5718–5729.
- [6] a) J. Gibson, A. P. Monkman, T. J. Penfold, *ChemPhysChem* **2016**, 17, 2956–2961; b) Y. Olivier, B. Yurash, L. Muccioli, G. D'Avino, O. Mikhnenko, J.-C. Sancho-García, C. Adachi, T.-Q. Nguyen, D. Beljonne, *Phys. Rev. Mater.* **2017**, 1, 075602; c) M. K. Etherington, J. Gibson, H. F. Higginbotham, T. J. Penfold, A. P. Monkman, *Nat. Commun.* **2016**, 7, 1–7.
- [7] a) T. J. Penfold, E. Gindensperger, C. Daniel, C. M. Marian, *Chem. Rev.* **2018**, 118, 6975–7025; b) C. M. Marian, *Annu. Rev. Phys. Chem.* **2021**, 72, 617–640; c) A. C. Albrecht, *J. Chem. Phys.* **1963**, 38, 354–365; d) I. Kim, K. H. Cho, S. O. Jeon, W.-J. Son, D. Kim, Y. M. Rhee, I. Jang, H. Choi, D. S. Kim, *JACS Au* **2021**, 1, 987–997; e) I. Kim, S. O. Jeon, D. Jeong, H. Choi, W.-J. Son, D. Kim, Y. M. Rhee, H. S. Lee, *J. Chem. Theory Comput.* **2019**, 16, 621–632.
- [8] M. Bracker, M. K. Kubitz, C. Czekelius, C. M. Marian, M. Kleinschmidt, *ChemPhotoChem* **2022**, e202200040.
- [9] G. A. Sommer, L. N. Mataranga-Popa, R. Czerwieniec, T. Hofbeck, H. H. Homeier, T. J. J. Müller, H. Yersin, *J. Phys. Chem. Lett.* **2018**, 9, 3692–3697.
- [10] a) J. Autschbach, *ChemPhysChem* **2009**, 10, 1757–1760; b) C. M. Marian, A. Heil, M. Kleinschmidt, *Wiley Interdiscip. Rev.: Comput. Mol. Sci.* **2019**, 9, e1394.
- [11] M. J. Frisch, G. W. Trucks, H. B. Schlegel, G. E. Scuseria, M. A. Robb, J. R. Cheeseman, G. Scalmani, V. Barone, G. A. Petersson, H. Nakatsuji, X. Li, M. Caricato, A. V. Marenich, J. Bloino, B. G. Janesko, R. Gomperts, B. Mennucci, H. P. Hratchian, J. V. Ortiz, A. F. Izmaylov, J. L. Sonnenberg, Williams, F. Ding, F. Lipparini, F. Egidi, J. Goings, B. Peng, A. Petrone, T. Henderson, D. Ranasinghe, V. G. Zakrzewski, J. Gao, N. Rega, G. Zheng, W. Liang, M. Hada, M. Ehara, K. Toyota, R. Fukuda, J. Hasegawa, M. Ishida, T. Nakajima, Y. Honda, O. Kitao, H. Nakai, T. Vreven, K. Throssell, J. A. Montgomery Jr., J. E. Peralta, F. Ogliaro, M. J. Bearpark, J. J. Heyd, E. N. Brothers, K. N. Kudin, V. N. Staroverov, T. A. Keith, R. Kobayashi, J. Normand, K. Raghavachari, A. P. Rendell, J. C. Burant, S. S. Iyengar, J. Tomasi, M. Cossi, J. M. Millam, M. Klene, C. Adamo, R. Cammi, J. W. Ochterski, R. L. Martin, K. Morokuma, O. Farkas, J. B. Foresman, D. J. Fox, *Gaussian 16 Rev. A.03*, **2016**.
- [12] a) J.-D. Chai, M. Head-Gordon, *Phys. Chem. Chem. Phys.* **2008**, 10, 6615–6620; b) J.-D. Chai, M. Head-Gordon, *J. Chem. Phys.* **2008**, 128, 084106.
- [13] C. Miller, O. Maass, *Can. J. Chem.* **1960**, 38, 1606–1616.
- [14] a) S. Grimme, M. Waletzke, *J. Chem. Phys.* **1999**, 111, 5645–5655; b) M. Kleinschmidt, C. M. Marian, M. Waletzke, S. Grimme, *J. Chem. Phys.* **2009**, 130, 044708; c) I. Lyskov, M. Kleinschmidt, C. M. Marian, *J. Chem. Phys.* **2016**, 144, 034104.
- [15] F. Plasser, *J. Chem. Phys.* **2020**, 152, 084108.
- [16] Y. Yoneda, H. Sotome, R. Mathew, Y. A. Lakshmana, H. Miyasaka, *J. Phys. Chem. A* **2019**, 124, 265–271.
- [17] W. W. Parson, *Modern Optical Spectroscopy*, Vol. 2, Springer, **2007**.
- [18] a) A. Pigliucci, G. Duval, L. M. L. Daku, E. Vauthey, *J. Phys. Chem. A* **2007**, 111, 6135–6145; b) B. Bagchi, B. Jana, *Chem. Soc. Rev.* **2010**, 39, 1936–1954; c) L. Reynolds, J. A. Gardecki, S. J. V. Frankland, M. L. Horng, M. Maroncelli, *J. Phys. Chem.* **1996**, 100, 10337–10354.
- [19] A. W. Franz, T. J. J. Müller, *Synthesis* **2008**, 2008, 1121–1125.
- [20] S. Fröbel, L. Buschhaus, T. Villnow, O. Weingart, P. Gilch, *Phys. Chem. Chem. Phys.* **2015**, 17, 376–386.
- [21] J. Mooney, P. Kambhampati, *J. Phys. Chem. Lett.* **2013**, 4, 3316–3318.
- [22] S. J. Strickler, R. A. Berg, *J. Chem. Phys.* **1962**, 37, 814–822.
- [23] a) A. Deshpande, A. Beidoun, A. Penzkofer, G. Wagenblast, *Chem. Phys.* **1990**, 142, 123–131; b) J. Furthner, A. Penzkofer, *Opt. Quantum Electron.* **1992**, 24, 591–601.
- [24] a) H. Satzger, W. Zinth, *Chem. Phys.* **2003**, 295, 287–295; b) I. H. van Stokkum, D. S. Larsen, R. Van Grondelle, *Biochim. Biophys. Acta Bioenerg.* **2004**, 1657, 82–104.
- [25] a) A. Schäfer, H. Horn, R. Ahlrichs, *J. Chem. Phys.* **1992**, 97, 2571–2577; b) F. Weigend, *Phys. Chem. Chem. Phys.* **2006**, 8, 1057–1065.
- [26] a) E. Cancès, B. Mennucci, J. Tomasi, *J. Chem. Phys.* **1997**, 107, 3032–3041; b) R. Cammi, S. Corni, B. Mennucci, J. Tomasi, *J. Chem. Phys.* **2005**, 122, 104513; c) G. Scalmani, M. J. Frisch, B. Mennucci, J. Tomasi, R. Cammi, V. Barone, *J. Chem. Phys.* **2006**, 124, 094107.
- [27] a) E. Runge, E. K. Gross, *Phys. Rev. Lett.* **1984**, 52, 997; b) M. A. L. Marques, E. K. U. Gross in *A Primer in Density Functional Theory* (Eds.: C. Fiolhais, F. Nogueira, M. A. L. Marques), Springer, **2003**, pp. 144–184; c) A. Dreuw, M. Head-Gordon, *J. Am. Chem. Soc.* **2004**, 126, 4007–4016; d) F. Furche, R. Ahlrichs, *J. Chem. Phys.* **2002**, 117, 7433–7447.
- [28] S. Hirata, M. Head-Gordon, *Chem. Phys. Lett.* **1999**, 314, 291–299.
- [29] a) A. D. Becke, *J. Chem. Phys.* **1993**, 98, 1372–1377; b) C. Lee, W. Yang, R. Parr, *Phys. Rev. B* **1988**, 37, 785–789.

Manuscript received: September 8, 2022

Accepted manuscript online: October 10, 2022

Version of record online: November 17, 2022

Chemistry–A European Journal

Supporting Information

A Thermally Activated Delayed Fluorescence Emitter Investigated by Time-Resolved Near-Infrared Spectroscopy

Wiebke Haselbach, Jeremy M. Kaminski, Laura N. Kloeters, Thomas J. J. Müller, Oliver Weingart, Christel M. Marian, Peter Gilch,* and Barbara E. Nogueira de Faria

1. Quantum chemical computations

The accuracy of the calculated TDDFT excitation energies, especially when they involved charge transfer excitations, depends on the range-separation parameter ω whose optimal value depends on the studied system. The optimization of ω for the ω B97X-D functional was carried out by applying Koopmans theorem.^[1] The optimal value ω was determined by minimizing the target function (Equation S1):

$$J^2 = \sum_{i=0}^1 [\varepsilon_{HOMO}^{\omega}(N+i) + IP(N+i)]^2, \quad \text{Equation S1}$$

where $IP(N) = E(N-1) - E(N)$, and $IP(N+1) = E(N) - E(N+1)$; here N is the number of electrons of the target molecule, $\varepsilon_{HOMO}^{\omega}$ is the HOMO energy and $IP(N)$ the vertical ionization potential.^[2] In Figure S1 is shown the parameter optimization for TAA-DCN in toluene where we focus on the range between 0.00 and 0.20 Bohr⁻¹. The optimal ω value is 0.15 Bohr⁻¹.

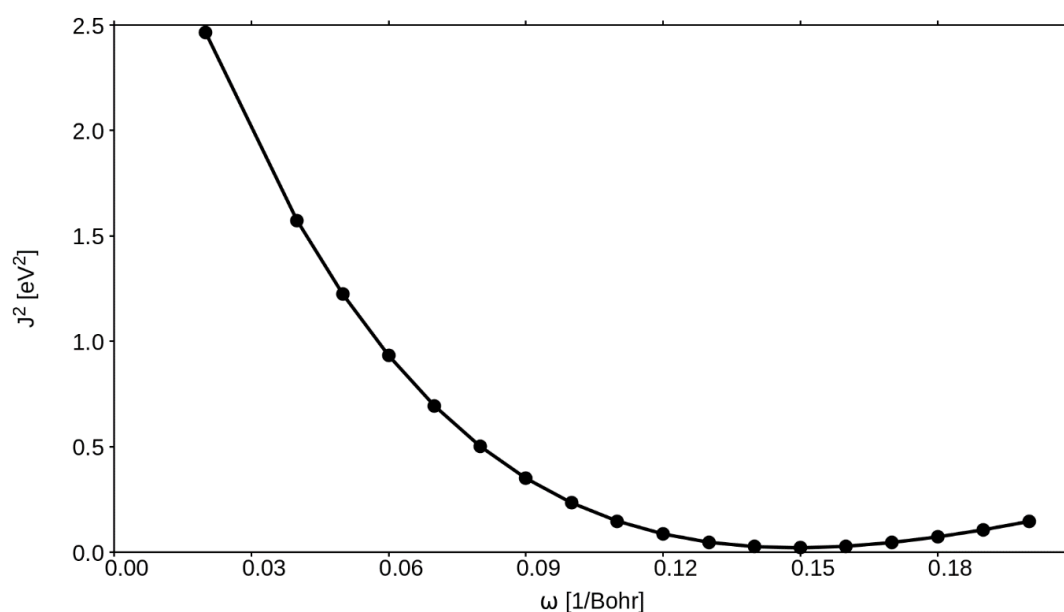


Figure S1. J^2 - ω plot of TAA-DCN in toluene for ω B97X-D functional and def2-TZVP basis set.

Comparison between rotamer 1 and rotamer 2

The Figures S2, S3, and S4 show the energy potential surfaces for TAA-DCN in toluene at OT- ω B97X-D/def2-SV(P) level of theory at the electronic state minima S_0 , S_1 , and T_1 respectively. Here, the choice of a smaller basis set (def2-SV(P)) is related to the higher computational cost of the def2-TZVP basis set. With the given minimum structures of the desired electronic (excited) state an interpolated path is calculated, resulting in several structures between the two minima. This is done by performing a relaxed scan along the dihedral angle connecting the donor and acceptor moiety. At every step, the dihedral angle is fixed while all other geometrical degrees of freedom are relaxed.

The lowest energy was chosen as origin, and all relative energies in meV are plotted against the dihedral angle between donor and acceptor moiety. Two rotamers can be identified in the graphs, where rotamer 1 presents the lowest energy at S_0 and S_1 geometry.

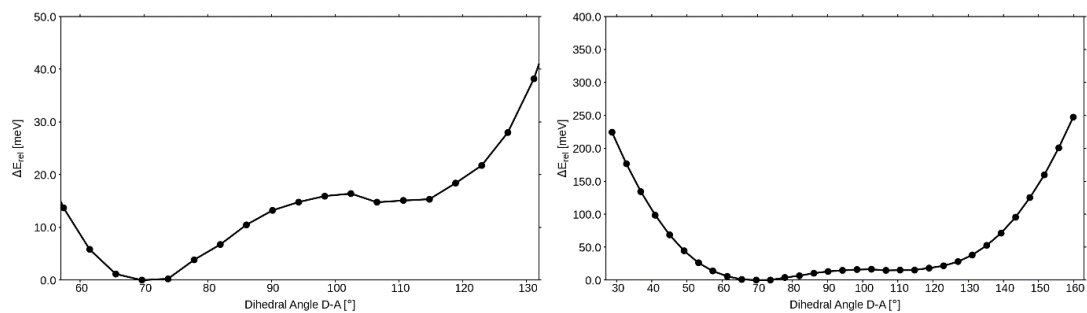


Figure S2. DFT energy profile at OT- ω B97X-D/def2-SV(P) level of theory along a linear interpolated pathway at the target electronic state minima S_0 between rotamer 1 ($\alpha = 70.2^\circ$) and rotamer 2 ($\alpha = 112.3^\circ$) for TAA-DCN with implicit toluene solvation via PCM. The same graph was plotted in a large scale for comparison with the different excited states and is shown on the right.

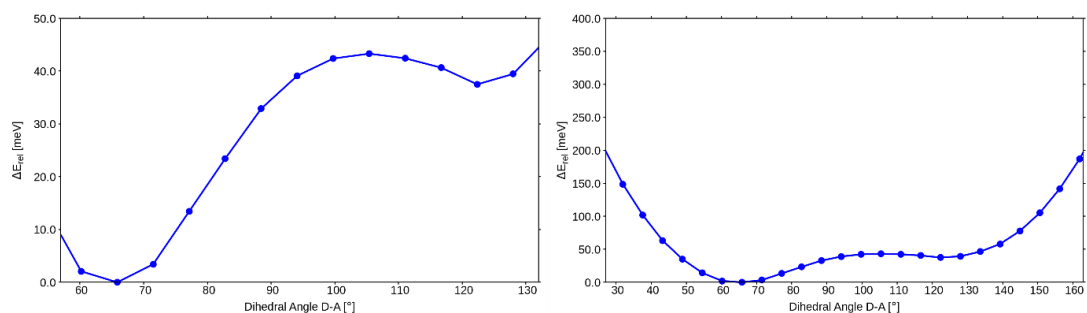


Figure S3. TDDFT energy profile at OT- ω B97X-D/def2-SV(P) level of theory along a linear interpolated pathway at the target electronic state minima S_1 between rotamer 1 ($\alpha = 65.9^\circ$) and rotamer 2 ($\alpha = 123.9^\circ$) for TAA-DCN with implicit toluene solvation via PCM. The same graph was plotted in a large scale for comparison with the different excited states and is shown on the right.

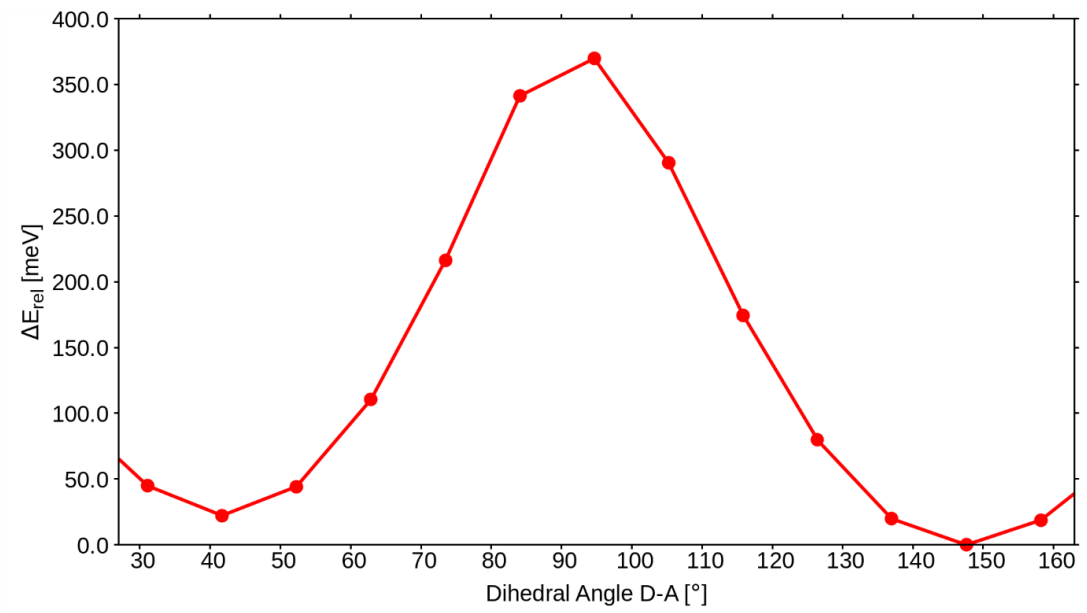


Figure S4. TDDFT energy profile at OT- ω B97X-D/def2-SV(P) level of theory along a linear interpolated pathway at the target electronic state minima T_1 between rotamer 1 ($\alpha = 41.4^\circ$) and rotamer 2 ($\alpha = 148.7^\circ$) for TAA-DCN with implicit toluene solvation via PCM.

The rotamer 1 was chosen in the paper for a comparison between the measured and computed $S_0 \rightarrow S_n$, $S_1 \rightarrow S_n$, and $T_1 \rightarrow T_n$ spectra. In Tables S1, S2 and S3, we include the vertical excitation energies, difference densities, and the respective oscillator strengths for both rotamers at the S_0 , S_1 , and T_1 optimized geometry. Difference densities (± 0.001)

of the excited states were obtained at the DFT/MRCI level of theory. A loss of electron density upon electronic excitation is shown in red, a gain in yellow.

Table S1. Vertical DFT/MRCI excitation energies, difference densities, and oscillator strengths for S_0 equilibrium geometry of TAA-DCN in toluene for rotamer 1 and rotamer 2. Energies are given in eV.

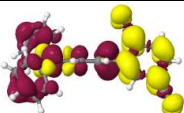

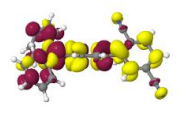
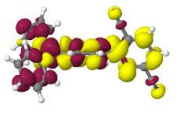
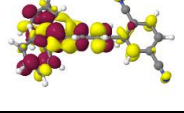
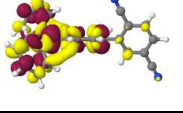
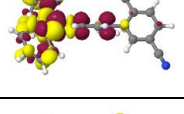
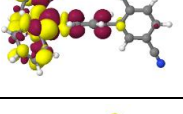
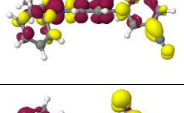
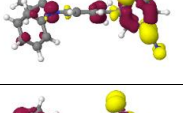
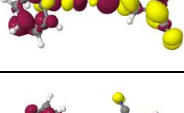
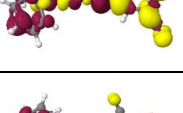
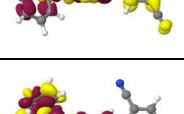
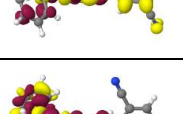
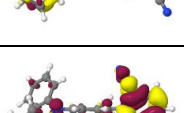
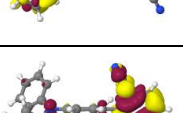
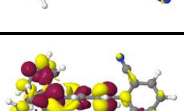
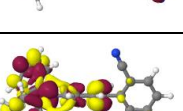


	Rotamer 1 ($\alpha = 70.2^\circ$)			Rotamer 2 ($\alpha = 112.3^\circ$)		
	S ₀ optimized geometry for TAA-DCN in toluene					
Electronic transition	Vertical Excitation	Oscillator Strength	Difference densities (+/-0.001)	Difference densities (+/-0.001)	Oscillator Strength	Vertical Excitation
S ₀ →S ₁	3.06	0.069			0.063	3.08
S ₀ →S ₂	3.83	0.205			0.343	3.80
S ₀ →S ₃	3.97	0.222			0.066	3.94
S ₀ →S ₄	4.26	0.251			0.257	4.26
S ₀ →S ₅	4.32	0.142			0.099	4.31
S ₀ →T ₁	2.90	-			-	2.93
S ₀ →T ₂	3.32	-			-	3.24
S ₀ →T ₃	3.46	-			-	3.46
S ₀ →T ₄	3.52	-			-	3.54
S ₀ →T ₅	3.60	-			-	3.62

Table S2. Vertical excitation energies, difference densities, and oscillator strengths for S₁ equilibrium geometry of TAA-DCN in toluene for rotamer 1 and rotamer 2. Energies are given in eV.

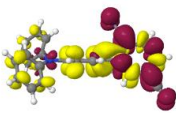
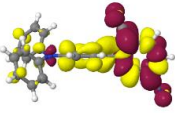
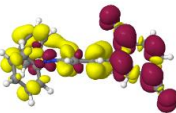
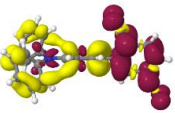
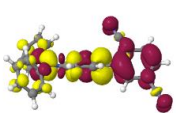
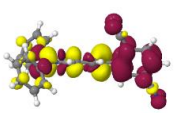
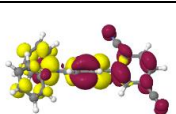
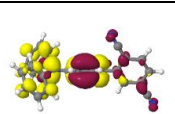
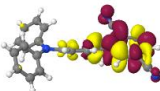
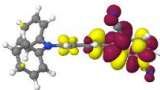
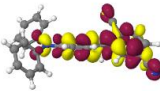
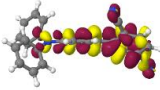
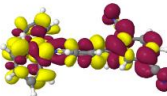
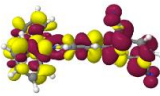
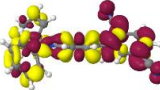
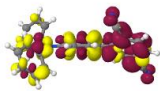
Electronic transition	Rotamer 1 ($\alpha = 65.9^\circ$)			Rotamer 2 ($\alpha = 123.9^\circ$)		
	S ₁ optimized geometry for TAA-DCN in toluene					
	Vertical Excitation	Oscillator Strength	Difference densities (+/-0.001)	Difference densities (+/-0.001)	Oscillator Strength	Vertical Excitation
S ₁ →S ₂	1.22	0.009			0.023	1.14
S ₁ →S ₃	1.38	0.034			0.000	1.32
S ₁ →S ₄	1.54	0.220			0.328	1.48
S ₁ →S ₅	1.64	0.029			0.001	1.63

Table S3. Vertical excitation energies, difference densities, and oscillator strengths for T₁ equilibrium geometry of TAA-DCN in toluene for rotamer 1 and rotamer 2. Energies are given in eV.

	Rotamer 1 ($\alpha = 41.4^\circ$)			Rotamer 2 ($\alpha = 148.7^\circ$)		
	T ₁ optimized geometry for TAA-DCN in toluene					
	Electronic transition	Vertical Excitation	Oscillator Strength	Difference densities (+/-0.001)	Difference densities (+/-0.001)	Oscillator Strength
T ₁ →T ₂	0.89	0.024			0.007	0.92
T ₁ →T ₃	1.17	0.295			0.347	1.19
T ₁ →T ₄	1.39	0.001			0.002	1.40
T ₁ →T ₅	1.53	0.007			0.009	1.55

2. Self-quenching of TAA-DCN in toluene triples.

The dependence of TAA-DCN triplet lifetime τ_T in toluene was traced by nanosecond transient absorption at 1200 nm and 780 nm. Probing at 780 nm was employed at the lowest concentration of $c = 1.3 \times 10^{-4}$ M since here the signal is higher. A plot of the inverse triplet lifetime τ_T^{-1} versus the concentration c , reveals a linear dependence. A fit according to (Equation S2):

$$\frac{1}{\tau_T} = k_0^T + k_{sq} \cdot [TAA - DCN]$$

Equation S2

affords an intrinsic lifetime $\tau_0^T = \frac{1}{k_0^T}$ of 30.1 μ s and a self-quenching constant k_{sq} of 9.7×10^7 M⁻¹s⁻¹.

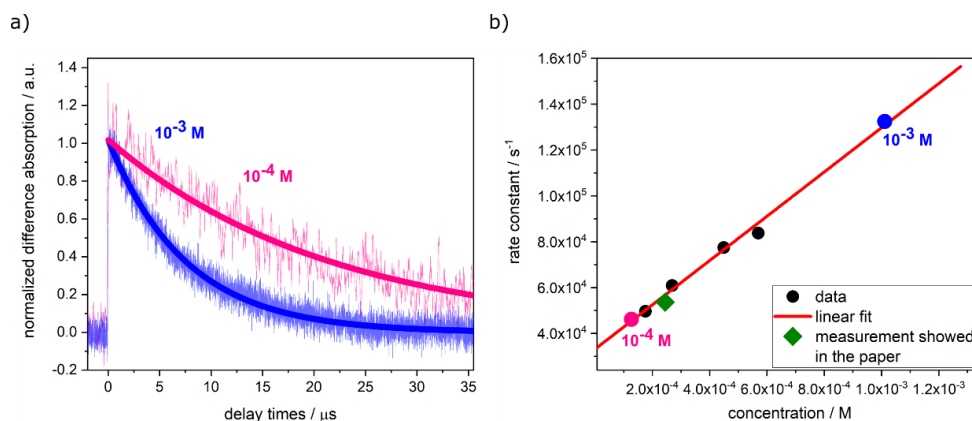
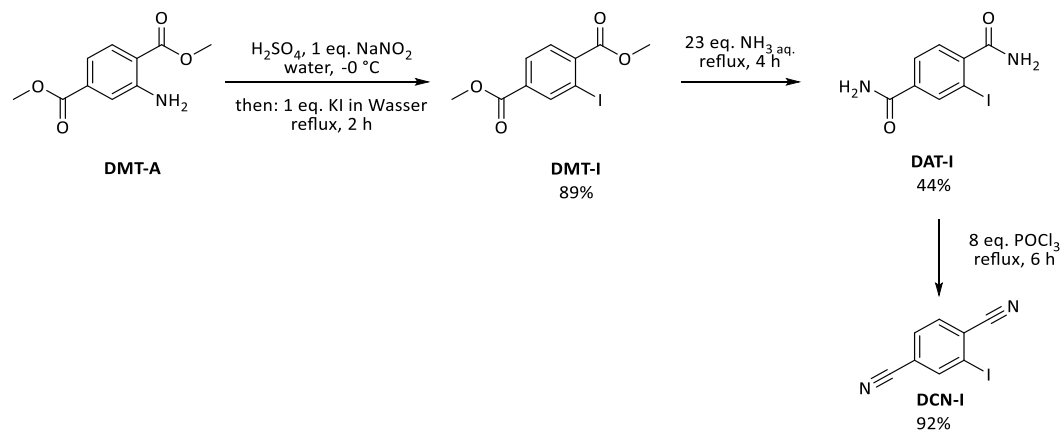


Figure S5. Dependence of the triplet lifetime on the TAA-DCN concentration: a) nanosecond transient absorption time trace at 1200 nm (blue line) and 780 nm (smooth data, pink line) for concentrations of 10^{-3} and 10^{-4} M, respectively, with the single exponential fits (thick lines). b) The inverse of the triplet lifetimes as a function of [TAA-DCN] (dots points), and a linear fit (red line) according to eq. S2. The inverse of the time decay retrieved from the global fit analysis of the nanosecond transient absorption map for the microsecond range is shown for comparison (rate constant showed as green diamond). The sample solutions (nitrogen-purged toluene) were excited at 355 nm.

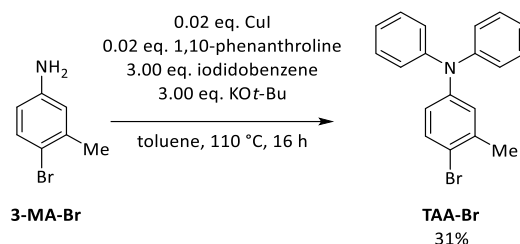
3. Synthesis and Characterization

All starting materials were synthesized via previously reported protocols.^[3] The acceptor 2-iodoterephthalonitrile (**DCN-I**) was synthesized starting from dimethyl-2-aminoterephthalate (**DMT-A**) in a Sandmeyer-like reaction with sodium nitrite for the formation of nitrosylium ion and potassium iodide for subsequent iodine exchange into 2-iodoterephthalate (**DMT-I**). Afterwards the ester moieties of **DMT-I** were treated with aqueous ammonia solution in a Schlenk vessel under reflux to form the corresponding amid moieties of 2-iodoterephthalamide (**DAT-I**). Dried and clean **DAT-I** was then further transformed into 2-iodoterephthalonitrile (**DCN-I**) by boiling in phosphoryl chloride.



Scheme S1. Synthesis route towards the acceptor DCN-I.

Donor compound 4-bromo-3-methyl-*N,N*-diphenylaniline (**TAA-Br**) was synthesized by Ullmann-coupling with iodobenzene and 4-bromo-3-methylaniline (**3MA-Br**) using copper(I)iodide and 1,10-phenanthroline as the reactive catalyst/ligand system under basic promotion of potassium *tert*-butoxide.



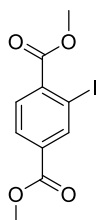
Scheme S2. Ullmann coupling towards donor TAA-Br starting from 3-MA-Br.

4. Analytical methods and instruments

All reactions were carried out in Schlenk or multi-neck flasks under nitrogen atmosphere and using the septum and syringe technique, unless otherwise indicated. Dried THF was taken from the MB-SPS 800 solvent drying system (M. Braun). The reaction temperature was adjusted for reactions not conducted at ambient temperature using silicone oil baths preheated to the indicated temperatures or cooling baths (ice/water for 0 °C or dry ice/isopropanol for -78 °C). Column chromatography was carried out on silica gel M60 (mesh 230 - 400, Macherey-Nagel, Düren, Germany). The column chromatographic separations were performed using the flash technique (overpressure of about 2 bars of compressed air). Silica coated aluminum foils (60 F254 Merck) were used for thin layer chromatography. Evaluation was performed under UV light (λ_{exc} = 254 and 356 nm) and staining with iodine. ^1H -, ^{13}C -, and DEPT-135-NMR spectra were recorded at 293 K on Bruker Avance III 600 (600 MHz), Bruker Avance DRX 500 (500 MHz), and Bruker Avance III 300 (300 MHz) instruments, respectively, unless otherwise noted. DMSO- d_6 served as solvent. As an internal standard, the residual proton signal of the corresponding solvents was used when recording the ^1H NMR spectra and ^{13}C NMR spectra (DMSO- d_6 , H 2.50, C 39.52). Spin multiplicities are abbreviated as follows: s: singlet; d: doublet; dd: doublet of doublet; ddd: doublet of doublet of doublet; dt: doublet of a triplet; t: triplet; q: Quintet; sp: septet; and m: multiplet. The quaternary carbon nuclei (C_{quat}) and the carbon nuclei of methine (CH), methylene (CH_2), and methyl (CH_3) groups were assigned based on DEPT-

135 spectra. Melting points (uncorrected) were measured on the Büchi B545 instrument. EI mass spectra were measured on the TSQ 7000 triple quadrupole mass spectrometer (Finnigan MAT). Indicated are all peaks with an intensity > 10% of the base peak, the mole peak, and any characteristic fragment peaks with an intensity < 10%. IR spectra were measured on the IRAffinity-1 instrument (Shimadzu) (single reflection ATR unit with diamond ATR crystal, wavenumber range: 4000 - 600 cm⁻¹). The intensities of the absorption bands are given as s (strong), m (medium), and w (weak). The elemental analyses were measured on the Perkin Elmer Series II Analyzer 2400 at the Institute of Pharmaceutical Chemistry, Heinrich Heine University.

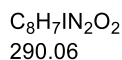
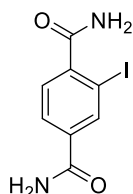
Dimethyl-2-iodoterephthalate (DMT-I)



In a 2L three-necked flask with KPG-stirrer and reflux condenser 21 g (1 equiv, 100 mmol) of dimethyl-2-aminoterephthalate were suspended in 320 mL of cold water before 62 mL concentrated sulfuric acid were added. The mixture was cooled down in an ice bath to 0 °C for 15 min. Afterwards, 6.9 g of sodium nitrite (1 equiv, 100 mmol) dissolved in 40 mL of ice water were added via a dripping funnel over 1 h. The resulting suspension was stirred additionally for 1 h at 0 °C before 16.6 g potassium iodide (1 equiv, 100 mmol) dissolved in 60 mL of water were added via a dropping funnel over 20 min at 0 °C. The solution was stirred at 0 °C until no gas bubbling was observed. Afterwards, the dark red suspension was heated in an oil bath for 2 h at 60 °C. The dark brown reaction mixture was then filtered and the obtained dark brownish solid recrystallized in 300 mL of methanol. Furthermore, the crystallized product was purified on silica via column chromatography with *n*-hexane/ethyl acetate (10:1) as solvent. The purified yellowish solid was dried under vacuum until the weight was constant.

yield: 89% (28.49 g, 89.00 mmol), yellow solid. **Mp.:** 78 °C. **R_f:** 0.19 (*n*-hexane/ethyl acetate = 10:1). **¹H NMR:** (300 MHz, DMSO-*d*₆) δ = 8.44 (d, ³*J* = 1.6 Hz, 1H), 8.03 (dd, ³*J* = 8.2 Hz, ⁴*J* = 1.6 Hz, 1H), 7.81 (d, ³*J* = 7.9 Hz, 1H), 3.89 (s, 3H), 3.88 (s, 3H). **¹³C NMR:** (75 MHz, DMSO-*d*₆) δ = 166.5 (C_{quat}), 166.2 (C_{quat}), 140.5 (CH), 132.9 (C_{quat}), 130.2 (CH), 128.7 (CH), 94.1 (C_{quat}), 52.8 (CH₃). **MS(EI)** *m/z* (%): 320 ([M]⁺, 65), 289 ([M - OMe]⁺, 100), 261 ([M - CO₂Me]⁺, 14), 246 ([M - CO₂Me - Me]⁺, 12), 229 ([M - (CO₂Me)₂]⁺, 6), 119 (14), 104 (13), 103 (24), 76 (18), 75 (22), 74 (29), 63 (11).

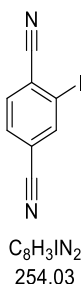
2-Iodoterephthalamide (DMA-I)



7.04 g (1 equiv, 22 mmol) of dimethyl-2-iodoterephthalate were suspended in a Schlenk vessel under nitrogen atmosphere in 35 mL of aqueous ammonia solution (25%) and then refluxed in an oil bath for 4 h at 100 °C. After the reaction the remaining white solid was filtered and washed with 100 mL of ice-cold water. The obtained product was dried under vacuum until the weight was constant.

yield: 55% (9.69 mmol, 2.81 g), transparent solid. **Mp.:** 295.2 °C. **¹H NMR:** (300 MHz, DMSO-*d*₆) δ = 8.32 (d, ⁴*J* = 1.6 Hz, 1H), 8.10 (s, 1H), 7.91 – 7.85 (m, 2H), 7.60 (s, 1H), 7.51 (s, 1H), 7.39 (d, ³*J* = 7.9 Hz, 1H). **¹³C NMR:** (75 MHz, DMSO-*d*₆) δ = 170.1 (C_{quat}), 165.8 (C_{quat}), 145.4 (C_{quat}), 137.9 (CH), 135.8 (C_{quat}), 127.4 (CH), 127.0 (CH), 92.7 (C_{quat}). **MS(EI)** *m/z* (%): 320 (70), 289 ([M]⁺, 100), 261 ([M - CO]⁺, 15), 246 ([M - CONH₂]⁺, 12), 149 (13), 119 ([M - I - CONH₂]⁺, 10), 105 (12), 104 (10), 103 (17), 77 (11), 75 (29), 74 (21), 73 (13), 69 (10), 60 (16), 57 (20), 55 (16).

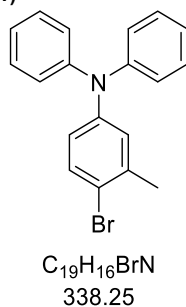
2-Iodoterephthalnitrile (DCN-I)



Under nitrogen atmosphere 3.2 g (1.0 equiv, 11 mmol) of 2-iodoterephthalamide were suspended in 8 mL (7.7 equivs, 84 mmol) of phosphoryl chloride and then heated in an oil bath for 6 h at 130 °C. Afterwards, the reaction mixture was cooled to room temperature and the remaining phosphoryl chloride was carefully quenched in an ice bath with ice water. The reaction solution was filtered, and the product was first washed with ice water and then dried under vacuum until the weight was constant.

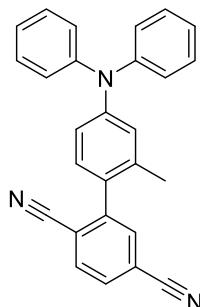
yield: 92% (9.2 mmol, 2.6 g), sand colored solid. **Mp.:** 219 °C. **R_f:** 0.13 (*n*-hexane/ethyl acetate = 4:1). **¹H NMR:** (300 MHz, DMSO-*d*₆) δ = 8.60 (dd, 4J = 1.4 Hz, 5J = 0.6 Hz, 1H), 8.02 – 8.11 (m, 2H). **¹³C NMR:** (75 MHz, DMSO-*d*₆) δ = 142.1 (CH), 135.0 (CH), 132.2 (CH), 123.5 (C_{quat}), 118.6 (C_{quat}), 116.5 (C_{quat}), 116.3 (C_{quat}), 101.0 (C_{quat}). **EA:** calcd. for C₈H₃IN₂ (254.0): C 37.82, H 1.19, N 11.03; Found: C 37.81, H 1.13, N 11.03. **MS(EI) *m/z* (%)**: 254 ([M]⁺, 100), 127 ([M – I]⁺, 80), 100 ([M – I – CN]⁺, 34), 75 ([M – I – (CN)₂]⁺, 12). **IR:** $\tilde{\nu}$ [cm⁻¹] = 1508 (w), 1452 (s), 1437 (w), 1379 (w), 1300 (w), 1281 (w), 1244 (s), 1196 (w), 1163 (w), 1155 (w), 1140 (w), 1123 (w), 1032 (w), 963 (w), 905 (w), 866 (w), 851 (m), 831 (m), 801 (m), 721 (w), 623 (s).

4-Bromo-3-methyl-*N,N*-diphenylaniline (TAA-Br)



In a Schlenk vessel 1.9 g (1.0 equiv, 10 mmol) of 4-bromo-3-methylaniline, 0.38 g (0.20 equivs, 2.0 mmol) of copper(I)-iodide, 0.36 g (0.20 equivs., 2.0 mmol) of phenanthroline, and 2.0 g (3.5 equivs, 35 mmol) of potassium hydroxide were added under nitrogen atmosphere and then dissolved in 30 mL of dry THF. Afterwards, 3.4 mL (3.0 equivs, 30 mmol) of iodobenzene were added, and the reaction mixture was heated in an oil bath for 24 h at 130 °C. The reaction mixture was cooled to room temp and washed three times with 60 mL of dichloromethane. The combined organic fractions were washed with 30 mL of brine and dried with anhydrous sodium sulfate. Afterwards, the organic solution was adsorbed on Celite® and further purified on silica via column chromatography with *n*-hexane/ethyl acetate (20:1) as solvent. After purification a red oil was obtained which was then crystallized in ethanol into a red solid. The obtained product was dried under vacuum until the weight was constant.

Yield: 31% (3.12 mmol, 1.05 g), red solid. **Mp.:** 143.6 °C. **R_f:** 0.78 (*n*-hexane/ethyl acetate = 20:1). **¹H NMR:** (300 MHz, DMSO-*d*₆) δ = 7.45 (d, 3J = 8.6 Hz, 1H), 7.30 (dd, 3J = 8.5, 4J = 7.4 Hz, 4H), 6.92–7.11 (m, 7H), 6.72 (dd, 3J = 8.6, 4J = 2.8 Hz, 1H), 2.23 (s, 3H). **¹³C NMR:** (75 MHz, DMSO-*d*₆) δ = 146.9 (C_{quat}), 146.9 (C_{quat}), 138.2 (C_{quat}), 132.9 (CH), 129.6 (CH), 125.5 (CH), 124.0 (CH), 123.3 (CH), 122.7 (CH), 117.0 (C_{quat}), 22.5 (CH₃). **MS(EI) *m/z* (%)**: 340 (18), 339 ([⁸¹Br-M]⁺, 96), 338 (25), 337 ([⁷⁹Br-M]⁺, 100), 258 (C₁₉H₁₆N⁺, 17), 257 (51), 257 (51), 256 (19), 243 (C₁₈H₁₃N⁺, 40), 242 (15), 180 (26), 167 (10), 166 (11), 155 (11), 153 (11), 152 (12), 129 (15), 128 (20), 127 (11), 120 (14), 115 (11), 77 (26), 51 (16).

4'-(Diphenylamino)-2'-methyl-[1,1'-biphenyl]-2,5-dicarbonitrile (TAA-DCN)

$C_{27}H_{19}N_3$
385.47

Under nitrogen atmosphere 0.34 g (1.0 equiv, 1.0 mmol) of 4-bromo-3-methyl-*N,N*-diphenylaniline were dissolved in 5 mL of dry THF in a Schlenk vessel. The solution was cooled down for 10 min to $-78\text{ }^{\circ}\text{C}$ in an isopropanol/dry ice-bath. At $-78\text{ }^{\circ}\text{C}$ 0.77 mL (1.2 equivs, 1.2 mmol) of freshly titrated *n*-BuLi (1.56 M) were added, and the reaction mixture was stirred for 20 min. Afterwards, 0.46 mL (1.4 equivs, 1.4 mmol) of trimethylborate were added at $-78\text{ }^{\circ}\text{C}$ and then stirred at room temperature for 20 min. For the following Suzuki coupling 0.058 g (0.05 equivs, 0.05 mmol) of $\text{Pd}(\text{PPh}_3)_4$, 0.23 g (1.1 equivs, 1.1 mmol) of 2-iodoterephthalnitrile, and 0.43 g (2.4 equivs, 2.4 mmol) of KO t -Bu were added before the reaction mixture was heated in an oil bath for 18 h at $80\text{ }^{\circ}\text{C}$. After the reaction the solution was quenched with 2 mL of ethyl acetate and then adsorbed on Celite®. The solvent was removed via evaporation and the adsorbed reaction mixture was purified on silica column with *n*-hexane/ethyl acetate (10:1) as a solvent. After the purification a yellow solid was obtained and further purified by crystallization in 10 mL of ethanol. The purified yellow solid was dried under vacuum until the weight was constant.

yield: 99% (0.99 mmol, 385 mg), yellow solid. **Mp.:** $164.9\text{ }^{\circ}\text{C}$. **R_r:** 0.14 (*n*-hexane/ethyl acetate = 10:1). **¹H NMR:** (600 MHz, DMSO- d_6) δ = 8.17 (d, 3J = 8.4 Hz, 1H), 8.05 (m, 2H), 7.39 – 7.32 (m, 4H), 7.17 (d, 3J = 8.3 Hz, 1H), 7.13 – 7.07 (m, 6H), 6.93 (d, 3J = 2.1 Hz, 1H), 6.85 (dd, 3J = 8.3 Hz, 4J = 2.3 Hz, 1H), 2.04 (s, 3H). **¹³C NMR:** (150 MHz, DMSO- d_6) δ = 148.1 (C_{quat}), 146.8 (C_{quat}), 145.4 (C_{quat}), 136.7 (C_{quat}), 134.2 (CH), 134.1 (CH), 131.5 (CH), 130.8 (CH), 129.7 (C_{quat}), 129.65 (CH), 124.69 (CH), 123.73 (CH), 123.22 (CH), 119.43 (CH), 117.45 (C_{quat}), 116.98 (C_{quat}), 116.35 (C_{quat}), 115.54 (C_{quat}), 19.67 (CH₃). **MS(EI) *m/z* (%)**: 386 (22), 385 ([M]⁺, 100), 166 (10). **EA:** calcd. for $C_{27}H_{19}N_3$ (385.5): C 84.13, H 4.97, N 10.90; Found: C 84.02, H 4.89, N 10.77. **IR:** $\tilde{\nu}$ [cm^{-1}] = 1607 (w), 1586 (m), 1477 (m), 1456 (m), 1418 (m), 1373 (m), 1337 (m), 1308 (m), 1271 (m), 1252 (s), 1192 (w), 1171 (w), 1126 (w), 1107 (w), 1067 (m), 1005 (m), 928 (w), 866 (w), 822 (m), 802 (m), 777 (m), 758 (s), 748 (m), 729 (m), 700 (s), 640 (m), 623 (s), 611 (m).

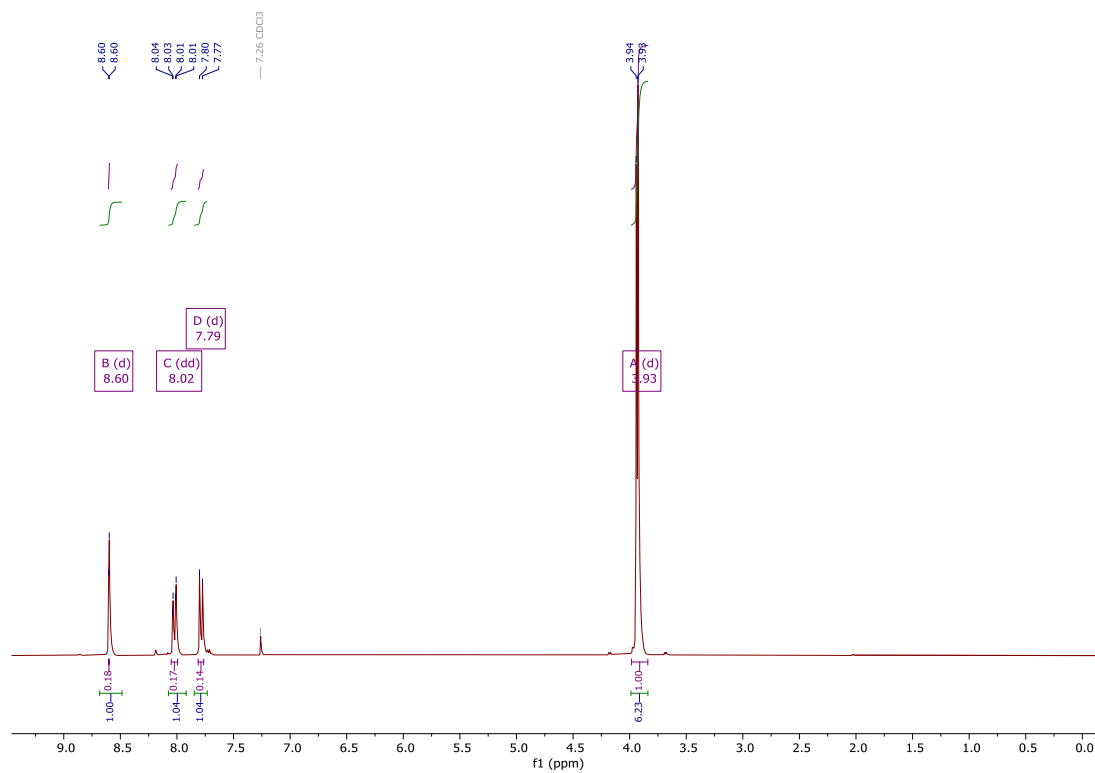


Figure S6. ¹H-NMR spectrum of Dimethyl 2-iodoterephthalate (DMT-I).

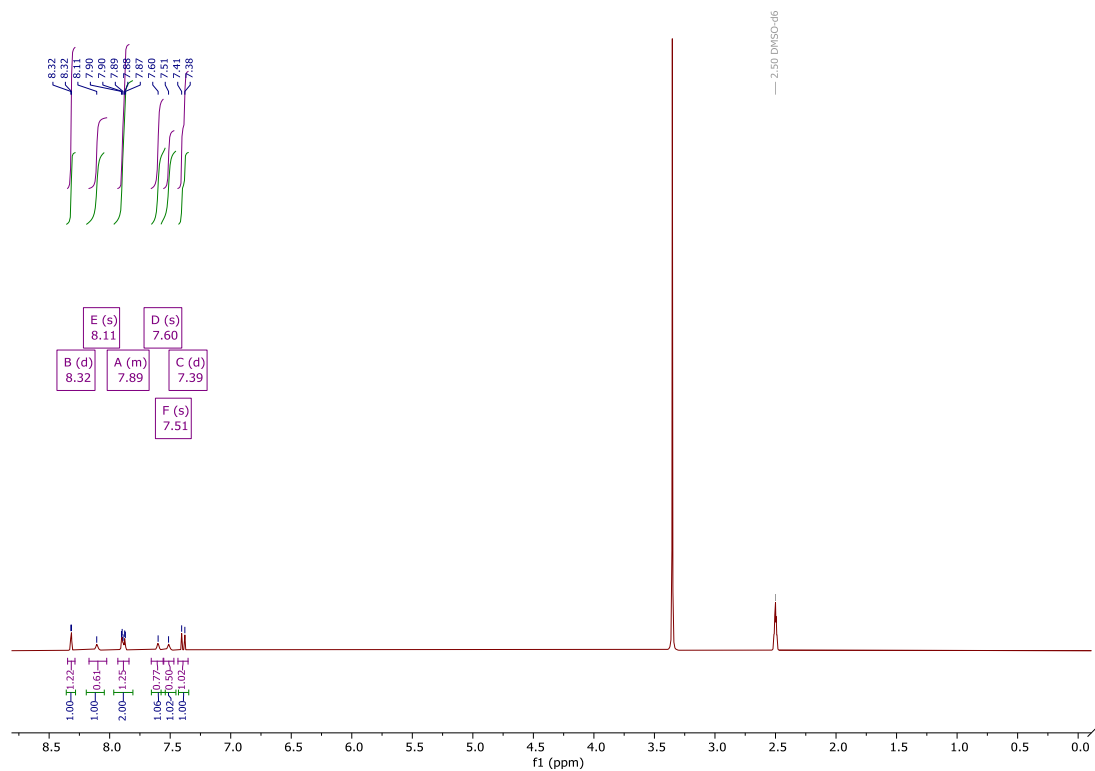
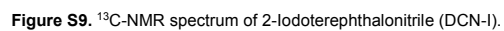
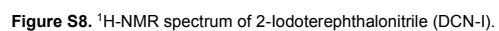


Figure S7. ¹H-NMR spectrum of 2-Iodoterephthalamide (DAT-I).



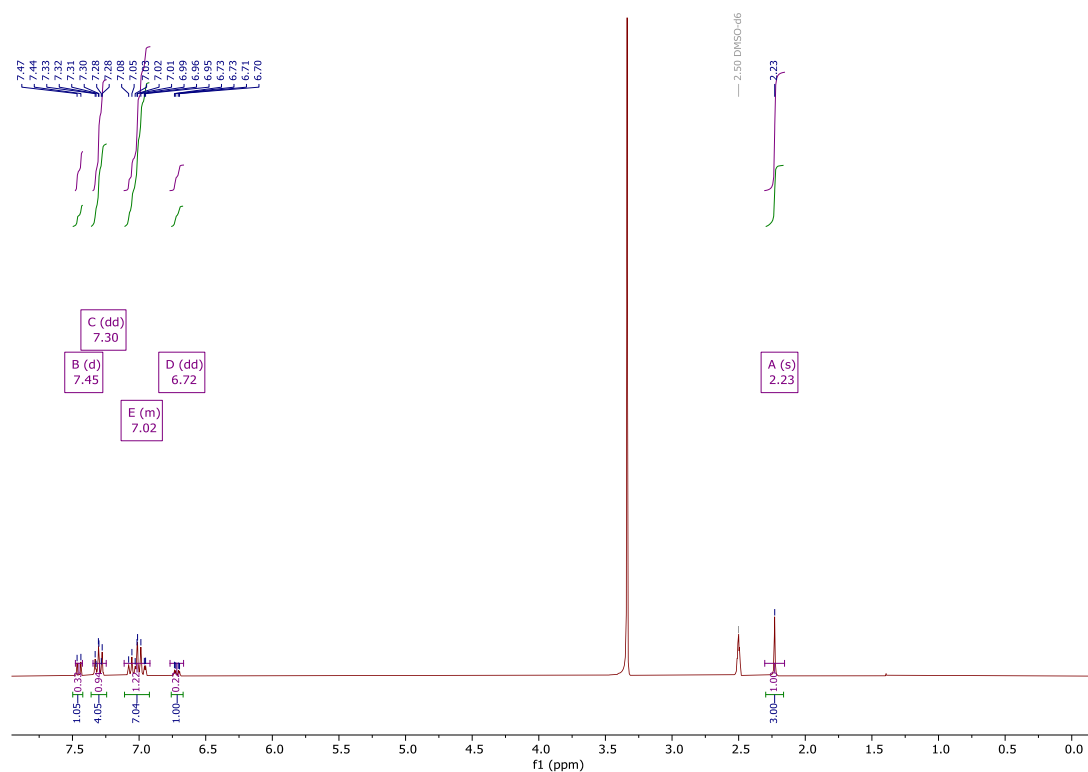


Figure S10. ¹H-NMR spectrum of 4-Bromo-3-methyl-*N,N*-diphenylaniline (TAA-Br).

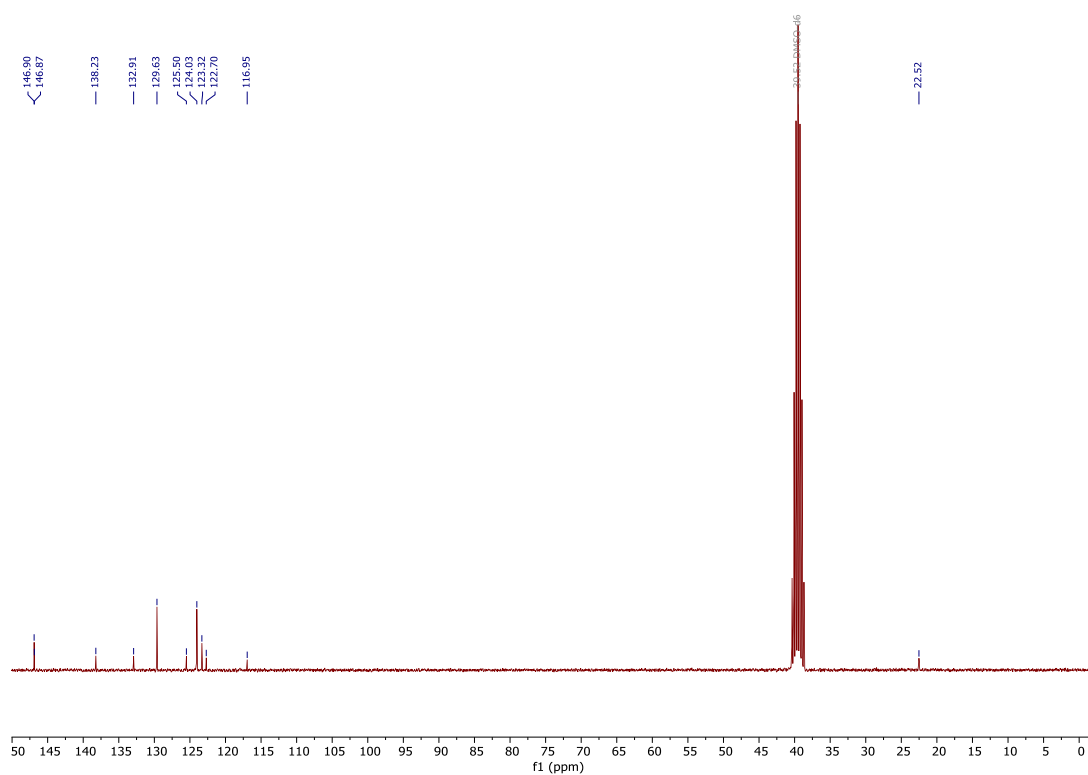


Figure S11. ¹³C-NMR spectrum of 4-Bromo-3-methyl-*N,N*-diphenylaniline (TAA-Br).

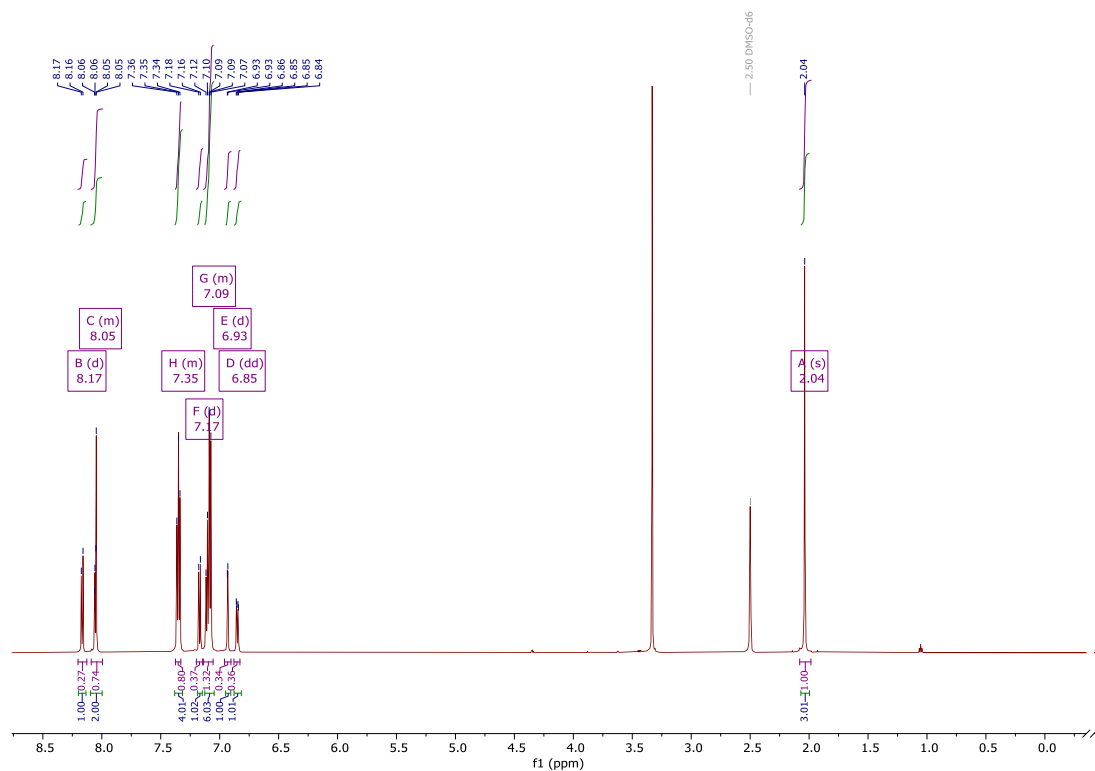


Figure S12. ¹H-NMR spectrum of 4'-(Diphenylamino)-2'-methyl-[1,1'-biphenyl]-2,5-dicarbonitrile (TAA-DCN).

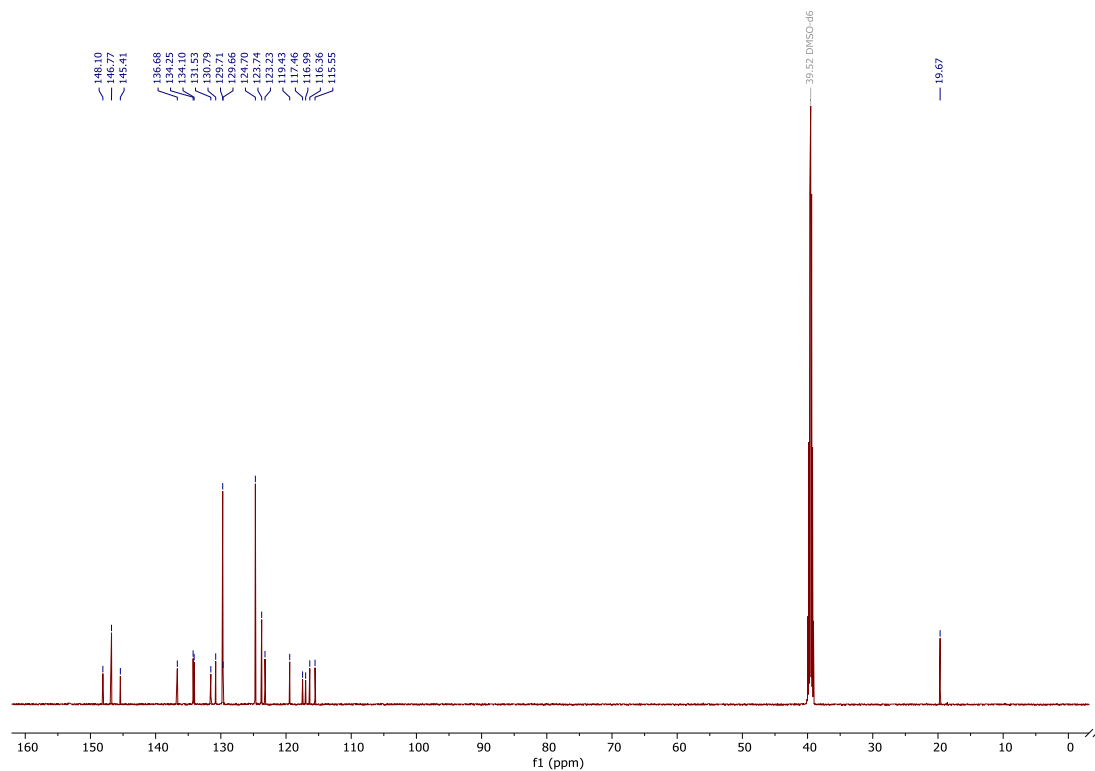


Figure S13. ¹³C-NMR spectrum of 4'-(Diphenylamino)-2'-methyl-[1,1'-biphenyl]-2,5-dicarbonitrile (TAA-DCN).

References

- [1] D. Jacquemin, B. Moore, A. Planchat, C. Adamo, J. Autschbach, *J. Chem. Theory Comput.* **2014**, *10*, 1677-1685.
- [2] a) R. Baer, E. Livshits, U. Salzner, *Annu. Rev. Phys. Chem.* **2010**, *61*, 85-109; b) L. Kronik, T. Stein, S. Refaely-Abramson, R. Baer, *J. Chem. Theory Comput.* **2012**, *8*, 1515-1531.
- [3] G. A. Sommer, L. N. Mataranga-Popa, R. Czerwieniec, T. Hofbeck, H. H. Homeier, T. J. J. Müller, H. Yersin, *J. Phys. Chem. Lett.* **2018**, *9*, 3692-3697.

Publication III

Highly Luminescent Blue Emitter with Balanced Hybridized Locally and Charge-Transfer Excited-States Emission

J. Wiefermann, **J. M. Kaminski**, E. Pankert, D. Hertel, K. Meerholz, C. M. Marian & T. J. J. Müller

ChemPhotoChem, 7(3):e202200265, 2023

DOI: 10.1002/cptc.202200265

Contribution: All quantum chemical investigations presented in this work, writing and visualization of results in section about quantum chemical calculations, revising the manuscript.



Highly Luminescent Blue Emitter with Balanced Hybridized Locally and Charge-Transfer Excited-States Emission



Julia Wiefermann^{+, [a]}, Jeremy M. Kaminski^{+, [b]}, Elisabeth Pankert,^[c] Dirk Hertel,^[c] Klaus Meerholz,^[c] Christel M. Marian,^[b] and Thomas J. J. Müller^{*, [a]}

Dedicated to Prof. Dr. A. Stephen K. Hashmi on the occasion of his 60th birthday

In this work, we perform an in-depth investigation of the optoelectronic properties of a blue emitter (4''-(diphenylamino)-2''-methyl-[1,1':4',1''-terphenyl]-4-carbonitrile), which was reported earlier. Lippert–Mataga analysis of the emission spectra obtained in solvents of varying polarity reveal charge transfer (CT) contributions to the first singlet excited state, S_1 . Multi-reference quantum chemical calculations clearly show a bal-

anced local excitation (LE) and CT character of the S_1 state and suggests the presence of a LE triplet state, T_2 , in its energetic vicinity. Finally, organic light emitting diodes (OLED) revealed blue emission at 451 nm and an external quantum efficiency (EQE) of 2%, corresponding to an internal quantum efficiency (IQE) of circa 10%.

Introduction

In recent years organic electronics paved its way into daily life and has steadily become a focus of research. Organic functional chromophores have attracted wide attention due to flexible processability, low power consumption, and the absence of toxic and expensive heavy metals as an advantageous aspect of sustainability and applicability.^[1] In the first and third generation of organic light emitting diodes (OLEDs) purely organic materials already found entry as emissive materials.^[2] Prerequisite for the application as emissive materials are high luminescence quantum yields in the solid state, good thermal and oxidative stability, and a high color purity.^[3] For full-color displays new materials are indispensable and especially efficient deep-blue emitters are highly demanded.^[4] Spin-

statistics dictate the formation of 25% singlet excitons and 75% triplet excitons upon hole-electron recombination.^[5] According to the underlying mechanism, emissive materials are divided into classical fluorescence,^[6] phosphorescence,^[7] thermally activated delayed fluorescence (TADF),^[8] and hybridized locally excited (LE) and charge transfer (CT) excited state (HLCT) emitters.^[9] In classical fluorescent materials, the triplet excitons remain wasted due to non-radiative deactivation pathways.^[10] And classical fluorescence emitters limit the internal quantum efficiency (IQE) of the OLED to 25%.^[2] For harvesting the remaining 75% triplet excitons phosphorescent heavy-metal complexes have been employed as emitters for the second generation of OLEDs.^[7b] Another approach for harvesting the triplet excitons is the use of TADF emitters. They characteristically possess a small energy gap (ΔE_{ST}) between the lowest lying singlet (S_1) and triplet (T_1) excited states. It enables thermally activated reverse intersystem crossing (rISC) upconversion of triplet excitons to generate singlet excitons, which radiatively relax rapidly as delayed fluorescence to the ground state. Theoretically, the IQE can be optimized up to 100%.^[11] For HLCT materials, a hybridized local and charge transfer excited state occurs, which leads to a high photoluminescence quantum yield (PLQY) Φ_{PL} and high exciton utilization efficiency by rISC from a higher-lying triplet state.^[12]

Here, we present an in-depth investigation of the optoelectronic properties of a highly luminescent blue organic emitter (4''-(diphenylamino)-2''-methyl-[1,1':4',1''-terphenyl]-4-carbonitrile) with balanced LE and CT contributions. The origin of emission is examined by advanced quantum chemical calculations and photophysical experiments. In addition, the suitability for application in OLED devices is investigated.

[a] J. Wiefermann,⁺ Prof. Dr. T. J. J. Müller
Institute of Organic Chemistry and Macromolecular Chemistry
Heinrich Heine University Düsseldorf
Universitätsstraße 1, 40225 Düsseldorf (Germany)
E-mail: ThomasJJ.Mueller@hhu.de

[b] J. M. Kaminski,⁺ Prof. Dr. C. M. Marian
Institute of Theoretical and Computational Chemistry
Heinrich Heine University Düsseldorf
Universitätsstraße 1
40225 Düsseldorf (Germany)

[c] E. Pankert, Dr. D. Hertel, Prof. Dr. K. Meerholz
Department of Chemistry
University of Cologne
Greinstraße 4–6
50939 Köln (Germany)

[†] These authors contributed equally to this work.



Supporting information for this article is available on the WWW under <https://doi.org/10.1002/cptc.202200265>



An invited contribution to a Special Collection on Emissive Materials for Organic Light Emitting Diodes



© 2022 The Authors. ChemPhotoChem published by Wiley-VCH GmbH. This is an open access article under the terms of the Creative Commons Attribution Non-Commercial License, which permits use, distribution and reproduction in any medium, provided the original work is properly cited and is not used for commercial purposes.

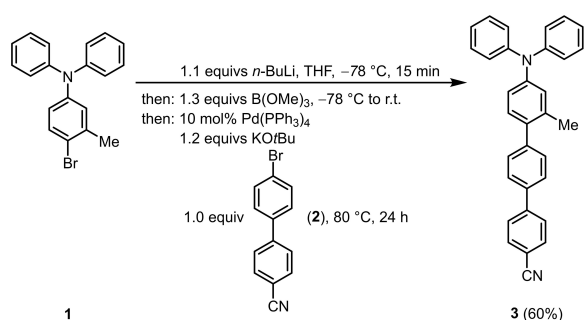
Results and Discussion

Synthesis

Recently, we showed that functional donor-acceptor TADF chromophores are efficiently accessed by one-pot methodologies.^[13] This approach was also successfully applied to study effects of extended π -conjugation with steric hindrance in a series of four terphenyl based blue emitters.^[14] Here, we selected the most intensely emissive molecule **3** with PLQYs of 0.96 and higher in solution (toluene, dichloromethane), in the solid state and in a PMMA film. The synthesis takes advantage of practical one-pot bromine-lithium exchange borylation-Suzuki (BLEBS) sequence^[15] starting from 4-bromo-3-methyl-*N,N*-diphenylaniline (**1**) as the donor part and 4'-bromo-[1,1'-biphenyl]-4-carbonitrile (**2**) as acceptor coupling partner (Scheme 1).

Photophysical properties

Absorption and emission spectra were recorded in nine solvents of variable solvent polarity with different orientation polarizations (Δf) (Figure 1). Evidently, the absorption is not significantly affected by the solvent polarity, indicating the weak dipole moment in the ground state. The compound reveals two distinctly separated absorption maxima in each



Scheme 1. BLEBS sequence for the synthesis of the *p*-phenylene bridged D-A compound **3**.

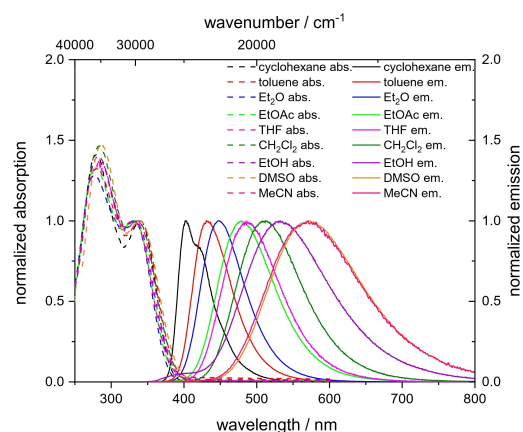


Figure 1. UV/Vis absorption (dashed) and emission spectra (solid) of compound **3** in different solvents normalized on the longest wavelength absorption band (recorded at $T = 293$ K, $c(\mathbf{3}) = 10^{-5}$ M for absorption spectra and $c(\mathbf{3}) = 10^{-6}$ M for emission spectra, $\lambda_{exc} = \lambda_{max,abs}$).

solvent. The absorption maximum at higher energy lies between 277 nm (diethyl ether) and 290 nm (THF). The absorption maximum at lower energy appears in a range from 330 to 340 nm.

The emission strongly shifts bathochromically for solvents of higher polarity, ranging from 404 to 572 nm ($\Delta\tilde{\nu} = 7,270$ cm^{-1}). This positive solvatochromism is easily visible to the naked eye and covers the color spectrum from blue (cyclohexane) to yellow orange (dimethylsulfoxide) accompanied by large Stokes shifts of up to $12,790$ cm^{-1} (Table 1, Figure 2).

Emission bands in nonpolar solvents, such as cyclohexane and toluene, have a FWHM (full width at half maximum) of 0.36 and 0.39 eV, respectively. In cyclohexane, a shoulder on the low energy side is observed, indicating some vibrational structure and a significant local contribution to the excited state of **3**.^[16] Emission bands become broader with increasing solvent polarity up to a FWHM value of 0.59 eV. The substantial solvatochromism indicates a CT character of the first excited singlet state. However, the high radiative rate constant of $2.53 \cdot 10^8$ s^{-1} in dichloromethane, derived from mono-exponential fitting of

Table 1. Selected photophysical properties of compound **3**.

	$\lambda_{max,abs}$ [nm] (ϵ [$\text{M}^{-1}\text{cm}^{-1}$])	λ_{em} [nm] (Φ_{PL}) ^[a]	τ [ns]	k_f [s^{-1}]	k_{nr} [s^{-1}]	Δf ^[b]	Stokes shift ^[c] [cm^{-1}]	FWHM ^[d] [nm] (eV)	CIE
cyclohexane	280 (40570), 340 (28620)	404 (0.97)	1.28	$7.58 \cdot 10^8$	$2.34 \cdot 10^7$	-10.00165	4660	49 (0.36)	0.159, 0.031
toluene	287 (33750), 339 (24830)	431 (0.99)	1.86	$5.32 \cdot 10^8$	$5.38 \cdot 10^6$	0.01324	6300	61 (0.39)	0.153, 0.059
Et ₂ O	277 (27600), 331 (21650)	448 (0.91)	2.15	$4.23 \cdot 10^8$	$4.19 \cdot 10^7$	0.16700	7890	70 (0.43)	0.150, 0.098
EtOAc	279 (32450), 330 (24360)	478 (0.83)	2.78	$2.99 \cdot 10^8$	$6.12 \cdot 10^7$	0.19964	9380	91 (0.48)	0.171, 0.264
THF	290 (39150), 335 (29100)	487 (0.88)	2.93	$3.00 \cdot 10^8$	$4.10 \cdot 10^7$	0.20728	9320	93 (0.46)	0.182, 0.312
CH ₂ Cl ₂	284 (37360), 336 (25580)	512 (0.99)	3.91	$2.53 \cdot 10^8$	$2.56 \cdot 10^6$	0.21710	10230	104 (0.48)	0.250, 0.455
EtOH	282 (47530), 330 (33750)	532 (0.50)	2.24	$2.23 \cdot 10^8$	$2.23 \cdot 10^8$	0.26301	12020	132 (0.59)	0.325, 0.471
DMSO	286 (34300), 339 (23290)	572 (0.49)	4.43	$1.11 \cdot 10^8$	$1.15 \cdot 10^8$	0.28874	11500	149 (0.55)	0.434, 0.505
MeCN	280 (43170), 330 (32560)	571 (0.63)	3.96	$1.59 \cdot 10^8$	$9.34 \cdot 10^7$	0.30542	12790	149 (0.55)	0.426, 0.504
in the solid state ^[14]	402	450 (0.98)	8.16	$1.20 \cdot 10^8$	$2.45 \cdot 10^6$	—	2650	46 (0.28)	0.150, 0.088
in 1 wt% PMMA film ^[14]	362	430 (0.96)	2.22	$4.32 \cdot 10^8$	$1.80 \cdot 10^7$	—	4370	61 (0.41)	0.155, 0.060

[a] Absolute quantum yields determined using an integrating sphere. [b] $\Delta f = \frac{\epsilon_f - 1}{2\epsilon_f + 1} - \frac{n^2 - 1}{2n^2 + 1}$. [c] $\Delta\tilde{\nu} = \frac{1}{\lambda_{max,abs}} - \frac{1}{\lambda_{max,em}}$. [d] Full width at half maximum.

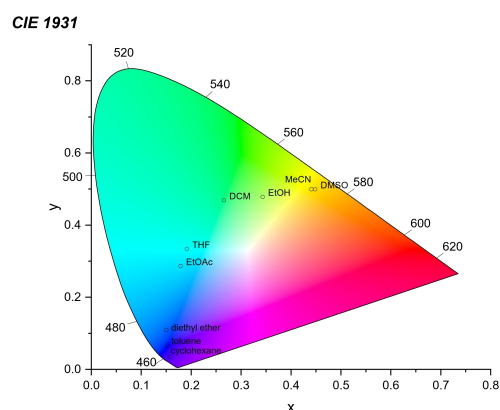


Figure 2. CIE diagram expressing the positive emission solvatochromicity of compound 3.

the luminescence decays and demonstrating a single emissive species,^[14] is untypical for pure CT transitions, typically occurring around 10^6 s^{-1} , and evidence for some LE contribution to the S_1 state.

Fluorescence lifetimes between 1–4 ns fall into a typical range for organic chromophores.^[17] In nonpolar solvents such as cyclohexane and toluene, the compound reveals short lifetimes of 1.28 and 1.86 ns, respectively. With increasing solvent polarity, the lifetime prolongates up to 4.43 ns in DMSO, with the exception of the lifetime in ethanol (2.24 ns), which is even shorter than in ethyl acetate (2.78 ns). This can be rationalized by nonradiative deactivation of the excited state by hydrogen bonding via amine and nitrile groups.^[18] The general trend of increased lifetimes in more polar solvents corresponds to the bathochromic shift in emission and the cubic dependence of the spontaneous emission probability on the transition frequency.^[17]

The emission solvatochromism is explained by a change in the dipole moment of the fluorophore upon excitation and dipole relaxation of the surrounding solvent molecules.^[18] Therefore, it was further assessed by applying the Lippert-Mataga model.^[19] The Stokes shift correlates linearly with the Lippert-Mataga polarity parameter Δf (Figure 3) indicative of a large change in dipole moment $\Delta\mu$ from the ground to the excited state upon excitation. From the slope of the fit using the Lippert-Mataga equation (see Equation S1) $\Delta\mu \approx 21 \text{ D}$ was obtained, where an Onsager radius of 5.60 \AA was estimated from the optimized geometry and crystal structural data.^[14]

Low-temperature measurements at 110 K in toluene/cyclohexane allow for estimating a $\Delta E_{S_1-T_1}$ value of 0.82 eV (see Figure S12) in good agreement with quantum chemical calculations (0.76 eV; see below). Therefore, we conclude that reverse intersystem crossing (rISC) of the T_1 population is highly unlikely,^[20] and **3** can be classified as typical singlet emitter.

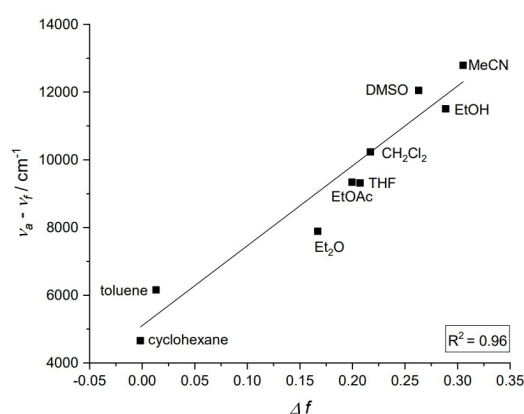


Figure 3. Lippert-Mataga plot for compound 3 ($R^2 = 0.96$).

Quantum chemical calculations

In order to rationalize why **3** is such a highly efficient emitter, its electronic and structural properties were analyzed using combined density functional theory (DFT) and multireference configuration interaction (MRCI) methods. Geometry optimizations of the excited states were performed using time-dependent density functional theory^[21] (TD-DFT) in conjunction with range-separated hybrid density functional ω B97X-D^[22] and the def2-TZVP^[23] basis set. During an optimal tuning procedure,^[24] the optimal value for the range-separation parameter was found to be $\omega = 0.14 \text{ a.u.}^{-1}$ (see Figure S16). The influence of solvation was considered via the polarizable continuum model^[25] (PCM) using the solvent excluding surface (SES) implemented in Gaussian16.^[26] Note, that the PCM includes only the instantaneous response of the solvent environment to the electronic excitation of the solute and does not account of solvent reorganization effects. Excitation energies, dipole moments and photophysical properties were calculated subsequently with the DFT/MRCI^[27] approach and the R2016^[28] parametrization, which is specially designed for organic systems consisting of various chromogenic units.

The calculated absorption spectrum of **3** in toluene solution comprises two strong and two medium strong singlet transitions in the wavelength region between 350 and 280 nm. The first peak in the experimental absorption spectrum ($\lambda_{\text{max}} = 339 \text{ nm}$) is assigned to the very intense $S_0 \rightarrow S_1$ transition found at 350 nm in our calculations with an oscillator strength of $f = 0.789$ and a huge change of the static electric dipole moment by more than 24 D indicating substantial contributions of LE as well as CT character.

The second peak with maximum at 4.32 eV ($\lambda_{\text{max}} = 287 \text{ nm}$) in toluene is composed of three electronic transitions according to our calculations, i.e., a medium strong ($f = 0.248$) local excitation (LE) on the donor moiety at 4.18 eV (297 nm), a strong ($f = 0.667$) excitation at 4.41 eV (281 nm) and a close-by weaker ($f = 0.177$) transition at 4.43 eV (280 nm), both with mixed CT and LE character on the acceptor moiety. Interestingly, four triplet excited states (3.02 eV, 3.27 eV, 3.39 eV,

3.42 eV) are lying energetically below the first excited singlet state (3.54 eV).

Analyses of the transition densities via the program package TheoDOR^[29] confirm that the first excited singlet state S_1 adopts a hybrid electronic structure of roughly 50% CT and 45% LE single excitation character in the Franck-Condon region ($S_1@S_0$, Figure 4D). The remaining 5% originate from double excitations or even higher excitations. The percentage of the CT and donor LE to the wavefunction slightly decreases in favor of the acceptor LE when the molecular geometry is relaxed in the S_1 state ($S_1@S_1$, Figure 4D). The change of the wavefunction composition is mainly brought about by a flattening of the torsional angle between the donor and acceptor units and a reduction of the C–C bond connecting them. The increased delocalization of the π -system affects a substantial enhancement of the emission oscillator strength ($f=1.455$) by roughly a factor of two compared to absorption. The natural transition orbitals (NTOs) also show that the *p*-phenylene bridge is fully involved in the electronic transition (Figure 4A) and cannot be considered an innocent spacer.

The fluorescence with calculated emission wavelength of 462 nm and radiative rate constant ($k_f=4.5\cdot10^8\text{ s}^{-1}$) is predicted to be highly anisotropic, with the electric transition dipole vector pointing along the axis connecting the donor and acceptor subunits. A ¹HLCT excited state with an optimal blend of LE and CT character can take advantage from both – having

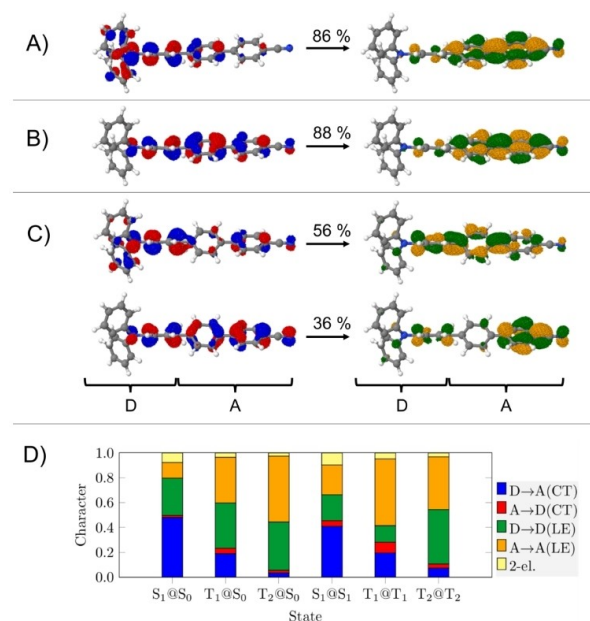
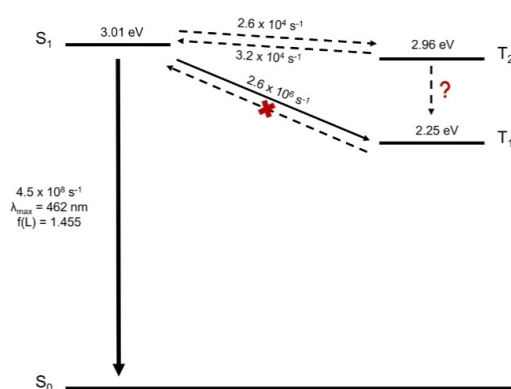


Figure 4. NTOs for (A) the S_1 state, (B) the T_1 state and (C) the T_2 state at their respective minimum geometries in toluene. The NTO from which the excitation takes place is shown in blue and red, the NTO into which the electron is excited is depicted in green and yellow. The numbers (86%, 88%, 56 + 36%) indicate the relative importance in describing the excitation by the given pair of NTOs. (D) Analysis of the excitation characters of the S_1 , T_1 and T_2 states at the S_0 geometry (Franck-Condon region) and at the respective minimum geometries of the excited states (D: donor and A: acceptor).

a strong and fast radiative fluorescence emission to compete with nonradiative pathways next to fast rISC from nearby ^3CT or ^3LE states via a hot exciton channel.^[9a]

In the following, the ability of compound **3** to undergo triplet-to-singlet up-conversion will be investigated in more detail. The optimized T_1 state shows about 30% CT and 65% LE character (Figure 4D). The NTOs (Figure 4B) suggest that the LE character mainly originates from the acceptor moiety. Its adiabatic energy is found to be 2.25 eV including zero-point vibrational energy (ZPVE) correction, resulting in a large singlet-triplet splitting between S_1 and T_1 of 0.76 eV, in good agreement with experiment (0.82 eV; see above). This result confirms the assumption that a thermally activated T_1 -to- S_1 up-conversion is energetically not feasible. Excitons populating the T_1 state can, therefore, not be harvested for the fluorescence process. The forward S_1 -to- T_1 ISC, for which we compute a rate constant of $k_{\text{ISC}}=2.2\cdot10^6\text{ s}^{-1}$ in Condon approximation using the VIBES program,^[30] cannot compete against the 200 times faster fluorescence, thus explaining the high PLQY value close to 1 observed in experiment. A very small adiabatic energy difference is found between the S_1 and T_2 state. The optimization of the T_2 geometry leads to an adiabatic energy of 2.96 eV including ZPVE correction, only 0.05 eV below the S_1 state. Due to the small energy gap, forward and backward ISC between S_1 and T_2 might therefore be possible.

T_2 is a multiconfigurational state that cannot be described by a single pair of NTOs (Figure 4C). With more than 80% LE character, evenly distributed on the donor and acceptor moiety (Figure 4D), one might expect its spin-orbit coupling to the S_1 state to be higher than between pure CT excited states. However, these expectations are not fulfilled because the rISC rate constant (T_2 to S_1) is only in the order of 10^4 s^{-1} in Condon approximation, i.e., by far not competitive with the non-radiative transition to the T_1 state. Therefore, triplet excitons will contribute to the luminescence to a minor extent only, if at all. An overview of the kinetic scheme based on our computational results is presented in Scheme 2.



Scheme 2. Adiabatic energies with ZPVE correction, rate constants for radiative (fluorescence) and nonradiative transitions (ISC and rISC) based on our theoretical results in toluene solution.

OLED fabrication

In order to assess the potential of compound **3** as an OLED emitter, we fabricated via evaporation in high-vacuum devices of the following structure: ITO/MoO₃ (6 nm)/NPB (60 nm)/mCP (10 nm)/EML (20 nm)/DPEPO (10 nm)/Bphen (20 nm)/LiF (3 nm)/Al (100 nm) (see SI/experimental for details) (Figure 5). Here, ITO (indium tin oxide) serves as transparent anode (bottom contact) and MoO₃ as hole-injection layer. NPB (*N,N'*-di(1-naphthyl)-*N,N'*-diphenyl-(1,1'-biphenyl)-4,4'-diamine) and mCP (1,3-bis(*N*-carbazolyl)benzene) were used as hole-transport materials, respectively. As emissive layer (EML), we tested compound **3** in a DPEPO-matrix (10 wt%) (bis[2-(diphenylphosphano)phenyl]-ether oxide) (**device 1**) and as a neat film (**device 2**). DPEPO and Bphen (bathophenanthroline) were utilized as electron-transport and hole-blocking layers, respectively. Finally, lithium fluoride and aluminium served as cathode material (top contact).

Both device types showed deep blue emission with an EL maximum at 451 nm and a FWHM of 60 nm. The respective CIE coordinates ($x=0.150$, $y=0.104$) fall within the range recommended by ITU-R for blue emitters in OLED displays. Comparison of the two devices shows, that **device 1** has a stronger "roll-off" at higher voltages as compared to **device 2**, indicating a better charge carrier balance in the latter case. We attribute this to a broader emission zone and reduced exciton density due to a higher number of recombination centers. Therefore, the brightness at an applied voltage of 8 V reached ca. 12 cd/m² (177 cd/m²) for **device 1** and **device 2**, respectively. Both devices reached a current (power) efficiency of ~2.8 Cd/A (~1.9 lm/W), corresponding to an EQE of ca. 2% and an IQE of ca. 10% for **device 2**, assuming an outcoupling efficiency of 20%.^[31] This is about 40% of the maximum to be expected for a singlet emitter, assuming 25% singlet formation efficiency upon recombination and 94% experimental PLQY. These results prove the potential of compound **3** as a singlet emitter, but

further optimization of the layer stack is needed to enhance the brightness and EQE of the device.

Conclusion

We performed an in-depth study of the strongly blue fluorescent twisted diphenylamino cyano terphenylene dye **3**. Its electronic properties classify compound **3** as a balanced HLCT photoluminescence emitter, further substantiated by quantum chemical calculations. Emission is strongly solvatochromic, exhibiting large Stokes shifts, while the absorption is not affected by solvent polarity. The analysis of the wavefunction contributions in the first excited state indicates a balanced HLCT state, responsible for high quantum yields also in polar solvents. Moreover, compound **3** reveals a strong and fast radiative emission. Regarding the molecular design the extension of the π -system by *p*-phenylene bridging is apparently crucial for obtaining balanced LE and CT contributions. The ligating *p*-phenylene bridge is strongly involved in the electronic transitions and, therefore, represents a handle for their finetuning and altering in future studies that are underway.

Application in OLED devices shows deep-blue emission in the range of recommended values for blue emitters in OLED displays by ITU-R, but the low IQE of about 10% suggests that only singlet excitons are harvested in these devices. The large energetic splitting of the first excited singlet and triplet states prevents the up-conversion of the T₁ population to the S₁ state by reverse intersystem crossing. Our calculations locate the T₂ state in close energetic proximity of the S₁. However, due to the low T₂-to-S₁ rISC rate constants, caused by the small mutual spin-orbit coupling between these states, only a low contribution of triplet excitons to the electroluminescence is expected.

Experimental Section

All experimental details, such as referenced and described, absorption and emission spectra, cyclic voltammetry, thermogravimetric analysis, differential scanning calorimetry, OLED characteristics as well as quantum chemical calculations are included in the Supporting Information.

Acknowledgements

The authors cordially thank the DFG (396890929/RTG 2482-1, Mu 1088/9-1) and the Fonds der Chemischen Industrie. Open Access funding enabled and organized by Projekt DEAL.

Conflict of Interest

The authors declare no conflict of interest.

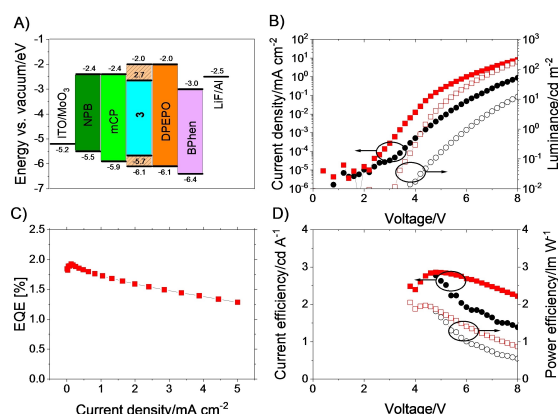


Figure 5. A) Energy diagram of **device 1** (EML: 10 wt% of compound **3** in a DPEPO matrix) and **device 2** (EML: **3** in neat film); B) Luminance (open symbols)-current density (solid symbols)-voltage (L-J-V) characteristics; C) EQE-current density characteristics; D) Current (solid symbols) and power (open symbols) efficiencies, respectively. The lines are guide to the eye.

Data Availability Statement

The data that support the findings of this study are available from the corresponding author upon reasonable request.

Keywords: density functional calculations · donor-acceptor systems · optoelectronics · organic light-emitting diodes · solvatochromism

- [1] a) S. E. Root, S. Savagatrup, A. D. Printz, D. Rodriguez, D. J. Lipomi, *Chem. Rev.* **2017**, *117*, 6467–6499; b) J.-H. Jou, S. Kumar, A. Agrawal, T.-H. Li, S. Sahoo, *J. Mater. Chem. C* **2015**, *3*, 2974–3002; c) N. Sun, C. Jiang, Q. Li, D. Tan, S. Bi, J. Song, *J. Mater. Sci. Mater. Electron.* **2020**, *31*, 20688–20729.
- [2] G. Hong, X. Gan, C. Leonhardt, Z. Zhang, J. Seibert, J. M. Busch, S. Bräse, *Adv. Mater.* **2021**, *33*, e2005630.
- [3] B. Geffroy, P. Le Roy, C. Prat, *Polym. Int.* **2006**, *55*, 572–582.
- [4] Y. Im, S. Y. Byun, J. H. Kim, D. R. Lee, C. S. Oh, K. S. Yook, J. Y. Lee, *Adv. Funct. Mater.* **2017**, *27*, 1603007.
- [5] S.-J. Su, E. Gonmori, H. Sasabe, J. Kido, *Adv. Mater.* **2008**, 4189–4194.
- [6] C. W. Tang, S. A. VanSlyke, *Appl. Phys. Lett.* **1987**, *51*, 913–915.
- [7] a) M. A. Baldo, S. Lamansky, P. E. Burrows, M. E. Thompson, S. R. Forrest, *Appl. Phys. Lett.* **1999**, *75*, 4–6; b) Baldo, Thompson, Forrest, *Nature* **2000**, *403*, 750–753.
- [8] H. Uoyama, K. Goushi, K. Shizu, H. Nomura, C. Adachi, *Nature* **2012**, *492*, 234–238.
- [9] a) T. Liu, X. Chen, J. Zhao, W. Wei, Z. Mao, W. Wu, S. Jiao, Y. Liu, Z. Yang, Z. Chi, *Chem. Sci.* **2021**, *12*, 5171–5176; b) W. Li, Y. Pan, R. Xiao, Q. Peng, S. Zhang, D. Ma, F. Li, F. Shen, Y. Wang, B. Yang, Y. Ma, *Adv. Funct. Mater.* **2014**, *24*, 1609–1614; c) N. Sharma, M. Y. Wong, D. Hall, E. Spuling, F. Tenopala-Carmona, A. Privitera, G. Copley, D. B. Cordes, A. M. Z. Slawin, C. Murawski, M. C. Gather, D. Beljonne, Y. Olivier, I. D. W. Samuel, E. Zysman-Colman, *J. Mater. Chem. C* **2020**, *8*, 3773–3783; d) S. Zhang, L. Yao, Q. Peng, W. Li, Y. Pan, R. Xiao, Y. Gao, C. Gu, Z. Wang, P. Lu, F. Li, S. Su, B. Yang, Y. Ma, *Adv. Funct. Mater.* **2015**, *25*, 1755–1762.
- [10] S. Reineke, M. A. Baldo, *Phys. Status Solidi A* **2012**, *209*, 2341–2353.
- [11] Z. Yang, Z. Mao, Z. Xie, Y. Zhang, S. Liu, J. Zhao, J. Xu, Z. Chi, M. P. Aldred, *Chem. Soc. Rev.* **2017**, *46*, 915–1016.
- [12] a) X. Tian, M. Yao, X. Liang, C. Zhou, S. Xiao, Y. Gao, H. Liu, S.-T. Zhang, B. Yang, *Dyes Pigm.* **2022**, 110463; b) J. Li, M. Zhang, T. Li, D. Guo, T. Tian, H. Zhang, *J. Mater. Chem. C* **2022**, *10*, 13124–13136.
- [13] G. A. Sommer, L. N. Mataranga-Popa, R. Czerwieniec, T. Hofbeck, H. H. H. Homeier, T. J. J. Müller, H. Yersin, *J. Phys. Chem. Lett.* **2018**, *9*, 3692–3697.
- [14] J. Wiermann, P. Schmeiack, C. Ganter, T. J. J. Müller, *Chem. Eur. J.* **2022**, e202200576.
- [15] A. Franz, T. Müller, *Synthesis* **2008**, 2008, 1121–1125.
- [16] J. Yang, Q. Guo, J. Wang, Z. Ren, J. Chen, Q. Peng, D. Ma, Z. Li, *Adv. Opt. Mater.* **2018**, *6*, 1800342.
- [17] in *Principles of Fluorescence Spectroscopy*; (Ed. J. R. Lakowicz), Springer US, Boston, MA, **2006**, pp. 205–235.
- [18] C. Reichardt, T. Welton, *Solvents and Solvent Effects in Organic Chemistry*; Wiley-VCH Verlag GmbH & Co. KGaA, Weinheim, Germany, **2010**, 384–386.
- [19] a) N. Mataga, Y. Kaifu, M. Koizumi, *BCSJ* **1956**, *29*, 465–470; b) E. Lippert, *Berichte der Bunsengesellschaft für physikalische Chemie* **1957**, 962–975.
- [20] a) C. Adachi, *Jpn. J. Appl. Phys.* **2014**, *53*, 60101; b) X. Liu, W. Liu, W. Dongyu, X. Wie, L. Wang, H. Wang, Y. Miao, H. Xu, J. Yu, B. Xu, *J. Mater. Chem. C* **2020**, *8*, 14117–14124.
- [21] a) E. Runge, E. K. U. Gross, *Phys. Rev. Lett.* **1984**, *52*, 997–1000; b) A. Dreuw, M. Head-Gordon, *J. Am. Chem. Soc.* **2004**, *126*, 4007–4016; c) F. Furche, R. Ahlrichs, *J. Chem. Phys.* **2002**, *117*, 7433–7447; d) S. Hirata, M. Head-Gordon, *Chem. Phys. Lett.* **1999**, *314*, 291–299; e) R. Beig, B.-G. Englert, U. Frisch, P. Hänggi, K. Hepp, W. Hillebrandt, D. Imboden, R. L. Jaffe, R. Lipowsky, H. v. Löhneysen, I. Ojima, D. Sornette, S. Theisen, W. Weise, J. Wess, J. Zittartz, C. Fiolhais, F. Nogueira, M. A. L. Marques, Eds, *A Primer in Density Functional Theory*, Springer Berlin Heidelberg, Berlin, Heidelberg, **2003**, 144–158.
- [22] a) J.-D. Chai, M. Head-Gordon, *Phys. Chem. Chem. Phys.* **2008**, *10*, 6615–6620; b) J.-D. Chai, M. Head-Gordon, *J. Chem. Phys.* **2008**, *128*, 84106.
- [23] a) A. Schäfer, H. Horn, R. Ahlrichs, *J. Chem. Phys.* **1992**, *97*, 2571–2577; b) F. Weigend, *Phys. Chem. Chem. Phys.* **2006**, *8*, 1057–1065.
- [24] a) D. Jacquemin, B. Moore, A. Planchat, C. Adamo, J. Autschbach, *J. Chem. Theory Comput.* **2014**, *10*, 1677–1685; b) R. Baer, E. Livshits, U. Salzner, *Annu. Rev. Phys. Chem.* **2010**, *61*, 85–109; c) L. Kronik, T. Stein, S. Refaely-Abramson, R. Baer, *J. Chem. Theory Comput.* **2012**, *8*, 1515–1531; d) L. Kronik, S. Kümmel, *Adv. Mater.* **2018**, *30*, e1706560.
- [25] a) E. Cancès, B. Mennucci, J. Tomasi, *J. Chem. Phys.* **1997**, *107*, 3032–3041; b) R. Cammi, S. Corni, B. Mennucci, J. Tomasi, *J. Chem. Phys.* **2005**, *122*, 104513; c) G. Scalmani, M. J. Frisch, B. Mennucci, J. Tomasi, R. Cammi, V. Barone, *J. Chem. Phys.* **2006**, *124*, 94107.
- [26] M. J. Frisch, G. W. Trucks, H. B. Schlegel, G. E. Scuseria, M. A. Robb, J. R. Cheeseman, G. Scalmani, V. Barone, G. A. Petersson, H. Nakatsuji, X. Li, M. Caricato, A. V. Marenich, J. Bloino, B. G. Janesko, R. Gomperts, B. Mennucci, H. P. Hratchian, J. V. Ortiz, A. F. Izmaylov, J. L. Sonnenberg, D. Williams-Young, F. Ding, F. Lipparini, F. Egidi, J. Goings, B. Peng, A. Petrone, T. Henderson, D. Ranasinghe, V. G. Zakrzewski, J. Gao, N. Rega, G. Zheng, W. Liang, M. Hada, M. Ehara, K. Toyota, R. Fukuda, J. Hasegawa, M. Ishida, T. Nakajima, Y. Honda, O. Kitao, H. Nakai, T. Vreven, K. Throssell, J. A. Montgomery, Jr., J. E. Peralta, F. Ogliaro, M. J. Bearpark, J. J. Heyd, E. N. Brothers, K. N. Kudin, V. N. Staroverov, T. A. Keith, R. Kobayashi, J. Normand, K. Raghavachari, A. P. Rendell, J. C. Burant, S. S. Iyengar, J. Tomasi, M. Cossi, J. M. Millam, M. Klene, C. Adamo, R. Cammi, J. W. Ochterski, R. L. Martin, K. Morokuma, O. Farkas, J. B. Foresman, D. J. Fox, Gaussian 16, Revision A.03, Gaussian Inc. **2016**.
- [27] a) C. M. Marian, A. Heil, M. Kleinschmidt, *Wiley Interdiscip. Rev. Comput. Mol. Sci.* **2019**, *9*; b) S. Grimme, M. Waletzke, *J. Chem. Phys.* **1999**, *111*, 5645–5655; c) M. Kleinschmidt, C. M. Marian, M. Waletzke, S. Grimme, *J. Chem. Phys.* **2009**, *130*, 44708.
- [28] I. Lyskov, M. Kleinschmidt, C. M. Marian, *J. Chem. Phys.* **2016**, *144*, 34104.
- [29] F. Plasser, *J. Chem. Phys.* **2020**, *152*, 84108.
- [30] a) M. Etinski, J. Tatchen, C. M. Marian, *Phys. Chem. Chem. Phys.* **2014**, *16*, 4740–4751; b) M. Etinski, J. Tatchen, C. M. Marian, *J. Chem. Phys.* **2011**, *134*, 154105.
- [31] W. Brütting, J. Frischeisen, T. D. Schmidt, B. J. Scholz, C. Mayr, *Phys. Status Solidi A* **2013**, *210*, 44–65.

Manuscript received: October 6, 2022
Revised manuscript received: December 21, 2022
Accepted manuscript online: December 22, 2022
Version of record online: January 18, 2023

ChemPhotoChem

Supporting Information

Highly Luminescent Blue Emitter with Balanced Hybridized Locally and Charge-Transfer Excited-States Emission

Julia Wiefermann⁺, Jeremy M. Kaminski⁺, Elisabeth Pankert, Dirk Hertel, Klaus Meerholz, Christel M. Marian, and Thomas J. J. Müller*

Supporting Information

Table of contents	
1 General considerations.....	2
2 Absorption and emission spectra.....	3
3 Estimation of ΔE_{ST}	9
4 Lippert plot	11
4.1 Lippert-Mataga equation.....	11
5 Cyclic Voltammetry (CV)	12
6 Thermal Properties.....	13
7 OLED fabrication	13
8 Luminance-current density-voltage characteristics (L-J-V).....	13
9 External quantum efficiency (EQE) and electroluminescence (EL) spectra.....	14
10 Computational details	14
11 ω -Scan	14
12 Absorption spectrum.....	16
13 Geometries (xyz) of optimized states.....	17
13.1 S_0	17
13.2 S_1	18
13.3 T_1	20
13.4 T_2	21
Literature	23

1 General considerations

All reactions were carried out in oven dried Schlenk glassware using septa and syringes under nitrogen atmosphere. Compound **3** was prepared according to our previously published protocol.^[1] Absorption spectra were recorded in cyclohexane, toluene, diethyl ether, ethyl acetate, tetrahydrofuran, CH₂Cl₂, ethanol, DMSO, and acetonitrile high performance liquid chromatography (HPLC) grade at 293 K on a Perkin–Elmer UV/Vis/NIR Lambda 19 spectrometer. For the determination of the molar extinction coefficients ϵ absorption measurements at five different concentrations were carried out. Emission spectra and fluorescence lifetimes were recorded in cyclohexane, toluene, diethyl ether, ethyl acetate, tetrahydrofuran, CH₂Cl₂, ethanol, DMSO and acetonitrile HPLC grade at 293 K on an Edinburgh FS5 spectrometer. PLQY measurements were performed using a C9920-02 absolute PL quantum yield measurement system by *Hamamatsu*. The setup uses a L9799-01 CW Xenon light source for excitation, an A10080-01 monochromator, an integrating sphere connected to a CCD spectrometer (C10027 Photonic Multichannel Analyzer by *Hamamatsu*). Measurements in solution were performed using an UV quartz cuvette. Solid states thin films were measured on glass substrates.

2 Absorption and emission spectra

2.1 4'-(Diphenylamino)-2'-methyl-[1,1':4',1''-terphenyl]-4-carbonitrile (**3**)

The spectroscopic data ($\lambda_{abs,max}$ (ϵ) and $\lambda_{em,max}$) are compiled in Table S1.

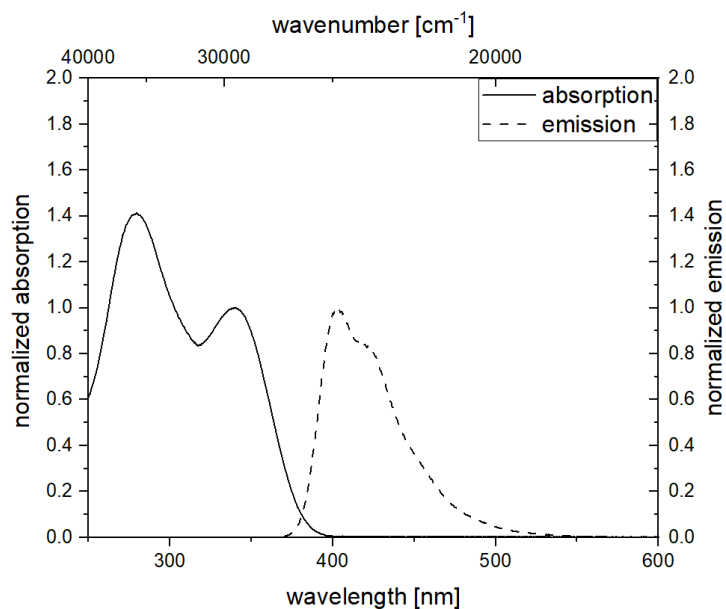


Figure S1: Recorded in cyclohexane, $T = 293$ K, $c(\mathbf{3}) = 10^{-5} - 10^{-6}$ M, $\lambda_{ex} = \lambda_{max,abs}$

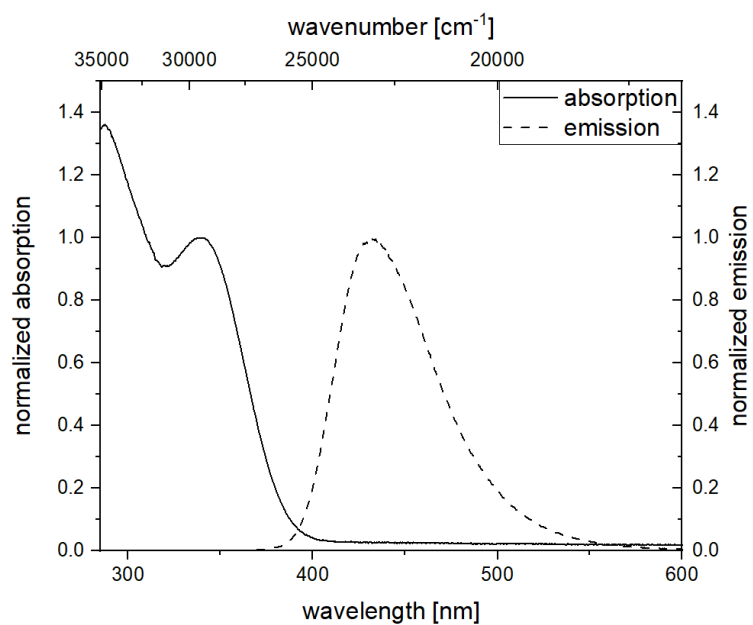


Figure S2: Recorded in toluene, $T = 293$ K, $c(\mathbf{3}) = 10^{-5} - 10^{-6}$ M, $\lambda_{ex} = \lambda_{max,abs}$

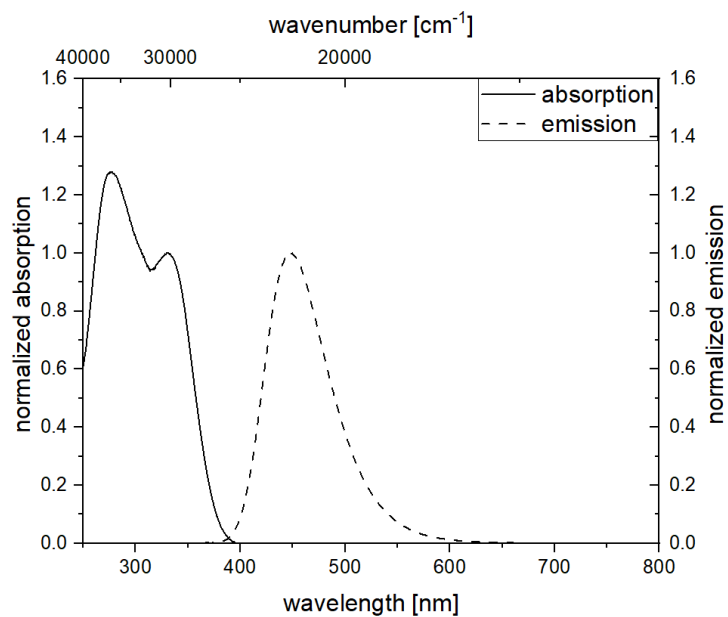


Figure S3: Recorded in diethyl ether, $T = 293$ K, $c(\mathbf{3}) = 10^{-5} - 10^{-6}$ M, $\lambda_{ex} = \lambda_{max,abs}$

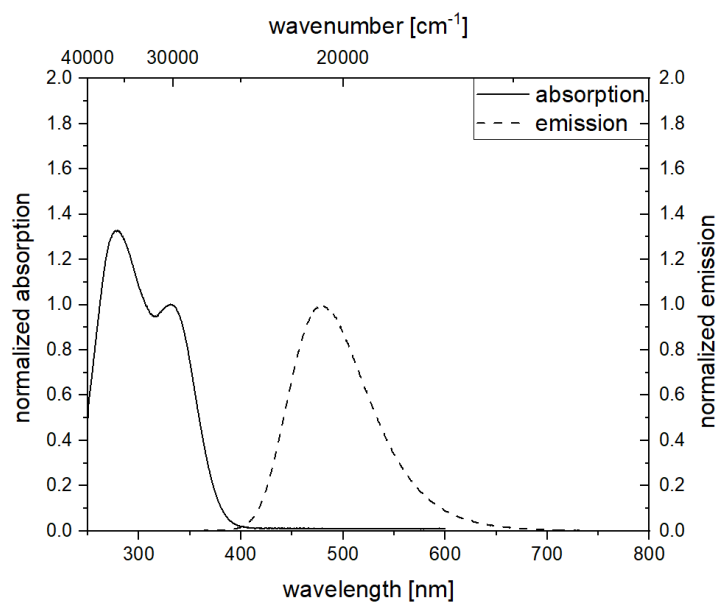


Figure S4: Recorded in ethyl acetate, $T = 293$ K, $c(\mathbf{3}) = 10^{-5} - 10^{-6}$ M, $\lambda_{ex} = \lambda_{max,abs}$

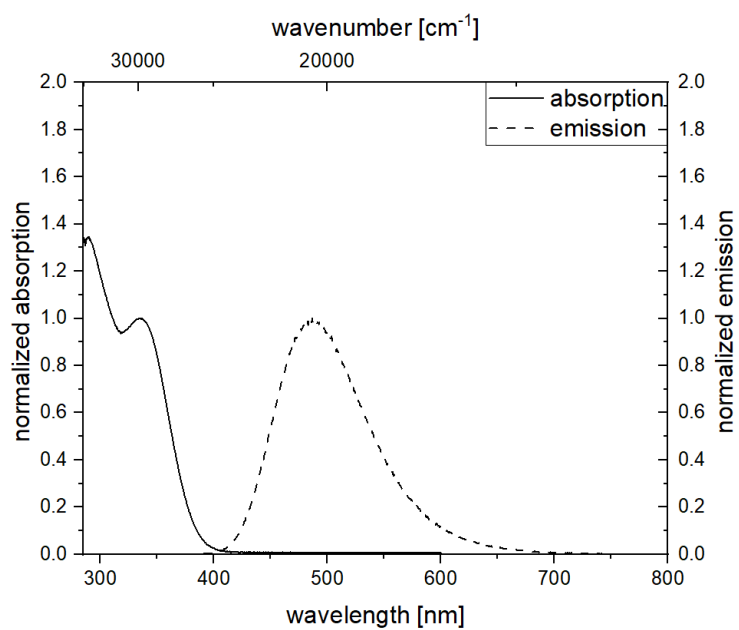


Figure S5: Recorded in tetrahydrofuran, $T = 293$ K, $c(\mathbf{3}) = 10^{-5} - 10^{-6}$ M, $\lambda_{ex} = \lambda_{max,abs}$

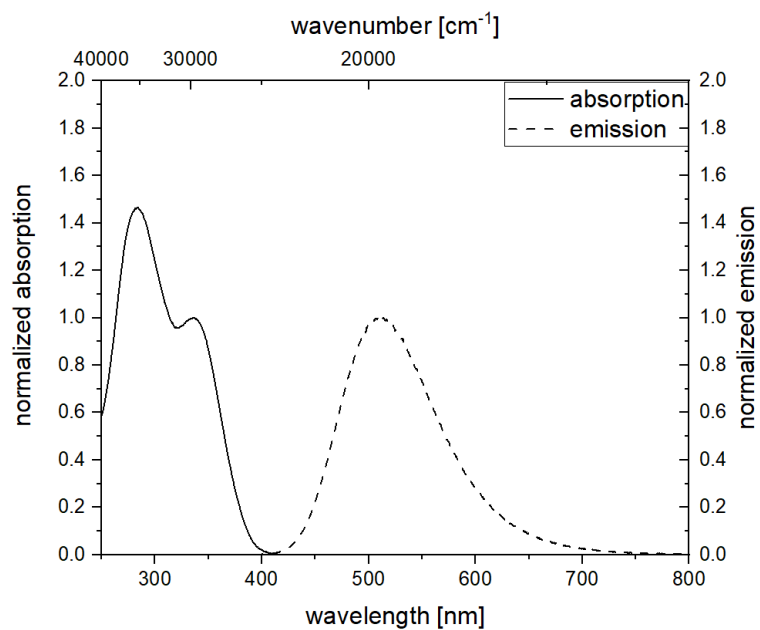


Figure S6: Recorded in dichloromethane, $T = 293$ K, $c(\mathbf{3}) = 10^{-5} - 10^{-6}$ M, $\lambda_{ex} = \lambda_{max,abs}$

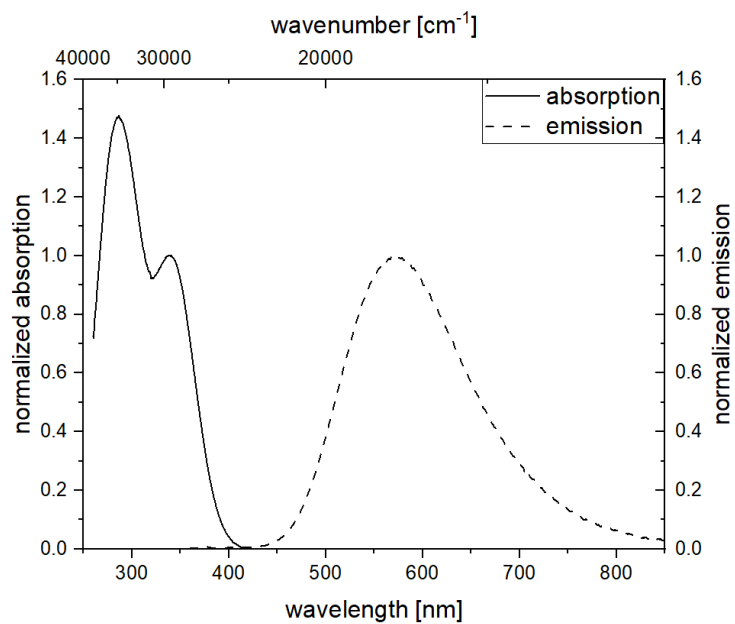


Figure S7: Recorded in DMSO, $T = 293$ K, $c(\mathbf{3}) = 10^{-5} - 10^{-6}$ M, $\lambda_{ex} = \lambda_{max,abs}$

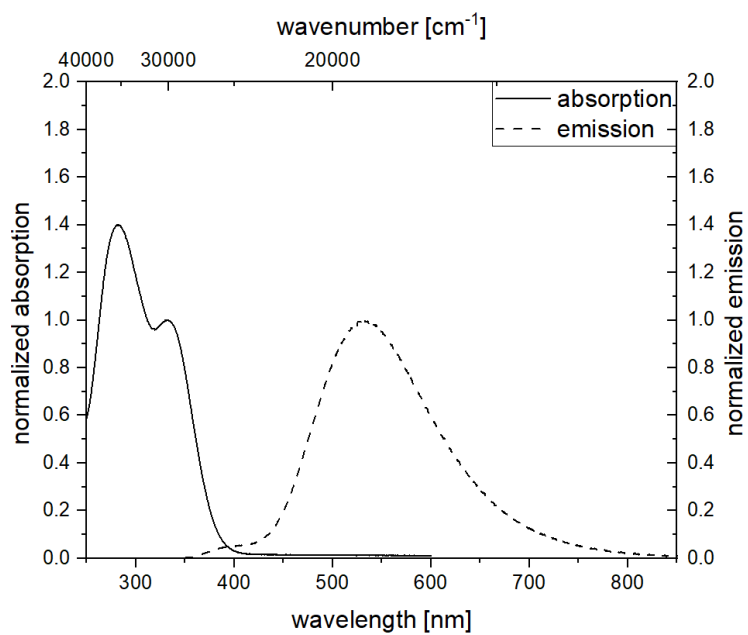


Figure S8: Recorded in ethanol, $T = 293$ K, $c(\mathbf{3}) = 10^{-5} - 10^{-6}$ M, $\lambda_{ex} = \lambda_{max,abs}$

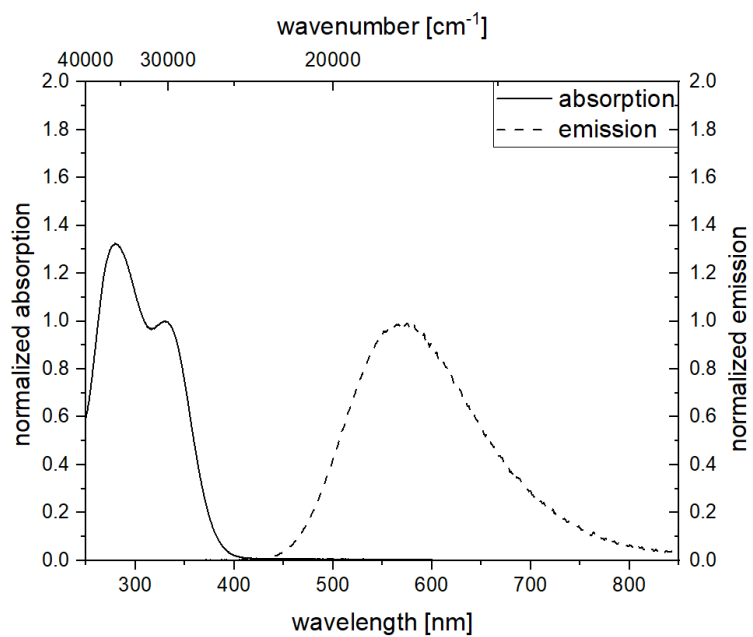


Figure S9: Recorded in acetonitrile, $T = 293$ K, $c(\mathbf{3}) = 10^{-5} - 10^{-6}$ M, $\lambda_{ex} = \lambda_{max,abs}$

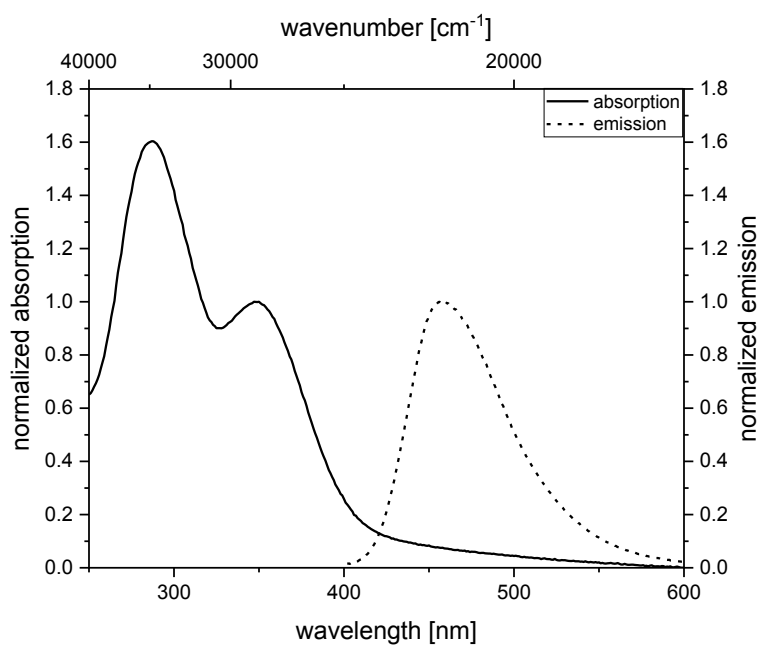


Figure S10: Recorded as 100 nm thin film on quartz glass, $T = 293$ K, $\lambda_{ex} = \lambda_{max,abs}$

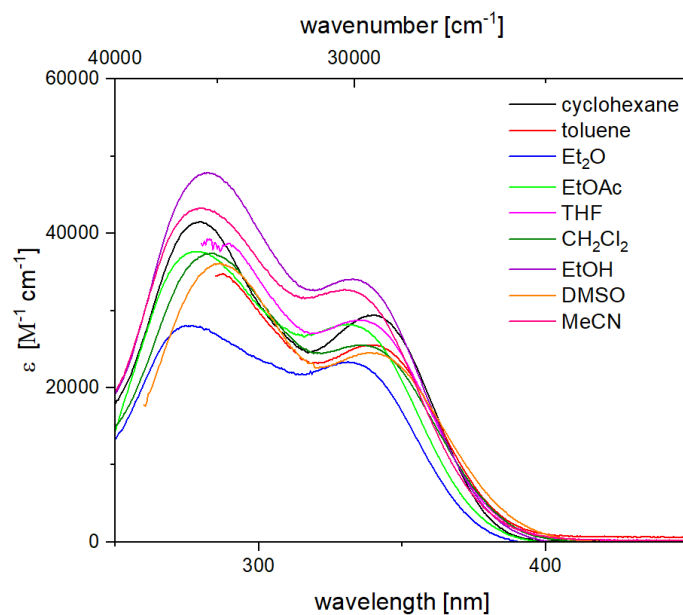


Figure S11: Absorption spectra recorded in solvents of different polarity, $T = 293\text{ K}$, $c(\mathbf{3}) = 10^{-5}\text{ M}$.

Table S1: Selected photophysical data of compound **3** in solvents of different polarity.

solvent	$\lambda_{abs, max} [\text{nm}] (\epsilon [\text{M}^{-1} \text{cm}^{-1}])$	$\lambda_{em} [\text{nm}]$
cyclohexane	340 (28620)	404
	280 (40570)	
toluene	339 (24830)	431
	287 (33750)	
Et ₂ O	331 (21650)	448
	277 (27600)	
EtOAc	330 (24360)	478
	279 (32450)	
THF	335 (29100)	487
	290 (39150)	
CH ₂ Cl ₂	336 (25580)	512
	284 (37360)	
EtOH	330 (33750)	532
	282 (47530)	
DMSO	339 (23290)	572
	286 (34300)	
MeCN	330 (32560)	571
	280 (43170)	

3 Estimation of ΔE_{ST}

For time-resolved emission measurements, the samples were placed in a cold finger cryostat (Optistat, Oxford instruments). The samples were excited using the third harmonic (355 nm) of a Nd:YAG laser (*InnoLas*) operated at a repetition rate of 10 Hz. The excitation intensity was adjusted using appropriate filters. The PL was collected and focused onto the entrance slit of a monochromator (Acton Spectra Pro 275, 150 l/mm, 2 nm spectral resolution) and detected by an intensified CCD camera (ICCD, PIMAX 4, *Roper Scientific*). The ICCD was operated in gated mode, which allows to vary and simultaneously delay the width of the detection window with respect to optical excitation. The instrument response function is about 1.7 ns. For temperature dependent measurements the sample was cooled down using liquid nitrogen. For phosphorescence lifetime measurements the repetition rate of the laser was reduced to 0.33 Hz, however, the rate could not be reduced further thus the excited molecules never depleted completely. For that reason we consider our measured lifetime as a good approximation only.

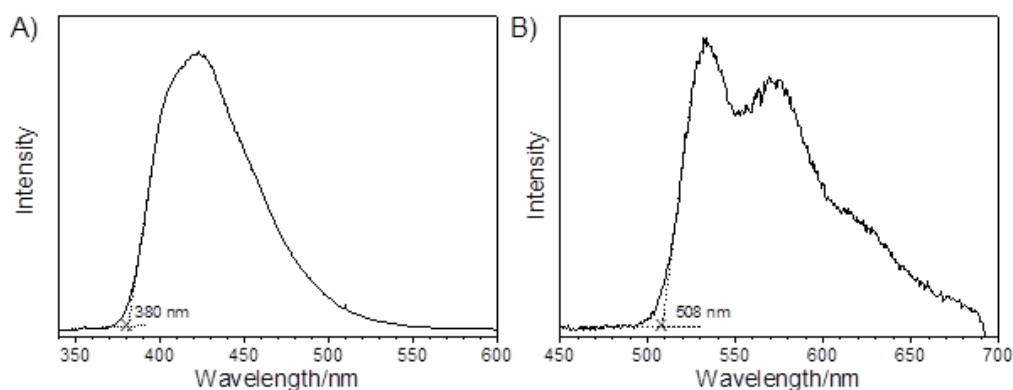


Figure S12: Fluorescence (A) and phosphorescence (B) spectra in toluene/cyclohexane (1:1) at 110 K, $c(\mathbf{3}) = 10^{-5}$ M, $\lambda_{ex} = 355$ nm. (A) was recorded with a gate of 100 ns with excitation, (B) was recorded with a gate of 200 ms and a delay of 10 ms. Cut-off wavelength of 380 nm (508 nm) for fluorescence (phosphorescence) indicate energy values of 3.26 eV (2.44 eV) and a ΔE_{ST} of 0.82 eV.

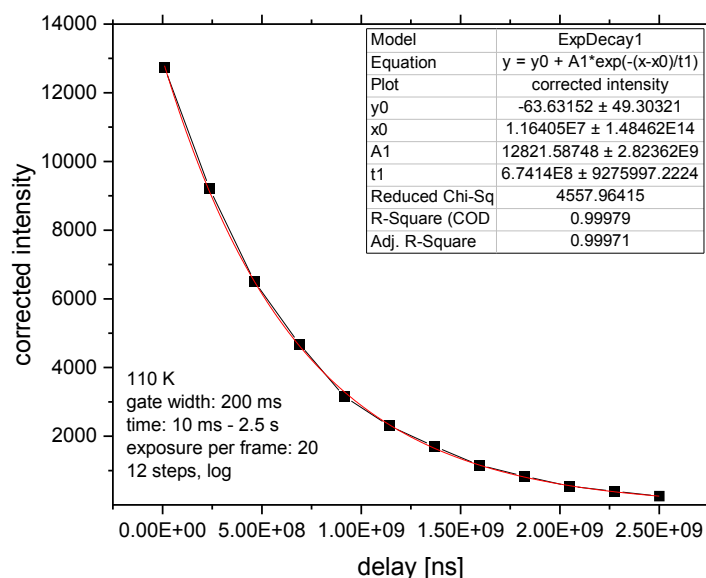


Figure S13: Phosphorescence decay in toluene/cyclohexane (1:1) at 110 K, $c(\mathbf{3}) = 10^{-5}$ M, $\lambda_{ex} = 355$ nm recorded with a gate of 200 ms and delay of 10 ms - 2.5 s. A minimum lifetime of 674 ms indicates phosphorescence type emission.

The lifetime can only be used as an order of magnitude estimate. The setup did not allow for excitation after passing of 10 lifetimes, thus the system never decays completely but remains in an equilibrium with constant T1 population. (The laser could only be operated at 0.33 Hz, not at 0.1 Hz).

4 Lippert plot

Table S2: Data for Lippert plot.

Solvent	$n_D^{20[2]}$	$\epsilon_r^{[2]}$	Δf	$\lambda_{\max,abs}$ [nm]	$\lambda_{\max,em}$ [nm]	Stokes shift [cm ⁻¹]
cyclohexane	1.4262	2.02	-0.00164973	340	404	4660
toluene	1.4969	2.38	0.01323509	339	431	6300
diethyl ether	1.3526	4.34	0.16699512	331	448	7890
EtOAc	1.3724	6.02	0.19963504	330	478	9380
THF	1.407	7.38	0.2072845	335	487	9320
DCM	1.4242	8.93	0.21710325	336	512	10230
DMSO	1.48	46.45	0.26300932	339	572	11500
EtOH	1.3614	24.55	0.28874639	330	532	12020
MeCN	1.3441	37.5	0.30541639	330	571	12790

4.1 Lippert-Mataga equation

$$\tilde{\nu}_a - \tilde{\nu}_f = \frac{2 \Delta f}{4\pi\epsilon_0 h c a^3} (\mu_E - \mu_G) + const$$

Equation S1: Lippert-Mataga equation.

 $\tilde{\nu}_a$: absorption maximum $\tilde{\nu}_f$: emission maximum μ_E : dipole moment in the excited state μ_G : dipole moment in the ground state ϵ_0 : vacuum permittivity constant ($8.8542 \cdot 10^{-12}$ As V⁻¹ m⁻¹)h: Planck's constant ($6.6256 \cdot 10^{-34}$ J s)c: the speed of light ($2.9979 \cdot 10^{10}$ cm s⁻¹)

a: Onsager radius (5.60 Å)

5 Cyclic Voltammetry (CV)

Cyclic voltammograms were recorded with an Autolab PGSTAT302N (Metrohm) workstation under argon atmosphere with a one-compartment cell. Disk shaped platinum ($A = 0.2 \text{ mm}^2$) was used as working electrode, a platinum grid as counter electrode and a silver wire as reference electrode. Tetrabutylammonium-hexafluorophosphate (TBAPF_6) from Fluka (puriss. Electrochemical grade) was used as supporting electrolyte (0.15 mol L^{-1}). Acetonitrile (Acros Seal), bubbled with argon for 30 min was used as solvent and the emitter was dissolved with a concentration of $10^{-3} \text{ mol L}^{-1}$. The voltammogram was recorded at scan rate of 10 mV s^{-1} . Ferrocene (Aldrich, 98%) was added at the end of the measurement for calibration.

The oxidation potential $E_{\text{ox}}^{1/2}$ is calculated as the average of the anodic and cathodic peak potentials, respectively.

To estimate the HOMO energy level the following equation is used

$$E_{\text{HOMO}} = -E_{\text{ox}}^{1/2} - 5.15 \text{ eV}$$

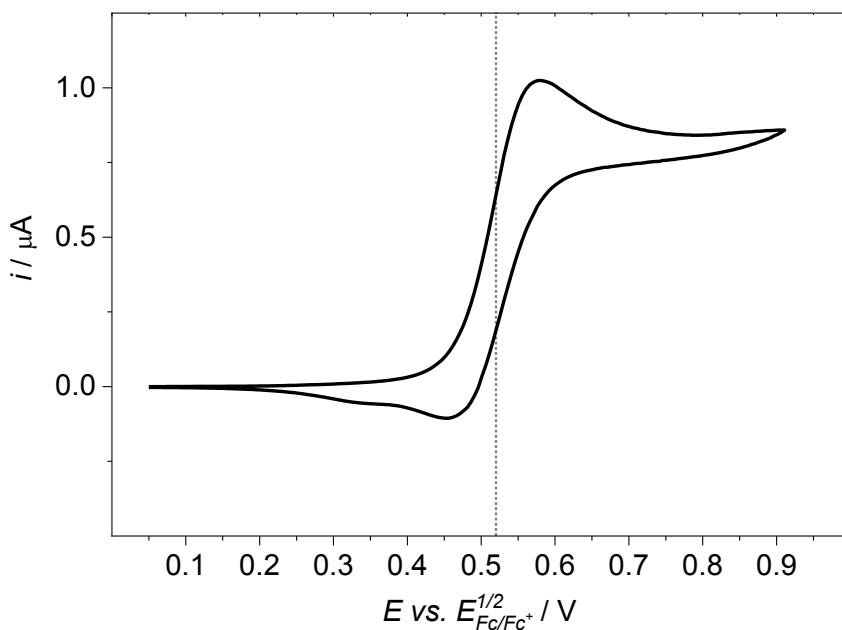


Figure S14: Cyclic voltammogram (CV) of compound **3** in MeCN/ TBAPF_6 at a scan rate of 10 mV s^{-1} . The determined $E_{\text{ox}}^{1/2}$ lies at 0.52 V .

6 Thermal Properties

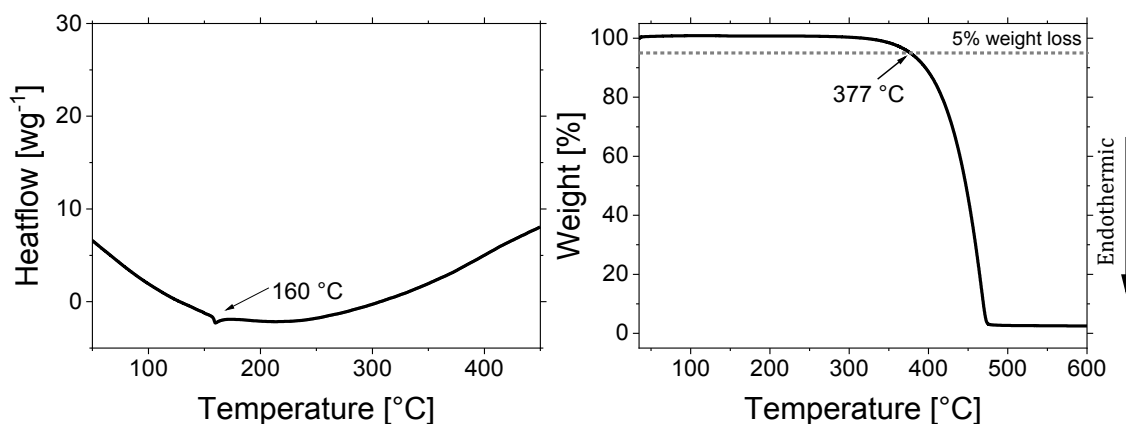


Figure S15: DSC and TGA curve of compound **3**.

Thermogravimetric analysis was performed with a TGA-DSC 1 by *Mettler-Toledo* at a heating rate of 10 °C min⁻¹ under nitrogen flow (30 mL min⁻¹).

7 OLED fabrication

OLED devices were fabricated using commercially available ITO-coated display glass (sheet resistance: 20 Ω cm⁻²). Prior to film deposition the pre-patterned substrates were cleaned in different steps in an ultrasonic bath with chloroform, acetone, detergent (Mucisol®) and deionized water. After cleaning the substrates were dried in nitrogen flow.

The evaporated materials are commercially available and were used as received. MoO₃ and all organic materials were deposited in a customized *Lesker* evaporation chamber. Devices were transferred from a glovebox under dry nitrogen atmosphere into the evaporation chamber. The evaporation process was started at a maximum of 5 × 10⁻⁶ mbar and a rate of 0.2-0.3 Å s⁻¹. The layer thickness was monitored via quartz sensors during the evaporation. After deposition of the organic material and without breaking the vacuum another shadow mask was used to define the active area (7.85 mm²) of the OLED and lithium fluoride and aluminum were evaporated as cathode materials.

8 Luminance-current density-voltage characteristics (L-J-V)

LJV characteristics were determined under argon atmosphere by use of a photodiode calibrated with a luminance meter Chroma Meter CS-100 (*Konica Minolta*). The photodiode was connected to a picoammeter (Keithley, model 6485) and a SourceMeter® (Keithley, model 2400).

9 External quantum efficiency (EQE) and electroluminescence (EL) spectra

EQE and EL measurements were performed under nitrogen atmosphere using an external quantum efficiency measurement system (C9920-11) by *Hamamatsu*. An integrating sphere, equipped with a custom-made device holder with electrical contacts is connected to a CCD spectrometer (C10027 Photonic Multichannel Analyzer by *Hamamatsu*). The voltage is increased stepwise by use of a SourceMeter® (*Keithley*, model 2400). An EL spectrum is recorded at every voltage step.

10 Computational details

The electronic ground-state geometry of the emitter was optimized with DFT at the ω B97X-D/def2-TZVP level of theory^[3] with $\omega = 0.14$ (after optimal tuning procedure in vacuo), including implicit toluene solvation via the polarizable continuum model (PCM)^[4] in the equilibrium limit using the solvent excluding surface (SES) implemented in Gaussian16.^[5]

Time-dependent DFT (TDDFT)^[6] was used for the optimization of the excited states (Tamm-Dancoff approximation (TDA) for excited triplet states^[7]). Analytic harmonic vibrational frequencies were computed by means of Gaussian16.

Excitation energies, dipole moments and photophysical properties were calculated using the DFT/MRCI method^[8] and the R2016^[9] parametrization (tight configuration selection threshold of $0.8 E_h$), which is specially designed for large multichromophoric systems. Up to 20 excited states in the singlet and triplet manifold employing closed-shell BH-LYP^[10] orbitals as the one-particle basis were considered. Kohn-Sham molecular orbitals and integrals were computed with the Turbomole suite of programs.^[11] Solute-solvent interactions were taken into consideration in this step by embedding the molecule in a field of point charges imported from preceding Gaussian16 DFT calculations.

Fragment-based analyses of the singlet and triplet DFT/MRCI wavefunctions were performed by the TheoDORE tool box.^[12] Spin-orbit coupling matrix elements (SOCMEs) between target singlet and triplet states were calculated with the spin-orbit coupling kit (SPOCK).^[13] Rate constants for ISC and rISC between excited singlet and triplet states were determined in the framework of Fermi's golden rule approximation and a time-dependent Fourier transform approach as implemented in the VIBES program.^[14] Temperature effects were accounted to the rate constants by assuming a Boltzmann distribution in the initial electronic state. Radiative rate constants were determined in Einstein's approximation.

11 ω -Scan

The accuracy of the calculated excitation energies, especially when they involved charge transfer excitations, depends on the range-separation parameter ω whose optimal values

depend on the studied system. The optimization of ω for the ω B97X-D functional was carried out by applying Koopman's theorem.^[15] The optimal value ω was determined from minimizing the target function:

$$J^2 = \sum_{i=0}^1 [\varepsilon_{HOMO}^\omega(N+i) + IP(N+i)]^2, \quad \text{Equation S2}$$

where $IP(N) = E(N-1) - E(N)$, and $IP(N+1) = E(N) - E(N+1)$; here N is the number of electrons of the target molecule, $\varepsilon_{HOMO}^\omega$ is the HOMO energy and $IP(N)$ the vertical ionization potential.^[16]

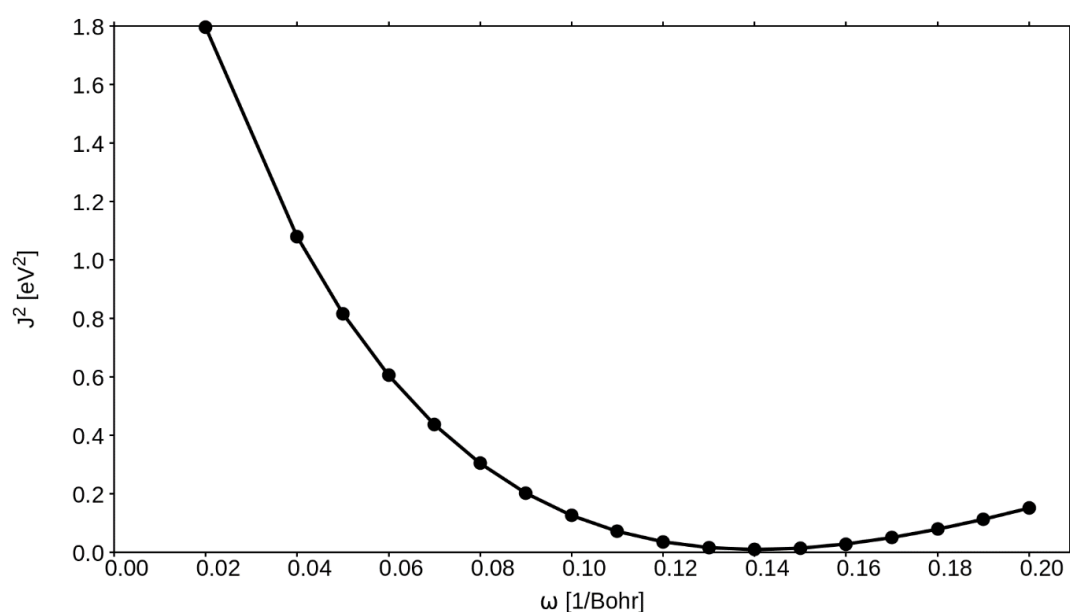


Figure S16. J^2 - ω plot in vacuo for the ω B97X-D functional and def2-TZVP basis set. The optimal value for ω is found to be 0.14 bohr⁻¹.

12 Absorption spectrum

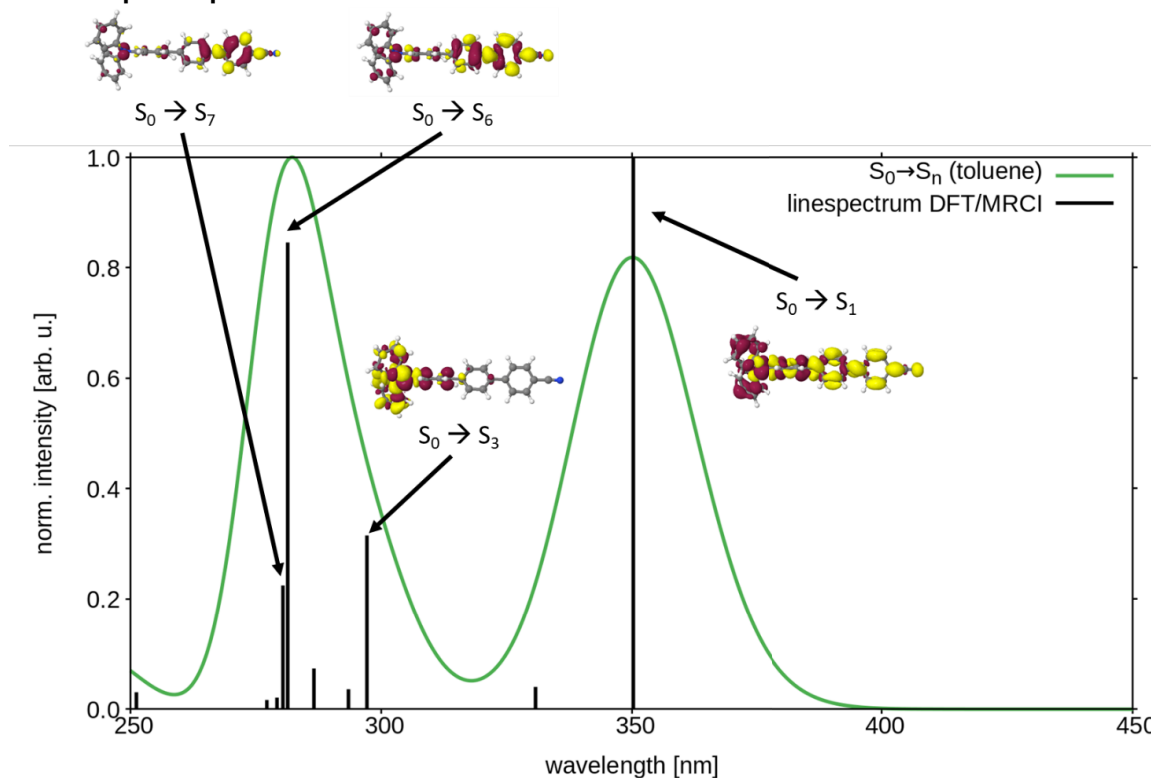


Figure S17. Calculated line spectrum (black) for $S_0 \rightarrow S_n$ transitions of the emitter with the DFT/MRCI approach and gaussian broadened (1000 cm^{-1}) spectrum (green). In the range of 250 nm and 400 nm four transitions, namely from the electronic ground state into the S_1 , S_3 , S_6 and S_7 state, produce two intense absorption bands at 350 nm and ca. 280 nm. Characterization of the transitions is done by difference densities (± 0.001). Electron density is transferred from the red to the yellow area.

13 Geometries (xyz) of optimized states

13.1 S₀

C	3.281339	8.192863	15.375076
H	3.531352	7.359586	14.730430
C	4.138365	9.282315	15.469405
H	5.062015	9.302538	14.906001
C	2.092712	8.167190	16.088291
C	3.795652	10.345558	16.295421
C	1.750648	9.229907	16.926364
H	1.424345	7.320595	16.001303
C	2.617622	10.319447	17.026097
H	4.456240	11.198856	16.384380
N	0.544612	9.203522	17.662060
H	2.362530	11.145963	17.676309
C	0.123097	8.008021	18.282672
C	-0.236046	10.375788	17.777686
C	-1.221643	7.642719	18.278094
C	1.039471	7.172538	18.918670
C	-0.826665	10.716813	18.995686
C	-0.426663	11.210890	16.675613
H	-1.938820	8.296196	17.796912
C	-1.674407	6.476176	18.885285
H	2.088375	7.436059	18.941734
C	0.601855	6.004114	19.514284
H	-0.680266	10.077196	19.856170
C	-1.597717	11.864049	19.102648
C	-1.184077	12.366061	16.795493
H	0.024438	10.952206	15.726605
C	-3.150528	6.172026	18.857970
C	-0.743045	5.630385	19.509715
H	1.324185	5.357758	19.998072
H	-2.048697	12.113459	20.054943
C	-1.778230	12.698531	18.006533
H	-1.320735	13.003097	15.930674
H	-3.405098	5.501546	18.033942
H	-3.478849	5.690670	19.779135
H	-3.726356	7.087357	18.723438

C	-1.134366	4.363161	20.177670
H	-2.374470	13.597203	18.095181
C	-1.815245	3.354759	19.494601
C	-0.796920	4.134226	21.512402
H	-2.078855	3.498177	18.454663
C	-2.148715	2.165604	20.121117
C	-1.134931	2.948068	22.143434
H	-0.266331	4.900046	22.064651
H	-2.689636	1.408500	19.567110
C	-1.817713	1.941841	21.458729
H	-0.846212	2.795948	23.176054
C	-2.179283	0.673978	22.130532
C	-2.629029	0.668685	23.454082
C	-2.079717	-0.546963	21.457104
C	-2.968860	-0.511879	24.088313
H	-2.735093	1.603920	23.987890
H	-1.712644	-0.569526	20.439420
C	-2.416835	-1.734988	22.078668
C	-2.864172	-1.722372	23.400985
H	-3.322952	-0.501115	25.110139
H	-2.327753	-2.673510	21.548762
C	-3.214772	-2.947644	24.050236
N	-3.497284	-3.934233	24.572678

13.2 S₁

C	3.598571	8.236156	15.852045
H	3.975101	7.397415	15.281155
C	4.384700	9.368551	16.030565
H	5.379833	9.412117	15.608196
C	2.323136	8.176116	16.388731
C	3.885072	10.445887	16.754608
C	1.824995	9.257032	17.119632
H	1.703660	7.302265	16.236738
C	2.614393	10.394927	17.301664
H	4.493544	11.328277	16.904204
N	0.526684	9.197348	17.679271
H	2.230389	11.227394	17.876011

C	0.083813	8.042806	18.300976
C	-0.307392	10.338696	17.597551
C	-1.279279	7.677182	18.267471
C	0.978404	7.210518	19.011631
C	-1.047968	10.745561	18.709281
C	-0.394180	11.057846	16.403848
H	-1.973642	8.328009	17.752284
C	-1.761997	6.537184	18.862014
H	2.024904	7.474340	19.077036
C	0.515700	6.086232	19.626139
H	-0.966880	10.194035	19.636509
C	-1.868232	11.858047	18.621118
C	-1.212552	12.172291	16.329531
H	0.174280	10.735460	15.541631
C	-3.249006	6.308741	18.812372
C	-0.850131	5.662255	19.562651
H	1.229023	5.462521	20.145901
H	-2.433759	12.172099	19.488754
C	-1.954626	12.576388	17.434124
H	-1.279215	12.722289	15.399901
H	-3.532327	5.603671	18.027477
H	-3.624964	5.915361	19.756944
H	-3.762282	7.246708	18.603268
C	-1.213707	4.430350	20.191770
H	-2.595190	13.445973	17.370192
C	-2.269847	3.582396	19.740307
C	-0.470207	3.930572	21.308642
H	-2.834437	3.853424	18.862202
C	-2.548610	2.385248	20.333701
C	-0.774692	2.750133	21.920777
H	0.326146	4.530177	21.728560
H	-3.349939	1.793995	19.913951
C	-1.828830	1.905252	21.468061
H	-0.178513	2.459654	22.774196
C	-2.140389	0.655106	22.104834
C	-1.525114	0.255268	23.324068
C	-3.084668	-0.256474	21.554798

C	-1.823650	-0.936343	23.935408
H	-0.811796	0.904626	23.810344
H	-3.579505	-0.028482	20.622057
C	-3.383716	-1.451032	22.160579
C	-2.760013	-1.818162	23.366205
H	-1.339551	-1.201032	24.866324
H	-4.102265	-2.120849	21.706621
C	-3.069057	-3.051314	23.995110
N	-3.320994	-4.056327	24.507597

13.3 T₁

C	3.648027	8.325478	15.882932
H	4.043180	7.508971	15.292253
C	4.418183	9.459595	16.108929
H	5.418562	9.529062	15.702389
C	2.362945	8.236062	16.395265
C	3.893191	10.504997	16.858834
C	1.840565	9.280698	17.157275
H	1.758144	7.358831	16.206212
C	2.614545	10.417530	17.387206
H	4.485935	11.391573	17.044284
N	0.526897	9.195146	17.684873
H	2.210082	11.228733	17.978270
C	0.088266	8.031134	18.307356
C	-0.326295	10.322711	17.568105
C	-1.266184	7.655613	18.270834
C	0.980821	7.202265	19.012594
C	-1.062242	10.765765	18.666516
C	-0.423155	11.003850	16.355672
H	-1.967150	8.304677	17.762214
C	-1.745830	6.508985	18.865338
H	2.027856	7.464757	19.075366
C	0.524385	6.067352	19.621584
H	-0.978258	10.243621	19.610670
C	-1.893213	11.868842	18.546058
C	-1.245337	12.114922	16.247530
H	0.148172	10.660535	15.503153

C	-3.234353	6.279101	18.812308
C	-0.834806	5.640129	19.560353
H	1.244558	5.445568	20.134627
H	-2.459318	12.205039	19.405282
C	-1.987215	12.550192	17.338767
H	-1.313744	12.636272	15.301386
H	-3.516404	5.597427	18.006505
H	-3.612640	5.861669	19.745167
H	-3.748837	7.221760	18.628752
C	-1.194761	4.404148	20.185253
H	-2.631852	13.414705	17.249794
C	-2.255316	3.552988	19.727341
C	-0.448776	3.899333	21.308663
H	-2.803250	3.823026	18.838307
C	-2.545622	2.366502	20.318286
C	-0.750678	2.727496	21.919770
H	0.343417	4.504206	21.728698
H	-3.323201	1.760669	19.876671
C	-1.824555	1.878521	21.469205
H	-0.176061	2.449370	22.791110
C	-2.145030	0.651630	22.105292
C	-1.355340	0.120793	23.175542
C	-3.280432	-0.130159	21.717326
C	-1.664864	-1.061372	23.788845
H	-0.476467	0.649361	23.513217
H	-3.930126	0.214590	20.926918
C	-3.593968	-1.310365	22.332839
C	-2.792944	-1.805947	23.383150
H	-1.041782	-1.434853	24.590489
H	-4.463712	-1.871159	22.017480
C	-3.115675	-3.030083	24.019737
N	-3.379113	-4.028383	24.538741

13.4 T₂

C	3.533959	8.258766	15.708688
H	3.886697	7.417250	15.126287
C	4.328597	9.391260	15.849643

H	5.305972	9.433015	15.387424
C	2.281887	8.200244	16.297439
C	3.857777	10.470402	16.593177
C	1.808688	9.284429	17.044393
H	1.657242	7.325272	16.176960
C	2.612019	10.420647	17.192845
H	4.472403	11.352866	16.716931
N	0.545672	9.215118	17.670349
H	2.255394	11.253458	17.784209
C	0.129214	8.031278	18.268521
C	-0.289499	10.352663	17.688319
C	-1.237946	7.628707	18.214466
C	1.051893	7.199482	18.965357
C	-1.033278	10.658618	18.833539
C	-0.408219	11.163425	16.553846
H	-1.944921	8.260554	17.692058
C	-1.677343	6.463080	18.789416
H	2.088834	7.496290	19.046589
C	0.614374	6.045089	19.549499
H	-0.935448	10.035531	19.712396
C	-1.874710	11.758372	18.839257
C	-1.246024	12.264048	16.574555
H	0.152972	10.919121	15.661670
C	-3.138211	6.108549	18.711596
C	-0.741289	5.625602	19.476025
H	1.322124	5.421565	20.082019
H	-2.439237	11.990573	19.733250
C	-1.986179	12.568484	17.714476
H	-1.332431	12.883063	15.690720
H	-3.327007	5.312584	17.987802
H	-3.511694	5.757199	19.675328
H	-3.725992	6.974999	18.410030
C	-1.129535	4.366631	20.140749
H	-2.644203	13.427295	17.723714
C	-1.793080	3.334605	19.462208
C	-0.805578	4.144643	21.487097
H	-2.019959	3.450055	18.410521

C	-2.135549	2.158481	20.096828
C	-1.130340	2.964080	22.123126
H	-0.305745	4.926805	22.045146
H	-2.621608	1.383097	19.519898
C	-1.815692	1.931898	21.450953
H	-0.884425	2.856891	23.171114
C	-2.173019	0.693070	22.121114
C	-1.479828	0.249603	23.281193
C	-3.232956	-0.128172	21.646845
C	-1.811292	-0.916832	23.916159
H	-0.646285	0.824839	23.659213
H	-3.808205	0.184051	20.786468
C	-3.579671	-1.292216	22.278116
C	-2.873252	-1.714336	23.428838
H	-1.258768	-1.240836	24.787534
H	-4.400662	-1.891050	21.908106
C	-3.224853	-2.918321	24.084126
N	-3.512563	-3.902006	24.619389

Literature

- [1] J. Wiefermann, P. Schmeinck, C. Ganter, T. J. J. Müller, *Chem. Eur. J.* **2022**, *28*, e202200576.
- [2] C. Reichardt, T. Welton, *Solvents and Solvent Effects in Organic Chemistry*; Wiley-VCH Verlag GmbH & Co. KGaA, Weinheim, Germany, **2010**.
- [3] a) J.-D. Chai, M. Head-Gordon, *Phys. Chem. Chem. Phys.* **2008**, *10*, 6615–6620; b) J.-D. Chai, M. Head-Gordon, *J. Chem. Phys.* **2008**, *128*, 84106; c) A. Schäfer, H. Horn, R. Ahlrichs, *J. Chem. Phys.* **1992**, *97*, 2571–2577; d) F. Weigend, *Phys. Chem. Chem. Phys.* **2006**, *8*, 1057–1065.
- [4] a) R. Cammi, S. Corni, B. Mennucci, J. Tomasi, *J. Chem. Phys.* **2005**, *122*, 104513; b) E. Cancès, B. Mennucci, J. Tomasi, *J. Chem. Phys.* **1997**, *107*, 3032–3041; c) G. Scalmani, M. J. Frisch, B. Mennucci, J. Tomasi, R. Cammi, V. Barone, *J. Chem. Phys.* **2006**, *124*, 94107.
- [5] M. J. Frisch, G. W. Trucks, H. B. Schlegel, G. E. Scuseria, M. A. Robb, J. R. Cheeseman, G. Scalmani, V. Barone, G. A. Petersson, H. Nakatsuji, X. Li, M. Caricato, A. V. Marenich, J. Bloino, B. G. Janesko, R. Gomperts, B. Mennucci, H. P. Hratchian, J. V. Ortiz, A. F. Izmaylov, J. L. Sonnenberg, D. Williams-Young, F. Ding, F. Lipparini, F. Egidi, J. Goings, B. Peng, A. Petrone, T. Henderson, D. Ranasinghe, V. G. Zakrzewski, J. Gao, N. Rega, G. Zheng, W. Liang, M. Hada, M. Ehara, K. Toyota, R. Fukuda, J. Hasegawa, M. Ishida, T. Nakajima, Y. Honda, O. Kitao, H. Nakai, T. Vreven, K. Throssell, J. A. Montgomery, Jr, J. E. Peralta, F. Ogliaro, M. J. Bearpark, J. J. Heyd, E. N. Brothers, K. N. Kudin, V. N. Staroverov, T. A. Keith, R. Kobayashi, J. Normand, K. Raghavachari, A. P. Rendell, J. C. Burant, S. S. Iyengar, J. Tomasi, M. Cossi, J. M. Millam, M. Klene, C. Adamo, R. Cammi, J. W. Ochterski, R. L. Martin, K. Morokuma, O.

- Farkas, J. B. Foresman, and D. J. Fox, *Gaussian 16, Revision A.03, Gaussian Inc. 2016*.
- [6] a) A. Dreuw, M. Head-Gordon, *J. Am. Chem. Soc.* **2004**, *126*, 4007–4016; b) C. Fiolhais, Ed, *A Primer in Density Functional Theory*; Springer-Verlag Berlin Heidelberg, Berlin, Heidelberg, **2003**; c) F. Furche, R. Ahlrichs, *J. Chem. Phys.* **2002**, *117*, 7433–7447; d) E. Runge, E. K. U. Gross, *Phys. Rev. Lett.* **1984**, *52*, 997–1000.
 - [7] S. Hirata, M. Head-Gordon, *Chem. Phys. Lett.* **1999**, *314*, 291–299.
 - [8] a) S. Grimme, M. Waletzke, *J. Chem. Phys.* **1999**, *111*, 5645–5655; b) M. Kleinschmidt, C. M. Marian, M. Waletzke, S. Grimme, *J. Chem. Phys.* **2009**, *130*, 44708; c) C. M. Marian, A. Heil, M. Kleinschmidt, *WIREs Comput. Mol. Sci.* **2019**, *9*;
 - [9] I. Lyskov, M. Kleinschmidt, C. M. Marian, *J. Chem. Phys.* **2016**, *144*, 34104.
 - [10] a) A. D. Becke, *J. Chem. Phys.* **1993**, *98*, 1372–1377; b) C. Lee, W. Yang, R. G. Parr, *Phys. Rev. B.* **1988**, *37*, 785–789.
 - [11] TURBOMOLE V7.5 2020. A development of University of Karlsruhe and Forschungszentrum Karlsruhe GmbH, 1989–2007, TURBOMOLE GmbH, since 2007; available from <http://www.turbomole.com>.
 - [12] F. Plasser, *J. Chem. Phys.* **2020**, *152*, 84108.
 - [13] a) B. A. Heß, C. M. Marian, U. Wahlgren, O. Gropen, *Chem. Phys. Lett.* **1996**, *251*, 365–371; b) M. Kleinschmidt, C. M. Marian, *Chem. Phys.* **2005**, *311*, 71–79; c) M. Kleinschmidt, J. Tatchen, C. M. Marian, *J. Comput. Chem.* **2002**, *23*, 824–833; d) M. Kleinschmidt, J. Tatchen, C. M. Marian, *J. Chem. Phys.* **2006**, *124*, 124101; e) B. Schimmelpfennig, *University of Stockholm* **1996**.
 - [14] a) M. Etinski, J. Tatchen, C. M. Marian, *J. Chem. Phys.* **2011**, *134*, 154105; b) M. Etinski, J. Tatchen, C. M. Marian, *Phys. Chem. Chem. Phys.* **2014**, *16*, 4740–4751;
 - [15] D. Jacquemin, B. Moore, A. Planchat, C. Adamo, J. Autschbach, *J. Chem. Theory Comput.* **2014**, *10*, 1677–1685.
 - [16] a) R. Baer, E. Livshits, U. Salzner, *Annu. Rev. Phys. Chem.* **2010**, *61*, 85–109; b) L. Kronik, T. Stein, S. Refaely-Abramson, R. Baer, *J. Chem. Theory Comput.* **2012**, *8*, 1515–1531.

Publication IV

Conformational, Host, and Vibrational Effects Giving Rise to Dynamic TADF Behavior in the Through-Space Charge Transfer, Triptycene Bridged Acridine–Triazine Donor Acceptor TADF Molecule TpAT-tFFO

H. Miranda-Salinas, A. Rodríguez-Serrano, J. M. Kaminski, F. Dinkelbach, N.

Hiromichi, Y. Kusakabe, H. Kaji, C. M. Marian & A. P. Monkman

J. Phys. Chem. C, 127(18):8607–8617, 2023

DOI: 10.1021/acs.jpcc.2c07529

Contribution: Quantum chemical investigation of ground and excited states belonging to conformer (Me→Ph) and computation of all (spin-)vibronic interactions including the calculation of (non-)radiative rate constants within the FC and FC+HT approximation, preparation of Figure 1, contributions to writing the quantum chemical sections and revising the manuscript.

Conformational, Host, and Vibrational Effects Giving Rise to Dynamic TADF Behavior in the Through-Space Charge Transfer, Triptycene Bridged Acridine-Triazine Donor Acceptor TADF Molecule TpAT-tFFO

Hector Miranda-Salinas, Angela Rodriguez-Serrano, Jeremy M. Kaminski, Fabian Dinkelbach, Nakagawa Hiromichi, Yu Kusakabe, Hironori Kaji, Christel M. Marian,* and Andrew P. Monkman*

Cite This: *J. Phys. Chem. C* 2023, 127, 8607–8617

Read Online

ACCESS |

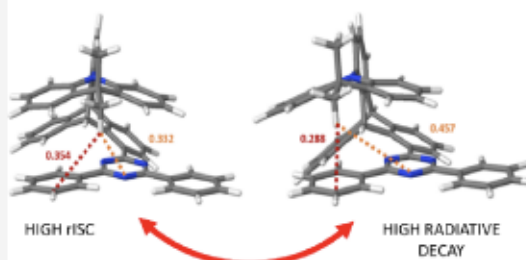
Metrics & More

Article Recommendations

Supporting Information

ABSTRACT: We present a joint experimental and theoretical study of the through-space charge transfer (CT) TADF molecule TpAT-tFFO. The measured fluorescence has a singular Gaussian line shape but two decay components, coming from two distinct molecular CT conformers, energetically only 20 meV apart. We determined the intersystem crossing rate ($1 \times 10^7 \text{ s}^{-1}$) to be 1 order of magnitude faster than radiative decay, and prompt emission (PF) is therefore quenched within 30 ns, leaving delayed fluorescence (DF) observable from 30 ns onward as the measured reverse intersystem crossing (rISC) rate is $>1 \times 10^6 \text{ s}^{-1}$, yielding a DF/PF ratio $>98\%$. Time-resolved emission spectra measured between 30 ns and 900 ms in films show no change in the spectral band shape, but between 50 and 400 ms, we observe a ca. 65 meV red shift of the emission, ascribed to the DF to phosphorescence transition, with the phosphorescence (lifetime $>1 \text{ s}$) emanating from the lowest ^3CT state. A host-independent thermal activation energy of 16 meV is found, indicating that small-amplitude vibrational motions ($\sim 140 \text{ cm}^{-1}$) of the donor with respect to the acceptor dominate rISC. TpAT-tFFO photophysics is dynamic, and these vibrational motions drive the molecule between maximal rISC rate and high radiative decay configurations so that the molecule can be thought to be “self-optimizing” for the best TADF performance.

VIBRATIONAL MOTION CONTROLS DYNAMIC THROUGH-SPACE TADF



INTRODUCTION

A new generation of triplet harvesting organic light-emitting diodes (OLEDs) uses thermally activated delayed fluorescence (TADF) emitter molecules to achieve nearly 100% internal efficiency,¹ without using heavy metals, via the mechanism of reverse intersystem crossing (rISC), harvesting the lowest energy triplet state (^3CT) to the singlet state (^1CT).² However, when the energy difference between these states approaches zero, the $^1\text{CT} \leftrightarrow ^3\text{CT}$ interconversion becomes spin-forbidden because the orbital angular momentum cannot change during the transition.³ Recently, we have shown that in organic TADF molecules, even when the ^3CT and ^1CT energy gap (ΔE_{ST}) is small ($<50 \text{ meV}$), rISC can be very efficient due to rISC mediated by a third triplet excited state through a non-adiabatic vibronic coupled spin–orbit coupling mechanism.^{4,5} Efficient TADF molecules usually have charge transfer excited states with effective spatial decoupling between the electron in the lowest unoccupied molecular orbital (LUMO) and its partner in the highest occupied molecular orbital (HOMO),⁶ which minimizes the electron exchange energy and ΔE_{ST} . This is most commonly achieved by conformational twisting of

the donor (D) relative to the acceptor (A) moieties, typically about a N–C bridging bond that naturally introduces a large dihedral angle, approaching 90° , giving effective decoupling of the electron and hole.⁷ This is an example of a through-bond charge transfer (TBCT) across a physical (conjugating) bridge bond between D and A.^{8,9} An electronically decoupled D–A charge transfer state can also form between separate D and A molecules when they are in close contact, forming a bimolecular exciplex state. In some cases, these exciplexes also show efficient TADF through the same non-adiabatic vibronic coupled spin–orbit coupling mechanism.¹⁰ In this case, the electronic decoupling is achieved by a large physical spatial separation of the electron and hole in the excited state. This is an example of through-space charge transfer (TSCT),

Received: October 26, 2022

Revised: April 12, 2023

Published: April 27, 2023



CT between the physically separated D and A. In both cases, the excited CT state has a very high dipole moment and is highly sensitive to its external environment, such as solvent polarity, leading to large solvatochromic shifts in solutions of increasing solvent polarity.^{11,12}

Alternatively, TSCT spatial separation can be achieved with an inert scaffold unit acting as the bridge between D and A units. Here, the spatial separation must be small enough to maintain some π -wavefunction interaction between them.^{13,14} In recent years, studies on TSCT have led researchers to come forward with designs that help to optimize this kind of CT state^{9,15,16} based on the success of exciplex systems that yield very efficient TADF but in uncontrolled and highly inhomogeneous systems.¹⁷ The strategy used by Wada *et al.*¹⁸ in **TpAT-tFFO** is by far better in this regard using D and A moieties that yield efficient second-order vibronic coupled spin–orbit coupling,^{4,19,20} combined with an (electronically inert) triptycene scaffold to optimize the spatial separation in a tilted face-to-face (tFF) alignment of acceptor and donor moieties, with an optimized separation distance (tFFO), a key factor to develop new and more efficient TSCT TADF materials. The system fulfills the requirements for a non-adiabatic vibronic coupled spin–orbit coupling mechanism, i.e., having near degenerate ¹CT, ³CT, and ³LE excited states. Recent studies on other TSCT systems have shown that the competition between TBCT and TSCT in a molecule can occur and also that the scaffold bridge unit can be involved in the CT states.²¹

Here, we present in-depth photophysical studies combined with results from high level DFT-MRCI theoretical calculations of **TpAT-tFFO**, which are described in detail in our sister paper,²² exploring the behavior of the TSCT states in different solvents and solid host matrix environments to fully understand TADF from such controlled TSCT molecules. The **TpAT-tFFO** molecule is composed of 9,9-dimethyl-9,10-dihydroacridine (**DMAC**) and 2,4-diphenyl-1,3,5-triazine (**dPT**) as D and A, respectively (Figure 1). These units are known to give CT states in a variety of D–A molecules²³ and

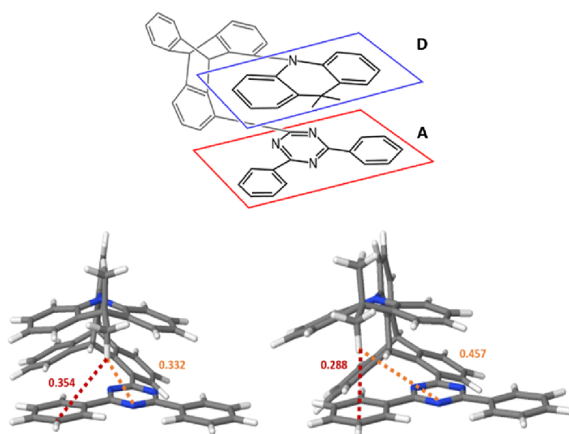


Figure 1. Chemical structure of **TpAT-tFFO** and the two lowest energy conformers found computationally, named S_0 (Me \rightarrow N) and S_0 (Me \rightarrow Ph). The conformers were named after the distances between the proximal methyl hydrogen atom of the **DMAC** donor and the triazine (orange) or phenyl (red) rings of the acceptor, given in nanometers.

D–A exciplexes. As an inert scaffold (bridge), a triptycene (**Tp**) unit is used to obtain the desired optimal spatial separation of D and A units.^{24,25} Using triptycene as a scaffold allows the D and A to take up a tFF configuration, which is believed to be critical for efficient magnetic coupling required for high spin–orbit coupling (SOC) and efficient TADF.¹⁸ Our computational analysis has identified two distinct stable low energy conformers of **TpAT-tFFO** (Figure 1), which however complicates the photophysics of **TpAT-tFFO**. These have very similar electronic structures and energies but have a large energy barrier for interconversion in the excited state, which should manifest in the solid-state photophysics of the material.

METHODS

Steady State. Photoluminescence measurements were obtained using drop cast films on sapphire substrates at 1% by weight for zeonex and 10% by weight for the other hosts, and for the solution measurement, concentrations of 20 μM were used. A Jobin Yvon Horiba Fluoromax-3 and a spectrophotometer Shimadzu UV–vis–NIR 3600 were used for emission and absorption measurements, respectively. All spectral onset energies were corrected using the Jacobian conversion of wavelengths to energies.

Time-Resolved Measurements. The time-resolved measurements were obtained using a gated iCCD camera (250–950 nm) system, and for the temperature-dependent measurements, a helium-closed cycle cryopump, with optical windows, Si thermodiode, and sample mount, attached directly to the cold head. TCSPC measurements were recorded with a Horiba DeltaFlex TCSPC system using a Horiba NanoLED 357 nm and SpectraLED 330 nm as light sources.

Computations. The computational protocol closely resembles the one followed in ref 26. In short, (time-dependent) density functional theory PBE0/SV(P) was utilized to compute equilibrium geometries and vibrational frequencies whereas excitation energies, transition dipole moments, and wavefunctions for subsequent spin–orbit coupling calculations were computed using a multireference configuration interaction approach employing the DFT/MRCI-R2016 Hamiltonian. Rate constants of radiative and nonradiative transitions were calculated including vibronic interactions at the Herzberg–Teller level of theory. For programs and further technical details of the calculations, we refer to a sister paper.²²

RESULTS

Absorption and emission spectra of **TpAT-tFFO** were measured in three different solvents (aerated and degassed): methylcyclohexane (MCH), toluene (PhMe), and acetonitrile (MeCN) (Figure 2a,b). The main absorption peak is seen at 271 nm ($\epsilon = 1.3 \times 10^5 \text{ cm}^{-1} \text{ M}^{-1}$), which matches well with both the absorption band of the **DMAC** donor unit²⁷ and the triphenyltriazine acceptor band.¹⁴ Calculations confirm that the local $\pi\pi^*$ excitations of both the acceptor (285 nm) and donor (275 nm) occur in this spectral region.

We further observe an absorption feature on the red edge of these strong $\pi\pi^*$ bands, at ca. 300–320 nm ($\epsilon = 7.5 \times 10^3 \text{ cm}^{-1} \text{ M}^{-1}$), which is more clearly seen in excitation spectra monitored at the peak of the CT emission band (Figure 3a and Figures S1–S6). Computational studies reveal this transition (labeled S_0 – S_3) to be a composite transition from the

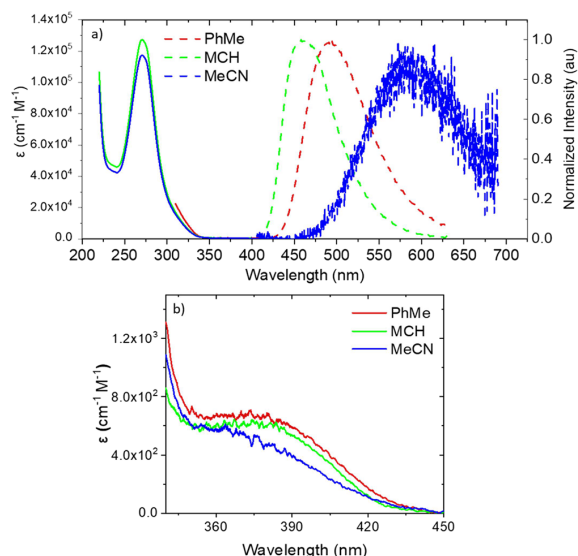


Figure 2. (a) Solution-state PL measurements, solid lines correspond to absorption and dashed lines correspond to emission (toluene absorption spectra were only 310 nm because of the solvent cutoff). (b) Absorption in the spectral region of 340–440 nm showing a weak solvent-dependent direct charge transfer transition below the lowest energy $\pi\pi^*$ transition.

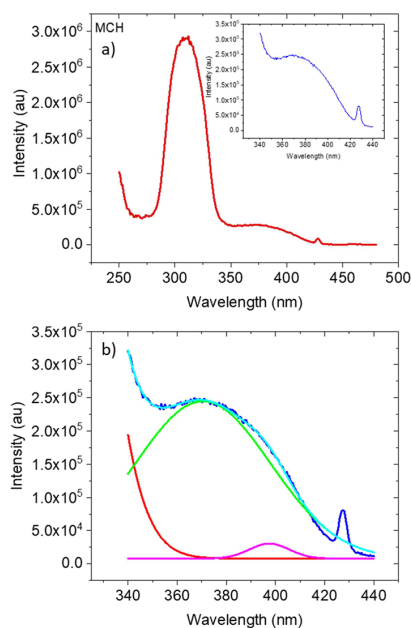


Figure 3. (a) Excitation spectrum of TpAT-tFFO dissolved in MCH; the inset shows well-resolved direct CT absorption below 340 nm and (b) close inspection of the 340–420 nm band (dark blue) fitted (light blue) with two exponential components (green and pink). The red curve represents the tail of the S_3 band. The spike at 427 nm is a solvent Raman band with a monitored emission wavelength of 490 nm.

tritycene bridge to the triazine CT state mixed with a local excitation on the triptycene, having moderate oscillator

strength $\epsilon = 5 \times 10^3 \text{ cm}^{-1} \text{ M}^{-1}$. Excitation spectra in aerated solution (Figure S7a) show that this transition gives prompt CT emission by pseudo-TBCT excitation. The excitation-dependent CT emission is constant for excitation between 300 and 370 nm (Figure S7b), showing that the triptycene bridge is involved in low energy excitations of the molecule. Further, excitation of the 300–320 nm band gives a weak but measurable emission in the range of 350–425 nm (Figure S7b), whereas excitation above 320 nm gives no such emission. This we believe arises from the triazine $\pi\pi^*$ state before charge separation occurs,²¹ indicative of the weak through-space electronic coupling between triazine and acridine units, allowing the triazine decay to compete to a small degree with the electron transfer step. Figure 2b and Figures S4–S6 also show a further, very low extinction absorption feature, *ca.* $\epsilon = 7 \times 10^2 \text{ cm}^{-1} \text{ M}^{-1}$ below this transition in the range of 340–420 nm, which we associated with direct through-space CT absorption. Again, this band is more clearly seen in the excitation spectra (Figures S1–S3). Gaussian deconvolution of the absorption and excitation spectra (Figure 3b and Figures S1–S3) reveals two Gaussian components, peak wavelengths of 370 and 395 nm, with extinction coefficients of *ca.* 6×10^2 and $3 \times 10^2 \text{ cm}^{-1} \text{ M}^{-1}$, respectively. The main 370 nm feature is assigned to the lowest lying S_0 – S_1 and S_0 – S_2 CT transitions of each conformer. Calculations suggest that depending on the molecular conformer, the ratios of extinction coefficients between the 275 nm $\pi\pi^*$ transition and these transitions will be *ca.* 10 for the S_0 (Me \rightarrow N) conformer and *ca.* 40 for the S_0 (Me \rightarrow Ph) conformer. Experimentally, we find a ratio very close to 40 between the two transitions (Figure 2b), indicating a predominance of the slightly more stable but higher CT energy S_0 (Me \rightarrow Ph) conformer at room temperature in solution. However, we cannot spectrally resolve the S_0 – S_1 and S_0 – S_2 pair of (direct CT) absorptions in solution (Figure 3b). Calculations suggest that the difference of the S_0 – S_1 and S_0 – S_2 energies for the conformers is only 20 meV. The extremely weak band observed at *ca.* 400 nm may be due to residual dimers/aggregates. However, excitation at this wavelength still results in an emission spectrum identical to TpAT-tFFO CT emission (Figure S4), most likely due to the residual tail absorption from the direct CT transitions.

In highly polar MeCN, we only observe a 360 nm band. These direct CT absorption bands show a little (instantaneous) blue shift with increasing solvent polarity, potentially indicating $n\pi^*$ character. Degassed excitation spectra (250–425 nm) show a uniform increase by nearly a factor of 100, indicating the very high DF contribution to the total emission spectra (Figure S4a).

The onsets of CT emission in MCH, PhMe, and MeCN are found to be 2.99, 2.86, and 2.57 eV, respectively (Figure 2a). Emission in MeCN is very weak compared to that observed in the less polar solvents. The solution measurements were made both in the presence of oxygen and degassed, and the effect of degassing the solutions is shown in Figure S5 where it is seen that oxygen quenches the CT emission very effectively, indicating the very large contribution of delayed CT emission to the overall luminescence of TpAT-tFFO. The largest DF contribution is observed in PhMe, accounting for some 98.70% of the total luminescence, followed by MCH with 93.62% and the smallest in MeCN with 88.87% (Table 1) and indicates very fast intersystem crossing rates from ^1CT , much faster than radiative decay rates.

Table 1. Degassed and Oxygenated Solution Measurement Data

solvent	τ_{PF1} [ns]	τ_{PF2} [ns]	τ_{DF1} [μ s]	τ_{DF2} [μ s]	k_{F} [10^5 s^{-1}]	k_{ISC} [10^6 s^{-1}]	k_{ISC} [10^5 s^{-1}]	DF/PF
MCH	8.0 ± 0.42	70.88 ± 18.89	1.64 ± 0.03		19.05 ± 1.48	11.31 ± 0.28	11.29 ± 1.00	93.62%
PhMe	7.9 ± 0.77	48.9 ± 6.37	4.4 ± 0.10		34.70 ± 1.91	12.54 ± 2.75	31.91 ± 1.63	98.7%
MeCN	14.71 ± 1.45	88.26 ± 26.60	0.62 ± 0.01	16.2 ± 0.65	36.89 ± 0.00	9.81 ± 0.00	0.74 ± 0.00	88.87%

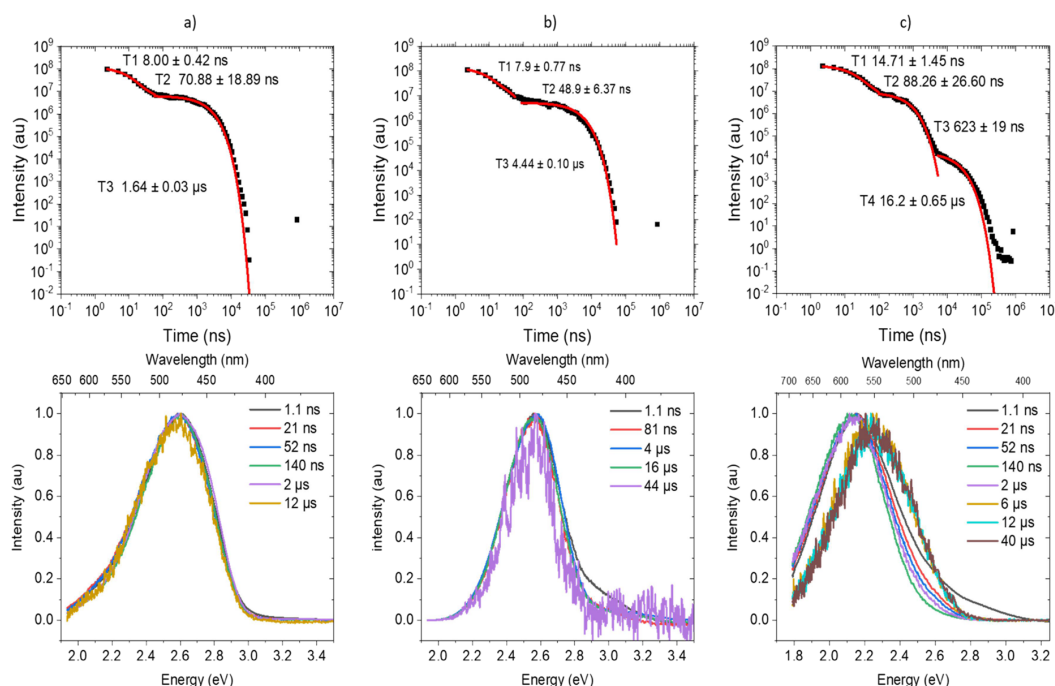


Figure 4. Time-resolved degassed measurements of TpAT-tFFO in (a) MCH, (b) PhMe, and (c) MeCN solutions.

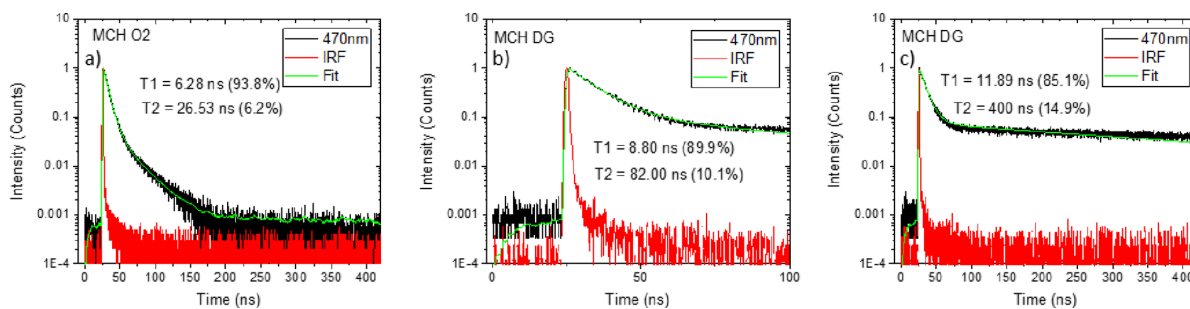


Figure 5. TCSPC decay measurements of TpAT tFFO in MCH measured in (a) aerated solution, (b) degassed, and (c) degassed in a longer time range.

To observe the differences that exist in the molecule while changing the medium, steady-state emission measurements were done in films for TpAT-tFFO; same as in solution, the compound shows only CT emission, with onsets at 2.96, 2.89, 2.86, and 2.93 eV for zeonex, UGH-3, mCBP, and CzSi host matrices, respectively. The carbazole containing hosts (mCBP and CzSi) show an additional emission peak at 371 nm, coming from the host because of the unavoidable overlap of host and guest absorption bands (Figure S6). The steady-state emission in the hosts shows little correlation between host properties such as dielectric strength and the CT energy in this molecule.²⁸

Time-resolved TpAT-tFFO emission in solution shows classic TADF decay kinetics. In toluene and MCH, we observe initial fast prompt and then delayed CT emission. However, the prompt decay has two decay components with lifetimes of 8 and 50–70 ns but only one Gaussian emission band. The delayed CT emission is mono exponential with a solvent-dependent lifetime of 1.6–4.4 μ s (Figure 4a,b and Figures S7 and S8). In aerated solutions, the DF emission is effectively quenched and only the two-prompt decay components are observed. Time-correlated single-photon counting (TCSPC) measurements in MCH (Figure 5a,b, toluene; Figure S7) are rather enlightening. In aerated MCH solution, we confirm two

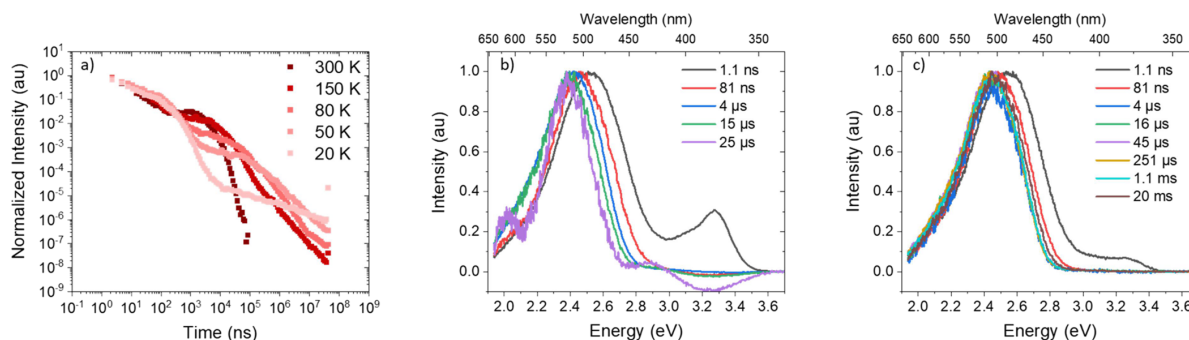


Figure 6. (a) Temperature-dependent decays and spectra of TpAT-tFFO using a mCBP matrix. Emission observed at very early times in the 350–425 nm region comes from the host mCBP as the absorption of the host overlaps with the TpAT-tFFO at the 355 nm laser excitation wavelength, at temperatures of (b) 300 K and (c) 50 K. Further temperatures are shown in Figures S14 and S15.

prompt decay lifetimes of 6.3 ns (94%) and 26.5 ns (6%); toluene is almost identical. In degassed MCH, the DF decay is very strong being the dominant component from about 30 ns onward, see the plateau in the TCSPC decays in Figure 5b,c. This completely skews the estimation of the second “prompt” decay time in degassed conditions, especially given its very low amplitude. However, in degassed solution, we observe the same emission spectra from 1 to 12–44 μs (Figure 4b). Given that we observe that DF dominates after *ca.* 30 ns, this implies that radiative decay of the prompt ¹CT state is very slow and so rapidly quenched by much faster ISC; in this kind of long-lived prompt emission, the presence of self-quenching by oxygen has been reported before.^{29,30} Also, rISC must be fast as well. Clearly, this TSCT TpAT-tFFO molecule has strong magnetic coupling between its CT and locally excited (LE) states. The relatively fast rISC then produces enough DF emission to be observed after 30 ns, but the rISC process still has a lifetime in the microsecond regime; simply put, it is not ultrafast. As all the prompt signals are quenched, we can see the DF signal from very earlier times.

From our calculations, we ascribed the two ¹CT decay components at the same emission wavelengths to arise from the two conformers of TpAT-tFFO (Figure 1). In the ground state, the energy barrier between the two conformers is shallow, allowing rapid interconversion between the two, especially in solution. However, in the excited state, the energy barrier for interconversion is much larger because of the larger molecular structural rearrangement required, allowing us to observe both emission decay components, but for long time DF emission, only one conformer contributes, as will be described later.

Taking the fluorescence quantum yield measured by Wada *et al.*¹⁸ in toluene, 84%, and the prompt lifetimes of the two conformers in aerated toluene measured by TCSPC, 8.4 and 30 ns, we calculate from the ratio of the areas of steady-state emission measured in aerated and degassed solutions that the PLQY of the prompt emission component is 2% (Figure S5). From this, we obtain radiative lifetimes of 420 ns and 1.5 μs and radiative decay rates of 2.38×10^6 and 6.67×10^5 s⁻¹, respectively, for the two conformer species. These are in good agreement with the rates determined from our kinetic fitting (Table 1) and with our calculated S₁ → S₀ (Me → N) radiative decay rate of 7.0×10^5 s⁻¹ and S₂ → S₀ (Me → Ph) radiative decay rate of 2.0×10^5 s⁻¹. These are very long indicative of weak coupling between the CT and ground state.

In MeCN, we observe more complicated photophysics with lifetimes and spectral components highly modified by the strongly polar environment (Figure 4c and Figure S9a) and are discussed in the Supporting Information.

Kinetic model fitting²⁹ of the decay curves yields rISC rates for the DF observed, in toluene of 3.2×10^6 and 1.1×10^6 s⁻¹ in MCH, which are very fast. In MeCN, taking the slow decay component to be true DF, we calculate a rISC rate of *ca.* 7.5×10^4 s⁻¹, in line with a much larger singlet–triplet gap. Data for TpAT-tFFO in degassed solution is given in Table 1. The peak in the DF/PF ratio in toluene indicates that in low polarity media, the ³CT state lies above the (mediating) ³LE state. In toluene, the energy gap between them is at its smallest, while in MeCN, the ³CT has dropped below ³LE opening up the singlet–triplet energy gap again, a behavior seen in many TADF materials.⁴

Time-resolved measurements of TpAT-tFFO in various hosts were also made as a function of temperature. All rate constants and lifetimes were determined using the fitting method reported by Haase *et al.*³¹ Measurements were made from 300 to 20 K. For TpAT-tFFO (10%) in the mCBP host (Figure 6b shows the 300 K decay and spectra), the emission has an onset energy of 2.818 ± 0.005 eV, which rapidly red-shifts over the first 100 ns by *ca.* 150 meV. This shift is found to be both host- and temperature-dependent but is not observed in MCH or toluene solution measurements. At 300 K, both prompt and delayed fluorescence CT decays are faster than at lower temperatures, showing that both ISC and rISC rates are thermally activated processes (Table 2). We also observe that the red shift of the CT state is less pronounced at low temperature (Figure 6b,c), which we take as an indication that in solid-state hosts, the D and A units have some conformational inhomogeneity yielding a distribution of CT energies and rISC rates.³⁶ At 300 K, a rISC rate of 1.1×10^6 s⁻¹ is found in mCBP (Table 2). As the temperature is

Table 2. Rate Constants for the Different Temperatures of the mCBP Matrix Time-Resolved Measurements

mCBP (10%)			
T [K]	K_F [10^5 s ⁻¹]	K_{ISC} [10^6 s ⁻¹]	K_{rISC} [10^5 s ⁻¹]
300	8.22 ± 0.1	8.97 ± 0.11	$11.21 \pm -$
150	4.99 ± 0.06	7.29 ± 0.10	$3.56 \pm -$
80	3.97 ± 0.03	2.05 ± 0.15	0.48 ± 0.04
50	6.98 ± 0.55	1.00 ± 0.02	$0.11 \pm -$

reduced, both ISC and rISC rates decrease, showing that ISC is also a thermally activated process, governed by a second-order vibrational coupling mechanism controlling ^1CT to ^3CT ISC in the direct analogue to rISC, the first clear observation of this fact in TADF materials.³ We also observe the onset of a long-time non-exponential tail in the DF emission at low temperature, even at 20 K. A very similar behavior is observed in the other small molecule hosts, CzSi and UGH-3 (Table 3)

Table 3. Onset Energies Measured Using Different Hosts: Zeonex, UGH-3, mCBP, and CzSi

host	^1LE (eV)	^1CT (eV)	^3CT (eV)	ΔE_{ST} (eV)
UGH-3		2.853	2.839	0.014
mCBP	3.495	2.818	2.800	0.018
CzSi	3.496	2.893	2.877	0.016
zeonex	3.489	2.943	2.930	0.013

and Figures S11–S13, S16, and S17 and Tables S1–S3). In mCBP at 20 K strong phosphorescence emission, an onset at 2.9 ± 0.005 eV is observed (even at 900 ms time delays; Figure 7c).

In all solid-state hosts, room temperature rISC rates are above $1 \times 10^6 \text{ s}^{-1}$ but not as high as found in toluene. We find that the energies of the ^1CT state change slightly from host to host, but from the temperature-dependent ISC and rISC rates,

we determine an identical thermal activation energy for the non-adiabatic coupling^{19,32} of *ca.* 17 meV (Figure S22), independent of the host. The vibrational mode that couples the triplet states to mediate the rISC mechanism is calculated to be the 1600 cm^{-1} (200 meV) breathing mode of the triazine unit, whereas 17 meV corresponds to a vibrational mode of 140 cm^{-1} . Our calculations indicate that such low energy torsional modes of D with respect to A units greatly affect both the ΔE_{ST} gap and SOCME, and so, freezing-out of these vibrational motions at low temperatures has a large effect on the rISC rate. This would explain the host-independent behavior of this activated process. As the temperature is reduced, we see a smaller monotonic red shift over the DF lifetime, and below 150 K, the DF emission is always *ca.* 50 meV higher than observed at 300 K. This is in line with the interconversion of the two conformers that requires thermal energy to overcome the large energy barrier of the structural reorganization. Thus, less of the lower GS energy conformer (Me \rightarrow Ph), which has a higher CT energy, will interconvert to the high GS energy but lower CT energy (Me \rightarrow N) species at low temperatures in the solid state, giving rise to the bluer DF emission at low temperatures. The prompt relaxation over 400 ns is then representative of contributions from the fast and slow conformers with much slower interconversion than in solution (Figures S12 and S13), along with the effects of inhomogeneity causing a distribution of rISC rates in both cases.

Importantly, in zeonex films, we observe only a very small red shift (20–30 meV) of the CT state energy from 1 ns (our time resolution) to 20 ms (Figures S19 and S20), in line with a very homogeneous D–A spatial conformation. As in MCH solution, the prompt emission has two decay components, *ca.* 8.1 and 100 ns, along with a mono exponentially decaying DF with a lifetime of 5.8 μs . Given that zeonex is a low-density amorphous polymer having non-symmetrical branched side chains, it therefore has a great deal of free volume to allow the D and A units of the TpAT-tFFO molecule to rearrange very rapidly after photoexcitation compared to the more hindered motion in the tightly packed small molecule host matrices. In this sense, zeonex acts very much like a viscous fluid and so the TpAT-tFFO behaves as in solution. In the time-resolved heat maps measured in zeonex, we observe a very small red shift (less than 5 nm), which could indicate the two conformer populations reaching equilibrium, but on a slower time scale than in MCH in line with the much greater “viscosity” of zeonex. Also, as with the small molecule hosts, we do observe the grow-in of a power law, long life-time DF tail (Figure S11). In all solid-state hosts, the rISC rate seems rather independent of the host.

Finally, using TpAT-tFFO zeonex and mCBP films at 20 and 80 K, respectively, time-resolved spectra at very long decay times were measured (Figure 7a and Figures S15 and S21). We observe no change in emission spectra from 30 ns until 50 ms, DF having the same onset energy as ^1CT prompt emission. In zeonex at 20 K, a gradual red shift from 50 ms until 400 ms is observed. Emission can be seen by eye even after 10 s, and our lowest laser repetition rate is 1 Hz, so we are limited to 900 ms delay time measurements. This ultralong-lived emission has an invariant spectral band shape. No change in the vibronic structure is seen, even at 900 ms. Comparing the band onset at 50 ms to that at 900 ms, we estimated a red shift of 50–75 meV (Figure 7b). Fitting the long-time emission decay in mCBP measured at 80 K gives two lifetimes, 50 ms and 1.1 s.

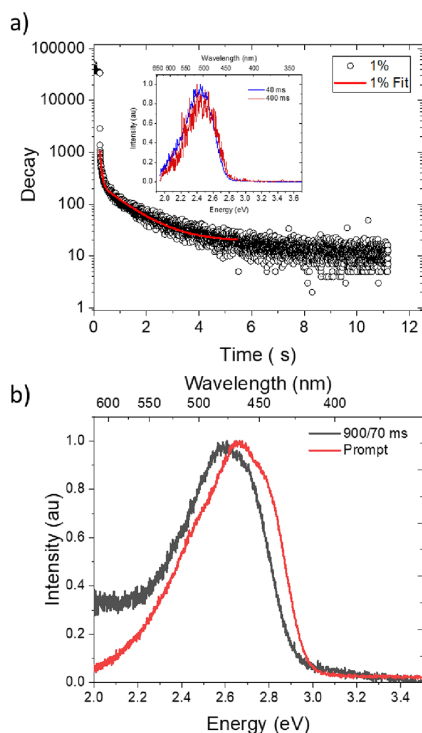


Figure 7. (a) Long-time decay of emission from a mCBP 1% TpAT-tFFO film fitted with a biexponential curve with lifetimes of 56 ms and 1.1 s. The inset shows the emission spectra recorded at 40 and 400 ms, showing that the two decay components come from energetically identical species. (b) Comparison of prompt fluorescence with 900 ms delayed phosphorescence measured at 20 K for a TpAT-tFFO zeonex film.

This we believe shows the emergence of phosphorescence from the DF at 50–100 ms.

DISCUSSION

In the solution-state measurements, we observe direct CT absorption indicating a ground state through-space interaction via the π -wavefunction overlap between D and A units in **TpAT-tFFO**. These bands show weak negative solvatochromism, indicating some n – π mixing in the orbitals involved. Clear TADF is observed from these CT states, and toluene gives an extremely large DF/PF ratio (98.7%), indicating the dominance of ISC over the radiative decay of the singlet CT state. Taking the lowest triplet energy from solid-state phosphorescence measurements, we estimated a very small singlet–triplet energy gap (<20 meV) in toluene, optimal for the largest rISC rate we observe. Such a small S–T gap indicates that the local ^3LE triplet state must be mediating the rISC in this TSCT system. **TpAT-tFFO** emission in toluene and MCH shows no spectral shift over all measurement times, yet the PF is biexponential. This is explained by the presence of two structural conformers, having nearly degenerate CT energies but different (slow) radiative decay rates, as we find from our computational modeling, where an energy difference of only 20 meV between energy states of each conformer is calculated. In both species, the ISC is an order of magnitude faster than radiative decay and so rapidly quenches the slow prompt emission. From TCSPC, we see the effect of this rapid quenching in that DF is observed to take over emission from 30 ns $k_{\text{ISC}} = 3.2 \times 10^6 \text{ s}^{-1}$, but as the prompt emission is quenched within 30 ns, we observe DF from this time onward. The calculated value for $k_{\text{ISC}} = 1 \times 10^7 \text{ s}^{-1}$ is in good agreement with the experimental value obtained here. In **TpAT-tFFO**, prompt emission is rapidly quenched by fast ISC, but rISC is also fast and rISC is very effective. Thus, the DF contribution is seen to be the major contribution to emission, see Figure S8. Hence, in toluene, where the exchange energy is minimal, the prompt component is very small but DF is very high, so overall, the PLQY is very high. PLQY is also enhanced because the ^3CT state is the lowest triplet state of the molecule. All triplets are effectively trapped in this state having both very weak very long-lived phosphorescence, which also indicates that non-radiative decay is virtually zero. The ^3CT state therefore acts as a triplet reservoir, allowing almost all triplets to be up-converted to the singlet state by the rISC mechanism.

Both conformers are found to have very long radiative lifetimes, 420 ns for the S_2 (Me \rightarrow N) conformer and 1.5 μs for the S_1 (Me \rightarrow Ph). These states have a large energy barrier for interconversion in the excited state; however, in the ground state, calculations show that vibrational torsional motion of the D with respect to the A units effectively drives interconversion of the conformers.

In the solid state, unsurprisingly, zeonex gives a very similar CT energy to MCH solution, with <5 nm red shift over time. Meanwhile, small molecule hosts that pack more closely hinder possible molecular reconfiguration and motion and we observe a slow red shift over tens of nanoseconds of the prompt emission. At low temperature, this relaxation slows down further, indicating possible interconversion of conformers or simple energy relaxation through a small thermally activated D–A rearrangement required to overcome the large reorganization energy between the two forms. As the (Me \rightarrow Ph) conformer is slightly more stable in the electronic ground

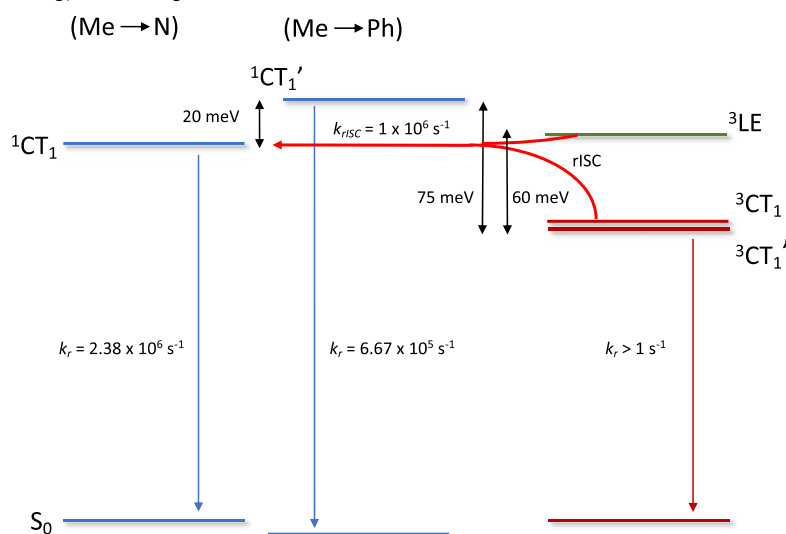
state, we should expect an increase in population (of this higher energy CT state) at lower temperatures relative to the (Me \rightarrow N) conformer. These long-lived (Me \rightarrow Ph) conformers give rise to the increasing (blue-shifted) long-time DF tail and bluer overall DF emission that we observe at low temperature, indicative of less efficient slower rISC from these species.

In the CzSi host, we observe only a very small time-dependent red shift at all temperatures, confirming the nature of the host molecule packing and its interactions with the emitter controlling this mechanism. High rISC rates are found in all solid-state hosts, above $1 \times 10^6 \text{ s}^{-1}$ and reaching $2.6 \times 10^6 \text{ s}^{-1}$ in UGH-3. In all cases, we observe that both ISC and rISC are temperature-dependent, clearly showing that both are mediated by vibronic coupling. From RT to 20 K, the rate of ISC decreases by an order of magnitude, whereas the rISC rate decreases by around 2 orders of magnitude, which indicates different mechanisms controlling these processes.

Given the similar small energy gaps found in all hosts, especially at room temperature, UGH-3 stands out with a rISC rate greater by a factor of 2 compared to the other hosts. As all hosts used have low polarizability, we believe that UGH-3 packs with **TpAT-tFFO** to give a more optimal D–A spatial overlap configuration that enhances the magnetic coupling (SOC) between them. This might not be the lowest energy equilibrium geometry of the molecule however but indicates the way to optimize TSCT rISC, e.g., by stabilizing the (Me \rightarrow N) fast rISC conformer, for example, in the case of **TpAT-tFFO**.

Our calculations reveal that the (Me \rightarrow Ph) conformer has lower SOC and vibronic coupling at lower temperature, and this supports our idea that a growing population of (Me \rightarrow Ph) conformers at low temperature gives rise to the observed increasing long-time non-exponential tail DF contribution. The conformers are unable to interconvert because of the host packing and lack of thermal energy to drive the interconversion over the large energy barrier in the excited state. Calculations also show that the optical transition probability is very sensitive to the singlet–triplet energy gap, and at low temperature, any frozen-in inhomogeneity will cause a large dispersion in the rISC rates. Thus, at room temperature, we observe no long-lived DF tail because all slow rISC (Me \rightarrow Ph) conformers can convert to fast rISC ones (Me \rightarrow N). Also, in solution, this conversion is fast so no tail is observed as well. In this case, thermal disorder is minimized at RT and the long-lived DF tail is greatest at low temperature. The vibrational mode that drives the interchange between the two conformers is shown in Figure S24 and can best be described as a torsional rocking motion of the D with respect to the A. From the experimental verification of the two interconverting near isoenergetic conformers having very different radiative lifetimes, ISC and rISC rates combined with the theoretical identification of the sensitivity of these parameters to the separation and orientation of the D and A units, we see that vibrational motion must play a very important role in dictating these important rates.

Further, at high temperatures, this thermal motion will enable each molecule to dynamically access a range of D and A spatial configurations such that both a fast rISC rate and a fast radiative decay rate molecular configuration can be dynamically accessed on the vibrational time scale. Thus, both highly efficient emission (PLQY >90%) and fast rISC ($>2 \times 10^6 \text{ s}^{-1}$) can be achieved simultaneously. Calculations show that

Scheme 1. Proposed Energy State Diagram^a

^aThe diagram is for the lowest energy states of the conformers (Me → N)¹CT₁ and ³CT₁ and (Me → Ph)¹CT₁' and ³CT₁', based on the S₀ (Me → Ph) reference following the nomenclature used in our sister theory paper (Figure S27 of ref 22). The (Me → N)–(Me → Ph) energy splitting is taken from theoretical estimates, and other energies are the experimentally determined values from the 50 ms delayed fluorescence and 900 ms phosphorescence measured at 20 K. The ³LE energy is taken as that previously reported by us for triaxene.¹⁴ The rISC rate is taken as the fastest rate calculated from the room-temperature delayed fluorescence decay. Radiative decay rates are experimentally determined as described in the text.

displacements along the low frequency mode 1 (Figure S27) accomplish the interconversion of the conformers in the electronic ground state and that two further low frequency vibrational modes, 9 and 12 (Figure S25), mostly affect the donor–acceptor interplanar distance and thus the ΔE_{ST} gap, oscillator strength, and rISC rate. These latter modes effectively cause rocking and distortion of the D and A units such that a D–A pair moves closer and further apart from each other and changes face-to-face orientation dynamically, changing the D–A wavefunction overlap. Our calculations indicate that vibrational motion along any of these three modes readily leads to S₁–T₃ crossing, i.e., ¹CT–³LE mixing (Figures S24 and S25), with mode 1 also causing large changes in the SOCME for the S₁–T₃ transition. Further, mode 9 and mode 12 have a major impact on the oscillator strength of the S₁ and S₂ states, respectively. Experimentally, we observe a host-independent thermal activation energy of 17 meV (140 cm⁻¹) fully in-line with reduced rISC because these low energy torsional modes are frozen out. These observations and calculations together strongly suggest that these thermally driven vibrational motions of the molecule (relative D–A motions) enhance rISC rates, not only by increasing vibronic coupling but also by allowing the molecule to sample very small ¹CT–³LE and ³CT–³LE ΔE_{ST} gap configurations. This motion also enhances rISC by increasing the SOC coupling while at the same time induces large changes in oscillator strength, increasing the radiative decay rate. Thus, the rISC and radiative decay rates will change in step with the different vibrational motions of the molecule, i.e., dynamic oscillations between high rISC and then high radiative decay, taking the two conformers having very different rates as well defined fixed high and low points. One can think of this as the molecule oscillating between high rISC rate and high radiative decay rate

configurations. This is dynamic photophysics on vibrational time scales.

In zeonex films, we clearly observe a transition from DF to phosphorescence between 50 and 400 ms, accompanied by a 50–75 meV red shift in emission but no change in the emission band shape. From comparison to our previous measurements of the phosphorescence from triaxene¹⁴ and the phosphorescence measured at 900 ms, we estimate that the phosphorescence in **TpAT-tFFO** is *ca.* 60–80 meV lower in energy than the triaxene acceptor. Calculations also consistently show that the first LE triplet state, T₃ (of the triaxene acceptor), is energetically above T₁, T₂, and ³CT states and that the T₃ state emission band should have the vibronic structure (Figure S23). Thus, the observed red shift from 50 to 400 ms in the spectra is not consistent with phosphorescence from the T₃ LE state. The calculated radiative rate constant for the T₃ phosphorescence is an order of 1 s⁻¹, whereas for the CT triplet states, T₁ and T₂, the decay rate is even slower, *ca.* 10⁻¹ s⁻¹ (in agreement with our visual observation of phosphorescence emission beyond 10 s). We are able to observe phosphorescence at such long times, indicating that whereas the ISC mechanism is still active at 20 K, rISC has been greatly slowed down, leaving a high CT triplet population that can decay radiatively. Additionally, in mCBP, we observe the long-lived phosphorescence at 80 K, and in zeonex, the phosphorescence is quenched at 80 K (Figure S21). This suggests that some molecular motion/reorganization present at 80 K in zeonex switches on TADF, whereas in the small molecule hosts with tight packing, this degree of freedom is hindered such that we still observe the phosphorescence at 80 K. Taken all together, especially the red shift in the spectra, the lack of vibronic structure, and the exceedingly long lifetime of the longest emission, we conclude that the weight of experimental and theoretical evidence supports this phosphor-

escence to come from a triplet charge transfer state (^3CT). This represents the strongest evidence so far for radiative decay of a triplet CT excited state.

In **TpAT-tFFO**, all the lowest energy singlet and triplet states are extremely close to each other energetically, so energy gaps are always very small, effectively nearly independent of temperature. In this case, the rISC rate must then depend far more on the dynamic vibrational coupling mechanisms, and vibrational adiabatic coupling only changes the state populations. As the average rISC rate slows down, a larger CT triplet population will build up leading to CT phosphorescence. As the ^3LE local state is above ^3CT , the possibility of triplet–triplet annihilation (TTA) through the highly immobile CT triplets contributing to the DF is remote,³³ compounded by the low concentration of **TpAT-tFFO** molecules in the high triplet energy hosts studied here.

From all of our results on the triplet states in **TpAT-tFFO**, we can understand why the TADF is so efficient in this TSCT system. **Scheme 1** shows the energy alignment of the three states directly involved in TADF. We see that even though the gap between ^1CT and ^3CT is approximately 50–75 meV, ^3LE is close to ^1CT , which means that they will have a large Franck–Condon overlap, so the rISC (and ISC) step will be very efficient, and most probably the non-adiabatic coupling between ^3CT and ^3LE dominates the temperature dependence of rISC. As discussed by Gibson and Penfold,¹⁹ this configuration of states should give rise to faster and more efficient rISC because the adiabatic coupling is active even at very low temperatures, with low energy torsional modes of D with respect to A greatly contributing to both high rISC and oscillator strength in a dynamic fashion. This is observable in the TSCT **TpAT-tFFO** because the triptycene scaffold holds the D and A units in an average position that ensures very small electron exchange energy such that the small amplitude motions have a large effect on rISC and radiative decay; hence, the triptycene scaffold is extremely important in **TpAT-tFFO** as well.

CONCLUSIONS

This study of the archetypical through-space charge transfer (TSCT) TADF material **TpAT-tFFO** reveals many new facets of the photophysics controlling rISC in TSCT excited states. We identify the role-played by two spatial molecular conformers, energetically separated by 20 meV, that readily interconvert in the ground state but have a large reorganizational energy barrier for interconversion in the excited state. We observe two prompt emission decay times (radiative decay rates of 2.38×10^6 and $6.67 \times 10^5 \text{ s}^{-1}$) but no time-dependent change in emission spectra, showing that the species are very close in energy, i.e., the two conformers. We show that ISC is thermally activated, mediated by a vibronic coupling mechanism. It is both efficient and very fast, $>10^7 \text{ s}^{-1}$, quenching prompt emission in 30 ns, so that more than 97% of light generated by **TpAT-tFFO** is delayed fluorescence. The DF thus becomes the dominant emission after only 30 ns. Notably, time-resolved measurements show no change in the emission spectral band shape and position from the nanosecond to more than 50 ms. The rISC rate is more strongly thermally activated than ISC, reducing by an order of magnitude more than the ISC rate at low temperature, fully in line with a second-order vibronic coupled SOC mechanism mediating rISC. However, we still observe DF at 20 K in films. The two conformers dictate delayed emission at long times and

low temperatures as the population of the slower rISC rate conformer increases as the temperature reduces because interconversion between conformers (over the large excited state reorganizational energy barrier) reduces, meaning that relatively more of this “slow” conformer persists giving rise to a growing long lifetime non-exponentially decaying DF tail. This DF tail is not due to disorder but a consequence of the energetics of conformer interconversion. This gives new insight into these often-seen long DF tails.

We discover that vibrational torsion motions of the D relative to the A units allow the molecule to dynamically access spatial and orientational D–A configurations, oscillation between high k_{rISC} and high radiative decay rates at vibrational frequencies, achieving both high overall PLQY and high rISC rates. Our theoretical models show us that the electron exchange energy (or singlet–triplet energy gap) and SOC are very sensitive to changes in the D–A spatial overlap. Thus, even small amplitude vibrational motions of the D and A relative to each other cause large dynamic variations of these rates on the vibrational time scale.

We observe host-independent, temperature-dependent rISC, with an activation energy of 17 meV (i.e., 140 cm^{-1}), and freezing-out these low energy torsional vibrational modes reduces rISC, by an order of magnitude more than the corresponding drop in ISC at low temperature. This dynamic behavior is a key difference in **TpAT-tFFO** (and we propose in other TSCT molecules) because the D and A units can move easily with respect to each other in space via many fast vibrational modes, with SOC being very sensitive to this motion, i.e., especially the face-to-face D–A overlap. Meanwhile, through-bond TADF systems with D and A directly bridged by a C–N bond for example have more limited relative motion, mainly slow torsional vibrational degrees of freedom. Finally, all calculations show that in **TpAT-tFFO**, the ^3CT triplet states are energetically lower than the lowest energy local ^3LE triplet state, in agreement with the triplet energy of triazene, and given that we observe no change in the emission spectral band shape, but a 50–75 meV red shift between DF at 50 ms and phosphorescence beyond 400 ms (lasting $>10 \text{ s}$), we conclude that phosphorescence in **TpAT-tFFO** comes from radiative decay of a charge transfer ^3CT triplet state. The relative energy gaps determined from our triplet state measurements and calculations, as shown in **Scheme 1**, indicate that ^1CT and ^3LE are close in energy and this is why ISC and rISC are both fast and highly efficient even at low temperature, confirming that **TpAT-tFFO** really defines the state of the art in TADF materials (**Figure S8**).

TpAT-tFFO is an excellent TADF emitter, yielding very high-performance devices. We believe this because in TSCT **TpAT-tFFO**, the D and A can move in three dimensions with respect to each other while still being held in near ideal low electron exchange energy configuration by the triptycene scaffold. For an exciplex TADF system, D–A configuration is random in the bulk in comparison. Vibrational motions allow the **TpAT-tFFO** molecules to dynamically sample different D–A spatial orientations, which have either very high rISC rates or very high radiative decay rates, so that on average, **TpAT-tFFO** is optimized both for the fastest rISC and highest radiative decay. This is an intrinsic property of the dynamic vibrational motion of the molecule, which indicates that the complete rigidity in these through-space TADF emitters would be detrimental. Instead, this degree of freedom enables the molecule to hunt through different conformations to “self-

optimize" itself for TADF efficiency. In this respect, **TpAT-tFFO** offers a template for the ideal TADF molecules.

■ ASSOCIATED CONTENT

SI Supporting Information

The Supporting Information is available free of charge at <https://pubs.acs.org/doi/10.1021/acs.jpcc.2c07529>.

Steady-state and time-resolved optical measurements, non-adiabatic energy gap estimate, theoretical vibrational couple modes and rate constants, and tables for different hosts (PDF)

■ AUTHOR INFORMATION

Corresponding Authors

Christel M. Marian – Institut für Theoretische Chemie und Computerchemie, Heinrich-Heine-Universität Düsseldorf, D-40225 Düsseldorf, Germany; orcid.org/0000-0001-7148-0900; Email: christel.marian@hhu.de

Andrew P. Monkman – OEM Research Group, Department of Physics, Durham University, Durham DH1 3LE, UK; orcid.org/0000-0002-0784-8640; Email: a.p.monkman@durham.ac.uk

Authors

Hector Miranda-Salinas – OEM Research Group, Department of Physics, Durham University, Durham DH1 3LE, UK; orcid.org/0000-0001-6403-5251

Angela Rodriguez-Serrano – Institut für Theoretische Chemie und Computerchemie, Heinrich-Heine-Universität Düsseldorf, D-40225 Düsseldorf, Germany

Jeremy M. Kaminski – Institut für Theoretische Chemie und Computerchemie, Heinrich-Heine-Universität Düsseldorf, D-40225 Düsseldorf, Germany

Fabian Dinkelbach – Institut für Theoretische Chemie und Computerchemie, Heinrich-Heine-Universität Düsseldorf, D-40225 Düsseldorf, Germany

Nakagawa Hiromichi – Institute for Chemical Research Kyoto University, Uji, Kyoto 611-0011, Japan

Yu Kusakabe – Institute for Chemical Research Kyoto University, Uji, Kyoto 611-0011, Japan; orcid.org/0000-0001-6598-2680

Hironori Kaji – Institute for Chemical Research Kyoto University, Uji, Kyoto 611-0011, Japan; orcid.org/0000-0002-5111-3852

Complete contact information is available at: <https://pubs.acs.org/doi/10.1021/acs.jpcc.2c07529>

Author Contributions

H.M.-S. undertook all of the photophysical measurements of **TpAT-tFFO**. N.H. and Y.K. carried out the synthesis of **TpAT-tFFO**. A.R.-S., J.M.K., and F.D. made the theoretical calculations on **TpAT-tFFO**. H.K. designed the **TpAT-tFFO** molecule. C.M.M. conceived the theoretical studies. A.P.M. conceived the photophysical measurements and analysis of the experimental results. All authors participated in the writing of the manuscript.

Notes

The authors declare no competing financial interest.

■ ACKNOWLEDGMENTS

H.M.-S. acknowledges the Mexican National Council for Science and Technology, CONACYT for his studentship

(2019-000021-01EXTF-00308). A.P.M. acknowledges the EPSRC for funding under grant number EP/T02240X/1. A.R.-S. was funded on DFG MA 1051/17-1, and F.D. and J.M.K. were supported by DFG 396890929/GRK 2482.

■ REFERENCES

- (1) Santos, P. L.; Ward, J. S.; Data, P.; Batsanov, A. S.; Bryce, M. R.; Dias, F. B.; Monkman, A. P. Engineering the singlet-triplet energy splitting in a TADF molecule. *J. Mater. Chem. C* **2016**, *4*, 3815–3824.
- (2) Dias, F. B.; Bourdakos, K. N.; Jankus, V.; Moss, K. C.; Kamtekar, K. T.; Bhalla, V.; Santos, J.; Bryce, M. R.; Monkman, A. P. Triplet harvesting with 100% efficiency by way of thermally activated delayed fluorescence in charge transfer OLED emitters. *Adv. Mater.* **2013**, *25*, 3707–3714.
- (3) Lim, B. T.; Okajima, S.; Chandra, A. K.; Lim, E. C. Radiationless transitions in electron donor-acceptor complexes: selection rules for S1 → T intersystem crossing and efficiency of S1 → S0 internal conversion. *Chem. Phys. Lett.* **1981**, *79*, 22–27.
- (4) Etherington, M. K.; Gibson, J.; Higginbotham, H. F.; Penfold, T. J.; Monkman, A. P. Revealing the spin-vibronic coupling mechanism of thermally activated delayed fluorescence. *Nat. Commun.* **2016**, *7*, 13680.
- (5) Gibson, J.; Monkman, A. P.; Penfold, T. J. The Importance of Vibronic Coupling for Efficient Reverse Intersystem Crossing in Thermally Activated Delayed Fluorescence Molecules. *ChemPhysChem* **2016**, *17*, 2956–2961.
- (6) Dias, F. B.; Penfold, T. J.; Monkman, A. P. Photophysics of thermally activated delayed fluorescence molecules. *Methods and Applications in Fluorescence*; IOP Publishing Ltd March 1, 2017, p 012001. doi: [10.1088/2050-6120/aa537e](https://doi.org/10.1088/2050-6120/aa537e).
- (7) Chen, X. K.; Kim, D.; Brédas, J. L. Thermally Activated Delayed Fluorescence (TADF) Path toward Efficient Electroluminescence in Purely Organic Materials: Molecular Level Insight. *Acc. Chem. Res.* **2018**, *51*, 2215–2224.
- (8) Oevering, H.; Verhoeven, J. W.; Paddon-Row, M. N.; Warman, J. M. Charge-transfer absorption and emission resulting from long-range through-bond interaction; exploring the relation between electronic coupling and electron-transfer in bridged donor-acceptor systems. *Tetrahedron* **1989**, *45*, 4751–4766.
- (9) Dekkers, A. W. J. D.; Verhoeven, J. W.; Speckamp, W. N.; Pasman, P.; De, Boer; Pasman, P.; De, Boer; Tickle, L.; Hess, J.; Vos, A.; Engberts, J. B. F. N. *For Bichromophoric*; 1982; Vol. 104.
- (10) dos Santos, P. L.; Dias, F. B.; Monkman, A. P. Investigation of the Mechanisms Giving Rise to TADF in Exciplex States. *J. Phys. Chem. C* **2016**, *120*, 18259–18267.
- (11) El-Gezawy, H.; Rettig, W.; Lapouyade, R. Solvatochromic behavior of donor - Acceptor-polyenes: Dimethylamino-cyanodiphenylbutadiene. *J. Phys. Chem. A* **2006**, *110*, 67–75.
- (12) Kautny, P.; Glöckhofer, F.; Kader, T.; Mewes, J. M.; Stöger, B.; Fröhlich, J.; Lumpi, D.; Plasser, F. Charge-transfer states in triazole linked donor-acceptor materials: Strong effects of chemical modification and solvation. *Phys. Chem. Chem. Phys.* **2017**, *19*, 18055–18067.
- (13) Wang, X.; Wang, S.; Lv, J.; Shao, S.; Wang, L.; Jing, X.; Wang, F. Through-space charge transfer hexaarylbenzene dendrimers with thermally activated delayed fluorescence and aggregation-induced emission for efficient solution-processed OLEDs. *Chem. Sci.* **2019**, *10*, 2915–2923.
- (14) Woon, K. L.; Yi, C. L.; Pan, K. C.; Etherington, M. K.; Wu, C. C.; Wong, K. T.; Monkman, A. P. Intramolecular Dimerization Quenching of Delayed Emission in Asymmetric D-D'-A TADF Emitters. *J. Phys. Chem. C* **2019**, *123*, 12400–12410.
- (15) Kumar, S.; Franca, L. G.; Stavrou, K.; Crovini, E.; Cordes, D. B.; Slawin, A. M. Z.; Monkman, A. P.; Zysman-Colman, E. Investigation of Intramolecular Through-Space Charge-Transfer States in Donor-Acceptor Charge-Transfer Systems. *J. Phys. Chem. Lett.* **2021**, *12*, 2820–2830.

- (16) Xue, Q.; Xie, G. Thermally Activated Delayed Fluorescence beyond Through-Bond Charge Transfer for High-Performance OLEDs. *Adv. Opt. Mater.* **2021**, *9*, 2002204.
- (17) Sarma, M.; Wong, K. T. Exciplex: An Intermolecular Charge-Transfer Approach for TADF. *ACS Appl. Mater. Interfaces* **2018**, *10*, 19279–19304.
- (18) Wada, Y.; Nakagawa, H.; Matsumoto, S.; Wakisaka, Y.; Kaji, H. Organic light emitters exhibiting very fast reverse intersystem crossing. *Nat. Photonics* **2020**, *14*, 643–649.
- (19) Gibson, J.; Penfold, T. J. Nonadiabatic coupling reduces the activation energy in thermally activated delayed fluorescence. *Phys. Chem. Chem. Phys.* **2017**, *19*, 8428–8434.
- (20) Marian, C. M. Mechanism of the Triplet-to-Singlet Upconversion in the Assistant Dopant ACRXTN. *J. Phys. Chem. C* **2016**, *120*, 3715–3721.
- (21) Miranda-Salinas, H.; Hung, Y. T.; Chen, Y. S.; Luo, D.; Kao, H. C.; Chang, C. H.; Wong, K. T.; Monkman, A. Controlling through-space and through-bond intramolecular charge transfer in bridged D–D′–A TADF emitters. *J. Mater. Chem. C* **2021**, *9*, 8819–8833.
- (22) Kaminski, J. M.; Rodríguezrodríguez-Serrano, A.; Dinkelbach, F.; Miranda-Salinas, H.; Monkman, A. P.; Marian, C. M. Vibronic effects accelerate the intersystem crossing processes of the through-space charge transfer states in the triptycene bridged acridine–triazine donor–acceptor molecule TpAT-tFFO. *Chem. Sci.* **2022**, *13*, 7057–7066.
- (23) Tsai, W.-L.; Huang, M.-H.; Lee, W.-K.; Hsu, Y.-J.; Pan, K.-C.; Huang, Y.-H.; Ting, H.-C.; Sarma, M.; Ho, Y.-Y.; Hu, H.-C.; et al. A versatile thermally activated delayed fluorescence emitter for both highly efficient doped and non-doped organic light emitting devices. *Chem. Commun.* **2015**, *51*, 13662–13665.
- (24) Harada, N.; Uda, H.; Nakasuji, K.; Murata, I. Interchromophoric homoconjugation effect and intramolecular charge-transfer transition of the triptycene system containing a tetracyanoquinodimethane chromophore. *J. Chem. Soc., Perkin Trans. 2* **1989**, *0*, 1449.
- (25) Kawasumi, K.; Wu, T.; Zhu, T.; Chae, H. S.; Van Voorhis, T.; Baldo, M. A.; Swager, T. M. Thermally Activated Delayed Fluorescence Materials Based on Homoconjugation Effect of Donor–Acceptor Triptycenes. *J. Am. Chem. Soc.* **2015**, *137*, 11908–11911.
- (26) Rodríguez-Serrano, A.; Dinkelbach, F.; Marian, C. M. Intersystem crossing processes in the 2CzPN emitter: a DFT/MRCI study including vibrational spin-orbit interactions. *Phys. Chem. Chem. Phys.*, **2021**, *23*, 3668–3678, DOI: 10.1039/d0cp06011a.
- (27) Dos Santos, P. L.; Ward, J. S.; Bryce, M. R.; Monkman, A. P. Using Guest-Host Interactions to Optimize the Efficiency of TADF OLEDs. *J. Phys. Chem. Lett.* **2016**, *7*, 3341–3346.
- (28) Stavrou, K.; Franca, L. G.; Monkman, A. P. Photophysics of TADF Guest-Host Systems: Introducing the Idea of Hosting Potential. *ACS Appl. Electron. Mater.* **2020**, *2*, 2868–2881.
- (29) Chakravorty, K.; Poole, J. A. The effect of dissolved molecular oxygen on the fluorescence of 9,10-dimethylantracene and 9,10-diphenylantracene. *J. Photochem.* **1984**, *26*, 25–31.
- (30) Pander, P.; Motyka, R.; Zassowski, P.; Etherington, M. K.; Varsano, D.; Da Silva, T. J.; Caldas, M. J.; Data, P.; Monkman, A. P. Thermally Activated Delayed Fluorescence Mediated through the Upper Triplet State Manifold in Non-Charge-Transfer Star-Shaped Triphenylamine-Carbazole Molecules. *J. Phys. Chem. C* **2018**, *122*, 23934–23942.
- (31) Haase, N.; Danos, A.; Pflumm, C.; Morherr, A.; Stachelek, P.; Mekić, A.; Brütting, W.; Monkman, A. P. Kinetic Modeling of Transient Photoluminescence from Thermally Activated Delayed Fluorescence. *J. Phys. Chem. C* **2018**, *122*, 29173–29179.
- (32) Penfold, T. J.; Dias, F. B.; Monkman, A. P. The theory of thermally activated delayed fluorescence for organic light emitting diodes. *Chem. Commun.* **2018**, 3926.
- (33) Suresh, S. M.; Duda, E.; Hall, D.; Yao, Z.; Bagnich, S.; Slawin, A. M. Z.; Bäessler, H.; Beljonne, D.; Buck, M.; Olivier, Y.; et al. A Deep Blue B,N-Doped Heptacene Emitter That Shows Both Thermally Activated Delayed Fluorescence and Delayed Fluorescence by Triplet-Triplet Annihilation. *J. Am. Chem. Soc.* **2020**, *142*, 6588–6599.

Conformational, Host and Vibrational Effects Giving Rise to Dynamic TADF Behaviour in the Through-Space Charge Transfer, Triptycene Bridged Acridine-Triazine Donor Acceptor TADF Molecule TpAT-tFFO

Hector Miranda-Salinas^a, Angela Rodriguez-Serrano^b, Jeremy Kaminski^b, Fabian Dinkelbach^b, Nakagawa Hiromichi ^c,
Yu Kusakabe^c, Hironori Kaji^c, Christel M. Marian^b and Andrew Monkman^{a,†}

^aOEM research group, Dept. of Physics, Durham University, Durham, UK, DH1 3LE

^bInstitut für Theoretische Chemie und Computerchemie, Heinrich-Heine-Universität Düsseldorf, Universitätsstraße 1, D-40225 Düsseldorf, Germany

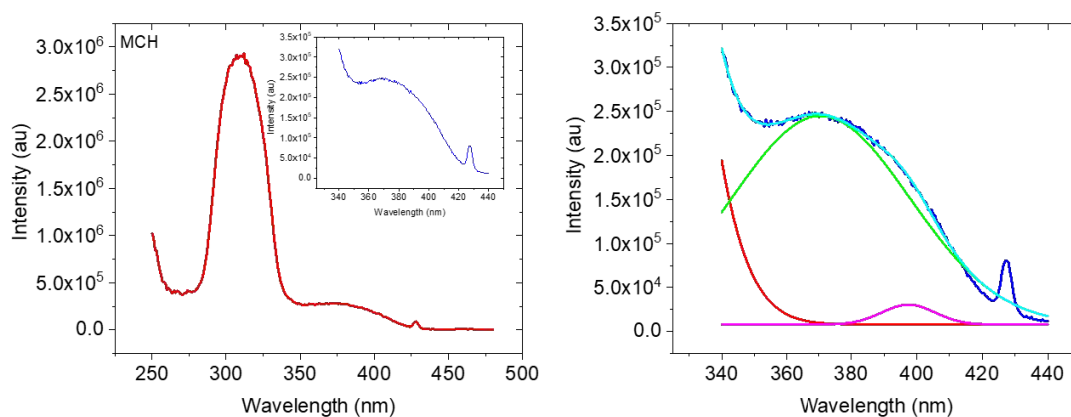
^c Institute for Chemical Research Kyoto University, Uji, Kyoto 611-0011, Japan

† a.p.monkman@durham.ac.uk

Supplementary information.

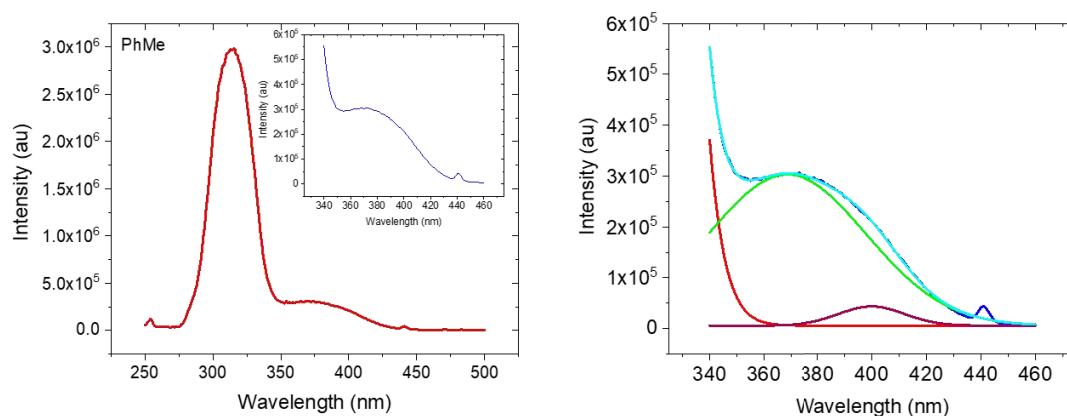
Solution state data

Excitation profiles



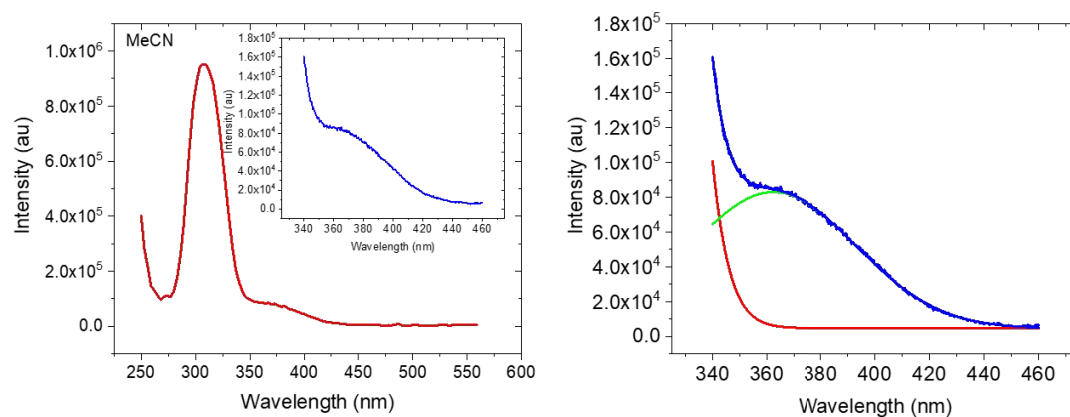
Model	Gauss		
Equation	$y=y_0 + (A/(w*\sqrt{\pi/2}))*\exp(-2*((x-xc)/w)^2)$		
Plot	Peak1(Intensity)	Peak2(Intensity)	Peak3(Intensity)
y0	7862.25392 ± 4687.13599	7862.25392 ± 4687.13599	7862.25392 ± 4687.13599
xc	293.01815 ± 113.59812	370.46715 ± 3.22124	397.45612 ± 1.359
w	40.50936 ± 49.35318	54.80797 ± 3.80708	16.2968 ± 3.80701
A	1.39169E8 ± 1.09134E9	1.62873E7 ± 1708902.65174	460446.69821 ± 225420.83745
Reduced Chi-Sqr	7.29062E7		
R-Square (COD)	0.9913		
Adj. R-Square	0.99089		

Figure S1. a) Excitation spectrum of TpAT-tFFO dissolved in MCH, inset shows well resolved direct CT absorption below the strong $\pi\pi^*$ transition, and b) close inspection of the 340 – 420 nm band, monitored emission wavelength 470 nm.



Model	Gauss		
Equation	$y=y_0 + (A/(w*\sqrt{\pi/2}))*\exp(-2*((x-xc)/w)^2)$		
Plot	Peak1(Intensity)	Peak2(Intensity)	Peak3(Intensity)
y0	5759.77753 ± 1822.34936	5759.77753 ± 1822.34936	5759.77753 ± 1822.34936
xc	261.91885 ± 127.1533	368.71422 ± 1.85728	399.88372 ± 1.21882
w	42.03195 ± 34.11045	58.33925 ± 1.71277	24.2438 ± 3.21309
A	1.91113E10 ± 2.31942E11	2.17442E7 ± 767161.41734	1144985.29435 ± 399134.74698
Reduced Chi-Sqr	2.17034E7		
R-Square (COD)	0.99886		
Adj. R-Square	0.99877		

Figure S2. a) Excitation spectrum of TpAT-tFFO dissolved in PhMe and b) close inspection of the 340 – 420 nm band, monitored emission wavelength 510 nm.



Model	Gauss	
Equation	$y = y_0 + (A / (w \cdot \sqrt{\pi/2})) \cdot \exp(-2 \cdot ((x - x_c) / w)^2)$	
Plot	Peak1(Intensity)	Peak2(Intensity)
y0	4683.12334 ± 186.54336	4683.12334 ± 186.54336
xc	239.3385 ± 81.02958	362.46644 ± 0.60549
w	49.4508 ± 19.71849	61.19907 ± 0.75052
A	2.36669E10 ± 1.69287E11	6008887.43175 ± 125620.10726
Reduced Chi-Sqr	853396.57333	
R-Square (COD)	0.9994	
Adj. R-Square	0.99938	

Figure S3. Excitation spectrum of TpAT-tFFO dissolved in MeCN and b) close inspection of the 340 – 420 nm band, monitored emission wavelength 570 nm.

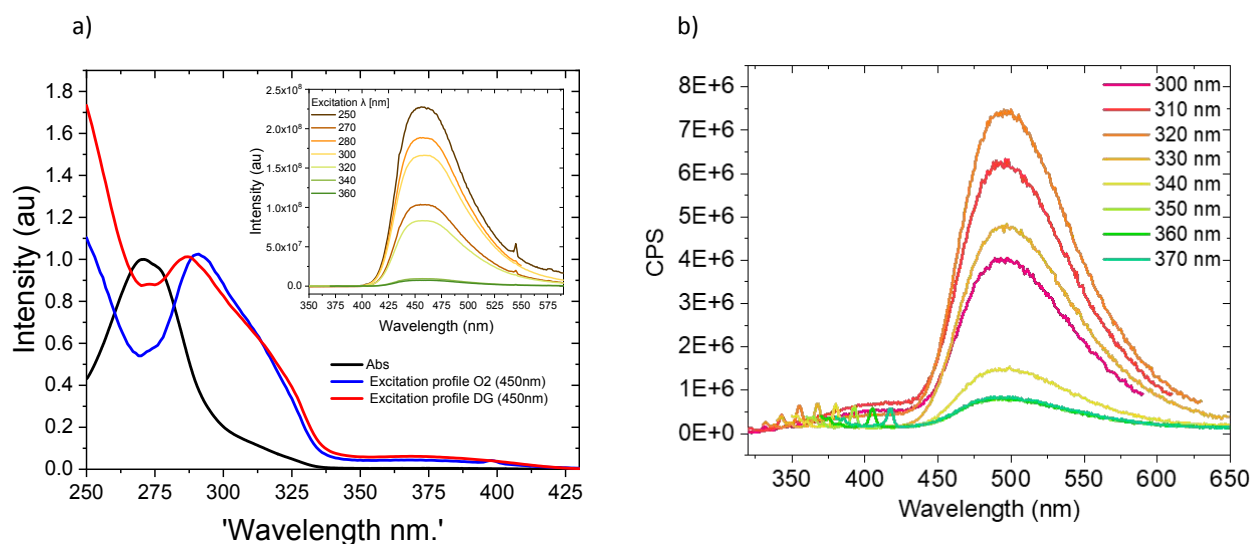


Figure S4. TpAT TFFO emission a) oxygen dependent excitation spectra and b) as a function of excitation wavelength in toluene.

As the S0-S3 (as well as the S0-S1 and S0-S2) transition led to prompt CT emission we can ascribe the primary electron transfer mechanism as hole transfer from A*D. The excitation spectra also indicate that the acceptor transition gives rise to far more CT production even though it has a much weaker extinction coefficient than the donor $\pi\pi^*$ absorption, consistent with hole transfer from A*D being the main ET channel.

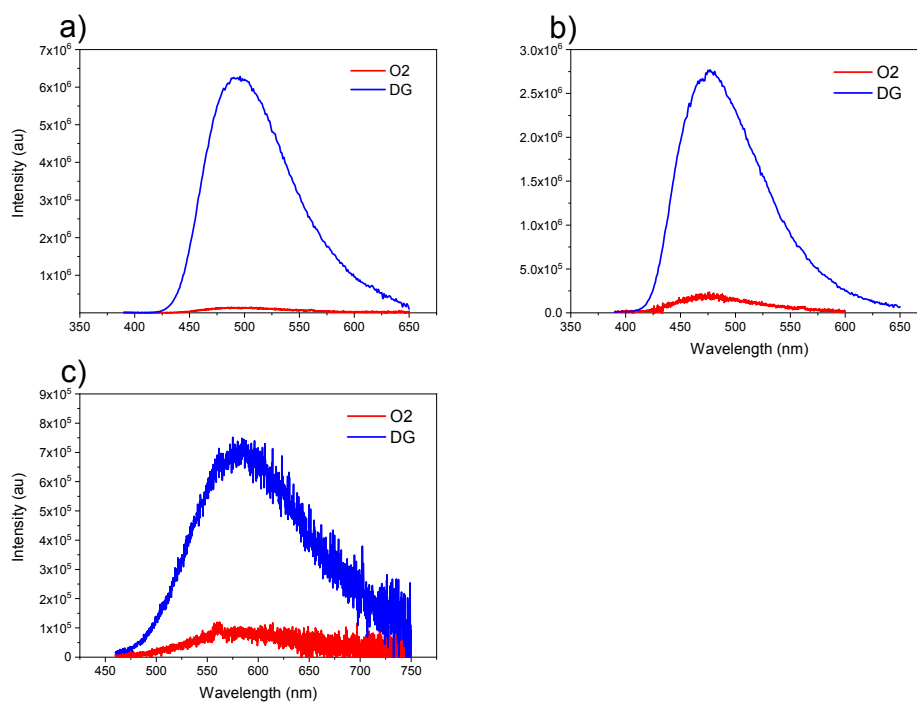


Figure S5. Degassed (blue) and in presence of oxygen (red) steady state emission comparison of TpAT-tFFO at 20 mM in a) PhMe, b) MCH and c) MeCN.

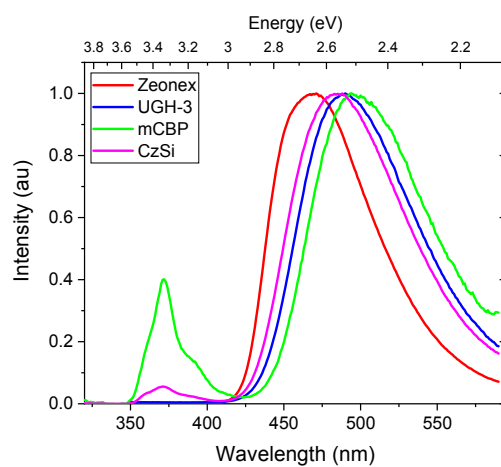
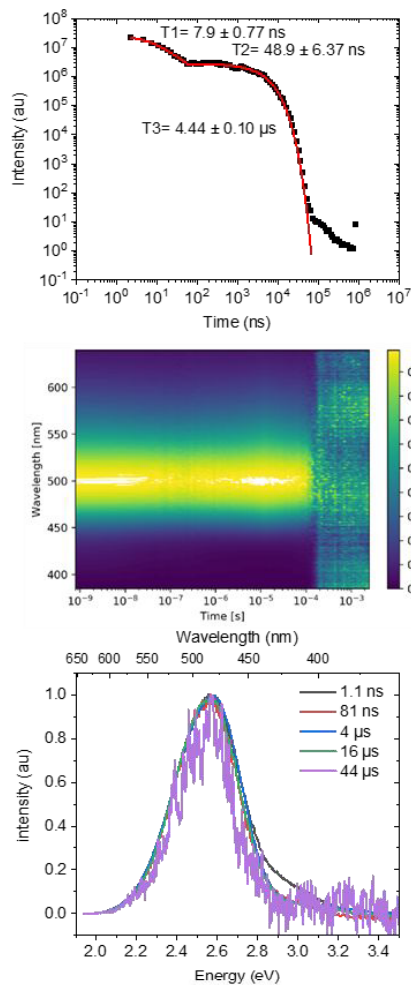


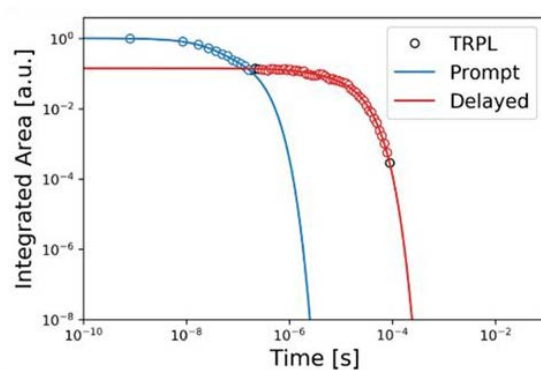
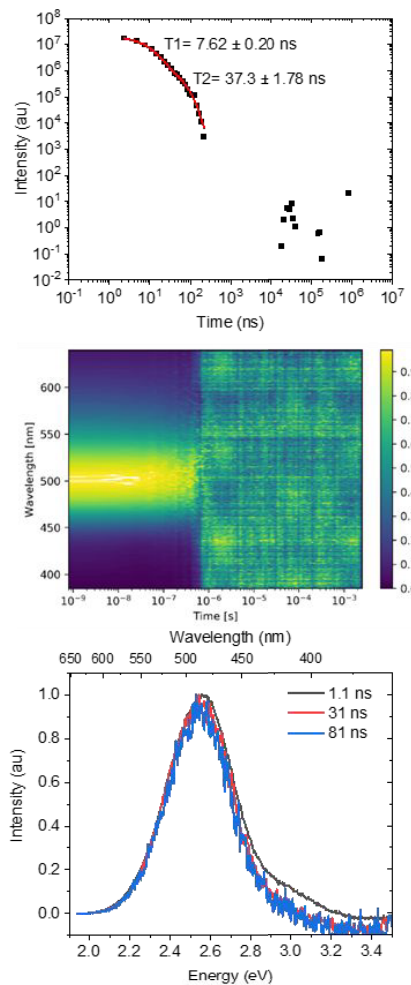
Figure S6. Solid state emission spectra using different hosts Zeonex 1% and the others 10% by weight.

Toluene data

a)



b)

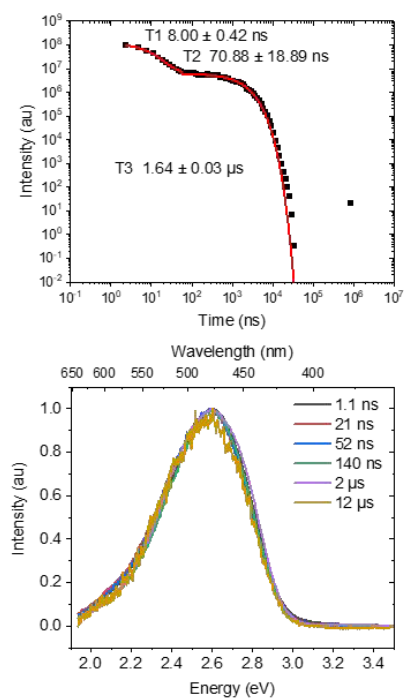


K_F	K_F Error	K_{ISC}	K_{ISC} Error	K_{rISC}	K_{rISC} Error
347006.2	19185.21	12543342	275080.2	3191554	163110.7

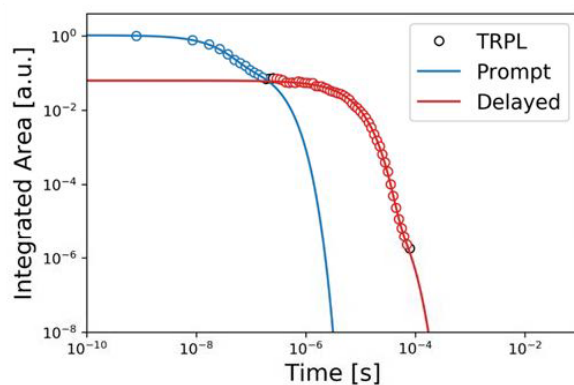
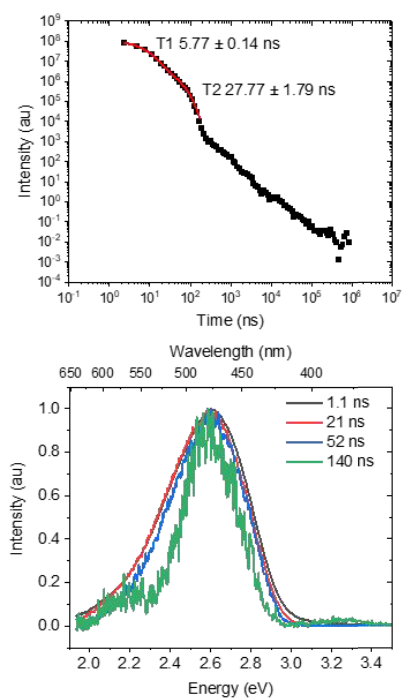
Figure S7. TpAT tFFO in PhMe a) degassed and b) oxygenated, time resolved decays, contour plots and their respective frames at different times.

MCH data

a)



b)

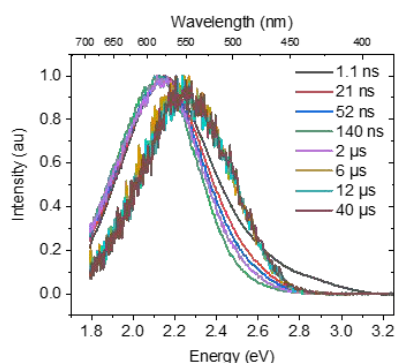
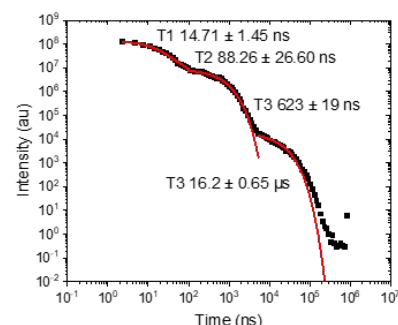


K^F	K^F Error	K^{ISC}	K^{ISC} Error	K^{rISC}	K^{rISC} Error
1905016	148020.8	11318695	28722.48	1129418	101105.4

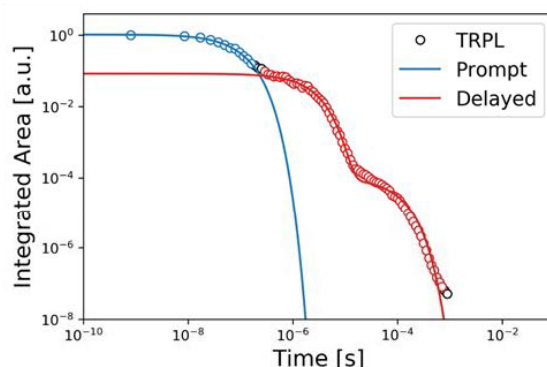
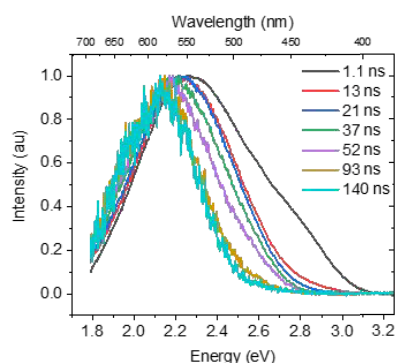
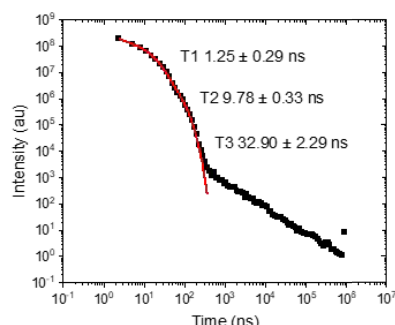
Figure S8. TpAT TFFO in MCH a) degassed and b) oxygenated, time resolved decays and their respective frames at different times.

MeCN data

a)



b)



K_F	K_F Error	K_{ISC}	K_{ISC} Error	K_{rISC}	K_{rISC} Error
3689300	161.0247	9814614	641.5399	74871.34	0.000928

Figure S9. TpAT TFFO in MeCN a) degassed and b) oxygenated, time resolved decays and their respective frames at different times.

In MeCN we observe rather more complicated photophysics with lifetimes and spectral components highly modified by the strongly polar environment, figure 4c (main manuscript) and 9a. In aerated solution, figure 9b, we observe multiple prompt decay components and spectral contributions, with large energy splitting of ca. 200 meV. In the first few nanoseconds we observe predominantly a gaussian feature at 550 nm (emission peak, lifetime 9.8 ns) having a high energy knee at 400–475 nm. This knee matches with the CT emission band observed in MCH, having a lifetime estimated at 1.25 ns (very close to our IRF however). These results then suggest that in highly polar MeCN there are aggregates or residual undissolved **TpAT-tFFO** even in low concentration solution. In this case it is difficult to conclude much about the early time photophysics. After some 50 ns, the CT emission has red shifted to 580 nm (onset 2.53 eV) having a lifetime of 33 ns, figure 9b. In degassed solution, figure 4c (main manuscript) and 9a, we observe the same two initial prompt CT components, with slightly longer lifetimes, but delayed CT emission from the low energy species at 580 nm rapidly dominates, clearly indicating that this band is giving a large DF contribution. This initial DF has a lifetime of 625 ns lasting for some 2 μ s only. This is very fast for TADF. Over the first 2 μ s this highly red shifted feature dominates, but at longer delay times (>2 μ s) weak DF emission is observed from the higher energy 550 nm state. This long-time decay

contribution is seen in the kinetics decays as well, figure 9b, having lifetime of 16 μ s. If we assume that a mediating local triplet state (for the rISC process) is close to 450 nm, then a CT state at 550 nm would be expected to have rather slow rISC as $\Delta E_{ST} \sim 0.35$ eV, therefore the emission intensity of MeCN is weaker than **TpAT-tFFO** in other solvents, due the lack of efficient rISC and having impact on the overall emission of the molecule. The observed short DF lifetime of the 580 nm species probably reflects a fast non radiative quenching of this state. We note that the PLQY of **TpAT-tFFO** in MeCN is very low (see figure 5c) and supports non-radiative quenching of this state out-competing rISC. We have no clear idea what this 580 nm state is, maybe some highly relaxed CT configuration having efficient TADF through mixing between the S_1 and S_2 triplet CT states mediating rISC instead of the 3LE state being involved. Or possibility this is a photodegradation species given the high fluence of 355 nm used during the time resolved measurements. We do not have enough clear evidence to be conclusive here.

TpAT-tFFO

TCSPC measurements measured in solution.

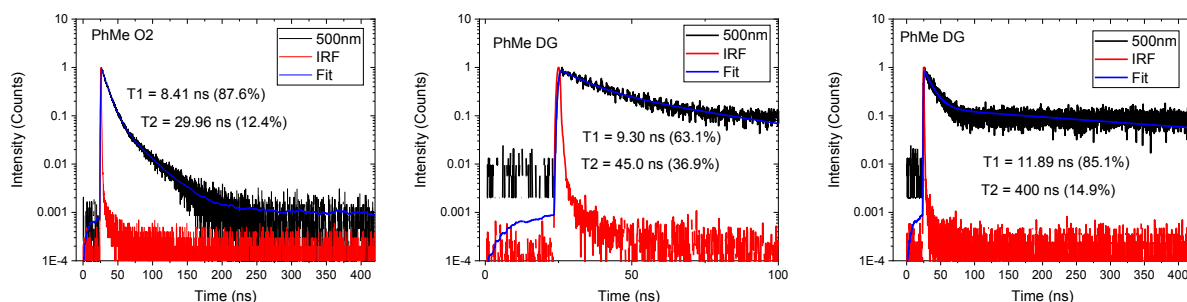


Figure S10. TCSPC decay measurements of TpAT tFFO in PhMe measure in aerated solution a), degassed b) and c) degassed in a longer time range.

Table S1. TCSPC Data for PhMe and MCH.

	T_1 (ns)	T_2 (ns)
PhMe O ₂	8.41 (87.6%)	30 (12.4%)
PhMe DG	9.3 - 12 (63-85%)	>400 (15%)
MCH O ₂	6.28 (93.8%)	26.53 (6.2%)
MCH DG	8.8 - 12 (89.9%)	>400 (15%)

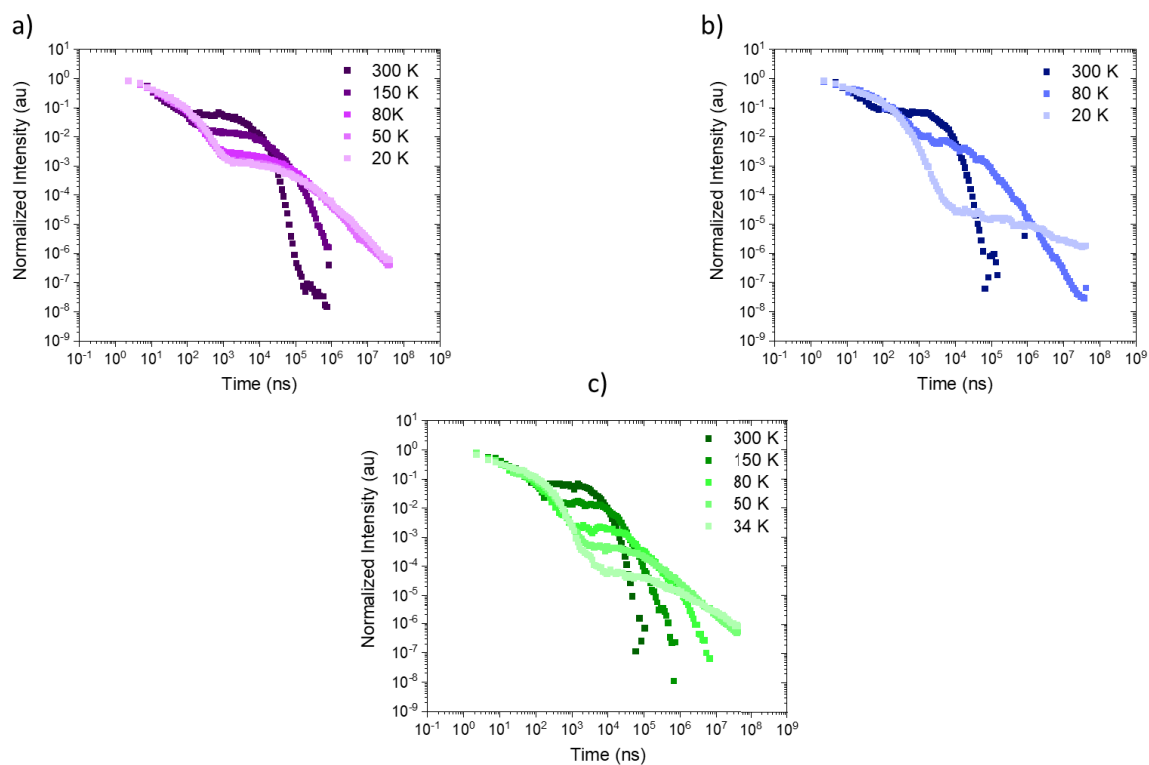


Figure S11 Decays for the time resolved measurements at different temperatures of a) zeonex, b) UGH-3 and c) CzSi.

UGH film data

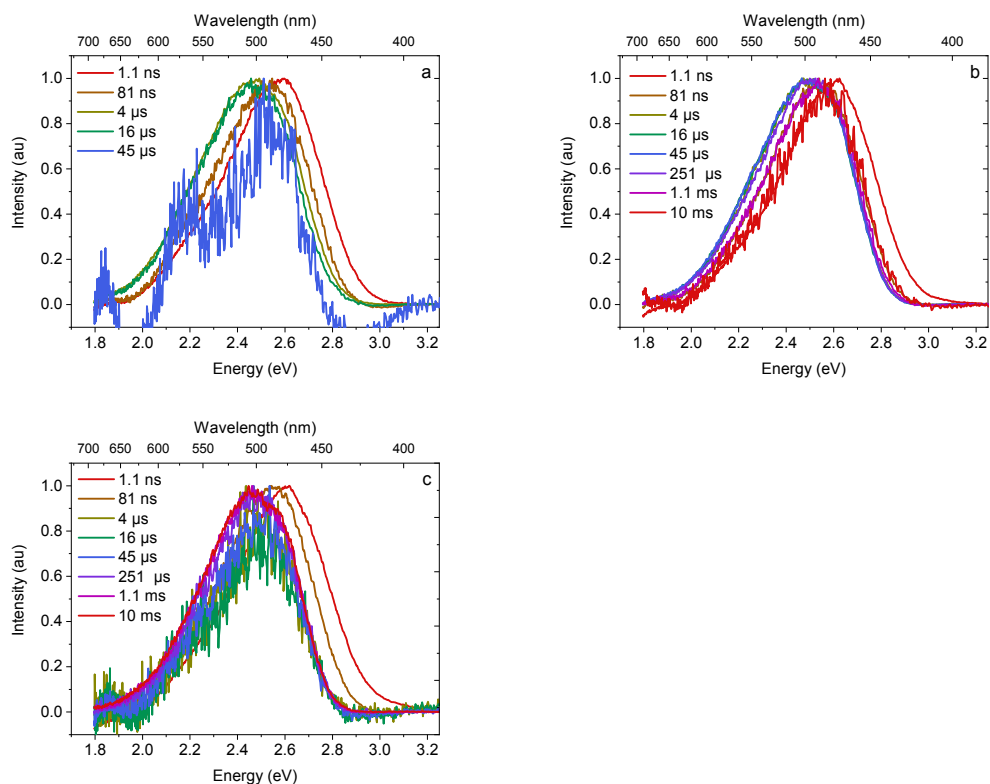
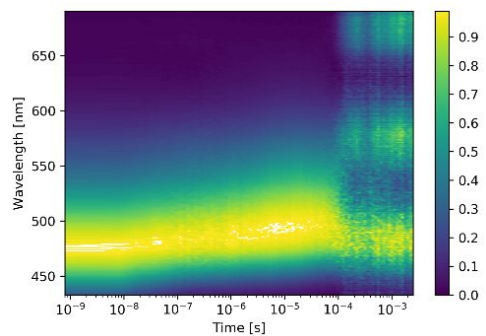
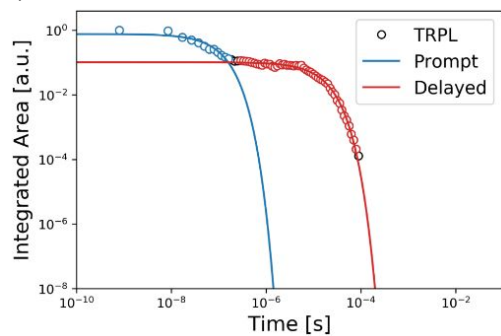
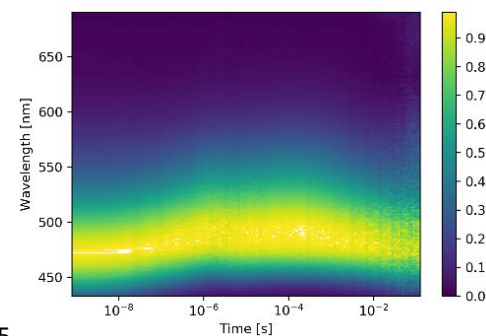
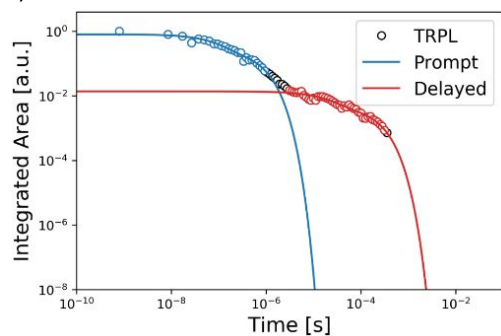


Figure S12. UGH-3 hosted film time resolved different frame times at a) 300 K, b) 80 K and c) 20 K.

a) 300K

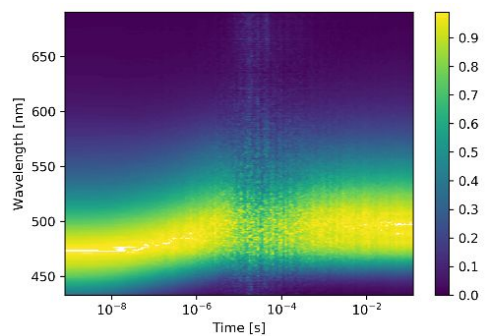
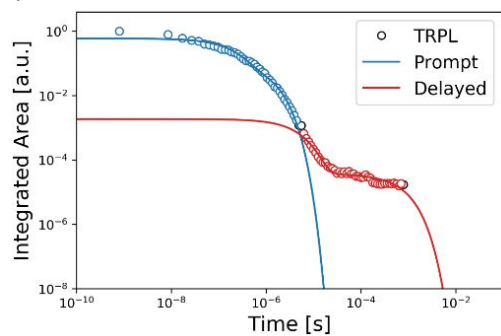


b) 80K



5

c) 20K



d)

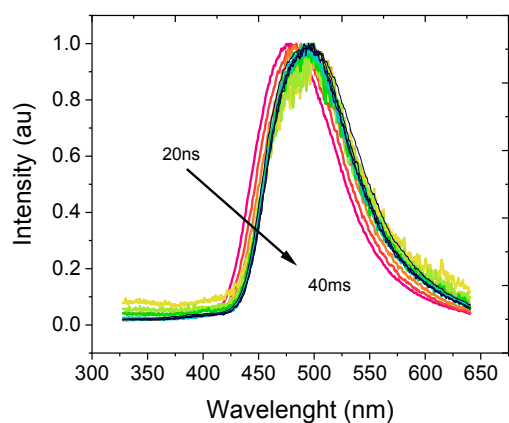


Figure S13. UGH-3 hosted film kinetic decay fitting and contour plot at a) 300 K, b) 80 K and c) 20 K. d) shows detailed time resolved spectra over a wide time scale measured at 80 K.

mCBP film data

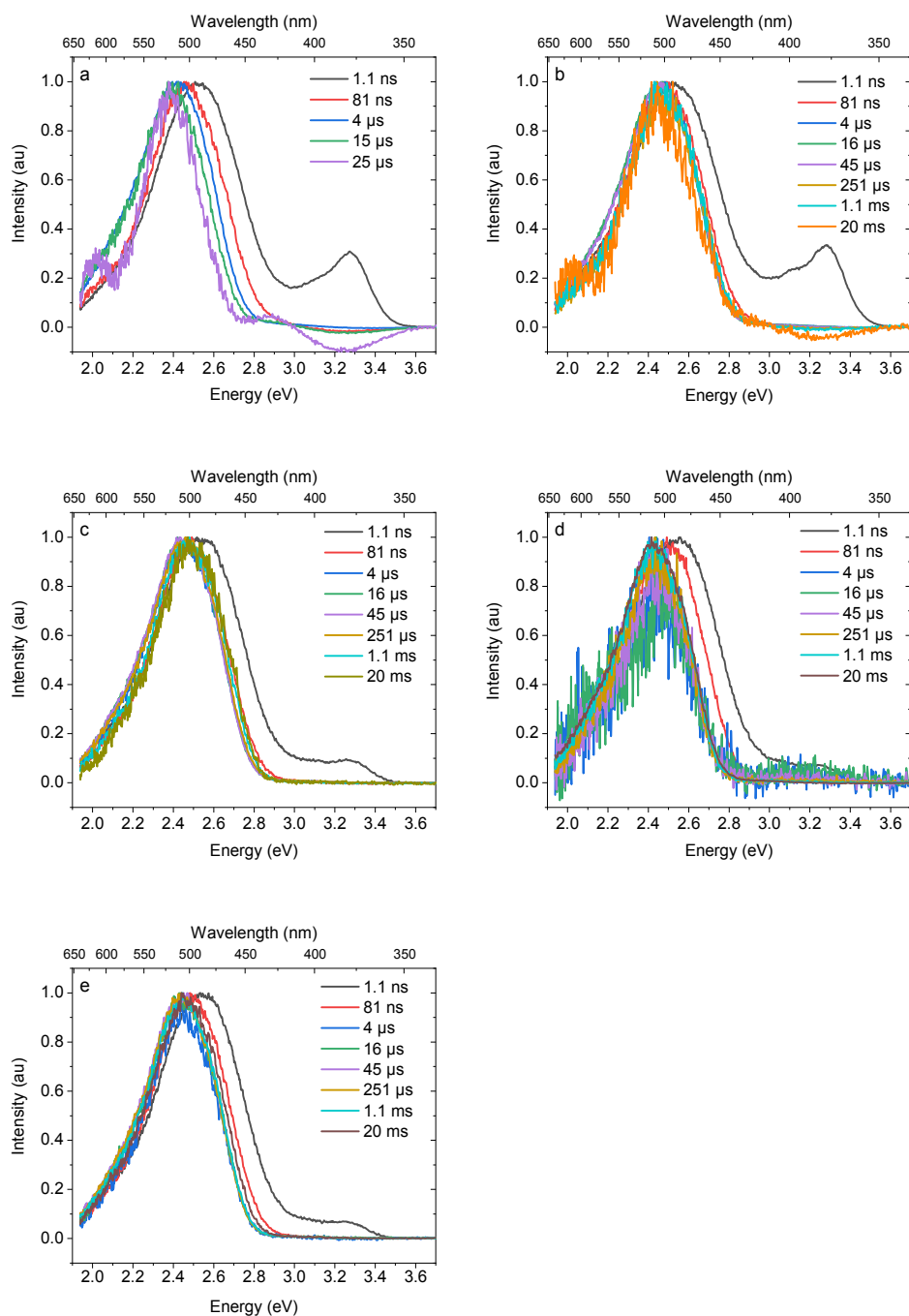
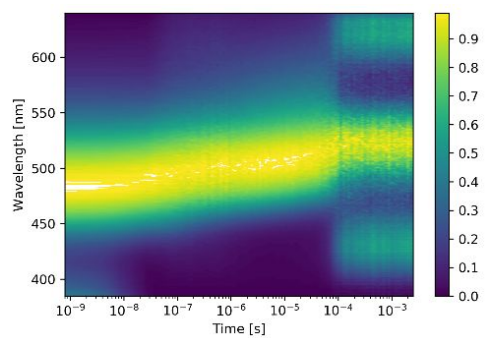
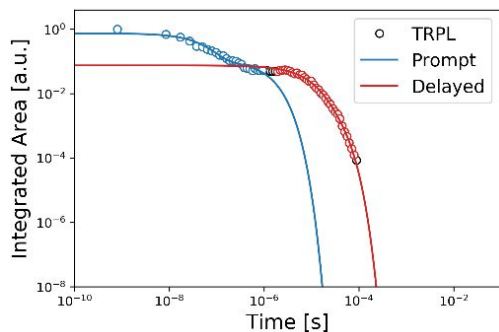
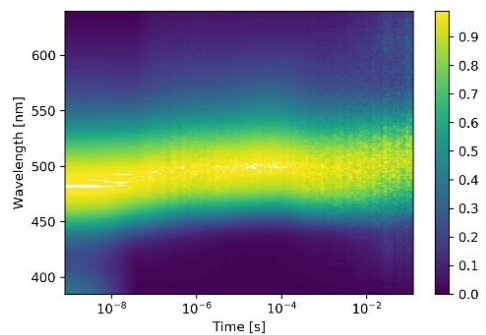
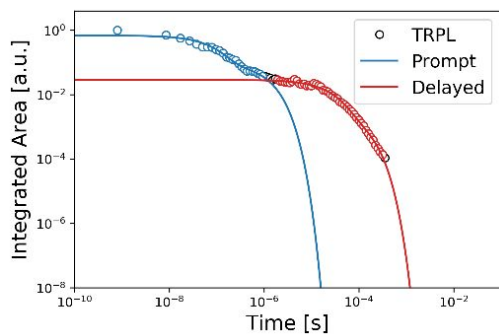


Figure S14. mCBP hosted film time resolved frames at a) 300 K, b) 150 K, c) 80 K, d) 50 K and e) 20 K.

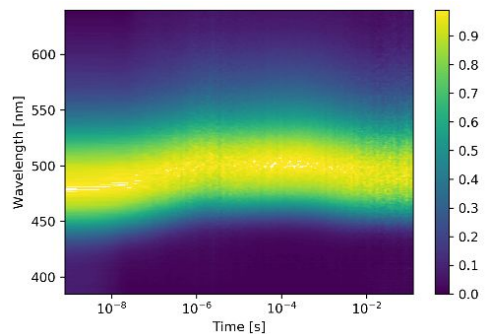
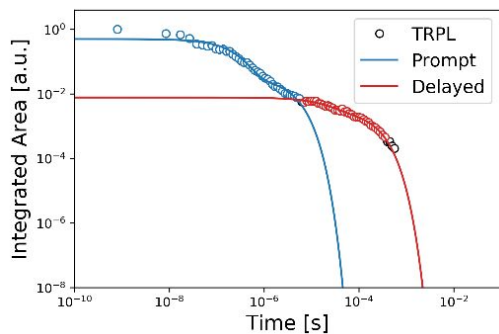
a) 300K



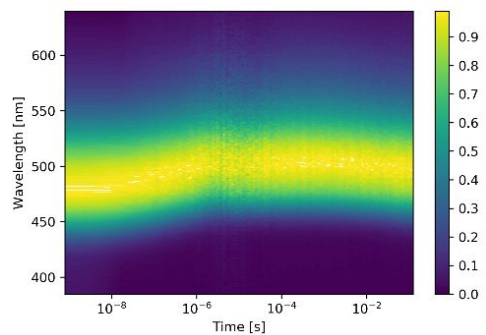
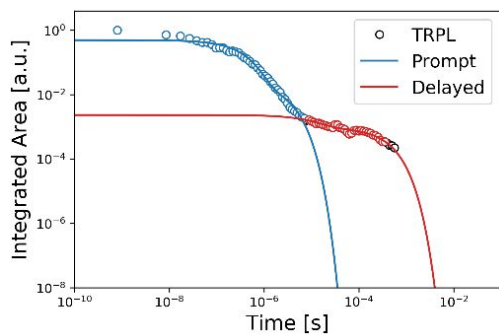
b) 150K



c) 80K



d) 50K



e) 20K

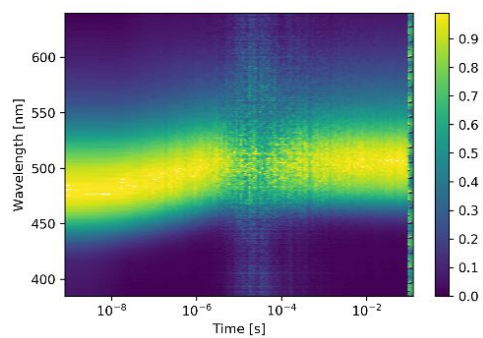
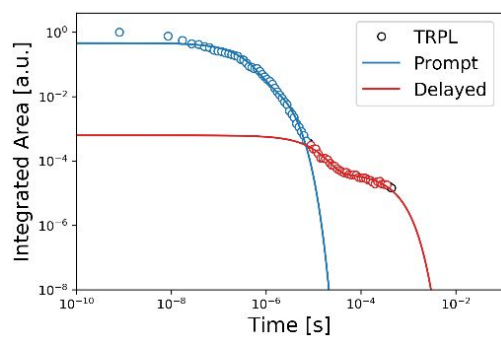


Figure S15. mCBP hosted film kinetic decay fitting and contour plot at a) 300 K, b) 150 K, c) 80 K, d) 50 K and e) 20 K.

CzSi film data

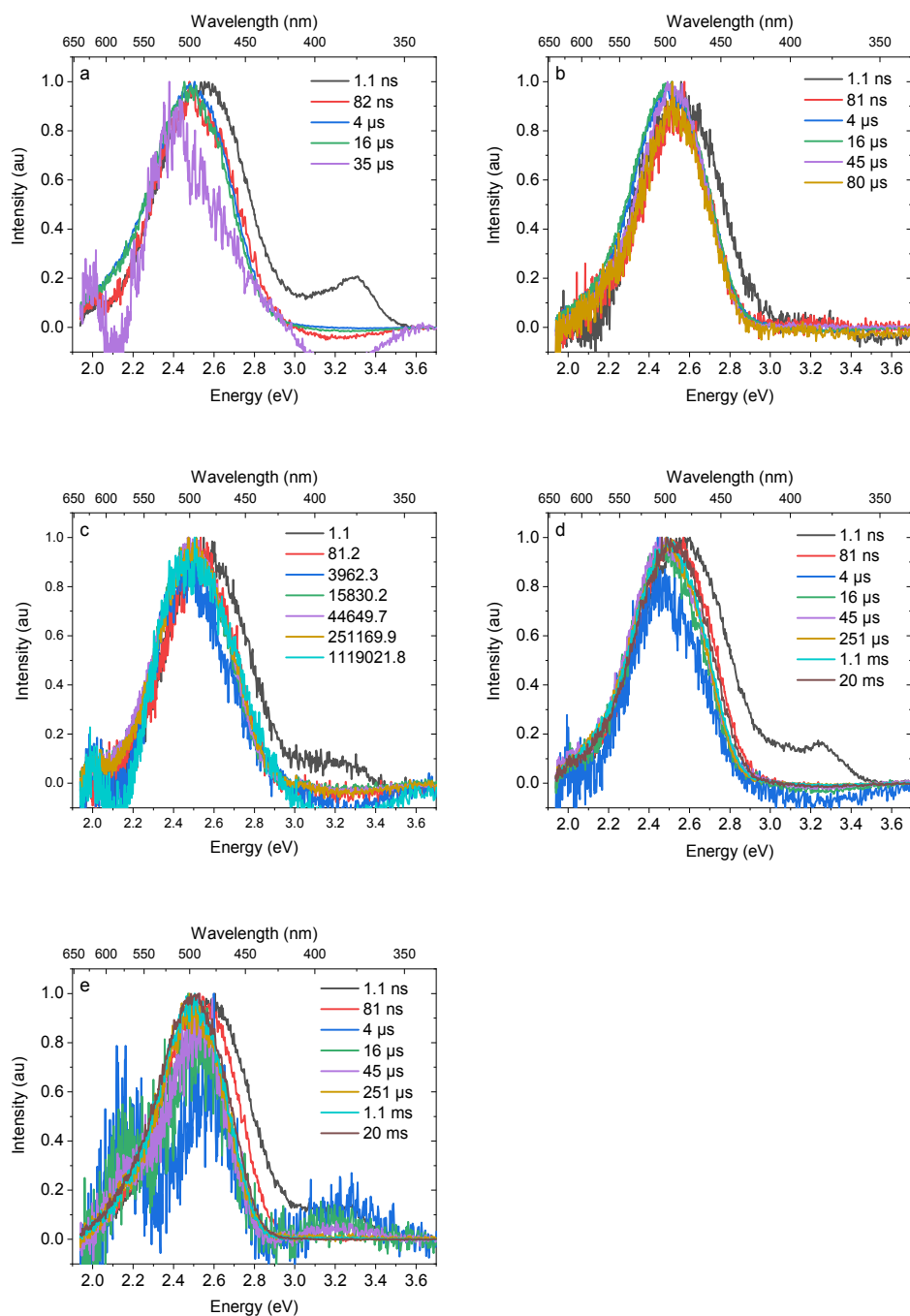
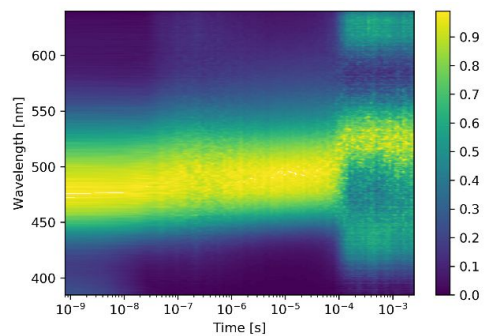
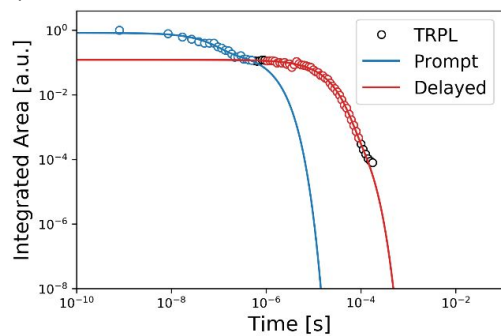
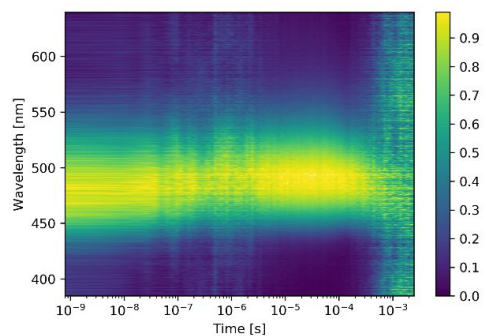
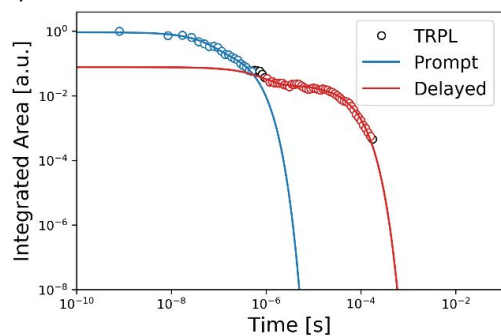


Figure S16. CzSi hosted film time resolved frames at a) 300 K, b) 150 K, c) 80 K, d) 50 K and e) 34 K.

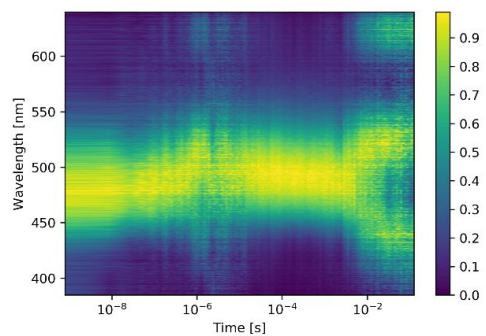
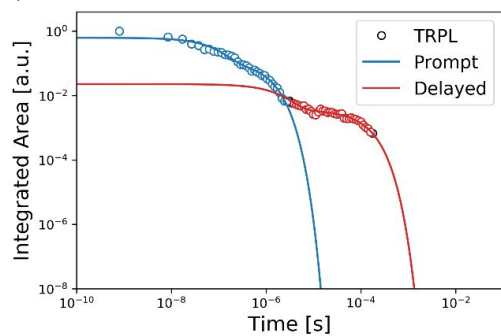
a) 300K



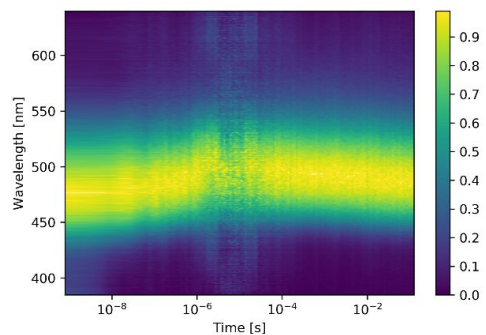
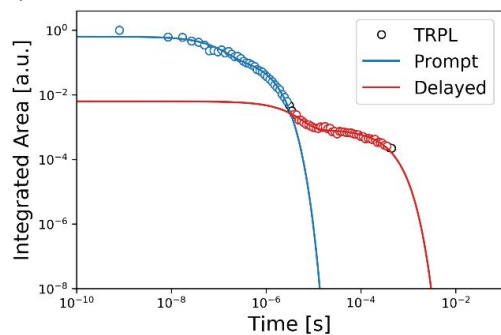
b) 150K



c) 80K



d) 50K



e) 34K

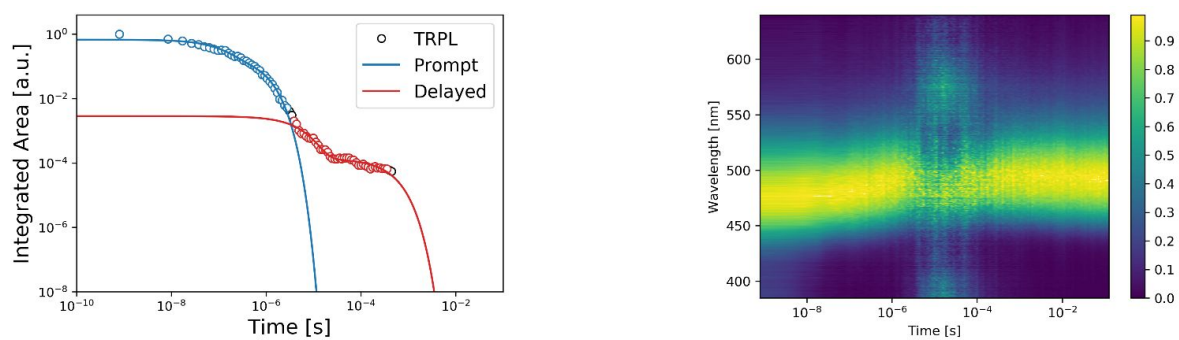


Figure S17 CzSi hosted film kinetic decay fitting and contour plot at a) 300 K, b) 150 K, c) 80 K, d) 50 K and e) 34 K.

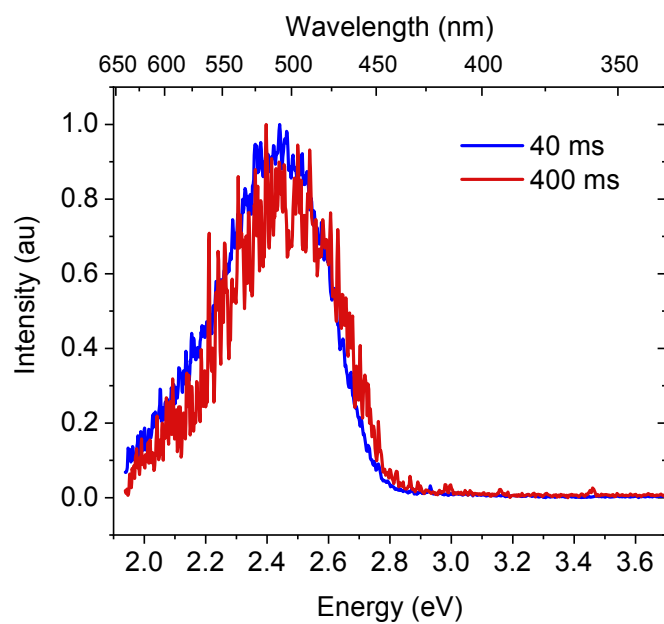


Figure S18 Comparison of emission 40 ms (blue) and 400 ms (red) in the mCBP hosted film at 20 K.

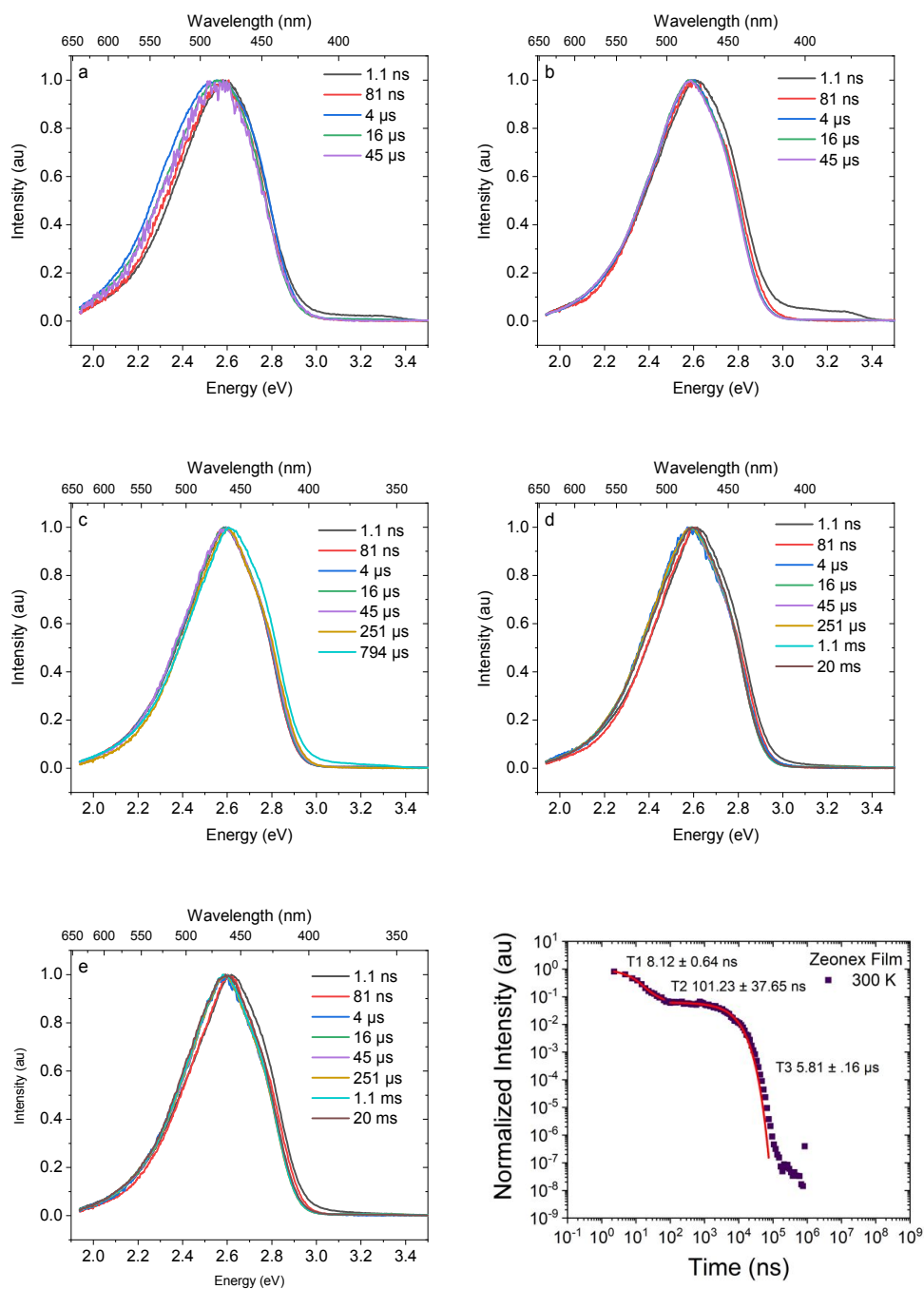
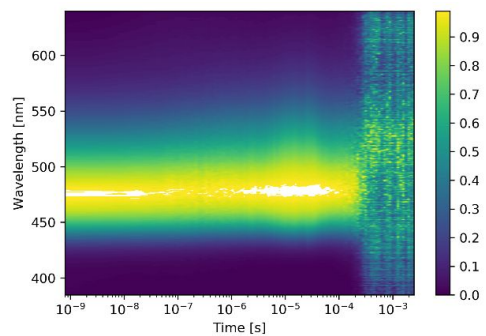
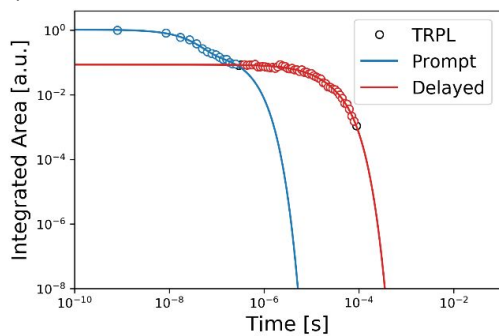
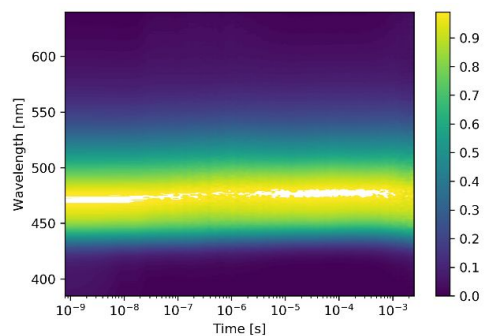
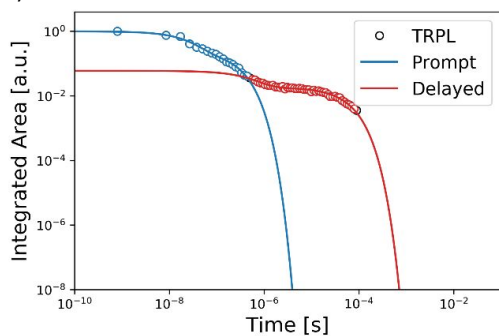


Figure S19. Zeonex hosted film time resolved frames at a) 300 K, b) 150 K, c) 80 K, d) 50 K and e) 20 K. f) shows the exponential fitting of the room temperature decay of emission.

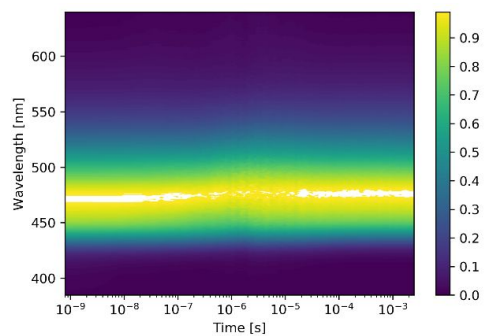
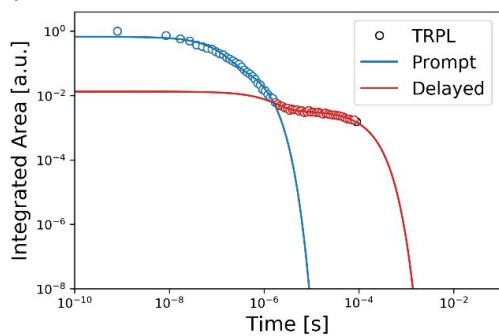
a) 300K



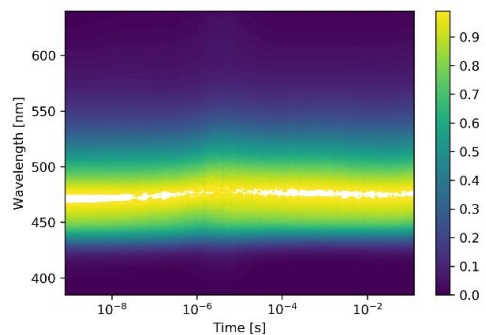
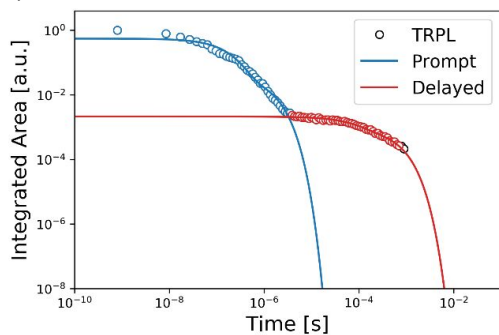
b) 150K



c).80K



d) 50K



e) 20K

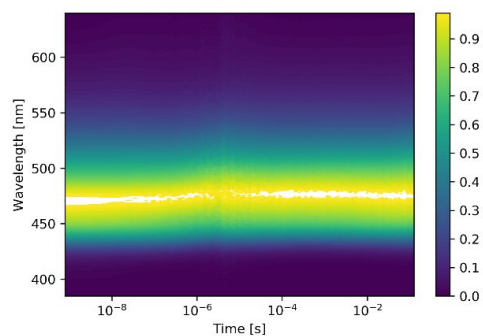
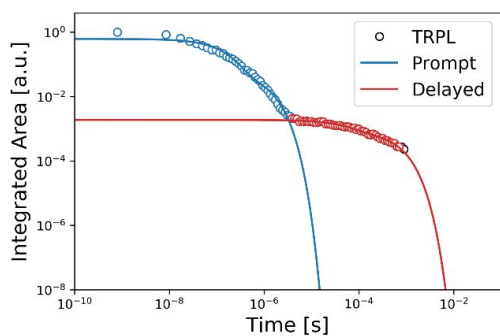


Figure S20 Zeonex hosted film kinetic decay fitting and contour plot at a) 300 K, b) 150 K, c) 80 K, d) 50 K and e) 20 K.

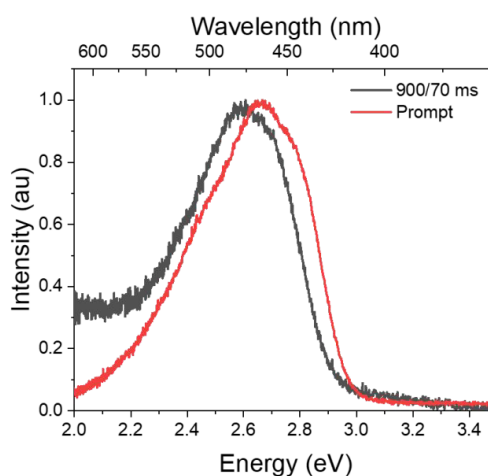
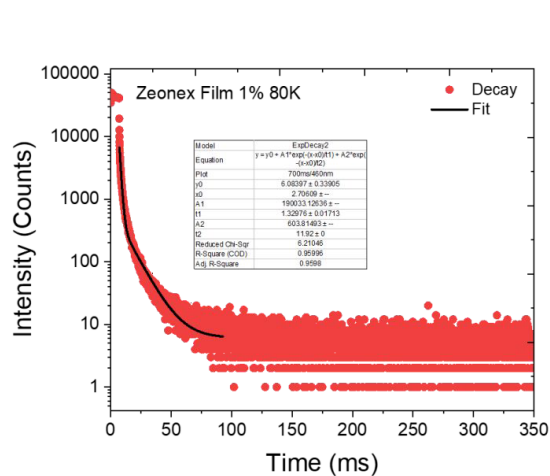


Figure S21 Zeonex hosted film TCSPC decay at 80K and spectra measured at 20K with 900 ms delay time and 70 ms integration time vs prompt emission.

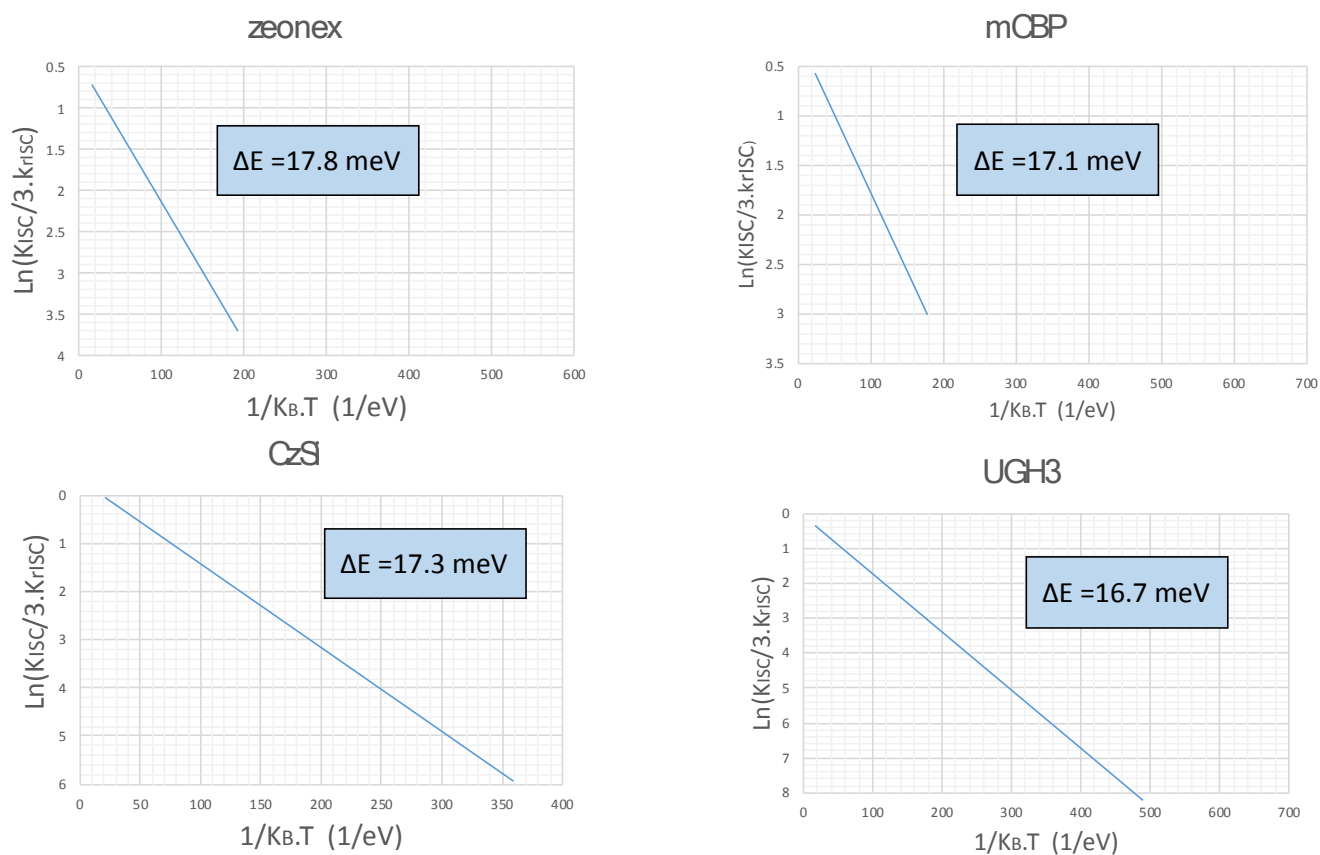


Figure S22. Plots of $\frac{k_{rISC}}{k_{ISC}} = \frac{1}{3} \exp\left[-\frac{\Delta E_{ST}}{k_B T}\right]$ to estimate the non-adiabatic energy gap between coupling CT and LE triplet states.

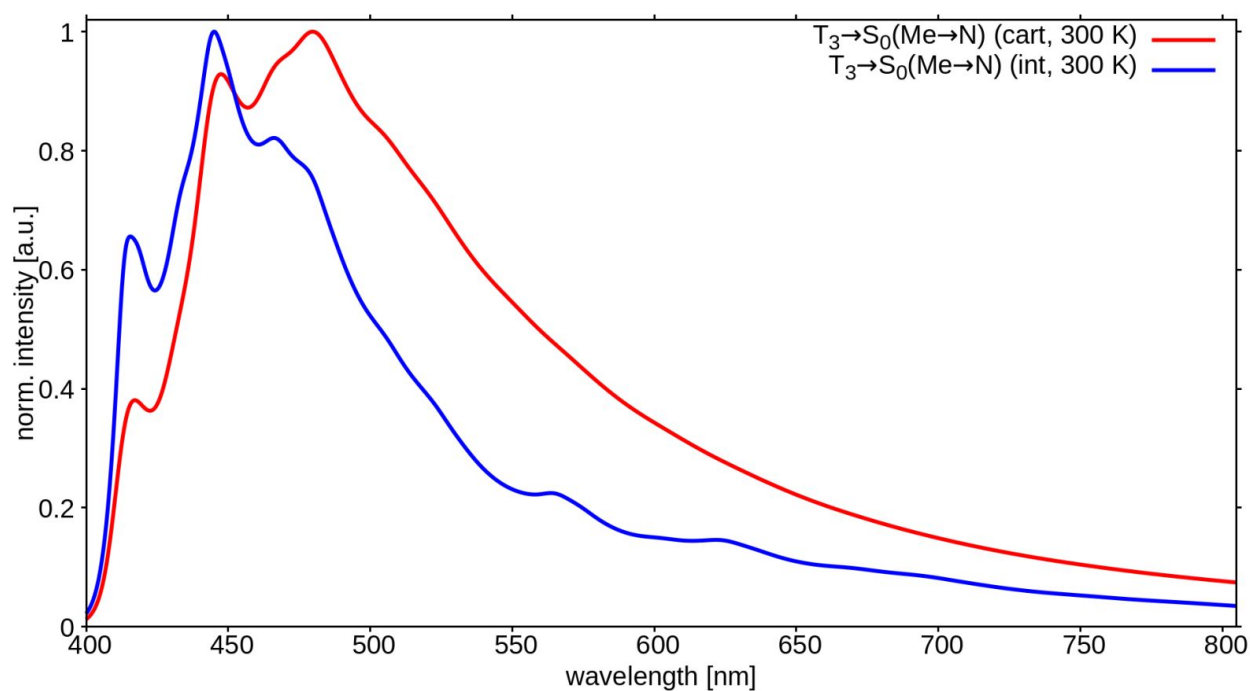


Figure S23 Theoretically calculate phosphorescence spectrum of the T_3 lowest energy local triplet state at 77K. Spectra in cartesian and internal coordinates are shown. The internal mode spectra are the most representative of what should be observed experimentally.

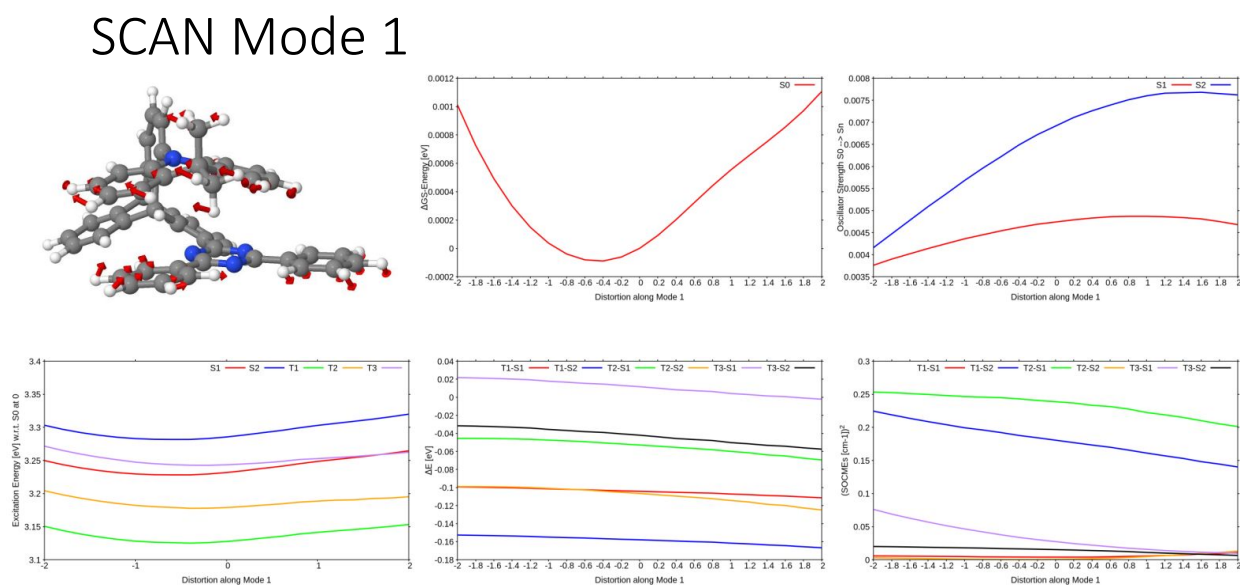
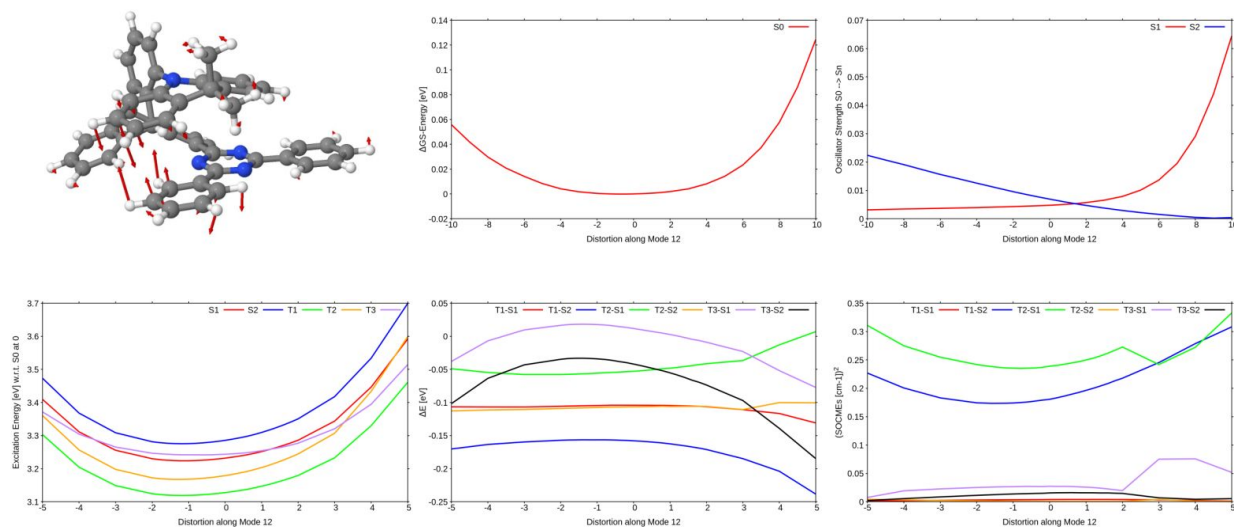


Figure S24 Vibrational mode that intercouple the two lowest energy TpAT-tFFO conformers

SCAN Mode 12



SCAN Mode 9

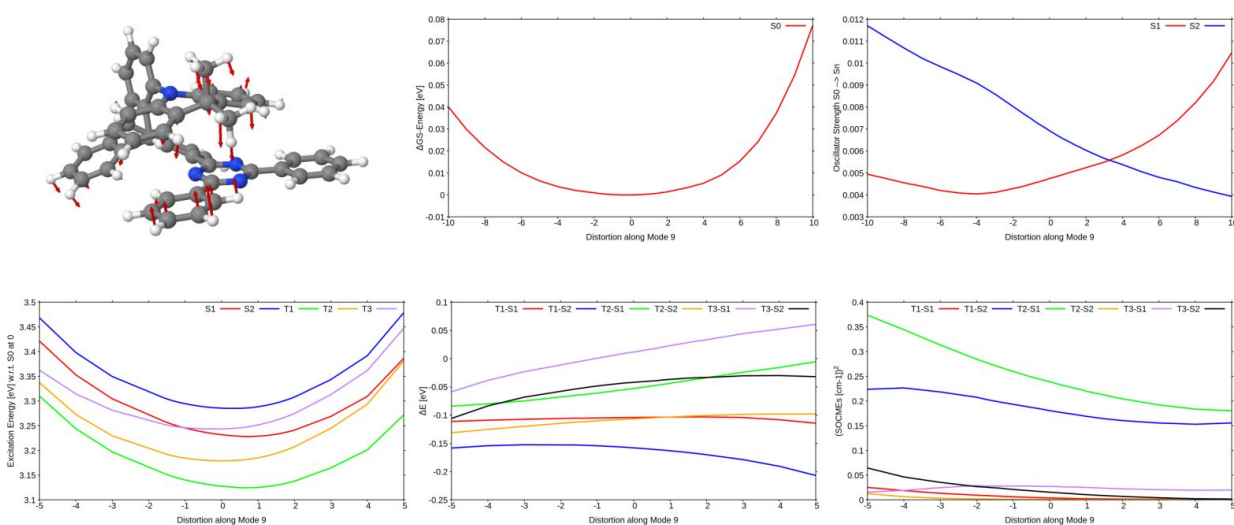


Figure S25 Vibrational modes that have major effect on D A wavefunction overlap and hence singlet triplet energy gap and oscillator strength. TpAT-tFFO conformers

Table S2 Rate constants for the different temperatures of the CzSi matrix time resolved measurements

CzSi (10%)			
T [K]	$K_F [10^5 \text{ s}^{-1}]$	$K_{ISC} [10^6 \text{ s}^{-1}]$	$K_{rISC} [10^5 \text{ s}^{-1}]$
300	3.95 ± 0.22	6.94 ± 0.3	14.48 ± 0.05
150	5.42 ± 0.03	5.10 ± 0.10	2.83 ± 0.14
80	5.72 ± 0.51	1.54 ± 0.10	0.44 ± 0.04
50	6.80 ± 0.06	1.00 ± 0.06	0.10 ± 0.01

Table S3 Rate constants for the different temperatures of the UGH-3 matrix time resolved measurements

UGH-3 (10%)			
T [K]	$K_F [10^5 \text{ s}^{-1}]$	$K_{ISC} [10^6 \text{ s}^{-1}]$	$K_{rISC} [10^5 \text{ s}^{-1}]$
300	$5.37 \pm \sim$	14.915 ± 0.24	26.06 ± 0.27
80	3.60 ± 0.28	1.74 ± 0.09	0.54 ± 0.04

Table S4 Rate constants for the different temperatures of the Zeonex matrix time resolved measurements

Zeonex (1%)			
T [K]	$K_F [10^5 \text{ s}^{-1}]$	$K_{ISC} [10^6 \text{ s}^{-1}]$	$K_{rISC} [10^5 \text{ s}^{-1}]$
300	5.28 ± 0.15	18.88 ± 0.05	2.09 ± 0.96
150	5.32 ± 0.04	7.47 ± 0.44	3.55 ± 0.03
80	9.49 ± 0.10	2.88 ± 0.16	0.54 ± 0.04
50	4.83 ± 0.43	2.39 ± 0.12	0.19 ± 0.01

Publication V

Balancing TADF Properties in π -Bridged Donor–Acceptor Systems by Sterical Constraints: The Best of Three Worlds

J. M. Kaminski, T. Böhmer & C. M. Marian

J. Phys. Chem. C, 128(33):13711–13721, 2024

DOI: 10.1021/acs.jpcc.4c03865

Contribution: Quantum chemical investigation of compounds **1-H**, **2-Me** and **3-ⁱPr** and computation of all relaxed scans, (hybrid) solvent model approaches and spin-vibronic interactions, preparation of Figures 3, 4 and 6, writing the first draft and revising the manuscript.

Balancing TADF Properties in π -Bridged Donor–Acceptor Systems by Sterical Constraints: The Best of Three Worlds

Published as part of The Journal of Physical Chemistry C virtual special issue “TADF-Active Systems: Mechanism, Applications, and Future Directions”.

Jeremy M. Kaminski, Tobias Böhmer, and Christel M. Marian*

Cite This: *J. Phys. Chem. C* 2024, 128, 13711–13721

Read Online

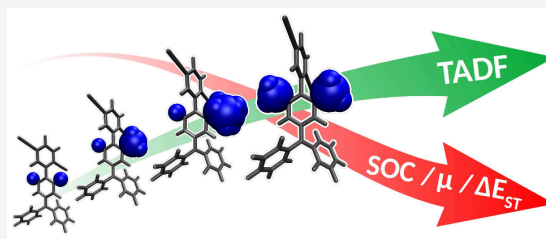
ACCESS |

Metrics & More

Article Recommendations

Supporting Information

ABSTRACT: Key parameters that steer the efficiency of thermally activated delayed fluorescence (TADF) are the energetic splitting ΔE_{ST} between S_1 and T_1 , their mutual spin–orbit coupling (SOC) and the transition dipole strength μ of the S_1 emission. Small ΔE_{ST} values, reasonable SOC and high values of μ are difficult to achieve simultaneously. Using high-level quantum chemical methods, we have investigated the course of these parameters as functions of the donor–acceptor torsion angle in a series of conformationally constrained triarylamine–terephthalonitrile systems. Potential energy surface crossings between triplet states of charge-transfer and local-excitation character close to 90° indicate that a three-state model of the TADF kinetics might not be appropriate. The smallest adiabatic ΔE_{ST} values are obtained for a hybrid solvent model comprising two explicit toluene molecules in addition to a polarizable continuum model of solvation. Due to the substantial geometrical displacements of the S_1 and T_1 potentials in the torsion angle, the adiabatic Hessian method does not provide meaningful rate constants for reverse intersystem crossing. The recently developed vertical Hessian approach remedies this problem.



INTRODUCTION

Organic light-emitting diodes (OLEDs) have emerged as a promising technology for display and lighting applications, particularly in compact devices such as smartphones and smartwatches.¹ The external quantum efficiency of an OLED is primarily determined by the total internal charge-to-photon conversion ratio, i.e., the internal quantum efficiency and the light out-coupling efficiency of the device.² From a technical perspective, achieving uniform performance across all primary colors remains an ongoing challenge. While highly luminescent red^{3–5} and green^{6–8} emitters are already known, there is still great interest to find deep-blue emitters with similar effectiveness.

The principle of thermally activated delayed fluorescence (TADF) has proven to be a promising approach to overcome the efficiency limitations of OLEDs.^{1,9} Initial studies on TADF date back to 1929.¹⁰ Since 2012, when Adachi and co-workers reported the first highly efficient TADF-based OLEDs,¹¹ a rapid development of TADF materials with excellent electroluminescence performance could be observed.¹² A key target in the design of novel TADF emitters is the energy difference between the lowest excited singlet and triplet states, ΔE_{ST} : A small ΔE_{ST} value is crucial for the efficiency of reverse intersystem crossing (rISC),^{13,14} a thermally activated non-radiative process necessary for converting optically dark triplet

excitons into singlet excitons which eventually emit delayed fluorescence. In this way, an internal quantum efficiency of 100% can be achieved by TADF emitters in principle, thereby maximizing the overall device performance. Challenges persist in the development and implementation of TADF-based OLEDs. These include the need for deep-blue TADF emitters, improvement of triplet state lifetimes, inhibition of exciton annihilation through aggregation in thin films, and ensuring operational stability.¹⁵ Addressing these challenges requires comprehensive research efforts to refine TADF systems for practical applications and industrial production.

A promising type of molecules in this regard are purely organic donor–acceptor (D–A) systems. In contrast to commercially available transition metal complexes, which often exhibit symmetrical, nearly spherical shapes, organic D–A systems have the advantage that their molecular structures resemble those of the host or matrix materials. Through the ordered structure of the molecules within the

Received: June 10, 2024

Revised: July 15, 2024

Accepted: July 23, 2024

Published: August 7, 2024



layers of an OLED device, the external quantum efficiency is significantly improved.¹⁶ In D–A compounds, electron and hole densities are spatially separated, yielding states of charge-transfer (CT) character as the lowest excited states with intrinsically very small singlet–triplet energy gaps. Unfortunately, spin–orbit coupling (SOC) between ¹CT and ³CT states, a prerequisite for efficient ISC and rISC, is very small as well. It was shown, however, that a locally excited (LE) triplet state in energetic proximity of the CT states can mediate the interconversion of singlet and triplet populations.^{17–19} From a theoretical perspective, accurately predicting the adiabatic energy difference between the excited singlet and triplet states remains a challenging task because it requires a balanced treatment of CT and LE states in the presence of a solvent environment.¹⁴

This study aims to shine light on how to modulate the characteristics of a known TADF emitter,²⁰ consisting of a triarylamine (TAA) donor and a 1,4-dicyanobenzene (terephthalonitrile, TPN) acceptor (Figure 1b). Dicyanobenzenes

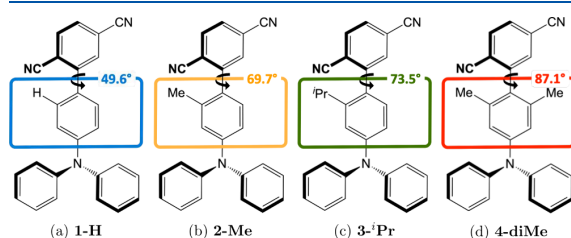


Figure 1. Investigated emitter series consisting of a triarylamine (TAA) donor and a terephthalonitrile (TPN) acceptor unit. Labeling: Consecutive numbers in the order of increasing substitutional effect plus name of the substituent. Differences are highlighted by colored boxes. The torsion angle between the phenylene bridge and the TPN acceptor of the most stable conformer is indicated in the upper right of each colored box.

have been commonly used as acceptor units since the development of the first TADF-based OLED emitters.¹¹ Due to their high photoluminescence efficiencies, dicyano-based N-heterocyclics have played an important role in the design of high-performance TADF materials.^{11,21} Triphenylamines show excellent hole-transporting capabilities. Moreover, their steric demand is able to diminish aggregation-caused quenching.²² Despite these advantageous properties and their high thermal and electrochemical stabilities, triphenylamine-based TADF emitters are rather uncommon.^{23,24} A problem appears to be the increased ΔE_{ST} value in comparison to D– π –A TADF emitters containing N-heterocyclic donors such as carbazole or dimethylacridine.²⁴ However, if the ΔE_{ST} values could be improved, triphenylamines might represent promising donors.

By means of quantum chemistry, we investigate the influence of the chemical substitution (Figure 1a–d) on key characteristics of this emissive system (oscillator strength, spin–orbit coupling, and rate constants for radiative and nonradiative processes) while the emission remains in the blue wavelength regime that is of strong interest. Furthermore, we discuss the challenges met in the simulation of their excited-state properties. Conclusions drawn from the observed trends are not considered system-specific but can be generalized and applied to improve the design principles for other TADF emitters.

METHODS

Molecular geometries and vibrational frequencies of the investigated TADF emitter series were determined with Gaussian 16²⁵ employing the optimally tuned, range-separated ω B97X-D density functional^{26,27} and the split-valence double- ζ def2-SV(P) basis set.^{28–30} The optimal tuning procedure followed the scheme recommended by many authors.^{31–35} It yields a value of $\omega = 0.15$ for the range separation parameter where Koopmans' theorem is fulfilled best (Figure S8). Geometries of singlet excited states were optimized with time-dependent density functional theory (TDDFT),^{36–38} for excited triplet states including the Tamm-Dancoff approximation (TDA).³⁹ Unless noted otherwise, the polarizable continuum model (PCM)^{40–42} was utilized to mimic the toluene environment using the solvent excluding surface (SES) implemented in Gaussian 16.

Excitation energies and excited-state properties were determined with the combined density functional theory and multireference configuration interaction (DFT/MRCI) method^{43,44} using the tight R2016⁴⁵ parameter set. Spin–orbit coupling matrix elements were computed in atomic mean-field approximation using SPOCK.^{46,47} Temperature-dependent vibronic spectra and (r)ISC rate constants were calculated with a recent extension⁴⁸ of the VIBES program,^{49,50} enabling the use of internal coordinates and the application of the vertical Hessian (VH) method which are better suited for a pair of potential energy surfaces with large displacements in a dihedral angle than Cartesian coordinates and the adiabatic Hessian (AH) approach. Numerical derivatives of the electric dipole transition moments and of the spin–orbit coupling matrix elements with respect to the normal coordinates, required for computing radiative or (r)ISC rate constants in Herzberg–Teller approximation,^{19,51,52} were generated with the GRADIENTATOR toolbox.^{53,54} A detailed analysis of the CT and LE contributions to the DFT/MRCI transition densities was carried out with a local version of the TheoDOR program.⁵⁵

RESULTS AND DISCUSSION

For each compound in the investigated D–A series (except for 4-diMe), two conformers can be found in the electronic ground state, even for seemingly symmetric bridges. In particular, the nonequivalency of the 1-H conformers is caused by the propeller structure of the TAA donor unit. The steric demand of the substituents at the bridge increases from 1-H to 4-diMe, entailing increasingly perpendicular D–A arrangements (Figure 1 and Table 1). The shallow potential energy surface of the electronic ground state may be the reason for finding only one 4-diMe conformer. A detailed analysis of the different conformers is omitted here, as this is the subject of a forthcoming paper.⁵⁶ The following results focus on the energetically most stable conformer of each compound.

Table 1. Torsion Angle/° between Donor and Acceptor for All Compounds in the Electronic Ground-State and in the Lowest Excited Singlet and Triplet States

	Compound			
	1-H	2-Me	3-iPr	4-diMe
S ₀	49.6	69.7	73.5	87.1
S ₁ (CT)	34.3	65.9	65.2	81.8
T ₁ (CT)	20.9	41.7	39.5	49.3

Absorption Spectra. Figure 2 shows the computed absorption spectra in toluene solution. Due to the multi-

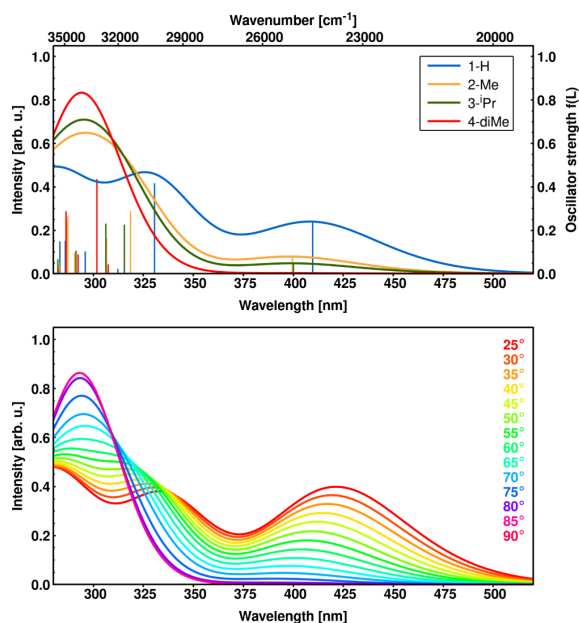


Figure 2. (Top) Computed absorption spectra of **1-H** (blue), **2-Me** (orange), **3-Pr** (green), and **4-diMe** (red) in toluene solution. (Bottom) Simulated absorption spectra of **2-Me** at fixed D–A torsion angles along a relaxed scan of the electronic ground-state relaxed PES. All DFT/MRCI line spectra were broadened with Gaussians of 4400 cm^{-1} full width at half maximum.

configurational character of the excited singlet wave functions (Tables S2–S5), the analysis of the transitions is not straightforward. A close look at the molecular orbitals (MOs) involved in the transitions (Figures S1–S4) further reveals that some of the frontier MOs are delocalized, thus further complicating the designation as CT or LE transition or an admixture thereof. To aid the assignment, we partitioned each molecule into a donor and an acceptor fragment and analyzed the corresponding DFT/MRCI one-particle transition density matrices by means of the TheoDOR⁵⁵ toolkit.

The first peak at ca. 400 nm is assigned to the $S_1 \leftarrow S_0$ transition. It is mainly characterized by an electron transfer from the highest occupied molecular orbital (HOMO) of the donor to the lowest unoccupied molecular orbital (LUMO) of the acceptor. We observe a clear correlation between the intensity of the $S_1 \leftarrow S_0$ absorption peak and the torsion angle between the donor and acceptor moieties: The larger this dihedral angle, the more pronounced is the CT character and the weaker is the oscillator strength of the $S_1 \leftarrow S_0$ transition. The intensity decrease is accompanied by a small blue shift of the absorption wavelength, ranging from **1-H** (410 nm) to **4-diMe** (396 nm). Note that the CT contributions to the corresponding T_1 states are markedly smaller, save for **4-diMe** with nearly orthogonal D–A orientation.

The $S_2 \leftarrow S_0$ transitions of **1-H**, **2-Me**, and **3-Pr** are dominated by a $\text{HOMO} \rightarrow \text{LUMO} + 1$ CT excitation mixed with varying amounts of LE_{TAA} configurations. The admixture of CT and LE character is most pronounced for **1-H** where the molecular planes of the phenylene bridge and the TPN

acceptor are twisted by about 50° , thus enabling substantial π -conjugation in $\text{LUMO} + 1$ (Figure S1). With increasing steric strain, the π -conjugation is diminished in this series and disappears completely in **4-diMe** where the $\text{HOMO} \rightarrow \text{LUMO} + 1$ CT excitation forms the leading term of the $S_4 \leftarrow S_0$ transition. The decrease of the π -conjugation in $\text{LUMO} + 1$ explains the strong blue shift of the excitation wavelength from 331 nm in **1-H** over 319 nm in **2-Me** and 315 nm in **3-Pr** to 286 nm in **4-diMe** and the concomitant reduction of the oscillator strength in this series (Table S1).

The $S_3 \leftarrow S_0$ and $S_5 \leftarrow S_0$ transitions are mainly characterized by LE_{TAA} contributions. To understand their intensity patterns, it is useful to study the donor fragment first. The absorption spectrum of the unsubstituted D_3 -symmetric triphenylamine molecule shows one strong E -symmetric $\pi\pi^*$ band with maximum at about 300 nm.⁵⁷ When the molecular point group is reduced to C_2 , the band splits into an A - and a B -symmetric component with perpendicular directions of the transition dipole vectors. In the D–A compounds investigated in this work, the A -polarized transition forms the lowest LE_{TAA} -type excitation. Its transition dipole and the dipole vectors of the CT excitations are arranged in a close to collinear fashion, i.e., they can strongly couple. Depending on the directions of the interacting dipoles, their combination can either enhance or reduce the oscillator strengths of the mixed LE/CT transitions. In the $S_2 \leftarrow S_0$ transition of **1-H**, these vectors point in the same direction and thus lead to an enhancement of absorption strength whereas their negative superposition causes the $S_3 \leftarrow S_0$ absorption to be weak. With decreasing CT contribution to the S_3 wave function of the emitter molecule, the $S_3 \leftarrow S_0$ absorption peak becomes more and more intense. This modulating effect is even more pronounced when an additional phenylene bridge is inserted between donor and acceptor, thus increasing their mutual distance.⁵⁸ The B -symmetric component of the LE_{TAA} transition can be associated with the $S_5 \leftarrow S_0$ transition. Because its transition dipole vector points in a direction perpendicular to the D–A axis, it cannot couple to a CT excitation. Hence, wavelengths and intensities of the $S_5 \leftarrow S_0$ transition are only marginally affected by the substitution.

The lowest-lying LE_{TPN} configuration, which gives rise to a shallow band with an onset at about 320 nm in the native TPN molecule in water solution,⁵⁹ contributes mainly to the $S_4 \leftarrow S_0$ transition in **1-H**, **2-Me**, and **3-Pr**. Its excitation wavelength does not vary strongly among these compounds, as may be expected for a predominantly local transition. Due to the increased steric hindrance between the cyano group in the ortho-position of the linkage and the substituents of the bridge, this transition is blue-shifted in compound **4-diMe**, where it forms the $S_6 \leftarrow S_0$ band with an excitation wavelength of 283 nm.

Interestingly, the impact of the substituents on the absorption spectra is not primarily driven by electronic effects. Rather, it seems to correlate with the torsion angle between the donor and acceptor units which varies between $\sim 50^\circ$ (**1-H**) and $\sim 87^\circ$ (**4-diMe**) in the respective minimum nuclear arrangements, see Figure 1 and Table 1. To prove this correlation, we computed the absorption spectrum of compound **2-Me** as a function of the torsion angle while optimizing all other geometry parameters of the ground-state potential energy surface (PES). The agreement between the computed absorption spectra of **1-H** to **4-diMe** (Figure 2, top) and the simulated spectra of compound **2-Me** for fixed torsion

angles between 25° and 90° (Figure 2, bottom) is striking and substantiates our assumption that the observed changes in the absorption profiles mainly have a steric rather than an electronic origin.

Torsional Effects on Excited-State Properties. The torsion angle between donor and acceptor does not only have strong impact on the absorption properties of the compounds. As shown in Figure 3, it affects several other excited-state

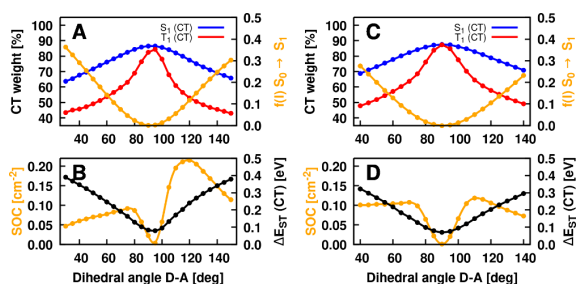


Figure 3. (A) CT character of the first excited singlet (blue) and triplet (red) state. Oscillator strength for the $S_1 \leftarrow S_0$ transition (orange) of 2-Me. (B) ΔE_{ST} (black) and sum of squared SOCMEs (orange) between S_1 and T_1 states of 2-Me. (C and D) Corresponding data for 4-diMe. All data were computed at the DFT/MRCI level of theory along a relaxed scan of the torsion angle in the electronic ground state.

properties of the emitters as well. In particular, we investigated the oscillator strength $f(I)$ of the $S_1 \leftarrow S_0$ transition of compound 2-Me and the CT contributions to the S_1 and T_1 states (Figure 3A), their mutual spin–orbit coupling matrix elements (SOCMEs), as well as the energy gap ΔE_{ST} (Figure 3B). Corresponding data for 4-diMe can be found in Figure 3C,D. Knowledge of their functional dependencies on the torsional coordinate is considered a key toward understanding the photophysics of these chromophores.

A perpendicular D–A orientation favors the CT character of the first excited singlet and triplet states and lowers their energetic splitting ΔE_{ST} to a minimum value. Concomitantly, the oscillator strength of the $S_1 \leftarrow S_0$ transition vanishes due to the missing overlap of hole and particle densities which are located on donor and acceptor, respectively. Direct SOC between states of CT character involving the same orbitals is expected to be close to zero as well.⁵² Accordingly, a strictly perpendicular arrangement does not seem to be as advantageous as expected when judging solely on the basis of ΔE_{ST} . Lowering the torsion angle to values describing nearly coplanar D–A arrangements strongly increases $f(I)$, but widens the energy gap. An increased ΔE_{ST} value, next to lowered SOC, minimizes the possibility of observing TADF. As a realistic compromise between these extremes, a twist of the donor and acceptor moieties by about $\pm 10^\circ$ away from orthogonality could markedly improve the situation: The mutual SOCME between S_1 and T_1 increases steeply while the CT weight of the S_1 and T_1 wave functions and the ΔE_{ST} values are still close to their optima.

Similar conclusions can be drawn for compound 4-diMe. The fact that the graphs for torsion angles $< 90^\circ$ and $> 90^\circ$, displayed in Figure 3C,D, are not perfect mirror images of one another, although the bridge is symmetrically substituted, is a consequence of the propellar structure of the TAA unit.

However, the qualitative picture changes when the nuclear frame is allowed to adapt to the electronic structure of the excited states. In particular, the S_1 – T_1 energy gap does no longer approach zero for a perpendicular orientation of donor and acceptor. Moreover, the data suggest that a three-state model of the excited-state decay, comprising only the S_0 , 1CT , and 3CT states and their mutual couplings, might not be sufficient. The reasons underlying this behavior are discussed below.

Geometry Relaxation Effects on the S_1 and T_1 States.

For all compounds, the minimum of the T_1 PES is located at much smaller torsion angles than the one of the S_1 PES (Table 1). Geometry relaxation of 2-Me in the S_1 state, for example, yields a minimum at 65.9° , whereas the minimum of the T_1 state is found at 41.7° . The eligibility of the applied quantum chemical methods to determine the equilibrium structures of the excited states may be judged from a convincing match of our results with recent time-resolved near-infrared spectroscopy measurements.⁶⁰ The disparity of the S_1 and T_1 equilibrium torsion angles is rooted in the fact that exchange interactions which stabilize triplet-coupled open-shell determinants with respect to singlet-coupled ones are much stronger in LE $\pi\pi^*$ states than in CT states where the overlap of the involved open-shell electron densities is small. Consequentially, the contributions of LE configurations to the T_1 wave function are much higher than to the corresponding S_1 wave function. Moreover, the percentage of LE contributions is seen to vary with the torsion angle in the investigated D–A compounds.

Relaxed scans of the first excited singlet and triplet PESs for fixed values of the torsional coordinate while optimizing all other nuclear degrees of freedom were computed at the TDDFT/ ω B97X-D level of theory. For 2-Me, properties derived from single-point DFT/MRCI calculations along these paths are shown in Figure 4. The analysis of the one-particle

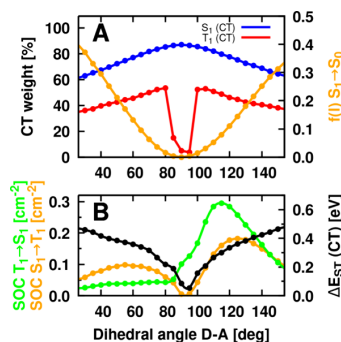


Figure 4. Properties of DFT/MRCI wave functions resulting from single-point calculations along relaxed TDDFT paths of the S_1 and T_1 states. (A) CT character of the first excited singlet (blue) and triplet (red) state. Oscillator strength for the $S_1 \leftarrow S_0$ transition (orange) of 2-Me. (B) ΔE_{ST} (black) and sum of squared SOCMEs between S_1 and T_1 states (ISC: orange, rISC: green) of 2-Me.

transition density matrix reveals that the S_1 state has predominantly CT character across the considered range of torsion angles, reaching its maximum at 90° . The large exchange interactions in LE $\pi\pi^*$ states stabilize 3LE states which are therefore energetically much closer to the CT states than their singlet counterparts. For this reason, the wave function of the T_1 state exhibits substantial contributions from LE configurations both on the TAA donor and TPN acceptor

moieties (Figures S5 and S6). The LE character is particularly pronounced at torsion angles close to planarity. With increasing interplanar D–A angle, the CT contributions to the T_1 wave function rise to about 50% until they suddenly drop as the torsion angle approaches 85° (Figure 4A), indicating a major change in the electronic structure of the T_1 state and a breakdown of the Born–Oppenheimer approximation. In the LE regime, the T_1 state originates mainly from a local excitation on the TPN acceptor moiety, $^3\text{LE}_{\text{TPN}}$, while the T_2 state is predominantly of CT type.

The change in the electronic structure of the T_1 state when switching from the CT to the LE regime is reflected in a sudden increase of the mutual S_1 – T_1 SOC close to an orthogonal D–A arrangement (Figure 4B). The leading configurations of the ^1CT and $^3\text{LE}_{\text{TPN}}$ states share the electron accepting orbital on the TPN moiety, but the hole orbitals are different. This means that the S_1 and $^3\text{LE}_{\text{TPN}}$ states are singly excited with respect to one another, an important property in view of the effective one-electron nature and symmetry properties of the SOC operator. The energetically accessible PES crossing of the T_1 and T_2 states therefore has interesting consequences for the ISC and rISC probabilities: A three-state equilibrium model, underlying the Arrhenius analysis of the prompt and delayed fluorescence decay times, is not considered appropriate for describing the kinetic scheme of ISC and rISC processes in **2-Me**. The analysis of the excited-state energy profiles of **1-H**, **3-iPr**, and **4-diMe** suggests similar excited-state decay characteristics for these compounds as well.

Emission Properties. For the theoretical simulation of emission properties, the commonly used adiabatic Hessian (AH) method^{61,62} results in featureless and very broad emission spectra (Figure 5a). Due to large-amplitude motions in low-frequency vibrational modes, the harmonic oscillator model, which uses the respective equilibrium geometry as offset for the Taylor expansion of the PES, is not appropriate. In the compounds studied in this work, mainly the torsional coordinate between donor and acceptor is involved. The vertical Hessian (VH) method for the computation of vibronic spectra⁴⁸ yields emission bands with spectral origins and peak maxima (Figure 5b) in excellent agreement with the experiment.⁶³

Because the harmonic approximation tends to overestimate the Franck–Condon (FC) factors between the initial vibrational level in the electronically excited state and higher vibrational quanta of torsional modes in the electronic ground state, the computed spectra are somewhat broader than their experimental counterparts (Figure 5b, shown for **2-Me**). The emission spectra of **1-H**, **2-Me**, and **3-iPr** are almost superimposable with maxima at 499, 495, and 496 nm, respectively, while the **4-diMe** emission ($\lambda_{\text{max}} = 513$ nm) is somewhat red-shifted. The oscillator strength of the $S_1 \rightarrow S_0$ emission follows the trend observed already for absorption, i.e., we see a large step between **1-H** and **2-Me**, very similar values for **2-Me** and **3-iPr** and a reduction by a factor of 10 when moving to **4-diMe** (Table 2). Pure radiative lifetimes (without consideration of competitive nonradiative channels) vary between 10 and 590 ns in this series. Radiative lifetimes in the 500 ns regime may appear long, but they are not untypical for organic D–A TADF emitters.

Singlet–Triplet Energy Gap ΔE_{ST} . The ability of a molecule to emit TADF critically depends on the size of the singlet–triplet energy gap ΔE_{ST} . In earlier work by Sommer et al.,²⁰ a value of 980 cm^{-1} (122 meV) had been derived for the

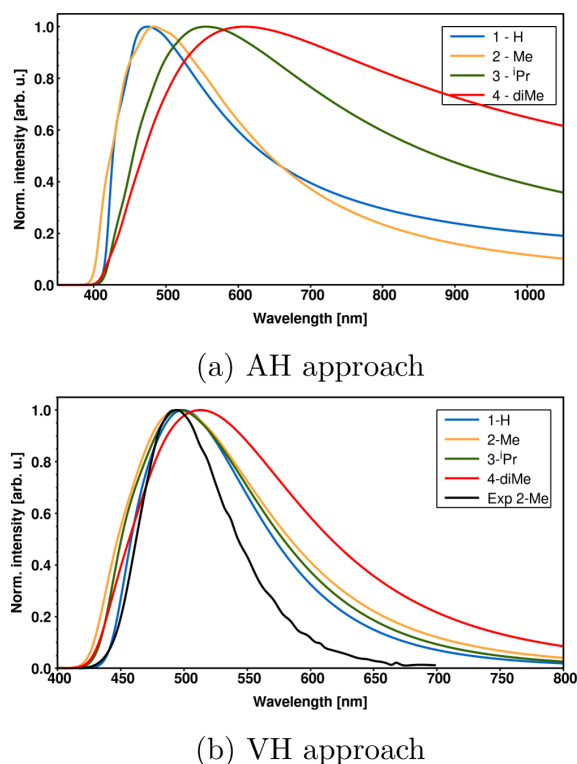


Figure 5. Computed emission spectra of **1-H** (blue), **2-Me** (orange), **3-iPr** (green), and **4-diMe** (red) in toluene solution at 300 K in comparison with an experimental emission spectrum of **2-Me** in toluene at 300 K.⁶³ (a) adiabatic Hessian approach and (b) vertical Hessian approach.

Table 2. Computed $S_1 \rightarrow S_0$ Emission Wavelengths/nm of DFT/MRCI Line Spectra (vert.), Adiabatic Hessian (AH), and Vertical Hessian (VH) Spectra^a

	Compound			
	1-H	2-Me	3-iPr	4-diMe
vert.	482	484	490	492
$f(l)$	0.348	0.090	0.071	0.006
$\tau_{\text{rad.}}$	10	39	51	590
AH	474	483	555	609
VH	499	495	496	513

^aOscillator strengths $f(l)$ and radiative lifetimes $\tau_{\text{rad.}}$ /ns are obtained from the Einstein relation at the S_1 minimum.

energy difference between the S_1 and T_1 states of **2-Me** on the basis of an Arrhenius plot. In the same work, a quantum chemically determined energy separation of 840 cm^{-1} (104 meV) was reported. Note, however, that this value resulted from single-point TDDFT calculations at the optimized S_0 geometry, i.e., in the absorption region. This vertical energy gap is therefore neither directly comparable to the 0–0 energy difference underlying the Arrhenius equations nor to the energy shifts derived from the maxima of the fluorescence and phosphorescence spectra. Since TADF is not an ultrafast process that proceeds on the subpicosecond time scale, the nuclear arrangement has the time to adapt to the electronic potentials of the S_1 and T_1 states, respectively.

The data presented in Table 1 reveal that the torsion angles of the S_1 and S_0 equilibrium structures are similar whereas T_1 has its minimum at markedly reduced values of the torsional coordinate. As a consequence, geometry relaxation in the excited state increases the ΔE_{ST} values substantially (Table 3). The consideration of zero-point vibrational energy corrections changes the overall picture only slightly.

Table 3. DFT/MRCI computed $S_1 - T_1$ energy differences $\Delta E_{ST}/\text{meV}$ in toluene solution

	Compound			
	1-H	2-Me	3- ⁱ Pr	4-diMe
$\Delta E_{ST, \text{vert}}^{a,b}$	341	192	162	73
$\Delta E_{ST, \text{adiab}}^a$	501	438	428	333
$\Delta E_{ST, \text{adiab}}^c$	—	263	—	—
$\Delta E_{ST, 0-0}^a$	510	481	463	322

^aPCM. ^bEvaluated at the S_0 minimum geometry. ^cHybrid solvent model, see text.

We thus have to face the situation that the computed $S_1 - T_1$ 0–0 energy gaps are significantly larger than expected for a TADF emitter. This may have a variety of reasons which are analyzed and discussed in the following.

In liquid solutions, the primarily excited solute does not only relax internal nuclear degrees of freedom. For all but ultrafast processes, the reorganization of the solvent environment has to be taken into consideration as well. Initially, the electronic ground state of the emitter molecule and the solvent are in equilibrium. Upon electronic excitation, the charge distribution changes almost instantaneously, effectuating that the solvent degrees of freedom must adapt to the new situation. Since solute and solvent have different response times, a slow evolution from the nonequilibrium to the equilibrium solvation occurs.

Solvent reorganization effects on spectroscopic properties are notoriously difficult to model, however. To simulate the coupling between the solute and solvent, typically a two step process is used in a polarizable continuum model (PCM): (i) Directly after the vertical transition process, the final state of the solute experiences an electrostatic field corresponding to a solvent polarization frozen to the initial state. (ii) A dynamic component of the solvent polarization rearranges to equilibrate with the final state charge density of the solute. While in linear response models the latter process is computed from the transition density, state-specific models like the corrected linear response (cLR) approach⁶⁴ incorporate solvent reorganization effects on the basis of electron density differences between initial and final states, including a density-dependent relaxation of the solvent polarization.⁶⁵

The cLR model works extremely well for CT excitations of polar transition metal complexes such as carbene coinage metal amides.^{66,67} In these compounds, the CT excitation reduces the static dipole moment of the molecule. Applied to **2-Me** that exhibits a much larger static dipole moment in the S_1 state than in the S_0 state, the cLR model apparently overshoots: The cLR corrections lower the emission energy in toluene solution by about 5000 cm^{-1} (Table S6) in comparison to a PCM environment. Considering the good agreement of the PCM-computed emission spectrum with its experimental counterpart (Figure 5b), this energy shift seems too strong and speaks against the applicability of the cLR model in the present case.

Recently, Mewes and co-workers advertised a state-specific ROKS/PCM approach,^{14,68} which appears to work well for many organic D–A systems but fails to reproduce the published experimental ΔE_{ST} value for a few emitter compounds including **2-Me**.²⁰ The adiabatic energy separations between the S_1 and T_1 states of **2-Me** in toluene, reported in that study, are significantly larger than the experimentally derived value and rather resemble the computational results of the present work.

Instead of employing a continuum model for describing solvation effects, explicit toluene molecules could be used to form a solvent shell. To obtain a representative, statistically balanced distribution, extensive molecular dynamics simulations would have to be carried out⁶⁹ which is beyond the scope of the present work. Here, we pursued a middle way and placed two toluene molecules close to the π -bridge using the Quantum Cluster Growth extension of the CREST program^{70,71} (Figure 6). These two toluene molecules were then

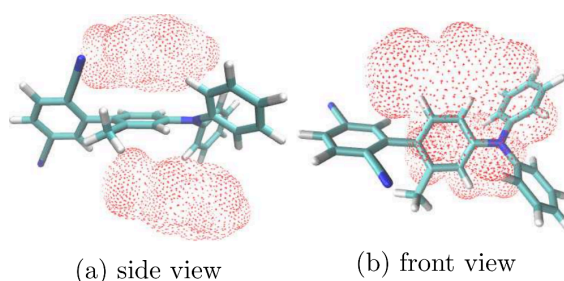


Figure 6. Optimized structure of **2-Me** in the electronic ground state with two explicit toluene solvent molecules. The red crosses indicate the van der Waals surfaces of the toluene molecules.

explicitly included in our quantum chemical calculations of the excited-state properties, and the whole complex was enclosed by a PCM cavity. While effects of this hybrid solvation model on the relaxed geometries are minimal, the electronic effect lowers the CT excitations in comparison to the implicit solvent model (Table S7). We do not see any indications for an exciplex formation. Rather, we attribute the preferential stabilization of the solute in the S_1 state to attractive interactions between its strong electric dipole moment and the highly polarizable π -electron clouds of the toluene molecules. As the electric dipole moment of **2-Me** in the T_1 state is much smaller than in S_1 , the explicit consideration of the solvent–solute interactions results in a decreased ΔE_{ST} gap as desired.

Rate Constants. The attempt to model explicit solvent interactions by two quantum chemically treated toluene molecules greatly improves the adiabatic singlet–triplet energy gap of **2-Me** from 0.44 eV (PCM) to 0.26 eV (hybrid solvent model). Within the harmonic oscillator model, the adiabatic Hessian (AH) approach⁴⁹ (Figure 7, left), commonly used so far in our group, yields room-temperature ISC rate constants of $3 \times 10^6 \text{ s}^{-1}$ (PCM) and $2 \times 10^6 \text{ s}^{-1}$ (hybrid solvent model) in FC approximation. As expected, the ΔE_{ST} value has larger impact on the rISC process, for which rate constants of $2 \times 10^{-2} \text{ s}^{-1}$ (PCM) and $6 \times 10^1 \text{ s}^{-1}$ (hybrid solvent model) are obtained. The computed ΔE_{ST} value is thus still too large to yield rISC rate constants which are compatible with the experimentally determined TADF lifetime of $\approx 30 \mu\text{s}$.²⁰

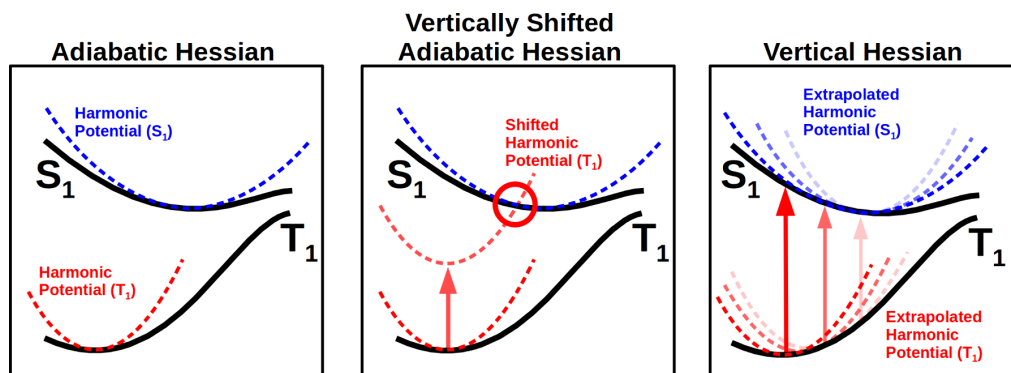


Figure 7. Schematic comparing the adiabatic Hessian (AH, left), vertically shifted adiabatic Hessian (center), and vertical Hessian (VH, right) approaches.

Could the crossing of the ^1CT and ^3CT PESs with the $^3\text{LE}_{\text{TPN}}$ PES in the neighborhood of a perpendicular conformation (see the [Geometry Relaxation Effects on the \$S_1\$ and \$T_1\$ States](#) section) play a decisive role? The spin-vibronic mechanism is known to substantially accelerate TADF in organic donor–acceptor compounds exhibiting a low-lying ^3LE state energetically close to the ^3CT and ^1CT states.¹⁹ For example, by including spin-vibronic interactions by means of a Herzberg–Teller-like expansion of the coupling, we could successfully explain the complicated excited-state decay behavior of the through-space CT TADF emitter TPAAT-tFFO^{72,73} and of the well-known through-bond CT TADF emitter DMAC-TRZ.^{74,75} Going beyond the FC approximation in the case of **2-Me** in an implicit solvent environment increases the rISC rate constant at room temperature merely to $9 \times 10^{-2} \text{ s}^{-1}$, a value still much too small to explain the experimentally observed TADF.

In a second attempt to remedy the problem, we simply adjusted the singlet–triplet energy gaps by vertically shifting the harmonic potentials of S_1 and T_1 (Figure 7, center). The rate constants computed for ΔE_{ST} values between 50 and 400 meV in AH approximation are presented in [Tables S8 and S9](#). With a decreasing singlet–triplet energy gap, the rISC rate constant increases by several orders of magnitude. Although the results meet our expectations at first sight, they are not fully credible. Since the S_1 and T_1 states are not nested, a strong energetic shift could lead to crossing potential energy surfaces. We observe this situation for **4-diMe** ([Tables S8 and S9](#), $\Delta E_{\text{ST}} < 100 \text{ meV}$) where rISC is faster than ISC.

Earlier theoretical studies suggest that the static picture underlying the AH approach is not sufficient to model the TADF process in conformationally flexible emitters.¹⁹ For example, Penfold and co-workers presented an extensive study using quantum nuclear dynamics to enlighten the excited-state processes in a copper phenanthroline complex undergoing large-amplitude flattening distortions.^{76–78} A similar dynamic mechanism was postulated for linear carbene metal amides, where the torsional motion about the metal–ligand bond plays a key role for the understanding of its photophysics.^{66,79} A simplified 3-state model that accounts for the spin-vibronic coupling of a ^1CT , ^3CT , and ^3LE state to a conformational degree of freedom associated with the torsion angle was presented lately by Dhali et al.⁷⁵ Their analysis is based on a scan of the torsional coordinate in the optimized electronic ground-state, however. For **2-Me**, the energy profiles of the

relaxed excited-state scans are quite different from the unrelaxed energy profiles along the ground-state scan. The simplified 3-state model of Dhali et al. therefore does not appear applicable in the present case.

The above-mentioned studies point toward a dynamic kinetic scheme in which the population transfer between the S_1 and T_1 surfaces and the radiative decay of the S_1 population to the S_0 potential occur at different points in coordinate space. For **2-Me**, the ΔE_{ST} gap is smallest for an orthogonal D–A orientation and, therefore, rISC is expected to occur primarily here. In contrast, the electric dipole transition probability is very low at 90° but increases appreciably as the torsion angle gets smaller (Figure 4 and [Table S11](#)). Fluorescence is therefore preferentially emitted in less twisted conformations.

To mimic the dynamic behavior of the ISC and rISC processes in **2-Me** without resorting to costly quantum dynamics simulations, we applied a vertical Hessian (VH) approach to determine rate constants at fixed torsion angles of the relaxed S_1 path (Figure 7, right). The VH method is well established for computing absorption and emission spectra,^{61,62,80,81} but it has, to our knowledge, so far not been applied by other groups to determine vibrational densities of states for nonradiative transitions such as ISC and rISC. Briefly, this method uses the gradients and Hessians of the initial and final electronic states at the fixed geometry of the initial state to extrapolate the course of the PESs and to compute FC factors. In the limit of strictly parabolic PESs, the VH and AH methods are supposed to yield identical results. The AH method is known to yield promising results for the onset of a vibronic spectrum and the 0–0 transitions. In contrast, in the strong coupling case, which is characterized by large geometric displacements of the minima in at least one vibrational coordinate,⁸² we expect the VH model to be more realistic, especially in cases in which these displacements are related to low-frequency modes. Details of the method and its implementation are presented in a separate paper by Böhmer et al.⁴⁸

Application of the VH method to the $S_1 \rightarrow T_1$ ISC in **2-Me** yields rate constants ranging between 10^6 and 10^7 s^{-1} upon variation of the torsion angle (Figure 8). Interestingly, the highest value is obtained for 60° , close to the equilibrium geometry of the S_1 state. In contrast, the reverse $S_1 \leftarrow T_1$ ISC process speeds up dramatically as the torsion angle increases. Starting from values of the order of 1 s^{-1} at the T_1 minimum, the rISC rate constant grows roughly exponentially to about 5

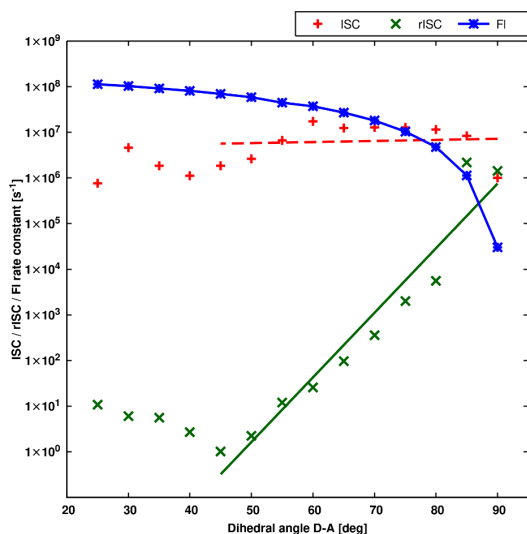


Figure 8. DFT/MRCI fluorescence rate constants of **2-Me** based on the Einstein relation, $S_1 \rightarrow T_1$ ISC and $S_1 \leftarrow T_1$ rISC rate constants in toluene (PCM) at 298 K. Note the logarithmic scale on the y-axis. The computed rate constants were supplemented by an exponential fitting from 45 (T_1 minimum) to 90 deg.

$\times 10^3 \text{ s}^{-1}$ for an angle of 80° . This value appears to be in the right ballpark in view of the experimentally observed delayed fluorescence lifetime of $357.5 \mu\text{s}^{63}$ of **2-Me**. The sudden jump of the rISC rate constant to values between 10^6 and 10^7 s^{-1} for torsion angles between 85° and 90° is only partially caused by the diminishing S_1 – T_1 energy gap. A large portion of this increase is due to the leading ${}^3\text{LE}_{\text{TPN}}$ character of the T_1 state in this regime and the concomitant enhancement of the SOC.

In the case of **4-diMe**, we computed ISC and rISC rate constants for a torsion angle of 81.8° , corresponding to the dihedral angle of the S_1 minimum structure. The VH method yields an extrapolated energy gap of 635 cm^{-1} and a rate constant of $k_{\text{ISC}} = 3.9 \times 10^6 \text{ s}^{-1}$ for the forward $S_1 \rightarrow T_1$ process, similar to the computed ISC rate constants of **2-Me**. The backward transition proceeds at a much shorter time scale in **4-diMe** than the corresponding process in **2-Me**. For $S_1 \leftarrow T_1$, the VH method yields an extrapolated energy gap of -716 cm^{-1} and a rate constant of $k_{\text{rISC}} = 4.6 \times 10^4 \text{ s}^{-1}$, in good agreement with the experimentally observed delayed fluorescence lifetime of $18.4 \mu\text{s}^{63}$ of **4-diMe**.

CONCLUSIONS

In this work, we have investigated the impact of chemical substitution on the TADF properties of triarylamine–terephthalonitrile emitters that exhibit blue emission wavelengths by means of advanced quantum chemical methods. The substituents, one (**2-Me**) or two methyl groups (**4-diMe**) or an isopropyl residue (**3-*i*Pr**), are attached to the donor in the ortho position of the donor–acceptor linkage. The inductive effects brought about by the substitution are found to be minimal. Rather, we attribute the variation of the photophysical properties among the compounds predominantly to the sterical strain exerted by the substituents. We could prove a clear correlation between the D–A twist angle and the absorption profile of a compound. For the respective most stable conformer, this dihedral angle varies between $\sim 50^\circ$

(**1-H**) and $\sim 87^\circ$ (**4-diMe**) in the electronic ground state. Similar dihedral angles are observed for the equilibrium structures of the S_1 states which exhibit ${}^1\text{CT}$ character. The corresponding T_1 states are markedly less twisted due to the admixture of ${}^3\text{LE}_{\text{TAA}}$ configurations. This disparity results in adiabatic ΔE_{ST} values which are much larger than the energy gaps determined from experimental data on the basis of Arrhenius plots.

Part of the problem seems to be caused by the continuum model of the solvent–solute interactions which does not fully account for the solvent reorganization effects following the primary excitation of the S_1 state. The shortcomings of the solvent model are not a specific problem of the methods employed in the present work but are a common phenomenon discussed in the literature. For **2-diMe**, a hybrid model was set up comprising two explicitly treated toluene molecules in addition to the surrounding self-consistent reaction field. The interaction between the highly polarizable π -electron clouds of the toluene molecules and the electric dipole moment of the solute in the excited state preferentially stabilizes the S_1 potential energy and improves the ΔE_{ST} value. However, the magnitude of the resulting adiabatic singlet–triplet energy gap still appears to be incompatible with the experimentally observed delayed fluorescence lifetimes.

Potential energy scans of the torsional coordinate in the excited state reveal the presence of a further low-lying electronic state, so far not discussed in the relevant literature. While the S_1 state retains ${}^1\text{CT}$ character at all considered nuclear arrangements, an energetically accessible crossing between states of ${}^3\text{CT}$ and ${}^3\text{LE}_{\text{TPN}}$ character is observed close to the perpendicular arrangement of the donor and acceptor moieties. Due to the presence of this conical intersection, a three-state kinetic model of the TADF processes resting only on the S_0 ground state and the ${}^1\text{CT}$ and ${}^3\text{CT}$ excited states and their mutual couplings appears inappropriate. Spin-vibronic interactions, accounted for by means of a Herzberg–Teller-type expansion of the S_1 – T_1 SOC, change the picture only marginally.

Like other conformationally flexible through-bond D–A systems, the TAA–TPN emitters face the situation that the vertical singlet–triplet energy gap is small and hence rISC is large only for a perpendicular alignment of the donor and acceptor units where the transition dipole moment and hence the emission probability vanish. While a static description of the TADF process, based on rate constants for an equilibrated population of the excited singlet and triplet state, is unable to deal with the problem, a quantum dynamical treatment is prohibitively expensive considering the microsecond time scale of the TADF kinetics. Relaxed scans of the excited state potentials and scans along the torsional coordinate in the electronic ground state yield qualitatively different results in the series of compounds, questioning the credibility of simplified dynamic models.

To mimic the dynamical behavior of a system undergoing large-amplitude motions without resorting to costly dynamics simulations, we here advocate the application of the vertical Hessian (VH) method. The VH method is well established for computing FC spectra, but has, to our knowledge, not been employed by other groups for determining rate constants of nonradiative transitions. This method uses the gradients and Hessians of the initial and final electronic states at the fixed geometry of the initial state to extrapolate the course of the PESs and to compute the FC factors and the vibrational

density of states. Due to the large displacement of the S_1 and T_1 minima in the torsional coordinate, we expect the VH model to yield more realistic rate constants than the commonly used adiabatic approaches.

Evidently, the steric demand of the substituents controls the D–A torsion angle and hence the ΔE_{ST} value. The ratio between $S_1 \rightarrow T_1$ ISC and $S_1 \leftarrow T_1$ rISC probabilities is negligibly small for the unsubstituted compound and maximizes in this series for the dimethylated compound. We therefore consider **4-diMe** the most promising candidate for showing TADF behavior. The increased percentage of the delayed component does not remedy the problem that its overall radiative rate constant of $\sim 2 \times 10^6 \text{ s}^{-1}$ is rather low but not untypical for an organic D–A compound.

■ ASSOCIATED CONTENT

SI Supporting Information

The Supporting Information is available free of charge at <https://pubs.acs.org/doi/10.1021/acs.jpcc.4c03865>.

Characterization of the excited singlet states in the absorption region showing the wave function composition and molecular orbitals of all compounds, emission spectra using the adiabatic Hessian approach, solvent shifts and rate constants according to various models, and procedure for the optimization of the range-separation parameter (PDF)

■ AUTHOR INFORMATION

Corresponding Author

Christel M. Marian – Institute of Theoretical and Computational Chemistry, Faculty of Mathematics and Natural Sciences, Heinrich Heine University Düsseldorf, 40225 Düsseldorf, Germany; orcid.org/0000-0001-7148-0900; Email: christel.marian@hhu.de

Authors

Jeremy M. Kaminski – Institute of Theoretical and Computational Chemistry, Faculty of Mathematics and Natural Sciences, Heinrich Heine University Düsseldorf, 40225 Düsseldorf, Germany

Tobias Böhmer – Institute of Theoretical and Computational Chemistry, Faculty of Mathematics and Natural Sciences, Heinrich Heine University Düsseldorf, 40225 Düsseldorf, Germany; orcid.org/0009-0004-2823-5300

Complete contact information is available at:

<https://pubs.acs.org/doi/10.1021/acs.jpcc.4c03865>

Author Contributions

J.M.K. and T.B. contributed equally to this work.

Notes

The authors declare no competing financial interest.

■ ACKNOWLEDGMENTS

The authors thank the Deutsche Forschungsgemeinschaft (DFG, German Research Foundation) for financial support through GRK 2482, project no. 396890929, and the members of the research training network ModISC, in particular Dragana Sretenović and Ralf Kühnemuth, for valuable discussions.

■ REFERENCES

- (1) Teng, J.-M.; Wang, Y.-F.; Chen, C.-F. Recent progress of narrowband TADF emitters and their applications in OLEDs. *J. Mater. Chem. C* **2020**, *8*, 11340–11353.
- (2) Tenopala-Carmona, F.; Lee, O. S.; Crovini, E.; Neferu, A. M.; Murawski, C.; Olivier, Y.; Zysman-Colman, E.; Gather, M. C. Identification of the key parameters for horizontal transition dipole orientation in fluorescent and TADF organic light-emitting diodes. *Adv. Mater.* **2021**, *33*, 2100677.
- (3) Kim, J. H.; Yun, J. H.; Lee, J. Y. Recent progress of highly efficient red and near-infrared thermally activated delayed fluorescent emitters. *Adv. Opt. Mater.* **2018**, *6*, 1800255.
- (4) Zhang, Y.; Zhang, D.; Cai, M.; Li, Y.; Zhang, D.; Qiu, Y.; Duan, L. Towards highly efficient red thermally activated delayed fluorescence materials by the control of intra-molecular π – π stacking interactions. *J. Nanotechnol.* **2016**, *27*, 094001.
- (5) Zhang, Y.-L.; Ran, Q.; Wang, Q.; Liu, Y.; Hänisch, C.; Reineke, S.; Fan, J.; Liao, L.-S. High-efficiency red organic light-emitting diodes with external quantum efficiency close to 30% based on a novel thermally activated delayed fluorescence emitter. *Adv. Mater.* **2019**, *31*, 1902368.
- (6) Braveenth, R.; Lee, H.; Kim, S.; Raagulan, K.; Kim, S.; Kwon, J. H.; Chai, K. Y. High efficiency green TADF emitters of acridine donor and triazine acceptor D–A–D structures. *J. Mater. Chem. C* **2019**, *7*, 7672–7680.
- (7) Zhou, D.; Tong, G. S. M.; Cheng, G.; Tang, Y.-K.; Liu, W.; Ma, D.; Du, L.; Chen, J.-R.; Che, C.-M. Stable tetradentate gold(III)-TADF emitters with close to unity quantum yield and radiative decay rate constant of up to $2 \times 10^6 \text{ s}^{-1}$: High-efficiency green OLEDs with operational lifetime (LT90) longer than 1800 h at 1000 cd m^{-2} . *Adv. Mater.* **2022**, *34*, 2206598.
- (8) Huang, Z.; Xiang, S.; Zhang, Q.; Lv, X.; Ye, S.; Guo, R.; Wang, L. Highly efficient green organic light emitting diodes with phenanthroimidazole-based thermally activated delayed fluorescence emitters. *J. Mater. Chem. C* **2018**, *6*, 2379–2386.
- (9) Endo, A.; Ogasawara, M.; Takahashi, A.; Yokoyama, D.; Kato, Y.; Adachi, C. Thermally activated delayed fluorescence from Sn^{4+} -porphyrin complexes and their application to organic light-emitting diodes-A novel mechanism for electroluminescence. *Adv. Mater.* **2009**, *21*, 4802–4806.
- (10) Perrin, F. La fluorescence des solutions—Induction moléculaire.—Polarisation et durée d'émission.—Photochimie. *Ann. Phys.* **1929**, *10*, 169–275.
- (11) Uoyama, H.; Goushi, K.; Shizu, K.; Nomura, H.; Adachi, C. Highly efficient organic light-emitting diodes from delayed fluorescence. *Nature* **2012**, *492*, 234–238.
- (12) Wong, M. Y.; Zysman-Colman, E. Purely organic thermally activated delayed fluorescence materials for organic light-emitting diodes. *Adv. Mater.* **2017**, *29*, 1605444.
- (13) Arjona-Esteban, A.; Szafranowska, B.; Ochsmann, J. In *Luminescence*; Pyshkin, S., Ed.; IntechOpen: Rijeka, 2019; Chapter 6.
- (14) Kunze, L.; Hansen, A.; Grimme, S.; Mewes, J.-M. PCM-ROKS for the description of charge-transfer states in solution: Singlet–triplet gaps with chemical accuracy from open-shell Kohn–Sham reaction-field calculations. *J. Phys. Chem. Lett.* **2021**, *12*, 8470–8480.
- (15) Liang, X.; Tu, Z.-L.; Zheng, Y.-X. Thermally activated delayed fluorescence materials: towards realization of high efficiency through strategic small molecular design. *Chem.—Eur. J.* **2019**, *25*, 5623–5642.
- (16) Naqvi, B. A.; Schmid, M.; Crovini, E.; Sahay, P.; Naujoks, T.; Rodella, F.; Zhang, Z.; Strohmriegel, P.; Bräse, S.; Zysman-Colman, E.; Brütting, W. What controls the orientation of TADF emitters? *Front. Chem.* **2020**, *8*, 750.
- (17) Nobuyasu, R. S.; Ren, Z.; Griffiths, G. C.; Batsanov, A. S.; Data, S. P.; Yan, Monkman, A. P.; Bryce, M. R.; Dias, F. B. Rational design of TADF polymers using a donor–acceptor monomer with enhanced TADF efficiency induced by the energy alignment of charge transfer and local triplet excited states. *Adv. Opt. Mater.* **2016**, *4*, 597–607.

- (18) Etherington, M. K.; Gibson, J.; Higginbotham, H. F.; Penfold, T. J.; Monkman, A. P. Revealing the spin–vibronic coupling mechanism of thermally activated delayed fluorescence. *Nat. Commun.* **2016**, *7*, 13680.
- (19) Penfold, T. J.; Gindensperger, E.; Daniel, C.; Marian, C. M. Spin-vibronic mechanism for intersystem crossing. *Chem. Rev.* **2018**, *118*, 6975–7025.
- (20) Sommer, G. A.; Mataranga-Popa, L. N.; Czerwieniec, R.; Hofbeck, T.; Homeier, H. H.; Müller, T. J.; Yersin, H. Design of conformationally distorted donor–acceptor dyads showing efficient thermally activated delayed fluorescence. *J. Phys. Chem. Lett.* **2018**, *9*, 3692–3697.
- (21) Cao, X.; Zhang, D.; Zhang, S.; Tao, Y.; Huang, W. CN-containing donor–acceptor-type small-molecule materials for thermally activated delayed fluorescence OLEDs. *J. Mater. Chem. C* **2017**, *5*, 7699–7714.
- (22) Chen, S.; Xu, X.; Liu, Y.; Yu, G.; Sun, X.; Qiu, W.; Ma, Y.; Zhu, D. Synthesis and characterization of n-type materials for non-doped organic red-light-emitting diodes. *Adv. Funct. Mater.* **2005**, *15*, 1541–1546.
- (23) Wang, S.; Yan, X.; Cheng, Z.; Zhang, H.; Liu, Y.; Wang, Y. Highly efficient near-infrared delayed fluorescence organic light emitting diodes using a phenanthrene-based charge-transfer compound. *Angew. Chem., Int. Ed.* **2015**, *54*, 13068–13072.
- (24) Lin, C.-Y.; Lu, C.-H.; Kuo, K.-H.; Wang, M.; Tang, Y.; Dou, Y.; Hu, B.; Wu, C.-C.; Wong, K.-T. Highly efficient blue thermally activated delayed fluorescence emitters with a triphenylamine-based macrocyclic donor. *Adv. Opt. Mater.* **2023**, *11*, 2202292.
- (25) Frisch, M. J.; Trucks, G. W.; Schlegel, H. B.; Scuseria, G. E.; Robb, M. A.; Cheeseman, J. R.; Scalmani, G.; Barone, V.; Petersson, G. A.; Nakatsuji, H. et al. *Gaussian 16*, revision A.03; Gaussian, Inc.: Wallingford, CT, 2016.
- (26) Chai, J.-D.; Head-Gordon, M. Long-range corrected hybrid density functionals with damped atom–atom dispersion corrections. *Phys. Chem. Chem. Phys.* **2008**, *10*, 6615–6620.
- (27) Chai, J.-D.; Head-Gordon, M. Systematic optimization of long-range corrected hybrid density functionals. *J. Chem. Phys.* **2008**, *128*, 084106.
- (28) Schäfer, A.; Horn, H.; Ahlrichs, R. Fully optimized contracted Gaussian basis sets for atoms Li to Kr. *J. Chem. Phys.* **1992**, *97*, 2571–2577.
- (29) Weigend, F.; Ahlrichs, R. Balanced basis sets of split valence, triple zeta valence and quadruple zeta valence quality for H to Rn: Design and assessment of accuracy. *Phys. Chem. Chem. Phys.* **2005**, *7*, 3297.
- (30) Weigend, F. Accurate Coulomb-fitting basis sets for H to Rn. *Phys. Chem. Chem. Phys.* **2006**, *8*, 1057–1065.
- (31) Baer, R.; Livshits, E.; Salzner, U. Tuned range-separated hybrids in density functional theory. *Annu. Rev. Phys. Chem.* **2010**, *61*, 85–109.
- (32) Kronik, L.; Stein, T.; Refaely-Abramson, S.; Baer, R. Excitation gaps of finite-sized systems from optimally tuned range-separated hybrid functionals. *J. Chem. Theory Comput.* **2012**, *8*, 1515–1531.
- (33) Kronik, L.; Kümmel, S. Dielectric screening meets optimally tuned density functionals. *Adv. Mater.* **2018**, *30*, 1706560.
- (34) Jacquemin, D.; Moore, B.; Planchat, A.; Adamo, C.; Autschbach, J. Performance of an optimally tuned range-separated hybrid functional for 0–0 electronic excitation energies. *J. Chem. Theory Comput.* **2014**, *10*, 1677–1685.
- (35) Bokareva, O. S.; Grell, G.; Bokarev, S. I.; Kühn, O. Tuning range-separated density functional theory for photocatalytic water splitting systems. *J. Chem. Theory Comput.* **2015**, *11*, 1700–1709.
- (36) Runge, E.; Gross, E. K. U. Density-functional theory for time-dependent systems. *Phys. Rev. Lett.* **1984**, *52*, 997–1000.
- (37) Marques, M. A. L.; Gross, E. K. U. In *A Primer in Density Functional Theory*; Fiolhais, C., Nogueira, F., Marques, M. A. L., Eds.; Springer: Berlin, 2003; pp 144–184.
- (38) Furche, F.; Ahlrichs, R. Adiabatic time-dependent density functional methods for excited state properties. *J. Chem. Phys.* **2002**, *117*, 7433–7447.
- (39) Hirata, S.; Head-Gordon, M. Time-dependent density functional theory within the Tamm–Dancoff approximation. *Chem. Phys. Lett.* **1999**, *314*, 291–299.
- (40) Cammi, R.; Corni, S.; Mennucci, B.; Tomasi, J. Electronic excitation energies of molecules in solution: State specific and linear response methods for nonequilibrium continuum solvation models. *J. Chem. Phys.* **2005**, *122*, 104513.
- (41) Tomasi, J.; Mennucci, B.; Cammi, R. Quantum mechanical continuum solvation models. *Chem. Rev.* **2005**, *105*, 2999–3094.
- (42) Scalmani, G.; Frisch, M. J.; Mennucci, B.; Tomasi, J.; Cammi, R.; Barone, V. Geometries and properties of excited states in the gas phase and in solution: Theory and application of a time-dependent density functional theory polarizable continuum model. *J. Chem. Phys.* **2006**, *124*, 094107.
- (43) Grimme, S.; Waletzke, M. A combination of Kohn–Sham density functional theory and multi-reference configuration interaction methods. *J. Chem. Phys.* **1999**, *111*, 5645–5655.
- (44) Marian, C. M.; Heil, A.; Kleinschmidt, M. The DFT/MRCI method. *WIREs Comput. Mol. Sci.* **2019**, *9*, e1394.
- (45) Lyskov, I.; Kleinschmidt, M.; Marian, C. M. Redesign of the DFT/MRCI Hamiltonian. *J. Chem. Phys.* **2016**, *144*, 034104.
- (46) Kleinschmidt, M.; Tatchen, J.; Marian, C. M. Spin-orbit coupling of DFT/MRCI wavefunctions: Method, test calculations, and application to thiophene. *J. Comput. Chem.* **2002**, *23*, 824–833.
- (47) Kleinschmidt, M.; Marian, C. M. Efficient generation of matrix elements for one-electron spin–orbit operators. *Chem. Phys.* **2005**, *311*, 71–79.
- (48) Böhmer, T.; Kleinschmidt, M.; Marian, C. M. Toward the improvement of vibronic spectra and non-radiative rate constants using the vertical Hessian method. *J. Chem. Phys.* **2024**, under revision.
- (49) Etinski, M.; Tatchen, J.; Marian, C. M. Thermal and solvent effects on the triplet formation in cinnoline. *Phys. Chem. Chem. Phys.* **2014**, *16*, 4740.
- (50) Etinski, M.; Tatchen, J.; Marian, C. M. Time-dependent approaches for the calculation of intersystem crossing rates. *J. Chem. Phys.* **2011**, *134*, 154105.
- (51) Etinski, M.; Rai-Constapel, V.; Marian, C. M. Time-dependent approach to spin-vibronic coupling: Implementation and assessment. *J. Chem. Phys.* **2014**, *140*, 114104.
- (52) Marian, C. M. Understanding and controlling intersystem crossing in molecules. *Annu. Rev. Phys. Chem.* **2021**, *72*, 617–640.
- (53) Dinkelbach, F.; Marian, C. M. Vibronic and spin–orbit coupling effects in the absorption spectra of pyrazine: A quantum chemical approach. *J. Serb. Chem. Soc.* **2019**, *84*, 819–836.
- (54) Rodriguez-Serrano, A.; Dinkelbach, F.; Marian, C. M. Intersystem crossing processes in the 2CzPN emitter: A DFT/MRCI study including vibrational spin–orbit interactions. *Phys. Chem. Chem. Phys.* **2021**, *23*, 3668–3678.
- (55) Plasser, F. TheoDORE: A toolbox for a detailed and automated analysis of electronic excited state computations. *J. Chem. Phys.* **2020**, *152*, 084108.
- (56) Sretenović, D.; Kloeters, L. N.; Kaminski, J. M.; Böhmer, T.; Schmeinc, P.; Sommer, G. A.; Chalani, M.; Felekyan, S.; Kühnemuth, R.; Reiß, G. J. et al. The effect of conformational constraints and oxygen quenching on TADF in donor-acceptor systems. **2024**, in preparation.
- (57) Amthor, S.; Noller, B.; Lambert, C. UV/Vis/NIR spectral properties of triarylamines and their corresponding radical cations. *Chem. Phys.* **2005**, *316*, 141–152.
- (58) Wiefermann, J.; Kaminski, J. M.; Pankert, E.; Hertel, D.; Meerholz, K.; Marian, C. M.; Müller, T. J. Highly luminescent blue emitter with balanced hybridized locally and charge-transfer excited-states emission. *ChemPhotoChem.* **2023**, *7*, e202200265.

- (59) Balan, B.; Gopidas, K. R. Photoinduced electron transfer in α -cyclodextrin-based supramolecular dyads: A free-energy-dependence study. *Chem. Eur. J.* **2006**, *12*, 6701–6710.
- (60) Haselbach, W.; Kaminski, J. M.; Kloeters, L. N.; Müller, T. J. J.; Weingart, O.; Marian, C. M.; Gilch, P.; Nogueira de Faria, B. E. A thermally activated delayed fluorescence emitter investigated by time-resolved near-infrared spectroscopy. *Chem. Eur. J.* **2023**, *29*, e202202809.
- (61) Götze, J. P.; Karasulu, B.; Thiel, W. Computing UV/vis spectra from the adiabatic and vertical Franck–Condon schemes with the use of Cartesian and internal coordinates. *J. Chem. Phys.* **2013**, *139*, 234108.
- (62) Ferrer, F. J. A.; Santoro, F. Comparison of vertical and adiabatic harmonic approaches for the calculation of the vibrational structure of electronic spectra. *Phys. Chem. Chem. Phys.* **2012**, *14*, 13549–13563.
- (63) Sretenović, D. Photophysical properties of chromophores studied by multimodal fluorescence spectroscopy. PhD thesis, Heinrich Heine University Düsseldorf, 2024.
- (64) Caricato, M.; Mennucci, B.; Tomasi, J.; Ingrosso, F.; Cammi, R.; Corni, S.; Scalmani, G. Formation and relaxation of excited states in solution: A new time dependent polarizable continuum model based on time dependent density functional theory. *J. Chem. Phys.* **2006**, *124*, 124520.
- (65) Guido, C. A.; Jacquemin, D.; Adamo, C.; Mennucci, B. Electronic excitations in solution: the interplay between state specific approaches and a time-dependent density functional theory description. *J. Chem. Theory Comput.* **2015**, *11*, 5782–5790.
- (66) Föller, J.; Marian, C. M. Rotationally assisted spin-state inversion in carbene–metal–amides is an artifact. *J. Phys. Chem. Lett.* **2017**, *8*, 5643–5647.
- (67) Lüdtkke, N.; Föller, J.; Marian, C. M. Understanding the luminescence properties of Cu(I) complexes: A quantum chemical perusal. *Phys. Chem. Chem. Phys.* **2020**, *22*, 23530–23544.
- (68) Froitzheim, T.; Grimme, S.; Mewes, J.-M. Either accurate singlet–triplet gaps or excited-state structures: Testing and understanding the performance of TD-DFT for TADF emitters. *J. Chem. Theory Comput.* **2022**, *18*, 7702–7713.
- (69) Parac, M.; Doerr, M.; Marian, C. M.; Thiel, W. QM/MM calculation of solvent effects on absorption spectra of guanine. *J. Comput. Chem.* **2010**, *31*, 90–106.
- (70) Pracht, P.; Bohle, F.; Grimme, S. Automated exploration of the low-energy chemical space with fast quantum chemical methods. *Phys. Chem. Chem. Phys.* **2020**, *22*, 7169–7192.
- (71) Spicher, S.; Plett, C.; Pracht, P.; Hansen, A.; Grimme, S. Automated molecular cluster growing for explicit solvation by efficient force field and tight binding methods. *J. Chem. Theory Comput.* **2022**, *18*, 3174–3189.
- (72) Kaminski, J. M.; Rodríguez-Serrano, A.; Dinkelbach, F.; Miranda-Salinas, H.; Monkman, A. P.; Marian, C. M. Vibronic effects accelerate the intersystem crossing processes of the through-space charge transfer states in the triptycene bridged acridine–triazine donor–acceptor molecule TpAT-tFFO. *Chem. Sci.* **2022**, *13*, 7057–7066.
- (73) Miranda-Salinas, H.; Rodríguez-Serrano, A.; Kaminski, J. M.; Dinkelbach, F.; Hiromichi, N.; Kusakabe, Y.; Kaji, H.; Marian, C. M.; Monkman, A. P. Conformational, host, and vibrational effects giving rise to dynamic TADF behavior in the through-space charge transfer, triptycene bridged acridine–triazine donor acceptor TADF molecule TpAT-tFFO. *J. Phys. Chem. C* **2023**, *127*, 8607–8617.
- (74) Stavrou, K.; Franca, L. G.; Böhmer, T.; Duben, L. M.; Marian, C. M.; Monkman, A. P. Unexpected quasi-axial conformer in thermally activated delayed fluorescence DMAC-TRZ, pushing green OLEDs to blue. *Adv. Funct. Mater.* **2023**, *33*, 2300910.
- (75) Dhali, R.; Phan Huu, D. K. A.; Bertocchi, F.; Sissa, C.; Terenziani, F.; Painelli, A. Understanding TADF: a joint experimental and theoretical study of DMAC-TRZ. *Phys. Chem. Chem. Phys.* **2021**, *23*, 378–387.
- (76) Eng, J.; Penfold, T. J. Understanding and designing thermally activated delayed fluorescence emitters: beyond the energy gap approximation. *Chem. Rec.* **2020**, *20*, 831–856.
- (77) Capano, G.; Penfold, T.; Chergui, M.; Tavernelli, I. Photophysics of a copper phenanthroline elucidated by trajectory and wavepacket-based quantum dynamics: a synergetic approach. *Phys. Chem. Chem. Phys.* **2017**, *19*, 19590–19600.
- (78) Capano, G.; Chergui, M.; Rothlisberger, U.; Tavernelli, I.; Penfold, T. J. A quantum dynamics study of the ultrafast relaxation in a prototypical Cu(I)–phenanthroline. *J. Phys. Chem. A* **2014**, *118*, 9861–9869.
- (79) Thompson, S.; Eng, J.; Penfold, T. J. The intersystem crossing of a cyclic (alkyl)(amino) carbene gold (i) complex. *J. Chem. Phys.* **2018**, *149*, 014304 DOI: 10.1063/1.5032185.
- (80) Hazra, A.; Chang, H. H.; Nooijen, M. First principles simulation of the UV absorption spectrum of ethylene using the vertical Franck–Condon approach. *J. Chem. Phys.* **2004**, *121*, 2125–2136.
- (81) Cerezo, J.; Santoro, F. FCclasses3: Vibrationally-resolved spectra simulated at the edge of the harmonic approximation. *J. Comput. Chem.* **2023**, *44*, 626–643.
- (82) Englman, R.; Jortner, J. The energy gap law for radiationless transitions in large molecules. *Mol. Phys.* **1970**, *18*, 145–164.

Supporting Information:

**Balancing TADF Properties in π -Bridged
Donor–Acceptor Systems by Sterical Constraints:
The Best of Three Worlds**

Jeremy M. Kaminski,^{†,‡} Tobias Böhmer,^{†,‡} and Christel M. Marian^{*,†}

[†]*Institute of Theoretical and Computational Chemistry, Faculty of Mathematics and
Natural Sciences, Heinrich Heine University Düsseldorf, Universitätsstraße 1, 40225
Düsseldorf*

[‡]*These authors contributed equally to this work.*

E-mail: christel.marian@hhu.de

Absorption Spectra

Table S1: DFT/MRCI-R2016 computed oscillator strengths $f(l)$, vertical absorption wavelengths $\lambda_{\text{abs}}/\text{nm}$ and wave function composition of low-lying electronic states at the respective ground-state geometry of the most stable conformer.

		Compound			
		1-H	2-Me	3- ⁱ Pr	4-diMe
$S_1 \leftarrow S_0$	λ_{abs} ($f(l)$)	410 (0.237)	400 (0.077)	400 (0.047)	396 (0.002)
	[% CT/LE _{TAA} /LE _{TPN}]	70/10/9	80/6/4	82/5/4	87/2/2
$S_2 \leftarrow S_0$	λ_{abs} ($f(l)$)	331 (0.417)	319 (0.289)	315 (0.226)	307 (0.044)
	[% CT/LE _{TAA} /LE _{TPN}]	40/41/9	31/59/2	26/64/2	7/85/0
$S_3 \leftarrow S_0$	λ_{abs} ($f(l)$)	312 (0.022)	307 (0.163)	306 (0.231)	302 (0.436)
	[% CT/LE _{TAA} /LE _{TPN}]	4/86/0	9/82/1	12/80/1	15/77/1
$S_4 \leftarrow S_0$	λ_{abs} ($f(l)$)	296 (0.103)	291 (0.096)	291 (0.106)	286 (0.247)
	[% CT/LE _{TAA} /LE _{TPN}]	25/4/58	15/6/68	18/7/64	63/24/4
$S_5 \leftarrow S_0$	λ_{abs} ($f(l)$)	286 (0.151)	287 (0.266)	292 (0.089)	286 (0.288)
	[% CT/LE _{TAA} /LE _{TPN}]	2/91/0	1/93/0	0/93/1	1/94/0

Table S2: Composition of the DFT/MRCI wave functions of the five lowest excited singlet states of 1-H at the ground-state geometry. The orbitals involved in the excitation are displayed in Figure S1.

State	%	Transition		
S ₁	81.2	H	→	L
	2.3	H-3	→	L
	2.1	H-1	→	L
	1.8	H	→	L+1
S ₂	76.3	H	→	L+1
	4.6	H	→	L+4
	1.6	H-3	→	L+1
	1.5	H-1	→	L+1
	1.1	H	→	L
S ₃	71.3	H	→	L+2
	2.5	H-2	→	L+1
	2.0	H-5	→	L+1
	1.8	H-2	→	L+4
	1.7	H-1	→	L+3
	1.4	H-2	→	L
	1.4	H-5	→	L
	1.2	H-3	→	L+5
	1.1	H-1	→	L+5
S ₄	23.4	H-7	→	L
	19.6	H-3	→	L
	15.2	H-1	→	L
	10.5	H-6	→	L+1
	4.3	H	→	L
	3.3	H-6	→	L
	2.5	H	→	L+4
	2.3	H-6	→	L+4
	1.8	H-2	→	L
	1.7	H	→	L+1
	1.2	H-3	→	L+1
S ₅	58.5	H	→	L+3
	16.9	H	→	L+5
	3.4	H-1	→	L+2
	2.8	H-3	→	L+3
	1.5	H-4	→	L+6
	1.2	H-2	→	L+7
	1.1	H-5	→	L+1
	1.1	H-5	→	L

S3

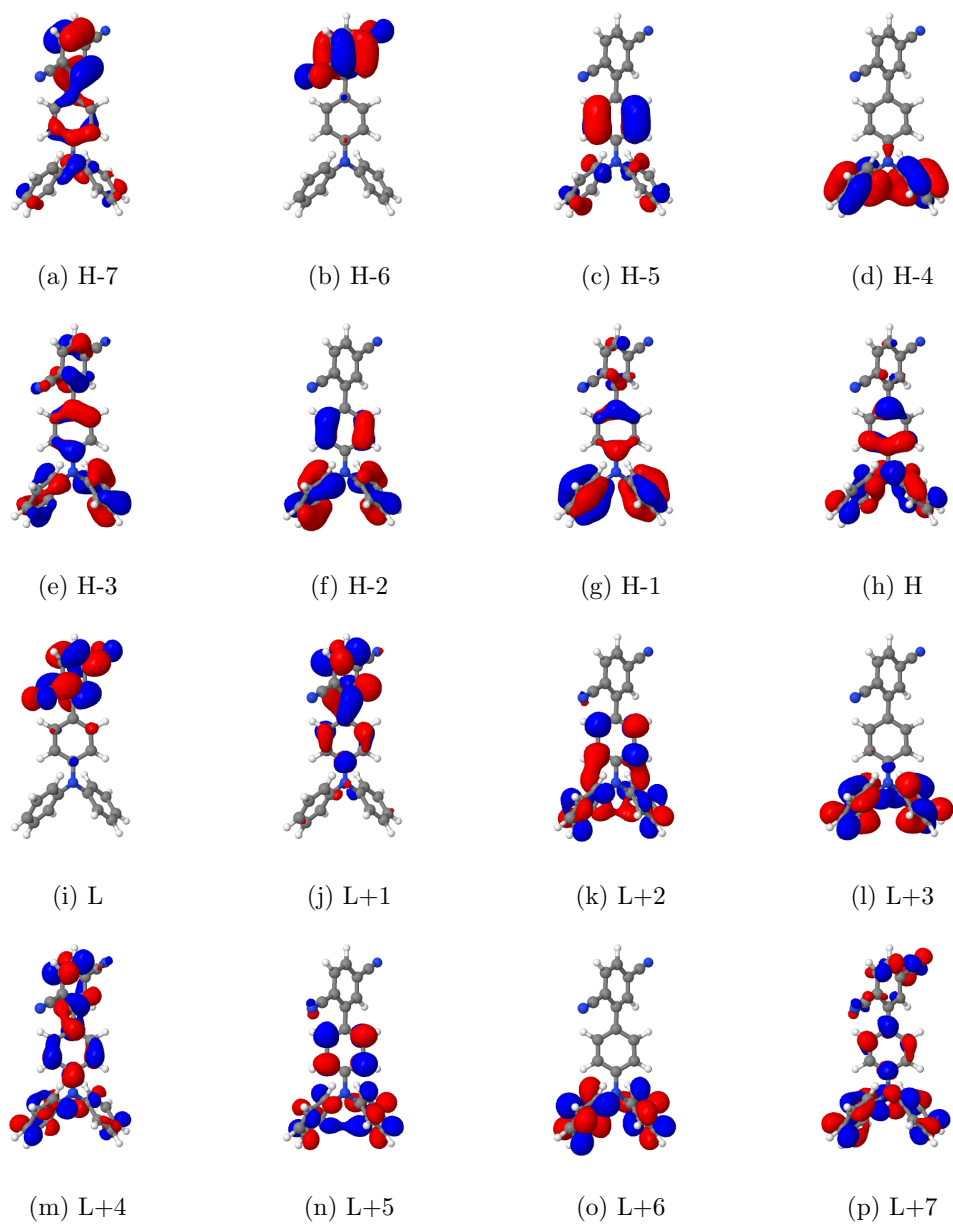


Figure S1: BH-LYP molecular orbitals (cutoff 0.03) mainly involved in the first five singlet excitations of **1-H** at the ground-state geometry.

Table S3: Composition of the DFT/MRCI wave functions of the five lowest excited singlet states of 2-Me at the ground-state geometry. The orbitals involved in the excitation are displayed in Figure S2.

State	%	Transition		
S1	84.4	H	→	L
	1.5	H-4	→	L
	1.3	H-3	→	L
S2	62.0	H	→	L+1
	10.9	H	→	L+3
	4.8	H	→	L+2
	3.6	H	→	L+4
	1.7	H-4	→	L+1
S3	69.0	H	→	L+2
	7.3	H	→	L+1
	2.4	H-1	→	L+3
	2.0	H-2	→	L+4
	1.7	H-1	→	L+1
	1.0	H-5	→	L+6
S4	39.6	H-7	→	L
	13.9	H-6	→	L+1
	8.4	H-3	→	L
	7.3	H-1	→	L
	5.2	H-4	→	L
	3.7	H	→	L+3
	2.0	H-4	→	L+1
	1.9	H	→	L
	1.5	H-6	→	L+3
	1.0	H	→	L+4
S5	62.4	H	→	L+4
	19.1	H	→	L+3
	3.9	H	→	L+5
	1.2	H-2	→	L+2

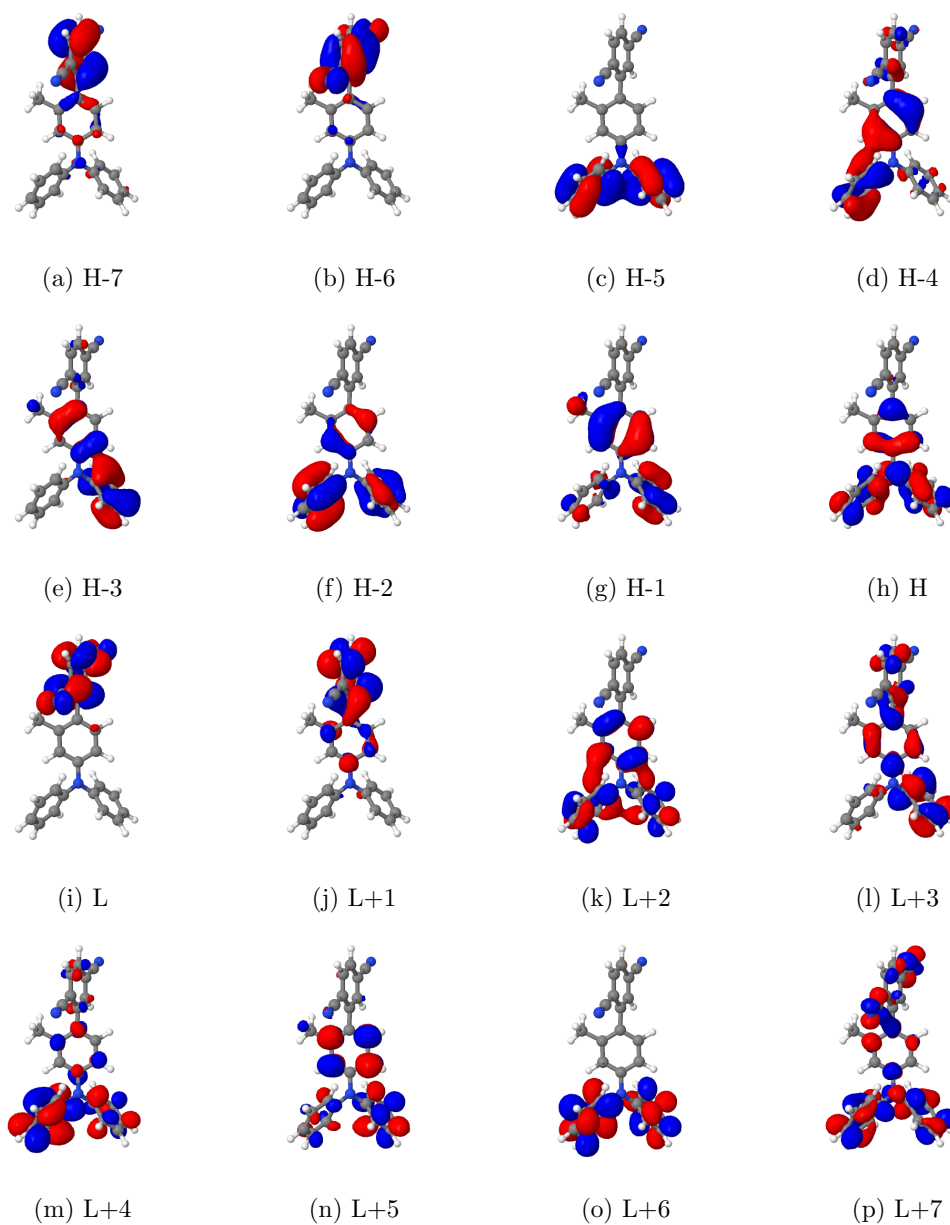


Figure S2: BH-LYP molecular orbitals (cutoff 0.03) mainly involved in the first five singlet excitations of **2-Me** at the ground-state geometry.

Table S4: Composition of the DFT/MRCI wave functions of the five lowest excited singlet states of $3\text{-}^i\text{Pr}$ at the ground-state geometry. The orbitals involved in the excitation are displayed in Figure S3.

State	%	Transition		
S1	85.0	H	→	L
	1.7	H-4	→	L
	1.0	H-3	→	L
S2	51.7	H	→	L+1
	17.6	H	→	L+3
	9.9	H	→	L+2
	1.6	H-4	→	L+1
	1.3	H-1	→	L+3
	1.2	H-1	→	L+2
	1.1	H	→	L+4
S3	65.4	H	→	L+2
	12.6	H	→	L+1
	2.0	H-1	→	L+3
	1.7	H-2	→	L+4
	1.4	H	→	L+3
	1.3	H-1	→	L+1
S4	38.2	H-7	→	L
	13.1	H-6	→	L+1
	10.2	H-1	→	L
	8.0	H-3	→	L
	5.7	H	→	L+3
	3.7	H-4	→	L
	1.8	H-4	→	L+1
	1.5	H	→	L
	1.3	H-6	→	L+3
	1.1	H-2	→	L
S5	76.1	H	→	L+4
	5.8	H	→	L+5
	2.3	H	→	L+3
	1.5	H-2	→	L+2
	1.0	H-8	→	L+4

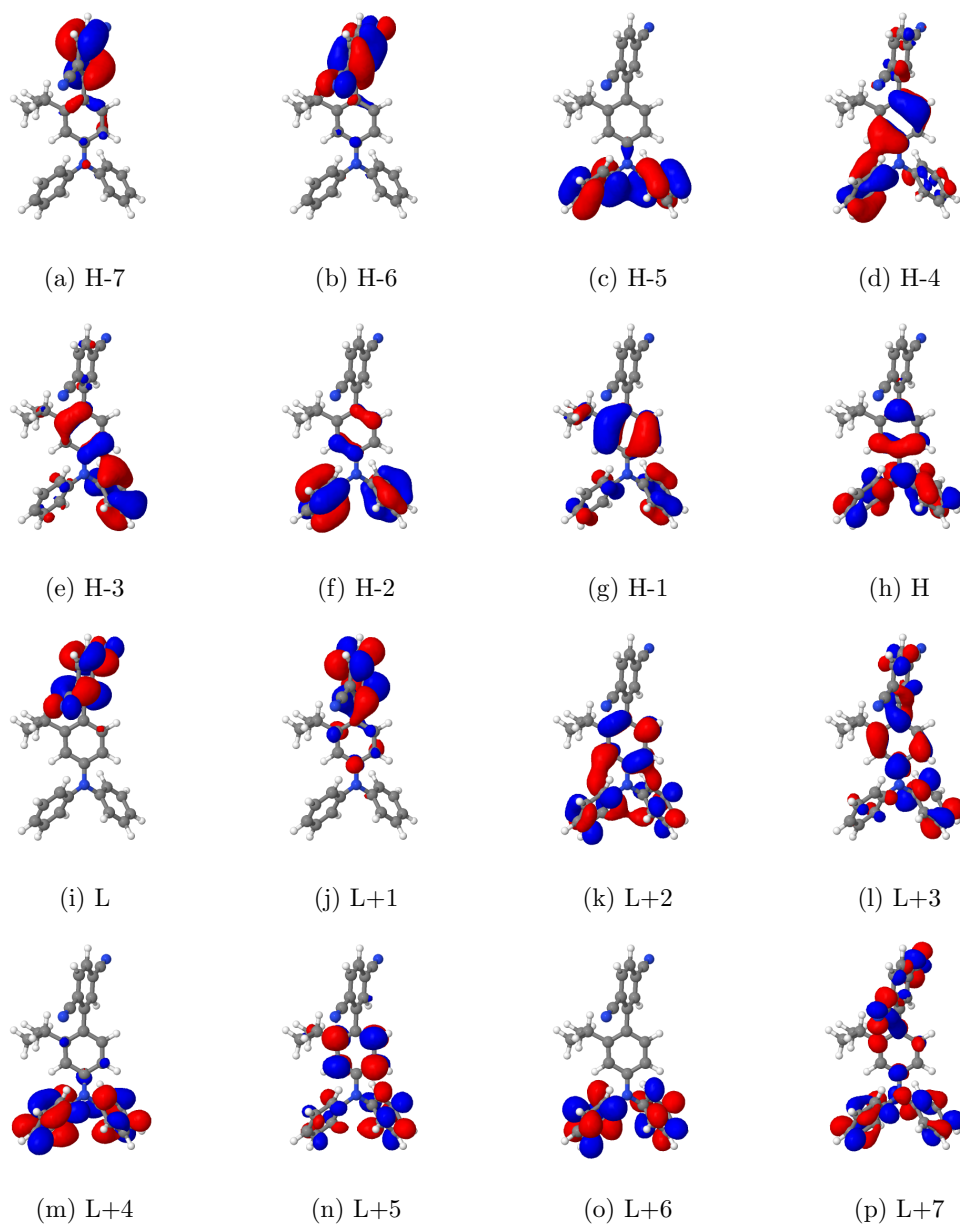


Figure S3: BH-LYP molecular orbitals (cutoff 0.03) mainly involved in the first five singlet excitations of **3-iPr** at the ground-state geometry.

Table S5: Composition of the DFT/MRCI wave functions of the five lowest excited singlet states of 4-diMe at the ground-state geometry. The orbitals involved in the excitation are displayed in Figure S4.

State	%	Transition		
S1	86.2	H	→	L
	2.9	H-4	→	L
	1.2	H-2	→	L
S2	63.8	H	→	L+3
	10.3	H	→	L+1
	4.8	H-1	→	L+2
	2.7	H-2	→	L+4
	1.3	H-4	→	L+6
	1.1	H	→	L+2
	1.0	H-5	→	L+5
S3	61.9	H	→	L+2
	17.5	H	→	L+1
	5.4	H	→	L+3
	1.0	H-7	→	L
	0.9	H-8	→	L+2
S4	53.0	H	→	L+1
	21.5	H	→	L+2
	4.8	H	→	L+3
	2.8	H-4	→	L+1
	1.8	H-7	→	L
	1.2	H-2	→	L+1
S5	83.0	H	→	L+4
	2.4	H	→	L+6
	1.5	H-2	→	L+3
	1.2	H-8	→	L+4
	1.0	H	→	L+3

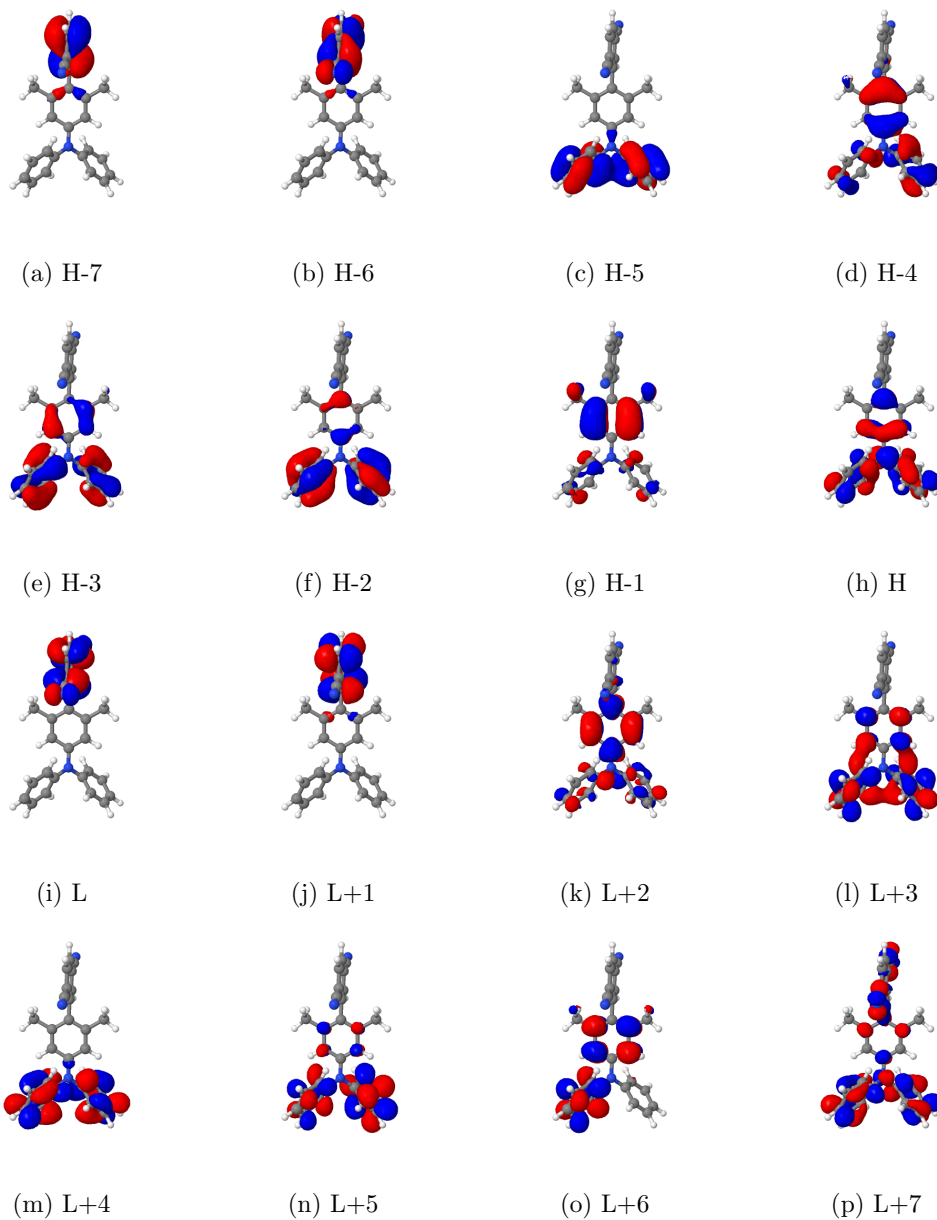


Figure S4: BH-LYP molecular orbitals (cutoff 0.03) mainly involved in the first five singlet excitations of **4-diMe** at the ground-state geometry.

Relaxed Interpolated Pathways

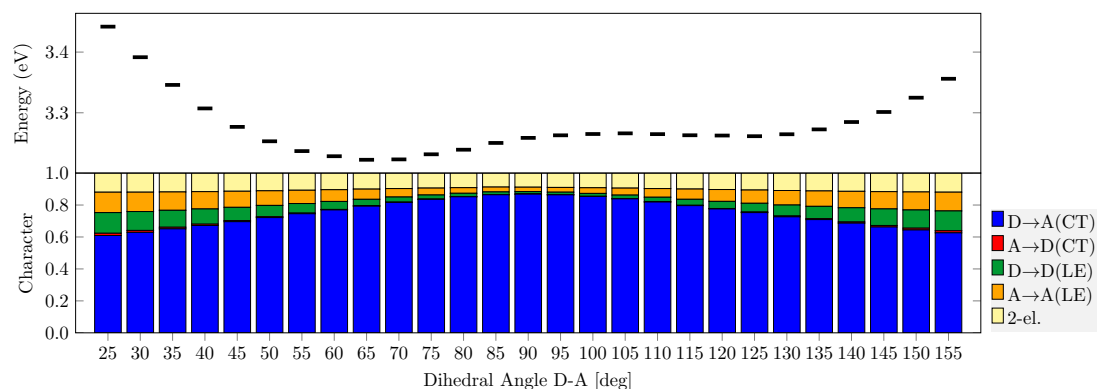


Figure S5: **2-Me**: Relaxed interpolated pathway for the lowest excited singlet state (S_1) at (TD)DFT/ ω B97X-D level of theory (**Top**). Detailed analysis of the excited state character based on the transition densities at every optimized geometry of the relaxed interpolated pathway (**Bottom**).

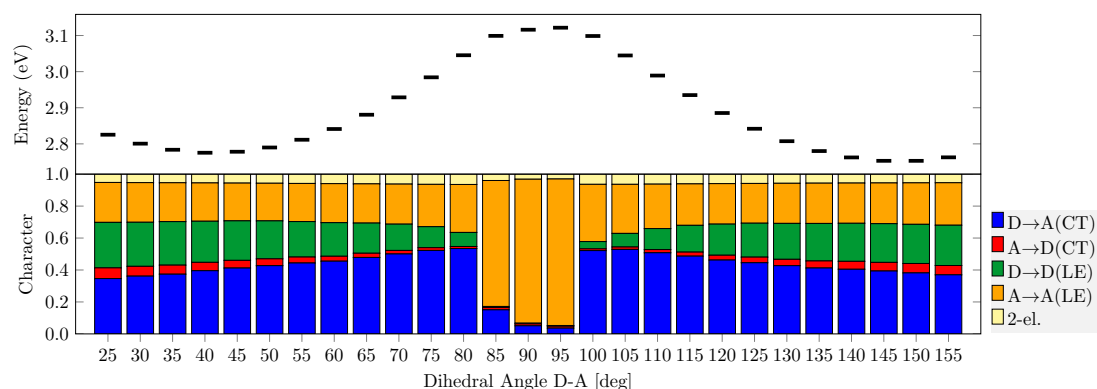


Figure S6: **2-Me**: Relaxed interpolated pathway for the lowest excited triplet state (T_1) at (TD)DFT/ ω B97X-D level of theory (**Top**). Detailed analysis of the excited state character based on the transition densities at every optimized geometry of the relaxed interpolated pathway (**Bottom**).

Emission Spectra

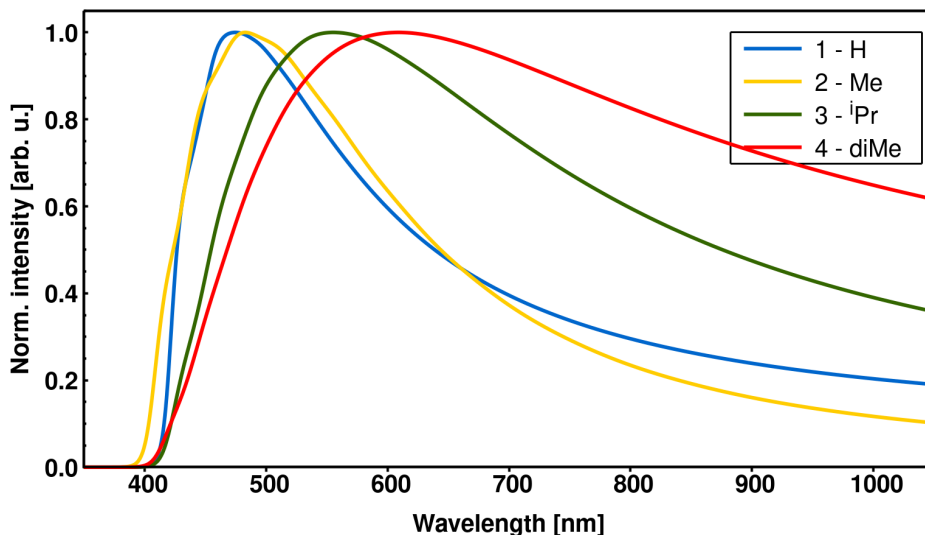


Figure S7: Computed emission spectra of **1-H** (blue), **2-Me** (yellow), **3-*i*Pr** (green) and **4-diMe** (red) in toluene solution at 300 K using the AH method.

Solvation Effects

Table S6: The influence of PCM and cLR models on the vertical emission wavelength λ_{em} (DFT/MRCI-R2016) and adiabatic energy of the S_1 excited state of **2-Me**.

	n-Hexane	Toluene	Ethylethanoate	DMSO
dielectric constant ϵ	1.8819	2.3741	5.9867	46.8260
Dihedral angle D-A S_0 [deg]	70.2	69.7	72.7	72.3
Dihedral angle D-A S_1 [deg]	66.3	65.4	58.5	56.0
$\lambda_{\text{em,PCM}}$ [cm^{-1} (nm)]	20536 (487)	20613 (485)	20533 (487)	20440 (489)
$\lambda_{\text{em,cLR}}$ [cm^{-1} (nm)]	16171 (618)	15530 (644)	12778 (783)	11962 (836)
E_{adia} (PCM/cLR) [eV]	2.96 / 2.36	2.94 / 2.23	2.94 / 1.87	2.92 / 1.73

Table S7: The influence of two explicit toluene solvent molecules (plus PCM) in comparison to implicit toluene solvation on different photophysical characteristics for 2-Me. Dihedral angle between donor and acceptor, absorption and emission oscillator strengths and wavelengths, vertical and adiabatic energies for S_1 and T_1 , electric dipole moments and CT weight of respective excited states.

	S_0		S_1		T_1	
	Implicit	Explicit	Implicit	Explicit	Implicit	Explicit
D-A [deg]	69.7	63.4	65.9	64.3	41.7	41.0
$E(S_1, \text{vert.})$ [eV (nm)]	3.10	2.90	2.56 (484)	2.35 (528)	2.53	2.37
$E(S_1, \text{adia.})$ [eV]	–	–	2.94	2.73	3.00	2.88
$\mu(S_1)$ [D]	26.97	24.32	24.66	23.16	19.66	18.53
S_1 [% CT/ LE_{TAA}/LE_{TPN}]	80/6/4	78/6/6	80/4/6	78/4/6	59/15/13	60/12/13
$E(T_1, \text{vert.})$ [eV (nm)]	2.91	2.72	2.36	2.19	2.03 (610)	1.95 (635)
$E(T_1, \text{adia.})$ [eV]	–	–	2.74	2.57	2.50	2.47
$\mu(T_1)$ [D]	20.28	20.07	20.32	20.67	13.71	14.16
T_1 [% CT/ LE_{TAA}/LE_{TPN}]	59/22/11	64/14/12	65/10/17	70/8/13	40/26/24	45/21/23
k_F [s^{-1}]	–	–	2.6×10^7	2.2×10^7	–	–
$\Delta E, \text{vert.}$ [eV]	0.19 / 0.18		–			
$\Delta E, \text{adia.}$ [eV]	–		0.44 / 0.26			

Non-radiative Rate Constants for Vertically Shifted PES

Table S8: ISC rate constants k_{ISC} for all compounds with respect to different energy gaps and the true adiabatic energy gap between the singlet and triplet state within the Franck-Condon approximation in s^{-1} .

E_{adia} [meV]	Compound			
	1-H	2-Me	3- <i>i</i> Pr	4-diMe
50	4.08×10^6	6.52×10^5	3.30×10^5	3.01×10^3
100	4.47×10^6	1.03×10^6	5.58×10^5	6.60×10^3
150	5.12×10^6	1.39×10^6	8.08×10^5	1.16×10^4
200	5.46×10^6	1.76×10^6	1.08×10^6	1.78×10^4
250	5.45×10^6	2.11×10^6	1.36×10^6	2.49×10^4
300	5.40×10^6	2.42×10^6	1.63×10^6	3.30×10^4
350	5.26×10^6	2.70×10^6	1.90×10^6	4.17×10^4
400	5.09×10^6	2.95×10^6	2.16×10^6	5.12×10^4
Actual ΔE	4.61×10^6	3.29×10^6	2.46×10^6	3.68×10^4

Table S9: rISC rate constants k_{rISC} for all compounds with respect to different energy gaps and the true adiabatic energy gap between the singlet and triplet state within the Franck-Condon approximation in s^{-1} .

E_{adia} [meV]	Compound			
	1-H	2-Me	3- <i>i</i> Pr	4-diMe
50	5.39×10^5	6.33×10^4	7.59×10^4	1.31×10^4
100	8.53×10^4	1.46×10^4	1.86×10^4	4.17×10^3
150	1.41×10^4	2.86×10^3	3.92×10^3	1.07×10^3
200	2.18×10^3	5.20×10^2	7.59×10^2	2.37×10^2
250	3.14×10^2	9.02×10^1	1.38×10^2	4.79×10^1
300	4.51×10^1	1.50×10^1	2.41×10^1	8.92×10^0
350	6.32×10^0	2.42×10^0	4.05×10^0	1.38×10^0
400	8.44×10^{-1}	3.82×10^{-1}	6.65×10^{-1}	–
Actual ΔE	4.80×10^{-2}	1.85×10^{-2}	6.65×10^{-2}	4.01×10^0

Comparison FC vs. FC/HT Rate Constants

Table S10: Calculated radiative and non-radiative rate constants within Franck-Condon approximation and HT-type scheme in s^{-1} for 1-H to 4-diMe.

	Compound			
	1-H	2-Me	3- ⁱ Pr	4-diMe
$k_{\text{F,FC}}$	1.0×10^8	2.6×10^7	2.0×10^7	1.7×10^6
$k_{\text{F,FC/HT}}$	–	1.9×10^7	–	2.6×10^6
$k_{\text{ISC,FC}}$	4.6×10^6	3.3×10^6	2.5×10^6	3.7×10^4
$k_{\text{ISC,FC/HT}}$	–	4.4×10^6	–	7.3×10^5
$k_{\text{rISC,FC}}$	4.8×10^{-2}	1.9×10^{-2}	6.7×10^{-2}	4.0×10^0
$k_{\text{rISC,FC/HT}}$	–	8.7×10^{-2}	–	1.3×10^1

Non-radiative Rate Constants within VH Approach

Table S11: Calculated fluorescence rate constants using DFT/MRCI-R2016 and non-radiative rate constants within the newly implemented VH approach in s^{-1} for 2-Me.

Dihedral angle D-A	k_{ISC}	k_{rISC}	k_{F}
25	1.0×10^6	1.0×10^0	1.1×10^8
30	1.1×10^6	1.4×10^6	1.0×10^8
35	1.2×10^7	2.2×10^6	9.1×10^7
40	1.2×10^7	2.2×10^0	8.1×10^7
45	1.3×10^7	2.7×10^0	7.0×10^7
50	1.3×10^7	5.6×10^0	5.9×10^7
55	1.7×10^7	6.1×10^0	4.5×10^7
60	1.8×10^6	1.1×10^1	3.7×10^7
65	1.8×10^6	1.2×10^1	2.7×10^7
70	2.6×10^6	2.6×10^1	1.8×10^7
75	4.6×10^6	9.6×10^1	1.0×10^7
80	6.7×10^6	3.6×10^2	4.8×10^6
85	8.4×10^6	2.0×10^4	1.1×10^6
90	7.6×10^5	5.6×10^4	3.0×10^4

Optimization of the range-separation parameter ω

In order to get reliable values for excited state energies on TDDFT level of theory for TADF emitters range-separated exchange functionals were proposed to bring remedy. However, these functionals need to be tuned and adapted to the system. This is done by varying the range-separation parameter ω that stands for the inverse distance which assigns the change from DFT to HF exchange terms.

Since TADF emitters usually consist of a donor and an acceptor moiety the range-separation parameter ω is tuned towards the ionization potential and the electron affinity applying Koopmans' theorem. As a matter of fact the value of J^2 is minimized in this procedure by determining the minimum of the target function:

$$J^2 = \sum_{i=0}^1 [\epsilon_{HOMO}^{\omega}(N+i) + IP(N+i)]^2 \quad (1)$$

with $IP(N) = E(N-1) - E(N)$, and $IP(N+1) = E(N) - E(N+1)$.

Here, N is the number of electrons of the target molecule, ϵ_{HOMO}^{ω} is the HOMO energy and $IP(N)$ the vertical ionization potential. In Figure S8 the parameter optimization for **2-Me** in toluene is shown in the range between 0.00 and 0.20 bohr⁻¹. The optimal ω was set to 0.15 a₀⁻¹ for all computations.

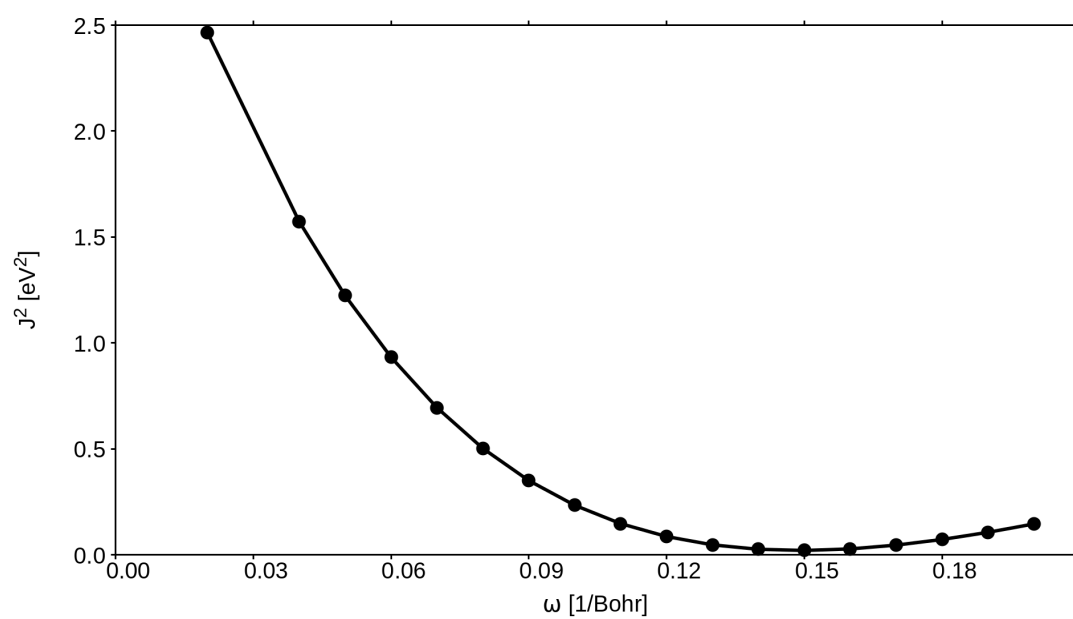


Figure S8: For the optimization of the range-separated hybrid density functional ω B97X-D a tuning procedure was performed. ω was set to 0.15 a_0^{-1} for all computations.

Publication VI

**How Donor–Bridge–Acceptor Orientation and Chemical Modification Affect the
TADF Abilities of Boron-Based Emitters**

J. M. Kaminski, T. V. Chu & C. M. Marian

ChemPhotoChem, e202500033, 2025

DOI: 10.1002/cptc.202500033

Contribution: All quantum chemical investigations of **DPACoOB**, **DMACoOB**, **DPAoOB** and **DPACoSB**, preparation of all figures, writing the first draft and revising the manuscript.

How Donor–Bridge–Acceptor Orientation and Chemical Modification Affect the Thermally Activated Delayed Fluorescence Abilities of Boron-Based Emitters

Jeremy M. Kaminski, Tu V. Chu, and Christel M. Marian*

The photophysical properties of a series of thermally activated delayed fluorescence emitters, comprising a nitrogen-based donor, a phenylene bridge and a boron-based acceptor, are investigated using a combination of density functional theory and multi-reference configuration interaction methods. In addition to singlet and triplet charge-transfer (CT) states, an acceptor-localized low-lying triplet state is found in all compounds.

The size of the singlet–triplet gap and the energetic order of the CT and locally excited (LE) states can be modulated by regioisomerism (*ortho*- or *para*-linkage) and the chemical modification of the subunits. Spin–vibronic interactions, introduced through a Herzberg–Teller-type approach, are found to accelerate the inter-system crossing process considerably provided that the CT and LE states are close in energy.

1. Introduction

In search for efficient blue thermally activated delayed fluorescence (TADF) emitters, boron-based donor–acceptor systems have gained increasing attention.^[1–9] This interest primarily arises due to the strong electron-accepting properties of the sp^2 -hybridized, tri-coordinate boron atom and the extended $p(B)-\pi^*(Ar)$ conjugation in triarylboranes. In combination with suitable donors comprising a tri-coordinate nitrogen atom such as diphenylamine (DPA), 9,9-dimethylacridane (DMAC) or 9,9-di-phenylacridane (DPAC), promising blue-light-emitting TADF compounds were developed, either as *ortho*-appended^[10,11] or *para*-appended^[12,13] donor–bridge–acceptor systems. These configurations give rise to electronically excited states of through-space charge-transfer (TSCT) and through-bond charge-transfer (TBCT) type, respectively. The acceptors comprised cyclic boryl compounds such as 9-boraanthryl (BA) or 10H-phenoxaboryl (OB) groups as well as open forms such as dimesitylboryl (B). To gain a deeper understanding of the observed trends, the authors performed quantum chemical calculations using Kohn–Sham density functional theory (KS-DFT) and time-dependent DFT (TD-DFT) methods. Herein, they focused mainly on the photophysical properties of the singlet and triplet CT states, S_{CT} and

T_{CT} . As we will show, a triplet LE state, $T_{LE(A)}$, is present in all these systems in energetic proximity of the CT states.

Due to spin statistics, singlet and triplet excited states are populated in a ratio of 1:3 in organic light-emitting diodes (OLEDs). TADF emitters harvest the triplet excitons by thermal upconversion of the T_{CT} population to the S_{CT} state, followed by delayed fluorescence. Requirements for efficient upconversion are a sufficiently small singlet–triplet energy gap, ΔE_{ST} , and a reasonable spin–orbit coupling (SOC) strength. The ΔE_{ST} value of CT states is related to the amount of exchange coupling between the donor and acceptor moieties. In face-to-face oriented TSCT systems, the distance between their π -planes can be used to tune the energy of the CT states and their splitting.^[14–17] In metal-free TBCT systems, it is typically the torsional angle between the donor and acceptor moieties that steers the ΔE_{ST} value.^[18–20] Because intersystem crossing (ISC) and reverse ISC (rISC) between S_{CT} and T_{CT} states of equal electronic structure are orbitally forbidden, spin–vibronic coupling with a nearby LE state is essential for enhancing the $S_{CT} \leftrightarrow T_{CT}$ transitions in TBCT and TSCT complexes.^[14,21–26] The enhancement is particularly pronounced if the LE state is of $n\pi^*$ -type or if out-of-plane vibrations mix some $n\pi^*$ -character into a $\pi\pi^*$ -excited state. Even in the absence of doubly occupied nonbonding orbitals, vibronic interactions can lift the orbital selection rules. In triarylborane phosphors, for example, $\sigma(B) \rightarrow \pi^*(B)$ transitions were shown to accelerate the ISC process.^[27]

In this work, we investigate the adiabatic energies of the low-lying CT and LE states and their relative energetic order in a series of emitter molecules (Figure 1) using a combination of DFT and multi-reference configuration interaction (MRCI) methods.^[28] For the most stable conformer of DPACoOB, consisting of a DPAC donor and an OB acceptor connected in *ortho*-position to a methylated phenylene (1-Me) bridge, the effect of spin–vibronic coupling on the ISC and rISC rates is explicitly evaluated. To investigate the influence of π -stacking versus $C-H \leftrightarrow \pi$ interactions, we replaced the DPAC donor by DMAC and DPA,

J. M. Kaminski, T. V. Chu, C. M. Marian
Institute of Theoretical and Computational Chemistry
Faculty of Mathematics and Natural Sciences
Heinrich Heine University Düsseldorf
40204 Düsseldorf, Germany
E-mail: Christel.Marian@uni-duesseldorf.de

Supporting information for this article is available on the WWW under <https://doi.org/10.1002/cptc.202500033>

© 2025 The Author(s). ChemPhotoChem published by Wiley-VCH GmbH. This is an open access article under the terms of the Creative Commons Attribution License, which permits use, distribution and reproduction in any medium, provided the original work is properly cited.

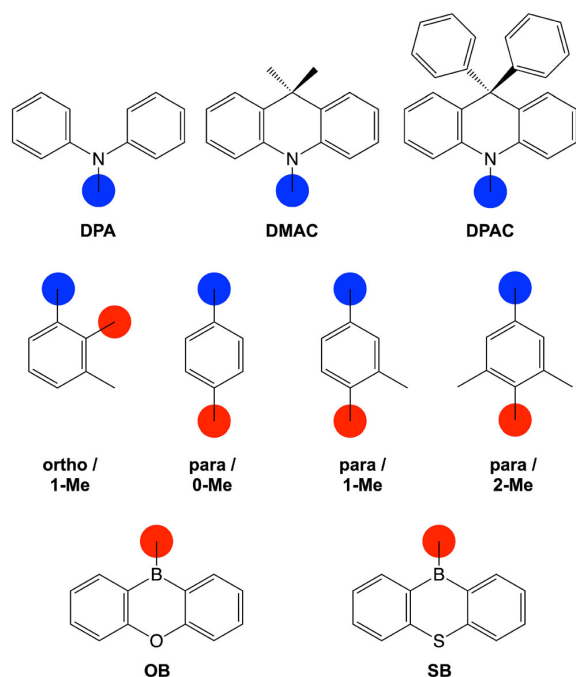


Figure 1. Investigated donor (upper panel), bridge (middle panel), and acceptor (lower panel) moieties. Electron-donating (blue circles) and accepting (red circles) units are cross-linked through a phenylene bridge at the 1,2-positions (*ortho*-regioisomers) or 1,4-positions (*para*-regioisomers).

respectively. By varying the number of methyl groups on the phenylene linker, we systematically study the impact of the steric repulsion between acceptor and linker on the donor–acceptor torsion angle and the photophysical properties of the *para*-appended combination of these substituents. Finally, chemical modification of the acceptor unit is employed to analyze the internal heavy-atom effect on the TADF properties in comparison to the originally used DPAC donor and OB acceptor.

2. Results and Discussion

2.1. The *Ortho*-Appended DPACoOB Emitter

DPACoOB is one of three molecules in a series studied by Mubarak et al.^[11] for which the influence of different acceptor moieties, namely BA, OB, and B on the luminescence was analyzed. These emitters have a rigid backbone due to the *ortho*-connectivity of donor and acceptor. The crystal structure of DPACoOB indicates the presence of π – π interactions between one phenyl group of DPAC and the OB plane. Additionally, a non-bonding electronic interaction between the nitrogen atom of DPAC and the boron atom of OB may be assumed. Hence, the boron atom is sterically and electronically protected, which improves the chemical and thermal stability of the emitter.^[11]

We found two conformers in the electronic ground state. As shown in Figure 2, they primarily differ in the orientation of the DPAC phenyl groups relative to the acceptor. In **conformer I**, one

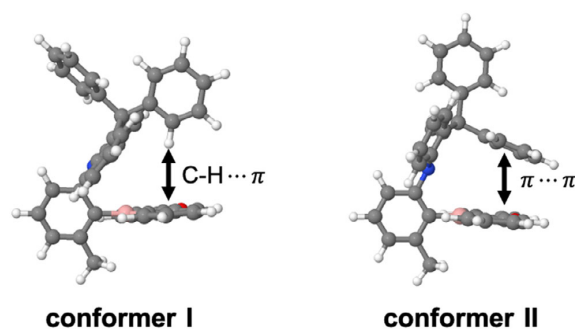


Figure 2. Optimized electronic ground-state conformers of DPACoOB at PBE0/def2-SV(P) level of theory in toluene. Conformers I and II exhibit either C–H \cdots π or π \cdots π interactions, respectively.

of these phenyl groups is perpendicular to the OB molecular plane and exerts C–H \leftrightarrow π interactions, similar to the corresponding DMAC compound studied in Ref. [10]. **Conformer II** is stabilized by π \leftrightarrow π interactions between one phenyl residue of the DPAC donor and the OB acceptor. In agreement with the crystal structure analysis,^[11] **conformer II** is preferred over **conformer I** in the electronic ground state. The DFT/MRCI-R2016 calculations place **conformer I** energetically 0.24 eV above **conformer II**. We therefore do not expect **conformer I** to be thermally populated in the electronic ground state.

The experimental absorption spectrum of DPACoOB at room temperature in toluene exhibits bands with maxima at 290 and 344 nm and a shoulder at 368 nm.^[11] A Gaussian-broadened line spectrum for **conformer II**, calculated at the DFT/MRCI-R2016^[28] level of theory, are shown in Figure 3. All bands exhibit a systematic hypsochromic shift of 0.10–0.15 eV relative to the experimental spectrum. The lowest-energy absorption band at 356 nm originates from the $S_1 \leftarrow S_0$ excitation, which is mainly a HOMO \rightarrow LUMO transition with donor-to-acceptor CT character. This explains the relatively small oscillator strength ($f = 0.043$) of this transition. The second absorption band with a maximum at 337 nm corresponds to the $S_2 \leftarrow S_0$ excitation, mainly a

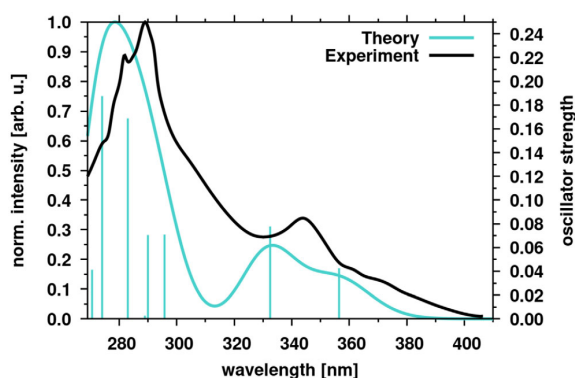


Figure 3. DFT/MRCI-R2016 absorption spectra for **conformer II** (turquoise) of DPACoOB in toluene in comparison to experimental results (black).^[11] The line spectrum was broadened by Gaussians with 2000 cm full width at half maximum.

HOMO-1 \rightarrow LUMO transition with LE character localized on the acceptor moiety. The most intense band in the considered wavelength regime arises from several LE transitions, localized either on the donor or acceptor units.

In contrast to the situation in the electronic ground state, the CT states of **conformer I** are located energetically below their counterparts in **conformer II** because the C–H \leftrightarrow π interaction stabilizes the negative charge of the **OB** acceptor in the CT states of **conformer I** to a much higher extent than the π -stacking interaction in **conformer II**. To ease the discussion of a possible conformational change in electronically excited DPACoOB molecules, all energy levels in **Figure 4** are drawn with respect to a common origin, that is, the ground-state energy of **conformer II**.

The level scheme (**Figure 4**) reveals significant changes in excitation energies, despite the moderate structural differences between the optimized S_0 and S_{CT}/T_{CT} geometries (**Table S3**, Supporting Information). In **conformer II**, the bonds connecting nitrogen, boron or oxygen with their direct neighbors differ by at most 0.02 Å in length between the S_0 and S_{CT}/T_{CT} equilibrium structures, leading to minor variations in the corresponding bond angles as well. However, the bite angle between the donor and acceptor moieties, as indicated by the B1–N1 distance, opens up markedly upon optimization of the CT state geometries. Simultaneously, the distance between the π -stacked DPAC phenyl residue and **OB** acceptor, reflected in the C41–O1 distance, shrinks. At the ground-state minimum geometry of **conformer II**, the energy difference between the S_{CT} and T_{CT} states is minimal ($\Delta E_{ST,vert} = 0.025$ eV), consistent with the value of 0.048 eV calculated by Mubarak et al.^[11] at the TDDFT(PBE0)/6-31G** level of theory. Decisive for the TADF properties, however, is the adiabatic value, $\Delta E_{ST,adia}$, or more precisely, the energy splitting $\Delta E_{ST,0-0}$ between the vibrational ground states of these electronic states (see below). Interestingly, the T_{CT} state is not the lowest triplet state at the ground-state geometry according to our calculations. Here, the T_1 state is mainly characterized by a local $\pi\pi^*$ excitation on the acceptor, $T_{LE(A)}$. It is therefore not surprising that the order of states changes when the nuclear arrangement is relaxed in the CT states (**Figure 4**).

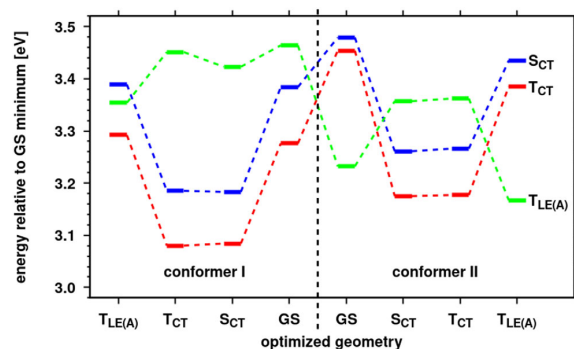


Figure 4. DFT/MRCI-R2016 energy level scheme of **conformer I** and **conformer II** of DPACoOB in toluene solution. All adiabatic excitation energies are given relative to the ground-state minimum energy of **conformer II** in eV.

A TheoDOR analysis^[29] of the one-particle transition density matrices, performed along a linearly interpolated pathway (LIP) connecting the Franck–Condon (FC) region with the optimized S_{CT} structure (**Figure 5** left), reveals that the electronic structure of the T_1 state changes gradually from a CT contribution of about 10% at the S_0 geometry to about 75% at the S_{CT} minimum geometry. In contrast, the S_1 state largely retains its CT character. Along this relaxation pathway, the S_1 and T_2 potential energy surfaces (PESs) intersect while T_1 and T_2 undergo an avoided crossing. We may therefore expect strong vibronic coupling between these states. A similar picture arises along a LIP connecting the T_{CT} and $T_{LE(A)}$ minima (**Figure 5** right). In addition to angular motions of the π -stacked DPAC phenyl residue, C–C stretching modes in the **OB** acceptor are excited. The low-frequency vibrational modes promoting the nonadiabatic couplings are torsional and rocking motions of the **OB** acceptor as well as a scissoring mode between the DPAC phenyl group and the acceptor moiety.

Difference densities of the S_{CT} , T_{CT} , and $T_{LE(A)}$ states of **conformer II** at their respective minimum geometries are displayed in **Figure 6**. The adiabatic excited-state energies lie all within a narrow range of ≈ 100 meV. Although the singlet–triplet energy splitting of the CT states ($\Delta E_{ST,adia} = 0.084$ eV, $\Delta E_{ST,0-0} = 0.085$ eV) increases compared to the FC region ($\Delta E_{ST,vert} = 0.025$ eV at the ground-state geometry), it remains small enough to facilitate TADF. Note that the experimental ΔE_{ST} value (0.020 eV), reported by Mubarak et al.^[11] was derived from the onsets of the fluorescence and phosphorescence spectra in toluene at 77 K, as the room-temperature fluorescence is substantially red-shifted in this medium. Adiabatically, the T_{CT} and $T_{LE(A)}$ states are almost degenerate according to our calculations.

The fluorescence rate constant of **conformer II** (**Table 1**) matches the expectations for a purely organic donor–acceptor system. Vibronic interactions increase the rate constant only marginally. The radiative lifetime of 185 ns, determined in Herzberg–Teller (HT) approximation, agrees very well with the measured

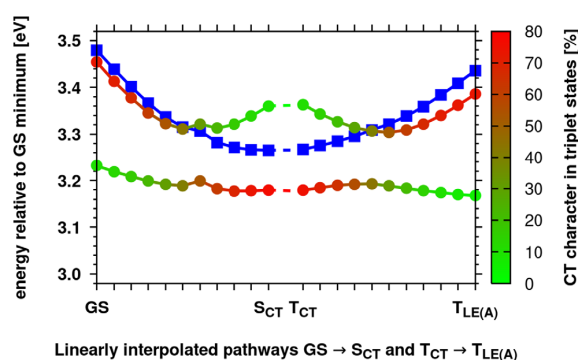


Figure 5. Linearly interpolated pathways between the optimized ground-state (S_0) and S_1 , as well as between the optimized T_1 and T_2 geometries (**conformer II**). DFT/MRCI-R2016 vertical energies of the relevant excited singlet (boxes) and triplet (circles) states relative to the ground-state minimum in eV. Along these pathways, the S state can be identified with the S state (blue), whereas the T and T states gradually change their character between T (red) and T (green).

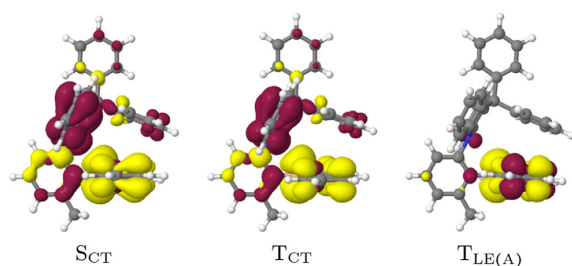


Figure 6. Difference densities (± 0.001) of the excited states of DPACoOB at their optimized geometries in toluene for conformer II. Areas losing electron density in comparison to the S state are shown in red, areas gaining electron density in yellow. Corresponding difference densities for conformer I are shown in Figure S2, Supporting Information.

Table 1. FC and FC + HT rate constants (F/ISC/rISC, s^{-1} , 300 K) between low-lying singlet and triplet state of DPACoOB for conformers I and II based on the computed DFT/MRCI energy gaps.

Process	Transition	Conformer I ^{a)}	Conformer II ^{a)}	Conformer II ^{b)}
F	$S_{CT} \rightarrow S_0$	8.7×10^5	5.2×10^6	5.4×10^6
ISC	$S_{CT} \rightarrow T_{CT}$	2.6×10^4	3.8×10^4	3.0×10^6
ISC	$S_{CT} \rightarrow T_{LE(A)}$	8.2×10^3	7.7×10^6	9.6×10^6
rISC	$S_{CT} \leftarrow T_{CT}$	2.2×10^2	4.4×10^2	7.9×10^4
rISC	$S_{CT} \leftarrow T_{LE(A)}$	1.3×10^5	1.3×10^4	7.6×10^4

^{a)}FC approach. ^{b)}FC + HT approach.

prompt fluorescence lifetime of 173.4 ns.^[11] While $S_{CT} \rightarrow T_{LE(A)}$ ISC can compete with radiative decay, the nonradiative $S_{CT} \rightarrow T_{CT}$ transition is relatively slow in FC approximation. According to the energy gap law for nested states (weak coupling limit),^[30] the rate constant for the latter process is expected to decrease exponentially with increasing ΔE_{ST} value. Indeed, test calculations employing 0–0 energy gaps in a range between 20 and 100 meV confirm these expectations (Figure S3 and Table S6, Supporting Information). In contrast, the $S_{CT} \rightarrow T_{LE(A)}$ transition, which tends toward the strong coupling limit as formulated by Englman and Jortner,^[30] appears to be nearly independent of the energy gap. The inclusion of spin-vibronic effects through a HT-like ansatz^[31] accelerates the ISC and rISC processes between the CT states by about two orders of magnitude (see Table 1), comparable to the impact of spin-vibronic interactions on the efficient TSCT emitter TpAT-tFFO.^[14,25,26] At variance with the findings for the FC approximation, the HT rate constants of this ISC process in DPACoOB do not obey the energy gap law for nested states. Due to the vibronic coupling between the CT and LE states, the $S_{CT} \rightarrow T_{CT}$ rates seem to inherit the energy dependence from the $S_{CT} \rightarrow T_{LE(A)}$ transition. Varying the 0–0 energy gap in a range between 20 and 100 meV in the VIBES program yields HT ISC rate constants ranging merely between 1×10^6 and $3 \times 10^6 s^{-1}$ (Figure 7 and Table S5, Supporting Information). As may be expected, the thermally activated $S_{CT} \rightarrow T_{CT}$ rISC process is much more sensitive with regard to the chosen $\Delta E_{ST,0-0}$ value. The calculated rate constant varies between approximately $2 \times 10^6 s^{-1}$ for $\Delta E_{ST,0-0} = 20$ meV and

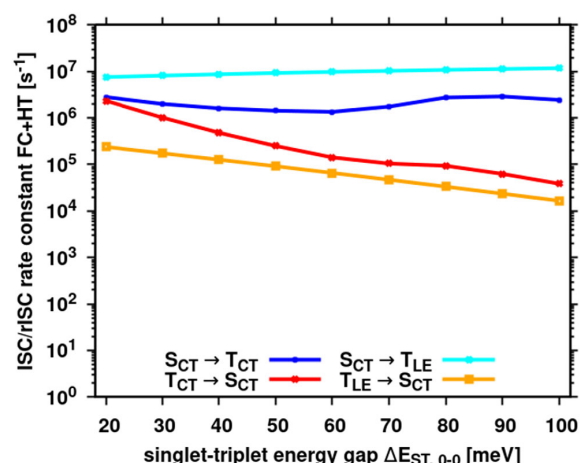


Figure 7. Computed rate constants for ISC and rISC between low-lying singlet and triplet states of DPACoOB (conformer II) in Herzberg–Teller (HT) approximation at 300 K with varying singlet–triplet energy gap. Note the logarithmic scale of the rate constants.

$4 \times 10^4 s^{-1}$ for $\Delta E_{ST,0-0} = 100$ meV. Employing the computed 0–0 splitting of 85 meV yields a rate constant of about $10^5 s^{-1}$ for the backtransfer of triplet excitons in conformer II of DPACoOB in HT approximation. Spin–vibronic coupling with the nearby $T_{LE(A)}$ state thus provides an explanation for the delayed fluorescence of this conformer in spite of a substantial singlet–triplet splitting.

Component-averaged derivatives of the SOC matrix elements (SOCMEs) with regard to nuclear displacements (Figure S4, Supporting Information) identify an in-plane deformation vibration of the acceptor involving the oxygen atom, normal mode 66 (Figure S5 and S6, Supporting Information), with a harmonic frequency of $665 cm^{-1}$ as the most prominent promoting mode of the $S_{CT} \leftrightarrow T_{CT}$ ISC and rISC processes. In the acceleration of the $S_{CT} \leftrightarrow T_{LE(A)}$ ISC and rISC processes, C–C stretching modes with harmonic frequencies around $1600 cm^{-1}$ (Figure S8 and S9, Supporting Information) play prominent roles. Despite larger SOC gradients (Figure S7, Supporting Information) the enhancement of the rISC rate constant by spin-vibronic coupling is smaller than in the $S_{CT} \rightarrow T_{CT}$ upconversion process, presumably due to a lower thermal population of the high-frequency modes.

Fluorescence spectra were calculated for the emissive S_{CT} state at different temperatures in toluene and compared to experimental data^[11] (see Figure 8). At 77 K, there is good agreement between the calculated ($\lambda_{max} = 409$ nm) and experimental ($\lambda_{max} = 422$ nm) spectra. As may be expected, the computed room-temperature HT spectrum exhibits a moderate bathochromic shift of $1302 cm^{-1}$ (0.16 eV) due to population of higher vibrational quanta, resulting in a λ_{max} value of 432 nm. Comparison with the corresponding FC spectrum (Figure S12, Supporting Information) shows that the inclusion of vibronic effects does not markedly alter the emission spectrum. The experimental spectrum shows a significantly larger red-shift of $3078 cm^{-1}$ (0.38 eV) to $\lambda_{max} = 485$ nm. This discrepancy suggests that the observed experimental shift cannot be attributed solely to the

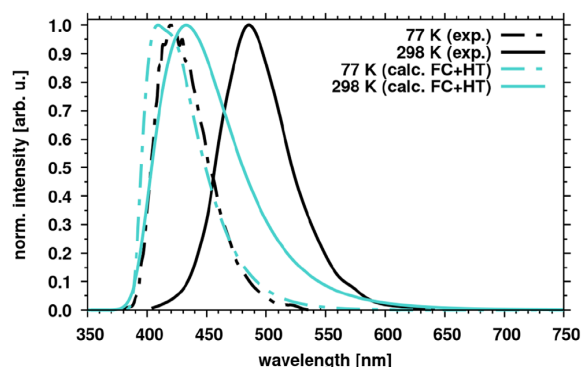


Figure 8. Calculated (turquoise) and experimental (black) emission spectra of DPACoOB (conformer II) in toluene at 77 K (dashed lines) and 298 K (solid lines). The theoretical spectra were determined in HT approximation.

temperature effect caused by a change in the Boltzmann population of the vibrational levels.

To explore the origin of this effect, we investigated whether the red-shifted emission could stem from **conformer I** as its S_{CT} minimum is energetically favored over the corresponding minimum of **conformer II** (see Figure 4). To populate the S_{CT} state of **conformer I**, an energetically accessible pathway has to be found. The inter-conversion of the conformer structures does not only require a reorientation of the phenyl group close to the **OB** acceptor. Energetically more demanding is the inversion of the (nonplanar) acridane unit (see Figure S14, Supporting Information). Nudged-elastic band calculations^[32,33] indicate barrier heights of ≈ 0.60 eV on the ground-state PES and of ≈ 0.40 eV on the S_{CT} PES, which are relatively difficult to overcome (see Figure S13, Supporting Information). We therefore consider the good agreement between the S_{CT} emission spectrum of **conformer I** with the experimental room-temperature spectrum to be accidental.

Analysis of the crystal structure reveals that the donor and acceptor units of two neighboring DPACoOB molecules adopt a T-shaped orientation (see Figure S15, Supporting Information). This raised the question whether the red-shifted room-temperature emission in toluene solution could originate from an excimer state. However, preliminary computational results for a dimer did not confirm this hypothesis. Alternatively, solvent reorganization effects could be the cause of the experimentally observed red shift. Although this process is not adequately described by the applied continuum solvent model, there are two experimental indications in favor of this assumption. First, the bathochromic shift of the DPACoOB room-temperature emission in the relatively rigid DPEPO film is much smaller than in toluene, which is expected to be solid at 77 K, but exhibits low viscosity at 298 K. Second, a similar dependence of the fluorescence wavelength was observed by Kitamoto et al.^[12] for a related *para*-appended compound where conformational effects are unlikely. Notwithstanding the shortcomings of our model in fully recovering the solvent reorganization in liquid toluene, we are confident that our computational approach captures the matrix effects on the dopant in the OLED device very well.

2.2. Chemical Modification of the Donor in *Ortho*-Appended Systems

Donor, bridge, and acceptor units can be systematically modified to fine-tune the photophysical properties of the emitter molecule. First, we investigate the impact of three distinct donor motifs, that is, DPAC, DMAC, and DPA on the adiabatic state ordering when they are cross-linked with the **OB** acceptor in *ortho*-position. DPAC and DMAC are relatively rigid, whereas DPA exhibits higher flexibility. As reported previously, the phenyl groups, attached to the acridane core in DPAC, contribute minimally to electronic excitations, but one of them plays a crucial role in nonbonding $\pi \leftrightarrow \pi$ interactions within the molecule (see also Refs. [10,13]). Conversely, DMAC features two methyl groups attached to the acridane frame, which facilitate $C-H \leftrightarrow \pi$ interactions. In DPA, the rigid tricyclic system is replaced with a more flexible structure. Here, the entire donor participates actively in electronic excitations, and one of its phenyl rings can orient toward the acceptor, enabling π - π stacking, a behavior similar to that observed in DPAC.

We do not expect the adiabatic excitation energy of the LE triplet state localized on the acceptor, $T_{LE(A)}$, to be strongly affected by donor modification. However, it is evident from Figure 9 that an increase of the $\pi \leftrightarrow \pi$ interaction, when going from DMAC through DPA to DPAC, slightly shifts the $T_{LE(A)}$ state to higher energies. In contrast, CT excited states are intrinsically sensitive to the choice of the donor. Like in **conformer I** of DPACoOB, $C-H \leftrightarrow \pi$ interaction between one methyl residue of DMAC and the negatively charged **OB** acceptor stabilizes the CT states of DMACoOB. This stabilization leads to an energetic arrangement of excited states (Figure 9) that enhances the TADF performance, in agreement with the experimentally observed higher ratio of delayed to prompt fluorescence.^[10] For DPA, the opening of the acridane ring markedly alters the hole distribution on the donor and further lowers the energy of the CT states. Consequently, the $T_{LE(A)}$ state comes to lie energetically higher than the S_{CT} state. This change prevents the $T_{LE(A)}$ state from serving as a mediator in the $S_{CT} \sim T_{CT}$ rISC process. It also becomes apparent that increasing flexibility of the molecule results in a higher ΔE_{ST} value. Compared to DPAC, this value

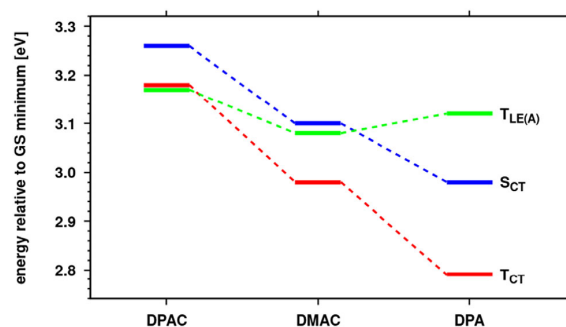


Figure 9. DFT/MRCI-R2016 energy level scheme of DPACoOB, DMACoOB, and DPAoOB. All adiabatic excitation energies are given relative to the ground-state minimum energy of the respective compound in eV.

approximately doubles when DPA is chosen as the donor. This result is in line with the conclusion drawn by Wu et al.^[34] who set up structure-property relationships for triarylboron-based TADF molecules comprising various donors and dimesitylboryl acceptors.

2.3. Regioisomerism: The *Para*-Appended DPACpOB Emitter

The *para*-linkage of the DPAC donor and the OB acceptor to the methylphenylene bridge in DPACpOB increases the energy gap between the S_{CT} and T_{CT} states substantially in relation to DPACoOB. Comparison of the level schemes in Figure 10 (1-Me) and Figure 9 (DPAC) reveals that the adiabatic S_{CT} energy is blue-shifted while the adiabatic T_{CT} energy is simultaneously red-shifted in DPACpOB, indicating a higher overlap of the hole and particle densities and, consequentially, a stronger donor-acceptor exchange interaction in the *para*-appended emitter. The adiabatic energy of the $T_{LE(A)}$ state varies minimally between the two regioisomers and hence comes to lie in the energy gap between the two CT states in DPACpOB. With a rate constant of $k_F = 3.8 \times 10^5 \text{ s}^{-1}$ in FC approximation, fluorescence is slowed down by an order of magnitude in comparison to DPACoOB, making it more susceptible to competitive nonradiative deactivation processes. $S_{CT} \leadsto T_{CT}$ ISC proceeds at a rate constant of $k_{ISC} = 8.0 \times 10^5 \text{ s}^{-1}$ in FC approximation (see also Table 2, 1-Me), thus reducing the prompt fluorescence quantum yield. Despite the increased singlet-triplet splitting, the $S_{CT} \leadsto T_{CT}$ rISC is not substantially slower than in its *ortho*-appended congener. We refrained from carrying out HT-type calculations for DPACpOB. However, as the $T_{LE(A)}$ state forms the first excited triplet state at the ground-state geometry and comes to lie adiabatically between S_{CT} and T_{CT} states, we expect spin-vibronic interactions to enhance the rISC rate by one to two orders of magnitude compared to its value of $k_{ISC} = 2.5 \times 10^2 \text{ s}^{-1}$ in FC approximation. All in all, we expect this *para*-appended regioisomer to be TADF active, but with lower luminescence quantum yields than the *ortho*-appended regioisomer.

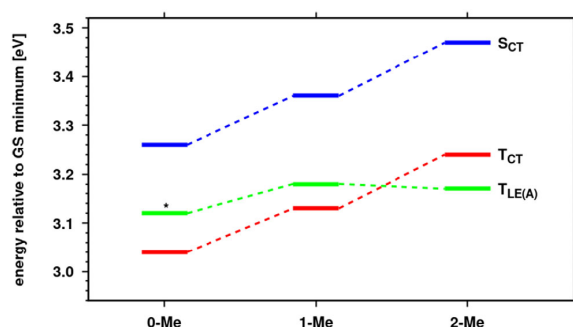


Figure 10. DFT/MRCI-R2016 energy level scheme of DPACpOB with modified bridge (0-Me, 1-Me, and 2-Me). All adiabatic excitation energies are given relative to the ground-state minimum energy of the respective compound in eV. For 0-Me, the asterisk symbolizes that the $T_{LE(A)}$ state energy was derived from the optimized $S_{LE(A)}$ geometry due to optimization failure.

2.4. Chemical Modification of the Bridge

In other *para*-appended donor-bridge-acceptor systems, the ΔE_{ST} value can easily be manipulated by introducing bulky substituents on the phenylene bridge.^[20,35] The question therefore arises whether the twist angle between the donor and acceptor moieties in DPACpOB can be changed in a similar way. The closer this angle is to 90°, the smaller ΔE_{ST} values are expected. For DPACpOB, we systematically explored the impact of varying numbers of methyl groups, i.e., 0-Me, 1-Me and 2-Me, on the phenyl bridge in *ortho*-position relative to the acceptor. Methyl groups have only minor electronic effects, making them ideal for analyzing conformational changes on the photophysical properties of the *para*-appended emitters.

Increasing the steric hindrance forces the bridge and the acceptor from a twisted conformation with a dihedral angle of 55° (0-Me) gradually into an orthogonal arrangement in the electronic ground state of 2-Me. Simultaneously, the dihedral angle between the donor and the bridge remains nearly orthogonal. Counterintuitively, the addition of methyl groups in *ortho*-position to the acceptor therefore reduces the dihedral angle θ between the donor and acceptor in the electronic ground state, bringing it closer to co-planarity (0-Me: 41°, 1-Me: 15°, 2-Me: 2°). Similar donor-acceptor twist angles are found for the T_{CT} state (see Table 2), where a change from 28° (0-Me) over 13° (1-Me) to 3° (2-Me) is observed. In the S_{CT} state, the trend is the same. The donor-acceptor twist angles are somewhat larger (0-Me: 50°, 1-Me: 31°, 2-Me: 21°), but they are far away from 90°.

The adiabatic excitation energy of the $T_{LE(A)}$ state remains nearly constant upon methyl substitution, whereas the S_{CT} and T_{CT} states increase in energy within this series (see Figure 10). Every additional methyl group raises the adiabatic energies of the S_{CT} and T_{CT} by $\approx 100 \text{ meV}$, despite the fact that the CT character of these states mildly increases, as indicated by the static dipole moments displayed in Table 2. The energy gap between the CT states is kept nearly constant at about 230 meV. While the addition of methyl groups to the linker therefore does not have the desired effect of reducing the ΔE_{ST} value, their impact can be used to position the CT states in the energetic proximity to the $T_{LE(A)}$ state.

The impact of the nuclear arrangement on the electronic structure is most pronounced in the T_{CT} state. Moving from the optimized geometry of the S_{CT} state to the T_{CT} minimum reduces the CT contributions to the T_{CT} wavefunction, thus explaining the substantial lowering of the static electric dipole moment and the increase of the SOCMEs with the S_{CT} wavefunction. For systems in which the LE state lies adiabatically between the CT states, we expect spin-vibronic interactions to improve the TADF abilities. Nevertheless, we consider the *para*-appended boron-based emitters to show inferior TADF performance in comparison to the *ortho*-appended ones.

2.5. Substituting Sulfur for Oxygen

SOC plays a crucial role in the ISC and rISC processes. To exert a heavy-atom effect, we modified the original acceptor

Table 2. Donor–Acceptor twist angle θ ($^\circ$), electric dipole moments μ (D), adiabatic energy difference ΔE_{adia} (cm^{-1}), component averaged SOCMEs (cm^{-1}) and FC rate constants (s^{-1} , 300 K) for ISC and rISC transitions in *para*-appended DPAC and OB for varying numbers of methyl substituents on the phenylene bridge.

Bridge	θ	Initial State	Final State	ΔE_{adia}	SOCME	$k_{\text{ISC}}/k_{\text{rISC}}$
0-Me	50	$S_{\text{CT}} (\mu = 26.18)$	$T_{\text{CT}} (\mu = 25.61)$	1759	0.081	2.8×10^4
1-Me	31	$S_{\text{CT}} (\mu = 27.97)$	$T_{\text{CT}} (\mu = 27.26)$	1909	0.082	8.0×10^5
2-Me	21	$S_{\text{CT}} (\mu = 29.44)$	$T_{\text{CT}} (\mu = 29.09)$	1826	0.064	5.2×10^4
0-Me	50	$S_{\text{CT}} (\mu = 26.18)$	$T_{\text{LE(A)}} (\mu = 5.52)$	1094	0.264	4.4×10^5
1-Me	31	$S_{\text{CT}} (\mu = 27.97)$	$T_{\text{LE(A)}} (\mu = 6.01)$	1504	0.090	4.7×10^3
2-Me	21	$S_{\text{CT}} (\mu = 29.44)$	$T_{\text{LE(A)}} (\mu = 6.43)$	2403	0.058	2.8×10^5
0-Me	28	$T_{\text{CT}} (\mu = 13.88)$	$S_{\text{CT}} (\mu = 22.07)$	-1759	0.444	1.5×10^2
1-Me	13	$T_{\text{CT}} (\mu = 15.19)$	$S_{\text{CT}} (\mu = 23.66)$	-1909	0.386	2.5×10^2
2-Me	3	$T_{\text{CT}} (\mu = 16.39)$	$S_{\text{CT}} (\mu = 24.70)$	-1826	0.343	2.1×10^2

10H-phenoxaboryl (OB) by substituting sulfur for oxygen, resulting in the acceptor unit 10H-phenothiaboryl (SB).

Our DFT/MRCI calculations reveal a small singlet–triplet energy gap between the CT states of the *para*-appended compound DPACpSB (Table S7, Supporting Information), which is smaller than in DPACpOB. Note, however, that the T_{CT} state does not constitute the first excited triplet state in DPACpSB. Adiabatically, the $T_{\text{LE(A)}}$ state lies more than 0.5 eV below the S_{CT} state, indicating that TADF is not to be expected for this compound. In the corresponding *ortho*-regioisomer, the $S_{\text{LE(A)}}$ and $T_{\text{LE(A)}}$ states are found at slightly lower energies while the S_{CT} and T_{CT} states are markedly stabilized (Table S7, Supporting Information). This red-shift is not sufficient, however, to bring the $T_{\text{LE(A)}}$ state in close energetic proximity to the CT states. On these grounds, we did not investigate the photophysical properties of these sulfur-containing compounds in more detail.

3. Conclusion

In search for suitable blue-light OLED emitters, the class of boron-based TADF emitters has proven to be highly promising. There are many ways to modify the molecular framework of a donor–bridge–acceptor system. In this quantum chemical study, we systematically investigate the influence of the donor–acceptor orientation in *ortho*- and *para*-arrangements on the TADF abilities. Moreover, the donor strength and rigidity is modulated and the impact of an internal heavy-atom effect on the photophysical properties is studied.

Starting with the experimentally verified TADF emitter DPACoOB,^[11] which consists of a DPAC donor and an OB acceptor connected in *ortho*-position to a methylated phenylene (1-Me) bridge, we found an acceptor-localized excited triplet state, $T_{\text{LE(A)}}$, in close energetic proximity to the previously known S_{CT} and T_{CT} states. This $T_{\text{LE(A)}}$ state couples vibronically to the T_{CT} state, thus enhancing the upconversion of the triplet population to the fluorescent S_{CT} state. This spin-vibronic mechanism accelerates the rISC by two orders of magnitude brings its rate constant in good agreement with the experimentally determined value.

When the phenyl residues of the acridane donor are replaced by methyl groups, the $C-H \leftrightarrow \pi$ interaction between DMAC and the negatively charged OB acceptor stabilizes the CT states of

DMACoOB. This stabilization has a two-fold effect. It leads to a red-shift of the emission and an energetic arrangement of the CT and LE states that is expected to enhance the TADF performance, in agreement with the experimentally observed higher ratio of delayed to prompt fluorescence in comparison to DPACoOB.^[10,11] The less rigid DPA donor further lowers the energy of the CT states and increases the ΔE_{ST} value, thus preventing the $T_{\text{LE(A)}}$ state from serving as a mediator in the $S_{\text{CT}} \leftrightarrow T_{\text{CT}}$ rISC process.

In the *para*-appended DPACpOB, fluorescence is slowed down by an order of magnitude in comparison to the *ortho*-appended DPACoOB, making it more susceptible to competitive nonradiative deactivation processes. Although the ΔE_{ST} value is markedly increased in this congener, the rISC rate constants are comparable in both systems. We therefore expect DPACpOB to be TADF active, but with lower luminescence quantum yields than the *ortho*-appended regioisomer.

Counterintuitively, the addition of methyl groups in *ortho*-position to the acceptor reduces the dihedral angle between the *para*-appended donor and acceptor units in the electronic ground state of DPACpOB, bringing them closer to co-planarity. Therefore, the addition of methyl groups to the linker does not have the desired effect of reducing the ΔE_{ST} value. However, their impact can be used to position the CT states in the energetic proximity to the $T_{\text{LE(A)}}$ state.

Introduction of a sulfur atom in the acceptor does not show the expected acceleration of the ISC and rISC processes due to an internal heavy-atom effect because the lowest excited triplet state adopts LE character in DPACpSB and DPACoSB and is located far below the CT states. We therefore expect these compounds to be nonemissive at room temperature.

Summarizing, chemical modification of the donor, bridge and acceptor in boron-based TADF emitters can be used to tune the energetic position of the CT states with regard to an acceptor-localized T which is an essential mediator for accelerating the rISC process by spin–vibronic interactions.

4. Computational Methods

The electronic ground and excited-state geometries were optimized with Gaussian16^[36] using (TD)DFT including the

Tamm–Dancoff approximation (TDA) for excited triplet states. Throughout, the def2-SV(P) atomic orbital basis set^[37] was employed in the calculations. Several density functionals were tested in the geometry optimization step of DPACoOB. Analysis of the data revealed that dispersion corrections,^[38] included either explicitly or through the density functional, lead to too strong intramolecular interactions and underestimate the distance between the phenyl residue of the DPAC donor and the OB acceptor by up to 0.3 Å. We finally opted for the PBE0^[39,40] density functional without dispersion corrections for all structure optimizations as this hybrid functional gave the best overall agreement with the X-ray parameters^[11] (Table S2, Supporting Information). Analytic harmonic vibrational frequencies were computed with Gaussian16. Solvation effects (toluene) were considered via the polarizable continuum model^[41] (PCM) using the solvent excluding surface (SES) implemented in Gaussian16. Note, that the PCM considers the solvent response to the electronic transition density and does not account for solvent reorganization effects, in contrast to state-specific solvent models based on the difference density. We have refrained from applying a corrected linear response solvent model in the present case because it was found to overshoot drastically in donor–acceptor compounds with highly polar CT excited states.^[20]

Molecular orbitals for subsequent excited-state calculations were generated with Turbomole^[42] employing the BH-LYP^[43,44] density functional. The auxiliary basis sets of Weigend^[45] were used for the resolution-of-the-identity approximation of the two-electron integrals. Excitation energies and photophysical properties were calculated with the DFT/MRCI method^[46,47] in the R2016 parametrization of the Hamiltonian^[28] with the tight configuration selection threshold of 0.8. This method performs much better than TDDFT (Figure S1, Supporting Information) in reproducing the general shape of the absorption spectrum of DPACoOB. Unlike TDDFT conjunction with the PBE0^[39,40] hybrid functional or the optimally tuned, long-range corrected LC-HPBE^[48] or B97X-D^[49] functionals, the DFT/MRCI-R2016 Hamiltonian^[28] yields balanced results for the CT and LE transitions (Table S1, Supporting Information). Fragment-based analyses of the DFT/MRCI-R2016 wavefunctions were performed with the TheoDOR tool box.^[29]

Radiative rate constants in Franck–Condon (FC) approximation were determined according to the well-known Einstein formula. To check whether vibronic effects accelerate fluorescence, electric dipole transition moments and their numerical derivatives were employed to compute fluorescence rate constants in HT approximation according to

$$k_{\text{f}}^{\text{HT}} = \int I^{\text{HT}}(\omega) d\omega = \frac{4}{3\hbar c_0^3} \frac{\int \omega^3 S^{\text{HT}}(\omega) d\omega}{\int S^{\text{FC}}(\omega) d\omega} \quad (1)$$

where $I^{\text{HT}}(\omega)$ is the frequency dependent intensity of the computed HT spectrum, \hbar is Planck's constant divided by 2π , c_0 is the vacuum speed of light and $S^{\text{HT}}(\omega)$ and $S^{\text{FC}}(\omega)$ are the HT and FC spectral densities, respectively, obtained by a fast Fourier transformation of the autocorrelation function in the time domain.^[31]

SOCMEs between target singlet and triplet states were calculated with the spin–orbit coupling kit (SPOCK)^[50,51] using the Breit–Pauli Hamiltonian in atomic mean-field approximation.^[52,53] Derivatives of the SOCMEs with respect to the mass-weighted normal coordinates were determined by two-point finite-difference techniques using a step size of 0.1 units. Rate constants for ISC and rISC in the framework of Fermi's golden rule were determined in FC or HT approximation by means of a Fourier transform approach, as implemented in the VIBES program.^[31,35,54] Temperature effects were included by assuming a Boltzmann distribution in the initial electronic state. The time correlation function was multiplied by a Gaussian damping function of 10 cm^{-1} full width at half maximum (FWHM) before numerical integration on a time interval of 3000 fs using 65536 grid points. The sensitivity of the computed rate constants with regard to variations of these technical parameters was found to be marginal (Table S4, Supporting Information). In the FC approximation, the rate constant for the $S_a \leadsto T_b$ ISC at a given temperature is computed as the sum of squared electronic SOCMEs between the initial singlet state S_a at its minimum geometry and the three triplet sublevels T_b , multiplied by the Boltzmann and FC weighted density of vibrational states according to

$$k_{\text{ISC},ab}^{\text{FC}}(T) = \frac{2\pi}{\hbar Z} \sum_{\alpha} |\langle \Psi_{T_b} | \hat{H}_{\text{SO}} | \Psi_{S_a} \rangle|_{Q_0}^2 \times \sum_k e^{-\frac{(E_{S_a} - E_{T_b})}{k_B T}} \sum_j |\langle v_{bj} | v_{ak} \rangle|^2 \delta(E_{ak} - E_{bj}) \quad (2)$$

where k_B is the Boltzmann constant and $Z = \sum_k e^{-\frac{(E_{S_a} - E_{T_b})}{k_B T}}$ the partition function of the initial state. In the HT approximation, the SOC is expanded as a function of the normal coordinates Q of the initial state about Q_0 and the expansion is terminated after the linear term yielding^[23,31,55]

$$k_{\text{ISC},ab}^{\text{FC+HT}}(T) = \frac{2\pi}{\hbar Z} \sum_{\alpha} \sum_k e^{-\frac{(E_{S_a} - E_{T_b})}{k_B T}} \times \sum_j \langle v_{bj} | \langle \Psi_{T_b} | \hat{H}_{\text{SO}} | \Psi_{S_a} \rangle |_{Q_0} \rangle \times \sum_A \left. \frac{\partial \langle \Psi_{T_b} | \hat{H}_{\text{SO}} | \Psi_{S_a} \rangle}{\partial Q_A} \right|_{Q_0} Q_A | v_{ak} \rangle \Big|^2 \times \delta(E_{ak} - E_{bj}) \quad (3)$$

Squaring this expression yields a pure FC term, a mixed FC/HT term and a HT/HT term. Similar formulas result for the reverse $S_a \leadsto T_b$ process.

Acknowledgements

This research was funded by the Deutsche Forschungsgemeinschaft (DFG, German Research Foundation)—GRK 2482/396890929.

Open Access funding enabled and organized by Projekt DEAL.

Conflict of Interest

The authors declare no conflict of interest.

Data Availability Statement

The data that support the findings of this study are available in the supplementary material of this article.

Keywords: DFT/MRCI · Herzberg–Teller expansion · regioisomerism · spin–orbit coupling · spin–vibronic interaction

- [1] L. Ji, S. Griesbeck, T. B. Marder, *Chem. Sci.* **2017**, *8*, 846.
- [2] G. Turkoglu, M. E. Cinar, T. Ozturk, *Molecules* **2017**, *22*, 1522.
- [3] S. K. Møllerup, S. Wang, *Trends Chem.* **2019**, *1*, 77.
- [4] Z. Huang, S. Wang, R. D. Dewhurst, N. V. Ignatév, M. Finze, H. Braunschweig, *Angew. Chem. Int. Ed.* **2020**, *59*, 8800.
- [5] S. S. Kothavale, J. Y. Lee, *Adv. Opt. Mater.* **2020**, *8*, 2000922.
- [6] H. Lee, D. Karthik, R. Lampande, J. H. Ryu, J. H. Kwon, *Front. Chem.* **2020**, *8*, 373.
- [7] H. J. Kim, T. Yasuda, *Adv. Opt. Mater.* **2022**, *10*, 2201714.
- [8] J.-Y. Yoo, S. W. Kang, T. H. Ha, C. W. Lee, *J. Mater. Chem. C* **2024**, *12*, 14045.
- [9] J. Park, S. Han, U. Jo, S. C. Kim, D. R. Lee, H. J. Ahn, J. Y. Kim, J.-H. Baek, J. Y. Lee, *Mater. Today* **2024**, *75*, 27.
- [10] J. Kim, T. Lee, J. Y. Ryu, Y. H. Lee, J. Lee, J. Jung, M. H. Lee, *Organometallics* **2020**, *39*, 2235.
- [11] H. Mubarak, W. Lee, T. Lee, J. Jung, S. Yoo, M. H. Lee, *Front. Chem.* **2020**, *8*, 538.
- [12] Y. Kitamoto, T. Namikawa, D. Ikemizu, Y. Miyata, T. Suzuki, H. Kita, T. Sato, S. Oi, *J. Mater. Chem. C* **2015**, *3*, 9122.
- [13] Y. H. Lee, D. Lee, T. Lee, J. Lee, J. Jung, S. Yoo, M. H. Lee, *Dyes Pigm.* **2021**, *188*, 109224.
- [14] Y. Wada, H. Nakagawa, S. Matsumoto, Y. Wakisaka, H. Kaji, *Nat. Photonics* **2020**, *14*, 643.
- [15] S. Kumar, L. G. Franca, K. Stavrou, E. Crovini, D. B. Cordes, A. M. Z. Slawin, A. P. Monkman, E. Zysman-Colman, *J. Phys. Chem. Lett.* **2021**, *12*, 2820.
- [16] Q. Li, J. Hu, J. Lv, X. Wang, S. Shao, L. Wang, X. Jing, F. Wang, *Angew. Chem. Int. Ed.* **2020**, *59*, 20174.
- [17] Y. Song, M. Tian, R. Yu, L. He, *ACS Appl. Mater. Interfaces* **2021**, *13*, 60269.
- [18] R. Dhali, D. A. P. Huu, F. Bertocchi, C. Sissa, F. Terenziani, A. Painelli, *Phys. Chem. Chem. Phys.* **2021**, *23*, 378.
- [19] F. Di Maiolo, D. K. A. Phan Huu, D. Giavazzi, A. Landi, O. Racchi, A. Painelli, *Chem. Sci.* **2024**, *15*, 5434.
- [20] J. M. Kaminski, T. Böhmer, C. M. Marian, *J. Phys. Chem. C* **2024**, *128*, 13711.
- [21] M. K. Etherington, J. Gibson, H. F. Higginbotham, T. J. Penfold, A. P. Monkman, *Nat. Comm.* **2016**, *7*, 13680.
- [22] R. S. Nobuyasu, Z. Ren, G. C. Griffiths, A. S. Batsanov, S. Data, P. Yan, A. P. Monkman, M. R. Bryce, F. B. Dias, *Adv. Opt. Mater.* **2016**, *4*, 597.
- [23] T. J. Penfold, E. Gindensperger, C. Daniel, C. M. Marian, *Chem. Rev.* **2018**, *118*, 6975.
- [24] C. M. Marian, *Annu. Rev. Phys. Chem.* **2021**, *72*, 617.
- [25] J. M. Kaminski, A. Rodriguez-Serrano, F. Dinkelbach, H. Miranda-Salinas, A. P. Monkman, C. M. Marian, *Chem. Sci.* **2022**, *13*, 7057.
- [26] H. Miranda-Salinas, A. Rodriguez-Serrano, J. M. Kaminski, F. Dinkelbach, N. Hiromichi, Y. Kusakabe, H. Kaji, C. M. Marian, A. P. Monkman, *J. Phys. Chem. C* **2023**, *127*, 8607.
- [27] Z. Wu, J. Nitsch, J. Schuster, A. Friedrich, K. Edkins, M. Loebnitz, F. Dinkelbach, V. Stepanenko, F. Würthner, C. M. Marian, L. Ji, T. B. Marder, *Angew. Chem. Intl. Ed.* **2020**, *59*, 17137.
- [28] I. Lyskov, M. Kleinschmidt, C. M. Marian, *J. Chem. Phys.* **2016**, *144*, 034104.
- [29] F. Plasser, *J. Chem. Phys.* **2020**, *152*, 084108.
- [30] R. Engelman, J. Jortner, *Mol. Phys.* **1970**, *18*, 145.
- [31] M. Etinski, V. Rai-Constapel, C. M. Marian, *J. Chem. Phys.* **2014**, *140*, 114104.
- [32] V. Ásgeirsson, B. O. Birgisson, R. Björnsson, U. Becker, F. Neese, C. Riplinger, H. Jónsson, *J. Chem. Theory Comput.* **2021**, *17*, 4929.
- [33] F. Neese, *WIREs Comput. Mol. Sci.* **2022**, *12*, e1606.
- [34] Z. Wu, F. Li, Y. Zhou, J. Fan, L. Lin, *Mater. Sci. Eng. B-Adv.* **2021**, *270*, 115203.
- [35] T. Böhmer, M. Kleinschmidt, C. M. Marian, *J. Chem. Phys.* **2024**, *161*, 094114.
- [36] Gaussian 16, Revision A.03, M. J. Frisch, G. W. Trucks, H. B. Schlegel, G. E. Scuseria, M. A. Robb, J. R. Cheeseman, G. Scalmani, V. Barone, G. A. Petersson, H. Nakatsuji, X. Li, M. Caricato, A. V. Marenich, J. Bloino, B. G. Janesko, R. Gomperts, B. Mennucci, H. P. Hratchian, J. V. Ortiz, A. F. Izmaylov, J. L. Sonnenberg, D. Williams-Young, F. Ding, F. Lipparini, F. Egidi, J. Goings, B. Peng, A. Petrone, T. Henderson, D. Ranasinghe, V. G. Zakrzewski, et al., Gaussian, Inc., Wallingford CT **2016**.
- [37] F. Weigend, R. Ahlrichs, *Phys. Chem. Chem. Phys.* **2005**, *7*, 3297.
- [38] S. Grimme, S. Ehrlich, L. Goerigk, *J. Comp. Chem.* **2011**, *32*, 1456.
- [39] J. P. Perdew, K. Burke, M. Ernzerhof, *Phys. Rev. Lett.* **1996**, *77*, 3865.
- [40] C. Adamo, V. Barone, *J. Chem. Phys.* **1999**, *110*, 6158.
- [41] J. Tomasi, B. Mennucci, R. Cammi, *Chem. Rev.* **2005**, *105*, 2999.
- [42] TURBOMOLE V7.5 2020, a development of University of Karlsruhe and Forschungszentrum Karlsruhe GmbH, 1989-2007, TURBOMOLE GmbH, since 2007; available from <http://www.turbomole.com>.
- [43] A. D. Becke, *J. Chem. Phys.* **1993**, *98*, 1372.
- [44] C. Lee, W. Yang, R. G. Parr, *Phys. Rev. B* **1988**, *37*, 785.
- [45] F. Weigend, *Phys. Chem. Chem. Phys.* **2006**, *8*, 1057.
- [46] S. Grimme, M. Waletzke, *J. Chem. Phys.* **1999**, *111*, 5645.
- [47] C. M. Marian, A. Heil, M. Kleinschmidt, *WIREs Comput. Mol. Sci.* **2019**, *9*, e1394.
- [48] O. A. Vydrov, G. E. Scuseria, *J. Chem. Phys.* **2006**, *125*, 234109.
- [49] J.-D. Chai, M. Head-Gordon, *Phys. Chem. Chem. Phys.* **2008**, *10*, 6615.
- [50] M. Kleinschmidt, J. Tatchen, C. M. Marian, *J. Comput. Chem.* **2002**, *23*, 824.
- [51] M. Kleinschmidt, C. M. Marian, *Chem. Phys.* **2005**, *311*, 71.
- [52] B. A. Heß, C. M. Marian, U. Wahlgren, O. Gropen, *Chem. Phys. Lett.* **1996**, *251*, 365.
- [53] B. Schimmelpfennig, *Atomic Mean-Field Integral (AMFI) Program*, University of Stockholm **1996**.
- [54] M. Etinski, J. Tatchen, C. M. Marian, *J. Chem. Phys.* **2011**, *134*, 154105.
- [55] J. Tatchen, N. Gilka, C. M. Marian, *Phys. Chem. Chem. Phys.* **2007**, *9*, 5209.

Manuscript received: January 31, 2025

Revised manuscript received: April 28, 2025

Version of record online:

ESI: How Donor–Bridge–Acceptor Orientation and Chemical Modification Affect the TADF Abilities of Boron-Based Emitters

Jeremy M. Kaminski,^[a] Tu V. Chu,^[a] Christel M. Marian*^[a]

[a] J. M. Kaminski, T. V. Chu, Prof. Dr. C. M. Marian*
Institute of Theoretical and Computational Chemistry, Faculty
of Mathematics and Natural Sciences, Heinrich Heine University
Düsseldorf, 40204 Düsseldorf, Germany
E-mail: christel.marian@hhu.de

Table S1. Wavelengths [nm] for the first two absorption bands and the absorption maximum for conformers **I** and **II** of **DPACoOB** at different levels of theory and experimental values. The energy difference [eV] between the experimental peak maximum and the corresponding calculated vertical excitation energy is given in parentheses. For RSH functionals, optimally tuned range-separation parameters were used: $\omega = 0.165$ for LC- ω HPBE, $\omega = 0.125$ for ω B97X-D.

Conf.	Method	Setup	$S_1 \leftarrow S_0$ (CT)	$S_2 \leftarrow S_0$ (LE(A))	$\lambda_{\max}^{\text{abs}}$
II	TDDFT	PBE0/GD3BJ	402 (+0.28)	317 (-0.31)	268 (-0.34)
II	TDDFT	PBE0	402 (+0.28)	317 (-0.31)	268 (-0.34)
II	TDDFT	LC-ωHPBE	380 (+0.11)	325 (-0.21)	290 (+0.01)
II	TDDFT	ωB97X-D	346 (-0.21)	305 (-0.46)	276 (-0.20)
II	DFT/MRCI	PBE0/GD3BJ	358 (-0.09)	332 (-0.13)	279 (-0.15)
II	DFT/MRCI	PBE0	356 (-0.11)	332 (-0.13)	279 (-0.15)
II	DFT/MRCI	LC-ωHPBE	359 (-0.08)	337 (-0.07)	280 (-0.14)
II	DFT/MRCI	ωB97X-D	358 (-0.09)	333 (-0.12)	279 (-0.15)
I	DFT/MRCI	PBE0	394 (+0.22)	337 (-0.07)	289 (± 0.00)
	Experiment ^[1]		368	344	289

Table S2. Geometrical parameters at the optimized ground-state geometries for **conformer II** of **DPACoOB** in toluene (PCM) using various density functionals in comparison to values retrieved from an X-ray structure analysis.^[1] Bond lengths in Å, angles in deg. For RSH functionals, optimally tuned range-separation parameters were used: $\omega = 0.165$ for LC- ω HPBE, $\omega = 0.125$ for ω B97X-D.

Parameter	XRAY	PBE0	PBE0+GD3BJ	ω B97X-D	LC- ω HPBE
B1 – N1	2.91	2.95	2.89	2.91	2.96
B1 – C21	1.58	1.58	1.58	1.58	1.59
B1 – C23	1.53	1.54	1.54	1.54	1.54
B1 – C29	1.53	1.54	1.54	1.54	1.54
C42 – O1	3.46	3.43	3.16	3.21	3.46
<OB – Ph-Me	83.7	89.8	86.8	86.5	87.0
<DPAC – Ph-Me	86.4	90.0	79.6	79.7	78.1
N1 – C16 – C21	118.0	119.5	118.3	118.4	119.4
C16 – C21 – B1	121.7	122.0	121.2	121.3	122.0
$\Sigma(\text{C} - \text{B} - \text{C})$	359.7	359.8	359.8	359.7	359.7

Table S3. Geometrical parameters at the optimized S_0 , S_{CT} , T_{CT} and $T_{\text{LE(A)}}$ geometries for **conformer II** of **DPACoOB** in toluene (PCM) at PBE0/def2-SV(P) level of theory in comparison to values retrieved from an X-ray structure analysis.^[1] Bond lengths in Å, angles in deg.

Parameter	XRAY	S_0	S_{CT}	T_{CT}	$T_{\text{LE(A)}}$
B1 – N1	2.91	2.95	3.04	3.00	3.00
B1 – C21	1.58	1.58	1.60	1.60	1.59
B1 – C23	1.53	1.54	1.53	1.53	1.54
B1 – C29	1.53	1.54	1.53	1.53	1.54
C42 – O1	3.46	3.43	3.40	3.40	3.50
C24/C30 – C25/C31	—	1.38	1.39	1.39	1.41
<OB – Ph-Me	83.7	89.8	89.9	89.4	83.9
<DPAC – Ph-Me	86.4	90.0	89.4	89.6	86.1
<OB – Ph	—	18.8	20.3	20.6	18.2
<DPAC (L/R)	—	14.6 / 14.6	12.1 / 12.1	12.1 / 12.1	13.7 / 13.6
<OB (L/R)	—	1.0 / 1.0	3.4 / 3.4	3.3 / 3.3	1.1 / 1.2
N1 – C16 – C21	118.0	119.5	119.6	119.2	120.0
C16 – C21 – B1	121.7	122.0	124.8	123.8	123.4
$\Sigma(\text{C} - \text{B} - \text{C})$	359.7	359.8	359.8	359.7	359.7

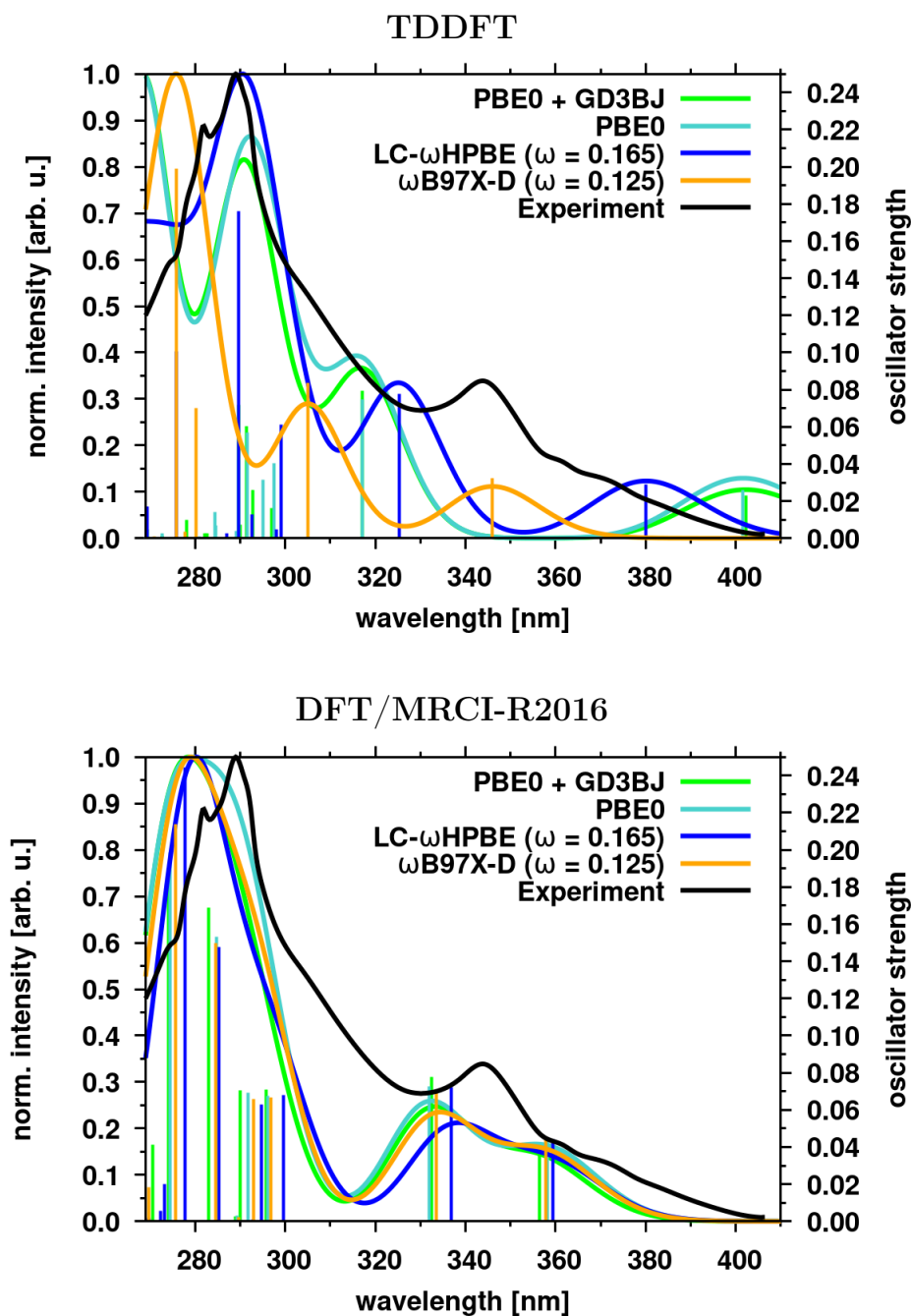


Figure S1. Absorption spectra of **DPACoOB** in toluene, calculated at TDDFT (top) and DFT/MRCI-R2016 (bottom) levels of theory in comparison to experimental results (black)^[1]. The line spectra were broadened by Gaussians with 2000 cm⁻¹ full width at half maximum. For the DFT/MRCI spectra in the bottom panel, the colors indicate the density functional employed in the geometry optimization of the electronic ground state.

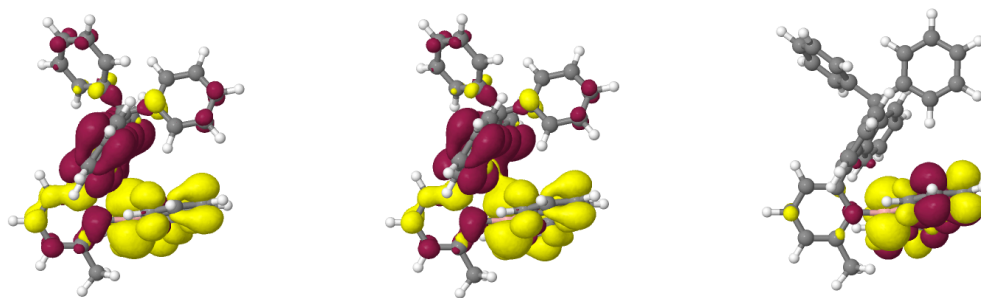


Figure S2. Difference densities (± 0.001) of the excited states at their optimized geometries in toluene (**conformer I**). Areas losing electron density in comparison to the electronic ground state are shown in red, areas gaining electron density in yellow.

Table S4. FC+HT rate constants (ISC/rISC, s^{-1} , 300 K) between low-lying singlet and triplet states of **DPACoOB**, conformer **II** for varying technical parameters (number of grid points and FWHM of the Gaussian damping function (cm^{-1})) of the Fourier transformation.

grid points	FWHM	$S_{CT \rightarrow T_{CT}}$	$S_{CT \leftarrow T_{CT}}$	$S_{CT \rightarrow T_{LE(A)}}$	$S_{CT \leftarrow T_{LE(A)}}$
65536	1	2.98×10^6	7.93×10^4	9.56×10^6	7.61×10^4
65536	5	2.98×10^6	7.93×10^4	9.56×10^6	7.61×10^4
65536	10	2.97×10^6	7.92×10^4	9.56×10^6	7.62×10^4
65536	20	2.94×10^6	7.90×10^4	9.56×10^6	7.63×10^4
262144	1	2.98×10^6	7.93×10^4	9.56×10^6	7.61×10^4
262144	10	2.97×10^6	7.92×10^4	9.56×10^6	7.62×10^4

Table S5. FC+HT rate constants (ISC/rISC, s^{-1} , 300 K) between low-lying singlet and triplet states of **DPACoOB**, conformer **II** for 0–0 singlet–triplet energy gaps (meV) ranging between 20 meV and 100 meV.

ΔE_{0-0}	$S_{CT \rightarrow T_{CT}}$	$S_{CT \leftarrow T_{CT}}$	$S_{CT \rightarrow T_{LE(A)}}$	$S_{CT \leftarrow T_{LE(A)}}$
20	2.80×10^6	2.32×10^6	7.57×10^6	2.39×10^5
30	2.00×10^6	1.02×10^6	8.14×10^6	1.75×10^5
40	1.60×10^6	4.81×10^5	8.70×10^6	1.27×10^5
50	1.43×10^6	2.52×10^5	9.25×10^6	9.19×10^4
60	1.35×10^6	1.42×10^5	9.79×10^6	6.60×10^4
70	1.75×10^6	1.05×10^5	1.03×10^7	4.71×10^4
80	2.75×10^6	9.40×10^4	1.08×10^7	3.34×10^4
90	2.89×10^6	6.30×10^4	1.13×10^7	2.36×10^4
100	2.44×10^6	3.87×10^4	1.18×10^7	1.66×10^4

Table S6. FC rate constants (ISC/rISC, s^{-1} , 300 K) between low-lying singlet and triplet states of **DPACoOB**, conformer **II** for 0–0 singlet–triplet energy gaps (meV) ranging between 20 meV and 100 meV.

ΔE_{0-0}	$S_{CT \rightarrow T_{CT}}$	$S_{CT \leftarrow T_{CT}}$	$S_{CT \rightarrow T_{LE(A)}}$	$S_{CT \leftarrow T_{LE(A)}}$
20	1.13×10^6	4.30×10^5	6.29×10^6	1.26×10^5
30	4.79×10^5	1.29×10^5	6.70×10^6	9.13×10^4
40	2.19×10^5	4.08×10^4	7.09×10^6	6.53×10^4
50	1.21×10^5	1.52×10^4	7.46×10^6	4.65×10^4
60	7.93×10^4	6.73×10^3	7.81×10^6	3.28×10^4
70	5.94×10^4	3.48×10^3	8.13×10^6	2.30×10^4
80	4.53×10^4	1.91×10^3	8.42×10^6	1.61×10^4
90	3.16×10^4	9.30×10^2	8.69×10^6	1.12×10^4
100	2.35×10^4	4.69×10^2	8.94×10^6	7.71×10^3

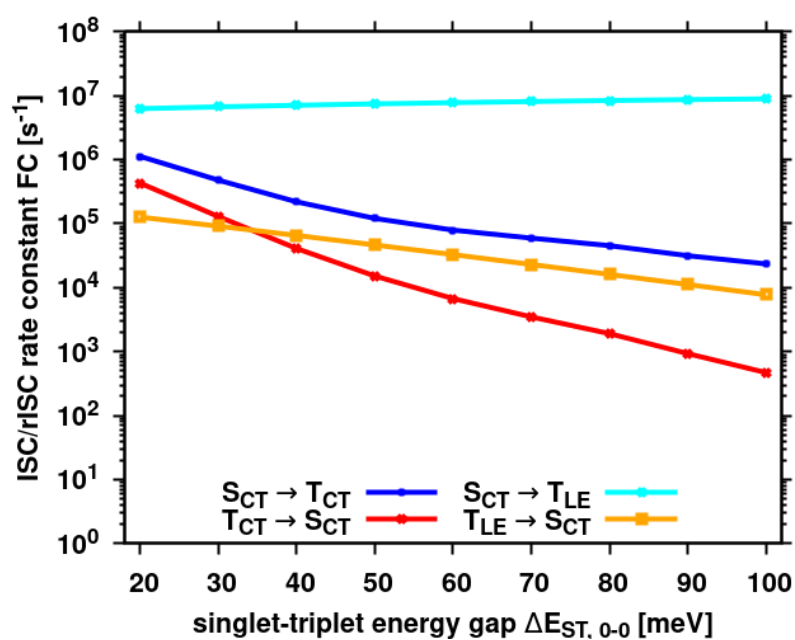


Figure S3. Computed rate constants for ISC and rISC between low-lying singlet and triplet states of DPACoOB (conformer II) in Franck–Condon approximation at 300 K with varying singlet–triplet energy gap. Note the logarithmic scale of the rate constants.

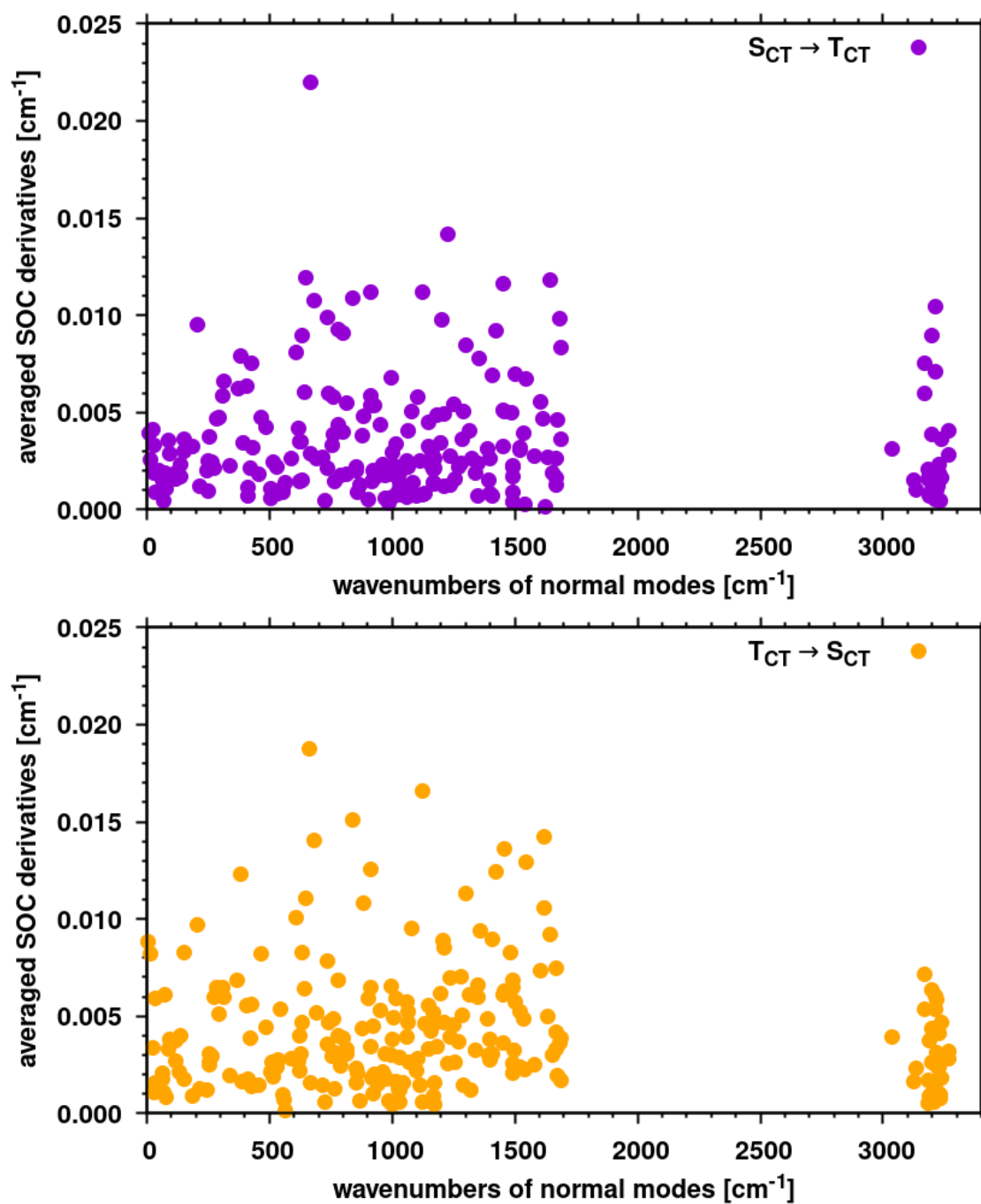


Figure S4. Component-averaged SOC derivatives for all vibrational normal modes of DPACoOB calculated for the S_{CT} → T_{CT} ISC process (purple) and the S_{CT} ← T_{CT} rISC process (orange) using a HT-like approach.

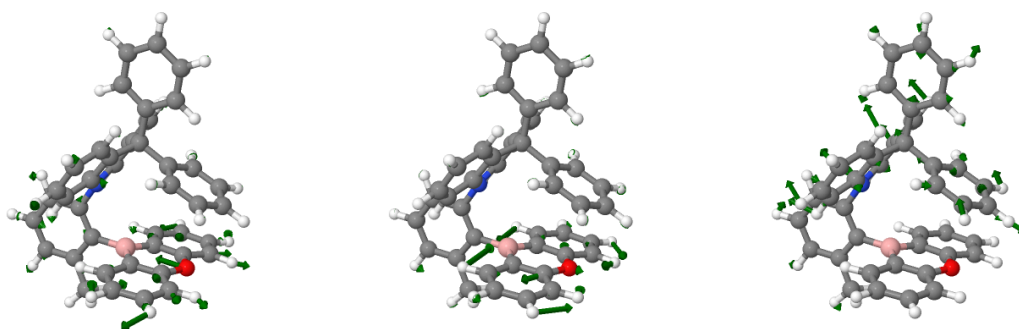


Figure S5. Displacement vectors of normal modes 66 (left), 147 (middle) and 65 (right) for which the highest component-averaged SOC gradients of the $S_{CT} \rightarrow T_{CT}$ ISC process are found.

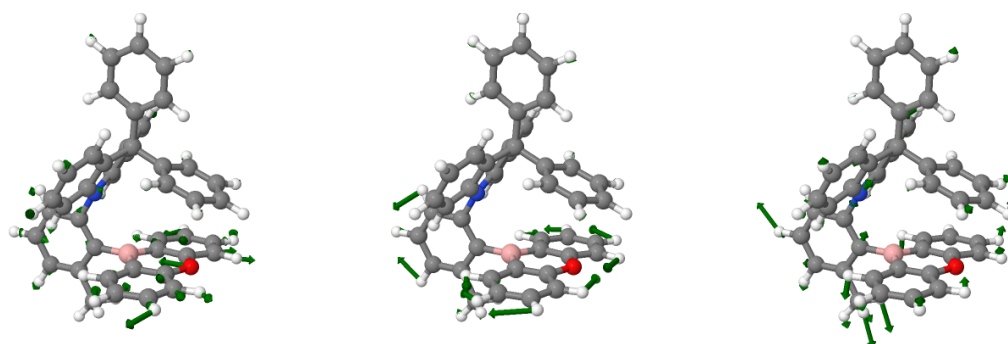


Figure S6. Displacement vectors of normal modes 66 (left), 130 (middle) and 86 (right) for which the highest component-averaged SOC gradients of the $S_{CT} \leftarrow T_{CT}$ rISC process are found.

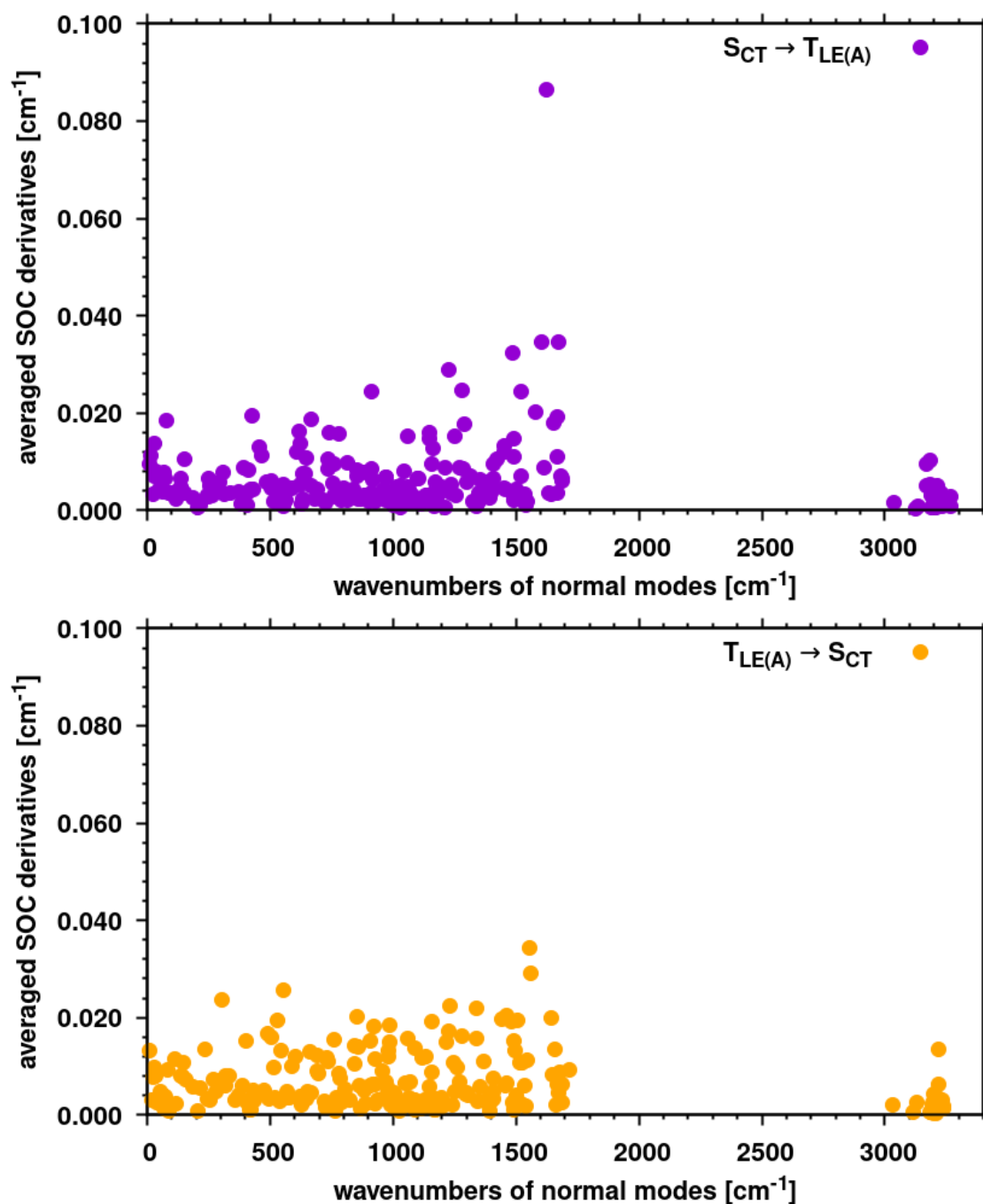


Figure S7. Component-averaged SOC derivatives for all vibrational normal modes of **DPACoOB** calculated for the $S_{CT} \rightarrow T_{LE(A)}$ ISC process (purple) and the $T_{LE(A)} \leftarrow S_{CT}$ rISC process (orange) using a HT-like approach.

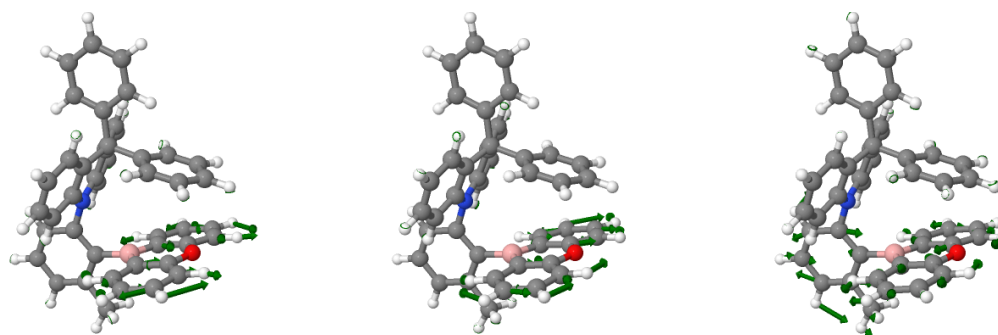


Figure S8. Displacement vectors of normal modes 189 (left), 187 (middle) and 196 (right) for which the highest component-averaged SOC gradients of the $S_{CT} \rightarrow T_{LE(A)}$ ISC process are found.

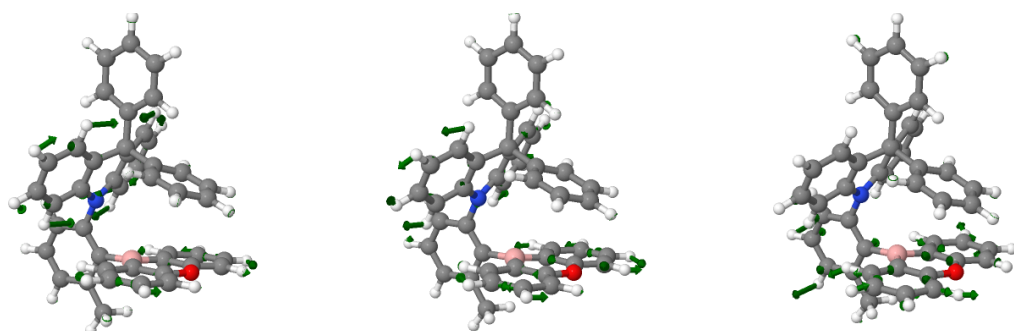


Figure S9. Displacement vectors of normal modes 187 (left), 188 (middle) and 54 (right) for which the highest component-averaged SOC gradients of the $S_{CT} \leftarrow T_{LE(A)}$ rISC process are found.

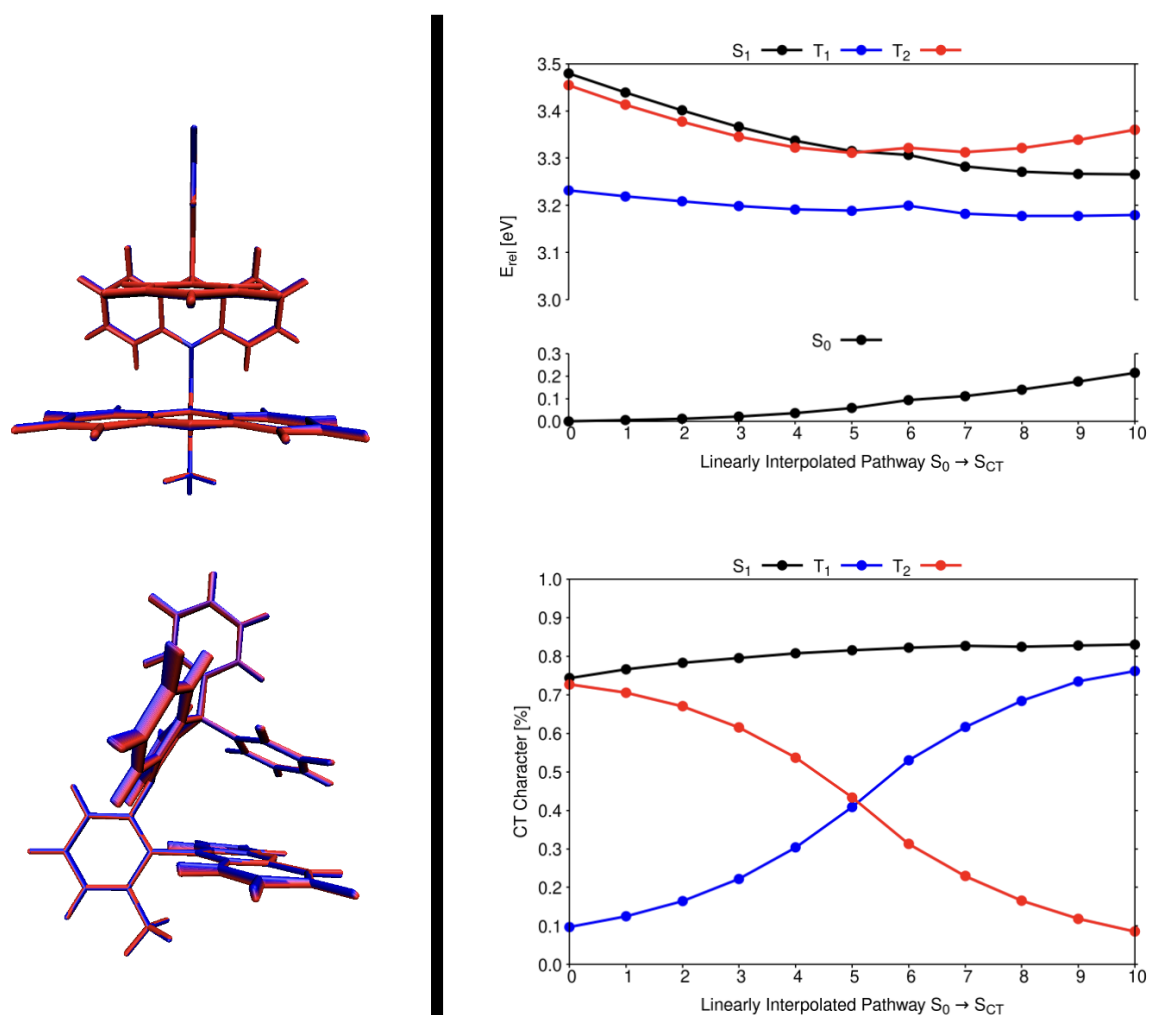


Figure S10. Linearly interpolated pathway between the optimized S_0 and S_{0CT} geometries (**conformer II**). Left panel: Overlays of structures connecting initial (blue) and final (red) geometries in front (top) and side (bottom) view. The structures are aligned on the phenyl bridge. Right panel: DFT/MRCI-R2016 vertical energies of the relevant excited states and respective dipole moments.

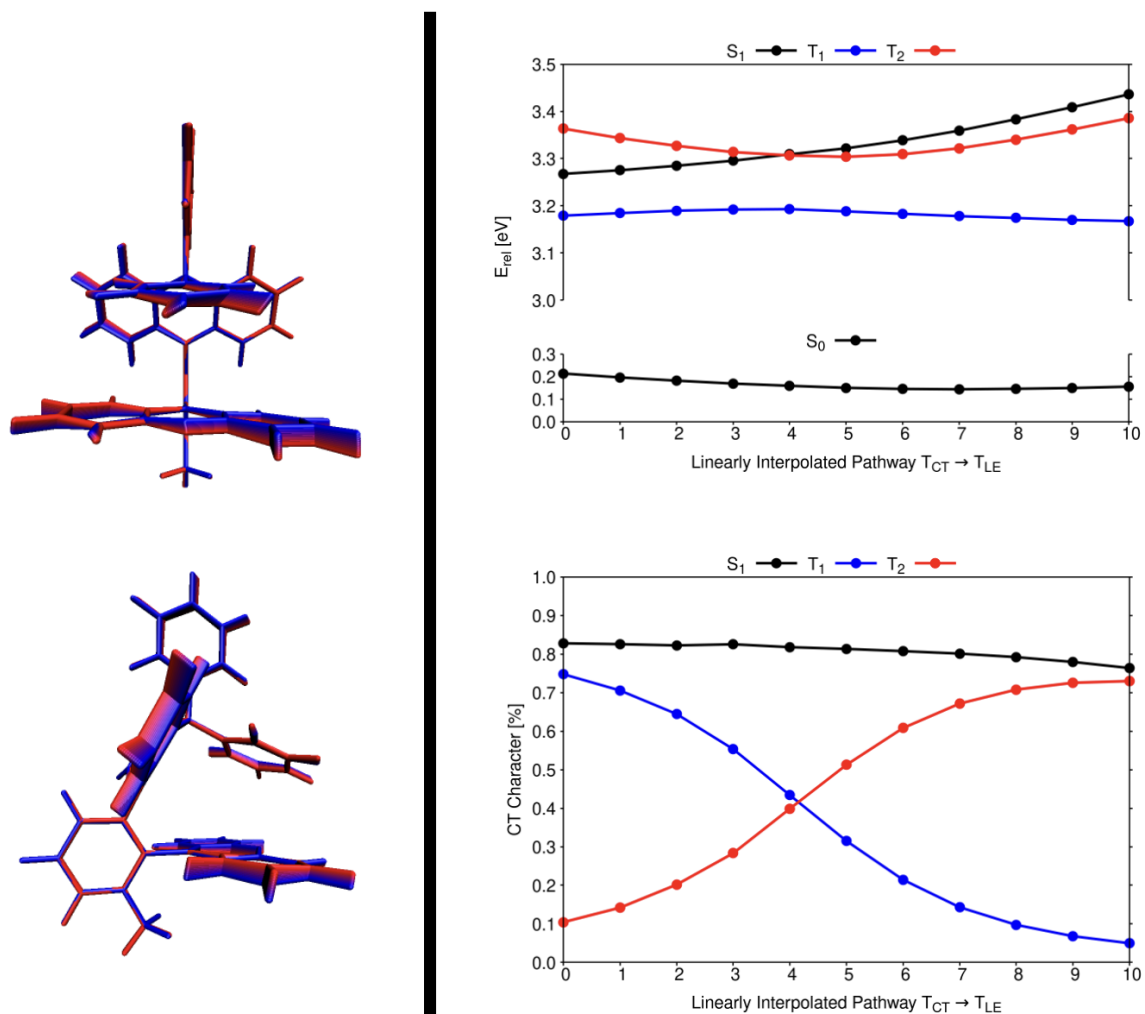


Figure S11. Linearly interpolated pathway between the optimized T_{CT} and $T_{LE(A)}$ geometries (**conformer II**). Left panel: Overlays of structures connecting initial (blue) and final (red) geometries in front (top) and side (bottom) view. The structures are aligned on the phenyl bridge. Right panel: DFT/MRCI-R2016 vertical energies of the relevant excited states and respective dipole moments.

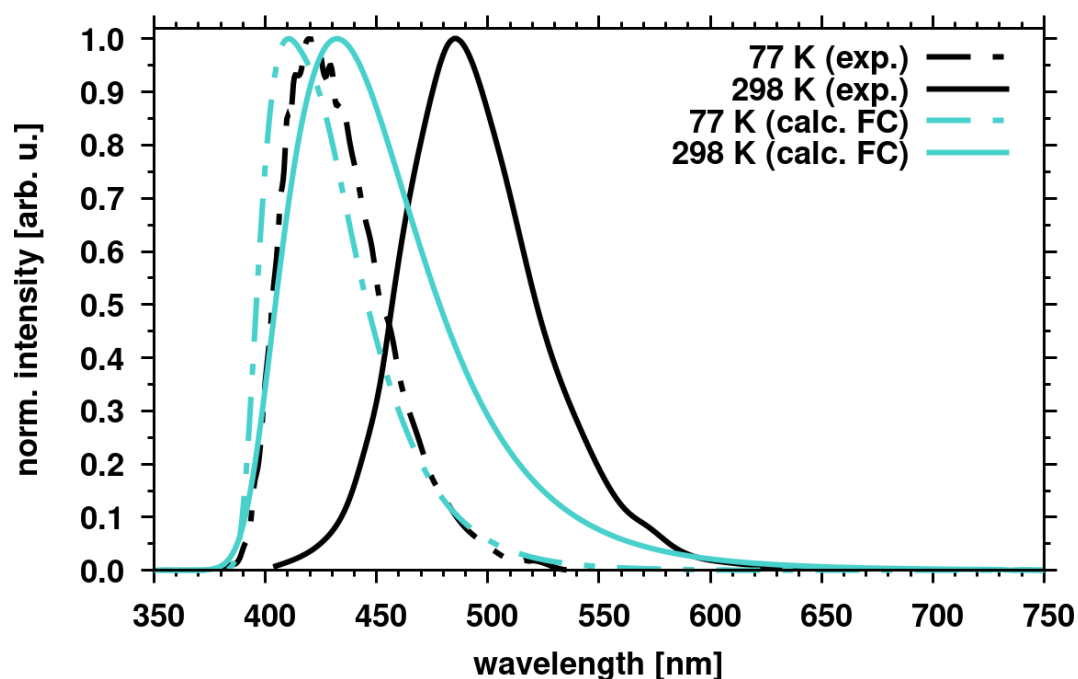


Figure S12. Calculated (turquoise) and experimental (black) emission spectra of **DPACoOB (conformer II)** in toluene at 77 K (dashed lines) and 298 K (solid lines). The theoretical spectra were determined in Franck–Condon approximation.

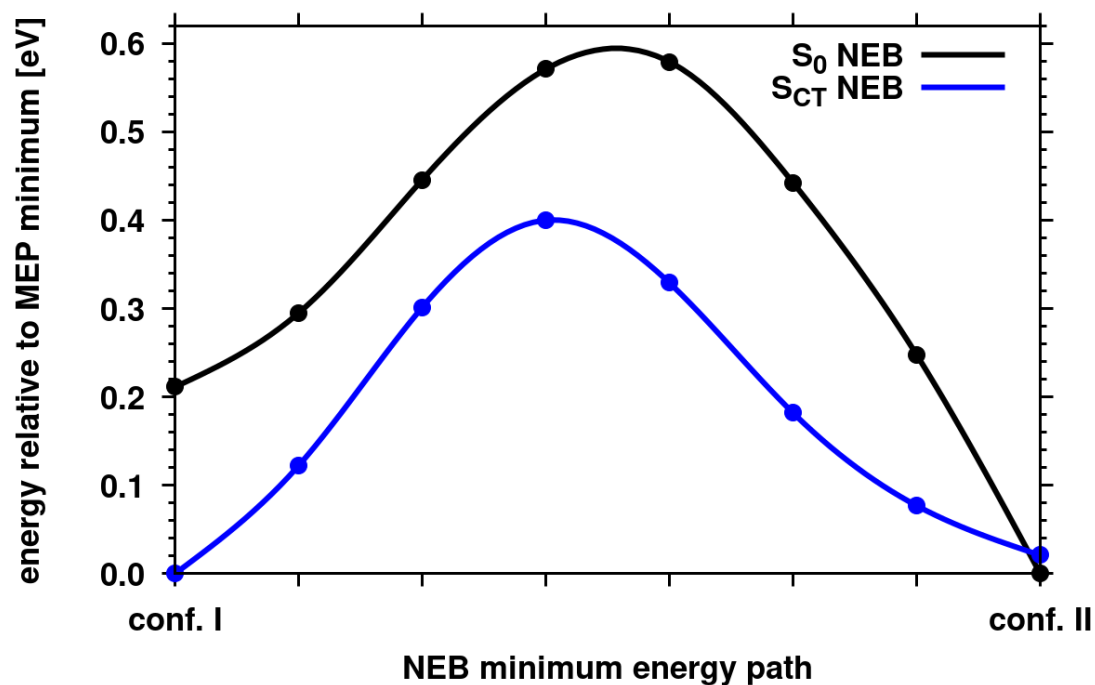


Figure S13. Minimum energy paths for the interconversion of **conformer I** and **conformer II** on the S_0 and S_{CT} PESs, determined by a nudged-elastic band approach.

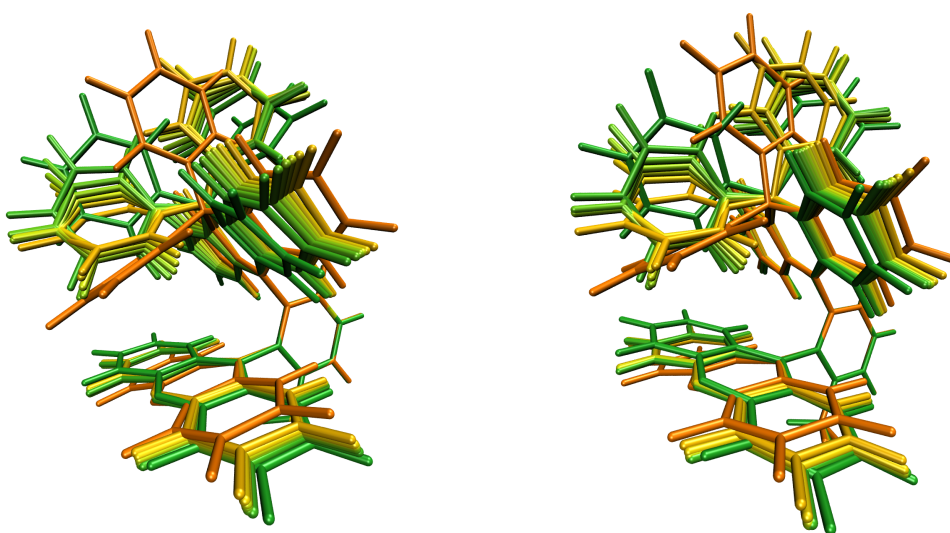


Figure S14. Overlay of the nuclear arrangements along the NEB minimum energy paths in the S₀ (left) and S_{CT} (right) states, respectively. The colors of the nuclear frames change gradually from green (**conformer I**) to orange (**conformer II**).

Hall: -P 1 #2
a=9.142Å
b=9.580Å
c=19.438Å
 $\alpha=78.874^\circ$
 $\beta=79.019^\circ$
 $\gamma=74.133^\circ$

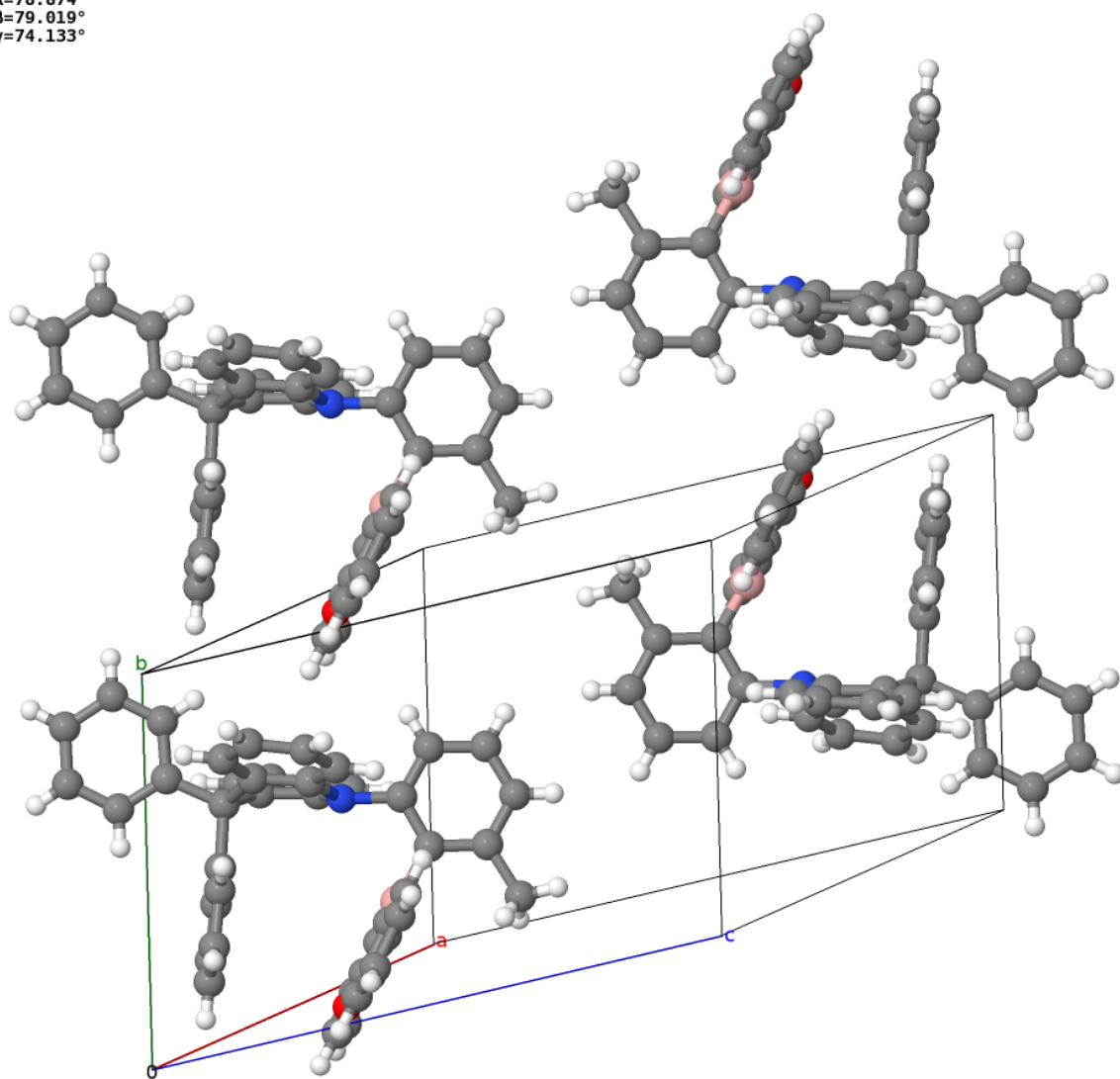


Figure S15. Dimerization of two emitter molecules, where the acceptor of the first stands perpendicular on the donor of the second. Cut from the crystal structure in 1 2 1 direction.

Table S7. DFT/MRCI excitation energies [eV] of low-lying singlet and triplet states of **DPACpSB** and **DPACoSB** in toluene at different molecular geometries. The energy of the respective ground-state minimum was chosen as offset. Due to a PES crossing between T_{CT} and $T_{LE(A)}$, the T_{CT} minimum could not be reached in the optimization procedure.

State	DPACpSB			DPACoSB		
	Optimized Geometry			Optimized Geometry		
	S_0	S_{CT}	$T_{LE(A)}$	S_0	S_{CT}	$T_{LE(A)}$
$S_{LE(A)}$	3.27	3.38	3.20	3.20	3.41	3.10
S_{CT}	3.58	3.36	3.55	3.46	3.04	3.39
$T_{LE(A)}$	2.89	3.03	2.82	2.84	3.07	2.75
T_{CT}	3.52	3.31	3.48	3.37	2.96	3.30

Table S8. *xyz*-coordinates [Å] of the S_0 geometry of DPACoOB, conformer II at PBE0/def2-SV(P) level of theory.

Atom type	x	y	z
H	4.739885	-0.646625	-0.343000
C	4.164278	-0.412222	-1.239576
C	4.603871	-0.872703	-2.475885
H	5.515270	-1.476335	-2.528404
C	3.899747	-0.553780	-3.635040
H	4.242224	-0.903285	-4.613113
C	2.740306	0.211488	-3.530356
H	2.171876	0.450120	-4.433016
C	2.263068	0.666649	-2.297696
C	3.000132	0.368664	-1.133496
H	2.350942	2.618161	2.126885
C	1.760863	2.874798	1.245905
C	1.785884	2.029975	0.122562
C	1.019323	2.369395	-1.010918
C	0.292449	3.563447	-0.997803
H	-0.295218	3.829142	-1.880361
C	0.277331	4.405200	0.112249
H	-0.309105	5.328167	0.095289
C	1.009600	4.044993	1.241479
H	1.011276	4.684923	2.129323
C	0.913840	1.370951	-2.162721
C	-0.174641	0.320843	-1.826020
C	-0.097616	-0.984563	-2.328374
H	0.776739	-1.293730	-2.960604
C	-1.119656	-1.906216	-2.101555
H	-1.028593	-2.919815	-2.503806
C	-2.242593	-1.544099	-1.359079
H	-3.041711	-2.268409	-1.173788
C	-2.326741	-0.252349	-0.841778
H	-3.193588	0.046429	-0.244420
C	-1.302596	0.666588	-1.070751
H	-1.386764	1.670719	-0.648341
C	0.569183	2.106657	-3.468521
C	1.446752	3.097748	-3.937890
H	2.352688	3.323034	-3.366900
C	1.184543	3.795350	-5.112505
H	1.885751	4.562768	-5.455263
C	0.030998	3.517941	-5.851630
H	-0.178010	4.065084	-6.776109
C	-0.847671	2.538612	-5.398346
H	-1.755541	2.309066	-5.964975
C	-0.579869	1.839325	-4.216470
H	-1.282935	1.074589	-3.878326
N	2.576123	0.871387	0.105384
C	3.335707	0.538698	1.278944
C	2.867243	-0.458622	2.143728
C	3.636736	-0.767065	3.292010
C	3.174856	-1.832180	4.250677
C	4.828568	-0.076930	3.530713
C	5.278475	0.914245	2.657458
H	6.213967	1.444144	2.860749
C	4.530746	1.223694	1.527823
H	4.862455	1.996258	0.828123
H	3.074600	-2.810663	3.747264
H	2.184225	-1.589315	4.675601
H	3.881712	-1.953143	5.087827
H	5.417549	-0.321485	4.421013
B	1.515058	-1.237933	1.873666
C	1.460727	-2.573328	1.108741
C	0.224160	-3.239358	1.007080
C	0.093011	-4.462794	0.334829
H	-0.889887	-4.937776	0.284851
C	1.212142	-5.038367	-0.245031
H	1.114883	-5.993906	-0.770031
C	2.464989	-4.408657	-0.160579
H	3.342893	-4.871292	-0.620297
C	2.575378	-3.200315	0.507095
H	3.548292	-2.704694	0.577283
C	0.165887	-0.791474	2.467077
C	-0.025376	0.379074	3.235654
H	0.839211	1.023640	3.420632
C	-1.263879	0.723806	3.750732
H	-1.385616	1.637026	4.349047
C	-2.368154	-0.110075	3.508747
H	-3.351063	0.153656	3.911839
C	-2.225997	-1.270636	2.765203
H	-3.070637	-1.935756	2.569177
C	-0.964120	-1.603913	2.252768
O	-0.913181	-2.758768	1.554470

Table S9. *xyz*-coordinates [Å] of the S_{CT} geometry of DPACoOB, conformer II at PBE0/def2-SV(P) level of theory.

Atom type	X	Y	Z
H	4.684126	-0.701376	-0.308800
C	4.116940	-0.484600	-1.212794
C	4.516763	-1.003178	-2.428963
H	5.400262	-1.644110	-2.479401
C	3.796267	-0.696247	-3.587833
H	4.115991	-1.090122	-4.556067
C	2.656829	0.106640	-3.510241
H	2.088532	0.324055	-4.417253
C	2.214198	0.626435	-2.298094
C	2.980866	0.356074	-1.133728
H	2.298255	2.543635	2.152377
C	1.697727	2.811440	1.284305
C	1.767628	2.010842	0.119008
C	0.968819	2.329354	-1.011167
C	0.190172	3.481020	-0.960515
H	-0.412296	3.750206	-1.830860
C	0.149922	4.285521	0.179788
H	-0.473881	5.183140	0.187401
C	0.895693	3.935701	1.310122
H	0.855786	4.550988	2.212184
C	0.891779	1.366301	-2.183958
C	-0.220629	0.317815	-1.871762
C	-0.146218	-0.985225	-2.381057
H	0.729469	-1.313471	-2.943535
C	-1.178031	-1.898199	-2.171128
H	-1.082399	-2.913138	-2.566510
C	-2.305164	-1.531396	-1.440122
H	-3.104429	-2.254765	-1.256102
C	-2.387827	-0.242412	-0.919499
H	-3.252644	0.057692	-0.321422
C	-1.355631	0.670031	-1.129705
H	-1.447179	1.665359	-0.691704
C	0.595111	2.131112	-3.483633
C	1.501395	3.115027	-3.908716
H	2.396584	3.319803	-3.312240
C	1.280244	3.835939	-5.077991
H	2.000428	4.598395	-5.390081
C	0.142338	3.586265	-5.849717
H	-0.034528	4.151370	-6.769766
C	-0.763281	2.612809	-5.437552
H	-1.658360	2.407102	-6.032235
C	-0.538602	1.889566	-4.261802
H	-1.259157	1.128980	-3.952205
N	2.665285	0.965505	0.062585
C	3.401998	0.600566	1.259065
C	2.900517	-0.401083	2.104786
C	3.691540	-0.687115	3.249878
C	3.237326	-1.746717	4.215201
C	4.884411	0.003857	3.487812
C	5.340888	0.993094	2.617004
H	6.275920	1.524068	2.817941
C	4.592647	1.297625	1.487574
H	4.921335	2.068149	0.783659
H	3.124810	-2.719393	3.705443
H	2.246122	-1.498396	4.633051
H	3.950836	-1.865328	5.047930
H	5.472356	-0.239157	4.379217
B	1.537873	-1.206208	1.861240
C	1.506806	-2.536171	1.108853
C	0.254607	-3.187816	0.952140
C	0.116799	-4.402546	0.289557
H	-0.881730	-4.841670	0.208424
C	1.243694	-5.043042	-0.248886
H	1.133853	-6.000273	-0.767401
C	2.499432	-4.448763	-0.099604
H	3.390702	-4.943334	-0.501085
C	2.621368	-3.230778	0.564574
H	3.616198	-2.787566	0.683924
C	0.214062	-0.757849	2.479430
C	0.009929	0.361951	3.331217
H	0.875917	0.982815	3.586539
C	-1.236743	0.691448	3.857247
H	-1.340667	1.566127	4.508616
C	-2.353174	-0.094078	3.559088
H	-3.338244	0.153354	3.965970
C	-2.195613	-1.220607	2.736813
H	-3.040634	-1.870491	2.491776
C	-0.943954	-1.538742	2.221498
O	-0.900677	-2.657937	1.444549

Table S10. xyz -coordinates [\AA] of the T_{CT} geometry of DPA-CoOB, conformer II at PBE0/def2-SV(P) level of theory.

Atom type	x	y	z
H	4.676103	-0.719754	-0.304056
C	4.105867	-0.503899	-1.206240
C	4.503950	-1.020588	-2.424302
H	5.388080	-1.660439	-2.477337
C	3.780830	-0.712858	-3.580635
H	4.098989	-1.104600	-4.550269
C	2.640432	0.088419	-3.499275
H	2.070693	0.307465	-4.404996
C	2.199280	0.605766	-2.285460
C	2.969230	0.335241	-1.123805
H	2.294275	2.522632	2.164377
C	1.687917	2.787652	1.299644
C	1.754842	1.987354	0.134308
C	0.952135	2.304204	-0.992956
C	0.170624	3.453830	-0.938751
H	-0.434223	3.722864	-1.807474
C	0.132005	4.257813	0.202098
H	-0.493940	5.153929	0.211851
C	0.882754	3.910113	1.329002
H	0.845121	4.525141	2.231296
C	0.877105	1.346128	-2.170065
C	-0.238963	0.298574	-1.869141
C	-0.165680	-1.001535	-2.386047
H	0.713630	-1.330082	-2.942622
C	-1.203625	-1.911110	-2.192152
H	-1.109051	-2.923526	-2.594228
C	-2.336048	-1.544021	-1.469581
H	-3.141067	-2.264408	-1.299286
C	-2.417088	-0.258575	-0.940022
H	-3.286050	0.041384	-0.347865
C	-1.378862	0.650515	-1.134377
H	-1.469929	1.643138	-0.690184
C	0.586530	2.118879	-3.466906
C	1.495343	3.104727	-3.882089
H	2.387740	3.305764	-3.280201
C	1.280298	3.832418	-5.048286
H	2.002392	4.596282	-5.352426
C	0.146124	3.587689	-5.827080
H	-0.025961	4.158110	-6.744752
C	-0.761880	2.612326	-5.424884
H	-1.654107	2.410406	-6.025129
C	-0.543387	1.882360	-4.252089
H	-1.265934	1.120457	-3.950513
N	2.657200	0.944813	0.074399
C	3.413175	0.595844	1.264601
C	2.922296	-0.399691	2.120096
C	3.719878	-0.677990	3.261362
C	3.271754	-1.732360	4.234914
C	4.912712	0.017935	3.485062
C	5.359742	1.002531	2.603501
H	6.294822	1.537237	2.794170
C	4.603067	1.298699	1.477033
H	4.924619	2.065728	0.766123
H	3.159252	-2.708437	3.731566
H	2.281410	-1.483228	4.654366
H	3.988056	-1.844725	5.066061
H	5.508338	-0.216899	4.373588
B	1.557264	-1.196274	1.867979
C	1.523211	-2.521080	1.106954
C	0.266715	-3.158941	0.930208
C	0.125287	-4.366502	0.255239
H	-0.876169	-4.795377	0.157855
C	1.252491	-5.012535	-0.276159
H	1.139751	-5.964173	-0.804275
C	2.511716	-4.431635	-0.107541
H	3.402867	-4.931288	-0.502930
C	2.637687	-3.220792	0.569783
H	3.635536	-2.790157	0.708258
C	0.231572	-0.740351	2.475987
C	0.028931	0.375840	3.332508
H	0.898991	0.982219	3.607880
C	-1.221925	0.716672	3.842464
H	-1.325147	1.587055	4.498506
C	-2.342500	-0.054108	3.523550
H	-3.330326	0.201845	3.918277
C	-2.186144	-1.177760	2.696843
H	-3.035144	-1.816095	2.435945
C	-0.931005	-1.507016	2.197036
O	-0.888817	-2.622214	1.414346

Table S11. xyz -coordinates [\AA] of the $T_{LE(A)}$ geometry of DPA-CoOB, conformer II at PBE0/def2-SV(P) level of theory.

Atom type	X	Y	Z
H	4.827689	-0.607793	-0.350450
C	4.259137	-0.381148	-1.253420
C	4.714989	-0.835224	-2.484404
H	5.636186	-1.424348	-2.529944
C	4.015298	-0.526843	-3.650844
H	4.373799	-0.868026	-4.626054
C	2.841158	0.216751	-3.556228
H	2.277082	0.445919	-4.464174
C	2.343844	0.662271	-2.328096
C	3.081308	0.384022	-1.156847
H	2.308239	2.570021	2.116390
C	1.713801	2.814290	1.235091
C	1.794674	1.990275	0.096682
C	1.021535	2.308225	-1.040322
C	0.233609	3.462280	-1.015476
H	-0.358619	3.711876	-1.899696
C	0.162956	4.281830	0.108878
H	-0.470659	5.173169	0.101003
C	0.902344	3.941215	1.241552
H	0.860404	4.565888	2.139127
C	0.973286	1.326687	-2.208658
C	-0.087970	0.234627	-1.913057
C	0.004043	-1.033097	-2.503195
H	0.868314	-1.282872	-3.123056
C	-0.989750	-1.991924	-2.312634
H	-0.888047	-2.973568	-2.785545
C	-2.099086	-1.707733	-1.516576
H	-2.877564	-2.461165	-1.361097
C	-2.196268	-0.456709	-0.909931
H	-3.052347	-0.219039	-0.270596
C	-1.200332	0.500935	-1.104936
H	-1.295714	1.471355	-0.612688
C	0.630476	2.077570	-3.506407
C	1.499644	3.086921	-3.951361
H	2.400918	3.309710	-3.372001
C	1.234515	3.806070	-5.112242
H	1.929290	4.587149	-5.436679
C	0.085853	3.533200	-5.860569
H	-0.125483	4.097332	-6.774225
C	-0.785582	2.537278	-5.429998
H	-1.690207	2.312106	-6.003508
C	-0.514663	1.815878	-4.262239
H	-1.212480	1.039116	-3.940994
N	2.655457	0.892155	0.071398
C	3.375318	0.549122	1.267205
C	2.853969	-0.410224	2.151002
C	3.609161	-0.695101	3.318293
C	3.113539	-1.717557	4.306085
C	4.816626	-0.031492	3.566656
C	5.306198	0.922847	2.664726
H	6.250954	1.436589	2.867265
C	4.581201	1.215741	1.516577
H	4.939287	1.961884	0.801005
H	2.942736	-2.693798	3.818709
H	2.147480	-1.412633	4.746996
H	3.833831	-1.863716	5.128462
H	5.386567	-0.267195	4.461901
B	1.474179	-1.164512	1.910104
C	1.360560	-2.456906	1.089353
C	0.106084	-3.117411	1.029789
C	-0.120724	-4.313930	0.328527
H	-1.124126	-4.746637	0.348645
C	0.937439	-4.921568	-0.369521
H	0.776268	-5.851764	-0.919309
C	2.184816	-4.310559	-0.334512
H	3.027156	-4.763666	-0.867187
C	2.393446	-3.107512	0.380373
H	3.390546	-2.658759	0.376741
C	0.172973	-0.734175	2.607060
C	-0.006957	0.382424	3.452146
H	0.849786	1.034149	3.647377
C	-1.248838	0.692353	4.040788
H	-1.328192	1.574152	4.684873
C	-2.372246	-0.100381	3.815783
H	-3.335316	0.141948	4.271314
C	-2.239416	-1.228298	2.992322
H	-3.079343	-1.897374	2.788053
C	-0.993960	-1.520205	2.419279
O	-0.978430	-2.638591	1.663799

Table S12. *xyz*-coordinates [Å] of the S_0 geometry of DPACoOB, conformer II at PBE0+GD3BJ/def2-SV(P) level of theory.

Atom type	x	y	z
H	4.826818	-0.599681	-0.320068
C	4.232770	-0.387651	-1.210207
C	4.647730	-0.867719	-2.447512
H	5.561582	-1.466318	-2.509484
C	3.916772	-0.574564	-3.597207
H	4.241229	-0.940817	-4.575030
C	2.754570	0.185421	-3.483931
H	2.162823	0.403644	-4.376522
C	2.301916	0.654945	-2.249068
C	3.063801	0.382577	-1.097480
H	2.442252	2.654557	2.147943
C	1.826286	2.891458	1.279209
C	1.845580	2.040604	0.162052
C	1.052432	2.352119	-0.957983
C	0.295559	3.525615	-0.942987
H	-0.315569	3.766430	-1.816496
C	0.278788	4.372123	0.163491
H	-0.332953	5.278325	0.153418
C	1.042682	4.040113	1.280747
H	1.043402	4.686718	2.163465
C	0.945924	1.332311	-2.086055
C	-0.104625	0.266308	-1.703407
C	-0.014248	-1.039364	-2.199312
H	0.860583	-1.340705	-2.779656
C	-1.028668	-1.966528	-1.966920
H	-0.931779	-2.980355	-2.365372
C	-2.151404	-1.609085	-1.222317
H	-2.944099	-2.338592	-1.031833
C	-2.240196	-0.319598	-0.700970
H	-3.103652	-0.027932	-0.096453
C	-1.224005	0.605490	-0.934928
H	-1.309002	1.608959	-0.512090
C	0.546577	2.031633	-3.390716
C	1.386822	3.034517	-3.897963
H	2.300377	3.289806	-3.352659
C	1.075937	3.703747	-5.076491
H	1.747300	4.482131	-5.451927
C	-0.089600	3.383236	-5.778340
H	-0.337235	3.908031	-6.706009
C	-0.930965	2.390550	-5.285224
H	-1.847019	2.128598	-5.823483
C	-0.614451	1.719722	-4.099585
H	-1.286327	0.943346	-3.727172
N	2.652107	0.897602	0.136615
C	3.386880	0.543544	1.313899
C	2.870528	-0.455069	2.142240
C	3.591870	-0.808914	3.304540
C	3.063457	-1.880898	4.217055
C	4.792642	-0.154398	3.591342
C	5.292503	0.842571	2.751446
H	6.234412	1.343300	2.994007
C	4.588438	1.195825	1.606048
H	4.957825	1.973084	0.931346
H	2.947412	-2.839658	3.680314
C	2.066120	-1.613448	4.610221
H	3.734588	-2.049063	5.074920
H	5.349355	-0.431107	4.492663
B	1.511182	-1.178962	1.800042
C	1.446784	-2.485358	0.996159
C	0.211815	-3.151967	0.899496
C	0.073086	-4.353329	0.192409
H	-0.907511	-4.833080	0.148703
C	1.179391	-4.893150	-0.443848
H	1.074273	-5.827003	-1.004739
C	2.428338	-4.254298	-0.374083
H	3.294971	-4.687380	-0.880988
C	2.550150	-3.076698	0.343949
H	3.519780	-2.575896	0.411093
C	0.159714	-0.704876	2.353572
C	-0.033037	0.496808	3.068591
H	0.834984	1.137216	3.246909
C	-1.280552	0.877828	3.533011
H	-1.407623	1.819291	4.074390
C	-2.385794	0.041457	3.305506
H	-3.375096	0.331964	3.672430
C	-2.238217	-1.153765	2.619960
H	-3.084877	-1.818114	2.431503
C	-0.971173	-1.514695	2.143674
O	-0.915789	-2.689612	1.480787

Table S13. *xyz*-coordinates [Å] of the S_0 geometry of DPACoOB, conformer II at LC- ω HPBE/def2-SV(P) level of theory.

Atom type	X	Y	Z
H	4.755761	-0.655258	-0.341096
C	4.176136	-0.419791	-1.243509
C	4.617170	-0.883393	-2.486185
H	5.534073	-1.491693	-2.539494
C	3.908456	-0.563077	-3.650704
H	4.252378	-0.915683	-4.635213
C	2.743581	0.206602	-3.545819
H	2.171241	0.446907	-4.454328
C	2.264664	0.665498	-2.306719
C	3.005856	0.364910	-1.137009
H	2.354229	2.626620	2.142723
C	1.759773	2.885194	1.256397
C	1.784453	2.036377	0.126977
C	1.014810	2.377555	-1.012892
C	0.283141	3.577424	-0.998789
H	-0.308189	3.845236	-1.887220
C	0.267742	4.422506	0.117461
H	-0.323208	5.351130	0.100812
C	1.003984	4.060981	1.252479
H	1.004913	4.704804	2.146387
C	0.910102	1.375733	-2.171702
C	-0.188800	0.322583	-1.839836
C	-0.114421	-0.987955	-2.349017
H	0.767380	-1.300383	-2.927385
C	-1.147453	-1.910299	-2.130607
H	-1.058693	-2.929300	-2.539380
C	-2.278847	-1.543622	-1.389796
H	-3.088347	-2.269163	-1.211767
C	-2.360764	-0.246559	-0.866213
H	-3.236181	0.056550	-0.270277
C	-1.325668	0.672993	-1.086852
H	-1.408608	1.683302	-0.660166
C	0.569003	2.118695	-3.484086
C	1.454379	3.114684	-3.949386
H	2.363920	3.338479	-3.369599
C	1.197300	3.819458	-5.129594
H	1.905759	4.591824	-5.469336
C	0.041315	3.543853	-5.878337
H	-0.164086	4.097010	-6.808578
C	-0.845399	2.559295	-5.429244
H	-1.756764	2.330863	-6.004609
C	-0.582945	1.853360	-4.242072
H	-1.293372	1.083704	-3.907157
N	2.578859	0.869878	0.110003
C	3.345839	0.537034	1.290512
C	2.875883	-0.465332	2.161043
C	3.651259	-0.773414	3.314036
C	3.187389	-1.843545	4.277992
C	4.849456	-0.078973	3.551991
C	5.300238	0.916552	2.673141
H	6.241966	1.450289	2.876228
C	4.546986	1.226500	1.538246
H	4.879455	2.003429	0.832624
H	3.085056	-2.827723	3.770840
C	2.190387	-1.508664	4.704955
H	3.898000	-1.966867	5.120936
H	5.443044	-0.324880	4.447758
B	1.519960	-1.247725	1.891315
C	1.467037	-2.586082	1.121987
C	0.224258	-3.253012	1.008000
C	0.092658	-4.481195	0.328624
H	-0.898340	-4.954737	0.269810
C	1.220284	-5.062631	-0.245354
H	1.124053	-6.023113	-0.776539
C	2.480425	-4.433852	-0.147304
H	3.366760	-4.902127	-0.602311
C	2.590094	-3.220514	0.526165
H	3.570749	-2.725673	0.607066
C	0.166696	-0.797906	2.485079
C	-0.023332	0.373685	3.266099
H	0.849593	1.016630	3.460439
C	-1.268204	0.721784	3.782725
H	-1.387797	1.637021	4.382653
C	-2.381901	-0.108284	3.530440
H	-3.371081	0.159443	3.935108
C	-2.242165	-1.269960	2.775419
H	-3.093972	-1.934901	2.570270
C	-0.972896	-1.606655	2.262638
O	-0.928818	-2.768554	1.550760

Table S14. *xyz*-coordinates [Å] of the S_0 geometry of DPACoOB, conformer II at ω B97X-D/def2-SV(P) level of theory.

Atom type	x	y	z
H	4.849726	-0.582981	-0.340630
C	4.248986	-0.370852	-1.225704
C	4.664480	-0.850134	-2.465550
H	5.581805	-1.442493	-2.529708
C	3.926277	-0.562455	-3.614213
H	4.249115	-0.927123	-4.592836
C	2.757556	0.190257	-3.496890
H	2.163809	0.397551	-4.390244
C	2.303823	0.660258	-2.259120
C	3.073449	0.393619	-1.108448
H	2.460294	2.687371	2.140225
C	1.843451	2.917863	1.270937
C	1.854272	2.058933	0.156408
C	1.052878	2.366089	-0.961996
C	0.297444	3.544215	-0.946137
H	-0.323571	3.785426	-1.811958
C	0.290585	4.398544	0.156718
H	-0.319344	5.305585	0.145281
C	1.062237	4.070769	1.272180
H	1.070696	4.721652	2.151252
C	0.940918	1.339696	-2.093604
C	-0.115671	0.268391	-1.705488
C	-0.028352	-1.041307	-2.199552
H	0.842197	-1.348927	-2.782121
C	-1.046411	-1.968326	-1.967887
H	-0.952134	-2.980875	-2.369447
C	-2.171527	-1.608755	-1.224083
H	-2.966955	-2.335490	-1.037138
C	-2.258265	-0.316690	-0.703246
H	-3.123584	-0.021500	-0.103688
C	-1.238418	0.608059	-0.936809
H	-1.330342	1.611032	-0.515597
C	0.538968	2.043458	-3.406081
C	1.379955	3.048452	-3.916856
H	2.295220	3.306840	-3.376074
C	1.068312	3.719386	-5.097014
H	1.740098	4.497179	-5.471908
C	-0.099575	3.399546	-5.800016
H	-0.347460	3.924634	-6.727040
C	-0.941748	2.405286	-5.305338
H	-1.858031	2.143233	-5.842484
C	-0.624239	1.733071	-4.117576
H	-1.300324	0.958331	-3.750540
N	2.660942	0.908697	0.132050
C	3.394771	0.548188	1.314399
C	2.874941	-0.454115	2.141006
C	3.595941	-0.811929	3.306300
C	3.065812	-1.890260	4.223082
C	4.799130	-0.158186	3.597140
C	5.302236	0.841749	2.758733
H	6.243974	1.340906	3.003579
C	4.599189	1.198662	1.611659
H	4.972257	1.977138	0.940773
H	2.954712	-2.850067	3.687775
H	2.069066	-1.623957	4.617663
H	3.735989	-2.057388	5.081755
H	5.356308	-0.434999	4.497846
B	1.510625	-1.180903	1.794766
C	1.448066	-2.497737	0.995644
C	0.216697	-3.177566	0.918162
C	0.081567	-4.391513	0.225827
H	-0.893594	-4.882562	0.196444
C	1.188465	-4.931473	-0.413888
H	1.086491	-5.873318	-0.961069
C	2.434807	-4.280811	-0.362006
H	3.301102	-4.714119	-0.868500
C	2.552726	-3.091041	0.340880
H	3.520938	-2.586143	0.395520
C	0.153193	-0.711151	2.354739
C	-0.045687	0.494138	3.067922
H	0.816009	1.145473	3.236757
C	-1.293374	0.863959	3.547583
H	-1.423629	1.805795	4.086779
C	-2.393611	0.012382	3.338581
H	-3.380898	0.292829	3.717420
C	-2.240464	-1.186560	2.656508
H	-3.082882	-1.860365	2.485476
C	-0.972756	-1.536083	2.164490
O	-0.912003	-2.720605	1.510881

Table S15. *xyz*-coordinates [Å] of the S_0 geometry of DPACoOB, conformer I at PBE0/def2-SV(P) level of theory.

Atom type	X	Y	Z
H	1.593736	2.013890	1.922507
C	0.855628	1.927311	1.124681
C	-0.359139	2.591499	1.237984
H	-0.560231	3.186571	2.133920
C	-1.313224	2.483629	0.227822
H	-2.280690	2.986243	0.312859
C	-1.001801	1.747364	-0.912111
H	-1.722885	1.698280	-1.732488
C	0.224381	1.093143	-1.063914
C	1.148641	1.135237	0.000118
H	4.432228	-1.234447	-0.262296
C	3.722796	-1.311870	-1.087132
C	2.595697	-0.466996	-1.116118
C	1.711359	-0.550716	-2.211690
C	1.923563	-1.551268	-3.166471
H	1.202894	-1.655508	-3.982016
C	3.018431	-2.408669	-3.116694
H	3.158036	-3.171193	-3.888026
C	3.937010	-2.260334	-2.079401
H	4.823206	-2.900276	-2.024492
C	0.624282	0.505954	-2.414585
C	1.247898	1.625099	-3.293145
C	1.358871	2.947844	-2.850148
H	0.987651	3.224364	-1.861065
C	1.940352	3.934660	-3.651496
H	2.012891	4.959078	-3.272760
C	2.424006	3.620943	-4.918019
H	2.879567	4.392691	-5.546134
C	2.323191	2.305112	-5.374660
H	2.698906	2.036502	-6.367043
C	1.748761	1.324824	-4.570337
H	1.688239	0.303238	-4.952424
C	-0.620952	-0.115911	-3.067120
C	-1.175453	-1.268310	-2.487851
H	-0.686450	-1.719536	-1.618645
C	-2.333795	-1.844391	-3.000157
H	-2.743115	-2.744454	-2.530564
C	-2.973050	-1.276008	-4.105292
H	-3.883894	-1.727793	-4.510257
C	-2.440232	-0.126726	-4.682240
H	-2.932459	0.335486	-5.543714
C	-1.274306	0.448225	-4.166023
H	-0.877098	1.354655	-4.629315
N	2.341587	0.413746	-0.059135
C	3.209675	0.361651	1.083419
C	2.881508	-0.420593	2.210248
C	3.850390	-0.539526	3.236152
C	3.594125	-1.413947	4.436863
C	5.068128	0.142266	3.129016
C	5.346084	0.958529	2.034662
H	6.295500	1.499035	1.975592
C	4.414452	1.064627	1.007500
H	4.616963	1.671464	0.120746
H	3.195442	-2.400639	4.142534
H	2.854096	-0.962351	5.121463
H	4.520467	-1.581401	5.010511
H	5.812296	0.031377	3.924755
B	1.447370	-1.072915	2.415466
C	0.926051	-2.335680	1.706377
C	-0.412730	-2.723095	1.920209
C	-0.975663	-3.838867	1.284591
H	-2.021914	-4.087228	1.479330
C	-0.188482	-4.602299	0.436980
H	-0.622595	-5.476129	-0.059038
C	1.158397	-4.268586	0.221007
H	1.776637	-4.878347	-0.443430
C	1.693573	-3.156243	0.848518
H	2.740149	-2.893365	0.678794
C	0.445431	-0.458832	3.420908
C	0.720881	0.637670	4.270520
H	1.719407	1.086695	4.232184
C	-0.226743	1.155371	5.136331
H	0.017444	2.001741	5.784615
C	-1.512220	0.587843	5.173341
H	-2.270836	0.993092	5.850140
C	-1.828598	-0.485774	4.358631
H	-2.820022	-0.945230	4.370341
C	-0.849300	-1.004082	3.497419
O	-1.245329	-2.056390	2.748945

Table S16. xyz -coordinates [\AA] of the S_{CT} geometry of DPA-CoOB, conformer I at PBE0/def2-SV(P) level of theory.

Atom type	x	y	z
H	1.673129	1.888286	2.020264
C	0.999769	1.942668	1.167670
C	-0.122391	2.742024	1.222155
H	-0.335481	3.310505	2.130122
C	-0.987583	2.798403	0.123333
H	-1.886368	3.419348	0.159934
C	-0.700699	2.066682	-1.027441
H	-1.375457	2.131297	-1.883346
C	0.427095	1.256021	-1.118632
C	1.281882	1.175885	0.009666
H	4.497613	-1.240193	-0.149323
C	3.879398	-1.239972	-1.045490
C	2.734360	-0.405494	-1.102589
C	1.923873	-0.401380	-2.264326
C	2.253220	-1.281428	-3.294439
H	1.609260	-1.329540	-4.173699
C	3.370281	-2.107189	-3.228891
H	3.595012	-2.783868	-4.057298
C	4.198388	-2.068496	-2.100915
H	5.082222	-2.708101	-2.038764
C	0.750049	0.556017	-2.430041
C	1.235669	1.611065	-3.460532
C	1.783896	2.828776	-3.037711
H	1.806974	3.082495	-1.974947
C	2.304854	3.743742	-3.954061
H	2.725024	4.686688	-3.591652
C	2.285809	3.461751	-5.317424
H	2.688681	4.179701	-6.037837
C	1.744300	2.252315	-5.753901
H	1.716993	2.014991	-6.821644
C	1.231525	1.337551	-4.836827
H	0.807723	0.403287	-5.211830
C	-0.513512	-0.214298	-2.861019
C	-0.794413	-1.446163	-2.252790
H	-0.096920	-1.882379	-1.529541
C	-1.970010	-2.133759	-2.546106
H	-2.161379	-3.090705	-2.052344
C	-2.891272	-1.601817	-3.448739
H	-3.813785	-2.142825	-3.679966
C	-2.629987	-0.370415	-4.046214
H	-3.346845	0.064799	-4.749176
C	-1.452267	0.319480	-3.751633
H	-1.273022	1.287522	-4.226560
N	2.397406	0.366525	-0.003934
C	3.225164	0.274098	1.186012
C	2.785127	-0.486185	2.286998
C	3.708557	-0.584094	3.365002
C	3.378579	-1.435303	4.559888
C	4.934611	0.089618	3.320492
C	5.301290	0.874921	2.228134
H	6.257743	1.405246	2.217778
C	4.439194	0.962445	1.141288
H	4.702841	1.551418	0.257827
H	3.000790	-2.423099	4.244813
H	2.578892	-0.979611	5.170574
H	4.262221	-1.580287	5.203753
H	5.623654	-0.005956	4.166465
B	1.316741	-1.106275	2.406546
C	0.796177	-2.287132	1.582403
C	-0.569033	-2.655595	1.718143
C	-1.136271	-3.717190	1.019656
H	-2.196743	-3.935002	1.174822
C	-0.351700	-4.485198	0.147307
H	-0.797976	-5.322905	-0.396947
C	1.004286	-4.177406	0.003234
H	1.637120	-4.780525	-0.656436
C	1.555966	-3.111406	0.708984
H	2.626409	-2.908912	0.609533
C	0.307440	-0.493269	3.391578
C	0.548526	0.566413	4.307546
H	1.556050	0.997061	4.353383
C	-0.439019	1.083353	5.143253
H	-0.197300	1.897734	5.834653
C	-1.734113	0.561522	5.101722
H	-2.518959	0.954984	5.754520
C	-2.021131	-0.481031	4.210503
H	-3.022104	-0.916964	4.145887
C	-1.022549	-0.986327	3.382924
O	-1.418429	-1.987920	2.546754

Table S17. xyz -coordinates [\AA] of the T_{CT} geometry of DPA-CoOB, conformer I at PBE0/def2-SV(P) level of theory.

Atom type	X	Y	Z
H	1.713864	1.881297	2.022138
C	1.022576	1.923689	1.183358
C	-0.101324	2.718904	1.252912
H	-0.299810	3.293405	2.160347
C	-0.987792	2.762830	0.168852
H	-1.889437	3.378814	0.217972
C	-0.714843	2.030102	-0.983793
H	-1.401935	2.090515	-1.830200
C	0.417506	1.226553	-1.091913
C	1.286623	1.147825	0.026653
H	4.509957	-1.257583	-0.180779
C	3.883864	-1.251577	-1.071480
C	2.735813	-0.419730	-1.111660
C	1.914094	-0.410998	-2.265882
C	2.237121	-1.282473	-3.305234
H	1.584471	-1.327117	-4.178300
C	3.357898	-2.104500	-3.256783
H	3.577129	-2.774236	-4.092292
C	4.196143	-2.071103	-2.135910
H	5.082358	-2.708573	-2.085948
C	0.736242	0.544370	-2.413452
C	1.216115	1.615120	-3.431135
C	1.754234	2.832633	-2.995032
H	1.774073	3.075474	-1.929735
C	2.268735	3.761401	-3.901217
H	2.681080	4.703742	-3.528342
C	2.252927	3.494137	-5.267528
H	2.650635	4.223006	-5.979812
C	1.721042	2.285262	-5.717355
H	1.696169	2.059204	-6.787617
C	1.215003	1.356789	-4.810482
H	0.798695	0.423407	-5.195892
C	-0.526368	-0.221605	-2.853603
C	-0.804916	-1.462339	-2.262715
H	-0.105982	-1.906556	-1.545843
C	-1.979058	-2.148129	-2.565594
H	-2.168596	-3.112578	-2.085896
C	-2.901983	-1.605265	-3.460086
H	-3.823469	-2.144897	-3.698572
C	-2.643366	-0.364990	-4.039961
H	-3.361438	0.078927	-4.736226
C	-1.466547	0.322667	-3.736326
H	-1.289029	1.297496	-4.197805
N	2.408518	0.346590	-0.005912
C	3.247060	0.254170	1.174544
C	2.801349	-0.490211	2.283636
C	3.723053	-0.586933	3.362924
C	3.384664	-1.422887	4.566087
C	4.956000	0.073202	3.309358
C	5.330613	0.841973	2.207422
H	6.292631	1.361947	2.191163
C	4.468786	0.927801	1.120064
H	4.736861	1.506296	0.231088
H	2.994884	-2.409132	4.260531
H	2.591346	-0.952749	5.174192
H	4.267308	-1.572757	5.210147
H	5.645082	-0.020265	4.155566
B	1.327889	-1.095314	2.394278
C	0.806053	-2.274552	1.566783
C	-0.560111	-2.639003	1.697263
C	-1.126740	-3.700364	0.997254
H	-2.188096	-3.916580	1.148236
C	-0.339839	-4.469632	0.129190
H	-0.785422	-5.306948	-0.416316
C	1.017183	-4.164737	-0.010635
H	1.651095	-4.769465	-0.667650
C	1.568060	-3.099424	0.696983
H	2.639542	-2.899911	0.603347
C	0.315292	-0.480902	3.375949
C	0.555415	0.578875	4.291435
H	1.564147	1.006057	4.341606
C	-0.433813	1.098403	5.123493
H	-0.192950	1.912193	5.815777
C	-1.729951	0.579736	5.075984
H	-2.516485	0.975324	5.725495
C	-2.016913	-0.460585	4.182871
H	-3.019052	-0.893057	4.113880
C	-1.015887	-0.969421	3.359805
O	-1.410977	-1.970031	2.522882

Table S18. *xyz*-coordinates [Å] of the T_{LE(A)} geometry of DPA-CoOB, conformer I at PBE0/def2-SV(P) level of theory.

Atom type	x	y	z
H	1.415613	1.843925	1.917798
C	0.701478	1.744601	1.100468
C	-0.546626	2.346072	1.203179
H	-0.795878	2.904197	2.111001
C	-1.472873	2.223375	0.168114
H	-2.464780	2.677723	0.244669
C	-1.100383	1.539041	-0.985819
H	-1.797989	1.483201	-1.825868
C	0.161094	0.951710	-1.126606
C	1.059226	1.004445	-0.040802
H	4.385067	-1.302514	-0.244126
C	3.697023	-1.382459	-1.086598
C	2.568875	-0.539295	-1.143621
C	1.710514	-0.630013	-2.260271
H	1.947299	-1.629769	-3.209714
H	1.251529	-1.728985	-4.047429
C	3.042280	-2.486129	-3.130990
H	3.204500	-3.247494	-3.899137
C	3.934515	-2.334107	-2.070905
H	4.819578	-2.973333	-1.992739
C	0.631610	0.429882	-2.480714
C	1.286431	1.592491	-3.276621
C	1.221091	2.922241	-2.845101
H	0.703504	3.167961	-1.915400
H	1.811000	3.952865	-3.582097
H	1.744061	4.981658	-3.214237
C	2.480740	3.676838	-4.770699
H	2.944024	4.483082	-5.347820
C	2.558283	2.354907	-5.213221
H	3.083979	2.115696	-6.143088
C	1.973986	1.330817	-4.472317
H	2.058315	0.304411	-4.837354
C	-0.568555	-0.167211	-3.232314
C	-1.183126	-1.315024	-2.706310
H	-0.774970	-1.770674	-1.798599
C	-2.297901	-1.878945	-3.318300
H	-2.755781	-2.775797	-2.888978
C	-2.832567	-1.302728	-4.474127
H	-3.709309	-1.744511	-4.957774
C	-2.239269	-0.159031	-5.000449
H	-2.649173	0.308489	-5.901267
C	-1.116677	0.403620	-4.383477
H	-0.669297	1.304879	-4.809511
N	2.285015	0.342024	-0.097591
C	3.177301	0.358993	1.029214
C	2.894232	-0.374851	2.203251
C	3.907218	-0.412494	3.197452
C	3.728087	-1.240969	4.443190
C	5.100826	0.297310	3.020561
C	5.324774	1.063908	1.878933
H	6.255694	1.627158	1.762788
C	4.359482	1.088722	0.878380
H	4.516712	1.655044	-0.044006
H	3.320719	-2.238772	4.204963
H	3.019765	-0.773249	5.150847
H	4.686947	-1.375709	4.971276
H	5.871980	0.245901	3.796869
B	1.472030	-1.024866	2.499809
C	0.856341	-2.239658	1.782717
C	-0.474121	-2.622828	2.104180
C	-1.161900	-3.690209	1.497047
H	-2.189266	-3.890867	1.811454
C	-0.519608	-4.460077	0.517611
H	-1.039441	-5.288778	0.031850
C	0.796266	-4.141217	0.194920
H	1.329362	-4.726125	-0.561147
C	1.470201	-3.066158	0.821177
H	2.504469	-2.865835	0.535668
C	0.564317	-0.415803	3.594128
C	0.862063	0.678244	4.434002
H	1.838545	1.164172	4.339416
C	-0.054327	1.179682	5.382175
H	0.240120	2.028838	6.007290
C	-1.319559	0.617931	5.534055
H	-2.028064	1.007924	6.268362
C	-1.667696	-0.463221	4.713430
H	-2.647101	-0.944531	4.773037
C	-0.737291	-0.947257	3.780578
O	-1.189486	-1.981456	3.041835

Table S19. *xyz*-coordinates [Å] of the S₀ geometry of DPACpOB, 0-Me at PBE0/def2-SV(P) level of theory.

Atom type	x	y	z
H	3.975809	-0.367188	0.832655
C	3.404711	-0.653870	-0.052112
C	4.033450	-1.324360	-1.096985
H	5.098411	-1.561928	-1.015320
C	3.319105	-1.677070	-2.240833
H	3.811224	-2.196601	-3.067580
C	1.958068	-1.381999	-2.310280
H	1.380490	-1.692708	-3.184422
C	1.300510	-0.733060	-1.264835
C	2.041341	-0.332907	-0.135682
H	0.460035	2.509280	2.222969
C	-0.126206	2.235606	1.343939
C	0.254604	1.128476	0.570637
C	-0.522321	0.758140	-0.544267
C	-1.619551	1.544994	-0.895557
H	-2.221968	1.254350	-1.759750
C	-1.983591	2.661467	-0.143745
H	-2.854607	3.256741	-0.431120
C	-1.239835	2.990561	0.988356
H	-1.519282	3.852605	1.601593
C	-0.215489	-0.586322	-1.194654
C	-0.758787	-1.698197	-0.266453
C	-0.131833	-2.947761	-0.197978
H	0.774679	-3.130778	-0.780265
C	-0.642878	-3.964331	0.608498
H	-0.132183	-4.931529	0.645786
C	-1.792485	-3.749247	1.367809
H	-2.191593	-4.544113	2.005196
C	-2.425011	-2.507922	1.309175
H	-3.326098	-2.321354	1.901511
C	-1.911067	-1.493836	0.501502
H	-2.414860	-0.524457	0.473582
C	-0.838012	-0.674604	-2.587596
C	-0.451825	0.260780	-3.559913
H	0.282823	1.028610	-3.299200
C	-0.987389	0.224851	-4.842895
H	-0.670671	0.956047	-5.584038
C	-1.926084	-0.752867	-5.183736
H	-2.349108	-0.783794	-6.192347
C	-2.316919	-1.686072	-4.228024
H	-3.050922	-2.457380	-4.480415
C	-1.776110	-1.646445	-2.939261
H	-2.093469	-2.386148	-2.200831
N	1.395983	0.382653	0.876092
C	2.041350	0.566264	2.131654
C	1.736602	-0.298695	3.182594
C	2.366492	-0.141985	4.415334
H	1.006680	-1.095719	3.015427
C	3.295045	0.889576	4.639686
C	3.575948	1.754529	3.566964
H	4.297766	2.566859	3.700415
C	2.968355	1.593130	2.324283
H	3.203898	2.265970	1.494760
H	5.115802	3.598411	9.817268
O	5.256922	1.395402	8.600842
C	4.592272	2.446613	8.072639
B	3.987936	1.067203	6.035961
C	4.769170	-0.063669	6.729130
C	5.353782	0.197435	7.983463
C	6.087564	-0.773906	8.678218
H	6.517411	-0.519286	9.649878
C	6.250884	-2.028358	8.113177
H	6.823514	-2.790001	8.651100
C	5.695571	-2.324323	6.857306
H	5.838966	-3.313662	6.414291
C	4.973030	-1.352640	6.185493
H	4.548468	-1.575427	5.201727
C	3.939492	2.388068	6.826085
C	3.258187	3.553742	6.407378
H	2.722709	3.528665	5.453225
C	3.245453	4.708586	7.171394
H	2.710027	5.596673	6.824582
C	3.921121	4.730530	8.402696
H	3.916153	5.638618	9.013167
C	4.590759	3.606813	8.591448
H	2.115739	-0.831024	5.228169

Table S20. xyz -coordinates [Å] of the S_{CT} geometry of DPACpOB, 0-Me at PBE0/def2-SV(P) level of theory.

Atom type	X	Y	Z
H	3.780459	-0.473795	1.004175
C	3.251126	-0.751289	0.092941
C	3.908079	-1.393230	-0.940995
H	4.969064	-1.632764	-0.839517
C	3.217359	-1.720934	-2.112405
H	3.736717	-2.217858	-2.935575
C	1.855720	-1.430205	-2.229495
H	1.313673	-1.721288	-3.131631
C	1.165959	-0.798335	-1.203158
C	1.881768	-0.425126	-0.038424
H	0.121508	2.025977	2.596762
C	-0.458152	1.824283	1.696339
C	0.021316	0.872580	0.764981
C	-0.737913	0.557405	-0.393181
C	-1.897601	1.282208	-0.636393
H	-2.474471	1.075221	-1.540310
C	-2.343206	2.255925	0.260978
H	-3.258127	2.812445	0.043109
C	-1.632340	2.506069	1.440450
H	-1.992514	3.249490	2.155167
C	-0.342451	-0.651684	-1.222744
C	-0.957264	-1.874614	-0.484615
C	-0.200109	-3.004375	-0.157825
H	0.860211	-3.055064	-0.411936
C	-0.784746	-4.092903	0.492650
H	-0.169713	-4.962835	0.739746
C	-2.136118	-4.072122	0.824636
H	-2.592597	-4.923455	1.337349
C	-2.902156	-2.951763	0.499541
H	-3.965649	-2.918986	0.752792
C	-2.316318	-1.864239	-0.140804
H	-2.935935	-0.996740	-0.378743
C	-0.838969	-0.537468	-2.664089
C	-0.479466	0.596093	-3.407009
H	0.114753	1.385260	-2.935396
C	-0.866837	0.729578	-4.736267
H	-0.578973	1.622705	-5.298404
C	-1.618130	-0.275682	-5.350059
H	-1.924144	-0.173413	-6.395190
C	-1.971649	-1.408949	-4.623026
H	-2.555134	-2.204977	-5.094512
C	-1.583814	-1.539814	-3.286706
H	-1.864184	-2.437088	-2.730401
N	1.251618	0.286170	0.964573
C	1.947507	0.510482	2.204466
C	1.795009	-0.408798	3.247831
C	2.475699	-0.201694	4.438534
H	5.716289	3.820854	9.484292
C	3.328944	0.914254	4.656777
C	3.440305	1.816428	3.563485
H	4.106486	2.679232	3.653205
C	2.775140	1.629127	2.361433
H	2.902189	2.335179	1.534703
H	1.134051	-1.271733	3.120995
C	4.967371	2.624884	7.871619
O	5.530228	1.543853	8.476962
B	4.094873	1.133532	5.997683
C	4.763912	-0.023772	6.779391
C	5.449925	0.279377	7.980172
C	6.106935	-0.686138	8.742280
H	6.605619	-0.371696	9.663155
C	6.122896	-2.016918	8.320441
H	6.637152	-2.774686	8.918984
C	5.487672	-2.359318	7.123048
H	5.509625	-3.394227	6.766315
C	4.833851	-1.382532	6.378894
H	4.368713	-1.671004	5.431749
C	4.252548	2.527401	6.653564
C	3.680912	3.742847	6.198198
H	3.070589	3.723243	5.290522
C	3.840381	4.952571	6.866413
H	3.376654	5.861347	6.469083
C	4.584182	5.004659	8.048972
H	4.721920	5.949238	8.583509
C	5.142299	3.828594	8.553685
H	2.316113	-0.915067	5.252031

Table S21. xyz -coordinates [Å] of the $S_{LE(A)}$ geometry of DPACpOB, 0-Me at PBE0/def2-SV(P) level of theory.

Atom type	x	y	z
H	3.959922	-0.196062	0.801255
C	3.405488	-0.484042	-0.093684
C	4.069767	-1.069064	-1.167111
H	5.148496	-1.239834	-1.099035
C	3.372840	-1.421077	-2.322274
H	3.892397	-1.873255	-3.171587
C	1.995194	-1.212765	-2.374066
H	1.433541	-1.524380	-3.258319
C	1.303122	-0.650843	-1.300513
C	2.023213	-0.248689	-0.158300
H	0.273609	2.372481	2.328033
C	-0.301662	2.099068	1.441707
C	0.150160	1.056656	0.617342
C	-0.610366	0.681730	-0.507674
C	-1.763970	1.403396	-0.816382
H	-2.352788	1.108465	-1.688540
C	-2.198943	2.457233	-0.013740
H	-3.112584	3.001233	-0.268789
C	-1.468868	2.787946	1.127213
H	-1.802537	3.600134	1.780269
C	-0.219019	-0.607932	-1.219906
C	-0.680278	-1.708302	-0.346187
C	0.005323	-3.018428	-0.379814
H	0.898446	-3.119271	-1.001532
C	-0.429767	-4.107937	0.373589
H	0.125458	-5.050062	0.330443
C	-1.560114	-3.997051	1.182994
H	-1.899457	-4.849286	1.779607
C	-2.249600	-2.786128	1.227244
H	-3.135812	-2.680629	1.860644
C	-1.812035	-1.698801	0.470907
H	-2.360070	-0.754870	0.523273
C	-0.844679	-0.670426	-2.613057
C	-0.519726	0.328012	-3.544198
H	0.173940	1.122563	-3.253217
C	-1.064682	0.320992	-4.823690
H	-0.795608	1.110240	-5.532379
C	-1.952629	-0.689740	-5.202281
H	-2.383082	-0.697833	-6.208212
C	-2.283874	-1.684606	-4.287149
H	-2.978382	-2.481933	-4.568889
C	-1.733300	-1.674124	-3.001931
H	-2.004102	-2.461932	-2.295406
N	1.344160	0.384036	0.885066
C	1.992250	0.571212	2.139144
C	1.766115	-0.344729	3.170847
C	2.391771	-0.179739	4.400416
H	1.083696	-1.180876	2.991736
C	3.264107	0.906194	4.666339
C	3.464044	1.816360	3.596801
H	4.155469	2.654484	3.728558
C	2.849855	1.655359	2.361421
H	3.035944	2.365101	1.549596
O	5.253389	1.425422	8.606301
H	5.496325	3.658057	9.685916
C	4.779255	2.532903	7.999429
B	3.958727	1.088213	6.042587
C	4.559553	-0.096187	6.860291
C	5.171133	0.173696	8.112525
C	5.758783	-0.804960	8.927363
H	6.197378	-0.496969	9.879659
C	5.780645	-2.137801	8.499079
H	6.229755	-2.912778	9.124388
C	5.227547	-2.443059	7.258958
H	5.240962	-3.473455	6.891848
C	4.642427	-1.434900	6.457264
H	4.248528	-1.716312	5.477037
C	4.123537	2.471992	6.741924
C	3.613692	3.699716	6.300044
H	3.041857	3.728929	5.368714
C	3.794035	4.907165	7.014018
H	3.386721	5.834989	6.601765
C	4.478863	4.924698	8.225458
H	4.624916	5.854939	8.779175
C	4.971307	3.714417	8.729231
H	2.167294	-0.894563	5.198203

Table S22. *xyz*-coordinates [Å] of the T_{CT} geometry of DPACpOB, 0-Me at PBE0/def2-SV(P) level of theory.

Atom type	X	Y	Z
H	3.818870	-0.405446	1.064286
C	3.268528	-0.808524	0.213995
C	3.900288	-1.621103	-0.712544
H	4.953300	-1.878212	-0.573923
C	3.199891	-2.083354	-1.829475
H	3.697267	-2.715796	-2.569255
C	1.860573	-1.729520	-2.008657
H	1.314201	-2.096242	-2.880237
C	1.196964	-0.928725	-1.086160
C	1.909781	-0.461781	0.041197
H	0.168746	2.351991	2.371686
C	-0.323050	2.136538	1.423831
C	0.145966	1.079323	0.615595
C	-0.569855	0.711283	-0.550654
C	-1.634292	1.510454	-0.953829
H	-2.177359	1.249121	-1.864772
C	-2.039216	2.614086	-0.200123
H	-2.878299	3.225933	-0.540931
C	-1.400248	2.902091	1.007905
H	-1.744391	3.729929	1.632719
C	-0.287961	-0.642604	-1.186621
C	-1.049898	-1.682782	-0.322474
C	-0.434733	-2.850017	0.141538
H	0.613314	-3.050773	-0.089806
C	-1.146083	-3.780809	0.901401
H	-0.640317	-4.684067	1.254735
C	-2.485960	-3.561783	1.208571
H	-3.042077	-4.288794	1.807290
C	-3.111098	-2.402265	0.747897
H	-4.163160	-2.214185	0.981019
C	-2.398287	-1.472328	-0.003312
H	-2.906925	-0.568310	-0.346213
C	-0.729204	-0.681521	-2.650119
C	-0.221497	0.286236	-3.529046
H	0.450137	1.061542	-3.147080
C	-0.559435	0.272739	-4.878169
H	-0.154853	1.038281	-5.546743
C	-1.410640	-0.716866	-5.376492
H	-1.678271	-0.729673	-6.437060
C	-1.912920	-1.686867	-4.513698
H	-2.576551	-2.469584	-4.892631
C	-1.573671	-1.669675	-3.157799
H	-1.971928	-2.440185	-2.493862
N	1.301125	0.389318	0.957088
C	1.950067	0.601725	2.201377
C	2.093396	-0.489205	3.088969
C	2.758633	-0.318360	4.284443
O	5.522174	1.433834	8.519459
C	3.350556	0.924656	4.672746
C	3.204682	1.989689	3.727051
H	3.695491	2.945824	3.928920
C	2.529894	1.846158	2.532219
H	2.492980	2.670377	1.813567
H	5.272410	3.523703	9.864361
H	1.629842	-1.448005	2.836364
C	4.728322	2.449203	8.088995
B	4.109107	1.102478	6.013880
C	5.038506	0.010369	6.607201
C	5.690858	0.272776	7.834109
C	6.570037	-0.631827	8.433381
H	7.027697	-0.359722	9.388229
C	6.850775	-1.844281	7.807887
H	7.538483	-2.554541	8.276461
C	6.257351	-2.132610	6.573835
H	6.486940	-3.071668	6.060433
C	5.381551	-1.220859	5.996034
H	4.952582	-1.455667	5.017725
C	4.004952	2.388891	6.875519
C	3.175785	3.507490	6.614284
H	2.549045	3.494742	5.717950
C	3.105846	4.609095	7.459022
H	2.449920	5.449128	7.209590
C	3.868183	4.638424	8.632170
H	3.826317	5.500953	9.303936
C	4.675616	3.548525	8.948704
H	2.793395	-1.160925	4.980461

Table S23. *xyz*-coordinates [Å] of the S₀ geometry of DPACpOB, 2-Me at PBE0/def2-SV(P) level of theory.

Atom type	x	y	z
H	4.096675	-0.539607	0.633834
C	3.462360	-0.875229	-0.189111
C	3.961605	-1.7751019	-1.148871
H	4.994527	-2.102956	-1.067307
C	3.160117	-2.165557	-2.212207
H	3.552412	-2.847823	-2.971441
C	1.838891	-1.723712	-2.284744
H	1.189829	-2.083251	-3.087062
C	1.310998	-0.865388	-1.320664
C	2.143794	-0.408002	-0.280991
H	1.055241	2.920705	1.660078
C	0.398939	2.608775	0.845056
C	0.590828	1.357184	0.243331
C	-0.274064	0.935853	-0.785197
C	-1.266590	1.805881	-1.235537
H	-1.941502	1.475338	-2.028957
C	-1.440110	3.063954	-0.658237
H	-2.231679	3.727450	-1.017418
C	-0.613654	3.451667	0.396103
H	-0.748009	4.428103	0.871453
C	-0.171880	-0.529160	-1.197877
C	-0.743577	-1.377546	-0.035916
C	-0.233800	-2.650807	0.243121
H	0.584854	-3.049706	-0.361097
C	-0.742698	-3.413593	1.293855
H	-0.321006	-4.403009	1.495736
C	-1.774565	-2.915805	2.089069
H	-2.168932	-3.509346	2.919447
C	-2.297474	-1.652433	1.814376
H	-3.107371	-1.246941	2.428517
C	-1.785817	-0.892818	0.762711
H	-2.196885	0.101331	0.570065
C	-0.913090	-0.792820	-2.505140
C	-0.517588	-0.100864	-3.660278
H	0.311398	0.610671	-3.598518
C	-1.161788	-0.306604	-4.875852
H	-0.835320	0.244659	-5.763002
C	-2.221320	-1.213562	-4.963317
H	-2.729918	-1.377390	-5.918154
C	-2.622742	-1.905910	-3.824474
H	-3.450744	-2.619320	-3.877903
C	-1.972613	-1.696386	-2.604815
H	-2.299303	-2.247657	-1.720111
N	1.625821	0.507454	0.636226
C	2.200727	0.628749	1.933900
C	1.664372	-0.138468	2.966175
C	2.191422	-0.057296	4.256874
C	1.608434	-0.888181	5.367589
C	3.274208	0.808134	4.512101
C	3.814579	1.583240	3.466863
C	4.970602	2.508501	3.735554
C	3.270527	1.486385	2.182372
H	3.680839	2.083215	1.362134
H	0.767668	-1.504972	5.010564
H	1.238370	-0.251575	6.191636
H	2.366964	-1.564657	5.801537
B	3.878769	0.906921	5.960334
C	5.015706	-0.002290	6.450433
C	5.492493	0.163796	7.763910
C	6.526412	-0.629071	8.280313
H	6.863094	-0.463262	9.306433
C	7.093955	-1.603548	7.474409
H	7.901298	-2.225512	7.872893
C	6.644163	-1.799265	6.157549
H	7.100437	-2.572154	5.532948
C	5.621825	-1.006563	5.663688
H	5.259583	-1.147356	4.639585
C	3.382229	1.920019	7.002712
C	2.345051	2.850496	6.771599
H	1.862516	2.850263	5.788239
C	1.937607	3.742980	7.748798
H	1.132356	4.455731	7.550785
C	2.568844	3.726711	9.004191
H	2.253223	4.428436	9.782260
C	3.590679	2.829519	9.272757
H	4.092316	2.802461	10.243016
C	3.989873	1.933259	8.271917
O	4.991364	1.090634	8.611156
H	0.824130	-0.803751	2.743278
H	5.844515	1.954369	4.123432
H	5.284838	3.041029	2.823208
H	4.708558	3.265102	4.497225

Table S24. xyz -coordinates [\AA] of the S_{CT} geometry of DPACpOB, 2-Me at PBE0/def2-SV(P) level of theory.

Atom type	X	Y	Z
H	3.723549	-0.846989	1.155487
C	3.179697	-1.130328	0.254471
C	3.764217	-1.943855	-0.698789
H	4.779277	-2.315690	-0.542097
C	3.061082	-2.275488	-1.861840
H	3.525312	-2.908301	-2.622178
C	1.756668	-1.811986	-2.050776
H	1.201072	-2.102131	-2.944857
C	1.137954	-1.005138	-1.105009
C	1.871240	-0.635591	0.049514
H	0.397163	2.240225	2.425214
C	-0.178308	2.047742	1.520026
C	0.189774	0.968969	0.681110
C	-0.575495	0.666190	-0.476323
C	-1.615332	1.521159	-0.818228
H	-2.191168	1.322326	-1.724597
C	-1.944119	2.616392	-0.015600
H	-2.766042	3.273667	-0.309673
C	-1.238166	2.860926	1.168203
H	-1.511173	3.701441	1.810107
C	-0.333478	-0.652114	-1.190994
C	-1.132904	-1.709424	-0.377726
C	-0.548286	-2.895740	0.077600
H	0.501699	-3.112344	-0.127367
C	-1.295841	-3.830970	0.796187
H	-0.813983	-4.749301	1.143394
C	-2.640553	-3.598059	1.068602
H	-3.224670	-4.329422	1.634178
C	-3.235372	-2.419795	0.615108
H	-4.291209	-2.221289	0.820033
C	-2.487062	-1.484600	-0.092916
H	-2.974303	-0.567429	-0.431413
C	-0.772688	-0.593044	-2.654022
C	-0.238747	0.413034	-3.471772
H	0.448430	1.149818	-3.043629
C	-0.569668	0.485398	-4.820887
H	-0.145103	1.279329	-5.442088
C	-1.438634	-0.455282	-5.379110
H	-1.700399	-0.401044	-6.439729
C	-1.965961	-1.463399	-4.576927
H	-2.643086	-2.208598	-5.004166
C	-1.634522	-1.532610	-3.220998
H	-2.051980	-2.332363	-2.605160
N	1.319859	0.236923	0.967087
C	2.010956	0.462381	2.212987
C	1.722978	-0.364652	3.291778
C	2.387586	-0.168305	4.506041
C	2.046952	-1.046513	5.676266
C	3.352208	0.860439	4.640019
C	3.623918	1.684123	3.519169
C	4.661080	2.767413	3.607112
C	2.951229	1.482552	2.311049
H	3.168229	2.108964	1.440004
H	1.173019	-1.685473	5.465415
H	1.837239	-0.433908	6.570311
H	2.897895	-1.696958	5.945844
B	4.113813	1.084601	6.012339
C	5.127456	0.076152	6.556056
C	5.765936	0.359016	7.790201
C	6.707678	-0.490942	8.360892
H	7.154502	-0.209206	9.318370
C	7.065879	-1.679483	7.707804
H	7.805918	-2.347747	8.157571
C	6.473353	-1.990275	6.480995
H	6.753041	-2.909812	5.955849
C	5.532223	-1.129038	5.922814
H	5.089477	-1.373977	4.950609
C	3.886577	2.324898	6.878397
C	2.979222	3.382811	6.604856
H	2.372275	3.318377	5.694544
C	2.824127	4.476254	7.452982
H	2.112047	5.268923	7.199558
C	3.571178	4.559961	8.630979
H	3.459214	5.413834	9.305484
C	4.467944	3.529371	8.949014
H	5.065286	3.555033	9.864563
C	4.611300	2.443586	8.091411
O	5.498461	1.492251	8.499073
H	0.970435	-1.152114	3.185772
H	5.602091	2.367729	4.023434
H	4.866540	3.215979	2.620593
H	4.340796	3.569372	4.295497

Table S25. xyz -coordinates [\AA] of the T_{CT} geometry of DPACpOB, 2-Me at PBE0/def2-SV(P) level of theory.

Atom type	x	y	z
H	3.750904	-0.771280	1.159502
C	3.168444	-1.160387	0.324125
C	3.704590	-2.115350	-0.522665
H	4.710506	-2.498380	-0.335191
C	2.970760	-2.562802	-1.624493
H	3.394549	-3.308371	-2.301920
C	1.694346	-2.051545	-1.868840
H	1.121014	-2.408819	-2.726748
C	1.124997	-1.104161	-1.025983
C	1.871831	-0.652934	0.085374
H	0.488172	2.544995	2.145912
C	-0.016774	2.319433	1.207312
C	0.318803	1.148681	0.494318
C	-0.421314	0.785986	-0.658984
C	-1.364093	1.683114	-1.148536
H	-1.921949	1.425097	-2.051303
C	-1.630410	2.885630	-0.490907
H	-2.375276	3.573535	-0.898680
C	-0.976997	3.182940	0.707703
H	-1.217902	4.095761	1.257675
C	-0.307911	-0.637772	-1.184789
C	-1.209563	-1.499691	-0.260201
C	-0.755778	-2.693331	0.310492
H	0.259763	-3.046208	0.119829
C	-1.590687	-3.459043	1.126823
H	-1.210389	-4.387078	1.563340
C	-2.894684	-3.045792	1.384367
H	-3.547283	-3.643372	2.027145
C	-3.359593	-1.858911	0.816392
H	-4.381556	-1.519761	1.008719
C	-2.523550	-1.093230	0.009009
H	-2.907640	-0.164041	-0.418282
C	-0.729825	-0.734067	-2.651093
C	-0.086931	0.087448	-3.588371
H	0.675608	0.796533	-3.250845
C	-0.405039	0.012015	-4.940285
H	0.105805	0.663496	-5.655291
C	-1.371890	-0.894736	-5.381913
H	-1.624249	-0.955939	-6.444500
C	-2.009272	-1.720458	-4.460193
H	-2.764566	-2.437675	-4.794331
C	-1.689672	-1.641074	-3.101792
H	-2.195021	-2.298696	-2.390980
N	1.363272	0.339044	0.914384
C	2.009647	0.551522	2.166277
C	1.934055	-0.462294	3.129462
C	2.569972	-0.307548	4.356261
C	2.405811	-1.368071	5.405910
C	3.336199	0.863037	4.629382
C	3.418633	1.868697	3.620664
C	4.273725	3.083398	3.834103
C	2.752809	1.711776	2.408787
H	2.856543	2.462860	1.619840
H	1.648217	-2.113960	5.113308
H	2.111165	-0.914613	6.368545
H	3.357757	-1.894495	5.596999
B	4.090537	1.034530	6.003512
C	5.247130	0.117588	6.420499
C	5.875942	0.350703	7.668451
C	6.945019	-0.415358	8.125342
H	7.375705	-0.182210	9.102962
C	7.446611	-1.456343	7.334676
H	8.286197	-2.058397	7.694231
C	6.871320	-1.706999	6.085568
H	7.265506	-2.508618	5.452300
C	5.802652	-0.932333	5.643887
H	5.377388	-1.122339	4.651932
C	3.725536	2.131547	7.011145
C	2.669409	3.069940	6.878198
H	2.045411	3.021953	5.978709
C	2.387795	4.024387	7.851295
H	1.562991	4.729460	7.704465
C	3.152714	4.076978	9.020192
H	2.942198	4.822332	9.792712
C	4.191177	3.156036	9.203405
H	4.804373	3.159290	10.108670
C	4.459305	2.206963	8.220584
O	5.477424	1.348295	8.505500
H	1.331426	-1.351790	2.920505
H	5.275596	2.791156	4.194929
H	4.381201	3.672716	2.908244
H	3.850151	3.738235	4.616400

Table S26. *xyz*-coordinates [Å] of the T_{LE(A)} geometry of DPACpOB, 2-Me at PBE0/def2-SV(P) level of theory.

Atom type	X	Y	Z
H	3.926775	-0.637185	0.858864
C	3.344525	-0.925026	-0.018346
C	3.919151	-1.711211	-1.012153
H	4.956728	-2.040527	-0.900199
C	3.187728	-2.064340	-2.145565
H	3.638601	-2.675211	-2.932539
C	1.860603	-1.650297	-2.254101
H	1.265860	-1.959062	-3.117454
C	1.255416	-0.882412	-1.258787
C	2.017678	-0.484781	-0.142574
H	0.690053	2.622650	2.017718
C	0.086951	2.355224	1.148167
C	0.371112	1.173044	0.447117
C	-0.427268	0.810301	-0.655601
C	-1.443042	1.672322	-1.069847
H	-2.062519	1.386287	-1.923549
C	-1.707819	2.861471	-0.391410
H	-2.516294	3.516931	-0.726841
C	-0.947087	3.187414	0.730837
H	-1.150508	4.107591	1.287110
C	-0.241645	-0.595652	-1.215342
C	-0.884029	-1.592263	-0.221485
C	-0.381842	-2.891522	-0.083430
H	0.494743	-3.196122	-0.660646
C	-0.977615	-3.803106	0.787422
H	-0.562938	-4.811745	0.879146
C	-2.088895	-3.430785	1.543196
H	-2.553481	-4.142894	2.232020
C	-2.598159	-2.139201	1.414499
H	-3.467308	-1.829574	2.003083
C	-1.999751	-1.230429	0.541974
H	-2.405756	-0.219110	0.460372
C	-0.865617	-0.718098	-2.604544
C	-0.392513	0.111210	-3.633088
H	0.410651	0.822242	-3.417406
C	-0.927923	0.041697	-4.914796
H	-0.542156	0.698717	-5.700333
C	-1.954389	-0.863581	-5.197918
H	-2.377597	-0.920587	-6.205355
C	-2.432531	-1.690953	-4.186009
H	-3.236118	-2.404414	-4.392586
C	-1.891376	-1.617870	-2.898872
H	-2.277964	-2.273884	-2.115685
N	1.433559	0.346370	0.813927
C	2.066747	0.524787	2.079558
C	1.657143	-0.262321	3.151896
C	2.255411	-0.118123	4.407292
C	1.793530	-0.972793	5.556511
C	3.282801	0.832079	4.594802
C	3.690275	1.626860	3.500602
C	4.789598	2.640822	3.668727
C	3.079448	1.466267	2.253432
H	3.394018	2.075651	1.400420
H	0.921182	-1.586611	5.277484
H	1.516753	-0.352408	6.427371
H	2.594413	-1.653985	5.896807
B	3.969810	1.001172	6.006517
C	4.996795	0.001767	6.553466
C	5.565602	0.234303	7.831556
C	6.515647	-0.605379	8.435844
H	6.894469	-0.340654	9.426027
C	6.950190	-1.753789	7.755065
H	7.687911	-2.419122	8.208615
C	6.420335	-2.017900	6.495813
H	6.747015	-2.906821	5.947077
C	5.465306	-1.159071	5.904740
H	5.075786	-1.395122	4.909584
C	3.668995	2.177674	6.943325
C	2.764582	3.232204	6.702244
H	2.204573	3.235830	5.761909
C	2.556795	4.273629	7.635477
H	1.843365	5.068092	7.394998
C	3.238232	4.305362	8.848236
H	3.075224	5.111222	9.566989
C	4.145090	3.271990	9.132939
H	4.709113	3.237603	10.068219
C	4.337651	2.247277	8.192062
O	5.224889	1.307378	8.569869
H	0.856824	-0.991236	2.991224
H	5.699570	2.174746	4.086679
H	5.053417	3.113897	2.708303
H	4.494299	3.439922	4.372478

Table S27. *xyz*-coordinates [Å] of the S₀ geometry of DMACoOB at PBE0/def2-SV(P) level of theory.

Atom type	x	y	z
H	4.797148	-0.611622	-0.329314
C	4.200159	-0.387216	-1.214650
C	4.623464	-0.839414	-2.460738
H	5.544217	-1.426577	-2.533341
C	3.890154	-0.530411	-3.602909
H	4.221386	-0.868171	-4.589134
C	2.713750	0.207542	-3.474420
H	2.134675	0.428046	-4.373620
C	2.248135	0.649709	-2.233627
C	3.025952	0.372347	-1.088295
H	2.452973	2.658139	2.161115
C	1.842201	2.903979	1.290969
C	1.830371	2.041963	0.182557
C	1.027669	2.355297	-0.936058
C	0.316639	3.557846	-0.926038
H	-0.295301	3.825723	-1.789914
C	0.344002	4.424316	0.166445
H	-0.231324	5.354334	0.144100
C	1.099973	4.081034	1.283790
H	1.129135	4.738178	2.158509
C	0.892338	1.320973	-2.047493
C	-0.111786	0.244011	-1.576065
C	-0.991585	-1.417136	2.025114
O	-0.960174	-2.523321	1.248199
H	0.881963	1.003803	3.492808
C	-0.005443	0.431668	3.205239
H	-1.363729	1.706473	4.292291
C	-1.255338	0.826049	3.652755
H	-3.381127	0.394883	3.618700
C	-2.388841	0.088771	3.272878
H	-3.134370	-1.618261	2.159031
C	-2.265591	-1.029023	2.462717
C	0.361853	1.929207	-3.346046
C	0.033375	-4.233811	0.023790
C	0.187027	-3.060165	0.774905
C	1.159196	-4.857400	-0.490715
H	-0.970567	-4.634472	-0.136863
C	2.438897	-4.324352	-0.265048
H	1.044762	-5.774950	-1.076319
C	2.570797	-3.160226	0.473496
H	3.320641	-4.824546	-0.675218
C	0.168547	-0.699609	2.376119
H	3.564078	-2.735979	0.649413
N	2.619046	0.879137	0.157705
C	3.379687	0.533764	1.326287
C	2.892077	-0.466322	2.176784
C	3.644153	-0.804018	3.325701
C	3.152550	-1.873652	4.263910
C	4.845522	-0.135817	3.580433
C	5.316815	0.858658	2.721831
H	6.259550	1.370072	2.938700
C	4.583325	1.196659	1.589958
H	4.933207	1.972587	0.903038
H	3.039197	-2.842593	3.744807
H	2.161905	-1.617772	4.681427
H	3.847034	-2.020964	5.107182
H	5.425207	-0.400233	4.471169
B	1.527032	-1.192370	1.843869
C	1.451647	-2.488444	1.015472
H	-1.102502	0.698194	-1.396783
H	-0.213890	-0.544411	-2.342804
H	0.221264	-0.231254	-0.638868
H	1.034263	2.710518	-3.740292
H	0.237092	1.153545	-4.118752
H	-0.635350	2.371977	-3.191673

Table S28. *xyz*-coordinates [Å] of the S_{CT} geometry of DMA-CoOB at PBE0/def2-SV(P) level of theory.

Atom type	X	Y	Z
H	4.207999	-0.937403	-0.305349
C	3.499426	-0.713514	-1.100691
C	3.482639	-1.473936	-2.249903
H	4.177959	-2.309414	-2.356769
C	2.561300	-1.179180	-3.261538
H	2.529932	-1.784016	-4.171488
C	1.680025	-0.110120	-3.113459
H	0.969076	0.094975	-3.916259
C	1.676253	0.690081	-1.972125
C	2.594826	0.364966	-0.939394
H	2.771059	2.722806	2.318344
C	2.086784	3.059839	1.541324
C	1.908238	2.273116	0.377447
C	0.991040	2.683612	-0.622596
C	0.301756	3.880242	-0.419717
H	-0.424563	4.212482	-1.164017
C	0.496050	4.662111	0.714804
H	-0.062579	5.593997	0.835096
C	1.395029	4.243389	1.701503
H	1.546531	4.840499	2.604184
C	0.674587	1.816215	-1.824128
C	-0.721257	1.182559	-1.584945
C	-0.750239	-1.663515	1.352066
O	-0.506026	-2.900241	0.836894
H	0.628108	1.079818	2.796829
C	-0.131199	0.415852	2.371705
H	-1.740383	1.772857	2.846781
C	-1.467263	0.805379	2.412257
H	-3.512329	0.252093	1.932520
C	-2.458497	-0.040771	1.907638
H	-2.836946	-1.986427	0.994934
C	-2.090042	-1.287252	1.381684
C	0.648236	2.669393	-3.107663
C	0.774368	-4.754885	0.266848
C	0.736009	-3.461496	0.779208
C	1.999002	-5.424904	0.142153
H	-0.166569	-5.226218	-0.031039
C	3.172419	-4.774967	0.532490
H	2.027593	-6.443150	-0.257039
C	3.116384	-3.480491	1.043746
H	4.138234	-5.283119	0.438585
C	0.294167	-0.823080	1.821165
H	4.051075	-2.986822	1.334908
N	2.631909	1.101228	0.224420
C	3.459625	0.634307	1.320990
C	3.021592	-0.458711	2.093779
C	3.862622	-0.806864	3.187148
C	3.453101	-1.906016	4.127892
C	5.064211	-0.124734	3.409640
C	5.482699	0.915236	2.579906
H	6.433227	1.425268	2.760417
C	4.666860	1.305833	1.524309
H	4.956149	2.126568	0.861286
H	3.515767	-2.896133	3.642252
H	2.401962	-1.782193	4.440416
H	4.092534	-1.922681	5.026366
H	5.690863	-0.416839	4.259132
B	1.735541	-1.331776	1.728314
C	1.898267	-2.764992	1.199825
H	-1.485024	1.973547	-1.495713
H	-0.990264	0.529799	-2.432817
H	-0.734959	0.582442	-0.659679
H	1.631726	3.131222	-3.298089
H	0.376455	2.058746	-3.982521
H	-0.103940	3.470267	-3.036052

Table S29. *xyz*-coordinates [Å] of the T_{CT} geometry of DMA-CoOB at PBE0/def2-SV(P) level of theory.

Atom type	x	y	z
H	4.229638	-0.924646	-0.281487
C	3.508220	-0.723002	-1.071262
C	3.492386	-1.497657	-2.210373
H	4.199636	-2.323517	-2.313542
C	2.556379	-1.229129	-3.217588
H	2.524876	-1.845921	-4.119479
C	1.665952	-0.167412	-3.076553
H	0.948425	0.021490	-3.877676
C	1.663255	0.649702	-1.946631
C	2.586927	0.342204	-0.912213
H	2.760695	2.749260	2.313551
C	2.076335	3.074069	1.531351
C	1.899524	2.269900	0.378331
C	0.979534	2.664235	-0.626666
C	0.288019	3.862033	-0.439800
H	-0.440259	4.181681	-1.187847
C	0.482133	4.661560	0.682619
H	-0.078164	5.594055	0.789703
C	1.383012	4.258551	1.674731
H	1.533696	4.868535	2.568951
C	0.664276	1.780613	-1.816946
C	-0.736738	1.159486	-1.579480
C	-0.742889	-1.630735	1.350339
O	-0.508182	-2.862816	0.820039
H	0.659110	1.088592	2.817697
C	-0.106233	0.434493	2.388292
H	-1.705582	1.795526	2.885838
C	-1.439933	0.831216	2.439955
H	-3.490288	0.293212	1.967368
C	-2.438230	-0.005065	1.933027
H	-2.834019	-1.938594	1.002959
C	-2.080668	-1.247775	1.392119
C	0.651984	2.617624	-3.111790
C	0.759631	-4.717977	0.224076
C	0.730072	-3.430148	0.751581
C	1.979869	-5.393275	0.089818
H	-0.184473	-5.180843	-0.076865
C	3.158466	-4.755711	0.484257
H	2.001217	-6.407335	-0.320458
C	3.111115	-3.466257	1.009366
H	4.120630	-5.269149	0.383078
C	0.307836	-0.801106	1.823178
H	4.048846	-2.981483	1.305400
N	2.628130	1.100089	0.239546
C	3.460585	0.648697	1.336966
C	3.033271	-0.454398	2.100042
C	3.876136	-0.808312	3.189392
C	3.475865	-1.922085	4.116599
C	5.070368	-0.115878	3.419082
C	5.477710	0.938446	2.601175
H	6.423233	1.455498	2.787856
C	4.659465	1.332293	1.548410
H	4.942444	2.160833	0.892525
H	3.545593	-2.905888	3.619188
H	2.423943	-1.810089	4.431320
H	4.115528	-1.945130	5.014721
H	5.700463	-0.410551	4.265161
B	1.746599	-1.316851	1.719267
C	1.897681	-2.746760	1.177009
H	-1.497134	1.955638	-1.508901
H	-1.003126	0.495127	-2.419167
H	-0.760884	0.573452	-0.645540
H	1.640240	3.069209	-3.302181
H	0.381001	1.997592	-3.980329
H	-0.094016	3.425470	-3.054894

Table S30. xyz -coordinates [\AA] of the $T_{LE(A)}$ geometry of DMA-CoOB at PBE0/def2-SV(P) level of theory.

Atom type	X	Y	Z
H	4.837741	-0.550122	-0.378952
C	4.218279	-0.343271	-1.253151
C	4.607903	-0.816575	-2.501567
H	5.528688	-1.401785	-2.589532
C	3.842218	-0.530625	-3.629667
H	4.148085	-0.885027	-4.618292
C	2.666340	0.204559	-3.482175
H	2.060486	0.404625	-4.368545
C	2.233526	0.667321	-2.237045
C	3.045074	0.416444	-1.107923
H	2.513168	2.722861	2.134574
C	1.878440	2.953690	1.277460
C	1.861568	2.085286	0.172726
C	1.023640	2.374492	-0.927653
C	0.287376	3.561615	-0.907966
H	-0.351772	3.810020	-1.757986
C	0.321898	4.435085	0.178688
H	-0.273224	5.352777	0.164938
C	1.110782	4.113482	1.280910
H	1.145329	4.776543	2.151105
C	0.875319	1.323545	-2.021093
C	-0.095846	0.236751	-1.501319
C	-0.963351	-1.439110	2.067447
O	-0.910402	-2.554722	1.313773
H	0.827625	1.058047	3.476216
C	-0.024414	0.433626	3.193052
H	-1.431206	1.686543	4.262941
C	-1.315643	0.794487	3.639043
H	-3.433859	0.325690	3.641256
C	-2.436246	0.042865	3.297911
H	-3.092522	-1.731769	2.197972
C	-2.255530	-1.095867	2.497439
C	0.296308	1.903131	-3.311975
C	0.022469	-4.271491	0.080079
C	0.220116	-3.088995	0.811334
C	1.128330	-4.926031	-0.484440
H	-0.994951	-4.655992	-0.027850
C	2.391164	-4.372662	-0.293927
H	0.993956	-5.846546	-1.056881
C	2.567867	-3.180084	0.442585
H	3.268826	-4.865734	-0.724007
C	0.205775	-0.697342	2.381641
H	3.576527	-2.773957	0.559901
N	2.680015	0.950621	0.133208
C	3.422713	0.577370	1.303555
C	2.925395	-0.433828	2.141661
C	3.688961	-0.775032	3.285267
C	3.204337	-1.852179	4.218873
C	4.892260	-0.112325	3.547269
C	5.365341	0.889233	2.698790
H	6.309157	1.397908	2.918139
C	4.628551	1.235832	1.572164
H	4.977493	2.017010	0.890338
H	3.094180	-2.817473	3.692821
H	2.210975	-1.604404	4.634049
H	3.900717	-1.999207	5.061427
H	5.472117	-0.386608	4.435209
B	1.557437	-1.179083	1.831924
C	1.486703	-2.483177	1.022289
H	-1.088154	0.678006	-1.298778
H	-0.207838	-0.565028	-2.252984
H	0.280129	-0.214148	-0.566793
H	0.944075	2.688860	-3.737552
H	0.161532	1.113952	-4.069200
H	-0.702821	2.332807	-3.134508

Table S31. xyz -coordinates [\AA] of the S_0 geometry of DPAAoOB at PBE0/def2-SV(P) level of theory.

Atom type	x	y	z
C	-4.724174	2.495039	-2.504622
C	-3.511883	3.105961	-2.183205
C	-5.109027	1.354328	-1.797991
C	-4.297100	0.826070	-0.798610
C	-3.073027	1.436420	-0.469082
C	-2.698319	2.593273	-1.175536
N	-2.251681	0.906445	0.539574
C	-0.861322	1.169862	0.538102
C	-0.239070	1.694578	1.678185
C	1.134545	1.928373	1.685307
C	1.902266	1.661362	0.552084
C	1.282842	1.153323	-0.592198
C	-0.085857	0.902035	-0.600512
C	-2.820202	0.242758	1.661920
C	-3.912561	0.829309	2.316723
C	-4.502729	0.186494	3.397374
C	-4.000465	-1.038020	3.835244
C	-2.896613	-1.626377	3.208334
C	-2.283996	-0.984611	2.106183
C	-2.398600	-2.964530	3.691911
H	-3.089312	-3.400914	4.431979
H	-1.404336	-2.884227	4.165935
H	-2.296744	-3.684768	2.860566
H	-5.362356	2.903543	-3.293326
H	-6.055338	0.856675	-2.033110
H	-4.616421	-0.068213	-0.258366
H	-1.760498	3.096465	-0.928623
H	-3.193935	4.008174	-2.715555
H	-0.842273	1.909089	2.564591
H	1.608021	2.329349	2.586688
H	2.980444	1.845946	0.559733
H	1.875650	0.933712	-1.485572
H	-0.568482	0.486647	-1.489088
H	-4.296378	1.790196	1.963782
H	-5.357585	0.644362	3.904721
B	-1.051112	-1.671961	1.389040
C	-1.168575	-2.390762	0.029735
C	-0.017790	-2.989507	-0.518093
O	1.182197	-2.975591	0.104302
C	1.374181	-2.417432	1.321251
C	0.350375	-1.762259	2.029436
C	-2.361224	-2.496419	-0.719539
C	-2.404637	-3.144131	-1.943437
C	-1.232376	-3.718865	-2.461222
C	-0.041153	-3.647589	-1.756001
H	-3.270738	-2.048834	-0.307576
H	-3.340975	-3.208622	-2.504830
H	-1.255316	-4.232132	-3.427652
H	0.880657	-4.093620	-2.137717
C	2.673883	-2.540200	1.834745
C	2.960805	-2.006216	3.080363
C	1.966718	-1.342506	3.818706
C	0.692330	-1.223821	3.290130
H	-0.085162	-0.697287	3.854032
H	2.203061	-0.920390	4.799689
H	3.971904	-2.104031	3.487988
H	3.431582	-3.059408	1.242602
H	-4.475231	-1.551613	4.677671

Table S32. *xyz*-coordinates [Å] of the S_{CT} geometry of DPaoOB at PBE0/def2-SV(P) level of theory.

Atom type	X	Y	Z
C	-4.893036	2.468096	-2.357033
C	-3.700663	3.129043	-2.051927
C	-5.222174	1.282468	-1.691864
C	-4.368174	0.752786	-0.735769
C	-3.156976	1.408576	-0.434341
C	-2.835511	2.611178	-1.097209
N	-2.291147	0.883428	0.529896
C	-0.910345	1.074021	0.399844
C	-0.143648	1.401100	1.532320
C	1.217429	1.626919	1.396646
C	1.825441	1.519620	0.142336
C	1.064429	1.188585	-0.983629
C	-0.299575	0.970380	-0.865649
C	-2.821280	0.231039	1.669152
C	-3.925936	0.849131	2.289479
C	-4.503167	0.256528	3.397945
C	-3.990494	-0.958674	3.859957
C	-2.895728	-1.582498	3.246992
C	-2.250015	-0.985994	2.134027
C	-2.440503	-2.920701	3.759496
H	-3.146106	-3.324143	4.504581
H	-1.442486	-2.855357	4.226741
H	-2.345707	-3.643111	2.930767
H	-5.570249	2.879573	-3.110364
H	-6.150163	0.757209	-1.932831
H	-4.614588	-0.183309	-0.231973
H	-1.923121	3.148347	-0.830286
H	-3.449880	4.068848	-2.551203
H	-0.631926	1.488749	2.505101
H	1.812737	1.879825	2.277332
H	2.901671	1.685301	0.042762
H	1.546439	1.076857	-1.958414
H	-0.893606	0.656590	-1.726743
H	-4.293245	1.807524	1.913279
H	-5.346067	0.734281	3.904686
B	-0.998072	-1.705164	1.454698
C	-1.041512	-2.289813	0.042454
C	0.140938	-2.878982	-0.477888
O	1.291013	-2.953182	0.247487
C	1.416914	-2.466130	1.514194
C	0.339628	-1.842419	2.192361
C	-2.161947	-2.312691	-0.830737
C	-2.108423	-2.852210	-2.114104
C	-0.917957	-3.407236	-2.589450
C	0.210878	-3.420821	-1.757488
H	-3.113304	-1.914046	-0.464233
H	-3.003136	-2.849746	-2.745846
H	-0.862045	-3.837705	-3.593729
H	1.158132	-3.855668	-2.088898
C	2.678110	-2.618878	2.083452
C	2.926637	-2.138636	3.376154
C	1.899312	-1.502051	4.076746
C	0.642656	-1.358031	3.492657
H	-0.146602	-0.844218	4.054162
H	2.080444	-1.116511	5.085839
H	3.916936	-2.263177	3.824456
H	3.457888	-3.116339	1.499795
H	-4.462228	-1.443628	4.720974

Table S33. *xyz*-coordinates [Å] of the T_{CT} geometry of DPaoOB at PBE0/def2-SV(P) level of theory.

Atom type	x	y	z
C	-4.748303	2.455361	-2.456956
C	-3.532221	3.068740	-2.147800
C	-5.144989	1.307148	-1.759839
C	-4.335449	0.770122	-0.771192
C	-3.099633	1.378139	-0.463030
C	-2.710485	2.544113	-1.158583
N	-2.276956	0.847347	0.532080
C	-0.883604	0.981607	0.433343
C	-0.142794	1.407376	1.556399
C	1.213355	1.652489	1.430457
C	1.850133	1.481787	0.192947
C	1.114280	1.070208	-0.924734
C	-0.246788	0.833494	-0.820812
C	-2.841935	0.238021	1.673577
C	-3.949088	0.870276	2.271924
C	-4.526527	0.301304	3.393165
C	-4.009233	-0.899857	3.891471
C	-2.912655	-1.537751	3.299439
C	-2.276312	-0.969667	2.166773
C	-2.447070	-2.857792	3.848040
H	-3.144582	-3.243468	4.609861
H	-1.446193	-2.774233	4.306467
H	-2.354951	-3.604900	3.040780
H	-5.391389	2.873125	-3.236292
H	-6.092050	0.817759	-2.002635
H	-4.636315	-0.137012	-0.244108
H	-1.780632	3.048723	-0.889182
H	-3.227337	3.978865	-2.671712
H	-0.653199	1.550766	2.511427
H	1.786120	1.977316	2.302818
H	2.923691	1.667736	0.101475
H	1.615757	0.916551	-1.884236
H	-0.821386	0.466009	-1.674051
H	-4.317241	1.818324	1.871395
H	-5.371849	0.788447	3.886818
B	-1.038115	-1.679510	1.468750
C	-1.114679	-2.297107	0.067329
C	0.057978	-2.881435	-0.473713
O	1.226697	-2.941383	0.221171
C	1.379404	-2.442175	1.478829
C	0.319622	-1.814611	2.176142
C	-2.257673	-2.341140	-0.771383
C	-2.234821	-2.895556	-2.048337
C	-1.050654	-3.445021	-2.548177
C	0.098672	-3.438560	-1.750197
H	-3.201398	-1.945058	-0.382909
H	-3.145722	-2.909394	-2.655867
H	-1.017983	-3.886439	-3.548803
H	1.039983	-3.869959	-2.102220
C	2.654841	-2.585533	2.021644
C	2.928538	-2.086937	3.299728
C	1.918142	-1.441215	4.016708
C	0.648626	-1.308262	3.458962
H	-0.130769	-0.789626	4.029405
H	2.123525	-1.039695	5.014573
H	3.929208	-2.203114	3.727082
H	3.423466	-3.088427	1.428205
H	-4.482169	-1.361385	4.764744

Table S34. xyz -coordinates [\AA] of the $T_{\text{LE(A)}}$ geometry of DPAAOB at PBE0/def2-SV(P) level of theory.

Atom type	X	Y	Z
C	-4.718021	2.388389	-2.547450
C	-3.493304	2.987987	-2.252970
C	-5.119662	1.283030	-1.795112
C	-4.312738	0.777727	-0.780196
C	-3.073339	1.374200	-0.479042
C	-2.683922	2.498649	-1.230431
N	-2.261400	0.867025	0.545388
C	-0.872112	1.131042	0.559982
C	-0.263623	1.655966	1.707691
C	1.108119	1.903449	1.729272
C	1.891050	1.649879	0.603518
C	1.285990	1.139616	-0.548343
C	-0.080552	0.876911	-0.571954
C	-2.840423	0.230391	1.681914
C	-3.910642	0.858825	2.333980
C	-4.495309	0.260846	3.443556
C	-4.004079	-0.957599	3.910891
C	-2.925823	-1.587606	3.279070
C	-2.319318	-0.999095	2.142290
C	-2.443097	-2.917806	3.795789
H	-3.108546	-3.305622	4.585190
H	-1.424275	-2.846582	4.217628
H	-2.394865	-3.667739	2.986411
H	-5.352949	2.779357	-3.347624
H	-6.077410	0.795649	-2.004703
H	-4.648268	-0.086529	-0.202381
H	-1.737949	2.996701	-1.005751
H	-3.161785	3.864895	-2.818571
H	-0.876704	1.861326	2.589262
H	1.566922	2.309253	2.636408
H	2.966794	1.847746	0.621462
H	1.888832	0.930890	-1.437949
H	-0.550012	0.462071	-1.467865
H	-4.278769	1.818583	1.960824
H	-5.332482	0.749950	3.951605
B	-1.098382	-1.705155	1.417801
C	-1.205373	-2.357132	0.026921
C	-0.044960	-2.940414	-0.548652
O	1.135378	-2.953146	0.104981
C	1.340807	-2.425576	1.323643
C	0.298952	-1.799932	2.052312
C	-2.358963	-2.444802	-0.777011
C	-2.347111	-3.047095	-2.049203
C	-1.180139	-3.600541	-2.579527
C	-0.010609	-3.547055	-1.813482
H	-3.295435	-2.029357	-0.395540
H	-3.273605	-3.079329	-2.631402
H	-1.175155	-4.066306	-3.567687
H	0.934564	-3.965613	-2.168751
C	2.665710	-2.551136	1.783901
C	3.014069	-2.024557	3.039285
C	2.025809	-1.391904	3.783053
C	0.697404	-1.279029	3.301519
H	-0.045368	-0.759060	3.914116
H	2.271720	-0.969366	4.762659
H	4.036725	-2.112473	3.412772
H	3.394869	-3.053956	1.143682
H	-4.470351	-1.433912	4.779985

Table S35. xyz -coordinates [\AA] of the S_0 geometry of DPACoSB at PBE0/def2-SV(P) level of theory.

Atom type	x	y	z
H	4.695521	-0.671179	-0.339397
C	4.124466	-0.438005	-1.238966
C	4.580767	-0.887183	-2.473252
H	5.498139	-1.482211	-2.519906
C	3.886019	-0.566689	-3.637469
H	4.240908	-0.907170	-4.614297
C	2.721698	0.191673	-3.539469
H	2.162938	0.435621	-4.446733
C	2.227931	0.635528	-2.308966
C	2.952053	0.331353	-1.138251
H	2.284161	2.571463	2.117886
C	1.693619	2.826272	1.236949
C	1.721558	1.981152	0.113913
C	0.964970	2.326016	-1.024443
C	0.236788	3.519535	-1.011241
H	-0.343037	3.789224	-1.897741
C	0.213098	4.357352	0.101397
H	-0.374379	5.279643	0.083775
C	0.941973	3.996007	1.232340
H	0.941526	4.634986	2.120870
C	0.878353	1.342268	-2.190503
C	-0.224479	0.294727	-1.898248
C	-0.146436	-1.000764	-2.425151
H	0.742549	-1.308437	-2.980897
C	-1.187627	-1.912977	-2.254129
H	-1.096439	-2.918637	-2.676283
C	-2.330768	-1.551500	-1.543252
H	-3.146268	-2.267477	-1.403899
C	-2.414001	-0.271938	-0.996611
H	-3.296110	0.024586	-0.420470
C	-1.370678	0.637371	-1.169398
H	-1.455440	1.632680	-0.726646
C	0.567153	2.100541	-3.492863
C	1.460466	3.094332	-3.925381
H	2.353888	3.305279	-3.329753
C	1.229370	3.812744	-5.093872
H	1.942276	4.581893	-5.407376
C	0.092094	3.553743	-5.864278
H	-0.092535	4.117258	-6.784110
C	-0.801764	2.571822	-5.447912
H	-1.697244	2.356489	-6.039316
C	-0.565373	1.851766	-4.271749
H	-1.280090	1.085489	-3.962866
N	2.509511	0.819910	0.100861
C	3.264675	0.488725	1.278813
C	2.797182	-0.503237	2.151732
C	3.573378	-0.804199	3.298601
C	3.117691	-1.863862	4.266493
C	4.766387	-0.113652	3.529581
C	5.212721	0.873693	2.650459
H	6.148464	1.405488	2.847458
C	4.460370	1.175656	1.522381
H	4.789434	1.944255	0.817068
H	3.003874	-2.843239	3.767751
H	2.134811	-1.613422	4.704855
H	3.835505	-1.986038	5.093967
H	5.358724	-0.354790	4.418581
B	1.437775	-1.291027	1.907433
C	1.441985	-2.625652	1.124374
C	0.276175	-3.408513	0.951217
C	0.310029	-4.616137	0.229750
H	-0.606237	-5.202248	0.105936
C	1.501846	-5.063969	-0.317909
H	1.518164	-6.004737	-0.877159
C	2.678861	-4.321042	-0.151564
H	3.620288	-4.676980	-0.579585
C	2.634916	-3.131430	0.556762
H	3.552931	-2.552313	0.689141
C	0.127464	-0.789048	2.561374
C	0.105205	0.402730	3.323278
H	1.040543	0.958012	3.436015
C	-1.046184	0.882663	3.925599
H	-1.023870	1.810364	4.504452
C	-2.243721	0.168028	3.783048
H	-3.163353	0.534542	4.249913
C	-2.270785	-1.011077	3.055276
H	-3.205162	-1.572156	2.952512
C	-1.094742	-1.493320	2.451217
S	-1.288811	-3.001847	1.600932

Table S36. xyz -coordinates [\AA] of the S_{CT} geometry of DPACoSB at PBE0/def2-SV(P) level of theory.

Atom type	X	Y	Z
H	4.619941	-0.574175	-0.494122
C	3.946594	-0.538548	-1.348725
C	4.254867	-1.233037	-2.499101
H	5.181157	-1.810335	-2.551024
C	3.368284	-1.211740	-3.582370
H	3.590190	-1.778412	-4.490206
C	2.197264	-0.465907	-3.502939
H	1.513614	-0.460833	-4.353094
C	1.868118	0.272972	-2.367438
C	2.748775	0.214516	-1.259746
H	1.809063	2.199716	2.096304
C	1.095596	2.324154	1.284511
C	1.318320	1.647860	0.058466
C	0.398572	1.795874	-1.011204
C	-0.709545	2.613585	-0.808825
H	-1.427425	2.741655	-1.621011
C	-0.926867	3.271245	0.399571
H	-1.811998	3.900708	0.521534
C	-0.014140	3.123668	1.451258
H	-0.179508	3.627011	2.406395
C	0.596731	1.113970	-2.358216
C	-0.635380	0.206940	-2.571733
C	-0.650781	-1.073239	-2.002459
H	0.222061	-1.453837	-1.463152
C	-1.782074	-1.882044	-2.093196
H	-1.764059	-2.873052	-1.631184
C	-2.921643	-1.426969	-2.754196
H	-3.808935	-2.062824	-2.827416
C	-2.923957	-0.149064	-3.311443
H	-3.813490	0.226482	-3.826357
C	-1.793306	0.662510	-3.215981
H	-1.823686	1.662026	-3.657389
C	0.801821	2.187429	-3.454871
C	1.421661	3.403496	-3.137261
H	1.688564	3.627329	-2.100678
C	1.707993	4.347477	-4.122946
H	2.191009	5.288513	-3.843262
C	1.379164	4.095194	-5.453404
H	1.597755	4.836093	-6.228028
C	0.767881	2.886942	-5.785819
H	0.501950	2.672314	-6.825212
C	0.486622	1.942865	-4.798876
H	0.002413	1.007548	-5.089564
N	2.445139	0.870038	-0.080307
C	3.332123	0.693837	1.056701
C	3.017955	-0.262021	2.038439
C	3.991074	-0.430040	3.059328
C	3.782154	-1.472808	4.122853
C	5.147460	0.359009	3.082020
C	5.390318	1.328640	2.110146
H	6.293882	1.943716	2.150580
C	4.475647	1.495490	1.077304
H	4.645738	2.230724	0.285356
H	3.557645	-2.454005	3.670610
H	2.918827	-1.221448	4.763902
H	4.672633	-1.574541	4.765579
H	5.877741	0.209662	3.884393
B	1.631431	-1.073836	2.073466
C	1.459181	-2.365604	1.259479
C	0.208178	-3.044588	1.166481
C	0.065668	-4.254478	0.485798
H	-0.913143	-4.746718	0.463645
C	1.158042	-4.842726	-0.162577
H	1.033965	-5.785650	-0.703195
C	2.405508	-4.213680	-0.087564
H	3.277570	-4.666281	-0.571872
C	2.544440	-3.021873	0.613022
H	3.537449	-2.565336	0.684130
C	0.541174	-0.625184	3.065398
C	0.754319	0.355982	4.075535
H	1.739678	0.833100	4.136988
C	-0.223203	0.738053	4.986761
H	0.001970	1.502437	5.735853
C	-1.486988	0.140140	4.952465
H	-2.264666	0.423448	5.667856
C	-1.741417	-0.842611	3.989510
H	-2.720607	-1.332789	3.954556
C	-0.761591	-1.204499	3.064409
S	-1.276822	-2.355762	1.827279

Table S37. xyz -coordinates [\AA] of the $T_{LE(A)}$ geometry of DPACoSB at PBE0/def2-SV(P) level of theory.

Atom type	x	y	z
H	4.687613	-0.703863	-0.329344
C	4.109615	-0.478327	-1.226060
C	4.540264	-0.952329	-2.458601
H	5.448019	-1.561374	-2.510098
C	3.832198	-0.639506	-3.618033
H	4.169659	-0.997452	-4.594761
C	2.677029	0.132149	-3.514975
H	2.107977	0.368218	-4.418020
C	2.206465	0.601798	-2.285250
C	2.950578	0.314695	-1.120634
H	2.275039	2.547139	2.145066
C	1.677340	2.799588	1.268696
C	1.725397	1.965191	0.135408
C	0.948957	2.296833	-0.995562
C	0.197036	3.475010	-0.971181
H	-0.392275	3.738445	-1.853427
C	0.162420	4.306058	0.146299
H	-0.442018	5.217401	0.135886
C	0.901146	3.951446	1.274087
H	0.887494	4.583328	2.167464
C	0.863066	1.318314	-2.164901
C	-0.249352	0.276469	-1.880843
C	-0.181331	-1.017014	-2.417455
H	0.708559	-1.330603	-2.967855
C	-1.234999	-1.917196	-2.267308
H	-1.153471	-2.917684	-2.703409
C	-2.381422	-1.549231	-1.562742
H	-3.213072	-2.251670	-1.450742
C	-2.453518	-0.273214	-1.002918
H	-3.339206	0.030417	-0.436058
C	-1.397498	0.623822	-1.155386
H	-1.475121	1.614867	-0.702682
C	0.560271	2.083756	-3.465386
C	1.462320	3.073308	-3.888788
H	2.354324	3.275268	-3.287921
C	1.241339	3.798552	-5.054926
H	1.960747	4.564323	-5.361654
C	0.105806	3.550713	-5.831619
H	-0.070905	4.119670	-6.749621
C	-0.796571	2.572973	-5.424025
H	-1.690734	2.366526	-6.020530
C	-0.570428	1.845852	-4.250152
H	-1.292129	1.083107	-3.948657
N	2.558638	0.845237	0.109611
C	3.320808	0.516750	1.286415
C	2.853490	-0.474028	2.162136
C	3.643524	-0.757123	3.305156
C	3.197909	-1.811208	4.282943
C	4.835558	-0.060010	3.526313
C	5.274633	0.922729	2.638000
H	6.209382	1.459853	2.825952
C	4.514141	1.213526	1.512067
H	4.834834	1.979158	0.799336
H	3.085415	-2.792352	3.787962
H	2.212395	-1.562839	4.715976
H	3.918344	-1.923739	5.110585
H	5.434102	-0.291255	4.414141
B	1.487838	-1.256156	1.899001
C	1.496983	-2.577882	1.104708
C	0.312018	-3.325773	0.828686
C	0.304771	-4.528692	0.108243
H	-0.642763	-5.048161	-0.070986
C	1.502307	-5.062057	-0.377381
H	1.505291	-5.996062	-0.942820
C	2.686732	-4.367458	-0.116287
H	3.639253	-4.765478	-0.481668
C	2.680043	-3.169374	0.605385
H	3.630777	-2.662785	0.794174
C	0.177723	-0.747357	2.533463
C	0.118190	0.385174	3.378136
H	1.047662	0.921433	3.590241
C	-1.071563	0.847077	3.950494
H	-1.046818	1.735996	4.589585
C	-2.286191	0.195283	3.720851
H	-3.217030	0.555953	4.164912
C	-2.280890	-0.940112	2.904679
H	-3.212531	-1.481432	2.707595
C	-1.081399	-1.391765	2.336422
S	-1.262546	-2.816068	1.357240

Table S38. *xyz*-coordinates [Å] of the S₀ geometry of DPACpSB at PBE0/def2-SV(P) level of theory.

Atom type	X	Y	Z
H	3.833417	-0.986257	1.118631
C	3.252753	-1.242545	0.230707
C	3.792902	-2.096257	-0.725554
H	4.795032	-2.507954	-0.570440
C	3.071604	-2.411079	-1.875981
H	3.493674	-3.073502	-2.636982
C	1.790394	-1.885842	-2.036502
H	1.205450	-2.156256	-2.919421
C	1.214037	-1.047465	-1.078835
C	1.971014	-0.693318	0.057053
H	0.819459	2.546843	2.140302
C	0.223167	2.310528	1.257211
C	0.441331	1.101381	0.575275
C	-0.349904	0.788324	-0.549278
C	-1.285866	1.724992	-0.995076
H	-1.895473	1.484208	-1.869844
C	-1.484743	2.935564	-0.333114
H	-2.232017	3.645740	-0.698219
C	-0.734192	3.214189	0.807895
H	-0.882764	4.151461	1.353099
C	-0.252406	-0.620761	-1.132661
C	-1.075600	-1.581966	-0.235798
C	-0.717705	-2.930181	-0.103699
H	0.180553	-3.303902	-0.601731
C	-1.487152	-3.810083	0.657926
H	-1.181496	-4.857694	0.743416
C	-2.633782	-3.359203	1.310815
H	-3.236025	-4.047196	1.912293
C	-2.998835	-2.019110	1.191995
H	-3.894165	-1.645967	1.701063
C	-2.227670	-1.142273	0.429303
H	-2.530191	-0.094637	0.355025
C	-0.768569	-0.641834	-2.578218
C	-0.134937	0.166974	-3.535829
H	0.711095	0.791440	-3.232736
C	-0.563809	0.187337	-4.859199
H	-0.051840	0.826847	-5.585107
C	-1.643428	-0.604766	-5.259927
H	-1.983166	-0.590594	-6.300136
C	-2.281028	-1.410781	-4.321510
H	-3.128094	-2.036884	-4.618805
C	-1.846346	-1.428468	-2.992007
H	-2.360913	-2.068186	-2.271202
N	1.458467	0.209644	0.982419
C	2.106546	0.420179	2.227175
C	1.673080	-0.274706	3.356795
C	2.291705	-0.102611	4.599672
C	1.801228	-0.865716	5.801011
C	3.377688	0.793086	4.714890
C	3.800983	1.482958	3.568540
H	4.641732	2.182103	3.637835
C	3.179423	1.305821	2.332999
H	3.523016	1.852795	1.450280
H	0.950096	-1.518195	5.546825
H	1.474506	-0.181393	6.604986
H	2.599468	-1.501004	6.225997
B	4.117571	1.035150	6.092762
C	5.331226	0.160406	6.485035
C	6.040144	0.344798	7.695650
C	7.141042	-0.467665	8.024923
H	7.676155	-0.306812	8.966183
C	7.545467	-1.470258	7.157493
H	8.402342	-2.097424	7.422466
C	6.863870	-1.680796	5.950012
H	7.185495	-2.472967	5.267897
C	5.782775	-0.875216	5.632128
H	5.249425	-1.033635	4.689065
C	3.638784	2.159886	7.040393
C	2.528297	2.969131	6.700033
H	2.024246	2.775855	5.747430
C	2.068547	3.983744	7.523410
H	1.206647	4.589615	7.229664
C	2.720733	4.228073	8.740526
H	2.370403	5.027788	9.401543
C	3.813113	3.463313	9.116935
H	4.319064	3.658299	10.067815
C	4.272537	2.432880	8.275710
S	5.652582	1.558115	8.888598
H	0.830056	-0.964580	3.252035

Table S39. *xyz*-coordinates [Å] of the S_{CT} geometry of DPACpSB at PBE0/def2-SV(P) level of theory.

Atom type	X	Y	Z
H	3.525212	-1.390386	1.484034
C	2.997132	-1.640319	0.564033
C	3.494739	-2.602975	-0.292924
H	4.418389	-3.127989	-0.038716
C	2.825886	-2.883963	-1.489551
H	3.230288	-3.624555	-2.184170
C	1.629914	-2.229987	-1.796907
H	1.106219	-2.475100	-2.723499
C	1.083604	-1.279927	-0.941510
C	1.809721	-0.942342	0.233163
H	0.811373	2.403741	2.197338
C	0.219594	2.199513	1.305173
C	0.411738	0.983457	0.607396
C	-0.366569	0.686991	-0.541277
C	-1.263845	1.647762	-0.992868
H	-1.865084	1.436296	-1.879734
C	-1.426281	2.862820	-0.322300
H	-2.138220	3.599482	-0.703153
C	-0.692531	3.128060	0.838559
H	-0.826762	4.070220	1.375174
C	-0.309683	-0.704271	-1.148985
C	-1.278431	-1.627424	-0.347288
C	-1.202362	-3.020308	-0.497345
H	-0.451623	-3.463529	-1.155566
C	-2.078426	-3.866054	0.177774
H	-1.996788	-4.947924	0.037714
C	-3.047311	-3.390914	1.032405
H	-3.730321	-4.002689	1.570375
C	-3.131600	-1.959235	1.194883
H	-3.884337	-1.527501	1.860943
C	-2.256538	-1.111785	0.511704
H	-2.355919	-0.034481	0.657819
C	-0.674689	-0.641837	-2.638111
C	0.175486	0.056187	-3.509639
H	1.089879	0.517152	-3.122094
C	-0.126773	0.173124	-4.862878
H	0.551609	0.719806	-5.524644
C	-1.292892	-0.403543	-5.372333
H	-1.532709	-0.313464	-6.435885
C	-2.147442	-1.091192	-4.515202
H	-3.066030	-1.543604	-4.900400
C	-1.840801	-1.209391	-3.156134
H	-2.525717	-1.749449	-2.498230
N	1.389525	0.101880	1.029389
C	2.068609	0.352794	2.280633
C	1.556696	-0.211118	3.446614
C	2.186383	0.006095	4.676773
C	1.590468	-0.596696	5.917139
C	3.361603	0.803797	4.747953
C	3.829091	1.363594	3.542773
H	4.731656	1.982969	3.566825
C	3.209668	1.152061	2.313611
H	3.608589	1.591957	1.394589
H	0.579436	-0.996942	5.731069
H	1.537042	0.154441	6.724715
H	2.220843	-1.416653	6.305777
B	4.147968	1.066319	6.108701
C	4.849089	-0.112755	6.814735
C	5.540303	0.033113	8.051740
C	6.220468	-1.024806	8.658246
H	6.745387	-0.854775	9.604841
C	6.234129	-2.294704	8.071672
H	6.761660	-3.119567	8.559709
C	5.576672	-2.480266	6.851405
H	5.588109	-3.462343	6.366073
C	4.918828	-1.416177	6.245699
H	4.439037	-1.579314	5.274138
C	4.319631	2.509329	6.629443
C	3.828551	3.652918	5.937123
H	3.281703	3.494123	5.002109
C	3.997102	4.954250	6.393718
H	3.591426	5.791511	5.815275
C	4.680582	5.195863	7.589979
H	4.827813	6.214454	7.960895
C	5.171969	4.105866	8.315353
H	5.705158	4.273182	9.257891
C	4.983091	2.800146	7.857891
S	5.548397	1.544387	8.962282
H	0.648749	-0.820759	3.394046

Table S40. xyz -coordinates [\AA] of the $T_{\text{LE(A)}}$ geometry of DPACpSB at PBE0/def2-SV(P) level of theory.

Atom type	X	Y	Z
H	3.697000	-1.311094	1.220883
C	3.112333	-1.544174	0.329234
C	3.576760	-2.493001	-0.575466
H	4.524977	-3.002355	-0.377063
C	2.849867	-2.780962	-1.729657
H	3.213625	-3.518575	-2.450598
C	1.636352	-2.129704	-1.944708
H	1.043708	-2.376074	-2.829560
C	1.134133	-1.191838	-1.038811
C	1.901227	-0.868682	0.099798
H	1.055267	2.559519	2.019891
C	0.454882	2.349514	1.133015
C	0.560944	1.096307	0.505278
C	-0.237002	0.819378	-0.624358
C	-1.061729	1.827865	-1.129631
H	-1.675321	1.614419	-2.008777
C	-1.146939	3.079497	-0.522085
H	-1.808722	3.846871	-0.933591
C	-0.394231	3.326959	0.624878
H	-0.455197	4.296728	1.128628
C	-0.276714	-0.615409	-1.148775
C	-1.220021	-1.444493	-0.238261
C	-1.000635	-2.811318	-0.022630
H	-0.125597	-3.295943	-0.463034
C	-1.879694	-3.570462	0.750524
H	-1.680861	-4.636132	0.902377
C	-2.999747	-2.977007	1.331200
H	-3.687797	-3.570192	1.941582
C	-3.228371	-1.616403	1.129150
H	-4.099673	-1.131935	1.581231
C	-2.346875	-0.860795	0.355682
H	-2.541839	0.205531	0.216059
C	-0.757442	-0.644186	-2.606488
C	-0.024145	0.059903	-3.575649
H	0.870111	0.612682	-3.271795
C	-0.414681	0.066103	-4.910976
H	0.175134	0.623302	-5.645621
C	-1.554689	-0.635782	-5.312781
H	-1.864350	-0.632521	-6.362437
C	-2.290683	-1.338248	-4.363214
H	-3.185768	-1.893237	-4.661145
C	-1.894411	-1.341786	-3.021600
H	-2.486182	-1.899846	-2.292221
N	1.453349	0.127189	0.971787
C	2.127008	0.329794	2.216359
C	1.624420	-0.272704	3.369584
C	2.244367	-0.101868	4.612989
C	1.674315	-0.789755	5.824650
C	3.405715	0.702426	4.715278
C	3.899805	1.285101	3.534238
H	4.801751	1.905586	3.585189
C	3.279177	1.112682	2.297913
H	3.681959	1.584119	1.396465
H	0.880091	-1.502673	5.547249
H	1.241914	-0.063625	6.536998
H	2.458157	-1.340361	6.374326
B	4.147216	0.969094	6.093675
C	5.545642	0.360807	6.354126
C	6.270206	0.565618	7.569256
C	7.537103	0.016770	7.824404
H	8.033628	0.216416	8.779947
C	8.158764	-0.783166	6.861413
H	9.144526	-1.214525	7.049316
C	7.480317	-1.014747	5.662652
H	7.942041	-1.642185	4.893194
C	6.215001	-0.462153	5.421554
H	5.718595	-0.675776	4.470147
C	3.500242	1.885085	7.159929
C	2.264178	2.539791	6.963535
H	1.746482	2.393404	6.010236
C	1.680087	3.371333	7.929160
H	0.716333	3.843467	7.711984
C	2.303009	3.608722	9.156133
H	1.847072	4.255441	9.909154
C	3.536830	2.996980	9.397099
H	4.060759	3.165224	10.343978
C	4.109595	2.165588	8.421309
S	5.646477	1.507761	8.885907
H	0.728090	-0.894864	3.281716

References

- [1] H. Mubarak, W. Lee, T. Lee, J. Jung, S. Yoo, M. H. Lee, *Front. Chem.* **2020**, *8*, 538.

Manuscript I

The effect of conformational constraints and oxygen quenching on TADF in donor–acceptor systems

D. Sretenović, L. N. Kloeters, **J. M. Kaminski**, T. Böhmer, P. Schmeinck, S. Felekyan, O. Opanasyuk, G. A. Sommer, M. Chalani, G. J. Reiß, C. Janiak, C. M. Marian, R. Kühnemuth, T. J. J. Müller & C. A. M. Seidel

Manuscript in preparation for *Chemical Science*

Latest version from 21.01.2025

Contribution: Quantum chemical investigation of compounds **1-H**, **2-Me** and **3-ⁱPr** and computation of all relaxed scans, contributions to writing of results regarding the quantum chemical calculations.

The effect of conformational constraints and oxygen quenching on TADF in donor-acceptor systems

Dragana Sretenović,^[a] Laura N. Kloeters,^[b] Jeremy M. Kaminski,^[c] Tobias Böhmer,^[c] Philipp Schmeinck,^[d] Suren Felekyan,^[a] Oleg Opanasyuk,^[a] Gereon A. Sommer,^[b] Mina Chalani,^[a] Guido J. Reiß,^[d] Christoph Janiak,^[d] Christel M. Marian,^{*,[c]} Ralf Kühnemuth,^{*,[a]} Thomas J. J. Müller^{*,[b]} and Claus A. M. Seidel^{*,[a]}

- [a] Dr. D. Sretenović, Dr. S. Felekyan, Dr. O. Opanasyuk, M. Chalani,
Dr. R. Kühnemuth, Prof. Dr. C. A. M. Seidel
Institut für Physikalische Chemie
Mathematisch-Naturwissenschaftliche Fakultät
Heinrich-Heine-Universität Düsseldorf
Universitätsstr. 1, 40225 Düsseldorf, Germany
E-Mail: ralf.kuehnemuth@hhu.de, cseidel@hhu.de
- [b] Dr. L. N. Kloeters, Dr. G. A. Sommer, Prof. Dr. T. J. J. Müller
Institut für Organische Chemie und Makromolekulare Chemie
Mathematisch-Naturwissenschaftliche Fakultät
Heinrich-Heine-Universität Düsseldorf
Universitätsstr. 1, 40225 Düsseldorf, Germany
E-Mail: ThomasJJ.Mueller@uni-duesseldorf.de
- [c] J. M. Kaminski, T. Böhmer, Prof. Dr. C. M. Marian
Institut für Theoretische Chemie und Computerchemie
Mathematisch-Naturwissenschaftliche Fakultät
Heinrich-Heine-Universität Düsseldorf
Universitätsstr. 1, 40225 Düsseldorf, Germany
E-Mail: christel.marian@hhu.de
- [d] Dr. P. Schmeinck, Dr. G. J. Reiß, Prof. Dr. C. Janiak
Institut für Anorganische Chemie und Strukturchemie
Mathematisch-Naturwissenschaftliche Fakultät
Heinrich-Heine-Universität Düsseldorf
Universitätsstr. 1, 40225 Düsseldorf, Germany

Manuscript stage: In preparation for *Chemical Science*. The current version can be subjected to further changes such as adding or removing text or figures as well as author contributions.

Keywords: TADF, Fluorescence, Spectroscopy, steric effects, MRCI calculations

Abstract

To be filled in

Introduction

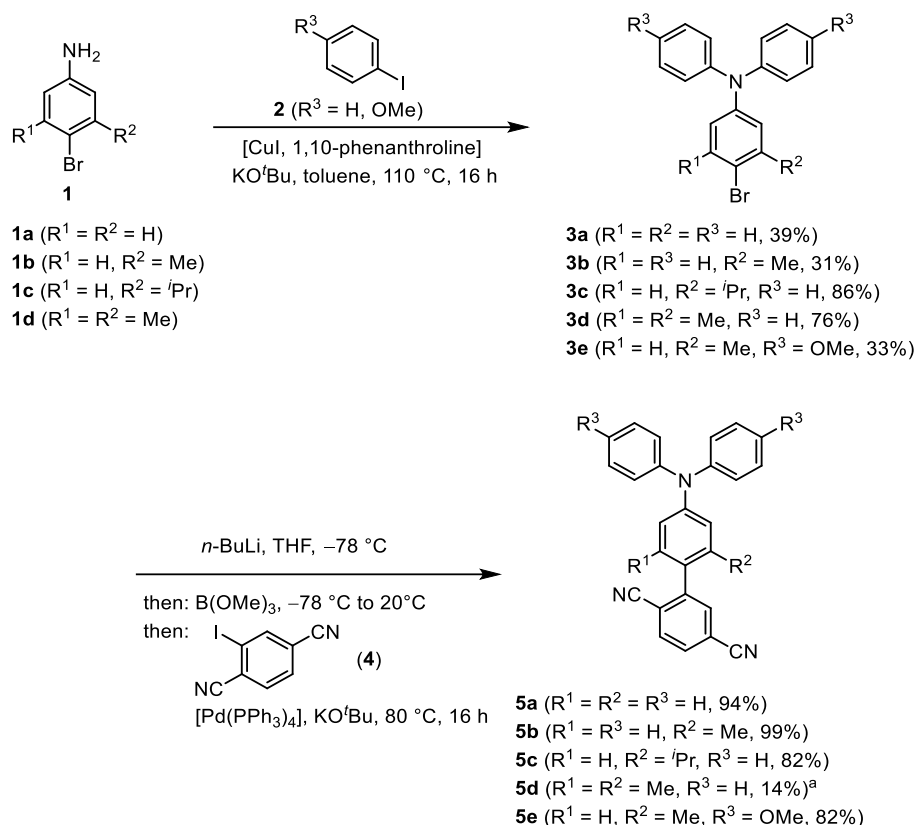
Thermally activated delayed fluorescence (TADF) has become an important design principle of metal free dyes and their applications range from non-doped organic light-emitting diodes (OLEDs),¹⁻³ over biomedicine⁴ to photocatalysis.⁵ In particular, increasing the energy efficiency of emitters in OLEDs takes enormous effort and has become the major interdisciplinary challenge for devising novel emissive molecules by synthesis, photophysics and theory.^{6, 7} One decisive key factor for enabling high internal quantum efficiency of TADF emitters is the singlet-triplet energy difference (ΔE_{ST}).⁸ Small ΔE_{ST} values allow for efficient reverse intersystem crossing (rISC) that leads to the depopulation of non-emissive triplet states T_1 into emissive singlet states S_1 . Realization of small singlet-triplet energy gaps by molecular motifs could be for example achieved in conjugated donor-acceptor systems with steric distortion.⁹ This steric distortion leads to the hole (donor) and electron (acceptor) of a conjugated donor-acceptor system and is achieved by conformational fixation, for instance in spiro systems or by bis-ortho disubstitution.

However, at complete orthogonalization of the donor and acceptor units, the emission transition dipole moment might reduce to zero, which causes a dramatic loss of emission quantum yield. Therefore, fine-tuning of ΔE_{ST} by conformational constraint of the angle between donor and acceptor parts warranting a small energy gap with a concomitant sufficiently large fluorescence rate constant appears to be an option for modulating singlet-triplet transitions.¹⁰ Besides this approach based upon conformational design, the presence of oxygen as a quencher of both singlet and triplet state might also affect the TADF characteristics of donor-acceptor dyes. Herein, we report the investigation of conformational effects on the photophysics as well as on TADF properties of a TADF system that we chose as a meaningful model.^{11, 12} Introducing substituents with different steric demand on the phenylene bridge of the reference system causes a conformational constraint in the ground state and this effect on the TADF properties is scrutinized by experimental and computational approaches. Photophysical measurements also consider the effects of oxygen quenching on the prompt and delayed fluorescence lifetimes.

Results and Discussion

Synthesis

Five donor-acceptor systems including the primordial system that already has been shown to possess TADF properties^{11, 12} are accessible by a concise two-step sequence. Starting from *para*-bromo anilines **1** and aryl iodides **2**, the brominated triphenylamine donor substrates **3** are synthesized by Ullmann coupling in the presence of catalytic amounts of copper iodide and 1,10-phenanthroline and potassium *tert*-butoxide as a base in 31–86% yield (Scheme 1).¹³ The donor substrates **3** subsequently react in a bromine-lithium exchange-borylation-Suzuki (BLEBS) sequence¹⁴ with 2-iodoterephthalonitrile (**4**) as an acceptor component to give after workup and purification by flash chromatography on silica gel the target compounds **5** in 14-99% yield.¹² While this one-pot sequence proceeds smoothly with Pd(PPh₃)₄ for monosubstituted phenyl bridges, the sterically demanding donor substrate **3d** with *ortho,ortho'*-disubstitution requires the catalyst system Pd₂(dba)₃/2-biphenyl)dicyclohexylphosphane (CyJohnPhos) and K₃PO₄ as a base in the Suzuki step to give the desired product **5d** in low yield. The molecular structures of the title compounds **5** were unambiguously assigned by comprehensive ¹H and ¹³C NMR spectroscopy and the molecular composition was determined by combustion analysis and/or mass spectrometry (see SI Chapter 1, Figures S1-S26).

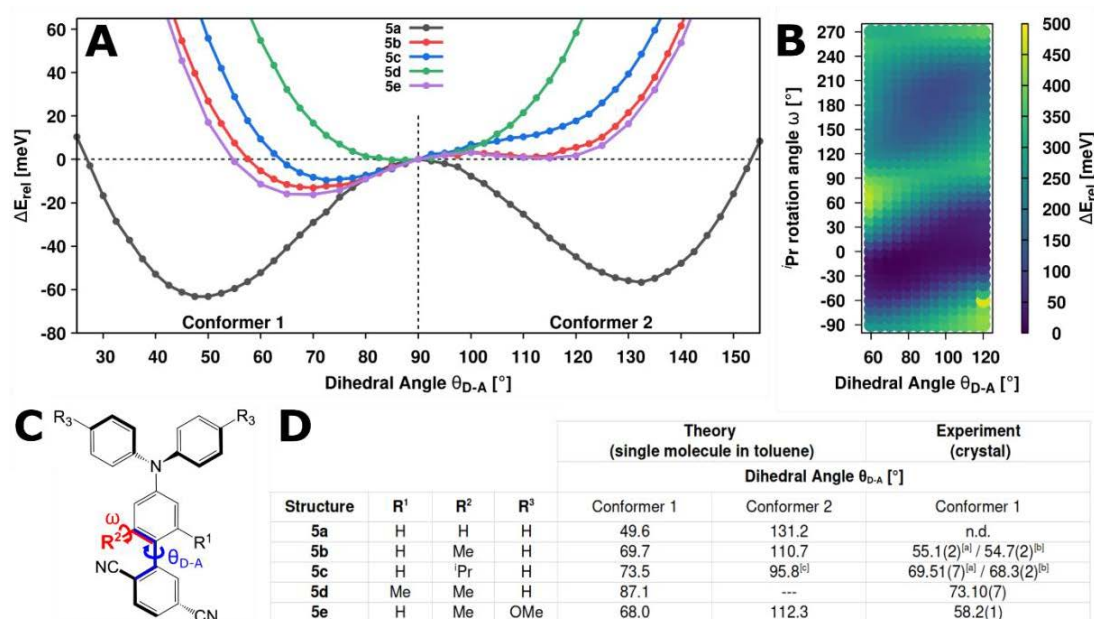


Scheme 1. Synthesis of donor-acceptor systems **5** with torsionally constrained phenylene-bridge via Ullmann arylation and one-pot bromine-lithium-exchange-borylation-Suzuki coupling (BLEBS) sequence [^aPd₂(dba)₃/2-biphenyl)dicyclohexylphosphane (CyJohnPhos) and K₃PO₄ are employed in the Suzuki step].

Geometric properties: Theory and experiment

Placing *ortho*-substituents on the phenylene bridge adjacent to the terephthalonitrile acceptor causes significant torsion of the donor-acceptor axes as seen in the crystal structure as well as from theoretical investigations (**Figure 1A, B and D**). One-dimensional relaxed KS-DFT scans of the ground-state potential energy surface along the donor-acceptor dihedral angle θ_{D-A} reveals two separate conformers for **5a**, **5b** and **5e**. A second conformer cannot be found for the corresponding relaxed scan of **5c**. Unlike for the other compounds the rotational degree of freedom for the sterically demanding isopropyl group (see ω in **Figure 1C**) has to be considered. Its steric demand possibly hinders rotation around the donor-acceptor ligating sigma bond (Figure S27). The rotational barrier was estimated from variable temperature (VT) NMR spectra (Figure S28). From the coalescence temperature ($T_c = 343$ K) the rate constant k_{T_c} and thereby the Gibbs free enthalpy of activation for rotation of the isopropyl group can be

calculated to $\Delta G_c^\ddagger = 74$ kJ/mol (for details, see SI Chapter 1.1).¹⁵ This value lies within the same order of magnitude for hindered *iso*-propyl rotations¹⁶ as well as for hindered *ortho,ortho'*-biaryl rotations.¹⁷ It can also be seen in a computed two-dimensional scan including the donor-acceptor dihedral angle and the isopropyl rotation (Figure 1B). The rotational barrier starting from the energetically most stable conformer (θ_{D-A} : 75° , ω : -5°) is computed to be marginally smaller (ca. 50 kJ/mol) than in experiment. For **5d** the donor-acceptor arrangement is nearly perpendicular, and due to the flat potential energy surface only one conformer could be confirmed.



[a] Molecule A. [b] Molecule B. See Figures S29-S33. [c] The second minimum of **5c** can only be seen in a two-dimensional scan in which θ_{D-A} and the isopropyl rotation angle ω are varied (see B).

Figure 1. **A.** One-dimensional relaxed KS-DFT scans of the ground-state potential energy surface of **5a-5e** along the donor-acceptor dihedral angle θ_{D-A} . **B.** Two-dimensional relaxed KS-DFT scan of the ground state potential energy surface of **5c** along the donor-acceptor dihedral angle θ_{D-A} including the ⁱPr rotation along rotation angle ω . **C.** General chemical structure of the investigated compounds **5a-5e**. **D.** Interplanar dihedral angles θ_{D-A} of the structures **5a-5e** from the relaxed ground-state KS-DFT scans and the crystal structure analyses (for more details, see SI Chapter 2).

The preceding experimental and theoretical investigations show that in solution and at room temperature the rotational degrees of freedom around the biaryl σ -bond are restricted and, therefore, these systems can be considered conformationally constrained in the electronic ground state.

Spectroscopy

We examined two factors influencing the photophysical properties in our study: the influence of steric torsion variations within the linker between the donor and acceptor (compound series **5a-5d**), and the increased donor strength (compound **5e**).

Compound **5a** has the smallest torsion angle, which results in the closest spatial proximity of its hole and electron densities. Thus, this compound has the highest absorption coefficient for its lowest-energy absorption maximum among all five compounds (Figure 2A). The theoretical S_0 - S_1 oscillator strengths (f) corroborates this trend (Figure 2B) of an increasing charge transfer character for compounds **5a-5d**. The theoretically predicted absorption and emission spectra are in excellent agreement with the experimental spectra (Figure 2C). From **5a** to **5d**, the increasing torsion angle leads to a more significant decoupling of the donor and acceptor, and consequently lower absorption coefficients (Figure 2D). The fluorescence emission maxima for compounds **5a-5d** in toluene are in the range of 490 nm to 500 nm. The donor variation in **5e** already significantly influences the fluorescence emission spectrum, shifting it bathochromically in comparison with its counterpart **5b** (dashed purple and red lines, respectively, Figure 2A and C).

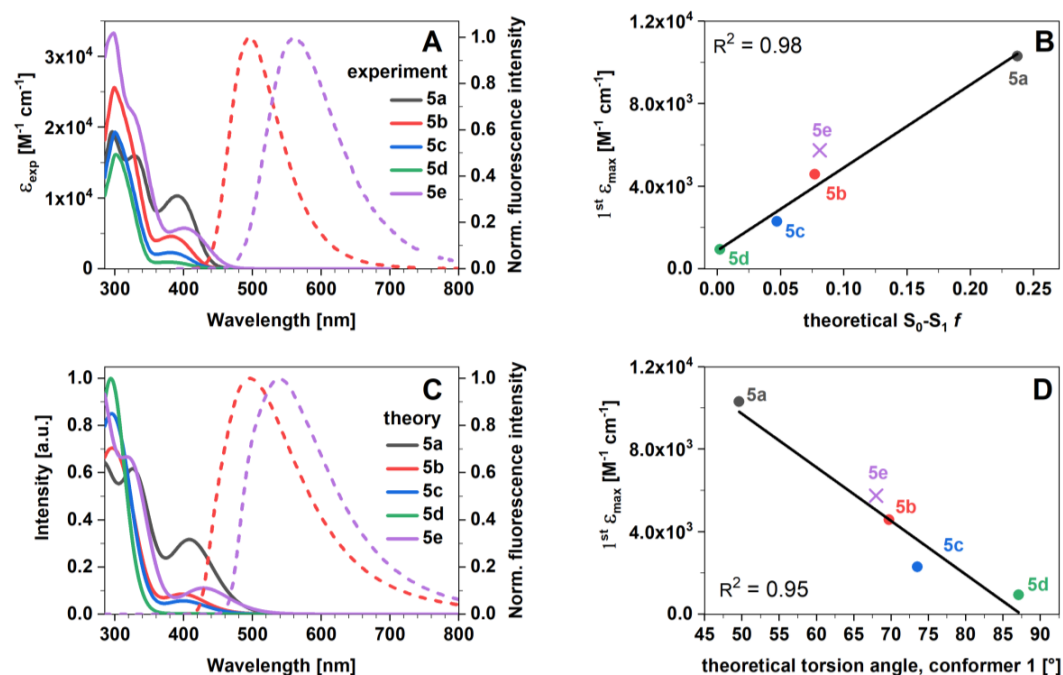


Figure 2. **A.** and **C.** *Left y-axis:* Experimental and theoretical absorption spectra of compounds **5a-5e** in toluene. The line spectra of all compounds were broadened with Gaussians of 4400 cm^{-1} . *Right y-axis:* Experimental and theoretical fluorescence emission spectra of compounds **5b** and **5e** in toluene (dashed red and purple lines, respectively). The corresponding spectra of compounds **5a**, **5c** and **5d** are similar to **5b** (see Figures S38 & S39). The range between 750 and 770 nm in the experimental spectra is excluded due to the presence of second-order diffracted excitation light. **B.** The correlation between the experimental absorption coefficient (ϵ_{exp}) and the theoretical oscillator S_0-S_1 strength f . The first absorption maximum ($1^{\text{st}} \epsilon_{\text{max}}$) was used for the correlation as it corresponds to the S_0-S_1 transition. **D.** The correlation between the first experimental absorption maximum ($1^{\text{st}} \epsilon_{\text{max}}$) and the theoretical torsion angle of conformer 1.

Both the absorption and fluorescence experimental spectra were transformed into the transition dipole moment representations¹⁸ (SI Chapter 3.1, Figure S38) to determine the 0-0 energies ($\tilde{\nu}_{00}$), the full widths at half maxima of the emission bands (emission FWHM) and the Stokes shift ($\Delta\tilde{\nu}_s$) (**Table 1**).

Table 1. Spectroscopic and photophysical parameters of compounds **5a-5e** in toluene. The wavelength maxima of the 1st and 2nd bands with the lowest absorption energies (λ_{\max}), absorption coefficients (ϵ), and fluorescence emission maxima (λ_{em}) refer to the spectra in the wavelength domain. 0-0 energies ($\tilde{\nu}_{00}$), full widths at half maxima of the emission bands (emission FWHM), and Stokes shift ($\Delta\tilde{\nu}_s$) were derived from the corrected absorption and fluorescence emission spectra (Figure S38).

Parameters (at 296 K)	5a	5b	5c	5d	5e
1 st λ_{\max} [nm]	391	382	381	377	401
1 st ϵ_{\max} [M ⁻¹ cm ⁻¹]	10309	4586	2289	941	5750
S ₀ -S ₁ f , theory [a]	0.237	0.077	0.047	0.002	0.081
λ_{em} [nm]	493	497	492	497	558
2 nd λ_{\max} [nm]	330	299	300	301	298
2 nd ϵ_{\max} [M ⁻¹ cm ⁻¹]	15979	25648	19324	16166	33333
$\tilde{\nu}_{00}$ [cm ⁻¹]	22472	22624	22676	22624	20790
Emission FWHM [cm ⁻¹]	3606	3990	3916	4106	4417
$\Delta\tilde{\nu}_s$ [cm ⁻¹]	5421	6022	6077	6385	7090
Lippert-Mataga slope [cm ⁻¹] [b]	22650	22191	24094	23810	19132 [c]
$\mu_E - \mu_G$ [D], theory [d]	19.1	22.9	22.7	24.0	25.3
$\Phi_{\text{PF}}^{\text{Air}}$ [e]	0.59	0.36	0.29	0.20	0.16
$\Phi_{\text{PF}}^{N_2}$ [f]	0.76	0.60	0.56	0.53	0.36
Φ_{DF} [g]	0.00	0.07	0.10	0.28	0.04
Φ_{TF} [h]	0.76	0.67	0.67	0.81	0.40
k_F^{SB} [10 ⁷ s ⁻¹] [i]	7.4	3.4	1.7	0.7	3.2
$\tau_F^{\text{SB Air}}$ [ns] [j]	8.0	10.6	17.0	29.1	5.1
$\tau_F^{\text{SB } N_2}$ [ns] [j]	10.3	17.6	33.0	77.1	11.6
$\langle \tau \rangle_F^{\text{Air}}$ [ns] [k]	7.3	12.3	14.7	17.5	10.8
$\langle \tau \rangle_F^{N_2}$ [ns] [k]	9.4	20.4	28.5	46.5	24.6
τ_{DF} at 296 K [μs]	-	1130	373.6	19.6	37.4

[a] Calculated S₀-S₁ oscillator strengths f . [b] See SI Chapter 3.2, Figure S40. [c] The fluorescence of **5e** was quenched in dimethylformamide and acetonitrile. These two data points were excluded from the Lippert-Mataga analysis (Figure S40E). [d] Theoretical values for the difference between the static dipole moments of the excited and ground states ($\mu_E - \mu_G$) in implicit toluene solution at DFT/MRCI level of theory. [e] The quantum yield of prompt fluorescence measured in air-saturated toluene ($\Phi_{\text{PF}}^{\text{Air}}$) was determined using the relative method with Rhodamine 6G in ethanol (air) as a reference ($\Phi_F^r = 0.94$).^{19, 20} [f] The quantum yield of prompt fluorescence for a nitrogen-purged solution ($\Phi_{\text{PF}}^{N_2}$) was calculated according to eq. 1. [g] The quantum yield of delayed fluorescence determined by TCSPC offset analysis (see SI Chapter 3.3, eqs. S11-S14). [h] The total fluorescence quantum yield calculated as $\Phi_{\text{TF}} = \Phi_{\text{PF}}^{N_2} + \Phi_{\text{DF}}$. [i] The radiative rate constants (k_F^{SB}) predicted by Strickler-Berg analysis²² (see SI Chapter 3.4). [j] The fluorescence lifetimes were estimated according to eqs. S15 and S16. [k] The fluorescence-weighted lifetimes of prompt fluorescence measured by TCSPC. Individual decay times and species fractions are compiled in SI Chapter 3.5, Tables S11-S15.

Compound **5a** had the highest fluorescence quantum yield in air-saturated toluene ($\Phi_{\text{PF}}^{\text{Air}}$) of 60%, measured relative to Rhodamine 6G in ethanol (air) as a reference ($\Phi_{\text{F}}^{\text{r}} = 0.94$).^{19, 20} To determine the prompt fluorescence quantum yield in nitrogen ($\Phi_{\text{PF}}^{N_2}$), we multiplied the quantum yield in air-saturated solution ($\Phi_{\text{PF}}^{\text{Air}}$) by the ratio of the fluorescence-weighted prompt fluorescence lifetimes in nitrogen and air, $\langle\tau\rangle_{\text{F}}^{N_2}$ and $\langle\tau\rangle_{\text{F}}^{\text{Air}}$ (eq. 1). The individual decay times and species fractions are compiled in Tables S11–S15 (SI Chapter 3.5). A significant increase in prompt fluorescence lifetime was observed in nitrogen-purged toluene solution (Figure 3A–E), indicating that singlet states are quenched to some extent by oxygen (SI Chapter 3.6.1).

$$\Phi_{\text{PF}}^{N_2} = \Phi_{\text{PF}}^{\text{air}} \cdot \frac{\langle\tau\rangle_{\text{F}}^{N_2}}{\langle\tau\rangle_{\text{F}}^{\text{Air}}} \quad 1$$

Triplet states are more sensitive to oxygen quenching than singlet states, as they have a longer lifetime and therefore the probability of collisions leading to quenching is higher.²¹ For compounds **5a–5e**, TADF was not detected in the air-saturated toluene solutions. However, in nitrogen, substantial variations in the TADF lifetimes were observed depending on the deoxygenation procedure used during sample preparation. This finding could be explained by the Stern-Volmer equation,²⁰ which predicts that for longer lifetimes small changes in quencher concentration may cause larger deviations in measured lifetimes (SI Chapter 3.6.2, Figure S46). Thus, sample preparation was one of the most challenging aspects of this study. To prevent the ingress of oxygen, all samples were stored in sealed glass ampoules after being thoroughly bubbled with nitrogen and subjected to the freeze-pump-thaw cycle (SI Chapter 3.7, Figure S47). The longest lifetimes obtained in this study are presented in Figure 3 and **Table 1**. To confirm the temperature dependence of the delayed fluorescence of compounds **5b–5e**, we conducted a series of time-resolved measurements in liquid solutions in a temperature range from 180 K to 300 K (Figure 3G–J), considering the melting point of toluene at 178.1 K (see SI Chapter 3.8). Time-resolved emission spectra of compounds **5b–5e** as additional evidence for TADF can be found in SI Chapter 3.9 (Figure S50).

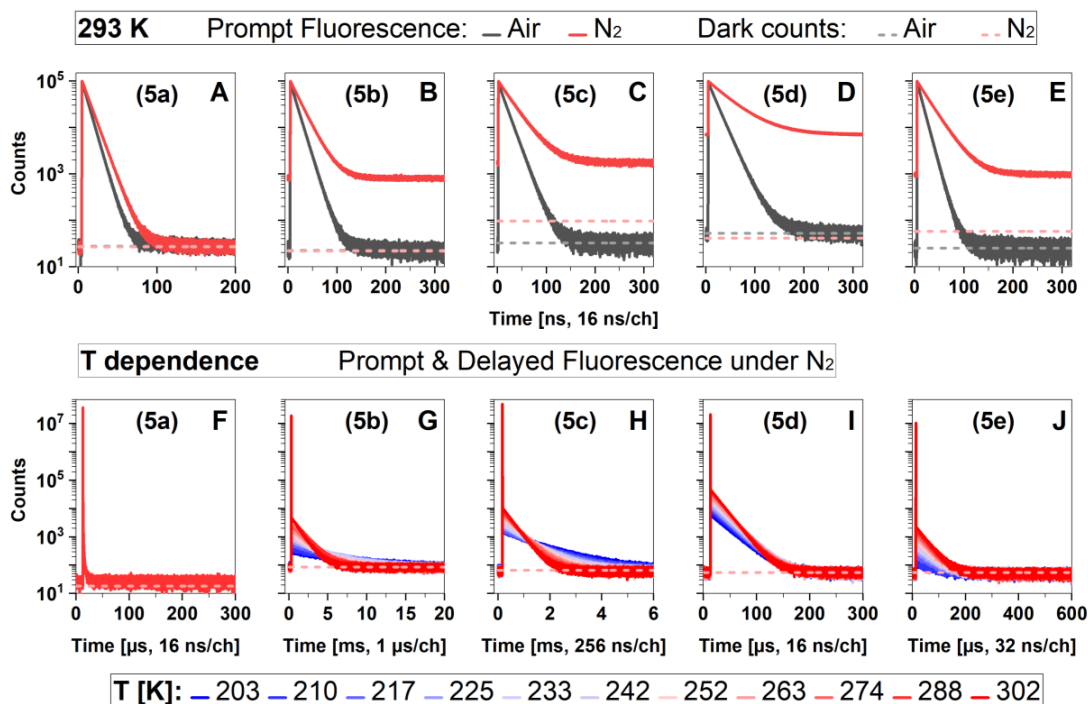


Figure 3. A-E: Prompt fluorescence of compounds **5a-5e** in air-saturated and nitrogen-purged solutions in toluene measured by TCSPC. F-J: Prompt and delayed fluorescence of compounds **5a-5e** in nitrogen-purged toluene solutions. The counts corresponding to the dark count rate of the detector (93 Hz) are indicated by a light grey or light red dashed line for air-saturated or nitrogen-purged solutions, respectively. The measurement conditions are described in detail in the Experimental Section.

Compound **5a** did not exhibit TADF under these conditions (Figure 3F). As the torsion angle increases from **5b** to **5d**, the quantum yield and the amplitude of TADF increase, and the TADF lifetime becomes shorter. This study presents an effective design strategy for improving TADF properties in compounds by fine-tuning the steric torsion at the donor-acceptor linker and ensuring a substantial spatial separation between hole and electron densities.

Compound **5e**, despite possessing nearly identical torsion angle as **5b** (Figure 1D), demonstrates enhanced TADF features due to its increased donor strength. However, due to the very low prompt fluorescence quantum yield of **5e**, compound **5b** remains brighter under nitrogen where both prompt and delayed fluorescence are operative (see Φ_{TF} in Table 1).

Kinetic model

The simplest model, consistent with theoretical predictions for this class of fluorophores,¹¹ is a three-state system with small energy gap between the excited S₁ and T₁ states. The corresponding rate matrix (eq. S22) has been solved analytically and yields relaxation times for prompt and delayed fluorescence, $1/k_p$ and $1/k_d$, respectively (eqs. S23 and S24). These two observables are not sufficient to independently determine all rate constants involved in this kinetic scheme. Tsuchiya *et al.*²³ presented an approach to incorporate quantum yields, in particular the relative fraction of the delayed fluorescence, $P_d = F_d/(F_p+F_d)$, as additional independent observable for each temperature. Assuming negligible direct relaxation of T₁ to the ground state, i.e., $k_{r_T} + k_{nr_T} \equiv k_T \ll k_{rISC}$, three primary rate constants (k_{ISC} , k_{rISC} and $k_S \equiv k_{rad_S} + k_{IC_S}$) now are readily available:

$$k_{rISC} = k_d(1 - P_d)^{-1} \quad 2$$

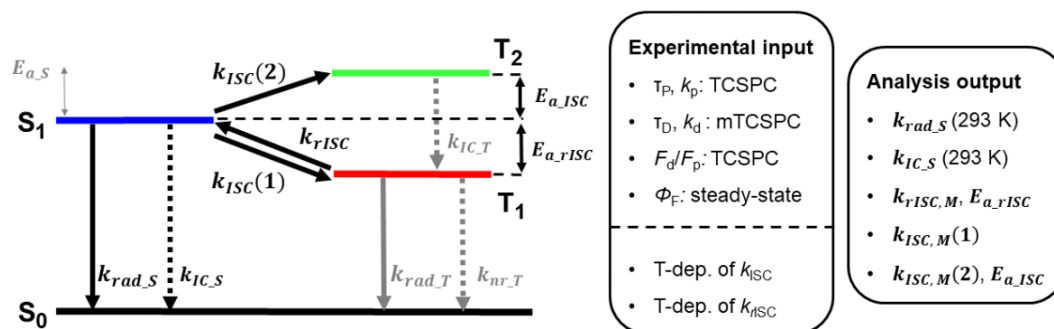
$$k_{ISC} = k_p P_d - k_d((P_d)^{-1} - 1)^{-1} \quad 3$$

$$k_{rad_S} + k_{IC_S} = k_S = k_p(1 - P_d) \quad 4$$

The disregard of k_T is justified by the observed temperature dependence of k_{rISC} (see Figure 4). The Marcus plots show no indication for the appearance of a second process depopulating T₁ at low temperatures. This would have to be expected since k_T is assumed to have a much smaller temperature dependence than k_{rISC} and should dominate the T₁ depopulation in that temperature range.

The derived intersystem crossing rates, $k_{ISC}(T)$, of compound **5b-5e** showed a clear increase with rising temperatures (Figure 4), indicating an activated process. Thus, we postulate an expanded kinetic model by adding a transition to a higher triplet state T₂ (Scheme 2).

Assuming $k_{IC_T} \gg k_{ISC}(2)$ this system behaves like a pseudo three-state system with $k_{ISC} = k_{ISC}(1) + k_{ISC}(2)$.



Scheme 2. 4-state system. *Experimental input:* The temperature-dependence of k_{ISC} and k_{rISC} were not directly obtained from the measurements. *Assumptions:* (i) Negligible direct relaxation of T1 to the ground state, i.e., $k_{rad,T} + k_{nr,T} \equiv k_T \ll k_{rISC}$; and (ii) Internal conversion from T2 to T1 is a very fast process, i.e., $k_{IC,T} \gg k_{ISC}(2)$. Thus, this system behaves like a pseudo three-state system. *Analysis output:* $k_{rad,S}$ and $k_{IC,S}$ follow the Arrhenius approach, while k_{rISC} and k_{ISC} are described using Marcus theory (denoted with a subscript 'M'). The activation energy $E_{a,ISC}$ always refers to the energy required for intersystem crossing from the S1 to T2 state, as no activation energy is required for intersystem crossing from S1 to T1. For further details, see equations 5-9.

Marcus & Arrhenius plots

Rate constants related to spin conversion processes are often described using Marcus theory.²⁴ For the rate constants of reverse intersystem crossing and intersystem crossing, we obtain:

$$k_{rISC} = \frac{k_{0,rISC}}{\sqrt{T}} e^{-(E_{a,rISC})/kT} \quad 5$$

$$\Rightarrow k_{rISC}\sqrt{T} = k_{0,rISC} e^{-(E_{a,rISC})/kT} \quad 6$$

and

$$k_{ISC} = \frac{k_{ISC,M}(1)}{\sqrt{T}} + \frac{k_{0,ISC,M}(2)}{\sqrt{T}} e^{-(E_{a,ISC}(2))/kT} \quad 7$$

$$\Rightarrow k_{ISC}\sqrt{T} = k_{ISC,M}(1) + k_{0,ISC,M}(2) e^{-(E_{a,ISC}(2))/kT}, \quad 8$$

respectively. The sums of the radiative and nonradiative rates from S1 to the ground state are described by an Arrhenius type approach:

$$k_{rad,S} + k_{IC,S} = k_S = k_{0,S} e^{-(E_{a,S})/kT} \quad 9$$

The temperature dependence of the rate constants described by the Marcus and Arrhenius approach (see equations 5-9) are shown Figure 4. The final primary kinetic parameters resulting from fits to the corresponding Marcus and Arrhenius plots are given in Table 2.

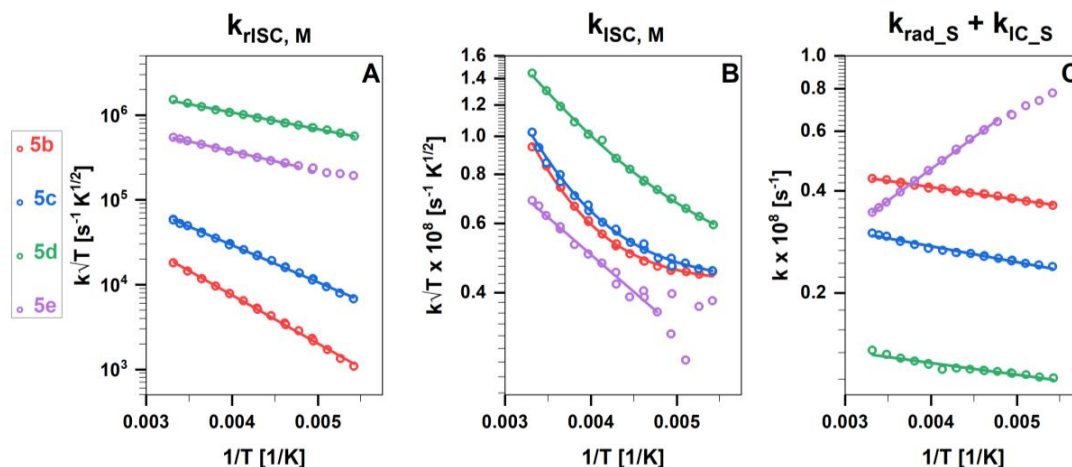


Figure 4. Temperature dependence of k_{rISC} (Panel **A**) and k_{ISC} (Panel **B**) is analysed using the Marcus approach (subscript 'M', see equations 5-8). Panel **C** shows the sum of radiative and nonradiative rate constants from S_1 to the ground state ($k_{rad,S} + k_{IC,S}$) based on the Arrhenius approach (eq. 9). The raw data can be found in SI Chapter 3.8, Figure S48 and Tables S17-S20. Data for compound **5e** below 220 K was excluded from the fits due to increased noise levels caused by aggregation (see Figure S52).

Table 2. The final primary kinetic parameters obtained from the fits shown in Figure 4. See equations 5-9 for further details.

Compound		5b	5c	5d	5e
$k_{ISC}(1)$	$[10^6 \text{ s}^{-1} \text{ K}^{1/2}]$	42.4 ± 0.4	42.6 ± 0.8	40 ± 2	0 (fixed)
$k_{0_ISC}(2)$	$[10^9 \text{ s}^{-1} \text{ K}^{1/2}]$	13 ± 3	6 ± 2	1.4 ± 0.2	0.29 ± 0.02
$E_{a_ISC,M}(2)$	[meV]	142 ± 5	122 ± 6	67 ± 3	38 ± 2
k_{0_rISC}	$[10^6 \text{ s}^{-1} \text{ K}^{1/2}]$	1.45 ± 0.09	1.64 ± 0.07	6.5 ± 0.2	3.19 ± 0.09
$E_{a_rISC,M}$	[meV]	113 ± 2	86.7 ± 0.8	39.0 ± 0.5	46.2 ± 0.6
k_{0_S}	$[10^6 \text{ s}^{-1}]$	57.5 ± 0.4	42.2 ± 0.7	17.2 ± 0.4	8.3 ± 0.1

E_{a_S}	[meV]	7.3 ± 0.2	9.3 ± 0.3	7.0 ± 0.5	-37.0 ± 0.3
k_{ISC} (296 K)	$[10^6 \text{ s}^{-1}]$	5.27	5.55	8.02	3.81
k_{rISC} (296 K)	$[10^3 \text{ s}^{-1}]$	0.99	3.18	82.6	29.6
k_{rad_S} (296 K)	$[10^6 \text{ s}^{-1}]$	29.0	19.6	11.2	14.3
k_{IC_S} (296 K)	$[10^6 \text{ s}^{-1}]$	14.3	9.7	1.9	21.2

With increasing steric hindrance from **5b** to **5d** we observe a reduction of the activation energies for intersystem crossing and reverse intersystem crossing, $E_{a_{ISC}}$ and $E_{a_{rISC}}$ respectively, while the activation energy E_{a_S} is very similar for all three compounds (Figure 4).

To prove the necessity of a 4-state model, we conducted relaxed TDDFT scans of the energy profiles of the first excited singlet and triplet states along the torsional coordinate. Figure 5 presents relaxed S_1 (first row) and T_1 (second row) scans, along with the corresponding static dipole moments (third row). The results obtained using DFT/MRCI are summarized in so-called state diagrams (fourth row). For compounds **5b** (left column), **5d** (middle column) and **5e** (right column), it is evident that the minima of the triplet states occur at significantly lower dihedral angles compared to the singlet states. As expected, the energy gap between the lowest excited CT states decreases when the donor and acceptor moieties are arranged orthogonally.

However, the results from the relaxed T_1 scans require a more detailed analysis. Notably, the static dipole moments of the triplet states exhibit significant changes near an orthogonal orientation of the donor and acceptor moieties. Between 85 and 95°, a state switch occurs, leading to the LE(TPN) triplet state becoming the lowest in energy. The DFT/MRCI state diagrams further corroborate this finding, clearly showing that for compounds **5b** and **5d**, the states switch, with the locally excited triplet state having its minimum geometry at 90°. In contrast, for compound **5e**, due to the increased donor strength, the CT and LE regimes are too energetically separated for such a state switch to occur.

From both a theoretical and experimental perspective, the application of a 4-state model is essential for accurately describing these systems.

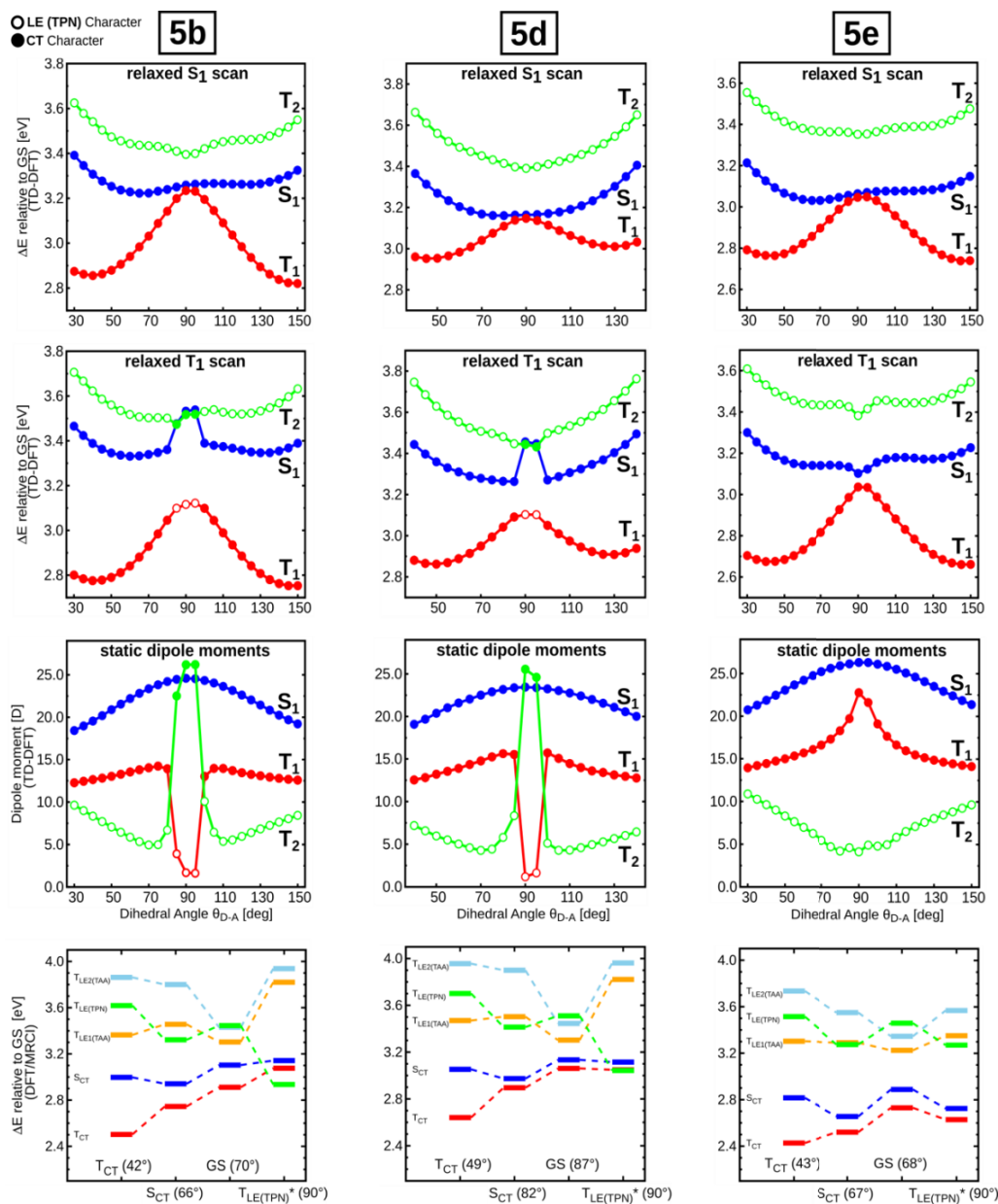


Figure 5. Relaxed scans of the lowest excited singlet and triplet state potential energy surface (S₁: first row, T₁: second row) as well as the static dipole moments of S₁, T₁ and T₂ states (third row) along the donor-acceptor dihedral angles for compound **5b**, **5d** and **5e** computed at TD-DFT level of theory. A change between CT (solid circles) and LE(TPN) character (hollow circles) can be observed close to orthogonality for compound **5b** and **5d**. Energy level diagrams comprising the vertical excitation energies for various excited states at different optimized geometries (x-axis) of compound **5b**, **5d** and **5e** computed at DFT/MRCI level of theory (fourth row). The * denotes that this geometry is not a minimum geometry but was optimized with a restricted dihedral angle between the donor and acceptor.

Discussion of kinetic parameters

From Figure 5 bottom panels we can extract the vertical energy differences between the lowest excited S_{CT} and T_{LE} states that are used to compute the rate constants using Marcus theory. We illustrated the influence of the steric constraints on these vertical energies from compound **5b** to compound **5d** (Figure 6A). From the resulting scheme we can estimate the transition barrier for the ISC process ($S_{CT} \rightarrow T_{LE}$) which decreases within the series. This agrees nicely with the experimental values (E_{a_ISC}) given in Table 2.

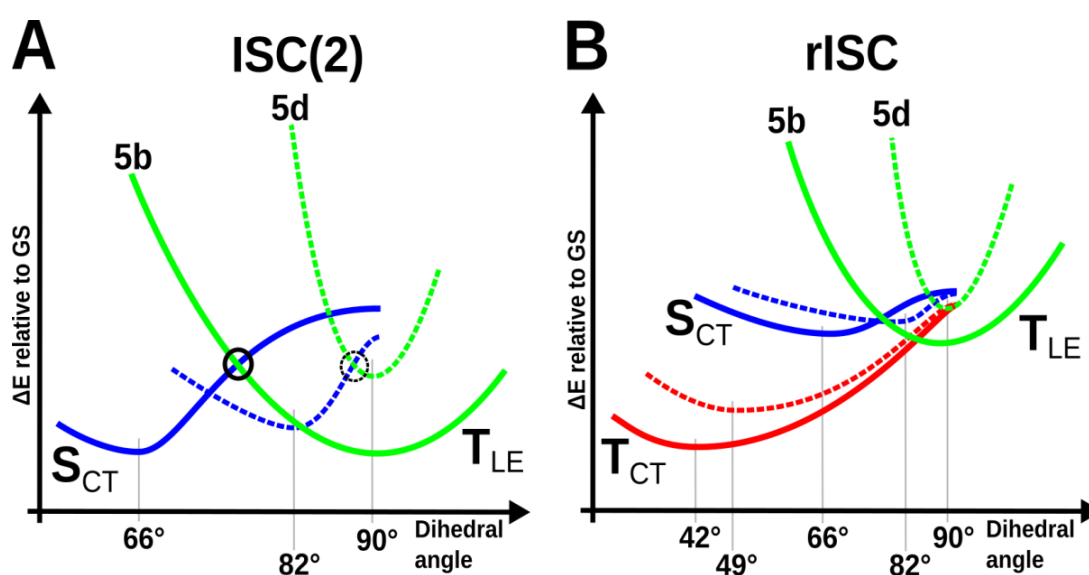


Figure 6. **A:** Schematic picture of the potential energy surfaces (PES) of S_{CT} and T_{LE} according to Marcus theory for **5b** (solid line) and **5d** (dashed line). The crossing point of the PES is an estimate for the transition barrier for (r)ISC process and is encircled in black. **B:** Schematic picture of the potential energy surfaces of S_{CT} , T_{CT} and T_{LE} involved in the excited-state decay pathway of **5b**.

Due to large geometrical changes one cannot simply draw a Marcus-like picture to understand the corresponding rISC process. Within a separate theoretical study of these systems²⁵ we conclude that the rISC process is strongly dependent on the dihedral angle and that it can only occur if donor and acceptor are aligned nearly perpendicularly to each other. In that region we see a strong correlation between the lowest excited CT states and the lowest excited LE state.

Discussion of previously published data on **5b**

The photophysical behaviour of compound **5b** has been investigated previously in Ref. 11. The general observation of TADF could only be confirmed qualitatively, the exact numbers for rate constants of ISC and rISC, k_{ISC} and k_{rISC} , and their dependence on temperature differ substantially in the current study. We have clear evidence that this deviation is caused by triplet quenching by residual oxygen in the previous measurements. A simple model assuming diffusion-controlled quenching was applied to simulate the effect (see Figure S51). Adding triplet quenching to the kinetic system will add an extra channel to depopulate the triplet and thus increase the apparent k_{rISC} , as reported. At the same time the temperature dependence of that rate will change, since the apparent activation energy for rISC ($E_{a,rISC}$) will now be affected by the temperature dependent diffusion coefficient of **5b** and O₂. We were able to quantitatively reproduce the published data and explain all experimental discrepancies using this approach (see SI Chapter 3.11).

Conclusion

To be filled in

Experimental Section

Spectroscopic conditions

Absorption spectra were measured on a Cary 4000 UV-Vis spectrophotometer (Agilent Technologies, USA), while fluorescence spectra were recorded on a Horiba Fluorolog FL3-22 spectrophotometer. Time-resolved measurements were conducted with a fluorescence lifetime and steady-state spectrometer FT300 (PicoQuant, Germany) equipped with a ColdEdge cryostat powered by a Sumitomo CH-204 cold head and HC-4E Helium compressor (Cryoandmore, Germany). Temperatures were regulated by a temperature controller, Model 335 (Lake Shore Cryotronics, USA), using a silicon diode sensor at the cold head. Sample temperatures were measured independently with a second diode (Model 540 group B, Scientific Instruments, USA; accuracy: ± 0.5 K) and used for all analyses. All samples were measured in UV Quartz Type Hellma QS 221.001 Fluorescence Cuvette Cells with an extension made of Quartz/Duran glass mixture. The light path was 10 mm. For the steady-state and time-resolved measurements in the nanosecond time regime, samples were excited with a supercontinuum laser excitation source (EXW-12 with EXTEND-UV spectral extension unit, NKT Photonics, Denmark). An excitation wavelength of 375 nm was set by tuning the frequency doubler. Time-correlated single photon counting (TCSPC) was achieved with HydraHarp 400 electronics (PicoQuant, Germany). The repetition rate was 4.88 MHz for **5a**, and 3.12 MHz for **5b-5e**. The time bin was 16 ps. For the time-resolved measurements in the microsecond and millisecond time ranges, samples were excited with a modulated continuous wave diode laser (Cobolt 375 nm MLD laser, Series 06-01, Hübner Photonics, Germany). In both cases, the excitation wavelength was 375 nm. A TCSPC and MCS board, Time Harp 260 (PicoQuant, Germany), provided photon counting and timing. The repetition rates were: 3.33 kHz for **5a** and **5d**, 0.05 kHz for **5b**, 0.15 kHz for **5c**, and 1.67 kHz for **5e**. The bin sizes were 16 ns for **5a** and **5d**, 1 μ s for **5b**, 256 ns for **5c**, and 32 ns for **5e**. Signal detection was achieved with a hybrid PMT detector (PMA Hybrid 40, PicoQuant, Germany). Emission was detected under magic angle conditions. The detection wavelength was 490 nm for compounds **5a-5d**, and 560 nm for **5e**. All time-resolved measurements were conducted with a scripted measurement routine.

Analysis of time- and temperature-resolved data

Prompt (ns) fluorescence decays

A multi-exponential model function was fitted to the data using Python based custom software (Pyfia) applying an iterative reconvolution procedure. The instrumental function (IRF) was acquired measuring scattered light off a diluted Ludox[®] solution. Almost always three decay components were needed to fit the data (see SI), the fastest decay reflecting the highly quenched fluorescence of the aggregates (see below). The second fastest fraction (average photon fraction 1-2 %) is most likely due to a small portion of less quenched species. This was found in **5b-5d**. The remaining prompt fluorescence of the monomers was found to be monoexponential.

Delayed (μ s & ms) fluorescence decays

To extract decay parameters from the time-resolved delayed fluorescence experiments a custom written LabView based batch routine was applied to fit a biexponential model function to the data. The short lifetime component represents the prompt fluorescence, broadened by the resolution of the experimental set-up ($\tau \approx 2 \mu$ s) and was not further processed. The delayed fluorescence of the monomers was found to be monoexponential.

Offset analysis

The well-separated decay times for prompt and delayed fluorescence allowed for determination of the relative delayed fraction in the ns-decays by calculating the virtually constant offset generated by the delayed signal. Here only the dark count rate of the detector of 93 Hz needed to be considered. For more details, see SI chapter 3.3.2.

Computational Details

Molecular geometries and vibrational frequencies were determined with Gaussian 16²⁶ employing the optimally tuned, range-separated ω B97X-D density functional^{27,28} and the split-valence double zeta def2-SV(P) basis set.²⁹⁻³¹ The optimal tuning procedure followed the scheme recommended in Ref. 32, yielding a value of $\omega=0.15$ for the range separation parameter. Geometries of singlet excited states were optimized with time-dependent density functional theory (TDDFT).³³⁻³⁵ For triplet states, the Tamm-Dancoff approximation (TDA)³⁶ was employed. The polarizable continuum model (PCM)³⁷⁻³⁹ was utilized to mimic the toluene solvent environment using the solvent excluding surface (SES) implemented in Gaussian 16. Excitation energies and excited-state properties were determined with the combined density functional theory and multireference configuration interaction (DFT/MRCI) method⁴⁰⁻⁴² using the tight R2016⁴³ parameter set. More detailed quantum chemical investigations of the emitter series were conducted in Ref. 25.

References

1. Y.-Z. Shi, H. Wu, K. Wang, J. Yu, X.-M. Ou and X.-H. Zhang, *Chemical Science*, 2022, **13**, 3625-3651.
2. X.-K. Chen, D. Kim and J.-L. Brédas, *Accounts of Chemical Research*, 2018, **51**, 2215-2224.
3. C. Adachi, *Japanese Journal of Applied Physics*, 2014, **53**, 060101.
4. F. Fang, L. Zhu, M. Li, Y. Song, M. Sun, D. Zhao and J. Zhang, *Advanced Science*, 2021, **8**, 2102970.
5. M. A. Bryden and E. Zysman-Colman, *Chemical Society Reviews*, 2021, **50**, 7587-7680.
6. S.-J. Zou, Y. Shen, F.-M. Xie, J.-D. Chen, Y.-Q. Li and J.-X. Tang, *Materials Chemistry Frontiers*, 2020, **4**, 788-820.
7. J. Bauri, R. B. Choudhary and G. Mandal, *Journal of Materials Science*, 2021, **56**, 18837-18866.
8. M. Zheng, Y. Li, Y. Wei, L. Chen, X. Zhou and S. Liu, *The Journal of Physical Chemistry Letters*, 2022, **13**, 2507-2515.
9. Paras, A. Dhiman and C. N. Ramachandran, *Chemical Physics Letters*, 2022, **801**, 139711.
10. P. Stachelek, J. S. Ward, P. L. Dos Santos, A. Danos, M. Colella, N. Haase, S. J. Raynes, A. S. Batsanov, M. R. Bryce and A. P. Monkman, *ACS Appl Mater Interfaces*, 2019, **11**, 27125-27133.
11. G. A. Sommer, L. N. Mataranga-Popa, R. Czerwieniec, T. Hofbeck, H. H. H. Homeier, T. J. J. Müller and H. Yersin, *The Journal of Physical Chemistry Letters*, 2018, **9**, 3692-3697.
12. W. Haselbach, J. M. Kaminski, L. N. Kloeters, T. J. J. Müller, O. Weingart, C. M. Marian, P. Gilch and B. E. Nogueira de Faria, *Chemistry*, 2023, **29**, e202202809.
13. C. Sambigao, S. P. Marsden, A. J. Blacker and P. C. McGowan, *Chemical Society Reviews*, 2014, **43**, 3525-3550.
14. A. W. Franz and T. J. J. Müller, *Synthesis*, 2008, **2008**, 1121-1125.
15. J. Sandström, *Dynamic NMR Spectroscopy*, Academic Press, 1982.
16. E. Rochlin and Z. Rappoport, *The Journal of Organic Chemistry*, 1994, **59**, 3857-3870.
17. M. S. Sundar, G. Singh, R. S. Ampapathi and A. V. Bedekar, *Journal of Molecular Structure*, 2017, **1147**, 495-501.
18. W. W. Parson, *Modern optical spectroscopy*, Springer, 2007.
19. M. Fischer and J. Georges, *Chemical Physics Letters*, 1996, **260**, 115-118.
20. J. Lakowicz, *University of Maryland School of Medicine Baltimore*, 2006, **132**.
21. H. Kautsky, *Transactions of the Faraday Society*, 1939, **35**, 216-219.
22. S. J. Strickler and R. A. Berg, *The Journal of Chemical Physics*, 1962, **37**, 814-822.
23. Y. Tsuchiya, S. Diesing, F. Bencheikh, Y. Wada, P. L. dos Santos, H. Kaji, E. Zysman-Colman, I. D. W. Samuel and C. Adachi, *The Journal of Physical Chemistry A*, 2021, **125**, 8074-8089.

24. Y. Tsuchiya, K. Mizukoshi, M. Saigo, T. Ryu, K. Miyata, K. Onda and C. Adachi, *Faraday Discussions*, 2024, **250**, 233-250.
25. J. M. Kaminski, T. Böhmer and C. M. Marian, *The Journal of Physical Chemistry C*, 2024, **128**, 13711-13721.
26. M. J. Frisch, G. W. Trucks, H. B. Schlegel, G. E. Scuseria, M. A. Robb, J. R. Cheeseman, G. Scalmani, V. Barone, G. A. Petersson, H. Nakatsuji, X. Li, M. Caricato, A. V. Marenich, J. Bloino, B. G. Janesko, R. Gomperts, B. Mennucci, H. P. Hratchian, J. V. Ortiz, A. F. Izmaylov, J. L. Sonnenberg, Williams, F. Ding, F. Lipparini, F. Egidi, J. Goings, B. Peng, A. Petrone, T. Henderson, D. Ranasinghe, V. G. Zakrzewski, J. Gao, N. Rega, G. Zheng, W. Liang, M. Hada, M. Ehara, K. Toyota, R. Fukuda, J. Hasegawa, M. Ishida, T. Nakajima, Y. Honda, O. Kitao, H. Nakai, T. Vreven, K. Throssell, J. A. Montgomery Jr., J. E. Peralta, F. Ogliaro, M. J. Bearpark, J. J. Heyd, E. N. Brothers, K. N. Kudin, V. N. Staroverov, T. A. Keith, R. Kobayashi, J. Normand, K. Raghavachari, A. P. Rendell, J. C. Burant, S. S. Iyengar, J. Tomasi, M. Cossi, J. M. Millam, M. Klene, C. Adamo, R. Cammi, J. W. Ochterski, R. L. Martin, K. Morokuma, O. Farkas, J. B. Foresman and D. J. Fox, *Journal*, 2016.
27. J.-D. Chai and M. Head-Gordon, *The Journal of Chemical Physics*, 2008, **128**.
28. J.-D. Chai and M. Head-Gordon, *Physical Chemistry Chemical Physics*, 2008, **10**, 6615-6620.
29. A. Schäfer, H. Horn and R. Ahlrichs, *The Journal of Chemical Physics*, 1992, **97**, 2571-2577.
30. F. Weigend and R. Ahlrichs, *Physical Chemistry Chemical Physics*, 2005, **7**, 3297-3305.
31. F. Weigend, *Physical Chemistry Chemical Physics*, 2006, **8**, 1057-1065.
32. O. S. Bokareva, G. Grell, S. I. Bokarev and O. Kühn, *Journal of Chemical Theory and Computation*, 2015, **11**, 1700-1709.
33. E. Runge and E. K. U. Gross, *Physical Review Letters*, 1984, **52**, 997-1000.
34. M. Marques and E. Gross, *Lecture Notes in Physics*, 2003, **620**, 144-184.
35. F. Furche and R. Ahlrichs, *The Journal of Chemical Physics*, 2002, **117**, 7433-7447.
36. S. Hirata and M. Head-Gordon, *Chemical Physics Letters*, 1999, **314**, 291-299.
37. R. Cammi, S. Corni, B. Mennucci and J. Tomasi, *The Journal of Chemical Physics*, 2005, **122**.
38. J. Tomasi, B. Mennucci and R. Cammi, *Chemical Reviews*, 2005, **105**, 2999-3094.
39. G. Scalmani, M. J. Frisch, B. Mennucci, J. Tomasi, R. Cammi and V. Barone, *The Journal of Chemical Physics*, 2006, **124**.
40. S. Grimme and M. Waletzke, *The Journal of Chemical Physics*, 1999, **111**, 5645-5655.
41. C. M. Marian, A. Heil and M. Kleinschmidt, *WIREs Computational Molecular Science*, 2019, **9**, e1394.
42. M. Kleinschmidt, C. M. Marian, M. Waletzke and S. Grimme, *The Journal of Chemical Physics*, 2009, **130**.
43. I. Lyskov, M. Kleinschmidt and C. M. Marian, *The Journal of Chemical Physics*, 2016, **144**.

SUPPLEMENTARY INFORMATION

The effect of conformational constraints and oxygen quenching on TADF in donor-acceptor systems

Dragana Sretenović,^[a] Laura N. Kloeters,^[b] Jeremy M. Kaminski,^[c] Tobias Böhmer,^[c] Philipp Schmeinck,^[d] Suren Felekyan,^[a] Oleg Opanasyuk,^[a] Gereon A. Sommer,^[b] Mina Chalani,^[a] Guido J. Reiß,^[d] Christoph Janiak,^[d] (Christel M. Marian,^{*[c]} Ralf Kühnemuth,^{*[a]} Thomas J. J. Müller^{*[b]} and Claus A. M. Seidel^{*[a]})

[a] Dr. D. Sretenović, Dr. S. Felekyan, Dr. O. Opanasyuk, M. Chalani,
Dr. R. Kühnemuth, Prof. Dr. C. A. M. Seidel
Institut für Physikalische Chemie
Mathematisch-Naturwissenschaftliche Fakultät
Heinrich-Heine-Universität Düsseldorf
Universitätsstr. 1, 40225 Düsseldorf, Germany
E-Mail: ralf.kuehnemuth@hhu.de, cseidel@hhu.de

[b] Dr. L. N. Kloeters, Dr. G. A. Sommer, Prof. Dr. T. J. J. Müller
Institut für Organische Chemie und Makromolekulare Chemie
Mathematisch-Naturwissenschaftliche Fakultät
Heinrich-Heine-Universität Düsseldorf
Universitätsstr. 1, 40225 Düsseldorf, Germany
E-Mail: ThomasJJ.Mueller@uni-duesseldorf.de

[c] J. M. Kaminski, T. Böhmer, Prof. Dr. C. M. Marian
Institut für Theoretische Chemie und Computerchemie
Mathematisch-Naturwissenschaftliche Fakultät
Heinrich-Heine-Universität Düsseldorf
Universitätsstr. 1, 40225 Düsseldorf, Germany
E-Mail: christel.marian@hhu.de

[d] Dr. P. Schmeinck, Dr. G. J. Reiß, Prof. Dr. C. Janiak
Institut für Anorganische Chemie und Strukturchemie
Mathematisch-Naturwissenschaftliche Fakultät
Heinrich-Heine-Universität Düsseldorf
Universitätsstr. 1, 40225 Düsseldorf, Germany

Manuscript stage: In preparation for *Chemical Science*. The current version can be subjected to further changes such as adding or removing text or figures as well as author contributions.

The results included in this Supplementary Information are limited to the spectroscopic and theoretical data necessary for a proper understanding of the manuscript. Information on the synthesis and crystallographic data of **5b** is already available in the original publication by Sommer *et al.*²⁹

Table of Contents

Chapter 1. Spectroscopy.....	3
1.1 Absorption and Steady-State Fluorescence Emission Spectra.....	3
1.2 Lippert-Mataga analysis.....	4
1.3 Delayed fluorescence quantum yields	8
1.3.1 Approach with the steady-state data.....	8
1.3.2 Approach with the time-resolved data (offset analysis).....	9
1.4 Strickler-Berg analysis.....	9
1.5 Analysis of prompt fluorescence decays	10
1.6 Oxygen quenching	15
1.6.1 Singlet quenching by oxygen.....	15
1.6.2 Triplet quenching by oxygen	17
1.7 Deoxygenation procedure	18
1.8 Temperature dependence of delayed fluorescence	20
1.9 An additional proof for TADF: TRES measurements.....	25
1.10 Rate matrix and solution.....	26
1.11 Discussion of previously published data on 5b.....	26
1.12 Aggregation at lower temperatures	28
Chapter 2. Analytical solution of kinetics for 3-state system (S_0, S_1, T_1).....	29
Chapter 3. Quantum Chemical Computations	35
Chapter 4. References.....	41

Chapter 1. Spectroscopy

1.1 Absorption and Steady-State Fluorescence Emission Spectra

Absorption and fluorescence spectra were redrawn in wavenumber scale ($\tilde{\nu}$). The absorption spectra were corrected by dividing the extinction coefficient by the wavenumber: $\epsilon(\tilde{\nu})/\tilde{\nu}$, and the fluorescence spectra by dividing the fluorescence intensity by $\tilde{\nu}^3$.¹² Subsequently, both the corrected absorption and fluorescence spectra were normalized to their respective maximum (Figure S1).

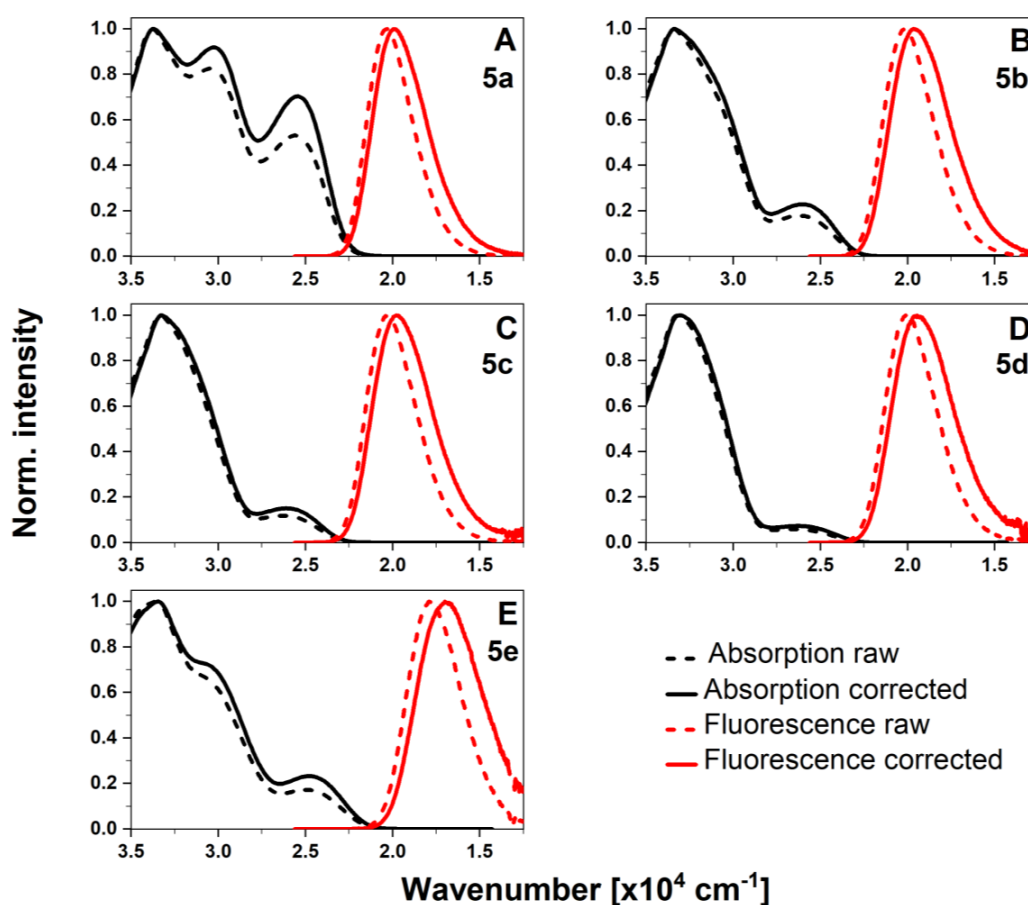


Figure S1. Absorption and fluorescence emission spectra of compounds **5a-5e** presented with and without corrections for comparison.

We derived several values from the corrected steady-state spectra, including the 0-0 energy ($\tilde{\nu}_{00}$), the full width at half maximum (FWHM) of the emission band, Stokes shift ($\Delta\tilde{\nu}_s$),

and radiative rate constants calculated according to the Strickler-Berg method (k_F^{SB}). All estimated values are compiled in Table 1 of the main text. The 0-0 energies ($\tilde{\nu}_{00}$) were determined as the intersection point between the corrected absorption and fluorescence emission spectra and ranged from 22472 cm⁻¹ (**5a**) to 22676 cm⁻¹ (**5c**). To calculate the FWHM of the emission band, we measured the distance in wavenumber units between two points with a normalized intensity of 0.5. The Stokes shift was determined as the distance between the first absorption maxima and the fluorescence maxima. To find the first absorption maximum, we deconvoluted the absorption spectra using a Gaussian fit. The calculated Stokes shift increased from 5421 cm⁻¹ for **5a** to 6385 cm⁻¹ for **5d**. These Stokes shift values were used in the Lippert-Mataga analysis^{13, 14} (Figure S3).

1.2 Lippert-Mataga analysis

Lippert-Mataga analysis is based on the Lippert-Mataga equation (eq. S1).^{13, 14}

$$\bar{\nu}_A - \bar{\nu}_F = \frac{2}{hc} \frac{(\mu_E - \mu_G)^2}{r^3} \cdot \Delta f + constant \quad \text{eq. S1}$$

In this equation, $\tilde{\nu}_A$ and $\tilde{\nu}_F$ represent the wavenumbers (cm⁻¹) of the absorption and emission, h is Planck's constant, c the speed of light, μ_G and μ_E indicate the dipole moments of the ground and excited states, and r corresponds to the radius of the cavity in which the fluorophore is situated.¹⁵ The orientation polarizability is defined as:

$$\Delta f = \frac{\varepsilon - 1}{2\varepsilon + 1} - \frac{n^2 - 1}{2n^2 + 1} \quad \text{eq. S2}$$

where ε is the dielectric constant, and n is the refractive index of the solvent.

Table S1. The solvents employed in this study with their corresponding refractive indexes (n), dielectric constants (ϵ) and calculated orientation polarizabilities (Δf) according to eq. S2.

Solvent	n	ϵ	Δf
Toluene	1.496	2.38	0.014
Methyl <i>tert</i> -butyl ether (MTBE)	1.369	2.60	0.074
Anisole	1.517	4.33	0.112
Chlorobenzene	1.525	5.62	0.143
Ethyl Acetate	1.372	6.08	0.201
THF	1.407	7.58	0.210
DCM	1.424	8.93	0.217
DMF	1.431	36.7	0.274
Acetonitrile	1.344	37.5	0.305

To generate Lippert-Mataga plots (Figure S3), we determined the difference of the absorption and emission maxima in wavenumbers by measuring the respective spectra of compounds **5a-5e** in toluene, methyl *tert*-butyl ether (tBuMeEther), anisole, chlorobenzene, ethyl acetate, tetrahydrofuran (THF), dichloromethane (DCM), dimethylformamide (DMF), and acetonitrile (MeCN). The measurements revealed a positive solvatochromic effect (Figure S2), typically associated with charge-transfer states and TADF.

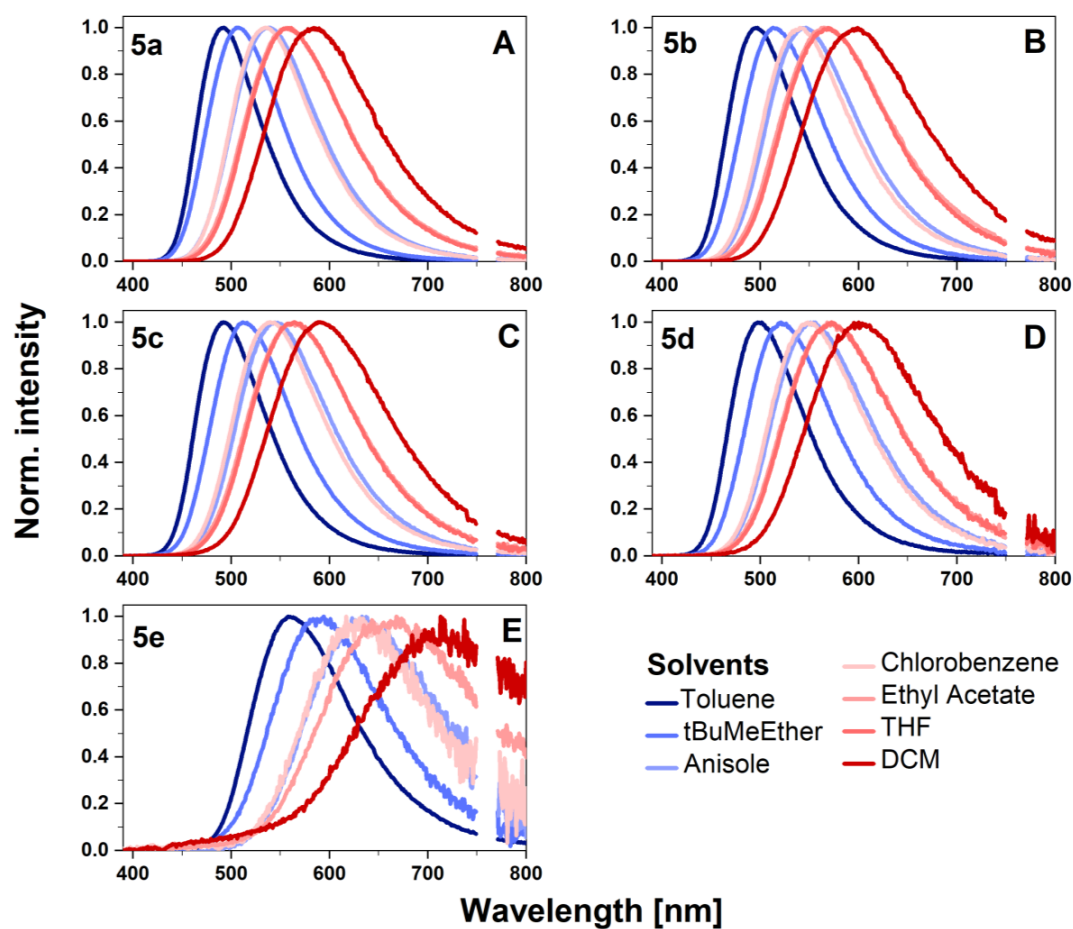


Figure S2. Fluorescence emission spectra of **5a-5e** (A-E) in the solvents indicated in the legend. Samples were excited at 375 nm. The range between 750 and 770 nm is excluded due to the presence of second-order diffracted excitation light.

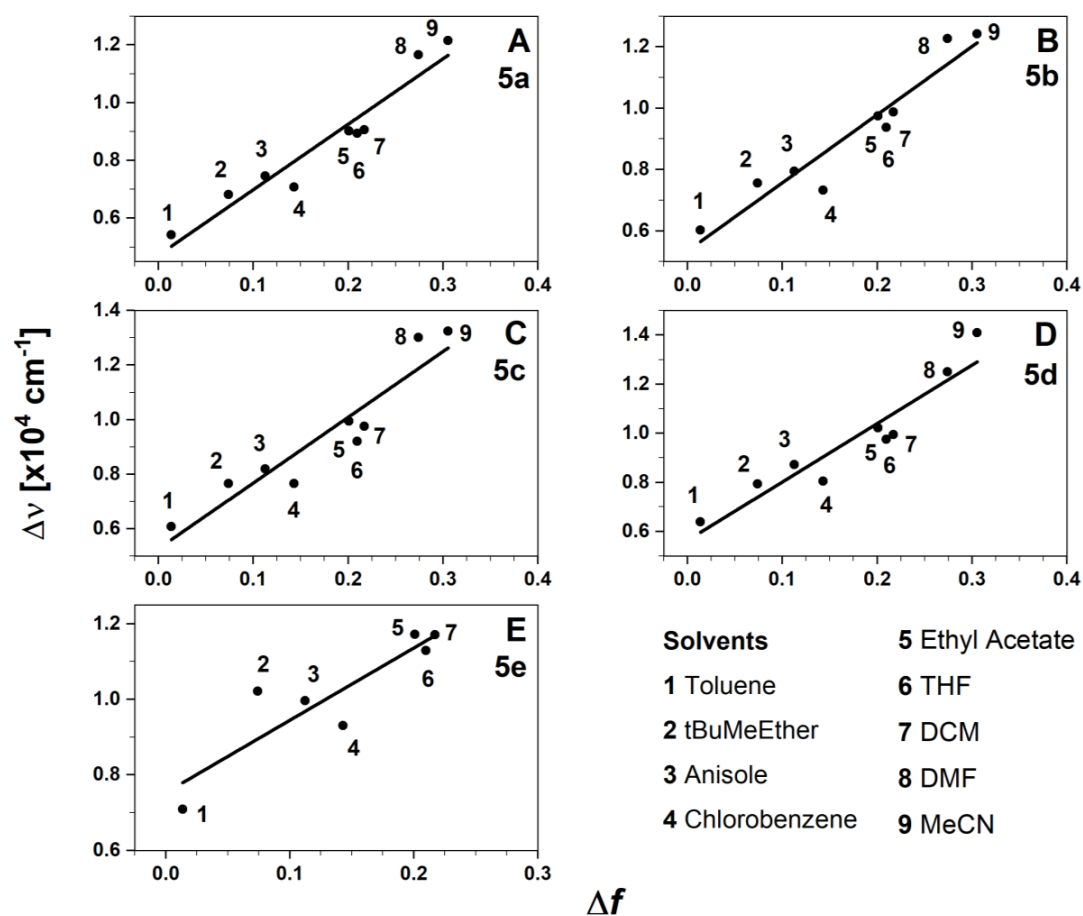


Figure S3. Lippert-Mataga diagrams for compounds **5a-5e** (A-E). The solvents used are marked with the numbers 1-9 and indicated in the legend. A linear regression is applied and the slopes are listed in Table S2. The Lippert-Mataga diagram of compound **5e** does not include DMF and MeCN, as the fluorescence is quenched in these solvents.

From the slope of the linear regression $\Delta\tilde{\nu}$ against Δf (Figure S3), the difference between the dipole moments of the ground and excited states can be estimated (eq. S3).

$$\mu_E - \mu_G = \Delta\mu = \sqrt{\frac{\text{slope} \cdot hc \cdot r^3}{2}} \quad \text{eq. S3}$$

However, it is evident that the assumption of a spherical molecular shape is not valid for compounds **5a-5e**, and as a result, the calculated $\Delta\mu$ values do not accurately reflect reality. To

estimate the molecular radius, we used the theoretically predicted $\Delta\mu$ values, along with the slopes obtained from the Lippert-Mataga analysis (see Table S2).

Table S2. Estimation of molecular radius based on the slopes obtained from the Lippert-Mataga analysis (Figure S3) and the theoretically predicted $\Delta\mu$ values.

	5a	5b	5c	5d	5e
Slope [cm⁻¹], exp.	22650	22191	24094	23810	19132
$\mu_E - \mu_G$ [D], theory	19.1	22.9	22.7	24.0	25.3
r (needed to get theory values) [Å]	5.5	6.2	6.0	6.2	7.0

1.3 Delayed fluorescence quantum yields

1.3.1 Approach with the steady-state data

One approach to determine the delayed fluorescence quantum yield (Φ_{DF}) uses steady-state data. In an air-saturated solution, only prompt fluorescence is observed due to the quenching of triplet states by oxygen. In a nitrogen-purged solution, both prompt and delayed fluorescence are operative. Thus, the integral of the steady-state fluorescence spectrum in air is proportional to Φ_{PF} , while in nitrogen is $\Phi_{PF} + \Phi_{DF}$.¹⁶ However, the quantum yield of delayed fluorescence cannot be simply calculated as the difference between the steady-state fluorescence integrals in air and nitrogen as indicated in Ref. 16, since singlet states are also quenched by oxygen to a certain extent (see Table 1). The increase in the steady-state emission signal in nitrogen is therefore not only due to the delayed fluorescence, but also to the enhanced prompt fluorescence. To obtain an estimate of the delayed fluorescence quantum yield, it is important to consider the prompt fluorescence quantum yield in nitrogen ($\Phi_{PF}^{N_2}$, see eq. 1 of the main text) and not in air (Φ_{PF}^{air}) in the context of the total fluorescence emission in absence of oxygen (Φ_{TF}), eq. S4.

$$\Phi_{TF} = \Phi_{PF}^{N_2} + \Phi_{DF} \quad \text{eq. S4}$$

The delayed fluorescence quantum yield is calculated from the eq. S5.

S8

$$\Phi_{DF} = \Phi_{TF} - \Phi_{PF}^{air} \cdot \frac{\langle \tau \rangle_F^{N_2}}{\langle \tau \rangle_F^{Air}} \quad \text{eq. S5}$$

1.3.2 Approach with the time-resolved data (offset analysis)

Another method to assess the quantum yields of delayed fluorescence involves integrating the time-resolved decays recorded within the nanosecond time range (Table 1). The region within the decay offset in nitrogen is important because it contains long lifetime components such as delayed fluorescence (eq. S6 and eq. S7). The quantum yield of delayed fluorescence is estimated by comparing the TCSPC decay offsets obtained under air and nitrogen in the nanosecond time range (see eq. S8 and eq. S9).

$$offset (Air) = dark\ counts + afterpulses \quad \text{eq. S6}$$

$$offset (N_2) = dark\ counts + afterpulses + F_{DF} \quad \text{eq. S7}$$

$$F_{DF} = \int offset (N_2) - \int offset (Air) \quad \text{eq. S8}$$

$$\Phi_{DF} = \frac{F_{DF}}{F_{PF}} \cdot \Phi_{PF}^{N_2} \quad \text{eq. S9}$$

where F_{DF} and F_{PF} are the integral fractions of delayed and prompt fluorescence.

1.4 Strickler-Berg analysis

The radiative rate constants (k_F^{SB}) were determined using the Strickler-Berg method,¹⁷ by integrating the absorption and fluorescence spectra. To compute the absorption integral, we focused on the absorption band with the lowest energy, identifying it through comparison with the corresponding corrected fluorescence spectrum. This fluorescence spectrum was mirrored at the 0-0 energy point and scaled to match the height of the corrected absorption spectrum.¹⁸ The calculated rate constants decreased from $7.4 \cdot 10^7\ s^{-1}$ for **5a** to $0.7 \cdot 10^7\ s^{-1}$ for **5d**. Furthermore, fluorescence lifetimes (τ_F^{SB}) were estimated based on the radiative rate constant, accounting for the fluorescence quantum yields (eq. S10 and eq. S11, Table 1).

$$\tau_F^{\text{SB air}} = \frac{\phi_{\text{PF}}^{\text{air}}}{k_F^{\text{SB}}} \quad \text{eq. S10}$$

$$\tau_F^{\text{SB } N_2} = \frac{\phi_{\text{PF}}^{N_2}}{k_F^{\text{SB}}} \quad \text{eq. S11}$$

However, the calculated lifetime values do not agree well with those measured by TCSPC, presumably due to the non-Condon effect.^{19, 20} As the torsion angle increases in the series **5a**-**5d**, the discrepancies in lifetimes also grow, ranging from 9% for **5a** to 66% for **5d**.

1.5 Analysis of prompt fluorescence decays

A bi-exponential fit function is applied to characterize the experimental TCSPC data. Each emissive species is presented with its fraction (x_i) and lifetime (τ_i). Species-averaged lifetime $\langle\tau\rangle_x$ (eq. S12) and intensity-weighted lifetime $\langle\tau\rangle_F$ (eq. S13) are given, as well as the reduced χ^2 value as a measure of the goodness of the fit. The value $\chi^2 = 1$ is obtained with an optimal fit.

$$\langle\tau\rangle_x = \sum_{i=1}^2 x_i \tau_i \quad \text{eq. S12}$$

$$\langle\tau\rangle_F = \frac{\sum_{i=1}^2 x_i \tau_i^2}{\sum_{i=1}^2 x_i \tau_i} \quad \text{eq. S13}$$

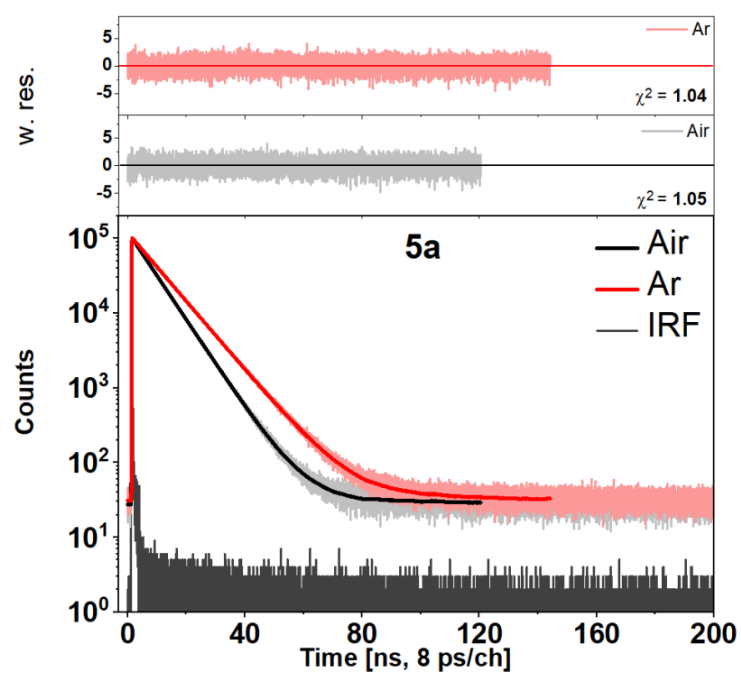


Figure S4. Prompt fluorescence of compound **5a** in air-saturated and nitrogen-purged solutions in toluene measured by TCSPC. Lifetime fit results with fixed lifetime fractions are shown in Table S3.

Table S3. Prompt fluorescence lifetime fit for compound **5a** with fixed lifetime fractions.

5a	x_1	τ_1 [ns]	x_2	τ_2 [ns]	$\langle\tau\rangle_x$ [ns]	$\langle\tau\rangle_F$ [ns]	χ^2
Air	0.96	7.37	0.04	0.76	7.09	7.34	1.05
Ar	0.96	9.44	0.04	0.17	9.06	9.44	1.04

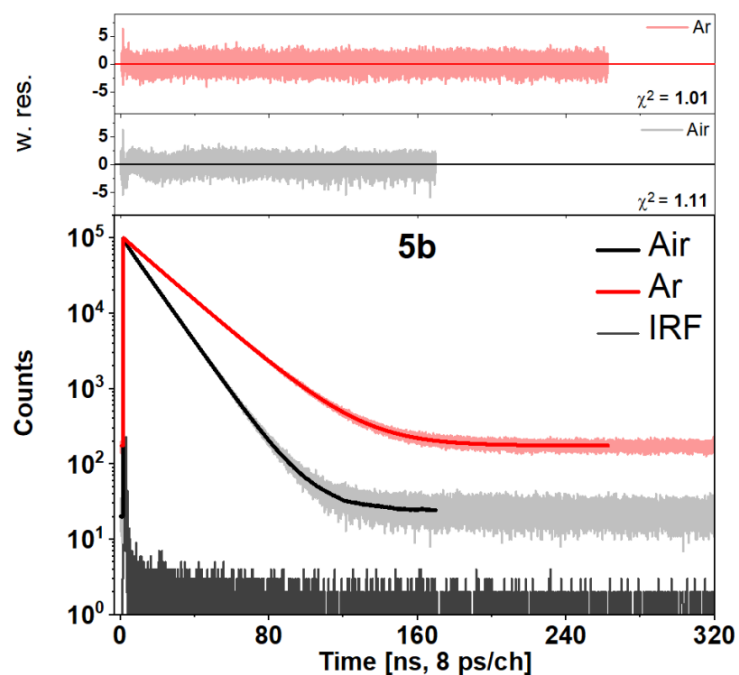


Figure S5. Prompt fluorescence of compound **5b** in air-saturated and nitrogen-purged solutions in toluene measured by TCSPC. Lifetime fit results with fixed lifetime fractions are shown in Table S4.

Table S4. Prompt fluorescence lifetime fit of compound **5b** with fixed lifetime fractions.

5b	x_1	τ_1 [ns]	x_2	τ_2 [ns]	$\langle\tau\rangle_x$ [ns]	$\langle\tau\rangle_F$ [ns]	χ^2
Air	0.89	12.46	0.11	1.50	11.22	12.29	1.11
Ar	0.89	20.91	0.11	14.83	20.23	20.41	1.01

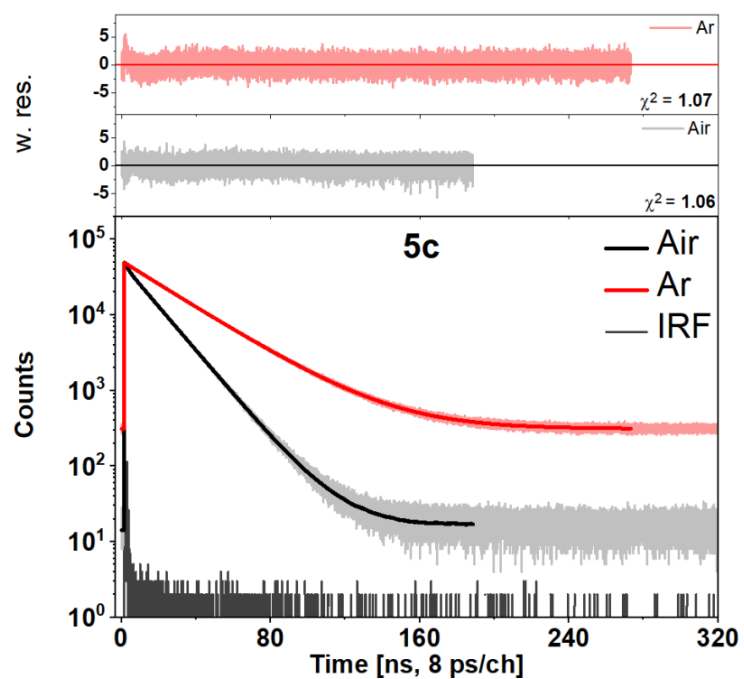


Figure S6. Prompt fluorescence of compound **5c** in air-saturated and nitrogen-purged solutions in toluene measured by TCSPC. Lifetime fit results with fixed lifetime fractions are shown in Table S5.

Table S5. Prompt fluorescence lifetime fit of compound **5c** with fixed lifetime fractions.

5c	x_1	τ_1 [ns]	x_2	τ_2 [ns]	$\langle\tau\rangle_x$ [ns]	$\langle\tau\rangle_F$ [ns]	χ^2
Air	0.85	14.96	0.15	1.66	13.01	14.71	1.06
Ar	0.85	29.40	0.15	21.09	28.18	28.49	1.07

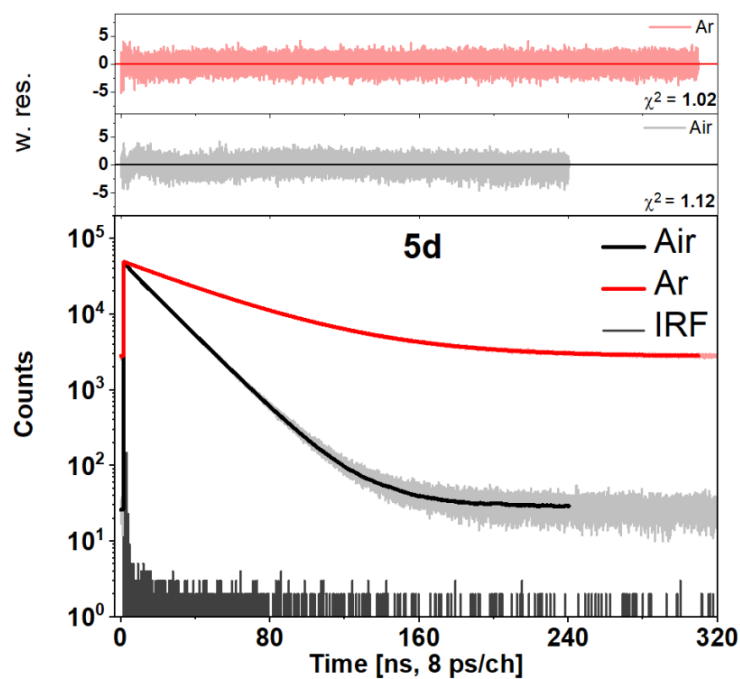


Figure S7. Prompt fluorescence of compound **5d** in air-saturated and nitrogen-purged solutions in toluene measured by TCSPC. Lifetime fit results with fixed lifetime fractions are shown in Table S6.

Table S6. Prompt fluorescence lifetime fit of compound **5d** with fixed lifetime fractions.

5d	x_1	τ_1 [ns]	x_2	τ_2 [ns]	$\langle\tau\rangle_x$ [ns]	$\langle\tau\rangle_F$ [ns]	χ^2
Air	0.90	17.74	0.10	2.22	16.20	17.53	1.12
Ar	0.90	47.64	0.10	30.74	45.96	46.52	1.02

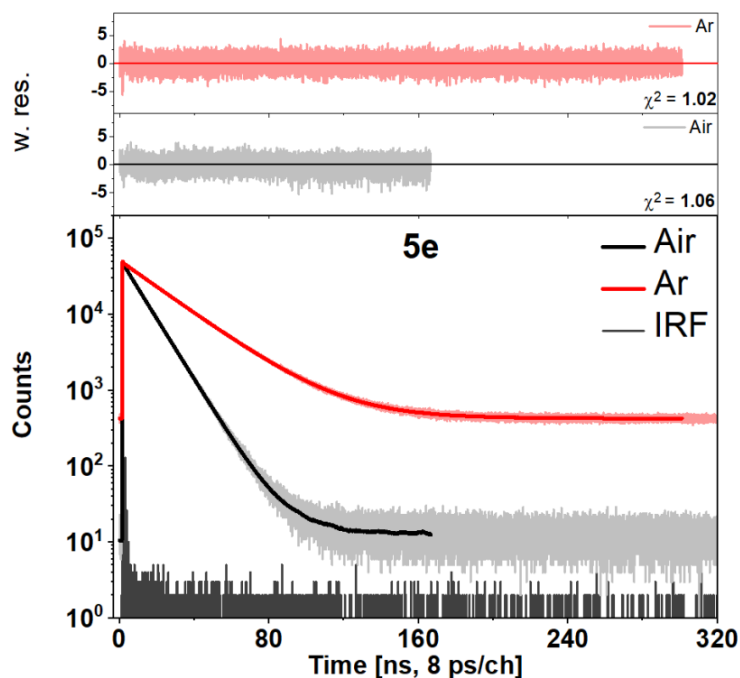


Figure S8. Prompt fluorescence of compound **5e** in air-saturated and nitrogen-purged solutions in toluene measured by TCSPC. Lifetime fit results with fixed lifetime fractions are shown in Table S7.

Table S7. Prompt fluorescence lifetime fit of compound **5e** with fixed lifetime fractions.

5e	x_1	τ_1 [ns]	x_2	τ_2 [ns]	$\langle\tau\rangle_x$ [ns]	$\langle\tau\rangle_F$ [ns]	χ^2
Air	0.91	10.87	0.09	0.95	9.94	10.78	1.06
Ar	0.91	24.60	0.09	0.39	22.34	24.56	1.02

1.6 Oxygen quenching

1.6.1 Singlet quenching by oxygen

By applying the Stern-Volmer equation (eq. S14), we predicted the prompt fluorescence lifetimes in air-saturated solutions [$\langle\tau\rangle^{\text{Air}}$] based on the measured prompt fluorescence lifetimes under nitrogen [$\langle\tau\rangle^{\text{N}_2}$] and a quenching constant derived from diffusion ($k_{q,\text{diff.}}$), since oxygen quenching is a diffusion-controlled process.²¹ The predicted and measured air-saturated prompt fluorescence lifetimes are in excellent agreement (Table S8).

$$\langle \tau \rangle^{\text{air}} = \frac{\langle \tau \rangle^{N_2}}{1 + k_{q,\text{diff.}} \cdot \langle \tau \rangle^{N_2} \cdot [\text{O}_2]} \quad \text{eq. S14}$$

The oxygen concentration $[\text{O}_2]$ in toluene is 1.8 mM at 20 °C and an O_2 partial pressure of 0.213 bar.²² The quenching constant ($k_{q,\text{diff.}}$) is calculated according to eq. S15.

$$k_{q,\text{diff.}} = 4\pi N_A (r_{\text{dye}} + r_{\text{O}_2}) (D_{\text{dye}} + D_{\text{O}_2}) \quad \text{eq. S15}$$

where N_A is the Avogadro constant, r_{dye} and r_{O_2} are the radii of the fluorescent dye and oxygen, and D_{dye} and D_{O_2} are the diffusivities of the fluorescent dye and oxygen, respectively. The dye radius, r_{dye} , is estimated in *PyMol* and via time-resolved anisotropy. The oxygen diffusivity in toluene is $D_{\text{O}_2} = 4.38 \cdot 10^{-9} \text{ m}^2/\text{s}$.²³ The dye diffusivity, D_{dye} , is calculated using eq. S16.

$$D_{\text{dye}} = \frac{k_B T}{6\pi\eta r_{\text{dye}}} \quad \text{eq. S16}$$

where k_B is the Boltzmann constant, T is the temperature, η is the toluene viscosity.

Finally, the quenching constant derived from diffusion is $k_{q,\text{diff.}} = 2.1 \cdot 10^{10} \text{ M}^{-1} \text{ s}^{-1}$.

Furthermore, we calculated the experimental quenching constants, $k_{q,\text{exp}}$, by using the measured lifetimes, and they are quite similar for all four compounds (around $2 \cdot 10^{10} \text{ M}^{-1} \text{ s}^{-1}$, Table S8) and in good agreement with the previously determined $k_{q,\text{diff.}}$.

Table S8. Predicted air-saturated prompt fluorescence lifetimes by the Stern-Volmer equation (eq. S14) and experimental quenching constants ($k_{q,\text{exp}}$) for compounds **5a-5d**. The species-averaged lifetimes, $\langle \tau \rangle_x$ are used. The ratio of predicted to the measured air-saturated prompt fluorescence lifetimes is equal to 1 for all four compounds.

Compound	Species-averaged lifetime, $\langle \tau \rangle_x$ [ns]			Ratio predicted / measured	$k_{q,\text{exp.}}$ [$\cdot 10^{10} \text{ M}^{-1} \text{ s}^{-1}$]
	Air (measured)	N ₂ (measured)	Air (predicted)		
5a	7.1	9.1	6.8	1.0	1.7
5b	11.2	20.2	11.5	1.0	2.2
5c	13.0	28.2	13.7	1.1	2.3
5d	16.2	46.0	16.9	1.0	2.2

1.6.2 Triplet quenching by oxygen

In our study, oxygen plays a crucial role as we have observed that the TADF properties of compounds **5b-5e** are highly dependent on the oxygen concentration in the toluene solution. It is known that oxygen efficiently quenches triplet states,²⁴ with longer lifetimes being more susceptible to quenching than shorter ones,²⁵ but the observed effect in our study was quite dramatic. This can be effectively illustrated by the Stern-Volmer plot (eq. S14, Figure S9). We calculated air-saturated lifetimes (τ^{Air}) for different oxygen concentrations with respect to specific oxygen-free lifetimes (denoted as τ^{N_2}).

The oxygen-free lifetimes include examples of (i): fast (21 ns, as prompt fluorescence of compound **5b**), (ii): slow (30 μs), and (iii): very slow (300 μs) processes. It becomes evident from Figure S9 that for fast processes such as prompt fluorescence, oxygen has limited time to act, and saturation is reached relatively quickly. Consequently, there is no difference in measured lifetimes if the concentration of oxygen in the solution is 10^{-5} M or 10^{-7} M, as both cases yield a lifetime of 21 ns. However, the scenario changes when observing slower processes, such as delayed fluorescence in the microseconds. Minor changes in oxygen concentration can lead to significant changes in measured lifetimes. In an air-saturated toluene solution, with a standard oxygen concentration of 1.8 mM,²² we have not detected any delayed fluorescence for this particular compound series. Standard deoxygenation methods, such as bubbling or freeze-thaw procedures, can reach oxygen concentrations in the range of 10^{-6} M to 10^{-7} M.²⁶ However, even when reaching an oxygen concentration of 10^{-7} M in the solution, we are limited by diffusion, and only lifetimes of approximately 1 ms can be experimentally measured. At lower temperatures, this limit is exceeded since diffusion is considerably slower.

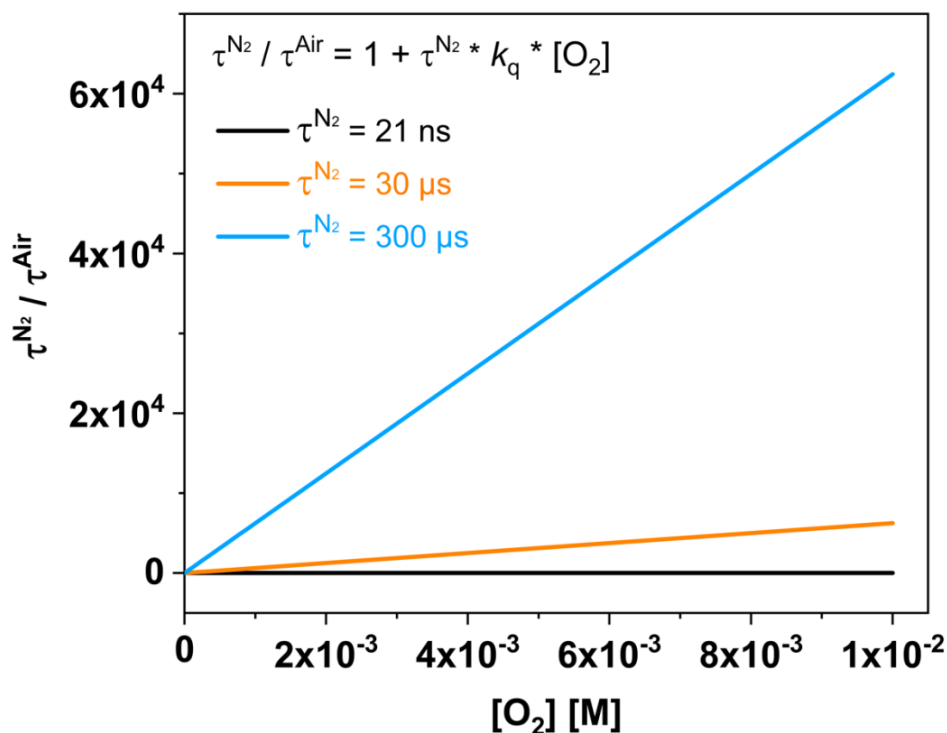


Figure S9. Oxygen quenching predicted by Stern-Volmer equation. Air-saturated lifetimes (τ^{Air}) are calculated for various oxygen concentrations in relation to specific oxygen-free lifetimes (τ^{N_2}) using the Stern-Volmer equation. The selected oxygen-free lifetimes represent different process speeds: (i) fast, $\tau^{N_2} = 21 \text{ ns}$; (ii) slow, $\tau^{N_2} = 30 \mu\text{s}$; and (iii) very slow, $\tau^{N_2} = 300 \mu\text{s}$.

1.7 Deoxygenation procedure

The experimental setup used for deoxygenation is shown in Figure S10. In the first step, the cryogenic UV-quartz cuvette [labelled (I)] was filled with the sample solution. One additional millilitre of solvent was added to the prepared sample to ensure that the concentration does not increase beyond the range suitable for fluorescence measurements during deoxygenation via inert gas bubbling. For this, nitrogen N5 (Air Liquide) was passed through the capillary in the sample [(II) to (III)] until the solvent level reached the initial value in the cuvette (approximately 30 min). The setup was then pressurized with nitrogen to 0.2 bar above ambient pressure and cooled to 77 K in a liquid nitrogen bath. The valve to the inert gas inlet [(II)] was closed, and the valve to the Schlenk line [(IV)] was opened. A high dynamic vacuum

S18

($5 \cdot 10^{-6}$ bar) was applied and the cuvette was flame sealed using a propane torch at the tapered position of the attached Duran glass tube [(V)].

The exact concentration of the deoxygenated sample was then determined by UV-Vis absorption. The oxygen impermeability of the resulting ampoules was verified by an unchanged lifetime of the delayed fluorescence even over a storing period of several months.

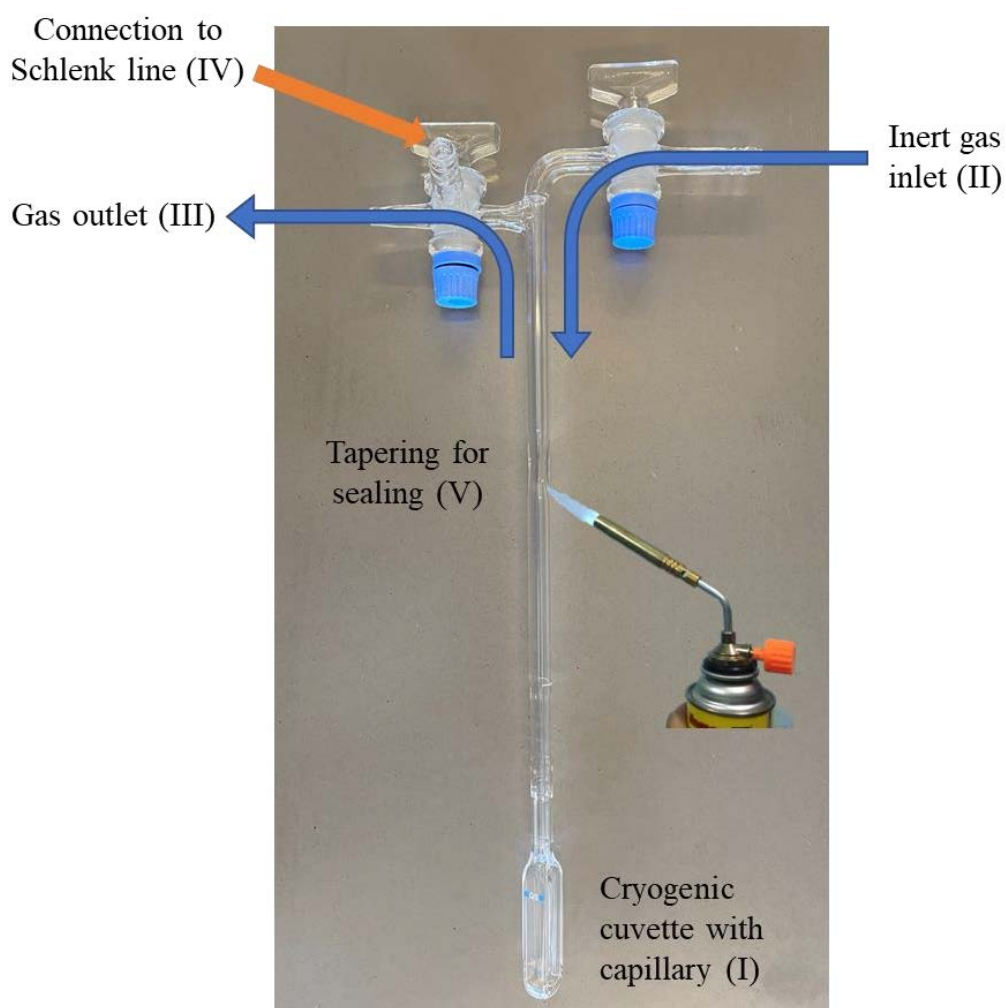


Figure S10. Setup used for degassing and sealing of the samples.

1.8 Temperature dependence of delayed fluorescence

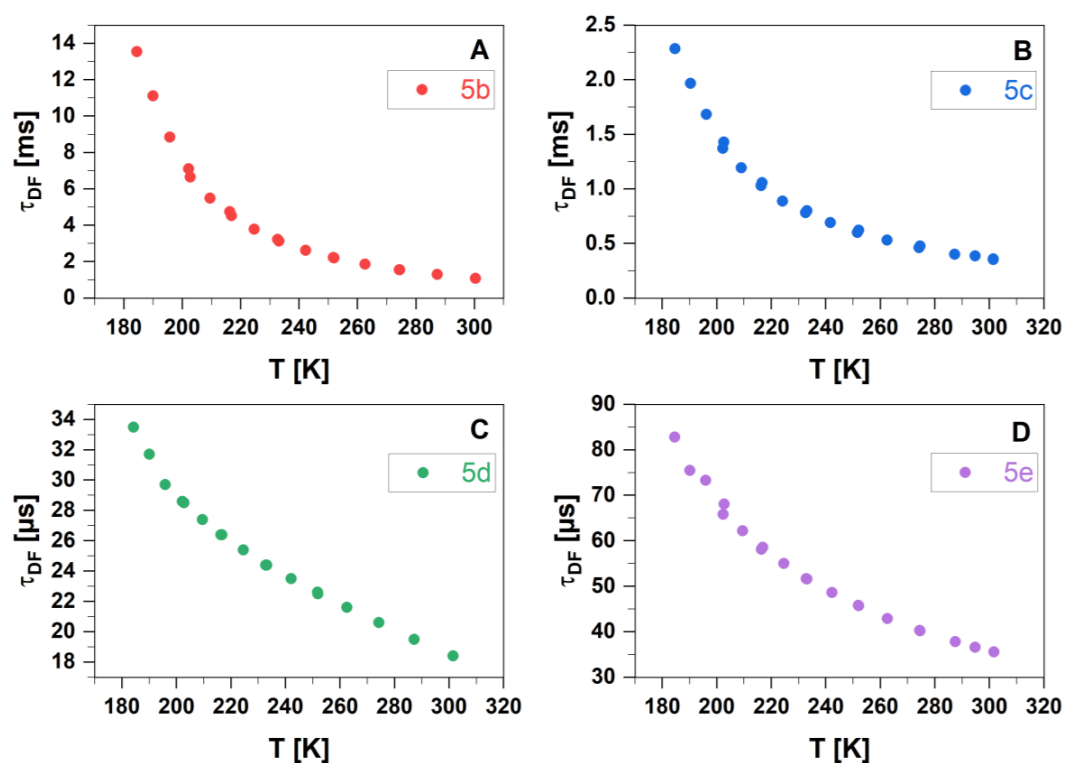


Figure S11. Temperature dependence of the delayed fluorescence lifetimes τ_{DF} of compounds **5b-5e** in liquid toluene. For all compounds, temperature series were firstly conducted from a lower to a higher temperature (i.e. from 200 K to 300 K) and then reversely (from 300 K to 182 K) to check the reproducibility of the measured data (Table S9 to Table S12).

Table S9. Temperature-dependent lifetimes of **5b**. The table contains the temperatures of the sensor and the sample (sensor T and sample T), the reciprocal sample temperature (1/Sample T), and the lifetime fit result of the measured delayed fluorescence lifetime (τ_{DF}).

Sensor T [K]	Sample T [K]	1 / Sample T [$\cdot 10^{-3}$ 1/K]	τ_{DF} [μ s]
200.0	202.7	4.9	6661.1
206.9	209.5	4.8	5485.7
214.3	216.8	4.6	4537.1
222.2	224.6	4.5	3782.7
230.8	233.1	4.3	3124.6
240.0	242.2	4.1	2617.4
250.0	251.9	4.0	2203.2
260.9	262.6	3.8	1856.6
272.7	274.4	3.6	1562.4
285.7	287.3	3.5	1309.0
300.0	300.4	3.3	1076.0
272.7	274.3	3.6	1559.3
250.0	251.7	4.0	2220.2
230.8	232.6	4.3	3232.1
214.3	216.3	4.6	4741.3
200.0	202.1	4.9	7096.9
193.5	195.7	5.1	8849.0
187.5	190.0	5.3	11112.3
181.8	184.4	5.4	13552.5

Table S10. Temperature-dependent lifetimes of **5c**. The table contains the temperatures of the sensor and the sample (sensor T and sample T), the reciprocal sample temperature (1/Sample T), and the lifetime fit result of the measured delayed fluorescence lifetime (τ_{DF}).

Sensor T [K]	Sample T [K]	1 / Sample T [$\cdot 10^{-3}$ 1/K]	τ_{DF} [μ s]
200.0	202.2	4.9	1370.9
206.9	209	4.8	1193.1
214.3	216.3	4.6	1029.1
222.2	224.1	4.5	888.0
230.8	232.6	4.3	782.5
240.0	241.7	4.1	690.6
250.0	251.6	4.0	601.5
260.9	262.5	3.8	530.6
272.7	274.2	3.6	462.0
285.7	287.2	3.5	402.0
300.0	301.4	3.3	354.0
300.0	301.4	3.3	357.7
293.0	294.7	3.4	386.8
272.7	274.5	3.6	477.3
250.0	252	4.0	622.7
230.8	233.1	4.3	800.7
214.3	216.6	4.6	1057.4
200.0	202.6	4.9	1430.5
193.5	196.1	5.1	1681.6
187.5	190.3	5.3	1967.7
181.8	184.7	5.4	2285.1

Table S11. Temperature-dependent lifetimes of **5d**. The table contains the temperatures of the sensor and the sample (sensor T and sample T), the reciprocal sample temperature (1/Sample T), and the lifetime fit result of the measured delayed fluorescence lifetime (τ_{DF}).

Sensor T [K]	Sample T [K]	1 / Sample T [$\cdot 10^{-3}$ 1/K]	τ_{DF} [μ s]
200.0	202.7	4.9	28.5
206.9	209.5	4.8	27.4
214.3	216.7	4.6	26.4
222.2	224.5	4.5	25.4
230.8	233.1	4.3	24.4
240.0	242.1	4.1	23.5
250.0	251.9	4.0	22.5
260.9	262.5	3.8	21.6
272.7	274.3	3.6	20.6
285.7	287.2	3.5	19.5
300.0	301.5	3.3	18.4
272.7	274.3	3.6	20.6
250.0	251.7	4.0	22.6
230.8	232.7	4.3	24.4
214.3	216.3	4.6	26.4
200.0	202.2	4.9	28.6
193.5	195.8	5.1	29.7
187.5	190.0	5.3	31.7
181.8	184.3	5.4	33.5

Table S12. Temperature-dependent lifetimes of **5e**. The table contains the temperatures of the sensor and the sample (sensor T and sample T), the reciprocal sample temperature ($1/\text{Sample T}$), and the lifetime fit result of the measured delayed fluorescence lifetime (τ_{DF}).

Sensor T [K]	Sample T [K]	$1 / \text{Sample T}$ [$\cdot 10^{-3} \text{ 1/K}$]	τ_{DF} [μs]
200.0	202.7	4.9	68.1
206.9	209.5	4.8	62.2
214.3	216.8	4.6	58.6
222.2	224.6	4.5	55.0
230.8	233.1	4.3	51.6
240.0	242.2	4.1	48.6
250.0	252	4.0	45.7
260.9	262.6	3.8	42.9
272.7	274.4	3.6	40.3
285.7	287.5	3.5	37.8
293.0	294.7	3.4	36.6
300.0	301.7	3.3	35.6
272.7	274.5	3.6	40.2
250.0	251.9	4.0	45.8
230.8	232.8	4.3	51.7
214.3	216.4	4.6	58.1
200.0	202.3	4.9	65.8
193.5	195.9	5.1	73.3
187.5	190.1	5.3	75.5
181.8	184.6	5.4	82.8

1.9 An additional proof for TADF: TRES measurements

To further investigate the spectral properties of delayed fluorescence, we conducted time-resolved emission spectroscopy (TRES) measurements. A spectral overlap between prompt and delayed fluorescence confirms that both types of emission originate from the same excited state (S_1). We integrated the specific areas under the time-resolved decay curves in microseconds to obtain the spectra of both prompt and delayed fluorescence (Figure S12). These spectra overlap for all four compounds (Figure S13 A-D), giving an additional verification to TADF.

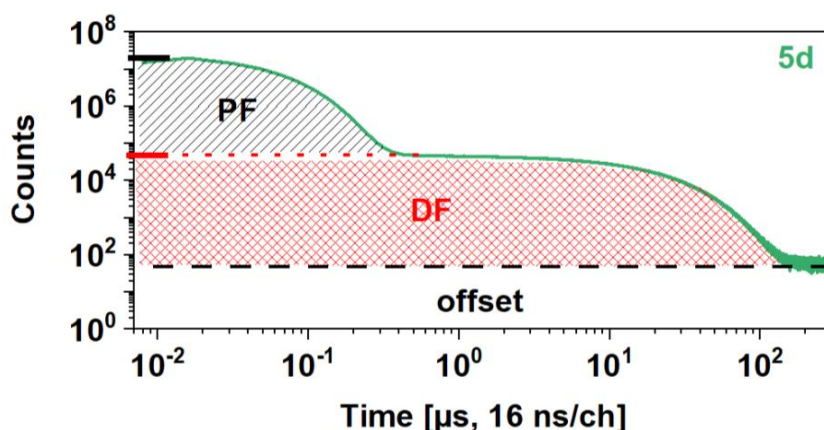


Figure S12. Integrated areas of prompt and delayed fluorescence under the time-resolved decay curves in microseconds for compound **5d**.

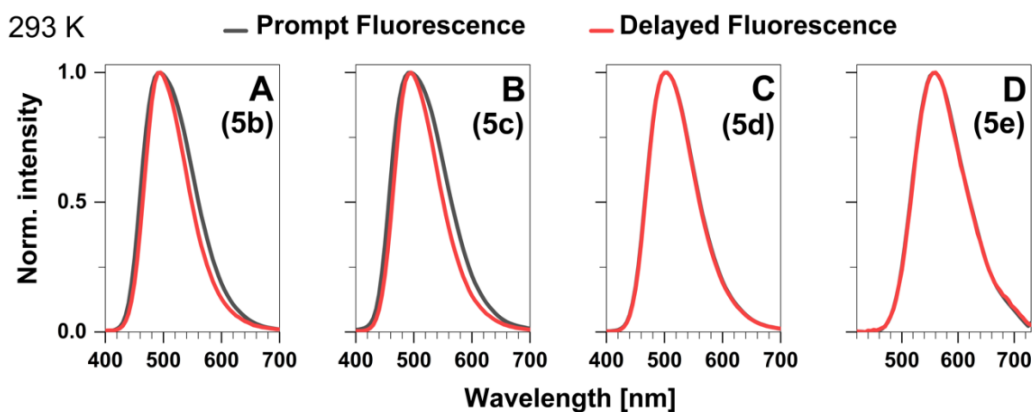


Figure S13. Time-resolved emission spectra of compounds **5b-5e** (A-D) in toluene at 293 K. Spectral overlap between prompt and delayed fluorescence is observed for all four compounds, indicating that both emissions originate from the same excited state.

1.10 Rate matrix and solution

The rate matrix for the excited 3-state kinetic system:

$$\begin{pmatrix} -(k_S + k_{ISC}) & k_{rISC} & 0 \\ k_{ISC} & -k_{rISC} & 0 \\ k_S & k_T & 0 \end{pmatrix} \quad \text{eq. S17}$$

has two relaxation times, the prompt and the delayed signal, as general solution:

$$k_p = -\lambda_2 = \frac{1}{2} \left(k_S + k_{ISC} + k_{rISC} + k_T + \sqrt{(k_S + k_{ISC} - k_{rISC} - k_T)^2 + 4k_{ISC}k_{rISC}} \right) \quad \text{eq. S18}$$

$$k_d = -\lambda_1 = \frac{1}{2} \left(k_S + k_{ISC} + k_{rISC} + k_T - \sqrt{(k_S + k_{ISC} - k_{rISC} - k_T)^2 + 4k_{ISC}k_{rISC}} \right) \quad \text{eq. S19}$$

with $k_S = k_{rad_S} + k_{IC_S}$ and $k_T = k_{rad_T} + k_{nr_T}$.

1.11 Discussion of previously published data on 5b

To simulate the effect of triplet quenching by O₂ the solution of the rate matrix for the delayed signal was used. Here the temperature-dependent rate constants as obtained from our kinetic analysis were inserted:

$$(k_{rad} + k_{IC}) = (k_{rad} + k_{IC})_0 e^{-Ea(1)/kT} \quad \text{eq. S20}$$

$$k_{ISC} = \frac{k_{ISC}(1)}{\sqrt{T}} + \frac{k_{0_ISC}(2)}{\sqrt{T}} e^{-Ea(2)/kT} \quad \text{eq. S21}$$

$$k_{rISC} = \frac{k_{0_rISC}}{\sqrt{T}} e^{-Ea(3)/kT} \quad \text{eq. S22}$$

Quenching by O₂ was introduced as the only process that depopulates T₁ to S₀:

$$k_T \equiv k_q \cdot \frac{[O_2]}{9} = \frac{2RT}{3\eta} \left(\frac{r_{dye}}{r_{O_2}} + \frac{r_{O_2}}{r_{dye}} + 2 \right) \cdot \frac{[O_2]}{9} \approx 5.0043 \cdot \frac{RT}{\eta} \cdot \frac{[O_2]}{9} \quad \text{eq. S23}$$

S26

The quenching rate was approximated by using the Stokes-Einstein equation, the radii of $r(\text{O}_2) = 84 \text{ pm}$ and $r(\mathbf{5b}) = 445 \text{ pm}$, and assuming a quenching efficiency of $1/9$ as upper limit given by spin statistics.²⁷ The viscosity of toluene in the temperature range studied was obtained from Ref. 28 and its eq. 1-5. With all parameters available now the delayed rate can be simulated for all relevant concentrations of O_2 .

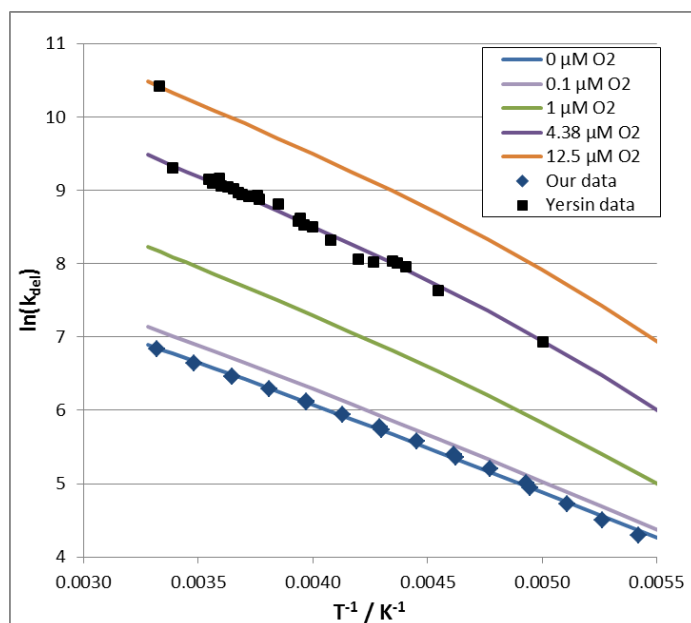


Figure S14. Temperature dependence of simulated delayed rate constant for different O_2 concentrations compared to experimental data and previously published data²⁹

The experimental data points from the original publication²⁹ (its Figure 4) were extracted using WebPlotDigitizer Ver. 4.7³⁰ and are consistent with a concentration of $4.38 \mu\text{M O}_2$. The single point on the $12.5 \mu\text{M}$ line corresponds to the reported decay time of $30 \mu\text{s}$ at 300 K (insert in Figure 4). The apparent Arrhenius-energy for the extracted data points is $E_a = 126 \pm 2 \text{ meV}$. For the limiting case, i.e. negligible rISC and quenching as dominating process to depopulate T_1 , an apparent Arrhenius-energy of $E_a = 129 \pm 2 \text{ meV}$ would be expected, just from the temperature dependence of the diffusion coefficient. It has to be noted that even in our measurements an effect of residual oxygen cannot be excluded. Thus, our reported rates for ISC and rISC as well as the activation energy for rISC would be upper limits for the system while the quantum yield for delayed fluorescence represents a lower limit.

1.12 Aggregation at lower temperatures

All samples showed signs of aggregation at lower temperatures, as indicated by a strong drop in total fluorescence intensity due to precipitation and the appearance of a highly quenched species ($\tau < 200$ ps) in the ns decays. In addition, compound **5e** formed a very long-lifetime species ($\tau \gg 1$ ms, $< 3.3\%$ of total signal, see Figure S15) below 220 K. Upon cooling down and heating up of the sample all the species attributed to aggregation showed more or less strong hysteresis regarding their relative amount and lifetime. This behaviour prevents us from evaluating the absolute fluorescence intensities as indicator for possible changes in quantum yields. It does not significantly affect the lifetime analyses since fluorescence decay times of monomers and aggregates are well separated. In the offset evaluation of the **5e** ns-decays the fraction of aggregates with long lifetime as estimated from the μ s decays was subtracted. Since the fraction of aggregates was not stable in time, and data from different measurements (ns and μ s decays) needed to be combined for this purpose, the data correction was only partially successful and an increased noise level in the corrected data (**5e** below 220 K) could not be avoided.

Aggregation in **5e**

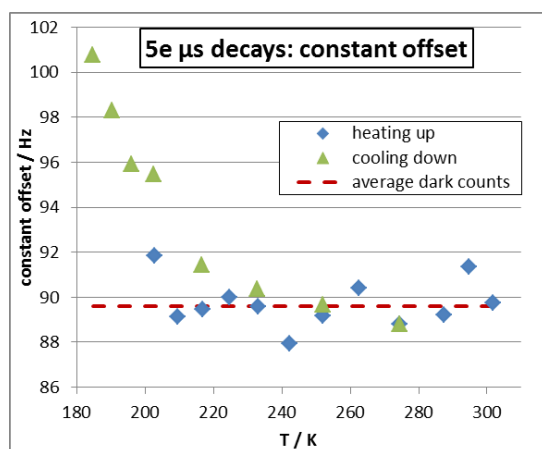


Figure S15. Aggregation in **5e**

Below 220 K the offset in the μ s decays measured for **5e** significantly exceeds the average dark counts of the detector, indicating the appearance of a species with lifetime much longer than the 600 μ s detection time window between excitation pulses.

Chapter 2. Analytical solution of kinetics for 3-state system (S₀, S₁, T₁)

The formal solution of dynamics equation for a 3-state system:

$$\frac{d\mathbf{a}(t)}{dt} = \mathbf{K} \mathbf{a}(t); \quad \mathbf{a}(t) = \begin{pmatrix} a_{S0}(t) \\ a_{S1}(t) \\ a_{T1}(t) \end{pmatrix}, \quad \text{eq. S24}$$

is:

$$\mathbf{a}(t) = e^{\mathbf{K}t} \mathbf{a}_0; \quad \mathbf{a}_0 = \mathbf{a}(t = 0) \quad \text{eq. S25}$$

The observed signal is defined by emission properties of involved states. In general, we can write:

$$a_{obs}(t) = \mathbf{a}_{em} \mathbf{a}(t) = \mathbf{a}_{em} e^{\mathbf{K}t} \mathbf{a}_0 \quad \text{eq. S26}$$

The transition rates matrix can be eigen-values decomposed (EVD) as:

$$\mathbf{K} = \mathbf{V} \mathbf{\Lambda} \mathbf{U};$$

$$\mathbf{V} = \begin{pmatrix} | & | & | \\ \mathbf{v}_0 & \mathbf{v}_1 & \mathbf{v}_2 \\ | & | & | \end{pmatrix}; \quad \mathbf{U} = \mathbf{V}^{-1} = \begin{pmatrix} - & \mathbf{u}_0 & - \\ - & \mathbf{u}_1 & - \\ - & \mathbf{u}_2 & - \end{pmatrix}; \quad \mathbf{\Lambda} = \begin{pmatrix} \lambda_0 & 0 & 0 \\ 0 & \lambda_1 & 0 \\ 0 & 0 & \lambda_2 \end{pmatrix}, \quad \text{eq. S27}$$

where \mathbf{V}, \mathbf{U} are matrixes consisting of right (columns) and left(rows) eigen-vectors. For the following derivation, it is more convenient to rewrite EVD in eq. S27 in the equivalent form of linear combination of eigen matrixes $\mathbf{\Gamma}_i$:

$$\mathbf{K} = \sum_i \mathbf{\Gamma}_i \lambda_i;$$

$$\mathbf{\Gamma}_i = \mathbf{v}_i \otimes \mathbf{u}_i, \quad \text{eq. S28}$$

Then the matrix exponential in eq. S25 and eq. S26 can be written as:

$$e^{\mathbf{K}t} = \sum_i \mathbf{\Gamma}_i e^{\lambda_i t} \quad \text{eq. S29}$$

The transition rate matrix \mathbf{K} for the system in absence of excitation (after excitation pulse) have the form:

S29

$$\mathbf{K} = \begin{pmatrix} 0 & k_{S10} & k_{T10} \\ 0 & -(k_{S10} + k_{ISC}) & k_{RISC} \\ 0 & k_{ISC} & -(k_{RISC} + k_{T10}) \end{pmatrix}, \quad \text{eq. S30}$$

where $k_{S10} = k_{S10,rad} + k_{IC}$. For this transition matrix in eq. S26 we can get next eigen values (negated rates):

$$\begin{cases} \lambda_0 = 0 \\ \lambda_1 = -k_p = -\frac{1}{2}(\Sigma k + \Delta k) \\ \lambda_2 = -k_d = -\frac{1}{2}(\Sigma k - \Delta k) \end{cases} \quad \text{eq. S31}$$

$$\Sigma k = k_{S10} + k_{ISC} + k_{RISC} + k_{T10}$$

$$\Delta k = \sqrt{4((k_{S10} + k_{ISC})(k_{RISC} + k_{T10}) - k_{ISC}k_{RISC})}$$

Note that the two expressions for the prompt and delayed rates k_p and k_d rates above can be rewritten in the form of two simple equations:

$$\begin{cases} k_p + k_d = k_{S10} + k_{ISC} + k_{RISC} \\ k_p k_d = k_{S10} k_{RISC} \end{cases} \quad \text{eq. S32}$$

The corresponding eigen-matrices are:

$$\begin{aligned} \mathbf{\Gamma}_0 &= \begin{pmatrix} 1 & 1 & 1 \\ 0 & 0 & 0 \\ 0 & 0 & 0 \end{pmatrix}; \\ \mathbf{\Gamma}_1 = \mathbf{\Gamma}_p &= \frac{1}{\Delta k} \begin{pmatrix} 0 & k_d - k_{S10} & k_d - k_{T10} \\ 0 & k_p - (k_{RISC} + k_{T10}) & -k_{RISC} \\ 0 & -k_{ISC} & -k_d + (k_{RISC} + k_{T10}) \end{pmatrix}; \\ \mathbf{\Gamma}_2 = \mathbf{\Gamma}_d &= -\frac{1}{\Delta k} \begin{pmatrix} 0 & k_p - k_{S10} & k_p - k_{T10} \\ 0 & k_d - (k_{RISC} + k_{T10}) & -k_{RISC} \\ 0 & -k_{ISC} & -k_p + (k_{RISC} + k_{T10}) \end{pmatrix} \end{aligned} \quad \text{eq. S33}$$

If the transitions $T_1 \rightarrow S_0$ are not emissive, the whole signal is detected as emission from the state S_1 . So, the emission vector takes form: $\mathbf{a}_{em} = (0 \ \Phi_{s1} \ 0)$, where Φ_{s1} is the quantum yield of a $S_1 \rightarrow S_0$ transition. Next, we assume that initial population of the state T_1 is neglectable, i.e. that an excitation pulse is so short that this state is not populated. This way we get $\mathbf{a}_0^T =$

S30

($a_{S0,0}$ $a_{S1,0}$ 0). Then, substituting \mathbf{a}_{em} , \mathbf{a}_0 and $\lambda_i, \mathbf{\Gamma}_i$ into eq. S29 and eq. S26, we get for the observed signal:

$$\begin{aligned} a_{obs}(t) &= a_p e^{-k_p t} + a_d e^{-k_d t} \\ a_p &= \Phi_{s1} a_{S1,0} \frac{1}{\Delta k} (k_p - (k_{RISC} + k_{T10})) \\ a_d &= \Phi_{s1} a_{S1,0} \frac{1}{\Delta k} ((k_{RISC} + k_{T10}) - k_d) \end{aligned} \quad \text{eq. S34}$$

In the experiment we can observe either ratio, either one of relative fractions (one of which will be dependent) of two exponential components of the decay:

$$\begin{aligned} \frac{F_d^{(a)}}{F_p^{(a)}} &= \frac{a_d}{a_p} = \frac{k_p - (k_{RISC} + k_{T10})}{(k_{RISC} + k_{T10}) - k_d}; \quad \frac{F_d^{(c)}}{F_p^{(c)}} = \frac{a_d}{a_p} \frac{k_p}{k_d} = \frac{k_p - (k_{RISC} + k_{T10})}{(k_{RISC} + k_{T10}) - k_d} \frac{k_p}{k_d} \\ p_d^{(a)} &= \frac{a_d}{a_p + a_d} = \frac{k_p - (k_{RISC} + k_{T10})}{k_p - k_d}; \quad p_d^{(c)} = \frac{a_d/k_d}{a_p/k_p + a_d/k_d} = \frac{1}{1 + \frac{F_p^{(c)}}{F_d^{(c)}}} \end{aligned} \quad \text{eq. S35}$$

Where the upper indices (a), (c) stand for amplitude (intensity) and counts variants of quantities, correspondingly.

Two equations from eq. S32 and one of equations from eq. S35 gives 3 independent equations relating 3 observed quantities and 4 transition rates. Obviously, such system is incomplete and cannot give solution for all 4 rates. So, we need to make some assumptions. For example, we can assume that k_{T10} is known. Then we can solve the system of 3 equations to get k_{S10} , k_{ISC} , k_{RISC} as functions of observables (here, for example, fluorescence rates and fractions) and k_{T10} :

$$\left\{ \begin{aligned} k_{RISC} &= k_p + k_d - \langle k \rangle^{(a)} - k_{T10} = \left(\frac{1}{k_d} + \frac{1}{k_p} - \langle \tau \rangle^{(c)} \right)^{-1} - k_{T10} \\ k_{S10} &= \frac{k_p k_d - \langle k \rangle^{(a)} k_{T10}}{k_{RISC}} \\ k_{ISC} &= \langle k \rangle^{(a)} - k_{S10} \\ \langle k \rangle^{(a)} &= (p_p^{(a)} k_p + p_d^{(a)} k_d) \\ \langle \tau \rangle^{(c)} &= \left(\frac{p_d^{(c)}}{k_d} + \frac{p_p^{(c)}}{k_p} \right) \end{aligned} \right. \quad \text{eq. S36}$$

S31

Note: $\langle k \rangle^{(a)} = k_p + k_d - k_{RISC} - k_{T10}$.

Oleg's contribution (not only about precipitation). I will put all contribution here. It probably should be separated later and placed to different parts according to context. Thus, discussion of the model should be placed closer to diagram plots below (see also the same plot at the beginning, before main text).

1. Fitting of TCSPC data

The TCSPC data for variety of temperatures were measured in two delay times regions: with ns- and ms- time resolution. The registered fluorescence decays were fitted using a quadratic programming optimization. As expected and observed fluorescence lifetimes differs by several orders of magnitude, no regularization was applied during optimization. The example fitted spectra of fluorescence lifetimes for different temperatures are shown at the Fig.

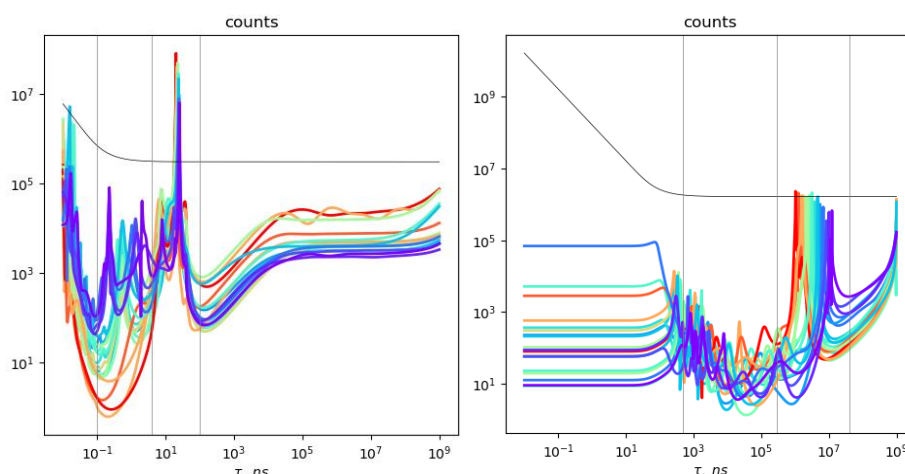


Figure S53 The fluorescence lifetime spectra for **5b** sample, obtained by the quadratic programming optimization fitting of TCSPC decays in ns- (left) and ms-ranges of delay times.

2. Precipitation

The total number of counts depend on the temperature – it drops several times with the decrease of a temperature. Also, this dependence reveal a hysteresis behaviour. See Fig... We assume that such behaviour evidences about the precipitation of solution at low temperatures.

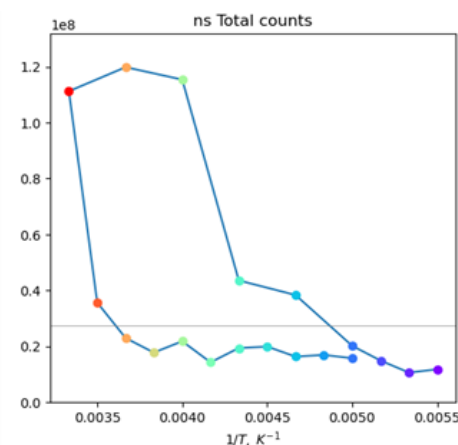


Figure S54. The temperature dependence of total number of counts for C2 sample.

3. Dominating fluorescence lifetimes

All samples reveal the presence of 2 dominating fluorescence lifetimes – one in each measurement with different delay time range. These lifetimes were calculated from the fitted spectra as average over the regions near dominating peaks (from minimum to minimum). To determine relative fraction of the prompt (shortest) lifetime only measurement in ns-region was used, as different excitation conditions of two measurements does not allow the quantitative comparison of their amplitudes. The prompt photon counts ($a_p^{(c)}$) were calculated as sum of counts around the dominating peak in the ns spectrum, and the delayed ($a_p^{(c)}$) counts are estimated as sum of all counts with lifetimes larger than last minimum of the ns-spectra, except the dark counts estimated from independent measurement. The resulting lifetimes and fractions for 5b sample are presented at the Fig. ... (Upper row)

4. The analysis of lifetimes using 3-state model

The presence of two dominating fluorescence lifetimes in the fitted decays witness in favour of 3-states (ground S_0 and two excited: S_1, T_1) model of an underlying kinetics (see. Scheme 1.). To resolve the transitions times we derived analytical expressions for we have derived the analytical expressions 3 independent observables: two characteristic times (τ_{DF}, τ_{PF}) their fractions (dependent on each other as $p_D = 1 - p_F$), for a supposed 3-state (see SI, chapter 4), assuming that the signal is observed from the radiative transitions from S_1 state only. As the 3-

state system of interest is characterised by 4 transition rates ($k_{10S} = k_{rSv} + k_{ICS}$, k_{ISC} , k_{rISC} , k_{10T}) and only 3 observables are available, the exact inverted solution for all rates is impossible. So, we had to make some assumption about transition rates: here we have assumed that k_{10T} is neglectable. Our derivation of observed quantities is analogous to one given by Adachi (JPCA125p08074_Exact solution TADF kinetics_Tsuchiya+Adachi_2021). Thus, the solution is almost the same, except the expression ???, where Adachi used approximation that $p_D \ll p_F$. This approximation is really applicable for the reasonable transition rates. However, it is not necessary, as the full solution is not much more complicated. The resolved transition rates for the 5b compound are presented at the Fig. ... (bottom row).

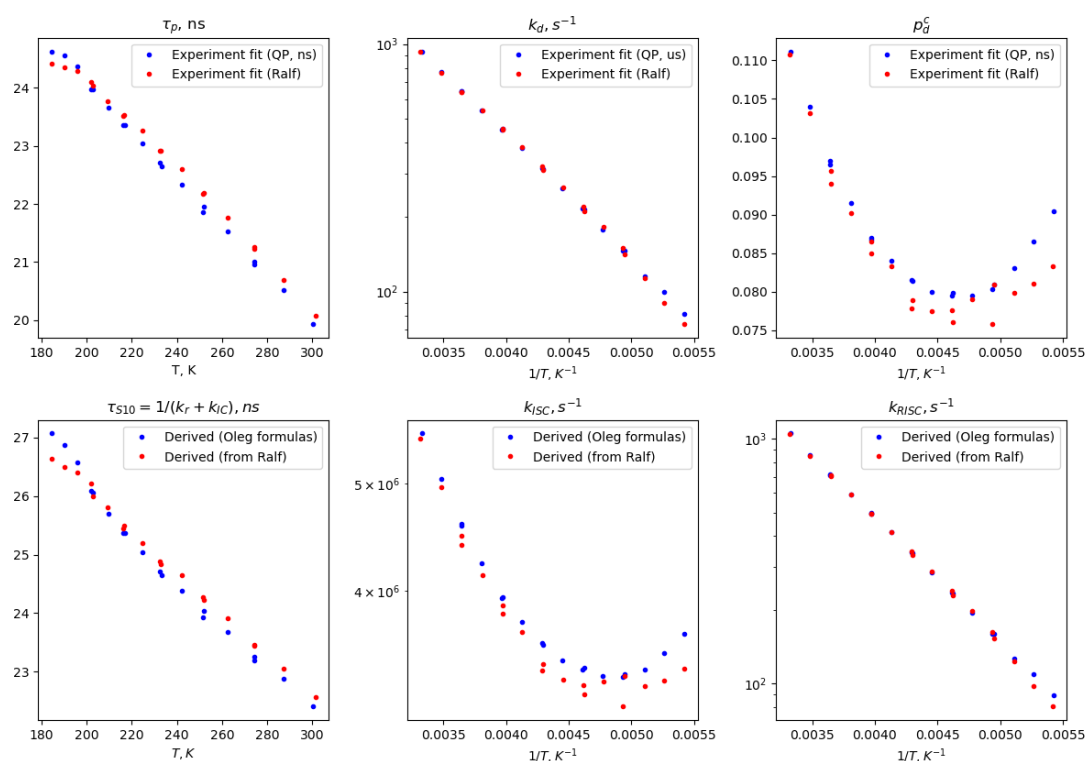


Figure S55. Fitted data analysis. **Top:** The fluorescence lifetimes (rates) and their fractions for 5b sample obtained from the data presented at Fig. ... **Bottom:** The transition rates calculated from fitted data according the relations presented at SI, chapter 4.

Chapter 3. Quantum Chemical Computations

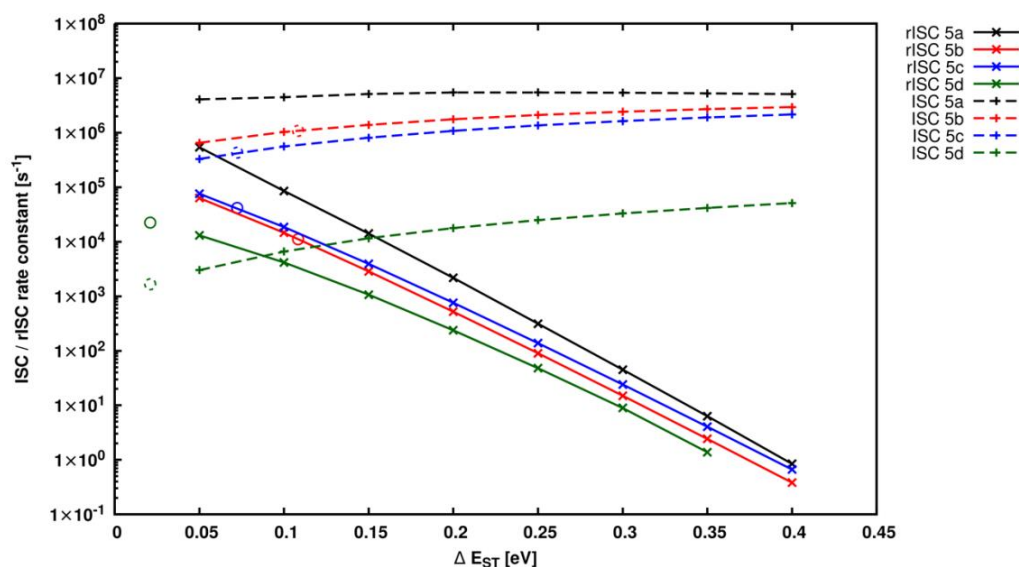


Figure S56. ISC and rISC rate constants for compound 5a to 5d. The adiabatic energy gap was successively decreased starting from 0.4 eV with an increment of 0.05 eV. Computed rate constants for the experimental energy gaps are highlighted in solid (rISC) and dashed (ISC) circles.

The potential energy surface (PES) and the according normal mode vibrations that are needed for the computation of nonradiative rate constants were computed at the optimized geometries of the lowest excited singlet and triplet state. In order to mimic the effect of a small energy gap between these states the adiabatic energy gap was decreased with an increment of 0.05 eV. The results clearly show that, unlike ISC, rISC (which is an uphill process that relies on thermal population of excited states in close energetic proximity) strongly depends on the energy gap. Rate constants were also computed for the experimental singlet-triplet gaps if given.

However, this approach leads to certain inaccuracies where the ISC rate constant is significantly lower than the rISC. Due to not recomputing the PES of the respective states at every given point a sole energetic shift leads to a crossing of two potentials and, thus, unphysical results.

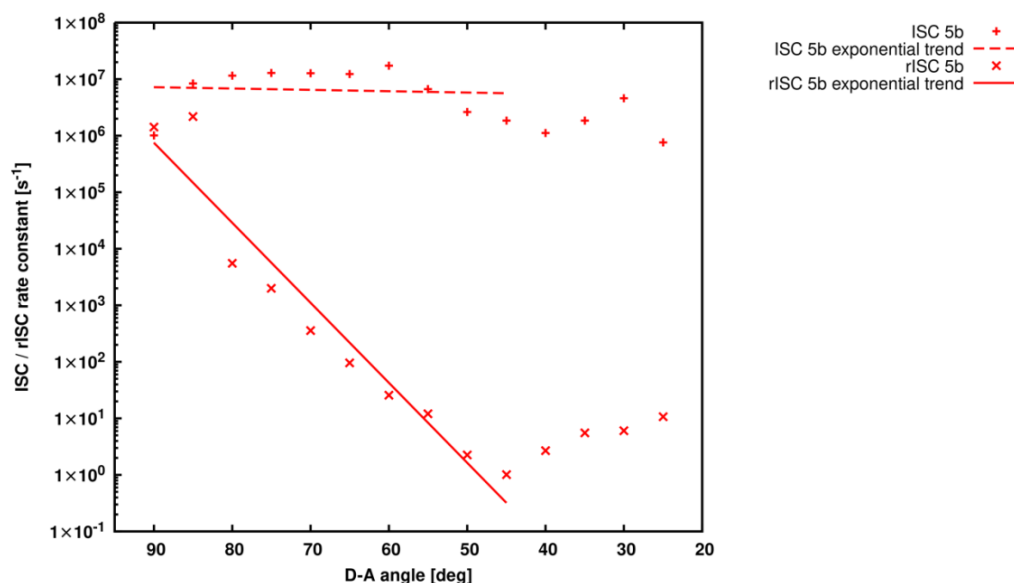


Figure S57: ISC and rISC rate constants computed for compound 5b. Results were obtained by performing a relaxed scan of the S1 and T1 geometry and using the VH-Method.

To ensure that reliable non-radiative rate constants are computed, relaxed scans were performed for the lowest excited singlet and triplet state geometries. In addition to a frequency analysis at the initial state geometry the Vertical Hessian (VH) method was used to extrapolate the PES alongside the normal mode vibrations of the respective final state. Unlike for a sole vertical shift of the PES shown in figure 1, figure 2 shows the ISC and rISC rate constants that were computed for different donor-acceptor angles and recomputed excited state potentials.

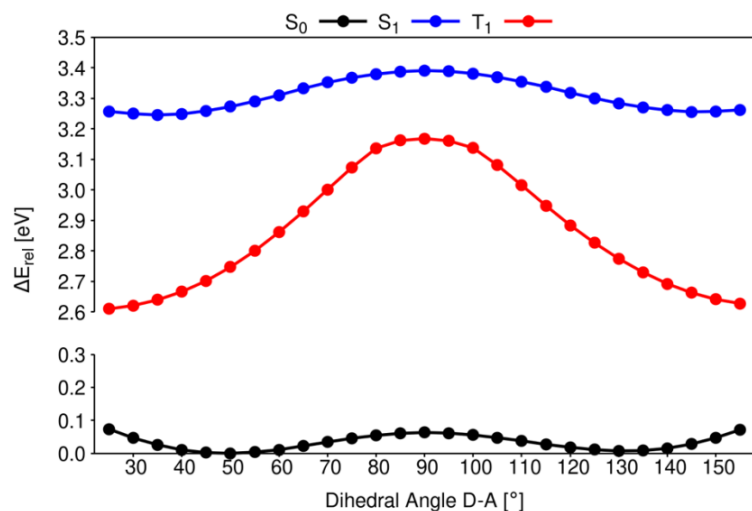


Figure S58. Relaxed interpolated pathway for compound 5a between 25 and 155 degrees for the electronic ground state and the lowest excited singlet and triplet state. Between 80 and 100 degrees the lowest optimized triplet state is of locally excited state character instead of charge-transfer character and thus in energy lower than expected.

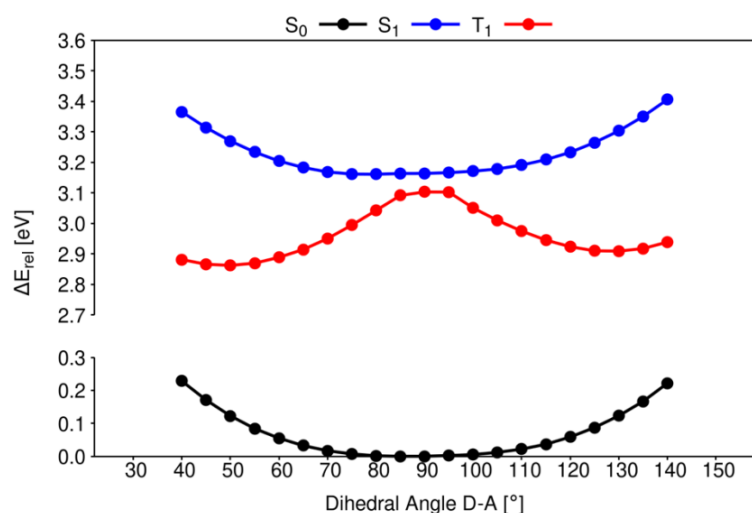


Figure S59. Relaxed interpolated pathway for compound 5d between 40 and 140 degrees for the electronic ground state and the lowest excited singlet and triplet state. Increased sterical hindrance by the methyl groups prevents a distortion beyond 40 and 140 degrees. Between 90 and 95 degrees the lowest optimized triplet state is of locally excited state character instead of charge-transfer character and thus in energy lower than expected.

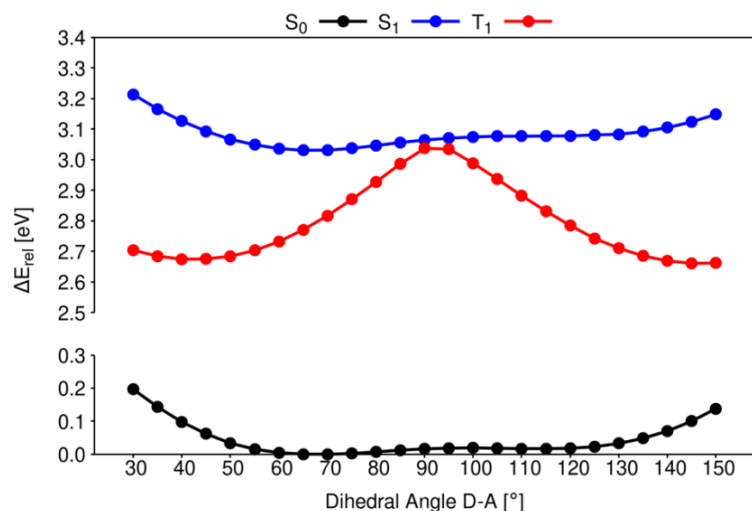


Figure S60. Relaxed interpolated pathway for compound 5e between 30 and 150 degrees for the electronic ground state and the lowest excited singlet and triplet. For all dihedral angles shown the lowest excited triplet state is of charge-transfer character.

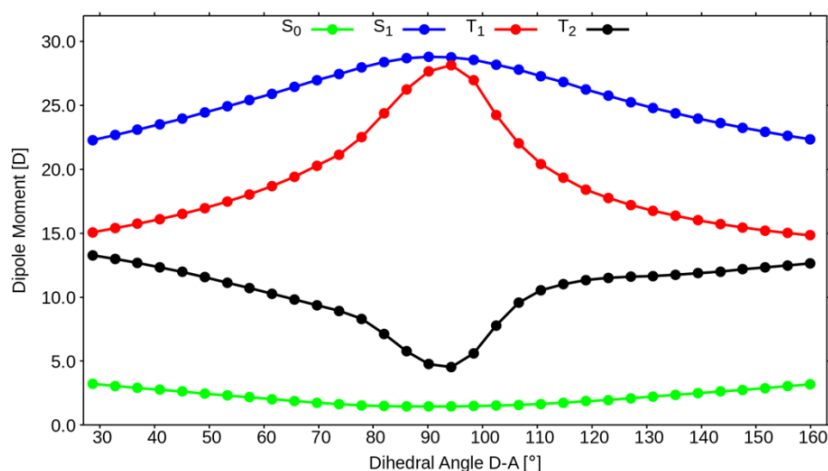


Figure S61. Dipole moment along the rotation of donor and acceptor for the electronic ground state and low-lying excited states of compound 5b. In this case In the case of a non-polar charge distribution in the electronic ground state the dipole moment can be used as a measure for the charge-transfer character.

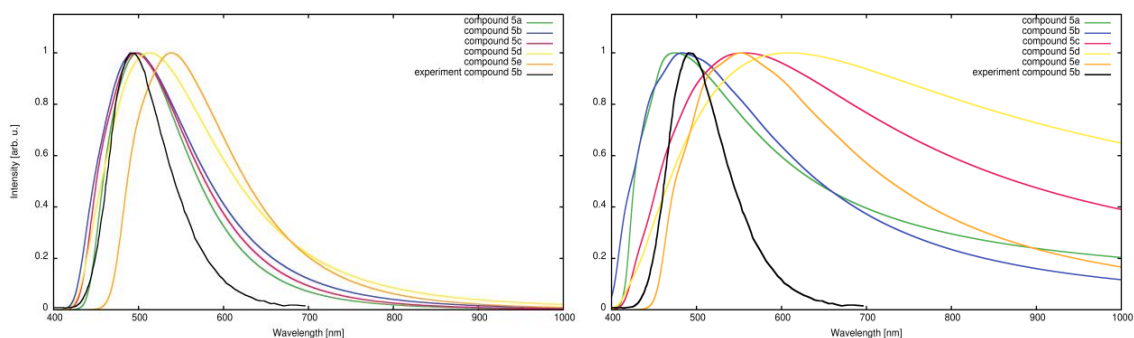


Figure S62. Emission spectra computed using the Vertical Hessian (VH, left) approach and the Adiabatic Hessian (AH, right) approach. The AH approach yields featureless broad spectra that do not allow for a meaningful comparison with the experiment. The VH method matches the spectral shape and emission maxima.

Table S21. Dihedral angle (C-C-C-C from substituent to ortho-CN) between donor and acceptor, energetic difference between the conformers and a torsional barrier estimated based on the interpolated relaxed pathway between the conformers.

	Compound				
	5a	5b	5c	5d	5e
Conf. 1, S_0 [deg]	49.6	69.7	73.5	87.1	68.0
Conf. 2, S_0 [deg]	131.2	110.7	95.8	---	112.3
$\Delta E_{\text{DFT}}(2 - 1)$ [meV]	7	15	112	---	17
$\Delta E_{\text{DFT/MRCI}}(2 - 1)$ [meV]	2	5	108	---	5
Energy Barrier 1 \rightarrow 2 [meV]	ca. 60	ca. 15	ca. 38	---	ca. 20

Table S22. Supplementary information for the absorption spectra consisting of oscillator strengths $f(L)$, band wavelengths and the percentage of charge-transfer, locally-excited character (% CT/LE) of the respective electronic states at DFT/MRCI-R2016, SVP level of theory.

	Compound				
	5a	5b	5c	5d	5e
$S_0 \rightarrow S_1$ $f(L)$	0.23692	0.07743	0.04683	0.00208	0.08110
$S_0 \rightarrow S_2$ $f(L)$	0.41659	0.28922	0.22606	0.04350	0.25488
$S_0 \rightarrow S_3$ $f(L)$	0.02198	0.16334	0.23080	0.43595	0.20215
$S_0 \rightarrow S_1$ [nm]	410	400	400	396	429
$S_0 \rightarrow S_2$ [nm]	331	319	315	307	331
$S_0 \rightarrow S_3$ [nm]	312	307	306	302	319
S_1 [% CT/LE]	70/20	80/10	82/9	87/3	81/9

Table S23. Dihedral angle between donor and acceptor for all compounds in the electronic ground state and the lowest excited singlet and triplet state.

	Compound				
	5a	5b	5c	5d	5e
Conf. 1, S_0 [deg]	49.6	69.7	73.5	87.1	68.0
Conf. 1, S_1 [deg]	34.3	65.9	65.2	81.8	66.6
Conf. 1, T_1 [deg]	20.9	41.7	39.5	49.3	43.0
Conf. 2, S_0 [deg]	131.2	110.7	95.8	---	112.3
Conf. 2, S_1 [deg]	147.0	122.4	---	---	117.5
Conf. 2, T_1 [deg]	161.5	147.6	145.9	128.4	146.8

Chapter 4. References

1. M. S. Sundar, G. Singh, R. S. Ampapathi and A. V. Bedekar, *Journal of Molecular Structure*, 2017, **1147**, 495-501.
2. E. Rochlin and Z. Rappoport, *The Journal of Organic Chemistry*, 1994, **59**, 3857-3870.
3. M. Hesse, H. Meier and B. Zeeh, *Spektroskopische Methoden in der organischen Chemie*, Georg Thieme Verlag, 2005.
4. C. F. Macrae, I. Sovago, S. J. Cottrell, P. T. A. Galek, P. McCabe, E. Pidcock, M. Platings, G. P. Shields, J. S. Stevens, M. Towler and P. A. Wood, *J Appl Crystallogr*, 2020, **53**, 226-235.
5. APEX2, *data collection program for the CCD area-detector system, Version 2.1-0*, Bruker Analytical X-ray Systems, Madison (WI), USA, 1997-2014.
6. SAINT, *data reduction and frame integration program for the CCD area-detector system*, Bruker Analytical X-ray Systems, Madison (WI), USA, 1997-2014.
7. G. M. Sheldrick, *SADABS: Area-Detector Absorption Correction*, University of Göttingen, Göttingen, Germany, 1996.
8. CrysAlis^{Pro}, Rigaku Oxford Diffraction/Agilent Technologies UK Ltd, Yarnton, England., release 1.171.40.103a, **2021**.
9. G. M. Sheldrick, *Acta Crystallogr C Struct Chem*, 2015, **71**, 3-8.
10. G. M. Sheldrick, *Acta Crystallogr A*, 2008, **64**, 112-122.
11. K. Brandenburg, *Brandenburg & H. Putz Gbr, Bonn (Germany)*, 2009-2022.
12. W. W. Parson, *Modern optical spectroscopy*, Springer, 2007.
13. E. Lippert, *Zeitschrift für Elektrochemie, Berichte der Bunsengesellschaft für physikalische Chemie*, 1957, **61**, 962-975.
14. N. Mataga, Y. Kaifu and M. Koizumi, *Bulletin of the Chemical Society of Japan*, 1956, **29**, 465-470.
15. J. Lakowicz, *Principles of Fluorescence Spectroscopy*, 3rd edition, Springer, **2006**.
16. F. B. Dias, T. J. Penfold and A. P. Monkman, *Methods Appl Fluoresc*, 2017, **5**, 012001.
17. S. J. Strickler and R. A. Berg, *The Journal of Chemical Physics*, 1962, **37**, 814-822.
18. A. Reiffers, C. Torres Ziegenbein, A. Engelhardt, R. Kühnemuth, P. Gilch and C. Czekelius, *Photochem Photobiol*, 2018, **94**, 667-676.
19. W. Haselbach, J. M. Kaminski, L. N. Kloeters, T. J. J. Müller, O. Weingart, C. M. Marian, P. Gilch and B. E. Nogueira de Faria, *Chemistry*, 2023, **29**, e202202809.

20. Y. Yoneda, H. Sotome, R. Mathew, Y. A. Lakshmanan and H. Miyasaka, *J Phys Chem A*, 2020, **124**, 265-271.
21. W. R. Ware, *The Journal of Physical Chemistry*, 1962, **66**, 455-458.
22. M. Montalti, A. Credi, L. Prodi and M. T. Gandolfi, *Handbook of photochemistry*, CRC press, 2006.
23. A. Schumpe and P. Luehring, *Journal of Chemical & Engineering Data*, 1990, **35**, 24-25.
24. P. Klán and J. Wirz, *Photochemistry of organic compounds: from concepts to practice*, John Wiley & Sons, 2009.
25. H. Kautsky, *Transactions of the Faraday Society*, 1939, **35**, 216-219.
26. N. J. Turro, *Modern molecular photochemistry*, University science books, 1991.
27. O. L. J. Gijzeman, F. Kaufman and G. Porter, *Journal of the Chemical Society, Faraday Transactions 2: Molecular and Chemical Physics*, 1973, **69**, 708-720.
28. F. J. Santos, C. A. Nieto de Castro, J. H. Dymond, N. K. Dalaouti, M. J. Assael and A. Nagashima, *Journal of physical and chemical reference data*, 2006, **35**, 1-8.
29. G. A. Sommer, L. N. Mataranga-Popa, R. Czerwieniec, T. Hofbeck, H. H. H. Homeier, T. J. J. Müller and H. Yersin, *The Journal of Physical Chemistry Letters*, 2018, **9**, 3692-3697.
30. <https://automeris.io/WebPlotDigitizer>.